Isolation, Characterisation and Software Development for Polymeric Wear Particles from In Vitro Joint Simulators

LAL, SAURABH

Isolation, Characterisation and Software Development for Polymeric Wear Particles from In Vitro Joint Simulators

SAURABH LAL

School of Engineering and Computer Sciences

Durham University

A thesis submitted for the degree of

DOCTOR OF PHILOSOPHY

2015

Abstract

Wear of the Ultra-high molecular weight polyethylene (UHMWPE) articulating against metal in joint replacements is one of the primary reasons for long-term failure of prosthesis due to implant loosening. Amount, size and morphology of wear debris are important factors that affect the clinical performance of a joint implant. Major developments in UHMWPE as an orthopaedic bearing material are radiation crosslinking and recent introduction of vitamin E as an antioxidant. This thesis aims to investigate the size and shape characteristics of UHMWPE wear debris produced by current state-of-the-art noncrosslinked and vitamin E containing highly crosslinked UHMWPE implants in artificial hip, knee and ankle joint articulations.

Current polyethylene wear debris isolation methods were assessed for isolating wear particles from serum based simulator lubricants. The limitations of current isolation methods were incomplete digestion, presence of impurities, bacterial contamination and low reproducibility. Consequently, a novel UHMWPE wear debris isolation method was developed to overcome these limitations. This method successfully isolated UHMWPE wear debris by digesting simulator lubricants using 5M potassium hydroxide and by purifying particles using a two-stage density gradient ultracentrifugation. High-resolution scanning electron microscopy was used to capture digital images of wear debris particles deposited on 15 nm pore size membrane filters.

Two current commercial size analysers Nanosight and Mastersizer were compared to SEM image analysis for characterising UHMWPE wear debris. Large size range and complex shape of wear debris made both Nanosight and Mastersizer unsuitable for complete characterisation of UHMWPE particles. Moreover, no shape analysis was available in both commercial particle analysers. Therefore, SEM image analysis was chosen for particle characterisation. Custom software was developed to automatically analyse SEM images and characterise particles using a range of size and shape descriptors.

The isolation and characterisation methods developed in this study were used to investigate the influence of crosslinking, addition of vitamin E and change in molecular architecture on size and morphology of wear debris. All wear particles analysed in this study were found to be predominantly submicron in size. Crosslinking reduced the size of UHMWPE wear debris for particles generated in knee and multidirectional pin-on-plate. Noncrosslinked direct compression

moulded (DCM) ArCom UHMWPE generated more elongated and fibrillar wear particles. Higher chain mobility and higher elongation to break was believed to be the reason for this particle morphology. Alternatively, highly crosslinked UHMWPE generated less elongated and more compact shaped particles.

Addition of vitamin E by blending, followed by crosslinking and annealing in ECiMA UHMWPE generated more elongated and fibrillar particles in comparison to vitamin E diffused highly crosslinked (E1) UHMWPE in hip. Multidirectional pin-on-plate wear testing of DCM UHMWPE moulded at 175°C and at 145°C generated similar particle size distribution and shapes.

Influence of type of joint articulation on size and morphology of wear particles was investigated by isolating and characterising E1 UHMWPE wear debris produced by ankle, knee, hip and multistation pin-on-plate articulation. E1 wear particles generated by ankle and knee had similar particle size and morphology. Moreover, both ankle and knee generated submicron as well as large micron sized particles. Submicron sized particles were more round, while large particles were elongated and fibrillar. Alternatively, hip generated mostly submicron-sized particles with rounder morphology. Wear particles generated in multidirectional pin-on-plate tester were also mainly submicron in size. However, morphology of these particles was more fibrillar and elongated.

In conclusion: Crosslinking, method of addition of vitamin E, change in processing conditions and type of joint articulation could influence the size and shape characteristics of UHMWPE wear debris.

Table of Contents

List of Illustrations

List of Figures

List of Tables

List of Abbreviations

AR	Aspect Ratio
ArCom	Argon Compressed
ASR	Articular Surface Replacement
ASTM	American Society For Testing And Materials
ATP	Adenosine Triphosphate
CFR	Carbon Fibre-Reinforced
CoCr	Cobalt Chromium Molybdenum Alloy
CrN	Chromium Nitride
DCM	Direct Compression Moulding
DFT	Discrete Fourier Transform
DLC	Diamond Like Carbon
DXA	Dual-Energy X-Ray Absorptiometry
E1	Vitamin E Diffused Highly Crosslinked UHMWPE
ECiMa	Vitamin E Blended Cold Iradiated Mechanically Annealed UHMWPE
ECD	Equivalent Circular Diameter
EDTA	Ethylenediaminetetraacetic Acid
EDX	Energy Dispersive X-Ray
FF	Form Factor
FDA	Food and Drug Administation
FLT3	Fms-related Tyrosine Kinase 3

FTIR	Fourier Transform Infrared Spectroscopy
GUR	Granular UHMWPE Ruhrchemie
GM-CSF	Granulocyte Macrophage Colony-Stimulating Factor
HDPE	High Density Polyethylene
HEPES	Hydroxy Ethyl Piperazine Ethane Sulfonic Acid
HGF	Hepatocyte Growth Factor
IL-1	Interleukin - 1
IL-1β	Interleukin - 1β
IL-6	Interleukin - 6
IL-8	Interleukin - 8
IL-10	Interleukin - 10
IP-10	Interferon Gamma-Induced Protein 10
ISO	International Organization For Standardization
LDPE	Low Density Poly Ethylene
LLDPE	Linear Low Density Polyethylene
MCP-1	Monocyte Chemoattractant Protein-1
MIG	Monokine Induced by Interferon-Gamma
NCS	Newborn Calf Serum
OPG	Osteoprotegrin
OXINIUM	Oxidised Zirconium
PBMNCs	Peripheral Blood Mononuclear Cells
PMMA	Polymethyl Methacrylate
PTFE	Poly Tetra Fluoro Ethylene
PEEK	Polyether Ether Ketone
PGE2	Prostaglandin E2

PIGF	Placenta Growth Factor
PVD	Physical Vapour Deposition
RANK	Receptor Activator Of Nuclear Factor-Kb
RANKL	Receptor Activator Of Nuclear Factor ĸB Ligand
ROI	Region of Interest
RGB	Red Green Blue
SARS	Severe Acute Respiratory Syndrome
SDS	Sodium Dodecyl Sulphate
SEM	Scanning Electron Microscopy
TiN	Titanium Nitrite
TiCN	Titanium Carbon Nitrite
TAR	Total Ankle Replacement
TKR	Total Knee Replacement
THR	Total Hip Replacement
Ti-6AL-4V	Titanium Aluminium Vanadium Alloy
TJR	Total Joint Replacement
TNF- α	Tumour Necrosis Factor - α
UHMWPE	Ultra High Molecular Weight Poly Ethylene
VEGF	Vascular Endothelial Growth Factor
ZTA	Zirconia Toughened Alumina

Declaration

The work in this thesis is based on research carried out at the School of Engineering and Computing Sciences, Durham University, UK. No part of this thesis has been submitted elsewhere for any other degree or qualification and it is all my own work unless referenced to the contrary in the text.

Acknowledgements

I would like to thank many people for their involvement, encouragement and support throughout my PhD.

My sincere gratitude to my principal supervisor Dr. Jun Jie Wu for providing me the opportunity to undertake this PhD and giving me the freedom and encouragement to work on my area of interest. Without her guidance and persistent help, this thesis would not have been completed!

To my co-supervisor Professor Roy Quinlan for offering me lab space and access to equipments in Biology Department and guiding me throughout my experimental work. Without his support and guidance, I would not have been able to conduct the particle isolation experiments at Biology Department.

To my co-supervisor Professor Roger Crouch for offering me valuable time and helping me think critically about my research work.

To Mr Leon Bowen for giving excellent training on SEM and offering continued help with using the equipments at GJ Russell Microscopy Facility. I would also like to thank Dr Budhika Mendis for offering help whenever needed.

To my colleague Miss Elaine Lovelady for being a great friend, and giving me support and encouragement throughout the PhD.

To my other colleagues Georgia Salpingidou, Qian Qian Wang, Martin Stanley and Daniel Giddings for making work enjoyable.

To my parents and brother Sumit Lal for their foundation and support to allow me to get where I am today.

To my girlfriend Xiaojie for always being there for me.

Chapter 1 - **Motivation**

Medical and public health advances in the last 150 years have doubled the lifespan of human beings [1]. Although life-threatening medical conditions have significantly reduced over these years, the need for effective long-term cure of age related diseases such as arthritis, cataract and cardiovascular disease has increased considerably.

Arthritis is an age-associated condition where treatments such as joint replacement surgery are very common and provide excellent relief from severe pain and joint stiffness. At present, severe arthritis in joints such as hip, knee, ankle and shoulder is surgically treated by replacing the diseased joint with a prosthetic joint. However, complications such as implant loosening and joint dislocation are also frequent, which make it necessary for patients to go through revision surgery. Over 6 % of total hip replacements need revision after 5 years and over 12% need revision after 10 years [2]. Knee and ankle replacements have either similar or inferior revision statistics [2]. Moreover, revision surgery is associated with high costs and high risk of failure [3]. Therefore, a lot of effort has gone into the development of longer lasting implants using superior materials and novel designs.

Conventional implant materials such as ultra high molecular weight polyethylene (UHMWPE) and metal have gone through several stages of developments. Moreover, alternative materials such as ceramics, ceramic coatings and composites have shown potential as orthopaedic biomaterials. Although a range of materials and their combinations are available, majority of the artificial joint implants use a combination of UHMWPE articulating against metal due to its predictable performance and reliability.

Wear is considered as one of the major reasons for the long-term failure of a joint prosthesis. Retrieval analysis of failed implants and characterisation of wear debris isolated from periprosthetic tissues have given insights into the *in vivo* wear and biological effects of wear debris. It has been estimated that around 100 million microscopic particles are released every day from the wear of UHMWPE in an artificial hip joint [4]. These particles primarily cause the loss of bone tissue surrounding the implant, known as osteolysis. Advances in the field of immunology and orthopaedic research have established the relationship between osteolysis and the amount, size and

shape of wear particles. Over the last two decades, characterisation of wear debris and investigation of its biological response have become important areas in orthopaedic research.

During the development of novel joint replacements, artificial joint simulators and wear testers are used to evaluate the wear properties of implant materials. Subsequently, wear particles isolated from the test lubricants are characterised for size and morphology to investigate the wear mechanisms and osteolytic potential of wear particles. Major developments in UHMWPE as an orthopaedic bearing material are the crosslinking of UHMWPE to reduce wear and introduction of vitamin E as an antioxidant to improve the oxidative stability. In addition, recent studies have shown added benefits of Vitamin E in reducing inflammation and osteolysis [5], [6]. Although it has been over a decade since vitamin E stabilised UHMWPE was clinically introduced [7] , very limited knowledge is available about the characteristics of wear debris produced by this biomaterial [6].

Therefore, it is crucial to conduct an in-depth comparison and analysis of wear debris produced in all primary joint articulations using conventional as well as latest generation UHMWPE as the bearing materials. This thesis is set out to achieve this goal by intensively investigating the characteristics of UHMWPE debris produced by the artificial wear testing of conventional UHMWPE and the latest generation of highly crosslinked vitamin E stabilised UHMWPE in knee, hip and ankle joints.

Chapter 2 begins with an overview of natural synovial joints, joint replacement surgery, implant materials and tribology of joint articulations. This is followed by a critical investigation of implant wear as the primary mode of clinical failure, influence of particle size and shape on biological response and cellular mechanisms of osteolysis. Finally, the methods of pre-clinical evaluation of wear, isolation of wear debris from simulator lubricants and characterisation of these particles are investigated.

Chapter 3 compares the existing state-of-the-art methods for isolation of UHMWPE wear debris and discusses their limitations, followed by description of a novel method developed for isolation of UHMWPE wear debris from simulator lubricants. A combination of base digestion and density gradient ultracentrifugation was chosen to isolate conventional UHMWPE and latest generation UHMWPE wear debris.

Chapter 4 investigates the particle characterisation methods, advantages and limitations of commercial size analysers and describes the methodology of custom software developed for detailed analysis of UHMWPE wear debris. Finally, the particle characterisation accuracy of existing image analysis software is compared with the custom software.

Chapter 5 describes the size and shape analysis results produced by isolation and characterisation of wear debris generated during joint simulator testing and multidirectional pin-on-plate testing of

conventional and latest generation UHMWPE components. Wear debris generated during early wear and long-term wear were compared for size and morphology.

Chapter 6 begins with a discussion about UHMWPE wear debris isolation and characterisation methods developed during the study. This is followed by an in-depth investigation of the effect of crosslinking, addition of antioxidants, the type of articulation on size and morphology of UHMWPE using results described in Chapter 5 and previous studies from literature. The principal mechanisms responsible for the wear of UHMWPE are also investigated.

Finally, Chapter 7 describes the key findings and discusses the future work.

Chapter 2 - **Literature Review**

2.1 **Introduction**

Over past five decades, arthroplasty has gone through several stages of developments. In 1950's first generation metal-on-metal hip prosthesis were introduced by surgeons such as McKee [8] and Ring [9]. However, these implants suffered from a high number of failures due to early loosening and bearing seizures. High frictional torque was initially thought to be the reason behind the implant loosening [10]. Conversely, later retrieval studies cited manufacturing issues and poor design tolerances as the causes of failure [11].

These early developments were followed by an era of very successful low friction metal -on-UHMWPE hip prosthesis introduced by Sir John Charnley in 1962 [12]. The combination of soft UHMWPE cup liner against hard metal head proved to be a nearly perfect solution for joint replacement surgery until early 1980s when implant loosening, known as ***late aseptic loosening*** became the primary concern for these prosthesis [13]. While the short-term performance of these implants was good, significant amounts of wear debris generated over the long-term use caused an immune reaction followed by osteolysis. Nonetheless, Charnley's low friction arthroplasty based UHMWPE-on-metal is still considered the gold standard for total hip arthroplasty.

During 1970s first generation ceramic such as alumina was introduced as a potential bearing material in Japan [14]. Since alumina is a very hard material, negligible wear was noticed during ceramic-on-ceramic wear testing. However, low toughness was a major concern in first generation ceramics such as alumina because it suffered from chipping and shattering, which was believed to cause a catastrophic joint failure upon a sudden impact.

The concerns over late aseptic loosening in metal-on-UHMWPE motivated researchers revisited metal-on-metal implants. Moreover, the long-term clinical performance of some McKee implants was quite impressive [15], [16]. This started a new era of second-generation metal-on-metal joint prosthesis. Improved designs and better tolerances showed encouraging wear testing results with metal-on-metal showing 10 - 100 times less wear in comparison to metal-on-UHMWPE [7], [17]. FDA approved the use of metal-on-metal implants on patients in 1999 and from late 1990s these implants were widely used in joint replacement surgeries [4]. However, problems with second generation metal-on-metal started cropping up in mid 2000s when complications such as metallosis

and pseudotumors and were reported in patients [18]–[21]. Increased wear due to edge loading was believed to cause these issues. Moreover, metal on metal hip resurfacing implants were found to have high revision rates due to femoral neck fracture and loosening of prosthesis[22]. Consequently, in 2010 Depuy Orthopaedics issued a voluntary recall of their Articular Surface Replacement (ASR) hips implanted since 2003 [23].

While metal on metal implants were gaining popularity in 1990s, a new generation of highly crosslinked UHMWPE was undergoing development with the motive to reduce the amount of wear in polyethylene. In 1998, highly crosslinked UHMWPE was clinically introduced in the market. Although crosslinking significantly improved the wear performance, but new issues such as oxidation and free radical release were also noticed[7].

The long history of failed implants made developers and researchers realize that thorough investigation of the modes of implant failure is one of the most important steps in development of new prosthesis. A number of studies since late 1980s analysed tissues from failed joint arthroplasties and found wear debris along with macrophages and giant cells indicating the biological reaction to these particles. With the scientific evidence gathered in last two decades, it is now believed that implant loosening, which is the biggest reason of clinical failure, is related to the wear and biological activity of wear debris. Moreover, it has been shown by several studies that the osteolytic potential of wear debris is dependent of its amount, size and shape [24], [25] . Therefore, preliminary assessment of wear, wear debris and its biological evaluation has become an important part of the joint implant development process and an essential step before the clinical use of implants in patients. This includes *in vitro* tribological assessment of wear in biomaterials using artificial joint simulators, isolation and characterisation of wear debris generated during the wear testing and biocompatibility testing of wear debris. The current study focuses on the isolation and characterisation of UHMWPE wear debris from a range of joint simulator tests.

Considering the multidisciplinary nature of this field, it is important to have basic knowledge of specific areas of biology, materials and engineering related to joint arthroplasty. Therefore, this chapter will give a brief overview of natural synovial joints, implant materials and basic principles of tribology in the beginning of this literature review. Then, the clinical modes of failure, especially implant failure will be investigated in detail. Afterwards, joint implant simulation, methods of wear debris isolation and characterisation will be investigated.

2.2 Natural Joints

Bones are rigid functional organs in the human body playing a major role in mechanical functions. They facilitate body movement, provide support and protect softer tissues. Three-dimensional manipulations of individual parts or the whole human body are achieved by interaction between bones with the help of skeletal muscles, cartilage, tendons and ligaments. The location of contact between two bones is defined as a joint. Adult human body contains over 200 joints [26]. Synovial joints are freely movable articulations containing synovial fluid. They provide locomotion of limbs by relative movement of one segment of bone past another while keeping the joint stable under load bearing conditions.

A synovial joint consists of several associated structures as shown in Figure 2.1. First, a layer of cartilage called articular cartilage covers the articulating surfaces and provides a smooth low friction. Second characteristic feature in a synovial joint is the joint capsule, which is an envelope to the articulation and provides stability. It consists of inner and outer synovial lining. The articular cavity encapsulated by the lining is known as synovial cavity. It is a highly vascular structure and produces synovial fluid, which is responsible for lubrication of the joint and jointly with articular cartilage it provides a smooth low friction articulation.

The ligament surrounds the capsule and provides additional stability to the joins by connecting one bone to another, while tendon connects the adjacent muscles to the bone. The connective tissue that joins the ends of ligament and tendon to the bone is enthesis. Bursa is a structure that intervenes between tendon and joint, or tendon and bone, and reduces the friction of one component moving over the other. [27]

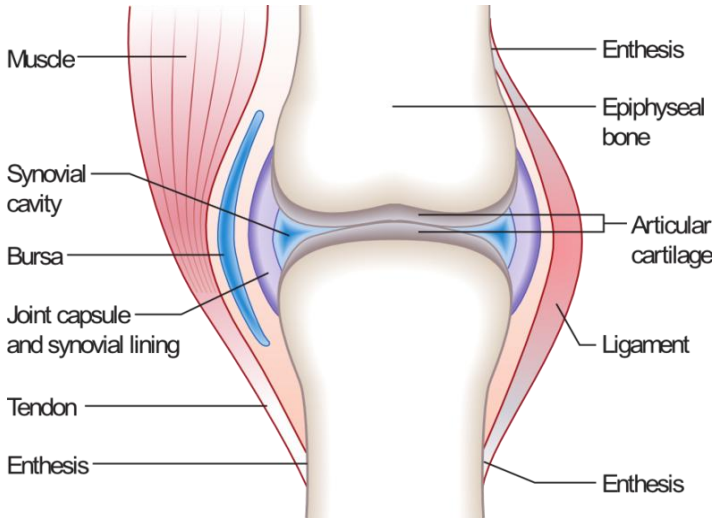

Figure 2.1 Synovial joint and associated structures in the human body

Based on the shape of articulating surface and/or the type of movement, synovial joints are classified into plane joint (sliding motion), hinge joint (uniaxial motion), saddle joint (biaxial motion), condylar joints (biaxial motion), ball and socket (multiaxial motion), pivot joint (uniaxial

rotation around central axis). Table 2.1 shows a list of joints responsible for major load bearing articulations in our body and their movements.

Table 2.1 Review of joints and their movements[28]

Joint	Type of joint	Type of movement
Hip	Ball and socket	Flexion/extension, adduction/abduction, rotation, circumduction
Knee	Bicondylar	Flexion/extension, tibial rotation
Ankle	Hinge	Internal/external axial rotation, dorsiflexion/plantar flexion, inversion/eversion [7]

The hip joint is an articulation between femur and acetabulum of the pelvis in our body. It allows rotation, movement of the upper part of the leg. Joint capsule of hip joint envelops the ball and socket articulation, and extends from the origin of the acetabular labrum to the base of femoral neck. The stability in the natural hip joint is provided by the joint capsule, ligaments and the muscles enfolding the joint [29]. The maximum compressive load through hip joint during a normal gait can be more than three times the body weight [7].

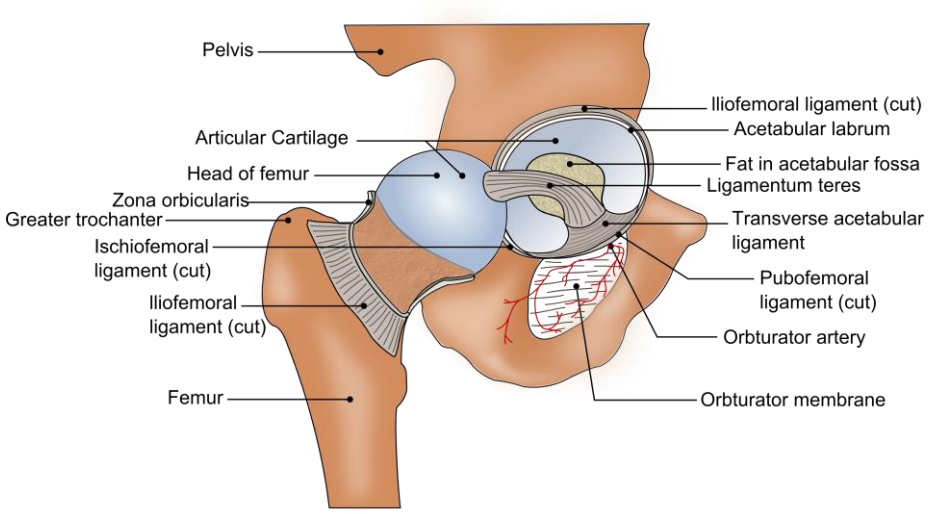

Figure 2.2 Anatomy of the hip joint

The knee joint is a combination of two different joints, the **tibiofemoral** and the **patellofemoral** joint. It allows the movement of lower leg relative to thigh while supporting the body's weight.

The **tibiofemoral** joint is a bicondylar articulation between tibia and femur. The distal end of femur consists of lateral and medial condyles, which are covered with smooth articular cartilage. The proximal end of tibia is covered with hard fibrous structure called menisci. Anterior and posterior cruciate ligaments provide vital stability to the knee by restricting its movement. Moreover, lateral collateral ligament and medial collateral ligament provide further stability to the joint.

The **patellofemoral** joint is composed of the patella, a flat bone located in front of the knee joint, and the patellar groove in front of the femur. The sliding movement of patella over the patellar

groove is facilitated by the presence of articular cartilage on both surfaces. The patellar tendon and quadriceps tendon ensure the structural stability of patella. The maximum compressive load through knee joint during a normal gait can be more than three times the body weight. Moreover, during activities such as standing up from a chair or squatting, the forces on the knee joint could be up to 7.6 times body weight [7].

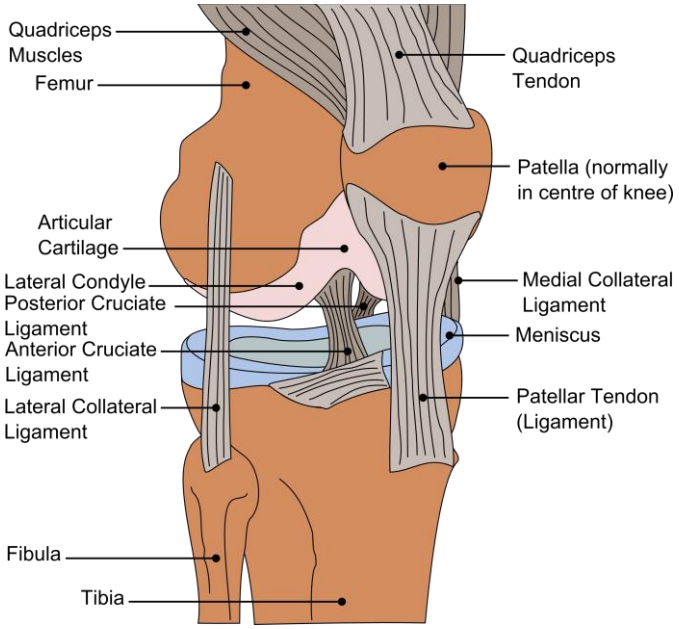

Figure 2.3 Anatomy of the knee joint

The ankle joint is a hinged joint formed by the lower end of tibia, lower end of fibula and talus. The distal end of tibia articulates against the proximal end of talus. Both articulating surfaces are covered by articular cartilage. A small portion of fibula also articulates against talus. The joint is held stable by tibiofibular, talofibular and calcaneofibular ligaments as shown in Figure 2.4. The maximum compressive load through ankle joint during a normal gait can be more than five times the body weight [7].

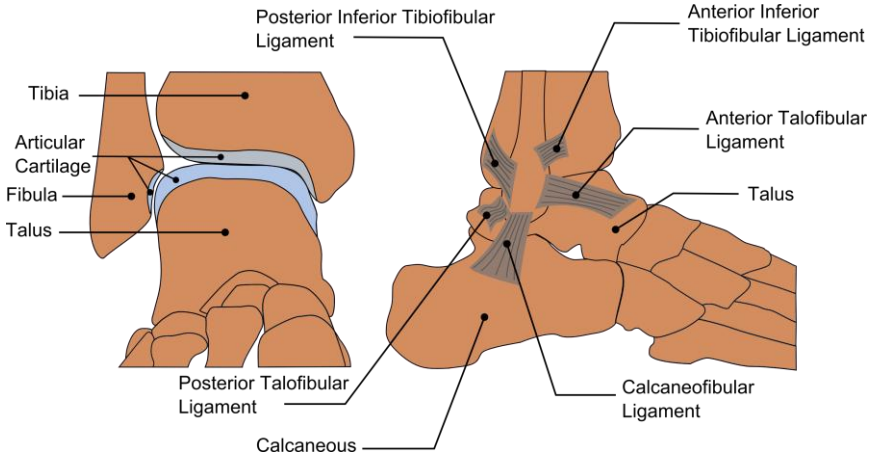

Figure 2.4 Anatomy of the ankle joint

2.2.1 **Arthritis and Joint Replacements**

Healthy joints can maintain low friction and low wear, even under loading conditions of several times a person's body weight during physical activities such as walking, running and climbing. Conversely, diseased joints may suffer from severe pain and disability in movement. Arthritis is the condition where inflammation of one or more joints causes pain, swelling and stiffness of joints. When degradation of articular cartilage and subchondoral bone leads to inflammation of bone tissue, it is known as osteoarthritis. In UK over 6 million people suffer from this condition in one or both knees and over 650,000 people in one or both hips. Moreover, radiological evidence of hip osteoarthritis has been found in over 1.5 million people [30].

The primary surgical method of treatment for osteoarthritis is the replacement of an arthritic joint surface with prosthesis, also known as Arthroplasty. It involves removal of the joint capsule, damaged articular cartilage and surrounding bone tissue, followed by shaping of the bone tissue to accommodate the implants and subsequently fixing the implants in place.

Figure 2.5 shows the above-mentioned steps in a total knee replacement surgery. A standard knee joint replacement involves removal of damaged articular cartilage from condyles, followed by reshaping of femur to accommodate the femoral component. Then, the proximal end of tibia is cut to accommodate a tibial tray. Finally, above components are fixed to the bone and a tibial insert placed in between both components.

The total joint replacement (TJR) in a hip involves removal of damaged cartilage from acetabulum and reshaping of acetabulum to accommodate an acetabular component. The femoral head is removed and the bone is shaped to accommodate a femoral stem inside the femur. A femoral head component is either part of stem or connected to stem by a modular taper junction. A liner goes in between head and acetabular component and facilitates ball and socket articulation of the hip.

The implants are fixed to the bone by using bone cement or by uncemented biological fixation. The bone cement is composed of polymethyl methacrylate (PMMA) polymer and the bonding of cement to the bone is achieved by interlocking of cement mantle with porous bone structure at cement-bone interface. The implant-cement interface is either bonded by using roughened implant surface or held in place by local stresses in an implant with smooth surface [29]. Additionally, the geometry of stem in a femoral component of hip implant is important to optimally load the cement mantle [31].

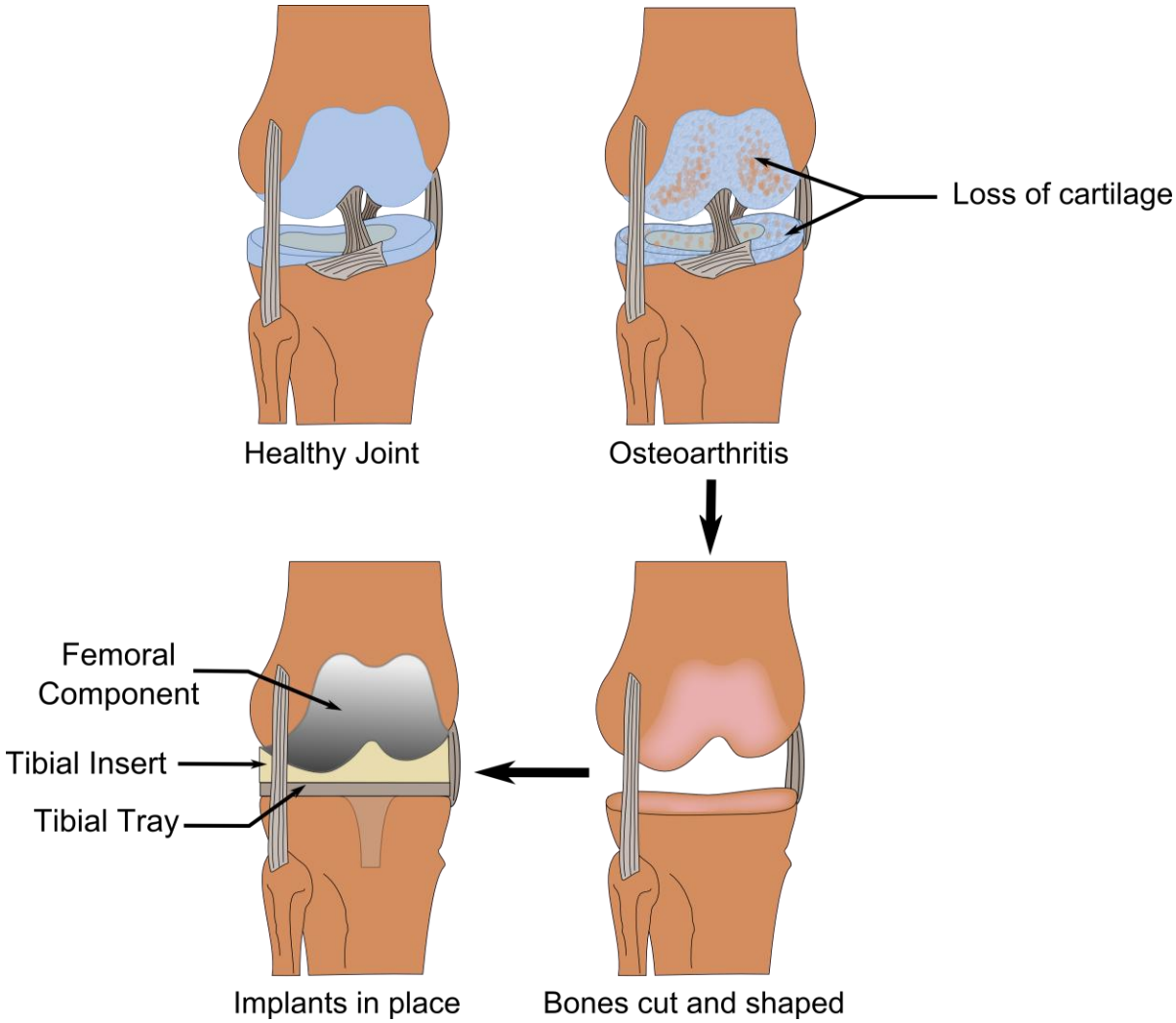

Figure 2.5 Illustration of a healthy knee (top left), osteoarthritic knee showing loss of cartilage (top right). Bones are cut and shaped, followed by fixation of the implants during the total knee replacement surgery (bottom).

The mechanical loosening of stem in cemented fixations of hip implants led to the development of cementless methods of fixation. Porous metal surfaces are used in cementless fixations to promote bone ingrowth. Moreover, the implant surface is coated with materials such as hydroxyapatite to promote osseointegration [29][32]. For knee replacement surgery the cemented fixation of tibial tray and femoral component is considered as the gold standard, while for hip replacement both cemented or cementless fixations are commonly used [29].

2.3 Implant materials

Appropriate selection of materials for manufacturing implants is one of the most crucial steps in the development of a joint prosthesis. Materials are selected primarily based on their biocompatibility, appropriate balance of mechanical and physical properties necessary for its functioning as a specific part of the implant , and good manufacturability [33].

Three major types of materials, which have been used for manufacturing implants, are metals, polymers and ceramics. These are described in sections below followed by other alternative bearing materials.

2.3.1 Polymers

Polymers are most commonly used biomaterials for arthroplasty. They are usually used as soft bearing material articulating against hard metal counterpart. A ***polymer*** is a molecule consisting of many (*poly*-) parts (-*mer*) linked together by chemical covalent bonds.

During the initial phases of development of joint prosthesis, PTFE was used as the bearing material. However, it was eventually replaced by UHMWPE in 1962 due to occurrence of severe wear when using PTFE [7]. Sir John Charnley introduced UHMWPE articulating against metal femoral head in 1962 and demonstrated clinically low wear rates [34]. Even today Charnely's low friction arthroplasty based UHMWPE-on-metal combination is considered as a gold standard for THR [7].

UHMWPE is a unique polymer with outstanding physical and mechanical properties. Most notable are its chemical inertness, lubricity, impact resistance, and abrasion resistance. These characteristics of UHMWPE have been exploited since the 1950s in a wide range of industrial applications. Over 90% of the UHMWPE produced in the world is used by industry [7]. Figure 2.6 shows chemical structures of ethylene and polyethylene molecules.

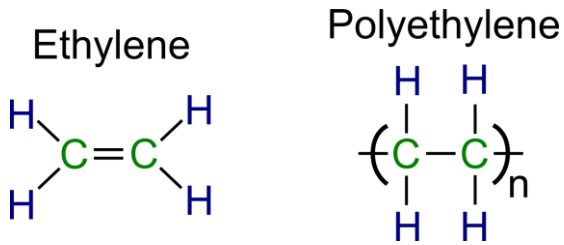

Figure 2.6 Chemical Structures of Ethylene and Polyethylene, n=number of repeating units

Several kinds of polyethylene can be synthesised depending on molecular length of chains and their architecture. These include low density poly ethylene (LDPE), linear low density polyethylene (LLDPE), high density polyethylene (HDPE) and ultra high molecular weight polyethylene (UHMWPE) [7].

A UHMWPE molecule is polyethylene composed of a large number of ethylene units joined by covalent bonding. Typically a UHMWPE molecule can consist of as many as 200,000 ethylene repeating units [7]. Moreover, it can have a crystalline as well as amorphous structure as shown in Figure 2.7.

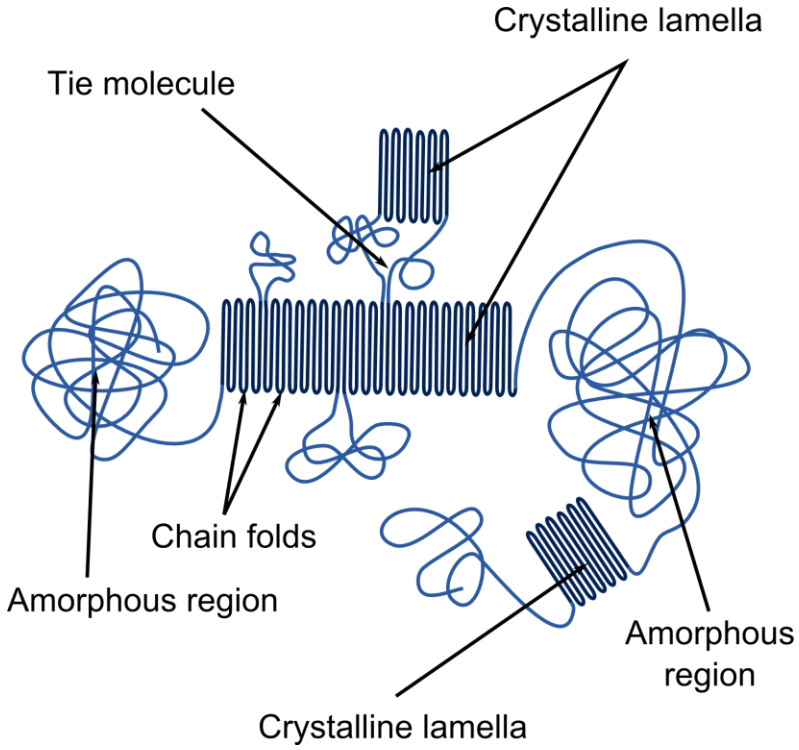

Figure 2.7 Crystalline and amorphous structure of UHMWPE. Amorphous region with randomly oriented chains, crystalline lalmellae with chain folds and tie molecules are shown by the arrows.

Although chemically UHMWPE is made up of only carbon and hydrogen, its structure and properties strongly depend on its processing. For this reason processing and manufacturing of UHMWPE bearing components is discussed in a separate section below.

Processing and manufacturing of UHMWPE implant components

During manufacturing UHMWPE, resin is prepared from UHMWPE powder of about 140µm in size. These resins are made by Ticona and at present come with trade names of GUR1020 and GUR1050. GUR stands for "Granular," "UHMWPE," and "Ruhrchemie". One key finding is that these resins are characterised by a fine network of submicron fibrils, interconnected to the micron sized spheroids [7].

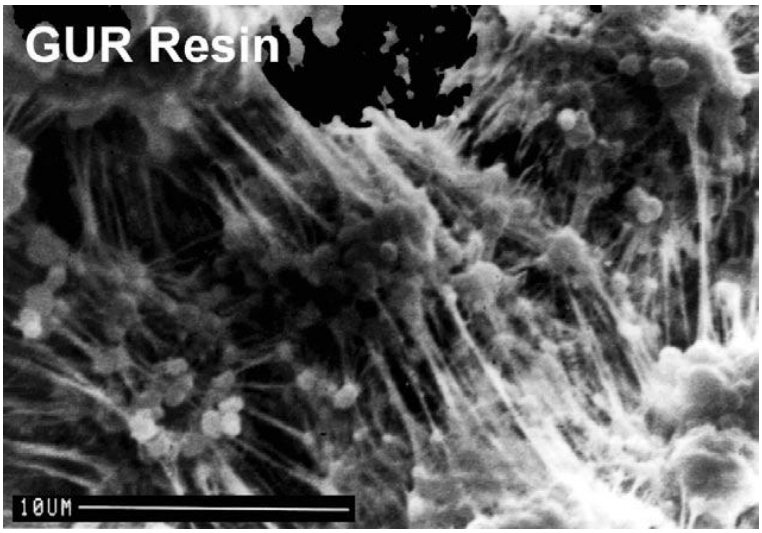

Figure 2.8 Submicron fibrils connected to micron sized spheroids in GUR resins[1]

The consolidation of the UHMWPE resin, to produce prosthesis components, is carried out by either compression moulding or ram extrusion. Thermoplastic processing techniques such as injection moulding, blow moulding cannot be used for UHMWPE since it does not flow like LDPE, LLDPE and HDPE.

Consolidation of resin requires a combination of pressure and temperature for a certain period to facilitate intermingling of UHMWPE molecular chains. However, consolidated structure has been found to retain the memory of its previous structure [35], [36]. Hot isostatic pressing is a two-step compression moulding technique used to improve the consolidation of UHMWPE. It consists of an initial cold isostatic pressing of resin, to remove most of the air, followed by hot isostatic pressing in an inert environment. ArCom™ polyethylene is a hot isostatic pressed UHMWPE manufactured by Biomet® Ltd. Argon is used as an inert gas during the hot isostatic pressing of ArCom.

Hot isostatic pressing could also be carried out as direct compression moulding (DCM) using individual moulds of finished components. The advantage of this method is nearly isotropic mixing along with an extremely smooth surface. DCM ArCom™ has been considered as a gold standard bearing material due to its low wear rates compared to conventional UHMWPE [7].

After consolidation, the UHMWPE components are machined and sterilised using irradiation or gas sterilisation. Until 1990s 25 to 40 kGy gamma radiation was used to sterilise the components, followed by packing them using air permeable packaging. In mid 1990s when clinical studies cited wearing of implant components as the primary reason for failure, it generated an interest into the effects of sterilisation methods on UHMWPE components. Although gamma sterilization had an added benefit of crosslinking the polymer chains, it also was responsible for long-term oxidation and degradation of material. An increase in material density and crystallinity was noticed due to

[1] S. M. Kurtz, UHMWPE Biomaterials Handbook. 2009
[2] S. Affatato, Wear of orthopaedic implants and artificial joints. 2012

the oxidation of UHMWPE in components that were packed using air permeable packaging [37]–[39]. Moreover, progressive embrittlement resulted in loss of mechanical properties [40]–[42].

In order to overcome this issue barrier packaging has been used after gamma sterilisation. However, the shelf life of these packaging is still debatable. Alternate methods such as gas sterilisation using ethylene oxide or gas plasma are now used in several contemporary UHMWPE implant components [7].

2.3.1.1.1 First generation of highly crosslinked UHMWPE

The benefits of crosslinking on wear resistance of UHMWPE were noticed as early as 1960s in Japan [43] and were clinically tested in 1970s in Japan and South Africa [7]. However, crosslinking was not widely accepted as a potential method for improving wear properties of UHMWPE until late 1990s. In 1998, orthopaedic manufacturers introduced the first generation of highly crosslinked UHMWPE. Ionizing radiation (gamma rays or electrons) dose of 50- 100 kGy have been used to cross-link the UHMWPE fibres [7].

Cross-linking has benefits of reduction in wear, however it reduces ductility, fatigue resistance and fracture resistance [44]. Moreover, irradiation releases free radicals from UHMWPE. To overcome these limitations, a thermal treatment step is performed after irradiation. The melt transition temperature of UHMWPE is around 137°C. Annealing is the heat treatment of material below the melt transition temperature; whereas re-melting is heat treatment above melt transition temperature. Crystallinity after thermal treatment is shown to be around 60% for annealed and 43% for re-melted UHMWPE [7]. Choice of an appropriate thermal treatment is a crucial step, because it can have an effect on oxidative stability, crystallinity, yield strength and ultimate tensile strength. Moreover, the choice between annealing or re-melting is a debated issue due to merits and limitations of both. Nonetheless highly crosslinked has been successful for both treatments. Over the last decade very few reports of fatigue failure such as rim fracture have been reported for highly crosslinked UHMWPE [45], [46].

Recent retrieved acetabular liner studies indicated no benefits in terms of resistance to surface damage in comparison to conventional UHMWPE [47], [48]. Moreover, highly crosslinked UHMWPE is believed to have long-term limitations due to oxidation such as decreased fatigue strength and delamination.

2.3.1.1.2 Second generation of highly crosslinked UHMWPE

With an increasing demand of large diameter hip prosthesis and long lasting implants for younger patients, there has been an introduction of second generation highly crosslinked UHMWPE. This is the latest generation of UHMWPE and has been developed with an aim to improve long-term oxidative stability and fatigue strength of highly crosslinked UHMWPE. Introduction of antioxidants such as α-tocopherol (Vitamin E) has been used to improve the oxidative stability.

Vitamin E is one of the most abundant antioxidants present in human body, with an ability to effectively minimise free-radical damage[49]. In second generation highly crosslinked UHMWPE, vitamin E is incorporated by two methods.

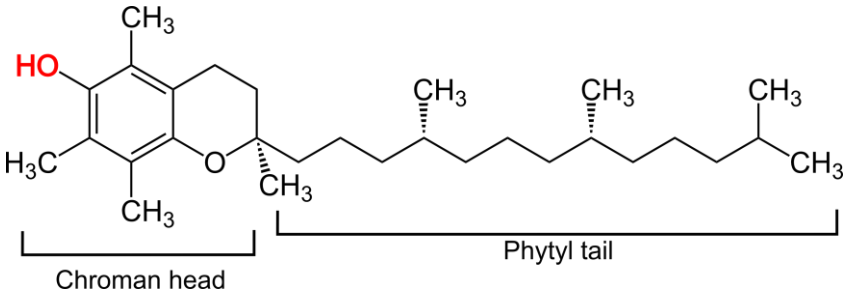

Figure 2.9 Chemical structure of α-tocopherol, showing chroman head and phytyl tail. The OH group highlighted in red donates the hydrogen atom to the radical and inhibits the subsequent oxidative chain breaking reactions.

First method is to blend Vitamin E into the resin prior to consolidation. Then, after consolidation, ionising radiation is used to cross-link the blend. However, studies have shown that crosslinking efficiency is reduced in the presence of vitamin E. Moreover, vitamin E concentrations of 0.3% or above were not recommended due to reduced crosslinking [50]–[52]. Since 2009, Ticona has started producing vitamin E blended resins, which come under trade names of GUR 1020-E and GUR 1050-E [12]. ECiMa™ is a vitamin E blended direct compression moulded polyethylene made by Corin.

Second method is to diffuse vitamin E into UHMWPE after irradiation. The aim of this method is to have enough vitamin E diffused into the surface to avoid any long-term oxidation. Moreover, this method does not affect the extent of crosslinking. In 2007, Biomet introduced vitamin E diffused highly crosslinked UHMWPE, named E1™.

2.3.1.1.3 Polyether ether ketone (PEEK)

PEEK and its composites have been explored as potential orthopaedic implant materials since 1980's [53]. The ability to match the mechanical properties to bone by addition of reinforcing materials such as carbon fibre made PEEK an attractive biomaterial for making implant components for bone-implant interface. For instance, Carbon fibre-reinforced PEEK (CFR PEEK) was used in making isoelastic stem in the Bradley hip prosthesis to reduce bone resorption due to stress shielding [53]. Other desirable properties of PEEK include high chemical resistance and good biocompatibility [54].

The wear characteristics of PEEK are found to be dependent factors such as extent of fibre reinforcement, surface roughness, temperature, sliding speed and contact pressure [53]. As a bearing material, CFR PEEK composites have been explored for hip and knee implants since 1990s. CFR PEEK has demonstrated low wear characteristics under specific conditions using multidirectional pin-on-plate tester [55], [56]. More recently, hip simulator testing of zirconia

toughened alumina against CFR PEEK showed low wear rates. However, friction was found to be relatively high for CFR PEEK [57]. Although CFR PEEK has shown potential, more investigation is needed to demonstrate its suitability as an orthopaedic bearing material.

2.3.2 **Metals**

Metals have been used as a biomaterial for manufacturing joint implants due to their suitable mechanical properties such as high fracture resistance and high strength. The first metal hip prosthesis was made by Wiles in 1938. Stainless steel was used to make femoral component and other components. As joint replacement surgery became popular, researchers started looking into alternative corrosion resistant, biocompatible and wear resistant alloys [33]. In 1950s McKee and Ring developed metal-on-metal joint prosthesis from cast cobalt chromium molybdenum (CoCr) alloy [7]. CoCr had excellent wear strength, good corrosion resistance, and high fatigue strength, and high modulus [33]. In late 1970s, titanium alloys gained popularity due to their excellent biocompatibility, corrosion resistance and lower modulus. Yet, titanium had low wear resistance, which made it unusable as a bearing material. Nonetheless, titanium has been important biomaterial due to above-mentioned characteristics and is used to make implant components such as femoral modular stem or acetabular shell. Titanium aluminium vanadium alloys (Ti-6AL-4V), initially developed for aerospace applications, are most commonly used for orthopaedic applications [33]. Cobalt nickel alloys have also been explored as potential orthopaedic biomaterials, but have not gained much popularity due to the metal allergy associated with nickel. Concerns over metal corrosion and biocompatibility limit the use to only the above metals/alloys.

CoCr based metal alloys are most commonly used bearing materials. As mentioned previously in Section 2.3.1 CoCr femoral head articulating against UHMWPE is considered as the gold standard bearing combination for THR. Moreover, CoCr articulating against CoCr is considered as the gold standard metal on metal bearing combination for TJR [7].

The manufacturing of CoCr has changed considerably since its first use as an implant material. In earlier days, investment casting was primarily used to manufacture implants. Whereas, contemporary implants are made by forging wrought CoCr. Wrought CoCr is more commonly used due to its superior hardness, yield strength and ultimate tensile strength. Moreover, it is shown to contain more uniform carbide structure [4]. Modern CoCr implants are either made from high carbon (>0.2% C) or low carbon (<0.05% C). Moreover, no significant difference in wear rates was shown between high carbon and low carbon metal on metal hip implants [58], [59].

In view of the metallic particles complications *in vivo*, recent innovation in orthopaedic implant research has been the introduction of hard ceramic-like coatings on metals. This combines high mechanical strength of metals with high wear resistance of ceramics. Physical vapour deposition (PVD) has been mostly used to deposit these coatings on metal substrate. Diamond like carbon (DLC) coating has been extensively investigated as potential implant bearing coating materials.

Studies have shown high hardness and extremely low wear rates of DLC coatings [60]. Other coatings include chromium nitride(CrN), chromium carbon nitride(CrCN), titanium nitride(TiN) and titanium carbon nitride(TiCN) [61]. Recently silicon nitride coating has also shown potential due to its high strength, low friction, low wear rates and dissolvable wear particles[62].

However, excellent coating adhesion can be challenging and possibility of delamination and catastrophic removal of coatings could potentially expose the substrate metal surface.

2.3.3 Ceramics

Ceramic are non-metallic inorganic solids prepared by heating and subsequent cooling. Alumina ceramics have been used since 1970s in THR [14], [63]. Alumina has a hardness of 1800-2000 (Vickers hardness, 0.1N), and is a hydrophilic material which gives it excellent wear properties with almost negligible wear and low friction articulation [7]. However, it is also a brittle material and has low fracture strength. Therefore, it has the possibility of chipping or shattering into small pieces under high mechanical impulse and has limited design options. Over last 35 years, alumina has been constantly improved by reducing its grain size, which has gradually improved its fracture strength. Another ceramic material that emerged in 1980s as an orthopaedic bearing material was zirconia due to its higher fracture toughness (8 $MPa.m^{1/2}$) than alumina (4 $MPa.m^{1/2}$)and a hardness of 1250 (Vickers hardness, 0.1N) [7]. However, zirconia is a metastable ceramic and can undergo phase transformation under certain temperature, humidity and stress conditions. This can cause roughening of bearing surface, which is clearly undesirable for a bearing material. In order to overcome this issue yttria or magnesia is added to stabilise zirconia. In 2000 unusually large number of fractures were reported in zirconia implants made by St. Gobain Desmarquest due to a change in manufacturing process, which lead to recall of implants and eventual suspension of zirconia ceramics [7]. For ceramic-on-ceramic implants, squeaking of hip bearings could be an issue reported by patients [7].

A new nanocomposite material was developed by CeramTec in 2000, called Zirconia-Toughened Alumina (ZTA). The advantages of this composite were high hardness, high strength and good fracture toughness. Commercially ZTA by CeramTec is known as BIOLOX Delta [7].

More recently, materials such as oxidised zirconium (OXINIUM) and silicon nitride have been introduced as implant materials. OXINIUM is a proprietary bearing material by Smith & Nephew Orthopaedics. It is prepared by oxidising the outer surface of zirconia to form zirconium oxide layer, which is about 5µm thick. This overcomes the stability issues with zirconia. However, oxidised zirconium layer could be dislocated as suggested by retrieval studies[64]. Silicon nitride is a latest generation ceramic with properties such as high modulus, high fracture toughness, good biocompatibility and dissolvable wear debris. Recently Amedica (Utah, USA) has commercialised silicon nitride for hip bearing applications.

2.4 Lubrication, Friction and Wear

Lubrication, friction and wear are important factors in joint arthroplasty. This section will briefly describe each of these factors.

2.4.1 Lubrication

Lubrication is the process by which the relative motion between surfaces is assisted by the presence of a lubricant. Depending on the thickness of the lubricant film and contact scenario, lubrication can be broadly divided into boundary lubrication and fluid film lubrication. Boundary lubrication occurs when a considerable amount of surface asperities interact with each other during the relative movement of surfaces as shown in Figure 2.10.

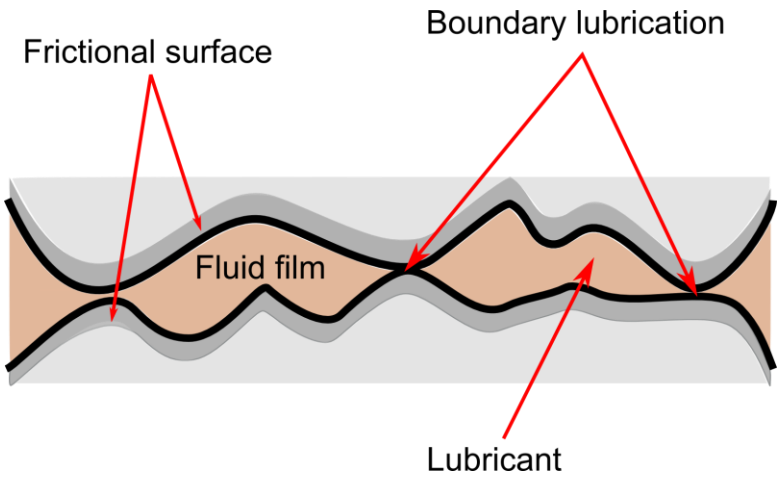

Figure 2.10 Schematic diagram showing boundary lubrication and fluid film lubrication between two surfaces sliding against each other in the presence of a lubricant.

Alternatively, fluid film lubrication occurs when surface asperities are separated by the presence of a lubricant film. Moreover, fluid film lubrication can undergo by three means. These are squeeze film, hydrodynamic and elastohydrodynamic lubrication.

Squeeze film occurs in the absence of tangential motion, primarily due to the squeezing out of fluid while viscosity is opposing the fluid movement. This creates pressure in the fluid, which opposes the load and allows fluid film lubrication for a certain period of time [65].

Hydrodynamic lubrication occurs in the presence of a thick film of fluid preventing the articulating surfaces to touch each other. The pressure in the film supports the load.

Elastohydrodynamic lubrication is similar to hydrodynamic lubrication. However, the pressure within the film is large enough to deform the articulating surface. This causes an increase in thickness of the film. Low elastic modulus materials can undergo electro hydrodynamic lubrication. Moreover, separation between the articulating surfaces could be achieved even at lower viscosities depending on the mechanical strength of articulating material.

Natural human synovial joints primarily undergo fluid film lubrication, which keeps the bearing surfaces (articular cartilage) separated by the fluid, creating smooth and low wear articulation. For natural synovial joints such as hip and knee, the squeeze film lubrication is believed to be the main lubrication state during the stance phase, causing a low friction movement of the joints [66]. In addition boundary lubrication is believed to occur briefly at the end of stance phase [66].

Artificial joints follow a mixed lubrication regime where boundary lubrication occurs along with fluid film lubrication. In boundary lubrication, a physically adsorbed protein film is formed on top of the bearing surfaces. The repulsion between the two films carries majority of the load. Surface asperities higher than the film make contact with opposite surface and cause wear. Therefore, during articulation of an implant, fluid film occurs at areas where asperities are small and fluid pressure plays a major role in supporting the load, while boundary lubrication occurs in areas where asperities at high enough to contact the counter surface and cause wear.

2.4.2 **Friction**

When two surfaces move against each other the shear stresses developed by the movement causes resistance known as friction. Basic principles of friction were explained by Amontons and Coulomb [66], [67]. It was stated that the frictional force is independent of an apparent area of contact and the sliding velocity. Moreover, the frictional force (F) is proportional to the normal load (L) and μ is coefficient of friction.

$$F = \mu L$$

For a surface, the apparent area of the contact is the area of contact surface dimensions. However, the frictional forces are only applicable at the actual area of contact, which is the contact area of asperities on the surfaces. In dry friction, each individual touching asperity contributes to the total frictional force. Moreover, very small contact area at each asperity causes high stresses, which could cause either removal of asperities due to abrasive wear or deformation of asperities causing adhesive wear (Detailed discussion in Section 2.4.3.1).

In the presence of a lubricant, interaction of asperities as well as the lubricant contributes to the overall frictional force between surfaces moving against each other. As mentioned in previous section, natural joints primarily undergo fluid film lubrication with synovial fluid as the lubricant, which prevents the asperities of articular surfaces to interact with each other. Consequently, a very low coefficient of friction has been observed in natural joints, which facilitates easy movement with low frictional torque [66]. In osteoarthritic joints, it has been believed that friction increases with the degradation of cartilage and change in rheological properties of synovial fluid. However, a study by Caligaris *et al.* demonstrated no significant change in coefficient of friction with progression of osteoarthritis in joints [68].

Similar to natural joints, the articulation of artificial joints needs to be in a low friction environment in order to minimise the frictional torque. For soft polymeric materials articulating against hard metals or ceramics, the viscoelastic behaviour of polymers causes formation of a transfer film of polymer at the countersurface. This transfer film is believed reduce friction during articulation. However, a noticeable difference was noticed between coefficient of friction under dry and serum lubricated conditions, indicating the influence of serum lubricant in further reducing the coefficient of friction as shown in Table 2.2.

For metal articulating against metal, the two articulating surfaces are composed of same material. Therefore, there is greater tendency for the surface asperities to fuse together and cause an increase in friction.

Table 2.2 A comparison between coefficient of friction for natural and artificial bearings under lubricated or dry conditions.

Bearing Type	Coefficient of friction	Lubrication
Cartilage- on-cartilage	0.001 - 0.03 [66]	Synovial fluid
UHMWPE-on-metal(CoCr)	0.05 - 0.10 [29]	Serum
UHMWPE-on-metal(CoCr)	0.15 [69]	Dry
Metal-on-metal (CoCr)	0.25 [29]	Serum

When articulating surfaces are not flat, friction factor is used to define frictional forces. For hip joints, friction factor (f) could be calculated from normal load (L), radius of head (R) and frictional torque (T) using following equation:

$$f = \frac{T}{LR}$$

Frictional torque in a hip is measured experimentally using friction hip simulator with a vertical dynamic load and a horizontal angular velocity. Typical friction factor values of different bearing combinations measured by previous studies are shown in Table 2.3.

Table 2.3 Friction factors for bearing combinations in the presence of bovine serum for artificial hip joints (adapted from [70]**)**

Bearing Combinations	Friction factor
UHMWPE-on-metal	0.06 - 0.08
UHMWPE-on-ceramic	0.04 - 0.08
Metal-on-metal	0.10 - 0.20
Ceramic-on-ceramic	0.002 - 0.07
Ceramic-on-metal	0.002 - 0.07

2.4.3 **Wear**

Wear is the removal of material from two or more surfaces articulating under a constant or variable load. In total joint arthroplasty, wear of implants is found to be one of the most important factors responsible for success of prosthesis. Different bearing combinations lead to different rates of wear as shown in Table 2.4.

Table 2.4 Volumetric wear rates and linear wear rates for different bearing combinations in hip implants (adapted from [70]).

Bearing Combinations	*In vitro* volumetric wear rate[a] (mm^3 / million cycles)	*In vivo* linear wear rate[b] (μm / year)
UHMWPE-on-metal(CoCr)	30 - 100	100 - 300
UHMWPE-on-ceramic	15 - 50	50 - 150
Cross-linked UHMWPE	5 - 10	15 - 30
Metal-on-metal (CoCr)	0.10 - 10	2 - 20
Ceramic-on-ceramic	0.02 - 1	1 - 20
Ceramic-on-metal	0.02 - 1	Not available

a. Volumetric wear rate was calculated by gravimetric analysis of implants tested in a hip simulator. **b**. Linear wear rate was measured by analysing radiographic images of hip implants in patients.

As mentioned previously, conventional UHMWPE articulating against metal has been the most commonly used bearing combination in total joint arthroplasty. Although this soft-on-hard combination provides low friction (Discussed in section 2.4.2), the wear of UHMWPE is several times in comparison to other current bearing combinations. On the other hand, first generation highly crosslinked UHMWPE exhibits wear rates comparable to metal-on-metal hip implants. Ceramic materials such as alumina and ZTA undergo lowest amount of wear. These differences in the amount of wear produced by different bearing combinations depend on the type and extent of fundamental mechanisms by which wear occurs during articulation. Next section will discuss these wear mechanisms. More details about wear specific to joint implants is discussed in Section 2.5.1

2.4.3.1 **Wear Mechanisms**

The fundamental processes by which two or more materials in relative motion undergo wear are known as wear mechanisms. There are four principle mechanisms of wear: adhesion, abrasion, fatigue, and corrosion wear. Other important wear mechanisms such as fretting wear and delamination originate from one or more of the above.

Adhesive wear

Adhesive wear occurs when temporary adhesion between surfaces articulating under a mechanical load leads to extraction of material from one or both surfaces [71]. In this type of wear, it is necessary for two surfaces to be in contact with each other. Therefore, adhesion mostly occurs in absence of a contaminant layer. Moreover, in this wear the asperities on a surface penetrate into the opposite surface causing plastic deformation and formation of micro junctions. Then, the sliding motion causes breaking of the junction either at the junction itself or at its base [29].

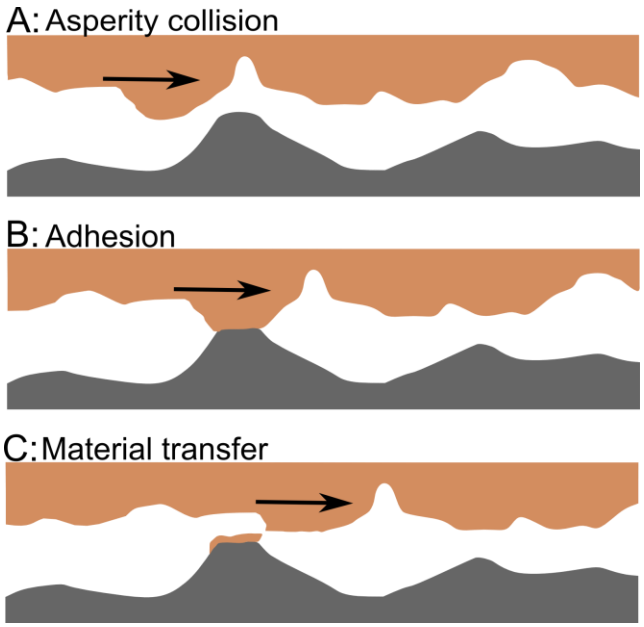

Figure 2.11 Schematic diagram showing three stages of adhesive wear. A) The collision of asperities on both surfaces. B) Adhesion (fusion) of asperities. C) Transfer of material from one surface to another.

Adhesive wear occurs often in softer materials such as polyethylene, where adhesion at a relatively harder counter surface such as CoCr is followed by stretching of polymer material resulting in formation of fibrillar particles. Previous studies have noticed formation of pits and voids on the articulating surface due to adhesive wear [72]. Moreover, this wear typically exhibits high volumetric wear and higher coefficients of friction between articulating surfaces.

Adhesive wear has also been found in retrieved metal and ceramic implants [29]. In metal-on-metal articulations adhesive wear is facilitated by fusion of material on both surface during the adhesion step (Figure 2.11) because the material used for both surfaces is similar.

Abrasive wear

When sliding motion between two surfaces of different hardness causes the removal of material from softer surface, it is known as abrasive wear. Furthermore, when one surface cuts material from another surface, it is known as two-body abrasive wear, while wear due to free moving particles between two surfaces is known as three body wear. The three mechanisms of abrasive

wear are ploughing, cutting and fragmentation. Ploughing occurs when grooves are formed on the surface of the softer material due to material displacement. The ridges formed are precursor to the material removal by other mechanisms such as cutting where material is directly removed from surface. Fragmentation is a wear mechanism that occurs in brittle materials. It is initiated with an indentation by an asperity of a counter surface, followed by crack propagation and removal of a fragment from surface.

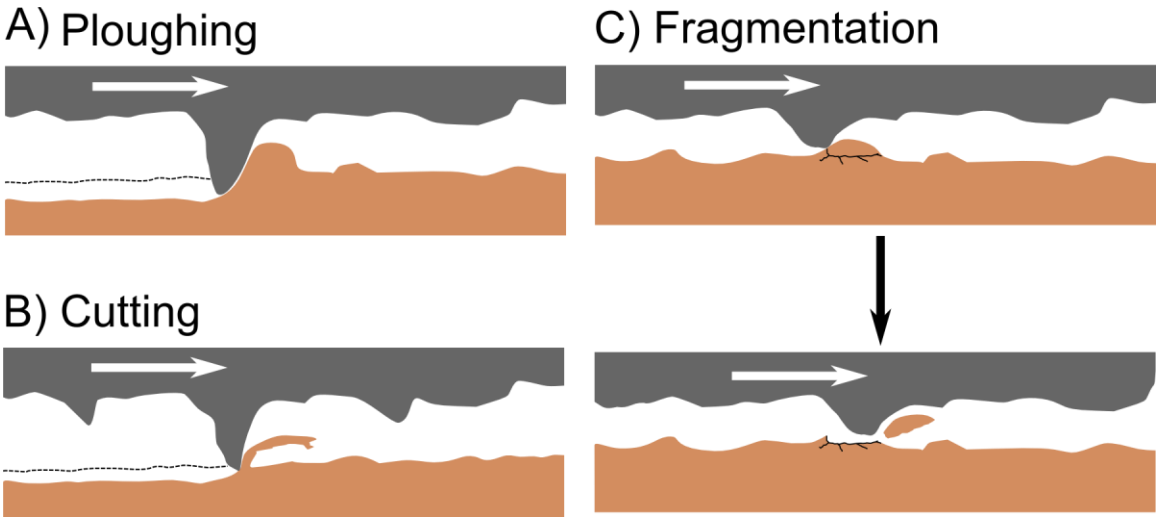

Figure 2.12 Schematic diagram showing three types of abrasive wear. A) Ploughing of soft material by a hard asperity. B) Cutting of soft material by a hard and sharp asperity. C) Fragmentation of a brittle material by a hard asperity.

In orthopaedic implants, abrasive wear is caused by rough metal components sliding against UHMWPE. Moreover, bone cement particles cause third body wear and damage the articulating surface. Surface roughness and the presence of third body particles are important indicators of abrasive wear [29].

Fatigue wear

When cyclic loading on a material causes accumulation of stresses that exceed intrinsic fatigue strength, wear particles are released from surface. This is known as fatigue wear. When individual asperities on the surface undergo fatigue wear, it is known as microscopic fatigue wear. Moreover, the cyclic loads are tangential in this type of wear as shown in Figure 2.13. Rolling of one body on another body can cause vertical cyclic loading which causes macroscopic fatigue wear. Since the cyclic loading can occur over a large area, accumulation of dislocations, formation of micro-cracks, nucleation of voids can spread rapidly to nearby areas, which could lead to catastrophic failure (Figure 2.13). Material defects serve as good sites for crack initiation and are avoided whenever possible.

In the past four decades it has been demonstrated that fatigue wear is predominantly responsible for joint implant failure, particularly for implants using polyethylene as a bearing material [29][71]. Polyethylene being a weaker material is more prone to fatigue wear. Material defects and plastic

flow parameters such as yield stress and ultimate tensile stress can greatly influence the wear properties of polyethylene. Moreover, studies have found the negative effect of ɣ-radiation and oxidative aging on fatigue threshold and crack propagation resistance[73].

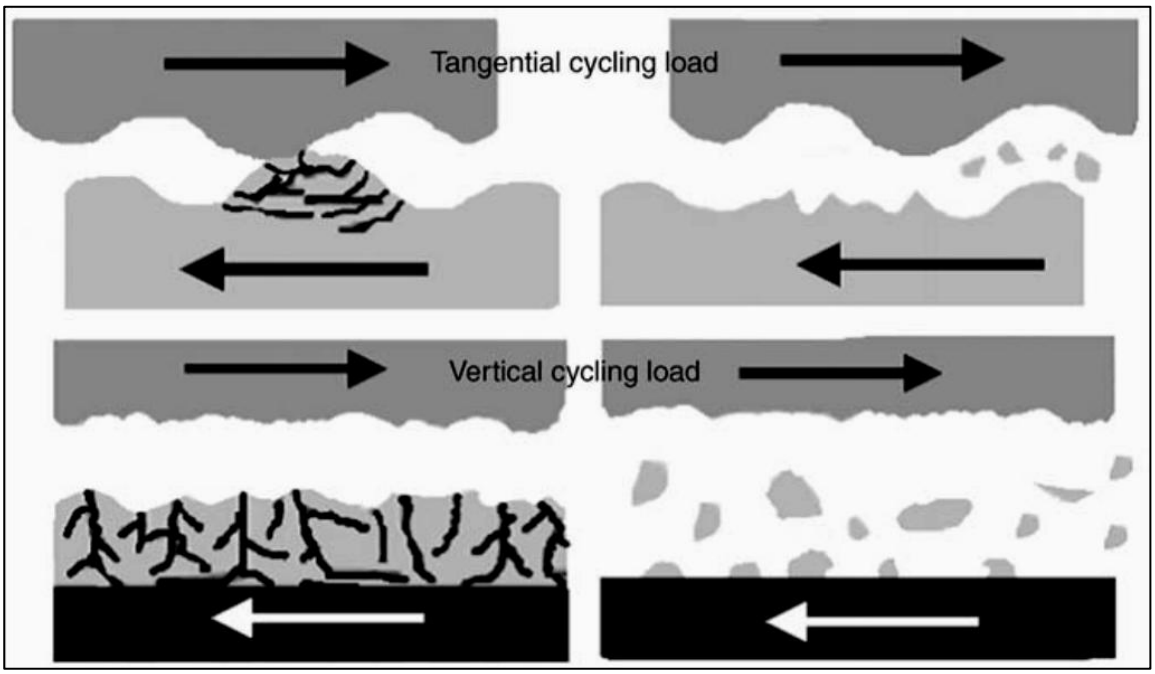

Figure 2.13 Schematic diagram showing fatigue wear by tangential and vertical cyclic loading[2]. Formation of surface cracks is shown on the left and release of wear particles due to wear of the asperities or whole surface is shown on the right.

For metals such as cobalt-chrome and titanium, the fatigue strength depends on their microstructure, surface and corrosion properties. Post-processing treatments have been found to improve fatigue strength of metals[73].

Corrosive wear

Combined degradation of a material by corrosion as well as wear is known as corrosive wear. Corrosion is the chemical transformation of a material at a surface due to the interaction with its surroundings. Most common form of corrosion in implants is the formation of metal oxides at wearing surface. As these oxides have different shear strengths in comparison to the bulk material, they tend to separate from surface causing generation of small cavities or pits, also known as *pitting*.

Small-amplitude oscillatory movement between two surfaces in combination with corrosion of material can cause another form of corrosive wear known as *fretting corrosion*. The primary cause of this wear is the micro-motion of misaligned couplings such as bolted joints or modular taper junctions. The mechanisms by which fretting wear occurs are abrasion, adhesion by oxidation products, plastic deformation and corrosion/oxidation of the surrounding area.

[2] S. Affatato, Wear of orthopaedic implants and artificial joints. 2012

Polymeric materials such as UHMWPE do not undergo corrosion. Therefore, corrosive wear is believed to be limited to metal components of joint implants.

2.5 Clinical Failure of Joint Replacements

In recent years, the need of revision surgery due to implant failure has created a big financial burden on government healthcare services and patients in many countries [3]. Although, implants are not supposed to last forever, in a successful scenario they are expected to at least last the lifetime of a patient. Clinical success of an implant is found to be dependent on two factors.

First is the robustness of initial implant fixation within few months after surgery. Inadequate fixation at the implant-cement interface is considered the reason behind rapid loosening of implants. Extensive de-bonding may cause generation of cement and implant debris due to micro-motion at implant-cement interface [74]. Moreover, this could initiate an osteolytic response to the debris and could potentially cause implant loosening [71]. Though successful initial fixation of an implant is a crucial step, it is not considered the major cause of failure of the implants.

Second factor of clinical success of prosthesis is its long-term clinical performance. Long-term failure is generally a combination of several mechanisms, however dominant mechanisms are observed to occur more often. Now this section will discuss the clinical factors affecting long-term performance of joint replacements in more detail.

2.5.1 Implant wear

Wear could be defined as the removal or displacement of one or more materials during the mechanical interaction between two surfaces. It is found to be one of the most important factors affecting the success of a joint prosthesis. Implant wear can have two major implications. Firstly, the physical wear can change an implants shape or can compromise its integrity due to excessive wear. Secondly, the material removed during wear could trigger an adverse biological reaction in the body, which could cause loosening of an implant and eventual failure.

2.5.1.1 Modes of Wear in Total Joint Replacement

Wear in artificial joint implant can occur at various sites and due to a number of prosthesis design problems and material limitations. McKellop identified a number of "modes" of wear, which describe the damage to implants and sources of wear debris generated in total joint arthroplasty. These modes are listed in Table 2.5.

Table 2.5 Modes of wear in total joint replacement (adapted from [71]**)**

Mode	Description	Examples
I	Primary articulating surface against primary articulating surface	• Femoral head against acetabular PE liner in THR • Distal femoral component against patellar and tibial PE insert in TKR • Distal tibial component against talar PE component in TAR
II	Primary articulating surface against secondary implant surface	• Femoral head against metal shell of acetabular component • Distal femoral component against metal backing of patellar component
III	Third-body wear	• Metal beads or macroscopic metal fragments from porous implants causing wear of femoral head and PE acetabular component in THR • Fragments of bone cement embedded in PE acetabular component in THR • Fragments of bone cement embedded in PE tibial insert in TKR • Fragments of bone cement embedded in PE talar insert in TAR
IV	Secondary implant surface against secondary implant surface	• Fretting at the interface of modular components • Fretting between screw and tibial tray in TKR • Fretting between screw and acetabular shell in THR • Femoral neck impingement against the acetabular metal rim • Wear between abnormally loose PE acetabular insert and acetabular shell • Wear between abnormally loose PE insert and the tibial tray in TKR • Abrasion between unbonded femoral stem and the neighbouring cement mantle

Mode I is the primary mode of wear in implants and is expected to occur during normal joint articulation. Moreover, it is responsible for generation of majority of wear debris.

Mode II is unintended wear of articulating surface against secondary implant surfaces that were not designed to articulate. For example, in a dislocated hip prosthesis femoral had could slide against metal acetabular shell causing wear of primary articulating surface. Such wear of ceramic head femoral heads against metal acetabular shell was observed by Bal *et al.* [75]. In a TKR the tibial component could also wear against metal backing of patellar component [71].

Mode III is the acceleration of wear in Mode A scenario by the presence of third body particles such as metal fragments or bone cement particles. These particles can scratch the articulating surfaces or can embed into softer materials such as polyethylene, which can eventually cause increase in wear [71].

Mode IV is the unintended wear of secondary implant surfaces against each other. For example, implant malposition could cause the impingement at the neck of femoral stem against acetabular metal shell in a THR, resulting in the release of wear debris. Another instance of this wear is abrasion between rough femoral stem and bone cement mantle, which causes generation of bone cement wear debris.

2.5.1.2 Modes of Surface Damage in UHMWPE

The damage to the TJR is caused by a combination of mechanisms. Hood *et al.* categorised the modes of surface damage in UHMWPE components of TKR [76]. Although these modes of surface damage were published in 1983, they have stayed relevant for last 3 decades. Seven modes of surface damage are following (adapted from [7]):

Pitting: These are surface defects of 2 to 3 mm in diameter and 1 to 2 mm depth, and are believed to be caused by fatigue wear. Wear debris generated by this damage mode is millimetre-sized and is considered to be too large to provoke an osteolytic response.

Embedded debris: Third body particles such as metal fragments or bone cement debris get embedded into polyethylene surface. This debris can cause third body wear (Mode III wear of TJR, section 2.5.1.1) and can scratch the metallic counter surface as well, causing further abrasive wear of polyethylene.

Scratching: Linear scratches produced at the articulating surface due to ploughing of the material by asperities on metallic counter surface, or by third body particles. It is caused due to abrasive wear.

Delamination: It involves removal of large sheets of polyethylene from the articulating surface due to a severe form of fatigue wear. Moreover, if the component is too thin, delamination could cause catastrophic damage to implant.

Surface deformation or creep: An irreversible change to surface geometry of polymer by plastic deformation. There is no wear debris generated in this mode of damage.

Burnishing: Burnishing is characterised by the polishing of the surface by adhesive/abrasive wear of the polymer. It is one of the important modes of damage because the wear debris produced by burnishing falls into biologically active size range. More detail about size dependence of biological response can be found in next section.

Abrasion: Shredding of the polymer from the bearing surface is characterised as abrasion. It is caused due to abrasive wear.

2.5.1.3 Wear in UHMWPE-on-metal implants and its Biological Effects

Wear and biological activity of UHMWPE as an implant bearing are interdependent and closely related topics, and therefore will be discussed together in this section.

When metal-on-polyethylene THR implants were developed in 1960s, an implant with low-friction and low wear rates was considered as an ideal candidate for THR. As these requirements were met by metal-on-UHMWPE hip implants by exhibiting low friction characteristics and wear rates less than 0.25mm/year, popularity and demand of total hip arthroplasty increased considerably in next two decades [34], [77]. Moreover, development of knee, ankle and shoulder prosthesis also occurred during these years. However, limited survivorship of THRs using metal-on-UHMWPE became apparent when majority of implants lasted to a maximum of 25 years [78]. These implants failed in the absence of any infection or mechanical failure, primarily due to the loosening of implants because of the bone loss (osteolysis) and inflammatory reaction in the surrounding tissues. Consequently, in late 1970s researchers analysed the tissues from failed implants and found large concentration of macrophages and voids formed from dissolution of PMMA particles during processing of the tissue [78].

In 1980s, PMMA debris released from bone cement was believed to be the main reason for osteolysis and this condition was termed as "cement disease". This led to development of cementless prosthesis in 1980s. But, this change in implant fixation couldn't solve the problem of osteolysis and led to an additional issue of biological reaction to metal debris released from stem-bone interface in a number of implants [79]–[81]. Moreover, metal debris was not always found in the retrieved tissues. A constant presence macrophages with UHMWPE wear debris in the regions of bone loss around both loose and adequately fixed implants led to the assumption that polymeric wear debris had a significant role in implant loosening [82], [83]. Several studies in early 1990s used histology in combination with polarised light microscopy to identify the location and characteristics of UHMWPE particles in tissues. Particles smaller than 5 microns were observed inside the macrophages and larger particles were observed to be surrounded by multi-nucleated giant cells [78]. Yet, the limited resolution of optical microscopes made it impossible to identify

any submicron particles. This led to an interest in isolation of particles from tissues in order to accurately characterise the wear debris.

In mid-1990s a number of studies demonstrated that UHMWPE wear particles isolated by digestion of peri-implant membranes in failed hip joint prosthesis were predominantly submicron in size [84]–[88]. Therefore, characterisation of particles using light microscopy was clearly insufficient. Moreover, these wear particles were isolated from interfacial membranes that surrounded the implant, and therefore gave an indication of ***Mode I*** abrasive and adhesive wear [71]. Hirakawa *et al.* isolated particles from failed hip implants with evidence of femoral neck impingement against acetabulum rim (***Mode IV*** abrasive and fatigue wear) and found a greater number of particles in interfacial membranes. This increase in wear was possibly due to an increase in ***Mode III*** wear of UHMWPE in the presence of third body metal particles. Another study by Schmalzried *et al.* compared polyethylene wear debris released from failed TKRs to wear debris released from failed THRs. Particles released in hip were found to be mostly submicron in size (similar to other studies), whereas particles released in knee were mostly between 2 - 20μm in size, indicating fatigue as the dominant wear mechanism in knee. Moreover, polarised light microscopy showed plump macrophages with birefringent cytoplasms, possibly due to the presence of submicron wear debris in tissues retrieved from hip. On the other hand, tissues retrieved from knee showed presence of giant cells surrounding large wear particles and few macrophages [89].

In 1997, Kobayashi *et al.* isolated and characterised UHMWPE particles from tissues at the areas with osteolysis and without osteolysis. A statistically significant difference and osteolysis was found in tissues with number of particles in excess of $1x10^{10}$ per gram of tissue [90]. In the same year Fisher *et al.* developed a method to quantify wear debris generated *in vivo* in terms of frequency distribution as well as mass distribution, which was applied by Tipper *et al.* to characterise wear debris from tissues of failed Charnley prosthesis [91]. Majority of particles were found to be 0.1 - 0.5μm in this study. However, large particles (size greater than 10μm) were also found in the form of fibrils, shards and platelets and these particles were accounted for a small fraction of total number of particles, but a large fraction of the mass of debris.

Richards *et al.* observed nanometre sized particles in failed Charnley THR hip periprosthetic tissues. The smallest particle identified was 30nm in diameter and majority of particles were in 0.1 to 1 μm size range. Particles in 1 to 10 μm size range represented highest fraction of wear volume, with 35% to 98% of total wear volume occupied by these particles [25].

The dissemination of polyethylene wear particles in periprosthetic tissue and other parts of the body has been studied by a few research groups. Urban *et al.* identified polyethylene and metal wear particles in lymph nodes, liver and spleen. Moreover, the majority of these particles were submicron in size [92]. Another study by Elfick *et al.* found the ability of the wear debris to disseminate away from point of origin to be inversely proportional to their size. Recently, Pokorny

et al. calculated the number of UHMWPE particles in different periprosthetic zones of a hip joint and found a variation in number of wear particles at each zone for different patients. Moreover, majority of particles were found in acetabular zone III and femoral zone 7 [93] (corresponding to the radiological zones of Gruen and DeLee, see Appendix IV).

2.5.1.3.1 UHMWPE wear debris comparison between different joint articulations

Several studies in literature have compared UHMWPE wear debris retrieved from failed hip implants to failed knee implants. Schmalzried *et al.* found majority of hip and knee wear debris to be smaller than 1µm. In addition, hip generated smaller particles in greater numbers, while knee generated larger particles in greater numbers. Moreover, a larger number of flakes and shreds were found in knee, while a larger number of fibrils were found in hip. The number of beads and granules were similar for both hip and knee [89]. Hirakawa *et al.* compared wear debris from failed THRs and TKRs and found a larger range of wear particles produced in knee in comparison to hip, while Kobayashi *et al.* found no difference significant in size of wear debris. Tipper *et al.* characterised polyethylene debris from early failure knee (<10 years) and early failure hip (< 10 years) implants and found similar size and aspect ratio for both knee and hip [94]. Later stage failure in hip showed significant difference in size and shape. Aspect ratio was shown to be higher in these particles due to their fibrillar morphology [94]. Another study by Tipper *et al.* compared wear debris produced during in knee and hip simulator testing of moderately crosslinked UHMWPE and found majority of wear debris generated in hip below 0.1 micron, while majority of wear debris produced in knee was in 0.1 - 1 µm size range.

Very few studies have compared wear debris from other articulations such as ankle and shoulder. Mabrey *et al.* compared size and morphology of UHMWPE knee, hip and shoulder wear debris from tissues obtained during revision surgery. Wear particles generated in hip were smaller in size compared to knee and shoulder. Moreover, hip wear particles were found to be more round, while knee and shoulder particles were found to have higher aspect ratio and elongation [95]. Another study by Kobayashi compared wear debris isolated from synovial fluid of well-functioning total ankle replacements and posterior stabilised total knee replacements. Ankle was found to produce wear debris with a mean size 0.81µm, while knee wear debris had a mean size of 0.78µm. Moreover, aspect ratio of ankle wear debris was about 1.57, whereas aspect ratio of knee wear debris was found to be about 2.30.

2.5.1.3.2 Wear and biological response of metal in UHMWPE-on-metal implants

UHMWPE undergoes majority of wear in UHMWPE-on-metal implants due to ***Mode I*** wear of softer UHMWPE against hard metal counter surface. However, metal components of the implant could also wear significantly in certain situations. Improper implant fixation could cause wear of metal components against bone or bone cement causing the release of metal debris (***Mode IV*** wear). In addition, one or more of: metal debris, bone and bone cement debris could cause third body abrasive wear of primary articulating metal surface (***Mode III*** wear). A number of studies

have observed an increase in roughness of metal counterparts in failed UHMWPE-on-metal prosthesis due to a combination of ***Mode III*** and ***Mode I*** wear [96]–[99]. This increase in roughness further accelerates the wear of UHMWPE components. Moreover, extensive wear of UHMWPE components could cause ***Mode II*** wear between primary articulating metal surface and secondary metal backing surface [71].

As discussed in Section 2.3.2 (page 16), CoCr and titanium are the most commonly used metals in joint implants. A number of studies have shown the adverse effects of wear debris in metal-on-metal implants. These primarily include metallosis, pseudotumors, and osteolysis. Metallosis is associated with blackening of tissues surrounding the implants due to excessive production of metal wear debris [100]. Pseudotumors are believed to be caused by metal hypersensitivity in patients [101]. In addition, the wear particles generated by metal implants were found to be nanoscale in size and disseminated to lymph nodes, liver, bone marrow and spleen [102].

Since late 1980s pseudotumors were found in a few patients due to improper implant fixation and extensive wear of metal components [103], [104]. With improvements in implant fixation methods, only a few incidences of clinical failure due to metal wear debris were observed in UHMWPE-on-metal prosthesis. Specifically, these incidences included loosening of implants, dislodgement of modular components and fracture of metal components [105]. More recently, a few studies showed occurrence of pseudotumors in well-fixed implants [106], [107]. Metal wear debris and ions produced by fretting and corrosion at modular junctions was believed to be the reason behind this adverse reaction [104], [106].

2.5.2 Other modes of clinical failure

Although implant wear is the primary mode of clinical failure of joint implants, other modes of failure cannot be ignored. These include dislocation, infection, inappropriate mechanical loading or stress-shielding.

Dislocation

Dislocation is an impingement of the femoral neck against acetabular shell followed by dislodgment of the femoral head from its acetabular shell. It is a condition which can occur in the initial stages of implant fixation as well as in later stages.

Dislocation has been extensively studied over last 30 years, and is mainly due to the design limitations of the implants. Early Charnley designs were prone to impingement in a seated position, which was corrected by reducing the femoral neck diameter [12]. Moreover, it was suggested by McKee and Farrar that large diameter bearings can reduce chances of dislocation by increasing the range of motion [108]. Still Charnley's low friction arthroplasty design with 28mm femoral head articulating against UHMWPE liner was a popular choice for manufacturers until 1990s when large bearings started to gain popularity. Moreover, in mid-1970s Bousquet *et al.* introduced a new dual

mobility concept for hip prosthesis. These implants combined Charnley's concept of a smaller head articulating against UHMWPE liner with McKee's concept of larger diameter bearing by making a dual articulation implant. Primary articulation was the femoral head articulating against polyethylene liner. Secondary articulation was engaged at large angles where instead of neck impingement polyethylene liner articulated against outer acetabular shell [109].

Clinical treatment of dislocation are changing/correcting the position of implant, replacement of loose components, revision of acetabular component, increasing the size of head and liner and using constrained or elevated liners [110].

Infection

Failure of an implant due to infection is found in nearly 1% to 5% of joint replacement surgeries. In addition, it is more common in knee replacement than hip, and is more likely to occur in revision surgeries than primary joint replacements [71]. Factors that contribute the risk of an infection are operating room condition, duration and complexity of surgery, host bone and soft tissue quality etc. Pathogens such as Staphylococcus epidermidis can readily attach to orthopaedic materials such as titanium, cobalt-chrome, PMMA and UHMWPE and create a protective environment to resist inflammatory response of the host [71], [111]. Infection is usually indicated by joint pain, redness, swelling and bone loss surrounding the implant. Ill defined bone loss surrounding the implant is one of the key radiographic indicators of an infection [71].

Stress-Shielding

After the joint replacement surgery, the mechanical load distribution throughout the joint is significantly changed in the patient. This may cause "stress-shielding" and subsequent re-modelling of the proximal bone tissue. Engh *et al.* used dual-energy x-ray absorptiometry (DXA) to calculate the periprosthetic bone density and found bone loss ranging from 7% to 52%. Moreover, the greatest bone loss occurred close to lesser trochanter. It was also noticed that patients with a low proximal bone density had the greatest bone resorption over time[112]. It is often found that bone resorption due to stress-shielding stabilises after two years. However, surgeons still try to preserve as much periprosthetic bone as possible [71].

2.6 Biological response to wear particles

2.6.1 Influence of particle size and shape on biological response

The biological response to wear debris released from the wear of implants involves interaction of cells such as neutrophils and macrophages with wear particles. The primary function of these cells is to clear pathogens, unwanted cells or cellular debris, and foreign materials such as chemicals, drugs, pollen by internalisation and subsequent degradation.

In immunology, foreign particles, antigens and other debris ingested by phagocytes are often termed as cargo. The size of the cargo has been found to be an important factor in deciding the cellular internalisation pathway and inflammatory response by macrophages [113]. Therefore, the size of endocytic vesicle formed during internalisation is also directly or indirectly influenced by the size of the cargo. Based on size of the endocytic vesicles, endocytosis is broadly divided into macroscale endocytosis and microscale endocytosis. A summary of primary endocytic mechanisms along with their size, morphology and cargo examples are shown in Table 2.6.

Table 2.6 A summary of endocytic mechanisms and their characteristics such as size, morphology and examples of cargo. (Table adapted from [113] and endocytic mechanism figures adapted from [114])

Endocytic Mechanism	Phagocytosis	Macropinocytosis	Clathrin-mediated	Caveolin-mediated	IL-2Rβ mediated
	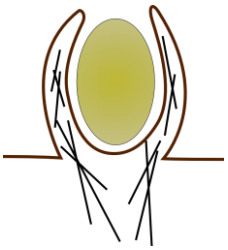			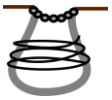	
Size	500nm or above	0.2 – 10μm	150 – 200nm	≈120nm	50 – 100nm
Morphology[1]	Cargo dependent	Ligand-dependent	Vesicular	Flask shaped	Vesicular
Examples of Cargo	Bacteria Apoptotic cells	Fluid (under specific stimuli), Specific bacteria and viruses	Ebola, SARS and few other viruses	Albumin, Cholera toxin, Tetanus toxin	IL-2Rβ ɣ cytokine receptor

1. Morphology mentioned here is endocytic vesicle morphology, not particle morphology.

Macroscale endocytosis includes internalisation mechanisms such as phagocytosis and macropinocytosis (cell drinking). Both of these mechanisms share common features such as slow kinetics and dependence on dynamic actin cytoskeleton to gain motility for ingesting particles. Actin is an intracellular ATP-binding protein essential for motility in cells [115]. Schematic diagrams of both mechanisms show actin cytoskeleton as straight black lines inside the membrane protrusions as shown in Table 2.6.

Phagocytosis is an endocytic mechanism used by macrophages to internalise large particles (size above 500nm). Underhill *et al.* divided the phagocytosis into five major steps of tasting, feeling, swallowing and digesting as shown in Figure 2.14. The first step of phagocytosis is the chemically identification (tasting) of the cargo. This is followed by getting information about overall size and morphology (feeling). Consequently, the cargo is ingested and is enclosed in a phagosome (swallowing). After the maturation of phagosome the cargo is broken down in lysosome (digesting).

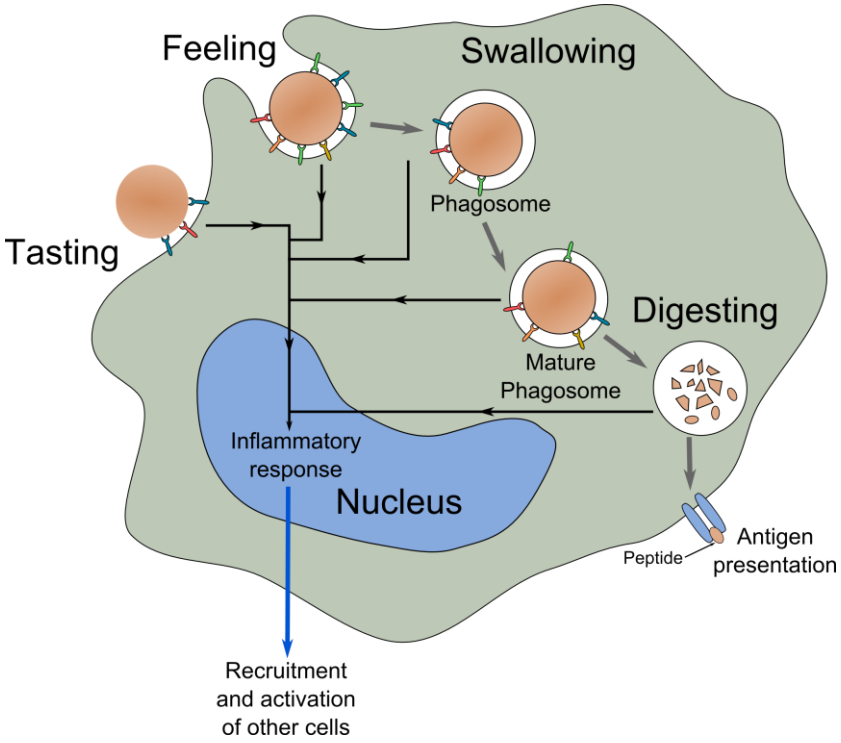

Figure 2.14 Information processing during tasting, feeling, swallowing and digesting stages of phagocytosis. Black lines and arrows indicate signalling within the cell during phagocytosis. Grey arrows indicate progression of phagocytosis process. Blue arrow indicates signalling for recruitment of other cells.(Figure adapted from [116])

Size and shape of the cargo are important factors during tasting and feeling stages of phagocytosis. Doshi *et al.* [117] compared spherical, ellipsoidal and rod-like particles and demonstrated that particles with longest dimension similar to rod shaped bacteria, i.e. 2 – 3 μm were readily phagocytised by macrophages. Moreover, Champion *et al.* [118]demonstrated that engulfing or spreading behaviour of macrophages was dependent on orientation and shape of particles as shown in Figure 2.15.

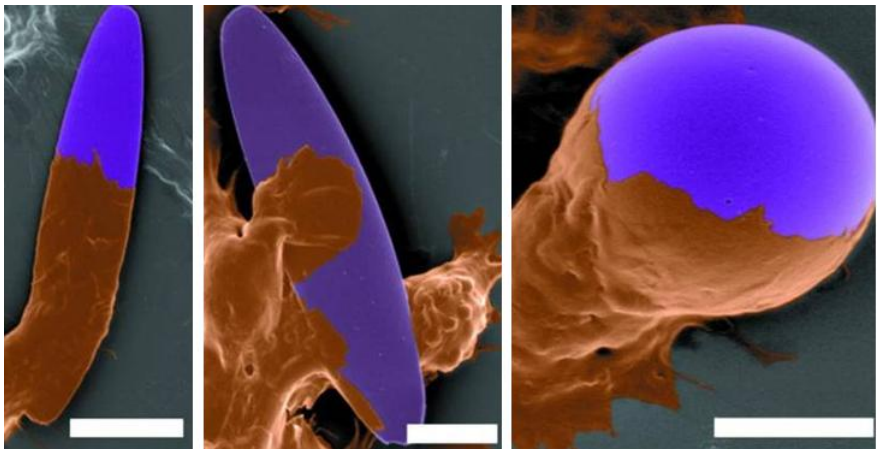

A) **B)** **C)**

Figure 2.15 Scanning electron micrographs of phagocytic cells ingesting particles at different orientations. Particles are coloured in purple and cells are coloured in brown. A) Cells engulfing majority of particle down the length. Scale = 10 µm. B) Cells in contact with the flat surface and spreading on particle. Scale = 5µm. C) Cells engulfing a spherical particle. Scale = 5µm. (Image adapted from Champion et al.[118]).

When phagocytes attempt to internalise particles but the large size or certain shape of the particle obstructs the internalisation process, it is known as frustrated phagocytosis. Studies have found that elevated levels of pro-inflammatory cytokines in macrophages undergoing frustrated phagocytosis [116]. Moreover, macrophages have been observed to fuse together to form multi-nucleated giant cells in order to internalise large particles. Additionally, it was found by Cannon et al. that phagocytic capacity of macrophages was dependent on available membrane for engulfing particles [119].

On the other hand, after successful internalisation of particles, phagocytes undergo the swallowing and digesting stages of phagocytosis. Biological particles such as cellular debris, viruses and bacteria undergo degradation by hydrolytic enzymes followed by the presentation of antigen peptides on cell surface as shown in Figure 2.14. However, synthetic particles such as UHMWPE wear debris are resistant to hydrolytic enzymes. Consequently, these particles remain undigested inside macrophages.

Histological analysis of wear debris, primarily released into the periprosthetic tissues, has revealed the internalisation of wear debris by macrophages and giant cells in these tissues (Section 2.5.1.3). Moreover, studies using polarised light microscopy have showed plump macrophages with birefringent cytoplasms. Majority of UHMWPE particles smaller than 10µm have been found to be internalised by macrophages, while giant cells have been observed to internalise particles with size larger than 10µm [89].

A few studies investigated the effect of large UHMWPE particle shapes on biological reaction to wear debris. It is believed that these particles would most likely have been internalised by phagocytosis. Yang *et al.* used a murine air pouch model to compare inflammatory response of

large micron sized globular and elongated UHMWPE particles. Elongated particles released higher levels of inflammatory cytokines in comparison to globular particles [120].

Macropinocytosis or 'Cell drinking' is a process by which cells engulf relatively large amount of surrounding liquid in comparison to their own volume. This process involves ruffling of plasma membrane, which traps the liquid. As the ruffles collapse back and fuse into plasma membranes, macropinosomes are formed. The particles trapped in liquid are ingested in this manner and finally broken down in lysosomes by hydrolytic enzymes [113], [116]. Previous studies have observed that membrane ruffling during macropinocytosis occurs in a number of ways (Figure 2.16) and could be activated by specific viruses to enter the cells [121]. Moreover, particles smaller than certain size or with specific shapes could only be able to enter the membrane ruffles as shown in Figure 2.17. This was demonstrated by a decrease in particle internalisation when macrophages were swollen osmotically to smoothen the membrane ruffles [117].

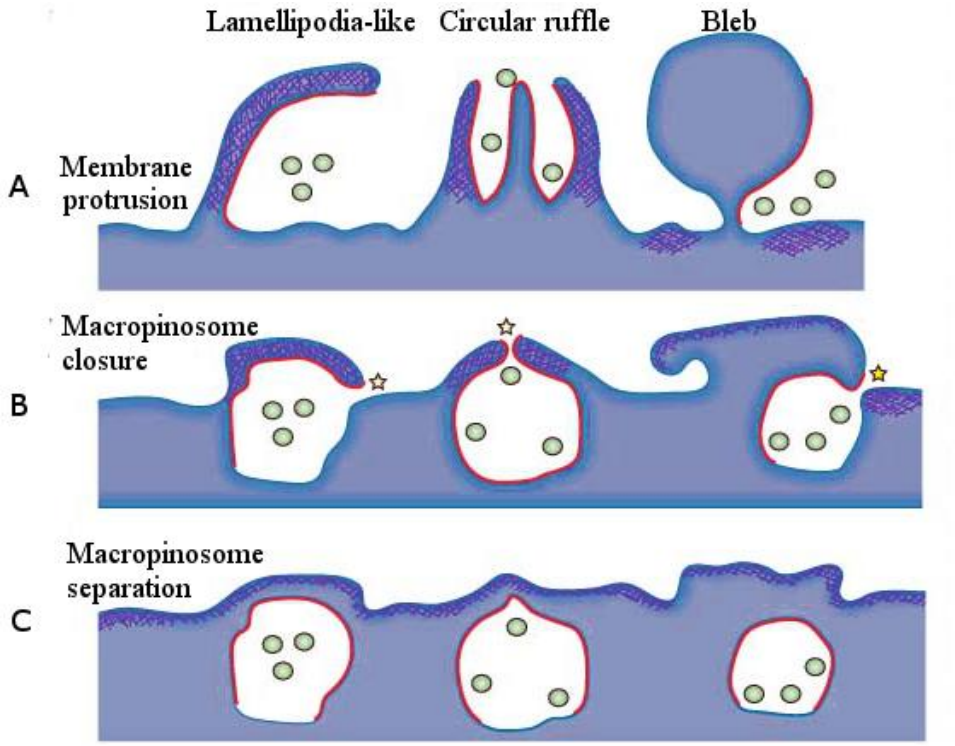

Figure 2.16 Three modes of macropinocytosis. **A) Membrane protrusions in the form of lamellipodia ruffles, circular ruffles and bleb B) Membrane protrusions folding back and fusing into plasma membrane. C) Separation of the macropinosome and its further movement into cytoplasm. (Figure adapted from Mercer et al. [121])**

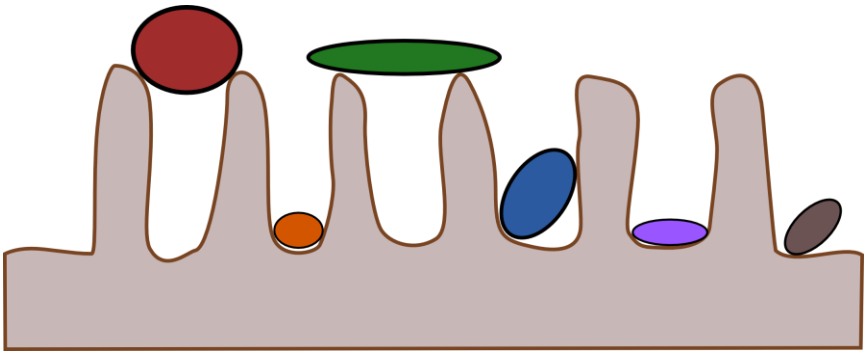

Figure 2.17 Role of membrane ruffling on initial attachment of cargo to the surface of macrophages. Higher attachment could occur for particles of certain size and geometry that fits inside membrane ruffles. (Figure adapted from Doshi *et al.* [117]).

Microscale endocytosis are actin-independent specialised mechanisms of endocytosis. Particles are internalised into pits with diameters smaller than 200nm. Clathrin-mediated endocytosis is the ingestion particles into 150 - 200nm clathrin coated pits and Caveolin-mediated endocytosis is the internalisation of particles into cholestrol-rich pits with diameter about 120nm. The small size of pits restricts the ingestion of large particles through these mechanisms.

Previous studies have believed that nanoscale and submicron sized UHMWPE and metal wear debris are potentially internalised by cells through macropinocytosis mechanisms [122].

Moreover, it is believed that majority of the mechanisms of endocytosis are a result of natural evolution. Immune cells have evolved over the years to protect the host organism against a range of bacteria, viruses and other undesirable debris. Consequently, studies have found higher uptake of particles with dimensions similar bacteria and entry of specific viruses by activating macropinocytosis [117], [121].

2.6.2 Cellular mechanisms of UHMWPE wear debris induced osteolysis

As mentioned previously in Section 2.2, the natural diarthodial joints are surrounded by a joint capsule. During joint replacement surgery, this synovial membrane is removed prior to the fixation of artificial prosthesis. After the surgery a pseudosynovial membrane gradually grows around the joint articulation, rich in macrophages, dendritic cells, osteoclasts, multi-nucleated giant cells and wear debris as observed in several studies [78], [123], [124]. Moreover, the interaction of these cells with wear debris showed presence of a biochemical mediators of inflammation, cellular recruitment and bone loss in periprosthetic membranes [125]–[129]. This overall process of wear debris induced inflammation osteolysis is shown in Figure 2.18.

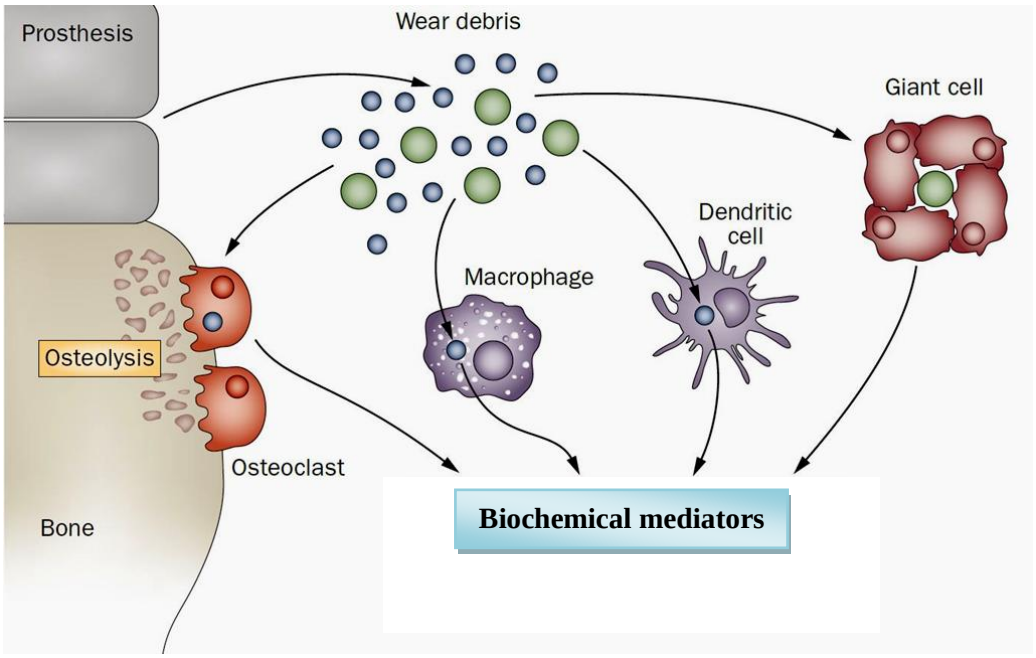

Figure 2.18 Schematic of periprosthetic bone loss and inflammation due to wear debris. Arrows represent the movement and interaction of wear derbris with cells such as macrophages, dendritic cells, giant cells and osteoclasts in periprosthetic tissues[3].

Since early 1990s, several researchers tried to associate the level of biochemical mediators present in retrieved tissues with the extent of osteolysis. However, no consistent pattern were observed [130][131]. Overall, these studies indicated the presence of biochemical mediators due to the activation of macrophages by wear debris and increased inflammatory response. The subsequent *in vitro* studies on the behaviour of macrophages in the presence of wear debris gave more insight into inflammatory response and osteolytic activity. Polyethylene wear particles were observed to stimulate mediators such as IL-1, IL-6, TNF- α, GM-CSF and PGE2. Moreover, bone resorption activity and inflammatory response of macrophages were shown to be dependent on size and quantity of wear debris [132]–[135]. A study by Green *et al.* used calcium-radio labelled mouse

[3] Source: Cobelli, N. *et al.* Nat. Rev. Rheumatol. 7, 600–608 (2011); published online 6 September 2011; doi:10.1038/nrrheum.2011.128

calvariae to assess the bone resorption activity by measuring the calcium ion release[133]. Particle dosage was expressed as volume of debris per cell. Bone resorption was stimulated by GUR 1120 polyethylene particles with a mean size of 0.24μm at a particle dose of 10 μm^3/cell, while particles with a mean size of 0.45 and 1.71 μm at a particle dose of 100 μm^3 per cell. Larger particles with a mean size of 1.71 μm and 88μm failed to activate any bone resorption activity. In regards to cytokine production, particles in the 0.1 - 1 μm size range at volumetric concentrations of 10-100 μm^3/cell have been considered as mainly biologically active [24].

In relation to the specific biochemical pathways leading to osteolysis, Udagawa *et al.* demonstrated the ability of mononuclear phagocytes to differentiate into osteoclasts in the presence of bone-marrow derived stromal cells or osteoblasts. Another study by Tanaka *et al.* demonstrated the importance of macrophage colony stimulating factor (M-CSF). Osteoclast formation was shown to be blocked in the presence of anti-M-CSF antibodies [136].

Significant developments occurred in late 1990s with the identification of a stromal cell-secreted protein, termed as osteoprotegrin (OPG), its ligand, termed as receptor activator of nuclear factor ĸB ligand (RANKL) [137]–[139] and a new TNF-family receptor, termed as receptor activator of nuclear factor-kB (RANK) [139]. RANKL has been shown to be expressed by a number of cells such as osteoblastic stromal cells, T lymphocytes and B-lymphocytes. When cleaved from the cell surface it can exist in the form of soluble RANKL. Moreover, Osteoclast precursors having RANK receptors can undergo osteoclastogenesis in the presence of RANKL and M-CSF. OPG is a soluble receptor and has an important role in balancing the extent of osteoclast formation by binding to the RANKL. Therefore, RANKL/OPG ratio is considered as a key parameter in regulating the bone resorption[138].

Effect of OPG and RANKL on osteoclast formation by macrophages derived from membranes of loosened hip implants were studied by Itonaga *et al.* Macrophages were found to differentiate into osteoclasts after addition of RANKL into cultures, even in the absence of osteoblasts. In addition, OPG was found to inhibit the osteoclast formation by hindering RANK-RANKL interactions between osteoblast-like cells and osteoclast precursor cells from membranes in a dose dependant manner[140]. Another study by Knoch *et al.* in 2005 used murine calvarial model to demonstrate the effect of OPG on suppression of UHMWPE particle-induced osteolysis [141].

As mentioned previously, mediators such as TNF-α, IL-1β, IL-6 and PGE2 are released by particle-activated macrophages. TNF-α and IL-1β have been recognised to have an important role in wear debris induced bone resorption by stimulating osteoblasts to express RANKL [142] and M-CSF [143]. Furthermore, TNF-α has been shown to assist the differentiation of osteoclast precursors in the presence of low levels of RANKL [144].

Moreover, Algan *et al.* demonstrated that the release of calcium ions (indicator of bone resorption) was significantly reduced when macrophage-PMMA conditioned medium (containing TNF-α) was

pre-incubated with anti-TNF-α antibody prior to its introduction into radio labelled mouse calvariae. Another study by Ingham *et al.* observed that with polyethylene particles stimulated release of TNF-α, IL-1β, IL-6 and PGE2 by murine macrophages and TNF-α was responsible for a statistically significant reduction in bone resorbing activity [145].

A recent study by Wang *et al.* on failed UHMWPE on metal hip implants has shown a higher RANKL expression and lower OPG/RANKL ratio in synovial fluid and osteoblastic stromal cells in the periprosthetic bone marrow of loosened THRs in comparison to primary THRs. Moreover, increased level of biochemical mediators such as IL-6, IL8, IL10, IP-10, MCP-1, MIG were found in the synovial fluid of loosened implants [146]. A few studies have also investigated the effect of UHMWPE particle shapes on biological reaction to wear debris. Yang *et al.* used a murine air pouch model to compare inflammatory response of large micron sized globular and elongated UHMWPE particles. Inflammatory response to elongated particles released higher levels of IL-1β and TNF-α cytokines in comparison to globular particles [120]. Another study by Ren *et al.* used similar murine air pouch model and showed higher level of RANK and RANKL gene expression in pouch tissue for elongated particles [147].

Second generation highly crosslinked UHMWPE was introduced to improve wear characteristics of UHMWPE as a bearing material as mentioned in Section 2.3.1. However, increased biological activity of wear debris has been observed in this material. Fisher *et al.* compared non crosslinked, moderately crosslinked and highly crosslinked polyethylene for inflammatory response and found a significant increase in TNF-α for crosslinked polyethylene debris in comparison to non crosslinked debris[148]. Another study by Illgen *et al.* showed elevated levels of TNF-α and VEGF for highly crosslinked polyethylene in comparison to conventional polyethylene.

More recently, antioxidants such as α-tocopherol (Vitamin E) have been added to highly crosslinked UHMWPE to improve the oxidation resistance and fatigue strength as mentioned in Section 2.3.1. Although the rationale behind using antioxidants was to improve the mechanical properties, a positive effect on its ability to reduce inflammation and osteolysis has also been observed recently. Balden *et al.* compared the inflammatory response of virgin UHMWPE to Vitamin E containing UHMWPE by stimulating peripheral blood mononuclear cells (PBMNCs) with particles and found a significant reduction in TNF-α, IL-1β, IL-6 and IL-8. This trend was also observed upon addition of liquid Vitamin E to UHMWPE particle stimulated PBMNCs [6]. Another study by Bichara *et al.* used murine calvarial bone model to compare the biological activity of Vitamin E-diffused highly crosslinked UHMWPE (E1, Biomet) to highly crosslinked virgin UHMWPE. After 10 days statistically significant reduction in bone resorption and inflammatory fibrous tissue was found with E1 particles in comparison to highly crosslinked virgin UHMWPE [5].

The cellular mechanisms of wear debris induced osteoclastogenesis are shown in Figure 2.19. The internalisation of wear debris by tissue macrophages and dendritic cells releases a range of cytokines and chemokines. This causes activation of osteoclast precursors by M-CSF cytokine, followed by the differentiation of osteoclast precursors into bone-resorbing osteoclasts via RANKL/RANK pathway. The cytokines and growth factors released by the macrophages also cause recruitment of other pro-inflammatory cells such as circulatory monocytes, macrophages and osteoclast precursor cells. Table 2.7 shows a list of biochemical mediators associated with osteoclastogenesis.

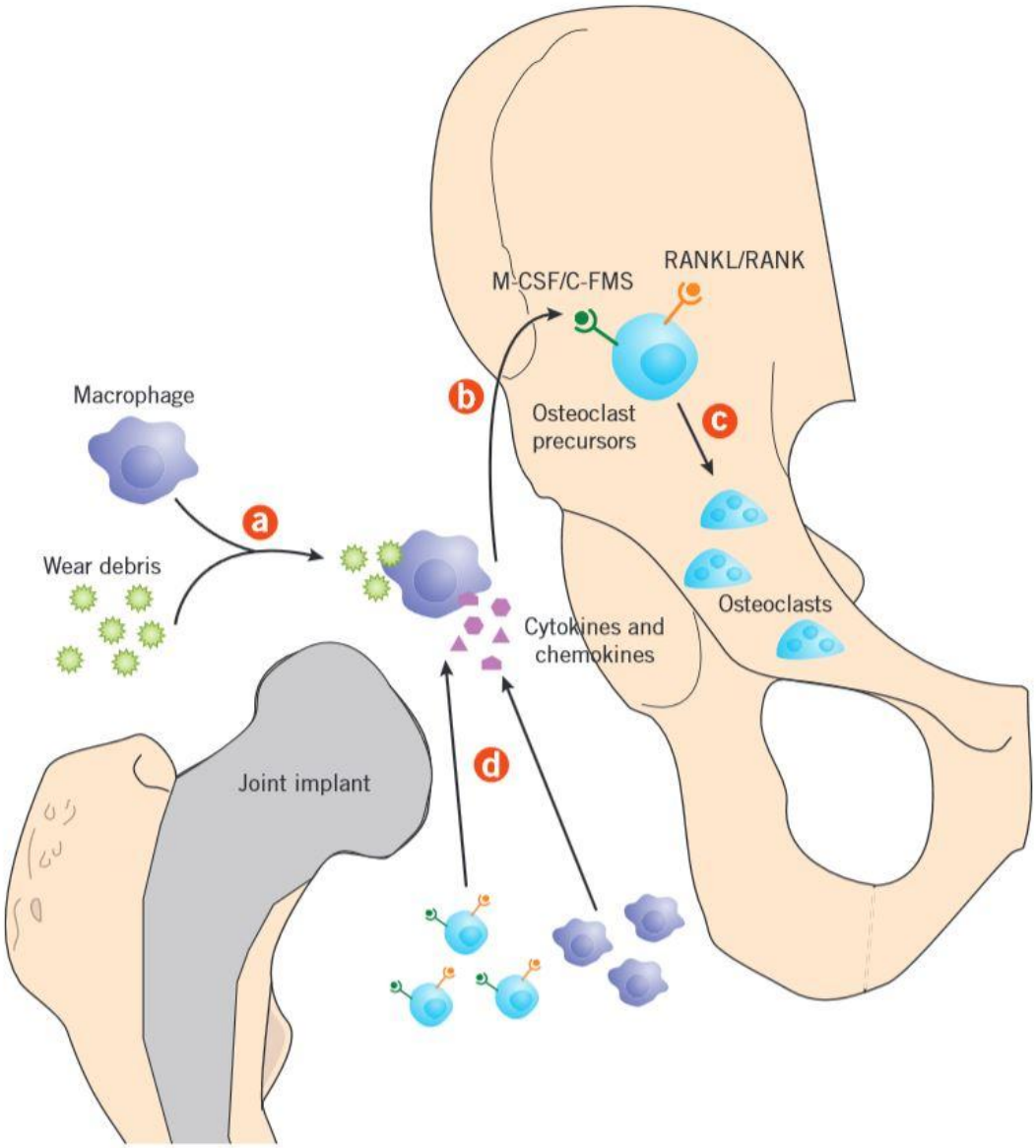

Figure 2.19 The cellular mechanisms of wear debris induced osteolysis. a) Internalisation of wear debris by macrophages and release of cytokines and chemokines. b) Activation of osteoclast precursors by M-CSF cytokine. c) Differentiation of osteoclast precursors into osteoclasts via RANKL/RANK pathway. d) Recruitment of circulatory monocytes, macrophages, osteoclast precursors and other pro-inflammatory cells to the affected region[4].

[4] Source: Lou, K.-J. SciBX5(25); doi:10.1038/scibx.2012.647

Table 2.7 List of cytokines and growth factors associated with osteoclastogenesis. (Table adapted from Adamopoulos *et. al.* [149]).

Cytokines and growth factors	Effect on osteoclastogenesis
TNF-α, IL-1, IL17, IL-23, RANKL, M-CSF	Promotion
IL-4, IL-12, IL-27, IL-33, OPG	Inhibition
GM-CSF, IL-6	Promotion and Inhibition
IL-34, VEGF, HGF, PIGF, FLT3 ligand	Support

Based on above studies the osteolytic effects of UHMWPE wear debris can be summarised into following:

- Macrophage interaction with UHMWPE wear debris releases a range of biochemical mediators that can have a direct or indirect effect on osteolysis.
- Size and amount of UHMWPE wear debris are important factors and have shown a direct effect on inflammatory response and bone resorption activity. UHMWPE particles in 0.1 - 1 µm size range are shown to be most biologically active.
- Shape of UHMWPE particles influences the inflammatory and osteolytic response.
- OPG-RANKL-RANK signalling between osteoblastic stromal cells and osteoclast precursors plays a key role in UHMWPE wear debris induced osteolysis.
- TNF-α is an important cytokine in determining the osteolytic potential of implant materials such as UHMWPE.
- Antioxidants such as α-tocopherol (Vitamin E) can significantly reduce the inflammatory response. E1 UHMWPE has shown to reduce inflammation as well as bone resorption.

2.7 **Pre-clinical Wear Evaluation of Joint Replacements**

Pre-clinical evaluation of the wear of joint implants is carried out by tribological testing of implant materials. Simple configuration wear testers are used for screening wear performance of implant materials, while artificial joint simulators test the wear of implants designed for clinical use. The design and features of these wear-testing devices have evolved considerably in last 40 years. The first wear tester was developed in 1960s and consisted of a polymer pin sliding on a stainless steel plate and simulated unidirectional motion [7]. In late 1990s, it was discovered that the wear rate of polymers such as polyethylene reported by unidirectional testers was much lower than clinical wear. Also, it was noticed that wear increased considerably when materials were subjected to multidirectional motion testing instead of unidirectional motion [150]. As a result, pin on plate reciprocators underwent key adaptation of the inclusion of rotational motion along with translational motion to simulate a multidirectional movement, which is closer to the movements in human synovial joints [151], [152]. Over the years, simple configuration wear testers such as pin-on-disc or multidirectional pin-on-plate testers have become the key devices for screening wear performance of implant materials. The contact pressures used during the wear testing are usually matched with the contact pressures observed *in vivo* for a particular type of joint. Figure 2.20 shows the schematic diagram of a multidirectional pin-on-plate tester developed at Durham University. Moreover, in recent years multidirectional pin-on-plate testers are used to generate a large volume of wear debris for biological studies [153].

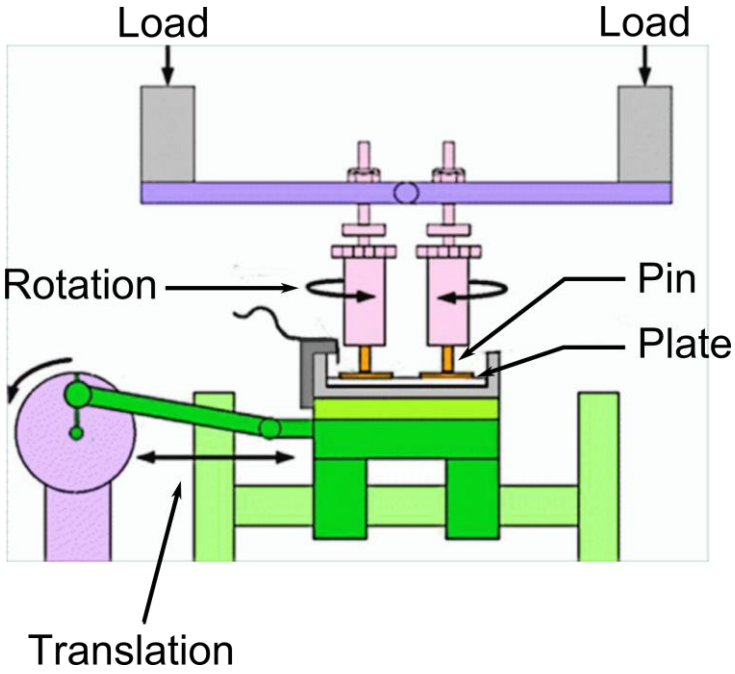

Figure 2.20 Multidirectional Pin-on-plate tester at Durham University. The multidirectional motion is achieved by translation of the plate and rotation of the pins at the same time.

Although simple configuration wear testers such as pin-on-disc or multidirectional pin-on-plate testers are good for screening materials based on their wear characteristics, the prediction of wear

in artificial joint implants needs more realistic wear testing. As seen previously in section 2.2, type of movements in human joints can vary significantly between different joint articulations. Moreover, the difference in implant design and biomechanics for each articulation could lead to different lubrication regimes and wear characteristics. Therefore, artificial joint simulators have been developed to test the wear performance of prosthesis under conditions as close as possible to the physiologic conditions.

Wear simulators specific to a joint can be broadly divided into categories based on the type of joint. Most common joint simulators are hip, knee, ankle and spine simulator. In some cases a joint simulator can be adapted to test a different joint. For example knee simulators are often adapted to test ankle joint prosthesis due to certain similarities in design and motion [154]. During the development of joint simulators, a number of designs and testing conditions were used at different research centres, which made it difficult to compare the wear results reported by studies conducted at different locations. Therefore, International Organization for Standardization (ISO) developed a set of standards to standardise the wear testing conditions. ISO 14242 and ISO 14243 are the standards for wear testing for hip and knee implants.

A hip joint simulator typically mimics the movement of the femoral component and applies loads equivalent to a simplified gait cycle. A single axis hip simulator reproduces flexion/extension movement, while a two-axis simulator reproduces either flexion/extension and abduction/adduction or flexion/extension and inward/outward rotation. A three axis simulator mimics all three movements in a hip such as abduction/adduction, flexion/extension and inward/outward rotation [155].

The simulation of a knee joint requires more complex movements due to the higher number degrees of freedom. Prosim Knee simulator can have six degrees of freedom with axial load, femoral flexion, tibial rotation (interior/exterior), tibial displacement (anterior/posterior) and abduction/adduction [156].

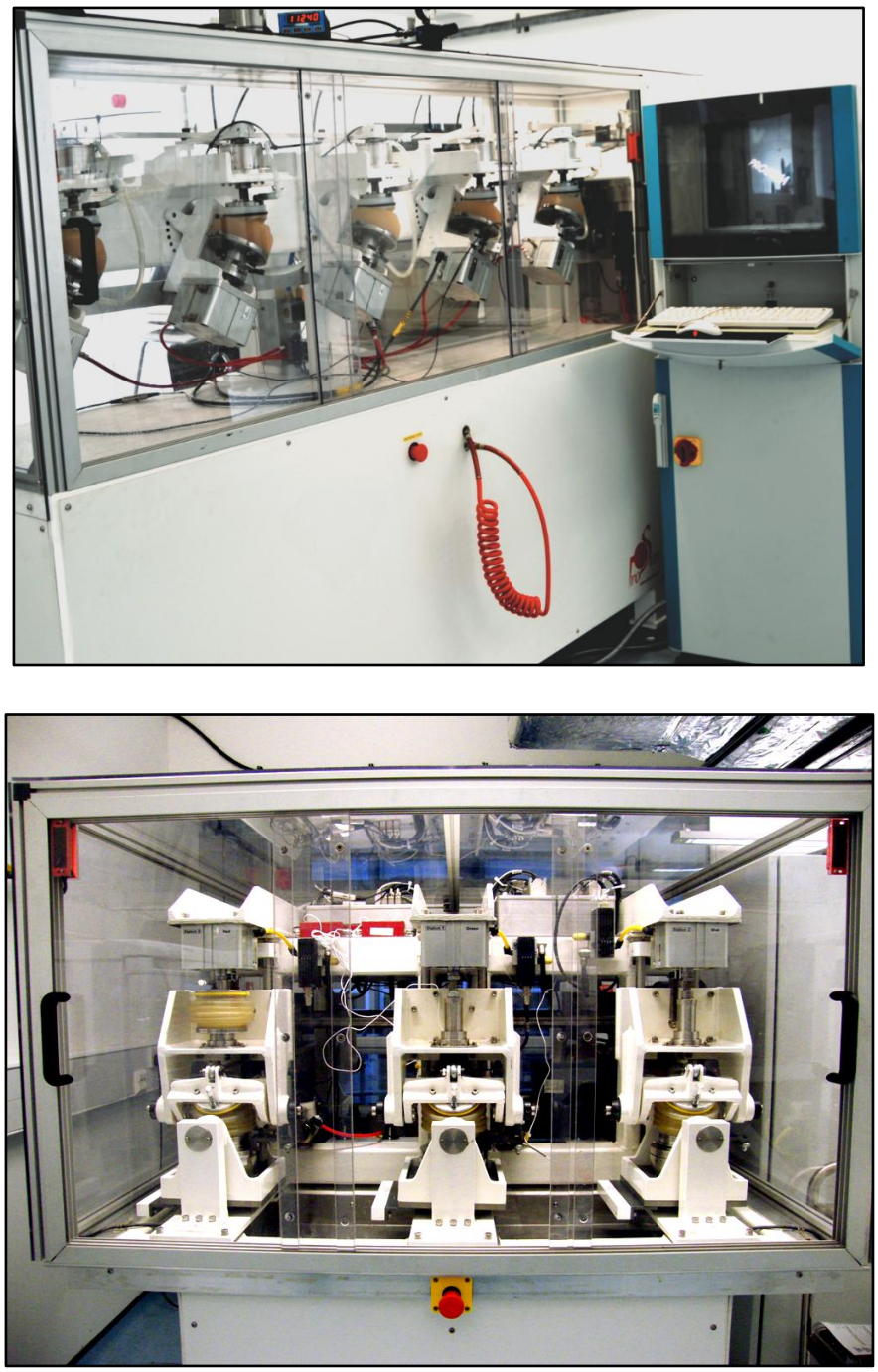

Figure 2.21 Prosim Hip Simulator (top image) and Prosim Knee Simulator (bottom image) at Durham University.

ISO standards (ISO 14242 and ISO 14243) specify 1 Hz as the frequency for simulator testing implants and at least 5 million cycles to predict the steady state wear characteristics [157], [158]. The number of cycles is an important parameter *in vitro* testing of joint implants. Each 1 million cycle represents about 1 year of implant use *in vivo*. However, actual usage of implants varies from patient to patient depending on their daily activities and lifestyle.

2.7.1 Importance of Lubricant for Pre-Clinical Evaluation

Natural synovial joints produce synovial fluid to lubricate bearing surfaces. Synovial fluid is a sterile non-Newtonian fluid composed of hyaluronic acid secreted by fibroblast-like cells in synovial membrane and dialysate of blood plasma. Unlike other body fluids derived from plasma, synovial fluid contains a large amount of proteins. Moreover, large protein molecules such as β-lipoprotein and fibrinogen are absent in synovial fluid due to their inability to penetrate the synovial membrane [159]. Albumin is the most abundant constituent of synovial fluid and occupies approximately 56% of its composition. Another constituent is hyaluronic acid, which is primarily responsible for maintaining the viscoelastic properties of synovial fluid. Aging and arthritis can reduce the viscosity of synovial fluid by a reduction in concentration and relative molecular weight of hyaluronic acid. Moreover, the amount of albumin is reduced to 42% in arthritic patients [160].

In order to achieve a realistic lubrication regime for testing artificial implants one may believe the possibility of using synovial fluid extracted from patients. However, the amount of synovial fluid, its limited availability and variability of composition between patients makes it impractical to use synovial fluid for *in vitro* tests.

Alternatively, serum obtained from blood is more readily available from animal sources and contains comparable constituents as in synovial fluid. Similar to synovial fluid, the major constituent of serum is albumin. Newborn Calf Serum (NCS) is the most commonly used lubricant for *in vitro* wear tests [154], [161], [162]. It is composed of proteins and phospholipids, which are believed to lubricate the joint articulation similar to proteins present in synovial fluid. A comparison between composition of Synovial fluid and NCS is shown in Table 2.8.

Table 2.8 A comparison between composition of synovial fluid from patients suffering from osteoarthritis and newborn calf serum (Table adapted from [163] **).**

Specifications	Synovial Fluid	Newborn Calf Serum
Protein Concentration	34.18 g/L	52 g/L
Albumin	68%	40%
α-1-globulin	3.5%	11.2%
α-2-globulin	7%	22.8%
β-globulin	10.5%	14.2%
ɣ-globulin	9.5%	11.8%
Ca	`1.55	2.70
Mg	0.4	1.06
Inorganic P	0.6	2.82
Fe	negligible	0.0157

NCS is often diluted with water to match the overall protein concentration of synovial fluid. Studies done in the past have investigated the effect of protein concentration on the wear rate and morphology of UHMWPE. An increase, followed by a decrease in wear rate was observed during wear testing of UHMWPE at increasing concentrations of bovine serum [164], [165].

A number of studies also compared wear characteristics of UHMWPE in water and serum. Large flake-like morphology was observed in water , while particles generated in bovine serum had submicron and elongated morphology [166][164]. McKellop *et al.* compared UHMWPE wear debris produced *in vivo* to the wear debris produced in a hip joint simulator using serum lubricant and found very similar particular morphologies [167].

Based on the optimum protein concentration for producing clinically relevant wear rates, ISO standards for hip (ISO 14242-1) and knee (ISO 14243-1) wear testing recommend the use of newborn calf serum diluted in deionised water, with a protein concentration of 20g/L as the lubricant for *in vitro* simulator tests [157], [158]. Therefore, majority of researchers use NCS with a protein content of 20g/l or more.

The limitations of serum as a simulator lubricant are the degradation and precipitation of serum proteins. Fang *et al.* observed a thermal unfolding of the secondary structure of albumin during tribological testing of UHMWPE against metal [160]. Frictional heat generated during joint articulation was believed to be the cause of this structural change in albumin. A number of studies have shown decrease in the wear of UHMWPE due to surface interaction with degrading proteins. A solid layer of precipitated proteins between bearings is believed to decrease the wear. Therefore, EDTA is often added to reduce calcification and protein precipitation. In addition, sodium azide is used to slow down the bacterial growth during the test.

The serum lubricant is not only important for creating suitable conditions for carrying out clinically relevant wear testing, but also for collecting UHMWPE wear debris released during the test. As mentioned in section 2.6, the size and morphology of wear particles are the key factors in determining the clinical success of a joint implant. Since these particles are surrounded by lubricant serum proteins, it is necessary to isolate them before carrying out particle characterisation. Moreover, the degradation and precipitation of serum proteins during wear testing make it more challenging to isolate the wear debris. Next section investigates the specialised methods used for isolating UHMWPE wear debris.

2.8 UHMWPE wear particle isolation

Clinical failure of implants due to inflammation and osteolysis is shown to be dependent on wear particle size and morphology (Section 2.6, page 33). Particle isolation from periprosthetic tissues and serum lubricants is an essential step prior to characterisation of wear debris. Following sections will discuss the methods developed in the past for isolation of wear debris from tissues as well as serum lubricants.

2.8.1 Isolation of wear particles from periprosthetic tissues

Wear particles disseminated from their point of origin mostly get trapped into the periprosthetic membranes and surrounding tissues. In late 1980s, the limitations of polarised optical microscopy to characterise the submicron particles became apparent. This created an interest in isolating wear debris from tissues in order to accurately characterise their size and morphology. From early to mid-1990s, several studies isolated and characterised wear debris from tissue samples. Lee *et al.* [168] used a commercial tissue solubiliser, while Kossovsky *et al.* and Shanbhag *et al.* [85] used strong base to digest tissues. Campbell *et al.* preferred an enzymatic digestion method using papain in their earlier studies. Margevicius *et al.* used an acid digestion based method and demonstrated no apparent changes in morphology before and after using nitric acid for digestion [84]. One significant improvement in particle isolation methodology was introduced by Campbell *et al.* in 1995 [169]. A combination of base digestion followed by isolation of UHMWPE particles using sucrose and isopropanol density gradients was used in this method, which became the basis for subsequently developed state of the art methods. In the same year Maloney *et al.* developed an enzyme digestion based isolation method that used papain to digest tissue samples. From mid 1990s until early 2000s majority of studies used the Campbell's method to isolate particles due to its sufficient sensitivity and reproducibility for conventional UHMWPE. In late 1990s, Tipper *et al.* introduced a new method for UHMWPE particle isolation from tissues. It used strong base to digest the tissues followed by methanol: chloroform extraction to isolate UHMWPE particles. Another study by Dean *et al.* modified Maloney's enzymatic digestion method by addition of a centrifugation step (100,000g) to isolate particles at the end of digestion. More recently in 2007 Slouf *et al.* compared acid base and enzymatic tissue digestion and isolation methods for UHMWPE isolation and suggested the use of acid digestion developed by Margevicius *et al.* for its convenience. Baxter *et al.* also compared tissue digestion methods and found 5M NaOH, 5M KOH and 15.8M HNO3 to be most effective [170]. In 2008 Richards *et al.* found nanometre sized particles (minimum size 30nm) in tissue samples by optimising Tipper's method [25]. More recently, Lapcikova *et al.* isolated tissue samples using nitric acid digestion and washing steps. Nanoscale UHMWPE wear debris were also found in this study [171].

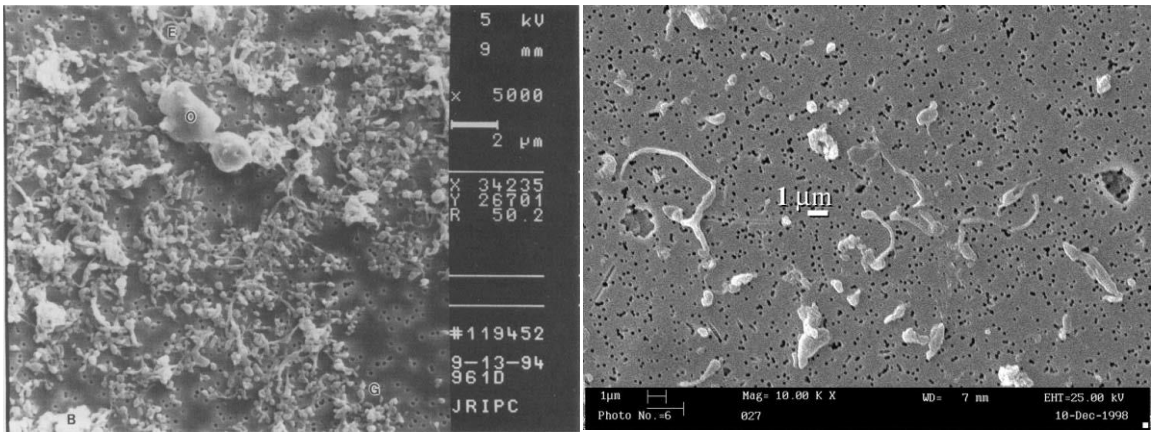

A) B)

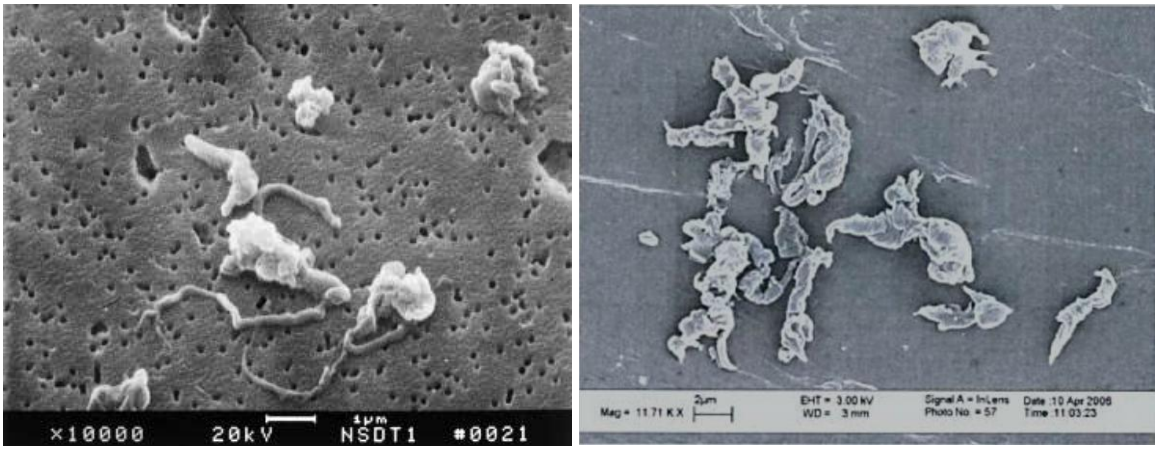

C) D)

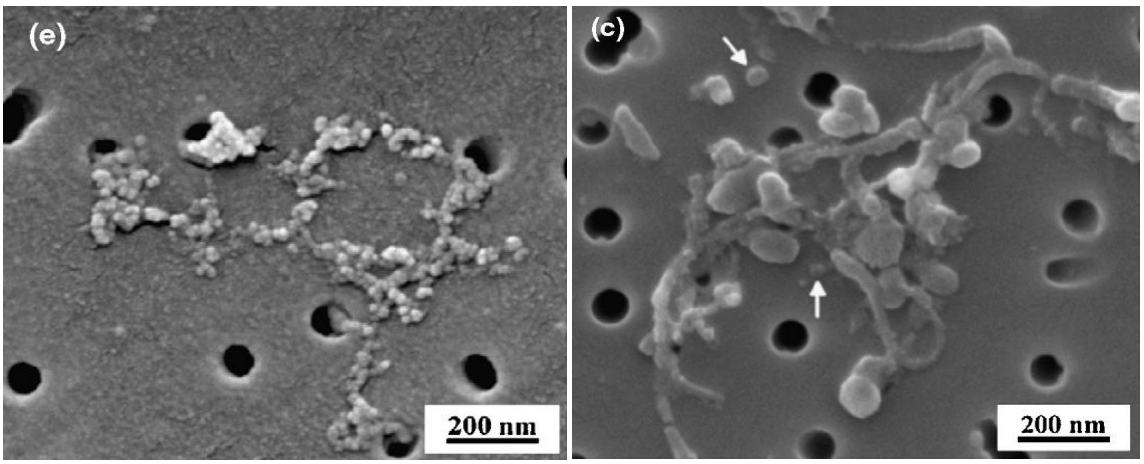

E) F)

Figure 2.22 Scanning electron micrographs of UHMWPE wear debris isolated from preiprosthetic tissues. A) Campbell's isolation method [169]**. B) Campbell's method used by Mabrey *et al.* [95] C) Dean's enzymatic digestion method** [172]**. D) Tipper's isolation method adapted by Richards *et al.* [25] E) and F) Lapickova's isolation method** [171]**. UHMWPE nanoparticle debris were observed by Lapcikova *et al.* as shown in micrographs. (Image sources[5])**

[5] Sources: Campbell *et al.* [169], Mabrey *et al.* [95], Dean *et al.* [172], Richards *et al.* [25], Lapickova *et al.* [171]

2.8.2 **Isolation of wear particles from serum lubricants**

By the end of 1990s, *in vitro* testing of implants using multidirectional pin-on-plate testers and artificial joint simulators became the standard methods of wear testing. These *in vitro* tests were done using 25% bovine serum as a lubricant, which contained about 17 grams/litre of serum proteins and phospholipids. During wear testing, submicron wear particles were generated and eventually were covered by protein agglomerates. Therefore, isolation of wear particles became necessary for particle characterisation. As particle isolation methods for periprosthetic tissues already existed, adaptation of these methods for serum lubricants was a natural choice. In 1996 Wang *et al.* adapted Campbell's isolation method [169] for serum lubricants and isolated wear debris from serum lubricant. Another study by Hailey *et al.* used base digestion followed by centrifugal washing to isolate UHMWPE wear debris. However, the isolated particles in this study appeared to be agglomerated similar to UHMWPE wear particles isolated from tissues by Shanbhag *et al.* [85]. In 1998, Besong *et al.* adapted Tipper's method to isolate UHMWPE particles from lubricant serum [173]. However, no wear debris images were shown in this study. Niedzwiecki *et al.* compared Campbell's base digestion method to simple enzymatic digestion and acid digestion based methods and found no significant difference between them for UHMWPE wear particle isolation on the basis of size distribution data and SEM images [174], [175]. Moreover, Scott *et al.* used Niedzwiecki 's method and demonstrated the importance of using small pore size membrane filters [176]. In 2001 Elfick *et al.* adapted Campbell's tissue digestion method for isolation of wear debris from serum samples [177].This method reduced the number of isolation steps by using only isopropanol density gradients. In 2003, Affatato *et al.* developed a simple debris isolation method using base digestion in combination with low speed centrifugation and demonstrated the usual UHMWPE wear particle morphology. Tipper *et al.* used their previously developed method and observed nanoscale wear debris with size down to 10nm in 2006 [178]. Since several isolation methods use centrifugation for separation of particles Zolotarevova *et al.* studied the effect of centrifugation on UHMWPE particles and found no significant difference in size distribution and morphology of particles. More recently in 2011, Billi *et al.* introduced a new enzymatic digestion based method. Particle isolation was carried out using a multi stage density gradient centrifugation and wear particles were deposited on a silicon wafer for characterisation. In the same year, the ISO standard for isolation of wear debris from simulator lubricants (ISO 17853:2011) chose Scott’s acid digestion method due to its ease of use and high reproducibility [179].

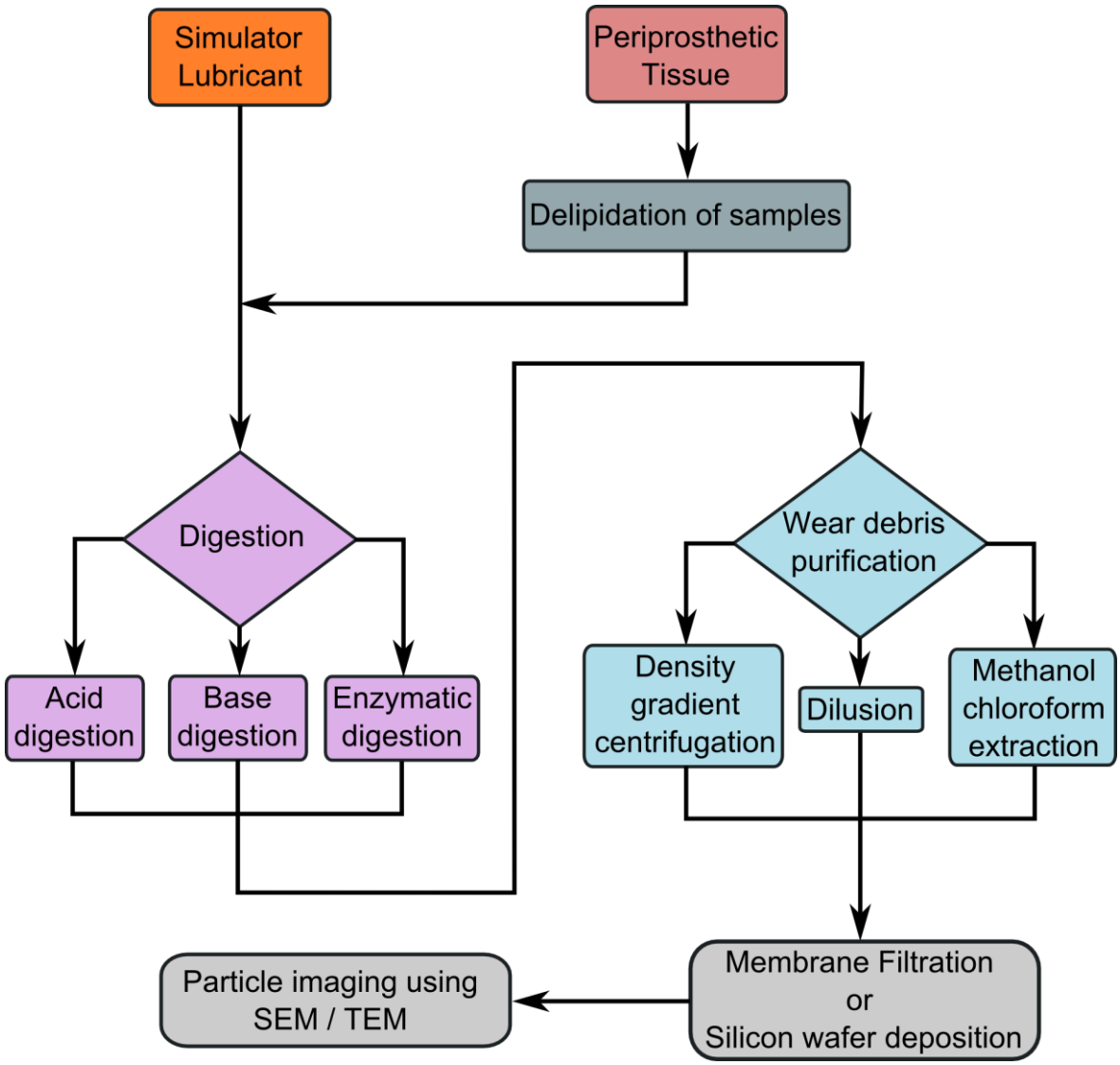

Figure 2.23 General UHMWPE particle isolation methodology used for isolating wear debris from periprosthetic tissues and serum based simulator lubricants. The digestion steps are shown by purple colour. Wear debris purification steps are shown by light blue colour. SEM sample preparation and imaging are shown by gray colour.

2.8.2.1 Methodologies for isolation of UHMWPE wear debris from serum lubricant

Wear debris isolation from serum lubricants can be broadly divided into two steps. These are serum digestion and wear debris separation. Following sections will discuss these steps in detail.

2.8.2.1.1 Serum digestion

Serum digestion is the solubilisation and hydrolysis of proteins. In addition, it can be carried out in three ways discussed below.

Acid digestion

Acid digestion was first used by Niedzwiecki *et al.* to digest serum lubricant [175]. Hydrochloric acid (37% v/v) was used at 5:1 ratio with serum lubricant and the digestion was carried out by stirring the solution at 60°C for 45 minutes. Scott *et al.* modified this method and used hydrochloric acid (37% v/v) at 4:1 ratio with serum [180]. Digestion was carried out at 50°C for 1 hour with continuous stirring.

Base digestion

Digestion with a strong base has been the most frequently used method to solubilise serum proteins. Wang *et al.* adapted Campbell's method for tissues and used 5M potassium hydroxide in a 2:1 ratio to digest serum and the digestion was carried out for 6 hours at 65°C [181]. Tipper *et al.* used 12M potassium hydroxide for 48hours at 60°C in earlier studies [182] and 5M potassium hydroxide with same temperature and duration in later studies [178][183]. Affatato *et al.* used 6M sodium hydroxide for 24 hours at 60°C [184]. Fang *et al.* used 5M sodium hydroxide at 4:1 ratio to serum for 24 hours at 65°C [166].

Enzymatic digestion

Enzymatic digestion uses a protease such as proteinase K to break down the serum proteins and lipids. Niedzwiecki *et al.* used proteinase K to digest the serum at physiological conditions (37°C and atmospheric pressure) along with magnetic stirring for 45 minutes [175]. Recently Billi *et al.* used a three-stage digestion process at physiological conditions with repeated addition of proteinase K and in the presence of Ca^{2+} to increase the efficiency of digestion. The duration of the digestion was over 45 hours in this method (Section 3.2.3) [185].

2.8.2.2 **Wear debris purification**

Purification of wear debris from digested proteins is as important as the serum digestion step. A number of methods have been used previously in an attempt to get wear debris free from proteins, lipids and other impurities. These methods are discussed below.

Density gradient centrifugation

Density gradient centrifugation is one of the most significant methods of wear debris purification due to its reproducibility and ability to achieve high degrees of separation. Campbell *et al.* originally introduced density gradients for wear debris separation in mid 1990s [169]. Sucrose density gradients were used to separate proteins from wear debris. A second gradient using layers of isopropanol banded UHMPWE particles between densities of 0.90 and 0.96 gms/cm^3 after centrifugation at 40,000rpm (200,000g) for 1 hour. Particles were isolated from the interface of two layers and were collected and dispersed on a filter. Elfick *et al.* modified Campbell's method by replacing sucrose gradient step with a simple centrifugation step of (104,000g for three hours) where UHMWPE particles along with lighter impurities made a thick layer (≈1mm) on top surface. This layer was harvested and re-suspended in filtered water. The second isopropanol gradient step was identical to Campbell's method [177]. In 2011, Billi *et al.* introduced a new density gradient method to separate wear debris (Section 3.2.3). The whole purification process was divided into three density gradient steps. First gradient washed the wear particles through layers of 6M urea and 4M Urea + 20% SDS. Second gradient further washed the particles through 20% SDS +3M Urea, 2% SDS and banded the particles within a continuous isopropanol gradient. Finally, Third density gradient is discontinuous gradients of isopropanol and band purified wear debris between two layers of density 0.89 gms/cm^3 and 0.98 gms/cm^3 [185].

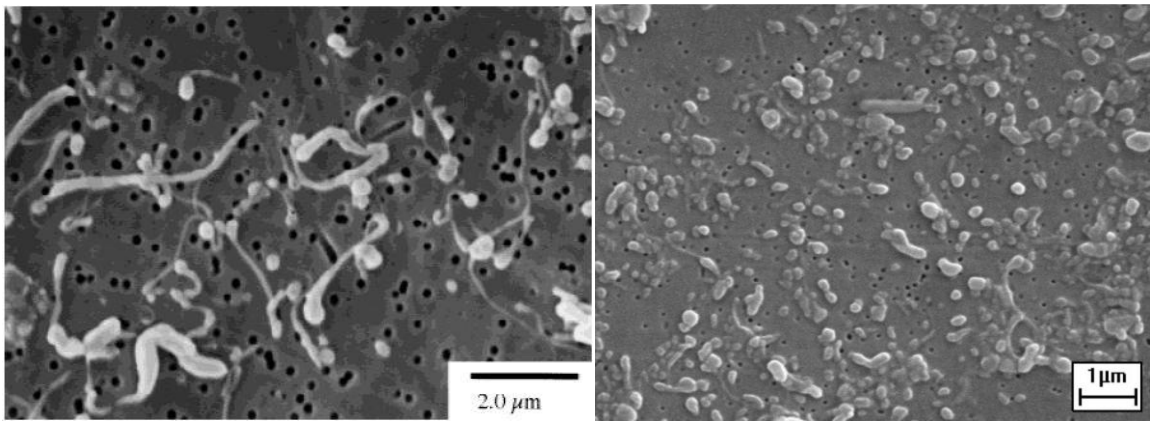

A) B)

Figure 2.24 Scanning electron micrographs of UHMWPE particles isolated from simulator lubricants using base digestion and density gradient ultracentrifugation. A) Campbell's method used by Niedzwiecki *et al.*[175]. B) Elfick's method [177]**. (Images sources[6])**

[6] Sources: Niedzwiecki *et al.*[175] and Elfick *et al.* [177]

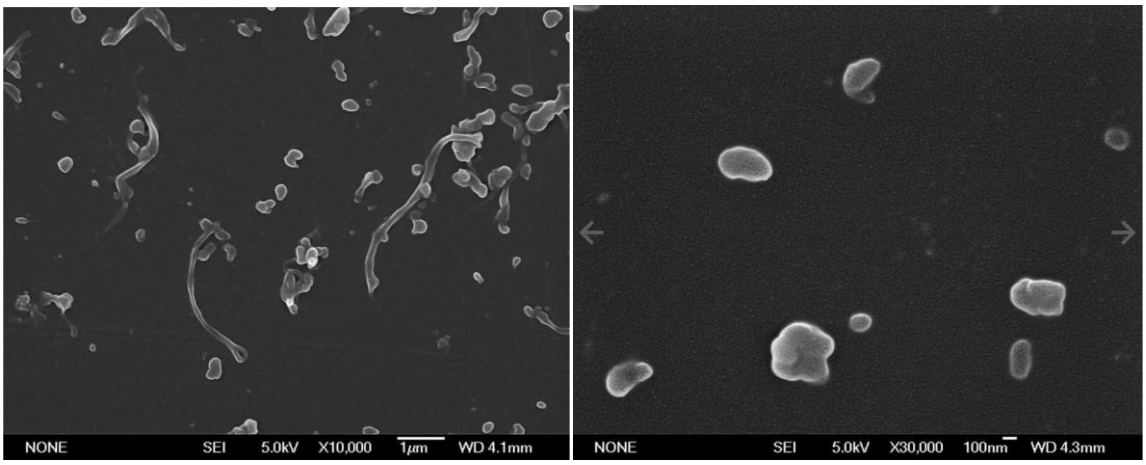

A) B)

Figure 2.25 Scanning electron micrographs of UHMWPE particles isolated from simulator lubricants using Billi's enzymatic digestion and density gradient ultracentrifugation method[185]**. A) Medium resolution micrograph showing UHMWPE wear debris. B) High resolution micrograph showing microscale and nanoscale UHMWPE wear debris. (Image source[7])**

Methanol Chloroform extraction

Tipper *et al.* introduced this method in late 1990s. The particles were purified by dissolution of lipids into the solvent layers. A 2:1 ratio of methanol: chloroform was added to the digest and incubated at room temperature for 24 hours. The samples were then centrifuged at 500g for 10 minutes and the wear debris was recovered as a supernatant layer. The methanol: chloroform / centrifugation steps were repeated until the supernatant was visibly clear. This process was repeated several times to ensure the complete removal of lipids.

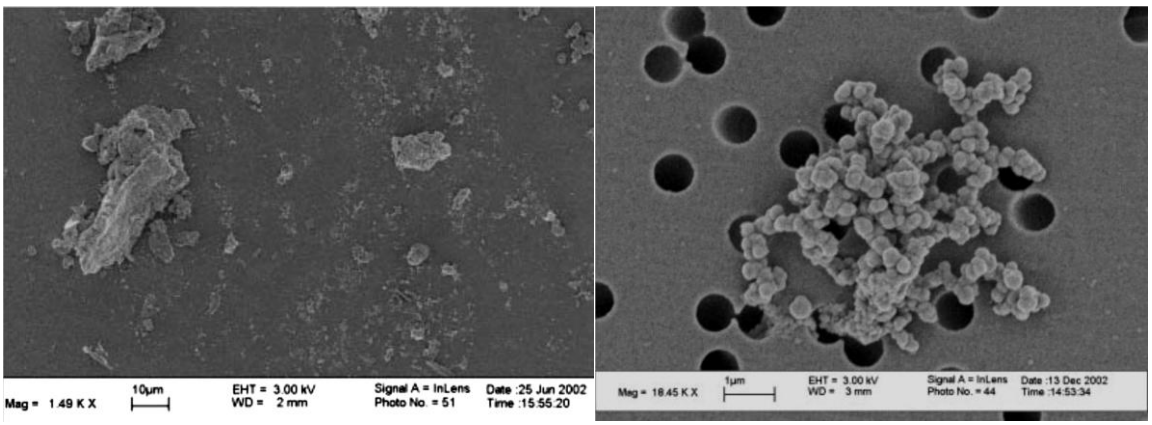

Figure 2.26 Scanning electron micrographs of UHMWPE particles isolated from simulator lubricants using Tipper's base digestion and methanol: chloroform extraction method. A) Medium resolution micrograph showing UHMWPE wear debris. B) High resolution micrograph showing nanoscale UHMWPE wear debris agglomerate. (Image source [8])

[7] Source: http://www.orthopaedicparticleanalysis.com; The Orthopaedic Biology, Biomaterials and Tribology Program (OrBBiT), Box 957358 Orthopaedic Hospital Research Center, Los Angeles, USA
[8] Source: Tipper *et al.* [178]

Membrane filtration

Membrane filtration uses a flat porous membrane filter to separate wear debris from solubilised and hydrolysed proteins. It is one of the easiest methods to implement but the duration of filtration depends on pore size and feed volume. Scott *et al.* used membrane filtration to purify UHMWPE particles after digesting the serum using hydrochloric acid. 1ml of digest was diluted with 100ml of methanol and filtered through a 0.05μm filter [176], [186].

Solubilised and hydrolysed proteins smaller than membrane pores pass through the filter, while wear particles larger than pores are collected on top [176]. Membrane filtration is also the most common method to visualize wear debris on top of a nanometre pore size filters using scanning electron microscopy.

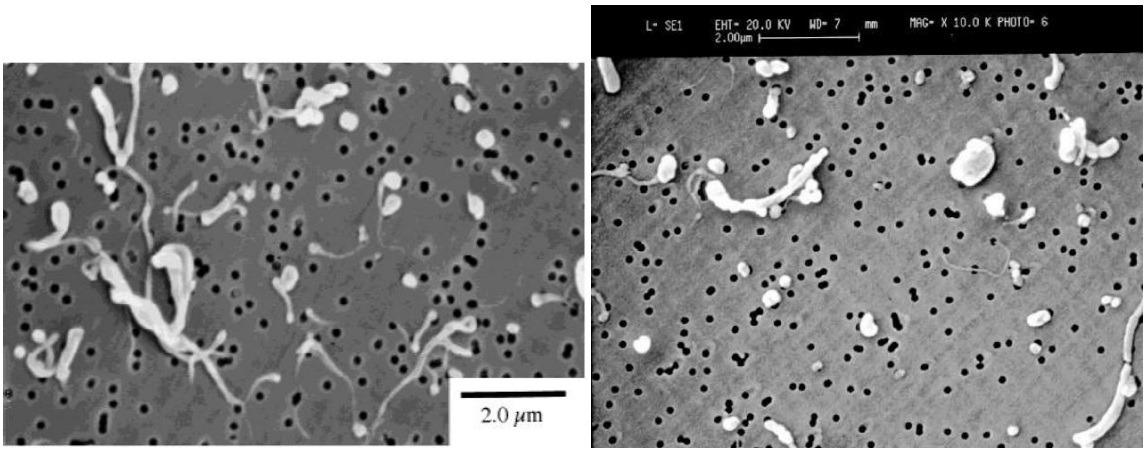

A) B)

Figure 2.27 Scanning electron micrographs of UHMWPE wear debris isolated from hip simulator lubricants using acid digestion and membrane filtration. A) Niedzwiecki's method [175]**. B) Niedzwiecki's method adapted by Scott *et al.*** [176]**. Both micrographs show UHMWPE wear debris with similar morphology demonstrating reproducibility of the method. (Image source[9])**

[9] Source: Niedzwiecki *et al.* [175] and Scott *et al.* [176]

Table 2.9 A list of methods previously used for isolation of UHMWPE particles from simulator lubricants and their characterisation using SEM image analysis.

Digestion Type	Digestion Method	Purification Method	Size Analysis	Shape Analysis	Reference
Acid	37 Vol% Hcl in 5:1ratio 60°C/45min Magnetic Stirring 350rpm	Membrane filtration	Yes(SEM)	No	*Niedzwiecki et al. 2000*[175]
Acid	37% w/v HCl in 4:1 ratio Stirred at 50◦C for 1 hour	Membrane filtration	Yes(SEM)	No	*Scott et al. 2001*[176]
Base	5M NaOH	Density gradient ultracentrifugation(40,000rpm) using sucrose and isopropanol	Yes(SEM)	No	*Niedzwiecki et al. 2000*[175]
Base	5N NaOH digested at 65◦C for in excess of 1 hour using ultrasonic agitation	Density gradient ultracentrifugation using isopropanol (40000rpm)	Yes Malvern Master sizer	No	*Elfick et al. 2001*[177]
Base	6 m NaOH solution at 60°C for 24 hours in an ultrasonic bath	Centrifuged at 4000 rpm for 70 minutes	Yes(SEM)	No	*Affatato et al. 2003* [184]
Base	5M KOH at 60 °C for 48 hours	Repeated Chloroform/Methanol (2 : 1) extraction, ice cold Ethanol lipid precipitation 24 hours and centrifugation at 15000g	Yes(SEM)	No	*Tipper et al. 2006*[178]
Enzyme	Proteinase K 37°C/45min Magnetic Stirring 350rpm	Membrane filtration	Yes(SEM)	No	*Niedzwiecki et al. 2000*[175]
Enzyme	Proteinase K, 8M Urea in the presence of Ca^{2+}	Three stage density gradient ultracentrifugation Step1: Using 6M urea,(4M Urea + 20% SDS) Step2: (20% SDS +3M Urea), 2% SDS, and continous isopropanol gradients Step3: Discontinous isopropanol gradients	Yes (SEM) Silicon wafer display	Yes Particles categorised into Fibril, Rod, Oval, Round and Irregular	Billi *et al.*, 2012[185]

2.9 **Wear debris characterisation**

Characterisation of wear debris was the main reason behind development of particle isolation methods in 1990s. Moreover, it is divided into four categories. These are particle display methods, chemical analysis, size analysis and shape analysis.

2.9.1 **Particle display methods**

Wear particles need to be displayed on a flat background with before imaging them using scanning electron microscopy (SEM). This has been done in a number of ways for wear debris analysis. Shanbhag *et al.* spread particles over super smooth carbon stubs and coated them with carbon before SEM examination, while majority of studies have used membrane filters to collect the particles on top of filters using a vacuum filtration unit. Initial studies used a 0.2µm pore size membrane filter [167], [169], whereas later studies used 0.1µm filter [90], [187]. In 2001, Scott *et al.* demonstrated the importance of small pore size membrane filters to minimise particle loss during filtration. Membranes with 0.2µm and 0.05µm pore size were compared and a significant difference in particle size distributions was noticed [176]. Recent studies have used 0.015nm pore size filters to minimise loss of particles even further. Tipper *et al.* used a series of filters (10, 1 and 0.1 µm) to collect particles in each size range[178]. Recently Billi *et al.* used a silicon wafer to display particles on a featureless background[185], [188].

Other studies using automatic size analysers needed particles to be suspended in a clear liquid. Therefore, no display of particles was required for size analysis [84], [177], [189], [190].However, shape analysis can only be carried out using SEM image analysis. Therefore, display of particles on a flat background is necessary for shape analysis.

2.9.2 **Chemical analysis**

A number of methods were used by particle characterisation studies to distinguish the UHMWPE particles from impurities based on their elemental composition or chemical bonding. This was an essential step prior to size and shape analysis. Moreover, it gave information about the chemical purity of particles after isolation. Energy Dispersive X-ray (EDX) analysis was the most commonly used method due to its easy accessibility. Scanning electron microscopes are usually equipped with EDX analysis capability. Moreover, EDX analysis can be done along with SEM imaging, which makes it a convenient method. Another method used by a few studies was Raman spectroscopy to identify particles from non-particle agglomerates on the basis of the peaks in the Raman spectrum made by chemical bonds present in the material [187], [191]. Both EDX and Raman spectroscopy could characterise individual particles. Fourier Transform Infrared Spectroscopy (FTIR) was another method used by a number of studies [185]. However, individual particles could not be characterised using this method, as opposed to above two methods.

2.9.3 **Size analysis**

During early 1990s, electron microscopy wasn't as developed as it is now. UHMWPE being a polymeric material had issues with electron beam contamination and charging. Therefore, commercial size analyzers were primarily used for size analysis of micron and submicron particles. However, with improvements in electron microscopy there was a growing use of computerised image analysis on SEM images for particle size calculation. Early studies by Margevicius *et al.*[84] and Hirakawa *et al.* [86] used automatic size analyzers such as Coulter Multisizer to obtain particle size distributions, while most of later studies used SEM image analysis. Moreover with improvements in electron microscopy and particle isolation methods, the smallest particle size reported went down from 530 nm (Shanbhag *et al.* [85]) to 200 nm (Campbell *et al.* [88]) ,and even further to 10 nm (Tipper *et al.* [178]).

Although SEM is a powerful technique to get information about size and morphology, it is a two-dimensional imaging technique. Therefore, it is unsuitable for calculation of particle volumes and volumetric size distribution of wear debris. For the same reason Elfick et. al. used low angle laser light scattering (LALLS) based Malvern Mastersizer in their studies [177], [189], [190] , because particle volumes and volumetric size distribution were natively calculated using this equipment. Other equipments such as Malvern Zetasizer and Nanosight have also been rarely used [7].

Literature includes size attributes such as Feret Diameter, Area Equivalent Circular Diameter and Particle length to quantify the particle size. The size data has been mostly presented in the form of a frequency (number %) distribution, mode diameter of particles and volumetric size distribution.

2.9.4 **Shape analysis**

Particle shape characterisation is carried out by analysing SEM images of wear debris. Attributes such as Circularity (or Roundness), Aspect Ratio, Convexity, Form Factor are mostly used to describe the shape of wear particles[95]. In 1996 Campbell *et al.* used image processing for shape analysis and reported UHMWPE particles to be “rounded or elongated” shape [169]. Moreover, In 1997 Stachowiak introduced a new attribute called Outline Fractal Dimension (OFD), which showed complexity of the boundary of a particle in 2D. Landry and Wirth also used OFD as a shape attribute along with elongation factor (EF) and other shape attributes mentioned above. In 2000, American Society for Testing and Materials used above-mentioned shape attributes as a part of ASTM Standard F1877-98 released for the classification and characterization of wear particles. This standard was reapproved in 2010 as ASTM F1877-05 with no noticeable changes [192]. Billi *et al.* and Mabrey *et al.* used ASTM methods to analyze shape of particles [95], [185].

Shape Categorisation

This has been the subject of a few studies. In 1996 Campbell found that the shapes of UHMWPE particles can be categorised as granules, beads, fibrils and other shapes [169], while Schmalzried

found them to be categorised as Beads, Granules, Fibrils, Shreds, and Flakes. In 2012 Billi *et al.* categorised the shapes as Fibril ,Rod, Oval and Round and Irregular[185]. One issue with shape categorisation has been the difficulty in comparing results between different studies as categorisation may vary between different research groups.

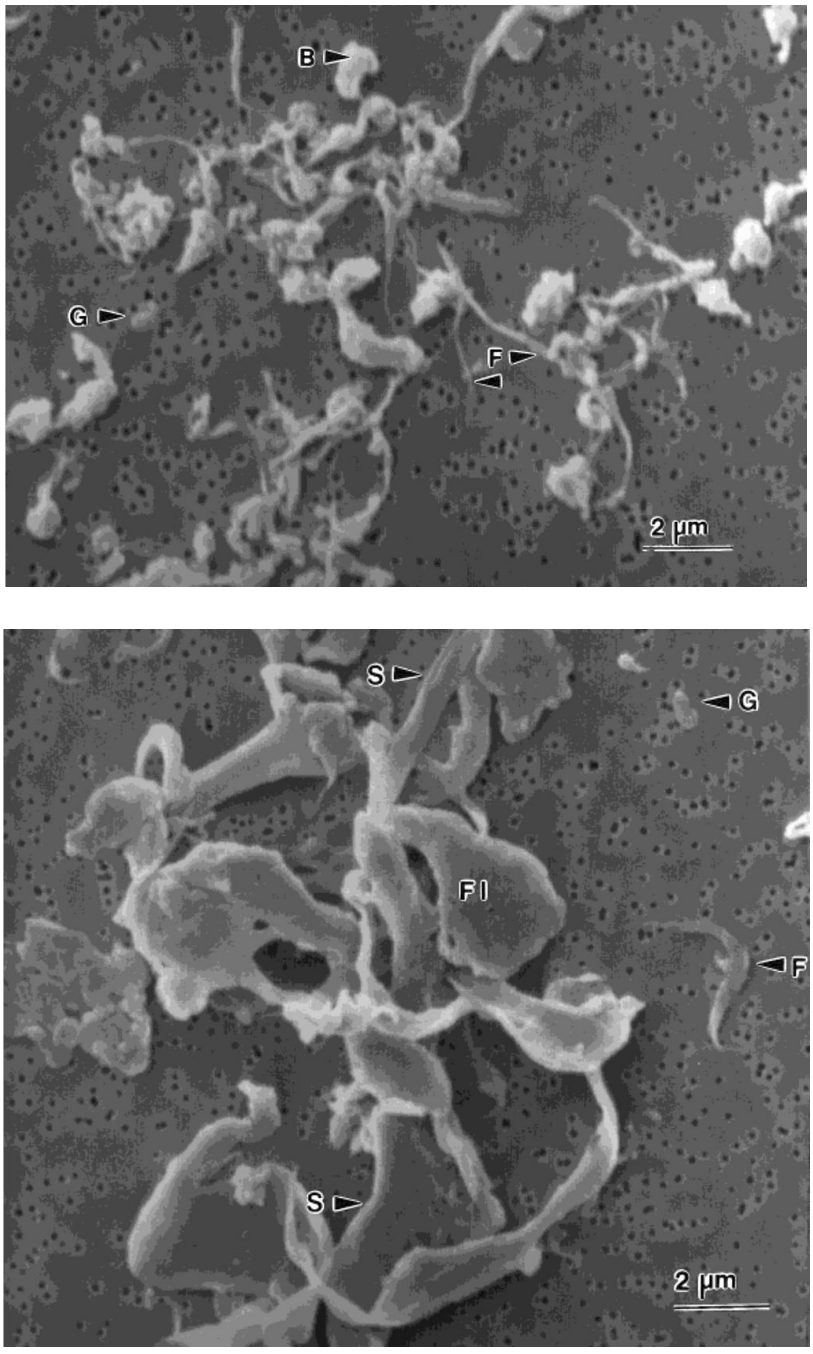

Figure 2.28 Scanning electron micrograph showing shape categorisation of UHMWPE wear debris by Schmalzried *et al.* [89]**. Black arrows show beads (B), shards (S), small fibrils (F), granules (G) and large flakes (FI). Scale bar = 2µm. (Image source[10])**

[10] Source: Schmalzried *et al.* [89]

2.9.5 **SEM image analysis**

Almost all of the SEM image analysis studies have used commercial image analysis software to analyze SEM images. Some commonly used Image analysis software are - Prism Image analysis program used by Stachowiak [193] , Image pro-Plus (Media Cybernetics Datacell Ltd.) used by Tipper *et al.*[178], NIH Image (National Institutes of Health, Bethesda Maryland) used by Wirth and Mabrey [95], [194], eXL II (Oxford Instruments Ltd. England) used by Scott [180]. Since all of these software are commercial products, the mechanisms used to analyse particles haven't been disclosed by these companies. Consequently, there has been no study in the past about the accuracy of particle detection algorithm used for wear particle analysis (especially smaller particles).

In 2007 Miroslav Slouf developed a method called SEMQ that calculated the particle size from area fraction covered by particles, but it was focused on quantification of overall wear, instead of individual particle analysis [195]. Therefore, this study did not provide any information on size distribution or shape analysis. Zhang *et al.* developed another method for shape analysis of metal nanoparticles. This method used Discrete Fourier Transform (DFT) to describe particle shape and texture[196]. However, the shape of metal particles is less complex than UHMWPE particles. Therefore, this method may not be applicable to characterise UHMWPE particles.

The main limitation of existing particle analysis methods was the lack of high-throughput shape analysis and particle image categorisation. This makes the particle characterisation very time consuming as mentioned by Billi *et al.* [185].

Chapter 3 - **Materials and Particle Isolation Methods**

3.1 **Introduction**

The serum proteins present in simulator lubricants constantly coat wear particles generated during the wear testing of UHMWPE implants as shown in Figure 3.1. Therefore, characterisation of wear particles requires the particles to be isolated from serum proteins using a suitable particle isolation method.

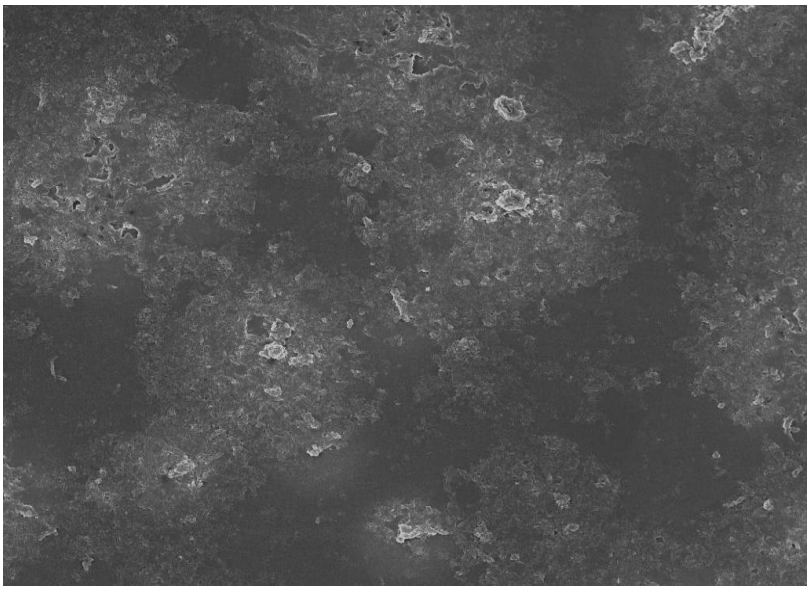

Figure 3.1 A scanning electron micrograph of UHMWPE wear particles surrounded by serum proteins on a membrane filter.

This involves digestion of the serum proteins using an acid, base or enzyme followed by a particle purification process as discussed in Section 0. Figure 3.2 shows a schematic diagram of particle isolation methodology used by current UHMWPE isolation methods.

To develop a novel method for isolation of both conventional and latest generation UHMWPE wear particles, current state-of-the-art isolation methods were tested for their performance. The key elements of each method with their advantages and limitations are described in following sections of this chapter.

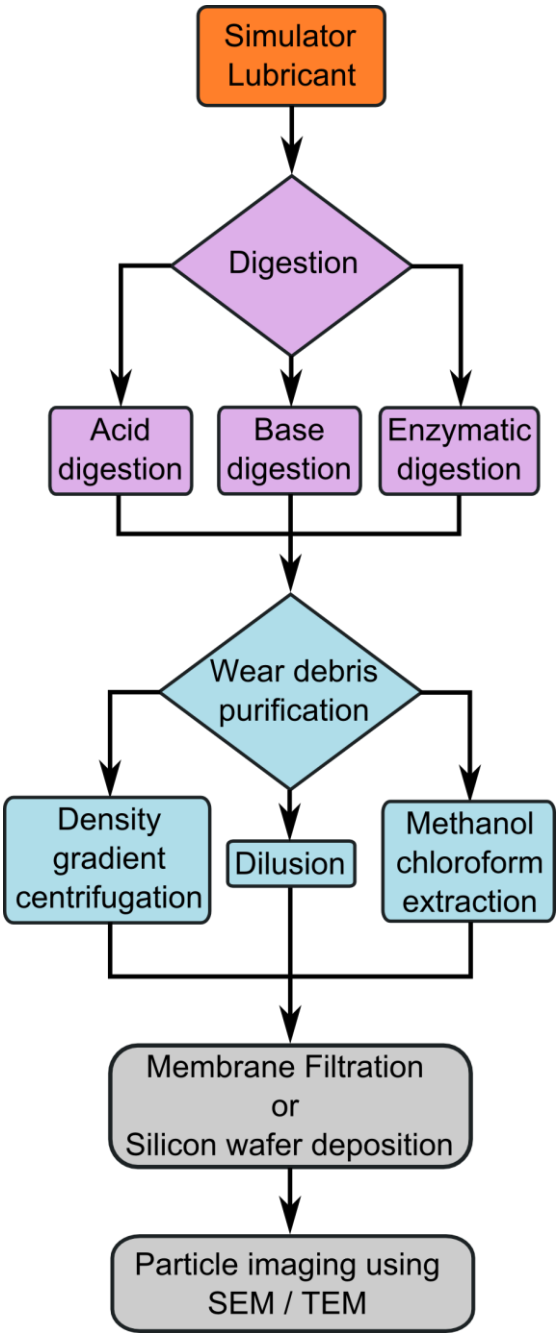

Figure 3.2 A schematic diagram showing methodology used to isolate wear debris from serum based simulator lubricants. The digestion steps are shown by purple colour. Wear debris purification steps are shown by light blue colour. SEM sample preparation and imaging are shown by gray colour.

3.2 Advantages and limitations of state-of-the-art methods

3.2.1 Acid digestion method by Scott[176]

In this method, a strong acid (12M hydrochloric acid) was used to break down serum proteins at 60°C. Magnetic stirring was used to increase the efficiency of digestion. To isolate UHMWPE wear particles, the digest was diluted about 100 times with methanol followed by membrane filtration using polycarbonate membrane. Protein fragments and other impurities were assumed

smaller than the pore size of the PC membrane filter. UHMWPE wear particles were collected on top of the membrane filter.

Since this method involved few steps, it was fast and easy to implement. In addition, the highly acidic environment reduced chances of bacterial growth in the solution.

However, filtration of a large volume (252.5ml) of liquid was required in this method. Since the rate of filtration is slower for smaller pore size, membranes of 0.05µm pore size were used to collect UHMWPE particles, as opposed to membranes of 0.015µm pore size. Furthermore, a few partially hydrolysed proteins were large enough to be left behind with UHMWPE particles during the membrane filtration as seen in Figure 3.4. The method also was not suitable to prepare wear particles for biological studies, as it could not provide purified particles in a liquid medium.

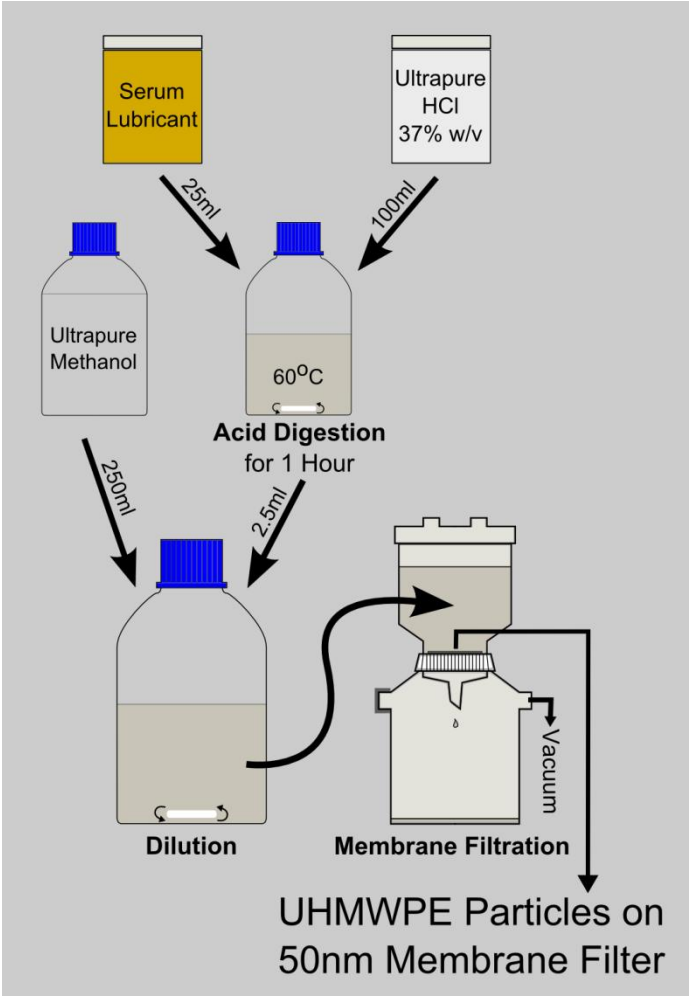

Figure 3.3 Schematic diagram of UHMWPE particle isolation using acid digestion method. Serum lubricant is digested, diluted and then vacuum filtered through a polycarbonate membrane filter. Isolated particles are collected on top of the membrane filter.

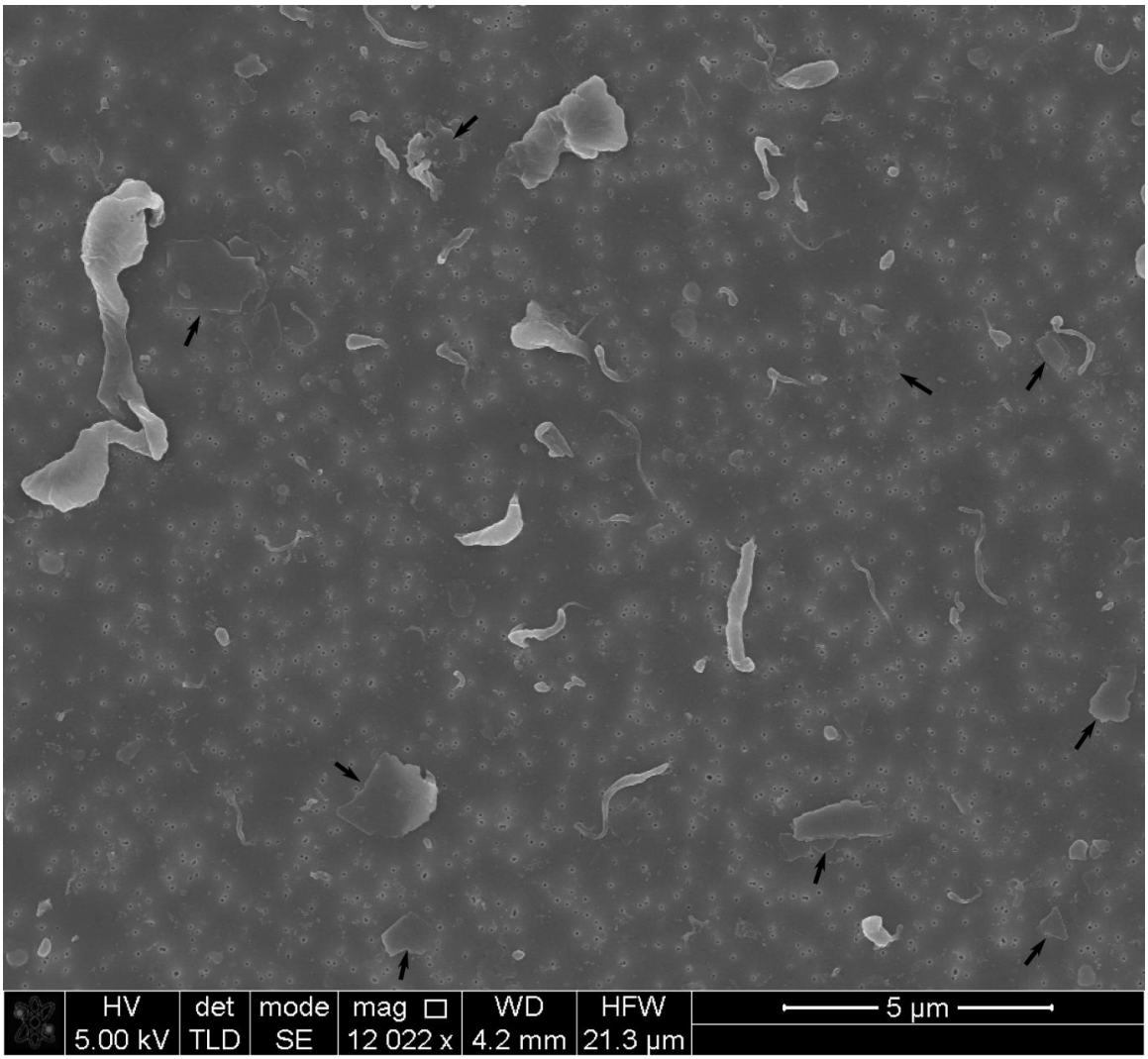

Figure 3.4 UHMWPE wear particles isolated using Scott's acid digestion method. Impurities are shown using black arrows. For comparison, scanning electron micrograph of UHMWPE particles isolated using the newly developed method is shown in Figure 3.18 and scanning electron micrograph of blank 50 nm membrane filter is shown in Appendix III.

3.2.2 **Enzymatic digestion by Niedzwiecki**[175]

In this method, enzymatic digestion was used to break down serum proteins at physiological conditions (37°C and atmospheric pressure). 25ml of the serum lubricant was diluted with equal amount of water to make a final volume of 50ml. Proteolytic enzyme proteinase K was added to the diluted serum lubricant and the solution was incubated at 37°C for 45 minutes with gyratory mixing. 25ml of the digest was then diluted by equal volume of ultrapure water to make a final volume 50ml and filtered through 0.05µm membrane filter. Protein fragments and other impurities were assumed to be smaller than the pore size of the PC membrane filter and were expected to be filtered through the membrane, leaving large UHMWPE wear particles collected on top of the membrane filter.

Even though this method was simple to implement, it had major limitations. The method was not able to completely isolate the wear particles from serum proteins. The enzymatic digestion for 45

minutes was not sufficient enough to break down the serum proteins. Consequently, the SEM images of wear particle showed a layer of impurity covering several areas of the membrane as seen in Figure 3.6.

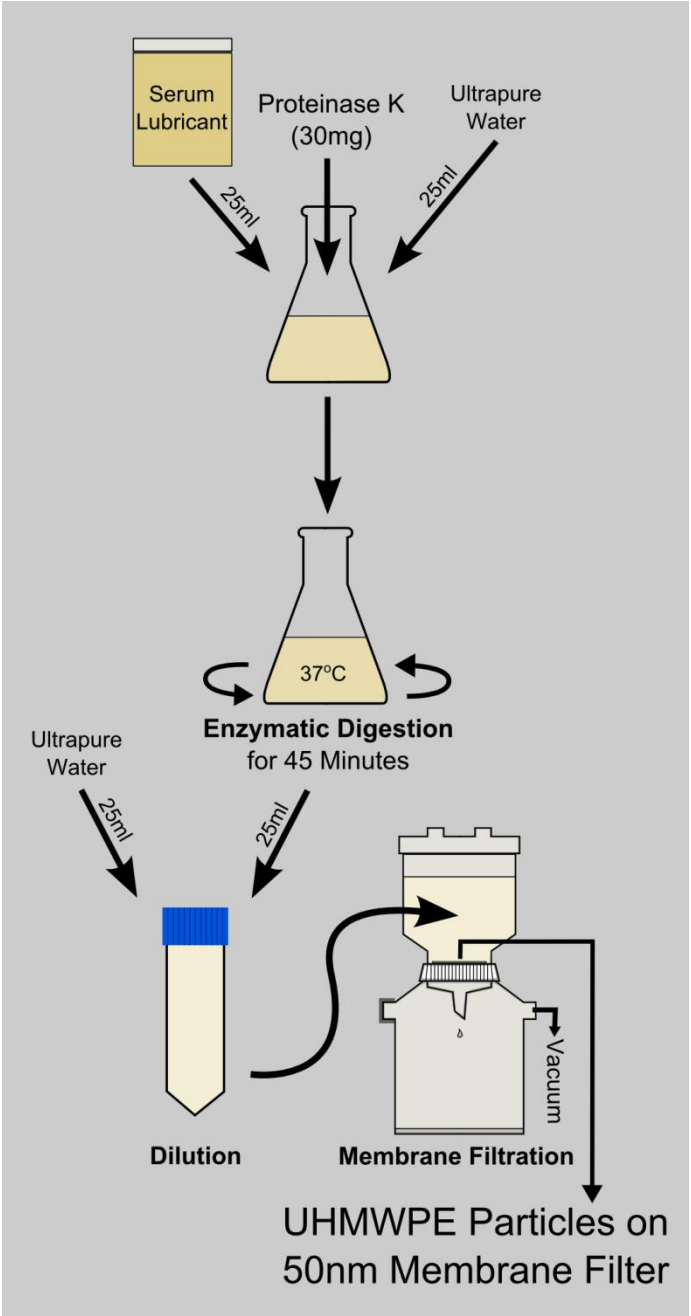

Figure 3.5 Schematic diagram of UHMWPE particle isolation using Niedzwiecki's enzymatic digestion method. Serum lubricant is digested by proteinase K, diluted with water and then vacuum filtered through polycarbonate membrane filter. Isolated particles are collected on top of the membrane filter.

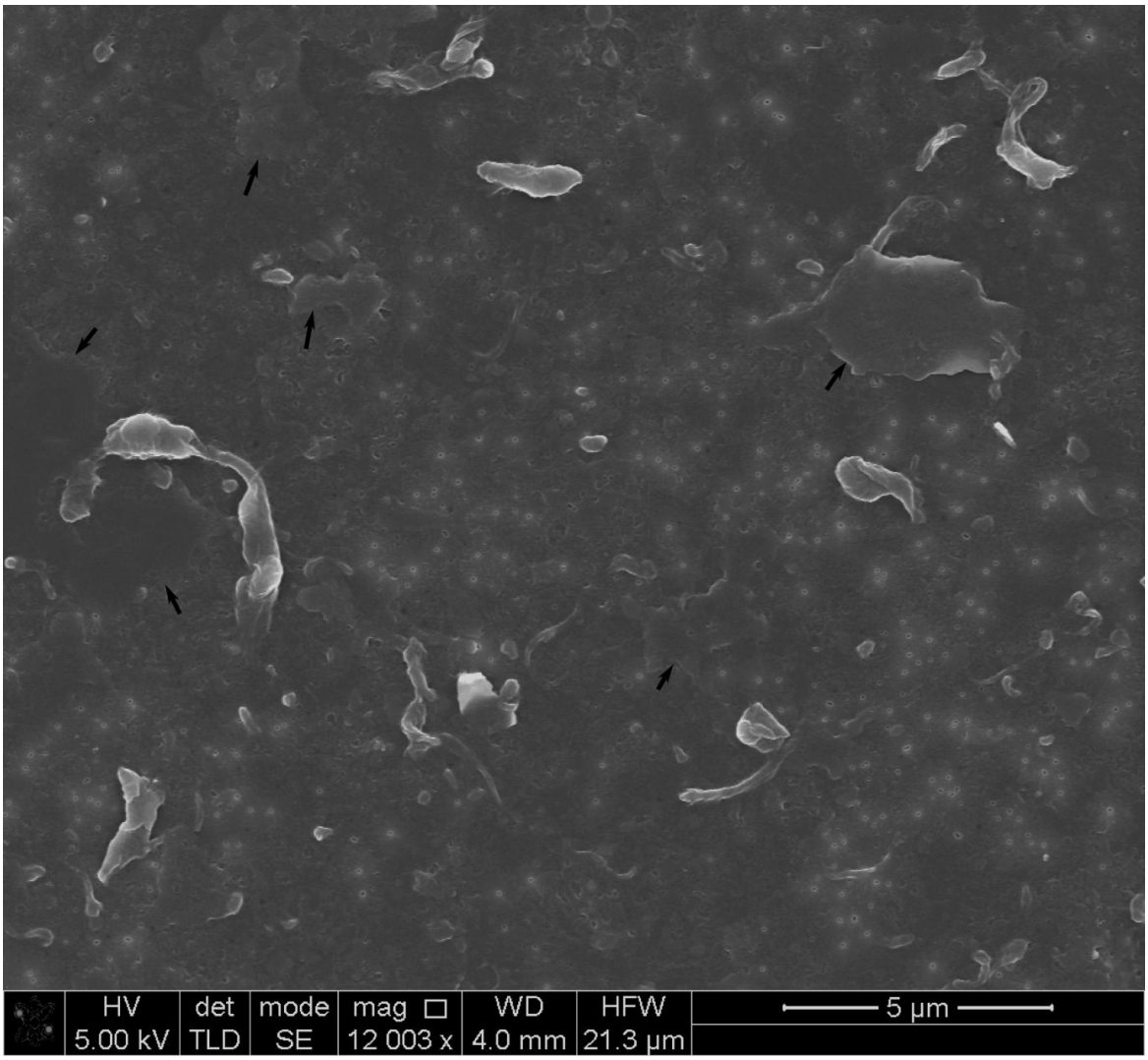

Figure 3.6 UHMWPE wear particles isolated using Niedzwiecki's enzymatic digestion method. Membrane filter appeared to be coated by contaminants. Visible impurities are shown using black arrows. For comparison, scanning electron micrograph of UHMWPE particles isolated using the newly developed method is shown in Figure 3.18 and scanning electron micrograph of blank 50 nm membrane filter is shown in Appendix III.

3.2.3 Enzymatic digestion method by Billi

With an intention to overcome the problems associated with current isolation methods, Billi developed a new UHMWPE wear particle isolation method in 2011. Enzymatic digestion followed by a multistep density gradient centrifugation process was used to isolate wear debris. In order to test the method, an adapted version was developed. The details of the method are described below.

Lubricant serum was mixed overnight in a shaker. Three millilitres of this lubricant was digested at physiological conditions (37°C and atmospheric pressure) along with gyratory mixing with repeated addition of proteinase K. The digestion was carried out in the presence of Ca^{2+} ions to increase the enzymatic efficiency of proteinase K. Since enzymatic digestion was carried out for long durations (over 40 hours) and at physiological conditions, sodium azide was used to retard bacterial growth. At the end of digestion, the sample was centrifuged through layers of sodium

dodecyl sulphate (SDS) to remove any remaining proteins and lipids. Isopropanol gradients were used to further purify and concentrate the particles.

Billi's method was the most comprehensive method tested this study and involved multiple steps of enzymatic digestion and density gradient centrifugations. However, it was found that the method was difficult to implement as it is at Durham. The original method had used a silicon wafer deposition method to display the UHMWPE particles and used a custom-made component to hold the silicon chip on the top of a centrifuge tube. Since centrifugation involved large forces (about 85,000g) and no information was available about the design of this component, it was decided to use 0.015µm membrane filter for the display of particles instead. According to the Billi's protocol[185], lyophilisation was used for drying urea, HEPES buffer and sodium azide before enzymatic digestion step. We followed the same methodology and lyophilized a liquid mixture of urea, HEPES buffer and sodium azide overnight in a 50ml tube. Perforated parafilm was used to seal the tube as shown in Figure 3.7. At the end of lyophilisation (freeze-drying) the tube contents were sticking to the sidewall and the parafilm (Figure 3.7). This made it difficult to recover all of the lyophilised mixture in the next step where lyophilised mixture was to be mixed in 3ml of serum using vortexing. It was believed that this step could have caused loss of particles. Moreover, the toxic nature of dry sodium azide made it necessary to carefully handle the lyophilised mixture in a sealed container during transportation. To ensure complete safety, one would require the freeze drier to be kept inside a Class II ventilated fume hood, which is not easy to implement.

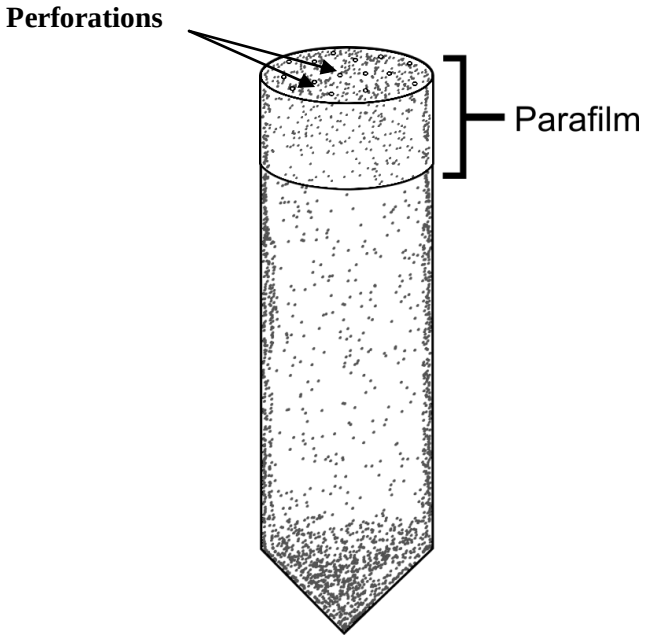

Figure 3.7 Mixture of urea, HEPES buffer and sodium azide at the end of lyophilisation. A significant amount of lyophilised contents were stuck to the tube walls and the parafilm.

Even though 0.04% sodium azide was used to avoid bacterial contamination during the isolation process, at the end of isolation rod shaped features were noticed as shown in Figure 3.10 which may be due to the presence of bacterial contamination. One may also believe that membrane

filtration step could introduce the bacterial contamination. However, this possibility was ruled out as filters were washed with hot water and detergent, followed by rinsing with ethanol. Besides, none of the other methods showed bacteria-like contamination with the same serum samples filtered at similar conditions.

It is also worth noting that this method only used 3ml of serum lubricant for isolation of wear particles, which made it only usable for particle analysis using electron microscopy. The amount of wear particles isolated using this method was not large enough to be used for particle sizing using automatic particle analyzers. In addition, the particles appeared to be agglomerated on membrane filter as seen in Figure 3.10. It might be possible that Billi's method was not optimised for displaying particles on membrane filter because it was designed to deposit particles on silicon wafers.

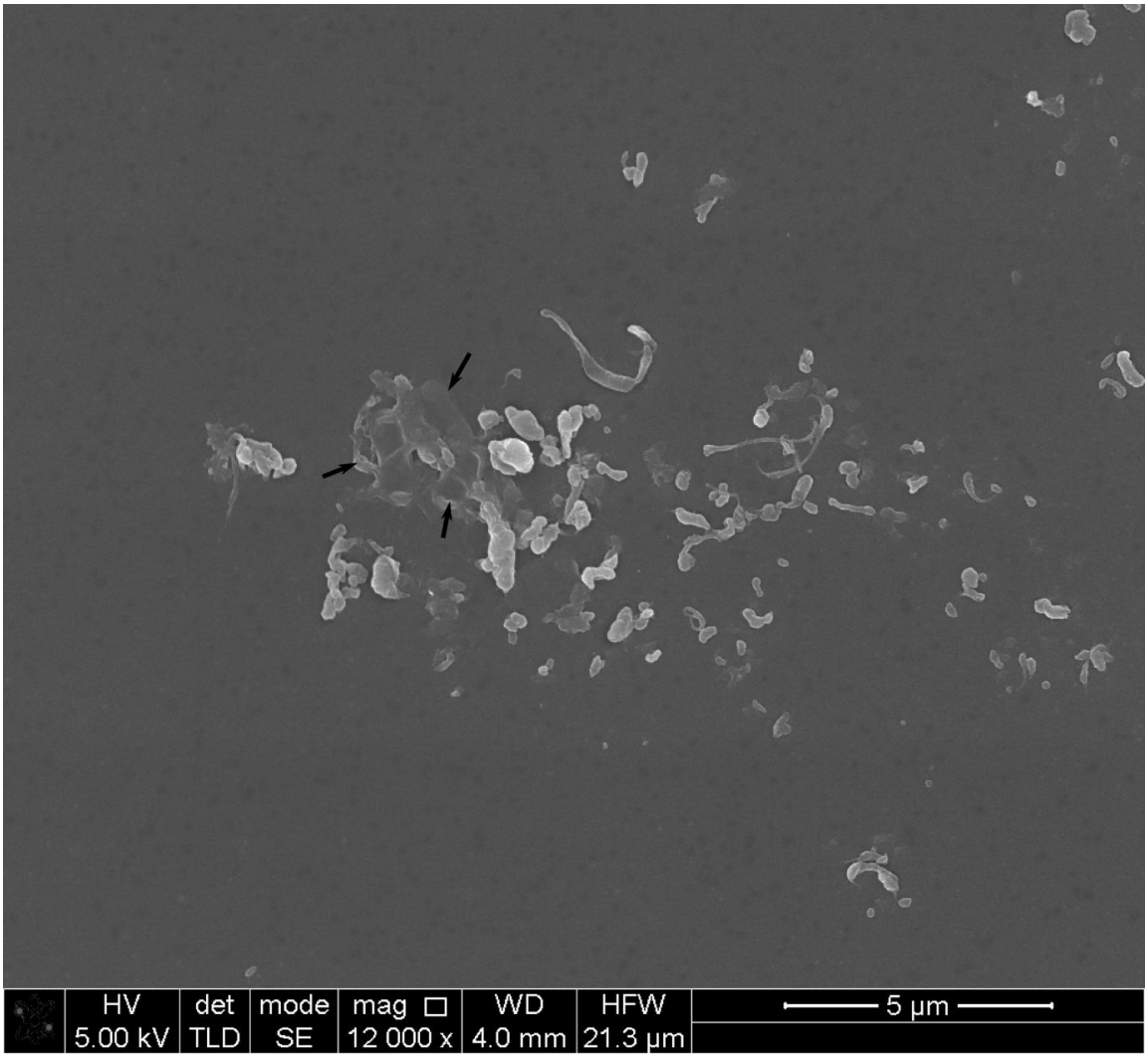

Figure 3.8 UHMWPE wear particles isolated using Billi's enzymatic digestion method. Agglomeration of particles was noticed as seen in the SEM image. Impurities are shown using black arrows. For comparison, scanning electron micrograph of UHMWPE particles isolated using the newly developed method is shown in Figure 3.18.

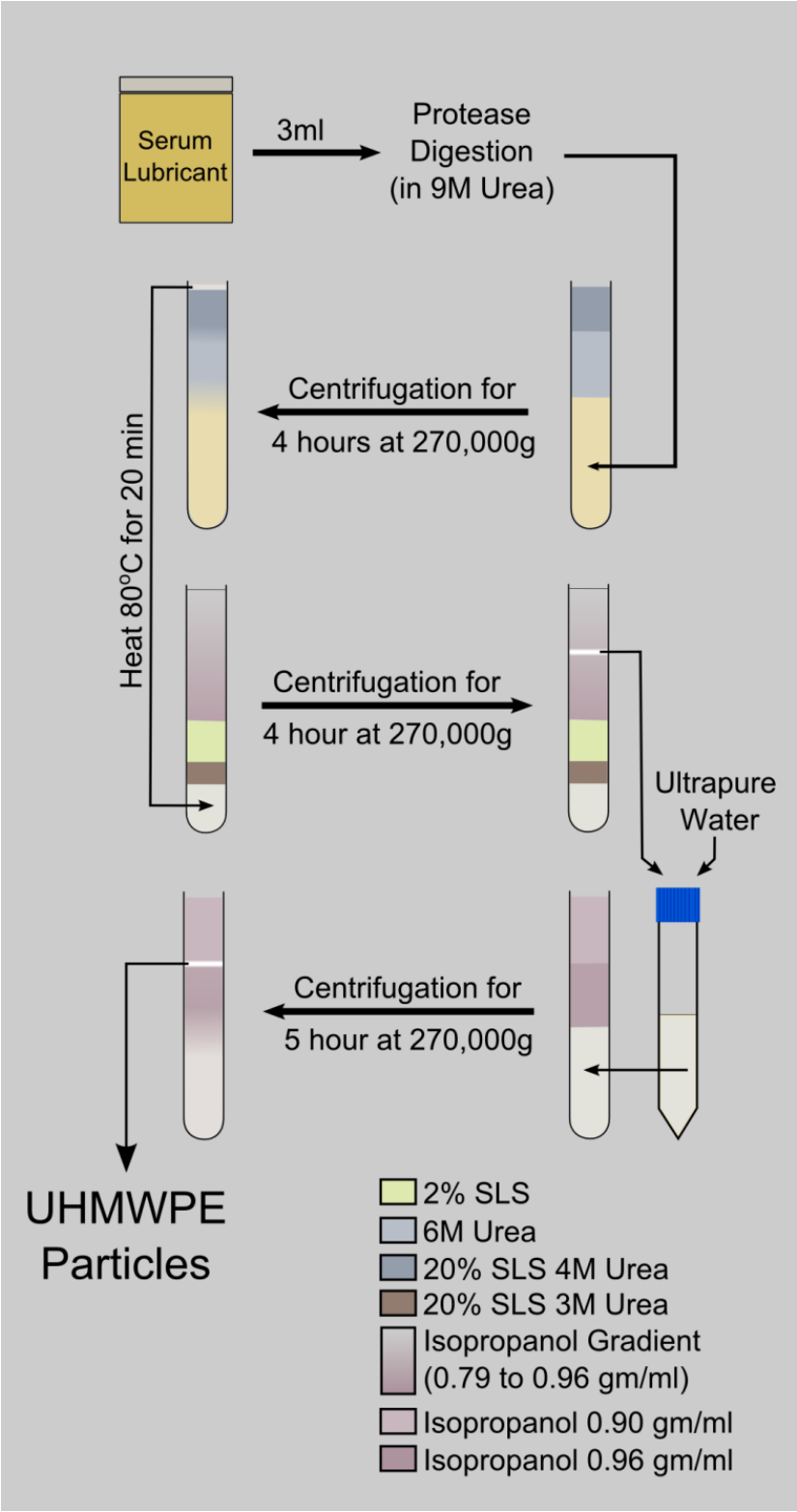

Figure 3.9 Schematic diagram of UHMWPE particle isolation using Billi's enzymatic digestion method. This method used enzymatic digestion, followed by three centrifugation steps to isolate UHMWPE wear debris.

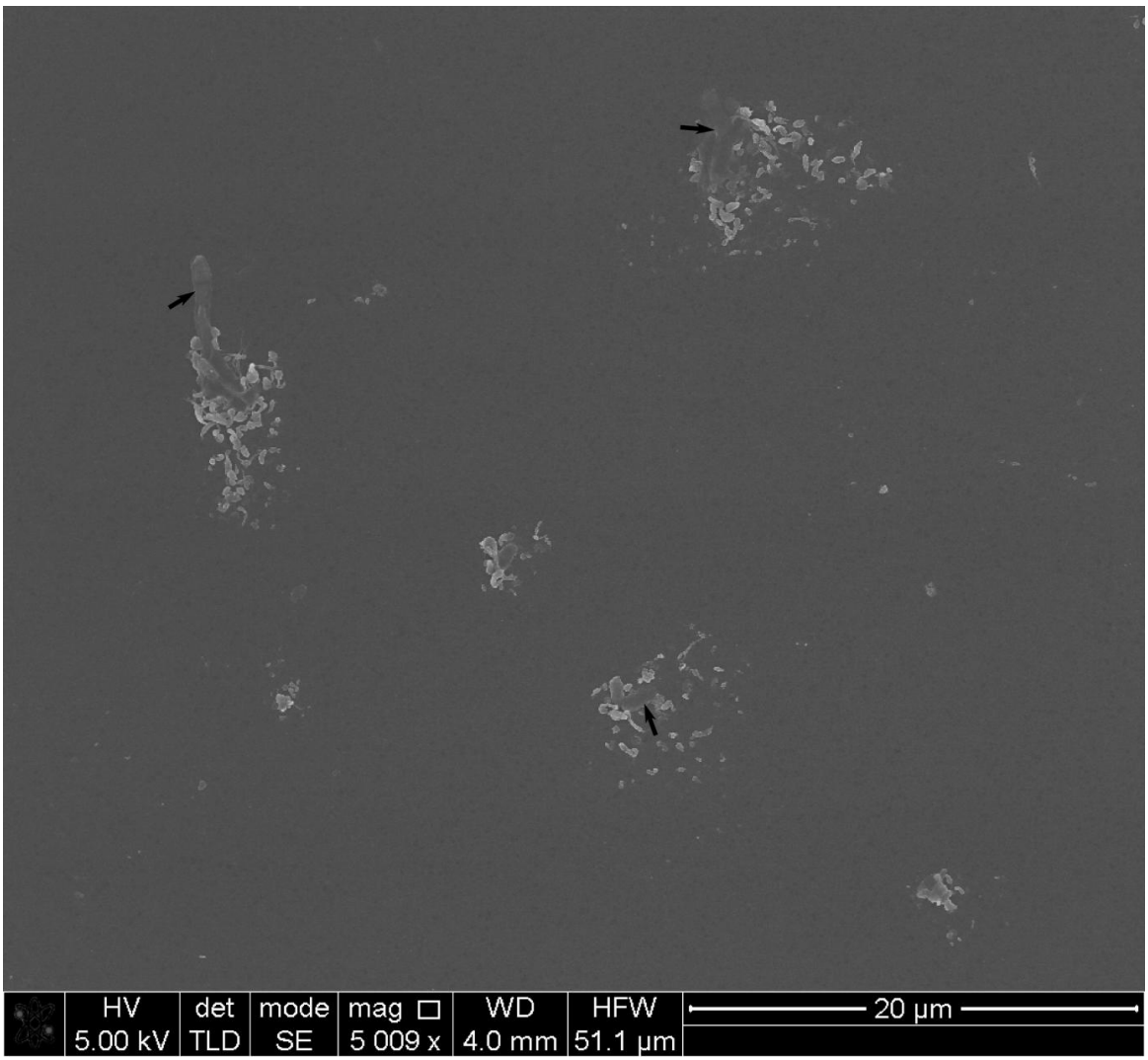

Figure 3.10 SEM image showing the contamination present in UHMWPE wear particles isolated using Billi's method. For comparison, scanning electron micrograph of UHMWPE particles isolated using the newly developed method is shown in Figure 3.18.

3.2.4 **Base digestion method by Tipper** [197]

This method used alkaline hydrolysis to break down the serum proteins. The serum samples were incubated in excess of 48hrs at 60°C to ensure the complete digestion of serum proteins. Methanol: Chloroform extraction was used thrice to separate UHMWPE wear particles from proteins and lipids. Additionally, ice-cold ethanol was used to precipitate lipids present in the solution. Finally, the solution was centrifuged at 15000g for 30 minutes and the supernatant was collected and filtered using polycarbonate membrane filter.

Although multiple stage protein and lipid extraction was used to isolate the UHMWPE particles, the method did not perform as well as expected. Unlike other methods, the final solution had a non-transparent (pale yellowish) colour, which was minimised by repeating the Methanol:Chloroform process several times. However, the large number of washing steps was

believed to cause loss of particles. Moreover, the low speed centrifugation may be an additional reason for loss of wear particles. As a visually clear solution was not achieved at the end of this method, samples were not suitable for automatic particle analysis using Mastersizer. Past studies that used this method showed recovery of nanoparticles [178] but were unable to obtain evenly dispersed nanoparticles like our method or Billi's SWD method. Figure 3.12 shows SEM images of UHMWPE particles isolated using this method.

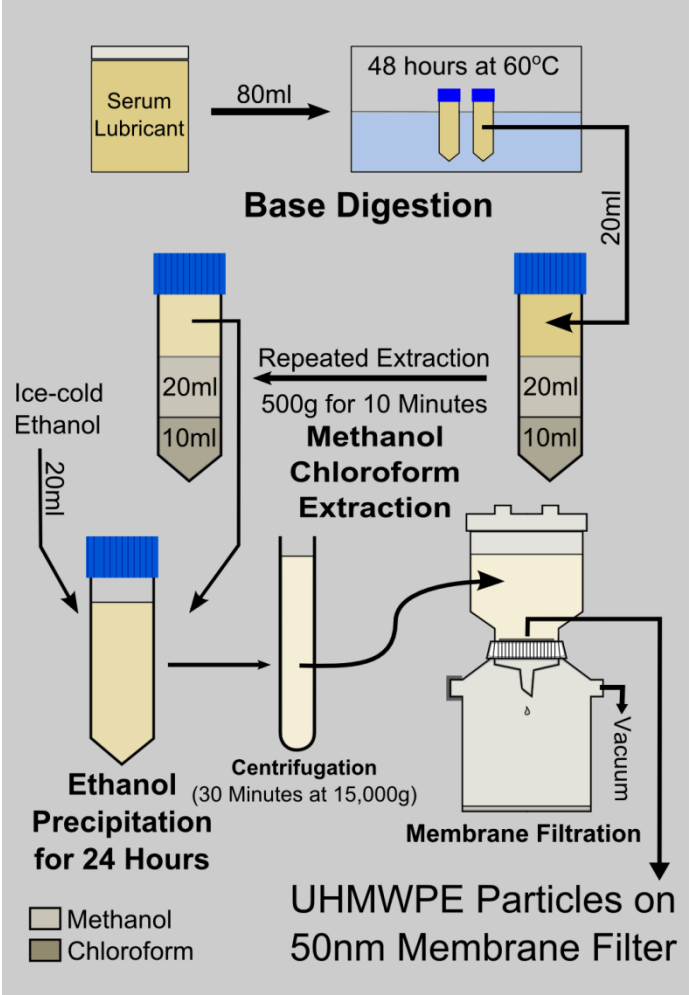

Figure 3.11 Schematic diagram of UHMWPE particle isolation using Tipper's base digestion method. Digestion using a strong base, followed by repeated methanol:chloroform extraction, ethanol precipitation, and centrifugation steps were used to isolate UHMWPE wear debris. Particles were collected on top of polycarbonate membrane filters.

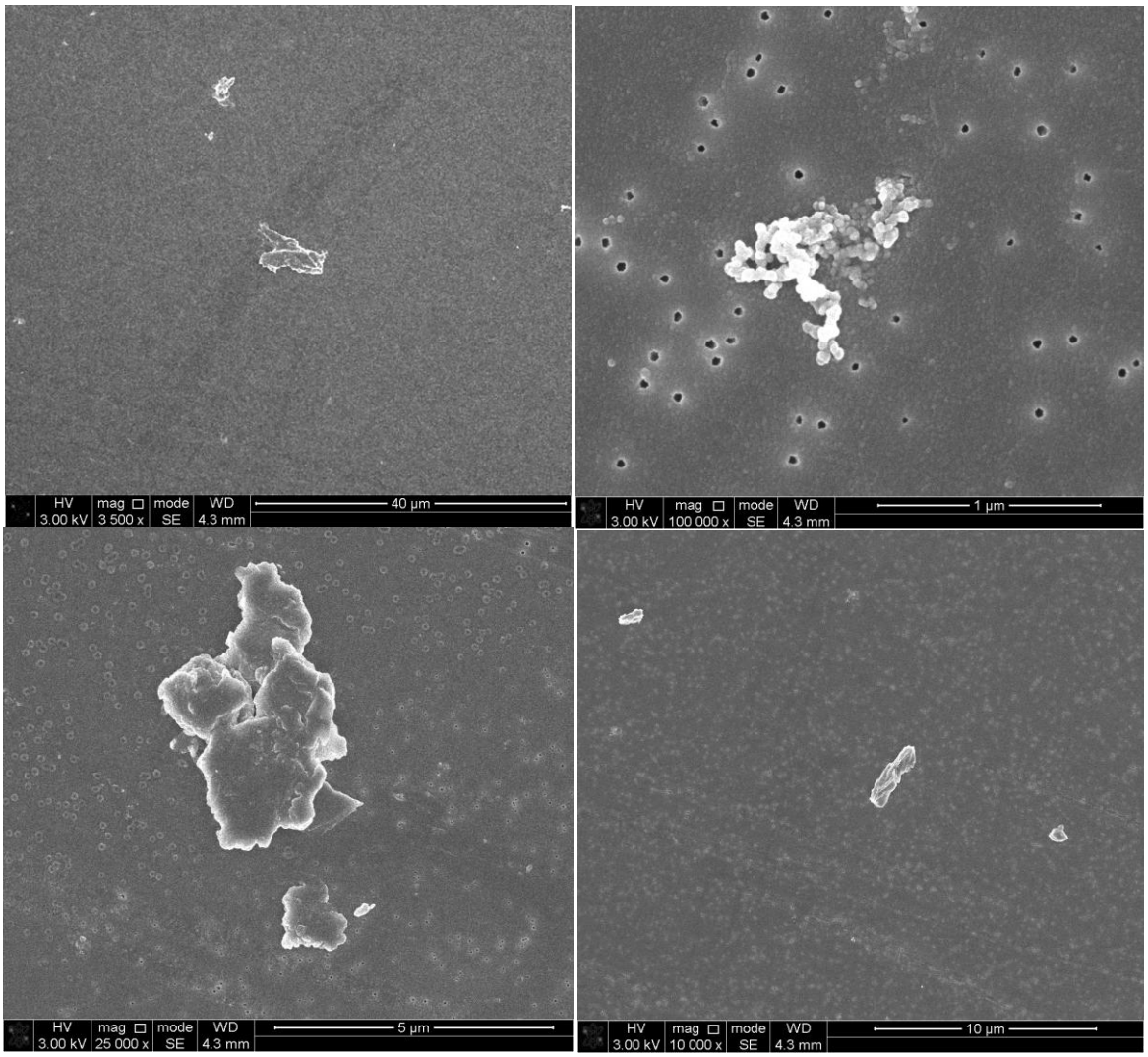

Figure 3.12 UHMWPE wear particles isolated using Tipper's base digestion method. For comparison, scanning electron micrograph of UHMWPE particles isolated using the newly developed method is shown in Figure 3.18 and scanning electron micrograph of blank 50 nm membrane filter is shown in Appendix III.

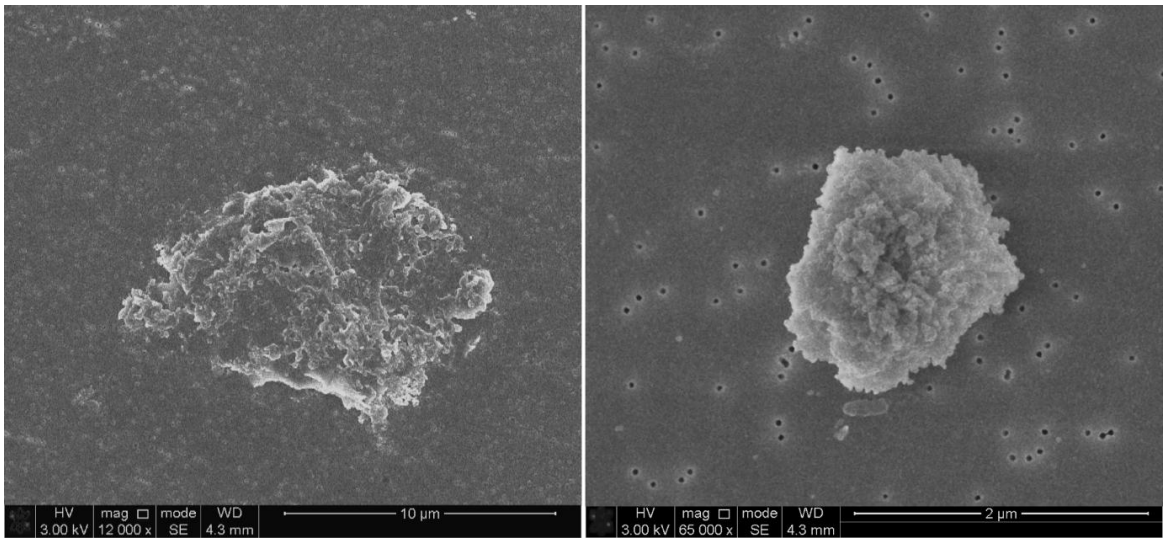

Figure 3.13 Possible impurities present after wear debris isolation using Tipper's base digestion method.

3.2.5 **Base digestion method by Elfick** [177]

This method was developed by Elfick *et al.* at Durham University and used a strong base (5M sodium hydroxide) to breakdown the serum proteins. The method itself was a modified version of base isolation protocol made by Campbell[88].

Serum digestion was carried out for 1 hour in a sonicated bath at 65 C, followed by a two-stage centrifugation process to isolate UHMWPE particles. The first stage of centrifugation concentrated UHMWPE particles as a pellicule and the second stage isolated the particles using an isopropanol density gradient. This method had fewer steps than Tipper's method and produced concentrated wear particles in a colourless medium. However, it needed a few modifications.

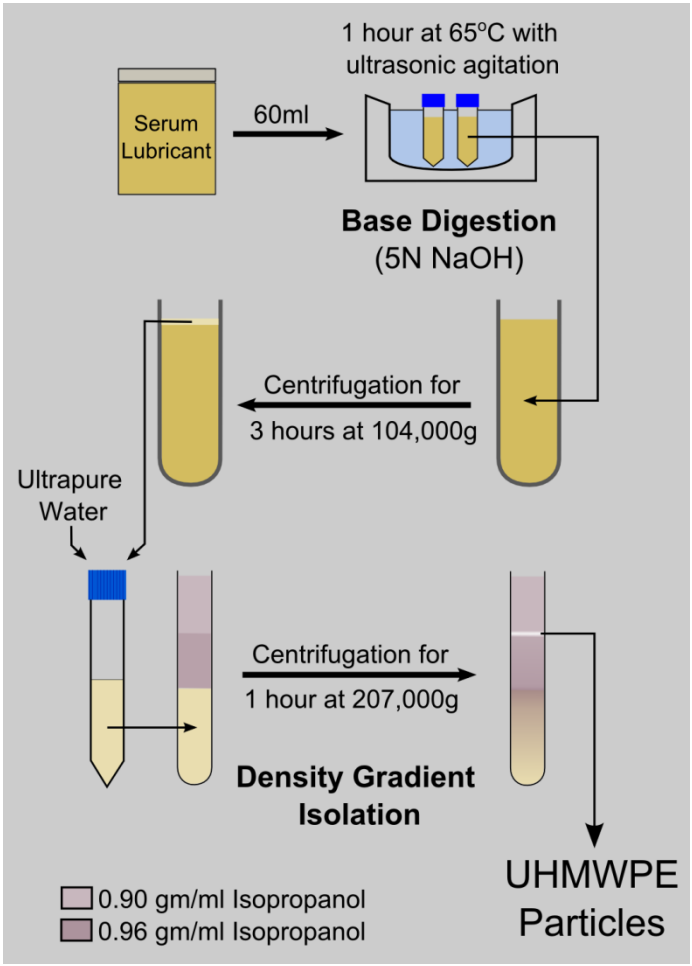

Figure 3.14 Schematic diagram of UHMWPE particle isolation using Elfick's base digestion method. The method used base digestion, followed by centrifugal concentration, and density gradient ultracentrifugation to isolate the wear particles.

The first stage of centrifugation required use of conventional open top centrifuge tubes for concentration of particles. However, this step had safety issues due to the possibility of a reaction between aluminium tube caps of the rotor buckets and the alkaline particle concentrate in case of any undesired spillage. Therefore, it was essential to use sealed centrifuge tubes. However, sealed

tubes need to be filled up to the top, which caused the pellicule to stick on inner surface of tubes. This was undesirable due to particle loss that could have occurred during this step.

Moreover, centrifugation time of 1 hour during second isolation step was found to be insufficient for samples with a large quantity of UHMWPE particles.

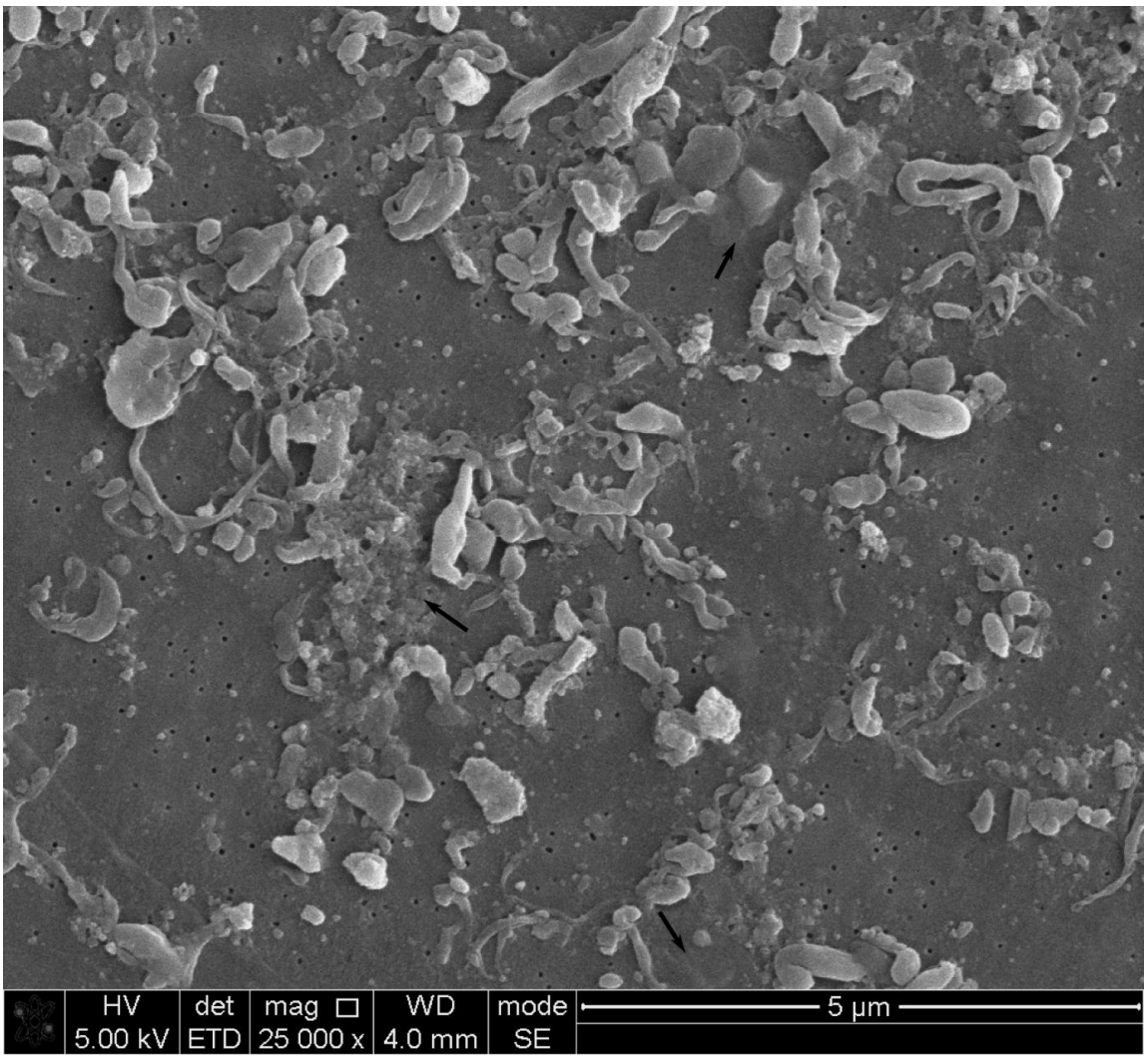

Figure 3.15 UHMWPE wear particles isolated using Elfick's base digestion method. Agglomeration of particles was noticed. Impurities were found attached to particles as shown using black arrows. For comparison, scanning electron micrograph of UHMWPE particles isolated using the newly developed method is shown in Figure 3.18 and scanning electron micrograph of blank membrane filter is shown in Appendix III.

3.3 Development of a novel method

3.3.1 Modified base digestion method

In order to overcome the limitations of above methods, a new UHMWPE wear particle isolation method was developed. Base digestion was used to digest the serum proteins due to its proven efficacy of digesting serum proteins as well as by previous studies (Discussed in Section 6.1, page 206). A two-stage density gradient centrifugation was used to purify the particles. The detailed description of the method is given in the sections below.

3.3.1.1 Serum Digestion

Frozen 250ml serum was thawed out at 37°C and was mixed overnight in a rocker. Number of freezing and thawing out steps was kept minimum by just performing it once. The whole method was designed to be scalable in case a larger volume of lubricant serum needed to be analysed. Lubricant serum was taken in multiples of 25ml. Each 25ml was pipetted into sterile 50 ml centrifuge tubes and then 7gms KOH was added in each tube to make 5M KOH solution. The tubes were then incubated for 24hours Hrs at 60°C in a water bath. At the end of 24 hours, tubes were vortexed thoroughly followed by sonication for 10 minutes. The digest was then kept again at 60°C for further 24 hours. The rationale behind above steps was the combination of a long digestion time (similar to Tipper's method [178]), with sonicated agitation (similar to Elfick's method [177]), to ensure complete digestion of serum proteins.

3.3.1.2 Particle Isolation

For isolation of UHMWPE particles from digested serum, a two-step density gradient ultracentrifugation was used. The isolation protocol was developed as a modified version of Elfick's density gradient isolation method previously developed at Durham University. All solutions used in this method were filtered using 0.05µm filters to minimize the introduction of any impurities. The pipettes and tubes were also rinsed using 0.05µm filtered ultrapure water before their use, for the above-mentioned reason.

Step 1

Each 25 ml digest was transferred to an Optiseal™ 30ml polyallomer tube and 3ml ultrapure water was layered on top followed by a layer of 0.90gms/ml isopropanol as shown in Figure 3.16.

Layering of ultrapure water between the digest layer and isopropanol layer served three purposes. Firstly, it helped avoiding formation of a dense pellet at the interface. Secondly, it removed impurities such as proteins and lipids heavier than water. Thirdly, it acted as a washing layer for UHMWPE particles. After centrifugation at 32000 rpm (175,000g) using Beckman SW32Ti rotor for 4 hrs the concentrated digest was collected at the interface between isopropanol and water layer.

The digest was then re-suspended in an equal volume of ultrapure water. The volume of re-suspended digest was approximately 6ml.

Step 2

An isopropanol density gradient, similar to the one used in Elfick's method [177], was used to isolate wear particles from the digest. 3ml of the re-suspended digest from step 1 was layered at the bottom of an Opentop™ 13.2ml polyallomer tube. Three layers of isopropanol (0.98gms/ml, 0.96gms/ml and 0.90gms/ml) were layered successively on top of the re-suspended digest as shown in Figure 3.16. The density gradient was centrifuged at 40,000rpm (274,000g) using the Beckman SW41 rotor for 4 hours.

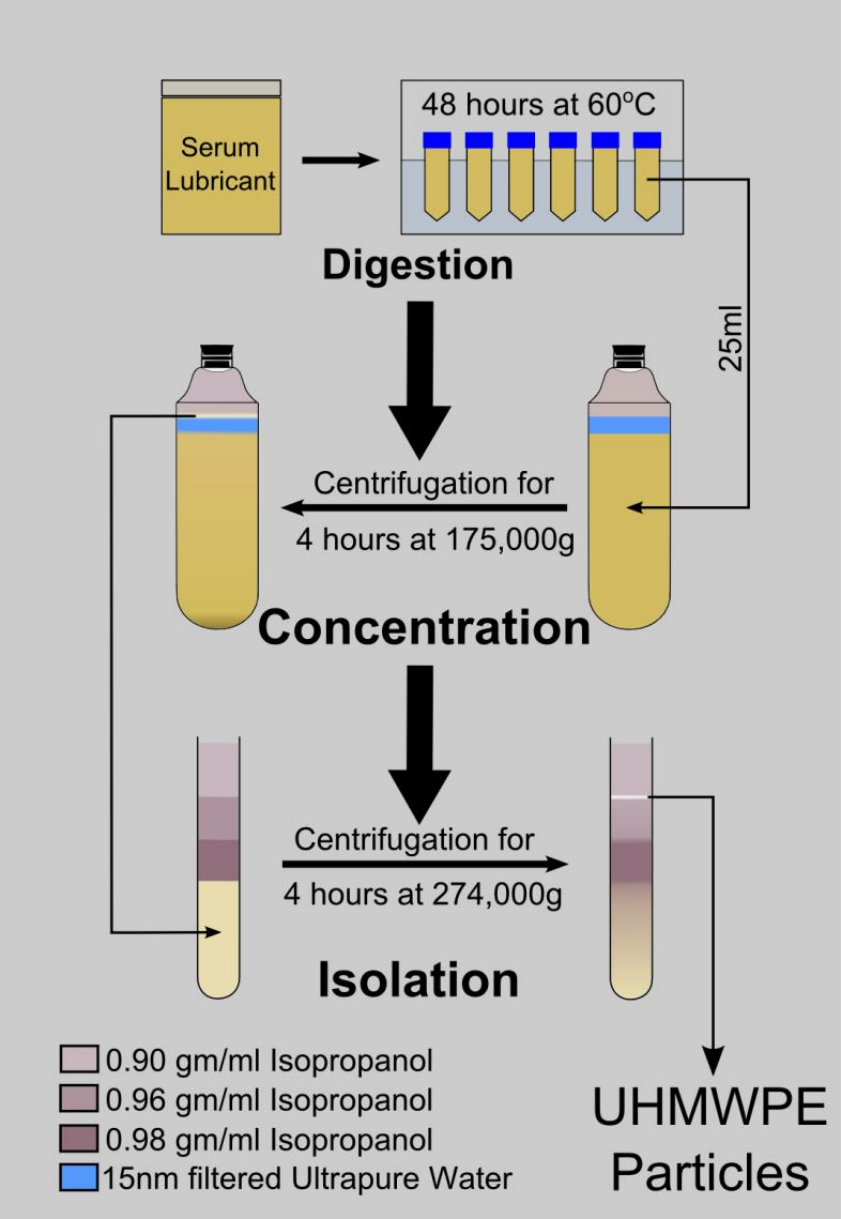

Figure 3.16 Schematic diagram of the modified base digestion method developed in the current study. The whole method was divided into digestion, concentration and isolation steps.

Since density of the UHMWPE particles is around 0.930 gms/ml [177] particles were banded between 0.90gms/ml and 0.96gms/ml isopropanol layers as shown in Figure 3.17.

Approximately 3ml of the particle concentrate was taken out of each tube using a sterile Pasteur pipette. The solutions from same samples were pooled together and were stored in sterile 15ml tubes at 4°C. Therefore, for every 25ml of serum lubricant taken for analysis, 6ml of final purified particle concentrate was obtained at the end.

In order to verify the complete removal of proteins, lipids and other impurities, control serum lubricants were also isolated. No banding was found between isopropanol layers at the end of step 2 (Figure 3.17). Moreover, SEM images of control serum showed no particles or impurities.

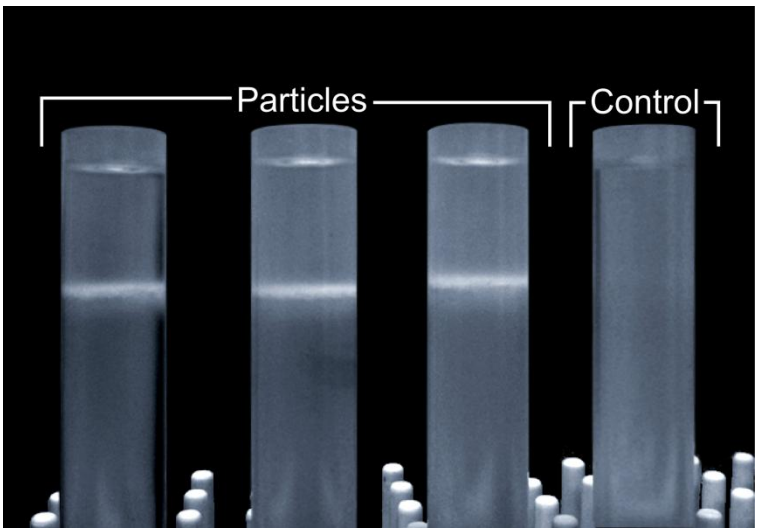

Figure 3.17 Purified UHMWPE particles seen as opaque white banding between 0.90gm/ml and 0.96gm/ml isopropanol layers after density gradient ultracentrifugation (isolation step). Control tube showed no visible bands due to absence on any UHMWPE particles in this sample.

This proved that the UHMWPE particles were completely separated from impurities by the end of the two isolation steps. SEM imaging further verified the capability of the method by displaying purified particles on a membrane filter Figure 3.18.

3.3.2 Preparation of SEM samples

As mentioned in previous section, each particle isolation used 25ml of serum and obtained particles in a final solution of 6ml at the end of isolation. 250 µl of this particle concentrate was diluted to 10ml in 0.93gms/ml isopropanol (pre-filtered with 0.015 µm filter) and then vortexed and sonicated twice for 10 minutes. Then, the particles were collected on top of a polycarbonate membrane filter using a vacuum filtration unit. After comparing membrane filters with pore size of 2um, 0.2um, 0.05um and 0.015um for particle display, we standardised upon a 0.05µm Whatman Nucleopore™ membrane filter for quick display of particles and 0.015µm filter for SEM analysis due to the minimum loss of particles with 15nm pore size (as explained Section 2.9.1, page 57) and a featureless background at magnifications ranging between 1000x - 20000x.

Figure 3.18 shows a SEM image of UHMWPE wear particles isolated from lubricant

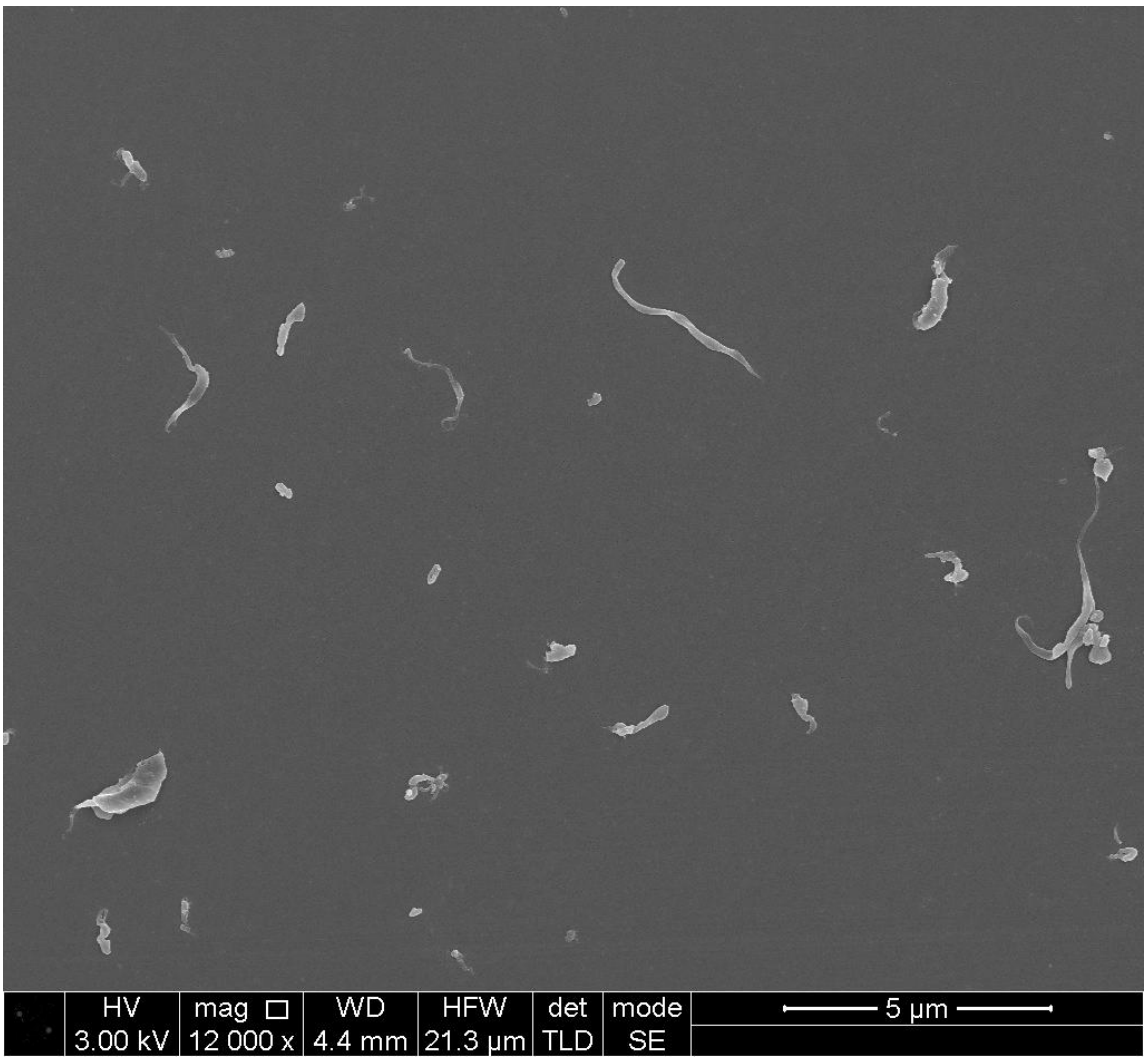

Figure 3.18 UHMWPE particles isolated by modified base digestion method and deposited on a 15nm pore size membrane filter. Unlike other methods, no contaminants were observed on the background filter.

3.3.3 **SEM Imaging**

FEI Heios Nanolab 600 SEM was used for imaging particles. The electron beam in SEM was set to 5kV voltage and 86pA current. A working distance of 4cm was used for imaging particles in high-resolution immersion mode. Since electron microscopy images tend to be noisy with lower dwelling times, a minimum dwelling time of 30µs was used. Images captured at 12000x, 15000x and 20000x magnification, Scale = 4µms were used for particle size/shape analysis and at other magnifications (3500x to 200,000x) for qualitative analysis. The dimensions of all captured images were 1024 pixels by 943 pixels. Moreover, a minimum of 100 images were captured for each sample, which captured 500 or more particles for characterisation.

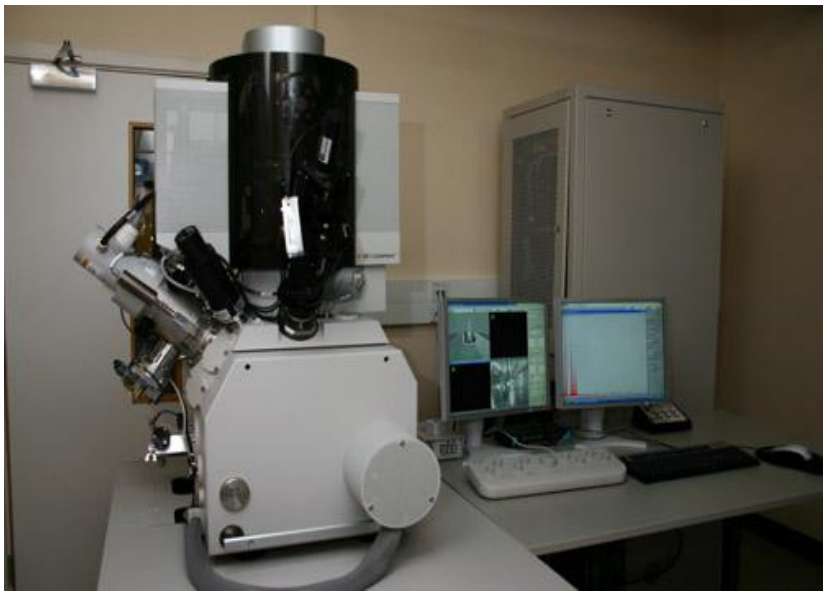

Figure 3.19 FEI Helios Nanolab™ 600 scanning electron microscope used for SEM imaging in the current study.

3.3.4 Energy Dispersive X-ray (EDX) analysis

EDX analysis was used to distinguish UHMWPE wear particles from the background or any impurities present in the samples. Figure 3.20 shows the EDX analysis of UHMWPE wear debris. SEM image shows the selection of a UHMWPE wear particle in red colour and selected of the background in blue colour. The EDX graph showed carbon (C), oxygen (O) and gold (Au) peaks for background, while only carbon (C) and gold (Au) peaks for UHMWPE wear particle. Samples were coated with gold. Therefore, a peak for gold was observed for both particle and background.

No oxygen peak was observed for UHMWPE because UHMWPE is only composed of carbon and hydrogen elements. Both carbon and oxygen peaks were observed for background because the background material was polycarbonate, which is composed of carbon, hydrogen and oxygen. Absence of any other elements indicated the complete isolation of UHMWPE and cleanliness of particle isolation and SEM sample preparation methodologies. EDX does not detect lighter elements such as hydrogen. Therefore, no peak was generated by hydrogen in EDX graph for both UHMWPE wear debris and background.

A)

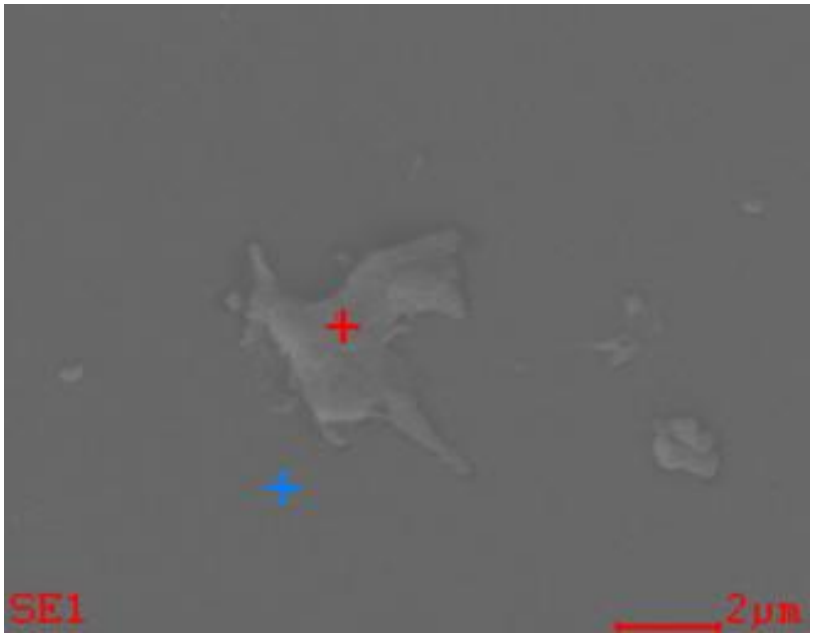

B)

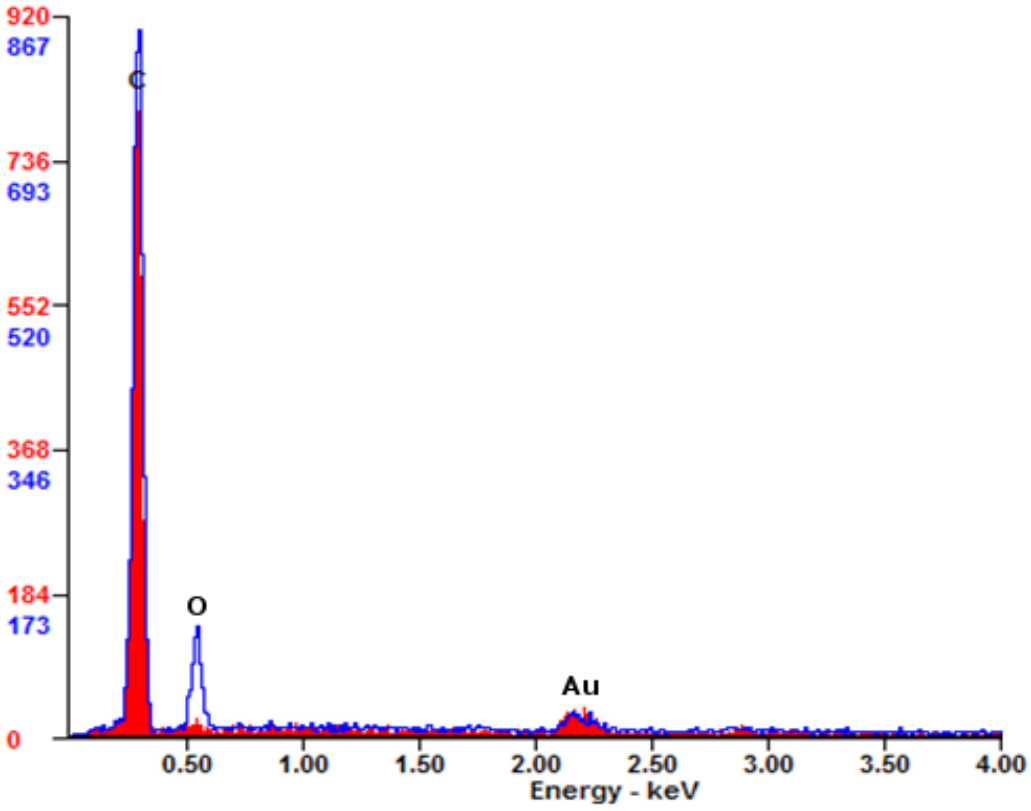

Figure 3.20 EDX analysis of UHMWPE wear debris isolated by using modified base digestion method of present study. A) SEM image showing a point selection inside UHMWPE particle (red cross) and point selection for background membrane filter (blue cross). B) Blue coloured graph showing carbon(C) and oxygen(O) peaks from polycarbonate filter and gold(Au) peak from gold sputter coating (in blue). Red coloured graph showing carbon(C) peak from UHMWPE particles and gold(Au) peak from gold sputter coating. No oxygen (O) peak was observed for UHMWPE particle due to the absence of oxygen in its elemental composition. Lack of nitrogen and sulphur peaks demonstrate complete removal of serum proteins.

Chapter 4 - **Advanced Software Development for Particle Analyses**

4.1 **Introduction**

Characterisation of particles is an important activity in academia and industry. Both sectors use a number of methods and equipments to characterise particles. When particles are micron sized or larger, the choices of methods and equipments are plenty. However, when the size of particles is submicron and nanoscale, only a few specialised techniques and equipments are capable of particle analysis. Particle characterisation becomes challenging when particle size varies from few nanometres to millimetres.

UHMWPE wear debris produced in joint implants exhibits a wide range of size distribution. Previous studies have found size of UHMWPE wear particles from as small as 10 nanometres to as large as few millimetres [178], [185]. Moreover, wide varieties of shapes have been observed for UHMWPE wear particles [89], [169].

The most accepted method to characterise particles of such large size range and wide variety of shapes is the combination of electron microscopy as an imaging technique, followed by particle analysis using computer software. Another option is the use of commercially available particle analysers. Several industries prefer commercial size analysers due to their ability to characterise particles in relatively short period of time and with sufficient accuracy. However, these particle analysers give no information about the shape of particles.

In this section, two current commercially available size analysers Mastersizer and Nanosight were compared for analysis of UHMWPE wear debris and their limitations were demonstrated. Afterwards, a comparison of commercial and freely available software was done for analysis of UHMWPE wear debris. Due to the limitations of the current particle analysis methods, new software was developed to efficiently and accurately characterise UHMWPE wear debris from SEM images. The image analysis methodology and implementation of the software have been described in the final section of this chapter.

4.2 Commercially available particle analysers

Two commercially available particle analysers Mastersizer and Nanosight were compared for their usability to analyse UHMWPE particles.

4.2.1 Mastersizer

Mastersizer is one of the most widely used automatic particle size analysers with a large 100nm - 3000µm size range. It is based on Low Angle Laser Light Scattering (LALLS) and uses Mie theory, also known as Lorenz–Mie theory to calculate the size of particles. Mie theory was developed to predict the way light is scattered by spherical particles and deals with the way light passes through, or is absorbed by particles. Each particle has its own characteristic scattering pattern. However, one needs a priori knowledge of the refractive index and absorption to calculate the particle size. Moreover, particles are assumed spherical in shape. For irregular particles scattering observed at wide angles can be significantly different to that seen for spherical particles. Analysis of the data produced by irregularly shaped particles can therefore lead to inaccurate results. For this reason, the Malvern Mastersizer 2000 system provides users with the ability to select an irregular-particle analysis mode. The mechanism behind this mode has not been disclosed by Malvern Instruments. However, it is thought to be based on combination of readings obtained from wide angle, large-angle and back scatter detectors in addition to the readings from focal plane detector.

The equipment itself consisted of a flow cell, protected by a glass window and outer cover. Sample was introduced into the cell with the help of tubes connected to a sample dispersion unit with an inbuilt pump. Before using the equipment the flow cell, rubber tubes and sample dispersion pump were cleaned by circulating ultrapure water. The cleanliness of the equipment could be checked by the live laser obscuration value shown for a circulating fluid. This value was indicative of the extent of laser obscuration by the sample. The equipment was only ready to use when obscuration value was near zero (indicated by a green colour). Moreover, according to the equipment instructions, 10% laser obscuration was recommended for particle size up to 3-4µm and 15% laser obscuration was recommended for particles of median size 50µm. In addition, it was mentioned that lower laser obscuration would adversely affect the accuracy of measurement. Therefore, a minimum of 10% value of laser obscuration was chosen as UHMWPE particles were predominantly submicron in size.

In order to test the ability of Mastersizer to analyse UHMWPE wear debris, large amount of isolated debris dispersed in 0.93gms/ml isopropanol were pooled together and divided into three parts. First part was used for Mastersizer, second for Nanosight (described in next section) and third part for SEM analysis. In order to keep good dispersion during measurement, the sample was circulated in 0.93gms/ml isopropanol. During measurement, it was noticed that the equipment required significantly large amounts of sample to reach 10% obscuration. The maximum

obscuration reached in the present study was 11.7%. The requirement of a large amount of wear debris by Mastersizer was a significant limitation because new generation materials produced very low wear. Isolating large quantities of wear particles from these samples wasn't practical. Therefore, the size distribution data shown here is only for comparison between different particle analysis techniques. Figure 4.1 shows a comparison between size distribution graphs produced by Mastersizer, Nanosight and SEM.

4.2.2 **Nanosight**

Nanosight is a nanoparticle size analyser that measures particle size in 10nm - 1000nm size range. It detects brownian motion of particles in a liquid medium by recording the movement of particles illuminated by shining a laser through the liquid in a flow cell. As the laser hits the surface of particles, it gets diffracted and causes the particles to appear as bright spots of light moving under brownian motion. This movement of particles is recorded using a digital video camera and analysed using Nanosight NTA software. This method also requires information about viscosity and temprature of liquid and calculated the particle size using Stokes-Einestien equation. Nanosight equipment consisted of a horizantal flow cell with a laser device adjacent to it. The flow cell had a transparent glass window to record the brownian motion using a video camera. Also, the flow cell was visible through an optical microscope. The purpose of the microscope was to locate the target area of cell for recording.

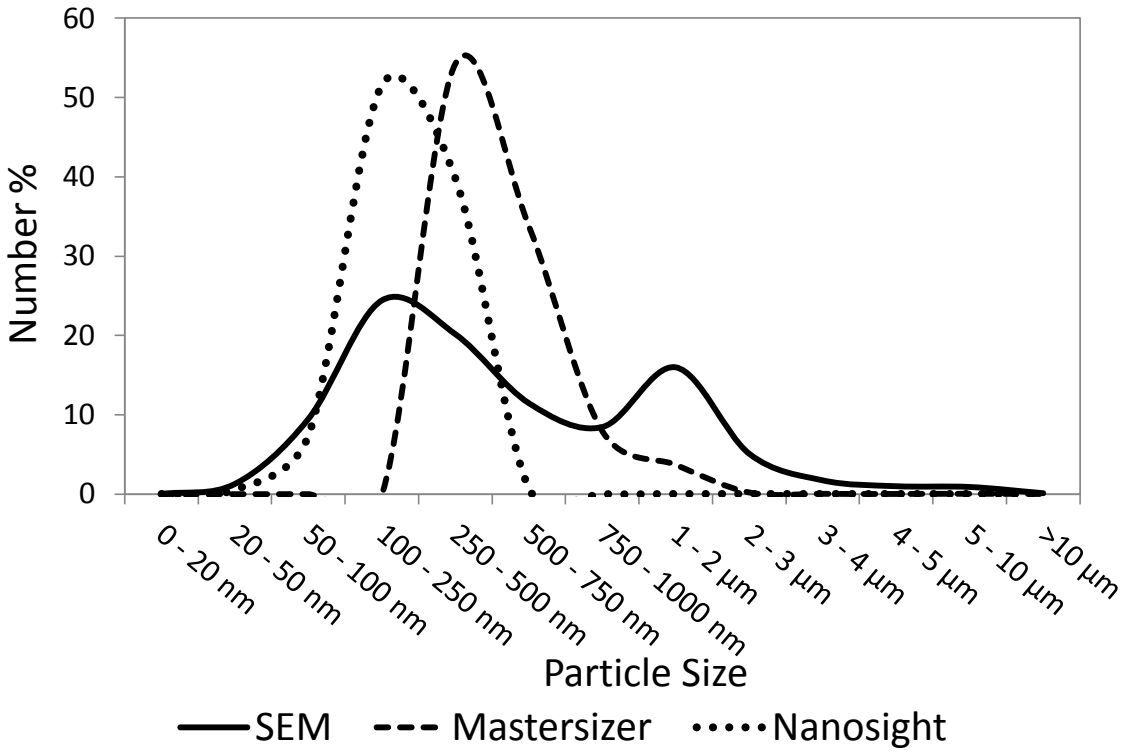

Figure 4.1 A comparison between frequency distributions of UHMWPE particles produced by SEM analysis, Mastersizer and Nanosight. SEM detected particles over 20 nm to 10 µm size range, while Nanisight detected only particles smaller than 750 nm and Mastersizer failed to detect particles smaller than 100 nm.

As mentioned previously, first part of the UHMWPE wear debris sample was used in mastersizer. Second part of this sample was analysed in Nanosight. Third part was analysed using SEM using the image analysis methodology mentioned in Section 4.3.2, page 86. A comparison of the three techniques showed limitations of Nanosight and Mastersizer (Figure 4.1). Mastersizer was only usable for particles larger than 100µm, while Nanosight ws only usable in 10 nm - 750 nm size range. Additionally, commenrical analysers such as Mastersizer and Nanosight dont provide any information on particle shape, while image analysis of SEM images can characterise particle size as well as morphology. Therefore, it was demonstated that SEM image analysis was the only viable technique for complete characterisation of UHMWPE wear debris.

4.3 Development of specialised software for wear particle analysis over 25nm to 100μm size range

The limitations of commercial size analysers for characterising UHMWPE wear debris were evident from size distribution comparisons discussed in previous section. Over the years SEM image analysis has become a standard technique for researchers to characterise a wide variety of materials. Particle characterisation using SEM image analysis has become a powerful technique to study behaviour and function of a large range of particles. However, this analysis is very much dependant on the ability of the computer software. Several studies in the past have used commercial software to analyse wear debris. But, these software are designed for generic processing of images or automated analysis of images with a very uniform background, which is challenging in SEM imaging. Often, a large number of steps are needed to characterise the wear debris for size and shape and its very time consuming as mentioned by Billi *et al.* [185]. Moreover, the accuracy of image analysis for characterisation has not been addressed in orthopaedic wear debris research community. Furthermore, even though image processing for shape analysis has progressed significantly, human eye is still considered as the best tool to identify differences in shapes. Therefore, proper categorisation of individual particle images for easy access is still missing in current image processing software. With the purpose of overcoming these limitations, new image analysis software was developed. Microsoft Visual Studio Development Environment was used to develop the software. Moreover, Intel® OpenCV was used as an image-processing library to implement the image processing functions. The library included a wide range of built-in image processing functions that were used during development of the software. In the following sections, the working principle and functioning of the software are described.

4.3.1 Working principle

The software analysis was divided into four stages as shown in Figure 4.2 . These were preliminary image processing, image segmentation, image measurements, shape analysis, particle image categorisation. All of these steps were applied in a sequential order in the software. Each stage is discussed in detail in following sections.

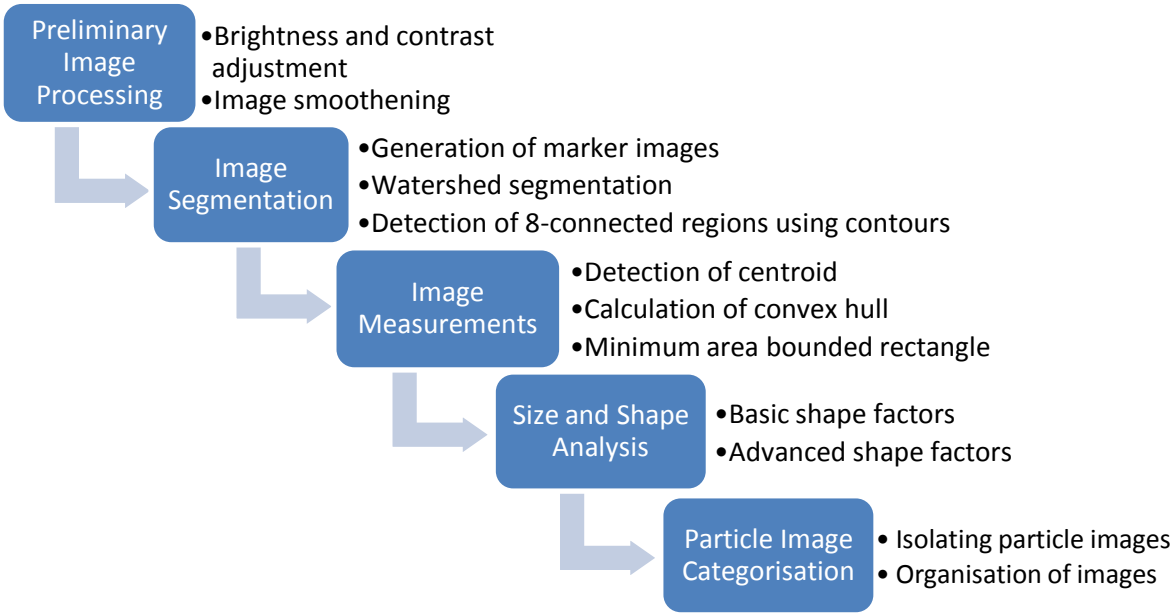

Figure 4.2 Working principle of the software. The software consists of five successive key steps and each step is divided into sub-steps.

4.3.2 Image processing steps

4.3.2.1 Preliminary image processing

Preliminary steps were necessary for an accurate segmentation of the regions of interest. Moreover, an image with a well spread out tonal distribution helped identify features more clearly.

Images captured using SEM tend to be noisy due to the background fluctuations. As mentioned in section 3.3.3 (page 78), a larger dwelling time could reduce the background noise. However, the noise could not be completely eliminated during the image acquisition as seen in Figure 4.3 . Moreover, presence of noise could hinder an effective segmentation of regions of interest. Therefore, in order to further reduce the noise a Gaussian smoothening filter was applied on the greyscale images during the pre-processing stage. Figure 4.4 shows an image after application of Gaussian filter.

As evident from SEM image of wear particles, the regions of interest were brighter than the background. In order to increase the accuracy of the segmentation the smoothened image was brightness and contrast adjusted to enhance the particle-background boundary details. Figure 4.5 shows an image after brightness and contrast adjustment.

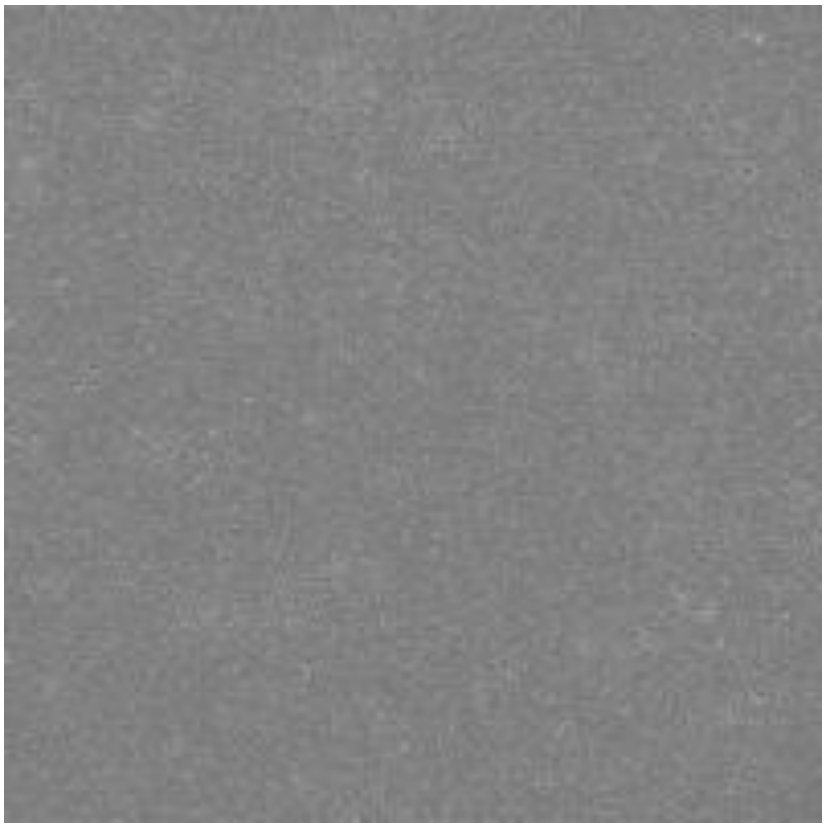

Figure 4.3 A magnified section of an electron microscopy raster image showing background noise.

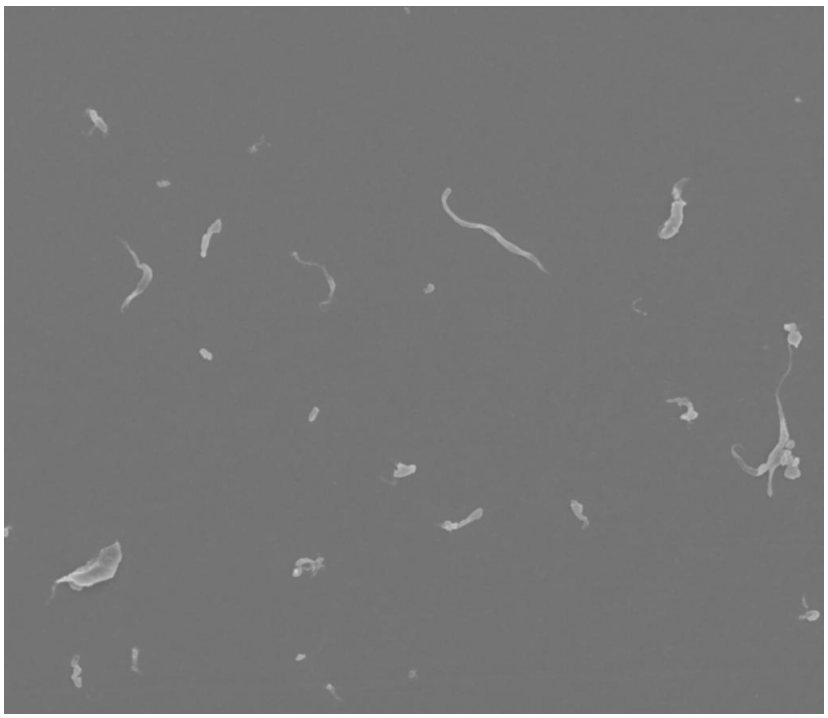

Figure 4.4 Scanning electron micrograph of UHMWPE particles after using Gaussian smoothening filter to minimise the background noise.

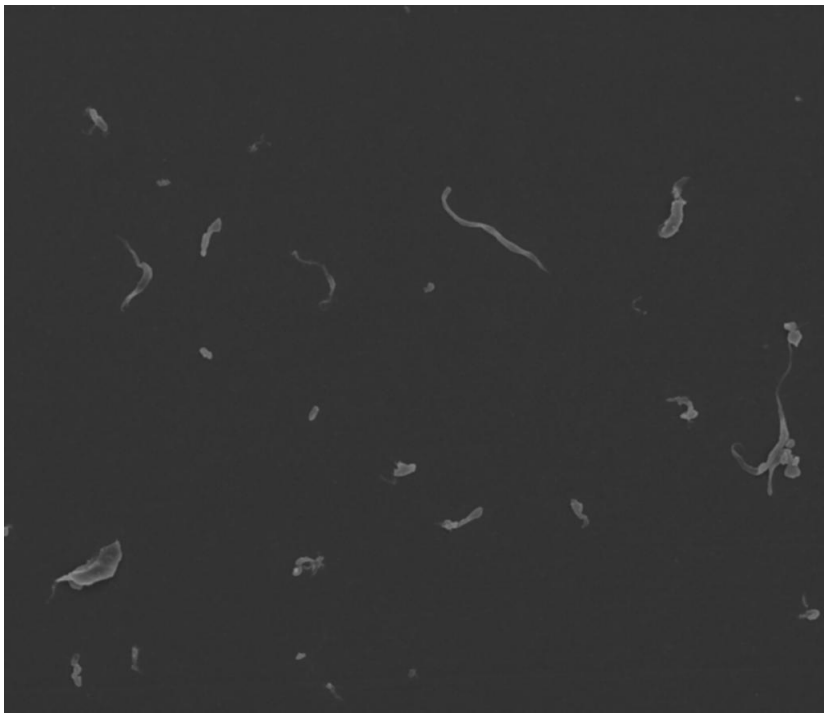

Figure 4.5 Scanning electron micrograph of UHMWPE particles after brightness and contrast adjustment.

4.3.2.2 Image segmentation

After pre-processing of the image, a watershed-based algorithm was used to segment the images. As this method needed an input of foreground and background pixel information of the image for segmentation, we devised an automatic threshold detection method to identify regions of foreground and background information. A marker image was then generated by thresholding the image using an intensity value obtained by clustering of the image histogram data using k-means. Afterwards, the marker image was input into a watershed segmentation method. Figure 4.6 shows a marker image used as an input for watershed segmentation method. At the end of watershed segmentation the particles were labelled as white and background as grey as shown in Figure 4.7.

The method of contours was used to recognise individual particles in the image. Since contour needed a binary image to identify the regions of interest, the watershed image was converted to a binary image, with the regions of interest shown in white and the background in black. Using the function cvFindContours the contour lines were drawn at the boundary of each particle. Moreover, each contour was given a unique RGB value to distinguish particles from each other. Figure 4.9 shows a contour image where each particle could be identified with its unique boundary colour (RGB value).

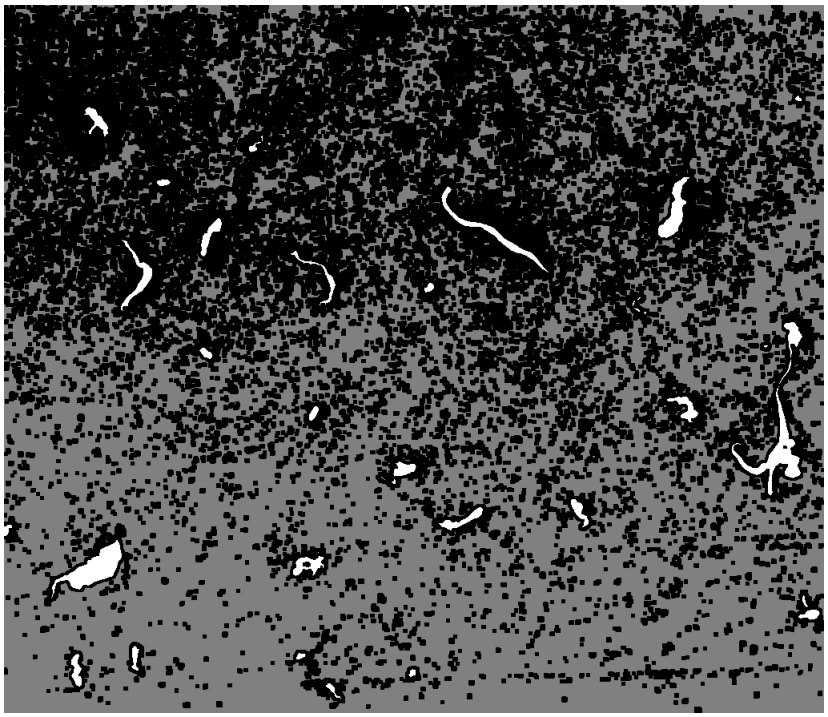

Figure 4.6 A marker image for watershed segmentation. Foreground is shown in white, background in gray and unknown region in black.

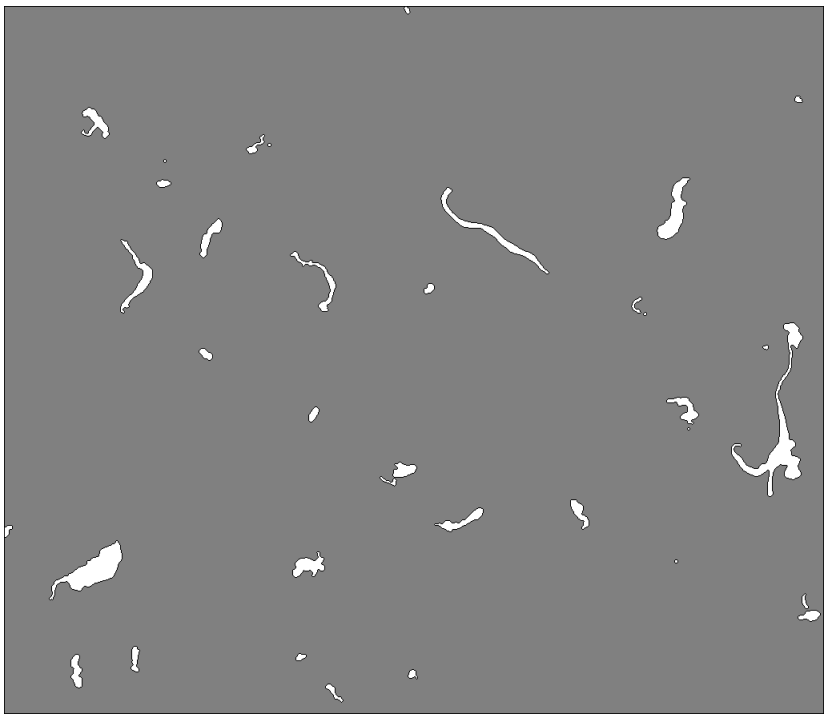

Figure 4.7 Segmented image of UHMWPE particles obtained after watershed segmentation. White regions are the segmented particles. Each particle is outlined by a thin black boundary. Gray region is the background.

Figure 4.8 Binary image obtained after thresholding the watershed segmented image. White region is the foreground and black region is the background.

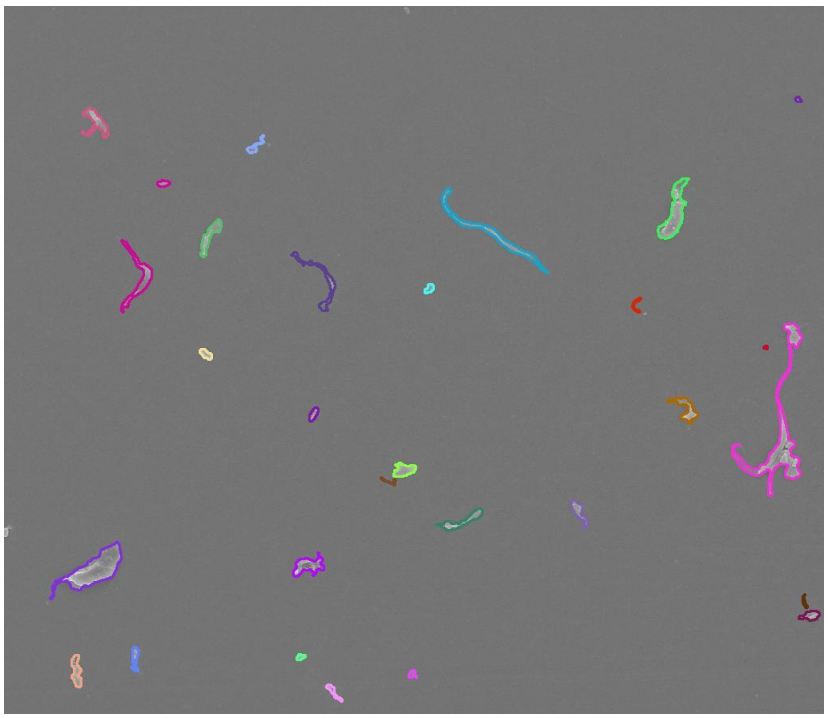

Figure 4.9 Image with particle contours. Each contour is assigned a unique coloured boundary.

4.3.2.3 **Image measurements**

Before characterisation of segmented particles, the particles touching the boundary were removed from analysis. This was done by traversing through the image boundary and using cvPointPolygonTest() function to identify the particles touching boundary pixels, followed by deletion of their contours. Non-touching particles were saved in a vector of structure. This structure had variables to store all necessary information of particles as shown in Figure 4.10. This included ParticleID[11], area, convex hull area, perimeter, all shape factors, contour and contour enclosing rectangle.

```
struct particle
    {
        int ParticleNo;
        string ParticleID;
        double area, hull_area, perimeter;
        double d_max, ecd;
        double aspect_ratio,elongation,roundness, form_factor,
        f_length, f_breadth, compactness, spreadness, complexity;
        CvSeq* particle_contour;
        CvRect Contour_Rectangle;
    };

std::vector<particle> particleData;
```

Figure 4.10 Vector of structure implementation for storing particle information. "particleData" is the vector of structure that stored information for each particle.

Area of each particle was calculated using cvContourArea().The convex hull , which is a bounding polygon similar to an elastic band wrapped around a particle, was determined using the cvConvexHull2() function. This was followed by calculation of the convex hull area by using cvContourArea() on convex hull contour. To identify the orientation and dimensions of the particle, minimum area rotated bounding rectangle was calculated using cvMinAreaRect2() function.

Concerning the shape factors aspect ratio, elongation, roundness, form factor, compactness and complexity were calculated using the formulas shown in Table 4.1 (page 93). Each of these shape factors was stored in the vector of structure particleData (Figure 4.10).

For display of analysed particles with their centre of mass, the location of centroid of each particle was calculated using cvMoments() function. It was worth noting that for particles with non-convex shape, the centroid may not lie within the bounds of the particle. The boundaries of segmented particles were overlaid on the original image by using cvDrawContours()function and exported as a new TIFF image using cvSaveImage().

4.3.2.4 **Particle image categorisation**

The characterisation step was followed by extracting individual particle images and categorising them based on size ranges. The size ranges chosen for UHMWPE wear debris were 0 - 100nm, 100nm - 1µm, 1 - 5µm, 5 - 10µm and 10 - 100µm. Moreover, a scale bar was imprinted on each

[11] ParticleID was unique number to identify each particle in each image. ParticleID format was img_**xxx_yyy**, where **xxx** was image number and **yyy** was particle number.

particle image. Images of particles within each size category were exported automatically into separate folders labelled with the size range as shown in Figure 4.11. Moreover, particles could be sorted based on size and shape parameters if desired.

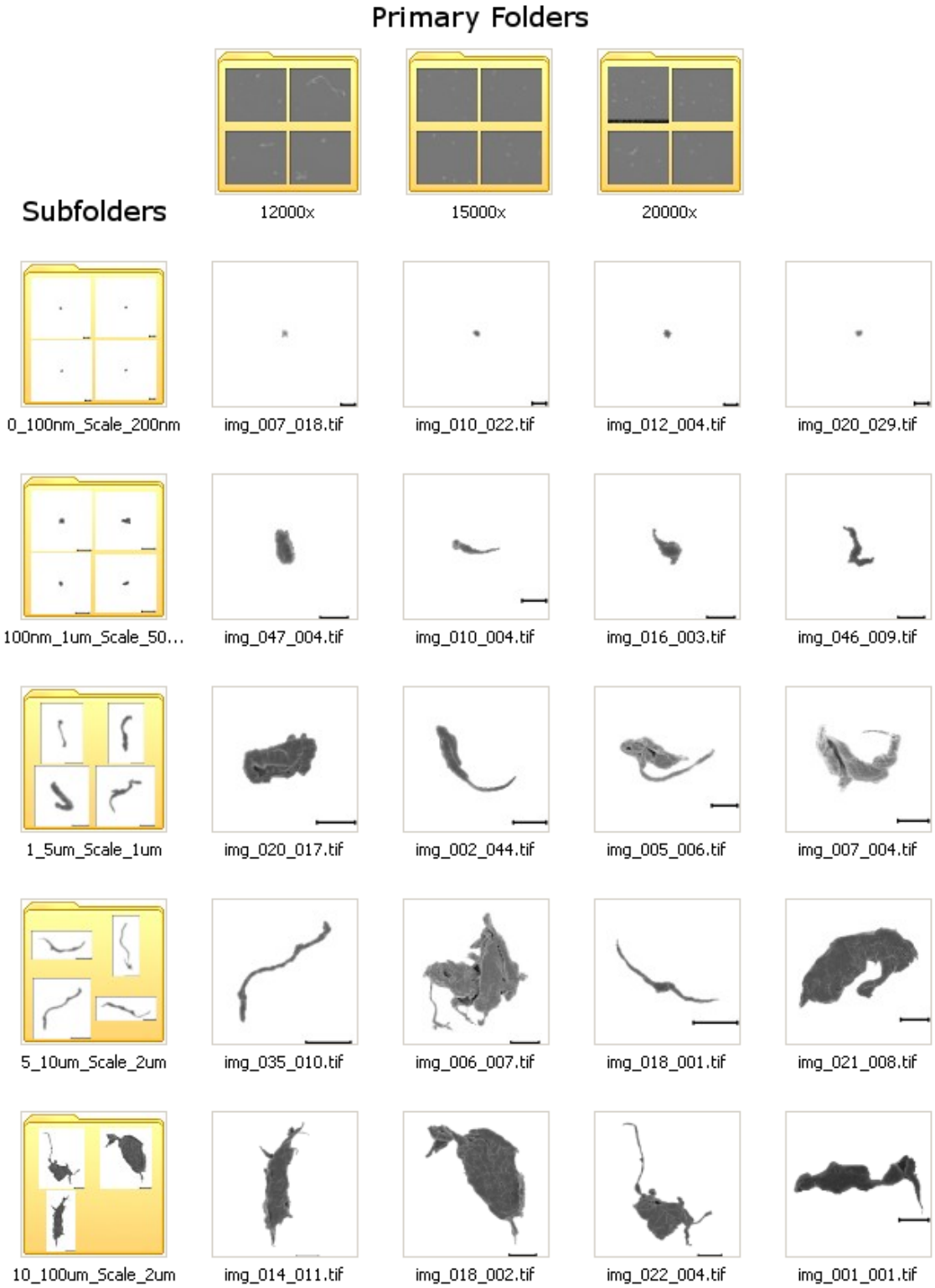

Figure 4.11 Particles categorised into three primary folders based on their magnifications and five subfolders based on their size. Scale bar information was also included in the names of subfolders.

4.3.2.5 **Shape descriptors used for particle analysis**

ASTM standard F1877 - 05 [192] suggests the use of aspect ratio, elongation, roundness and form factor for characterisation of wear particles. These factors were implemented in the custom software to evaluate the basic shape of particles. In addition, compactness and complexity were also implemented in the software. A description and the formula for calculation of each shape factor are given in Table 4.1. Both compactness and complexity are dependent on the convex hull area of a particle, and therefore provide additional information on simple/complex shape of the particles.

Table 4.1 Description of the shape factors. Aspect ratio, elongation, roundness and form factor are the shape factors used in ASTM F1877-05 standard for characterisation of wear particles. Compactness and complexity are additional shape factors used for further analysis.

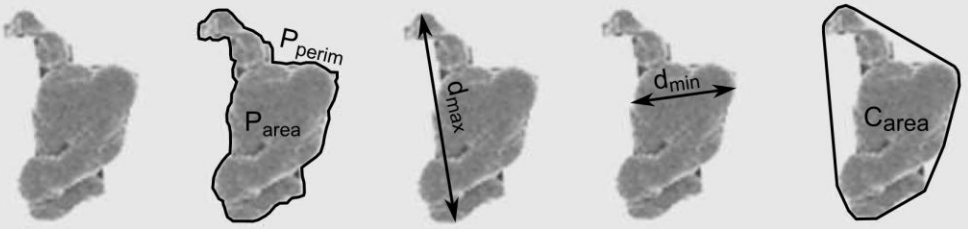

Shape Factor	Description	Formula
Aspect Ratio (AR)	Measure of the ratio of major diameter to the minor diameter (higher value indicates more long/narrow shape)	$\frac{d_{max}}{d_{min}}$
Elongation (E)	Measure of how long the shape is (higher value indicates more elongated/fibrilar shape)	$\frac{Fiber\ Length(FL)}{Fiber\ Width(FW)}$
Roundness (R)	Measure of how circular the shape is (higher value indicates more circular shape)	$\frac{4 \times P_{area}}{\pi \times {d_{max}}^2}$
Form Factor (FF)	Measure how circular the shape is but more sensitive to the variations in boundary roughness (higher value indicates more circular and smooth shape)	$\frac{4 \times \pi \times P_{area}}{{P_{perim}}^2}$
Compactness	Measure of how compact the shape is (higher value indicates more compact shape)	$\frac{\sqrt{C_{area}}}{P_{perim}}$
Complexity	Measure of complex the shape is (lower value indicates more complicated/fibrilar shape)	$\frac{P_{area}}{C_{area}}$

4.3.2.6 **Particle data representation**

At the end of categorisation, the particle data for all of the analysed images was exported into Microsoft excel supported .csv (comma separated value). The data was represented using frequency (number %) distribution and shape factor distribution graphs for each shape factor.

4.3.2.7 Testing of segmentation of particles

Analysed images were manually checked for any false recognitions and false non-recognitions. Data entries of the false recognitions (ghost particles) were manually deleted from the exported .csv file. Moreover, a very small fraction of particles were left undetected by the software. In such cases the parameter Twidth (explained in Table 4.2) was adjusted until all particles were included during segmentation.

Table 4.2 List of parameters used in the custom wear debris analysis software and their values used for analysis of SEM images of UHMWPE particles.

Parameter Name	Description	Value/ Range of Values
height	Height of the SEM image (without information bar) in pixels	884
brightness	Image brightness	10 - 35
contrast	Image contrast	80 - 90
Twidth	Upper threshold - Lower threshold (for generation of the marker image)	4 - 10
conversion_factor	Conversion factor to convert the size from pixels into nanometres	1/80 (at 20,000x magnification) 1/60 (at 15,000x magnification) 1/48 (at 12,000x magnification)

Table 4.3 List of key OpenCV functions used in the custom wear debris analysis software.

Function Name	Description
cvSmooth	Smoothening of the image
CvHistogram	Generation of histogram of the image
cv::kmeans	K means clustering of the histogram data
cvThreshold	Thresholding of the grayscale image
cv::watershed	Watershed segmentation of the image
cvFindContours	Find contours from a binary image
cvPointPolygonTest()	Test whether a point is inside or outside a contour
cvContourArea()	Calculate area of a contour
cvMinAreaRect2()	Calculate the pixel locations of minimum area rectangle of a contour
cvMoments()	Calculate moments of a contour
cvConvexHull2()	Calculate convex hull of a contour
cvDrawContours()	Print contours on an image
cvSaveImage()	Save the analysed images in TIFF format

4.3.3 **Flow chart**

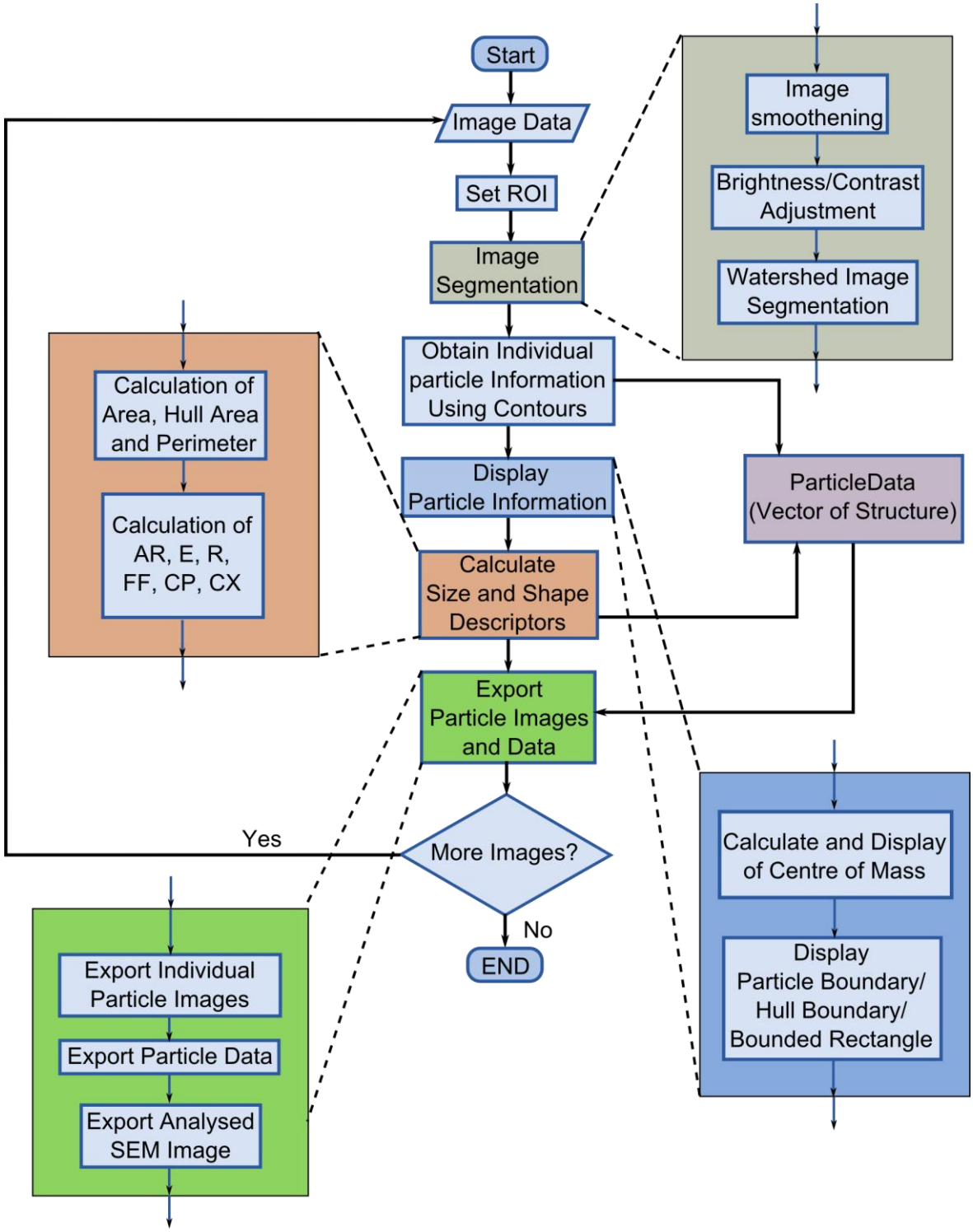

Figure 4.12 A flowchart of the custom image analysis software developed in current study. All key functions are coloured in gray, blue, green and red. The vector of structure 'ParticleData' is coloured in blue.

ROI: Region of Interest, AR: Aspect Ratio, E: Elongation, R: Roundness, FF: Form Factor, CP: Compactness, CX: Complexity

4.4 Comparison with other software using simple shapes

As mentioned previously, a number of software have been used in the past to analyse particles from digital images. In this section two commonly used software Image Pro Premier and ImageJ were compared with the custom software. The rationale behind comparing these two software was the fact that Image Pro Premier is an industry leading image analysis software and ImageJ is free software commonly used in academia. Latest versions of both software available at the time of analysis were used for comparison. These were Image Pro Premier (Version 9.1) and ImageJ version 1.46r. Moreover, the comparison was based on area and perimeter because other shape factors are primarily derived from them. A range of sizes were used for each shape to test the convergent/divergent nature of algorithms used for calculation of area and perimeter. In case of convergent results, the percentage error in calculation decreased with an increase in particle size. Alternatively, divergent results meant an increase in percentage error with an increase in particle size, which is not desirable for any image analysis software. Figure 4.13 shows the test shapes used for comparison. The rationale behind using these particular shapes was their ability to test area and perimeter detection for straight boundary, curved boundary, pointed corners, convex boundary and concave boundary. Moreover, smaller size of curved shapes tested for higher curvatures. For instance, smaller circle had a higher radius of curvature compared to large circle.

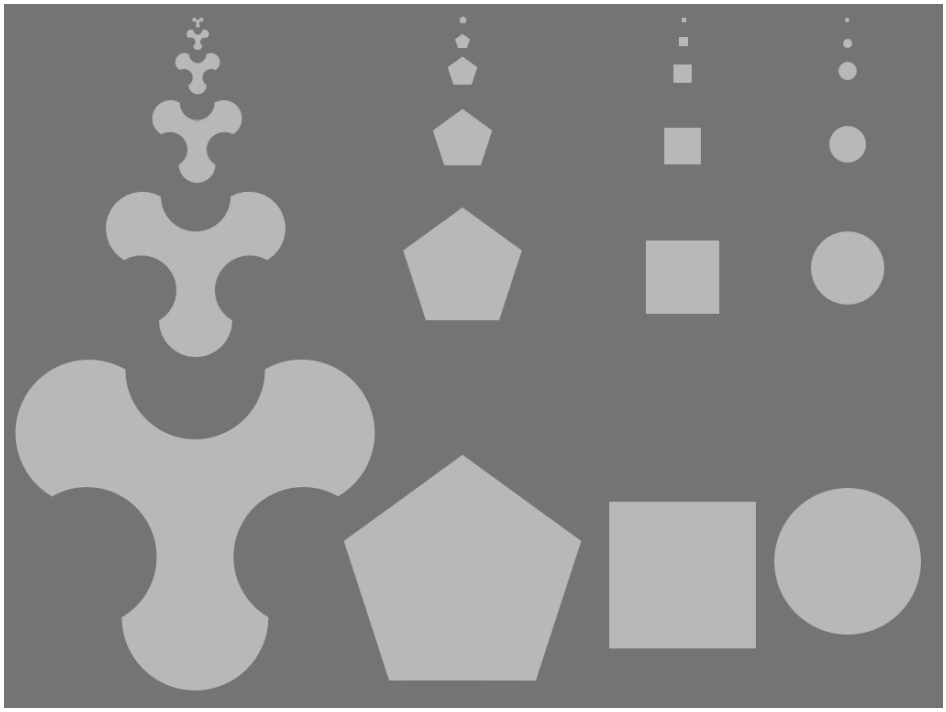

Figure 4.13 Image showing simple shapes used for comparison of area and perimeter using ImageProPlus, ImageJ and custom software.

After analysis, the percentage error data in area and perimeter were plotted for each software as shown in Figure 4.14 and Figure 4.15. It was noticed that Image Pro Plus and custom software gave convergent area and perimeter results for all of the shapes, while circle, pentagon and convex/concave shape gave divergent results for perimeter calculation in ImageJ. Moreover,

maximum percentage error in all of the comparisons was 23.6% by Image Pro Premier in the calculation perimeter of circle (diameter 5 pixels). ImageJ gave a maximum percentage error of 12.7% in calculation of perimeter of convex/concave shape (size 5 pixels). The custom software gave maximum error of 11.2% in calculation of perimeter for the same convex/concave shape mentioned above for ImageJ. Therefore, the custom software was similar or better in all the results compared to the other two, indicating accurate results given by the custom software.

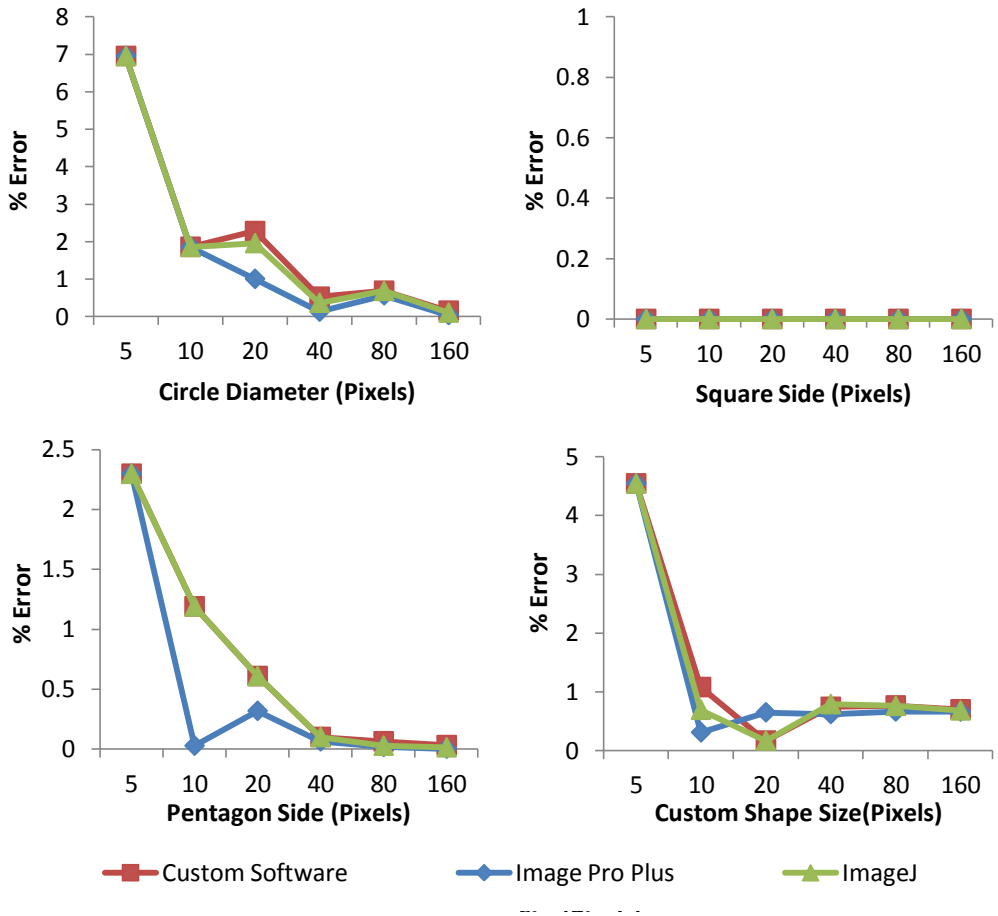

Figure 4.14 A comparison between percentage errors in area measurement using custom software, Image Pro Plus and ImageJ.

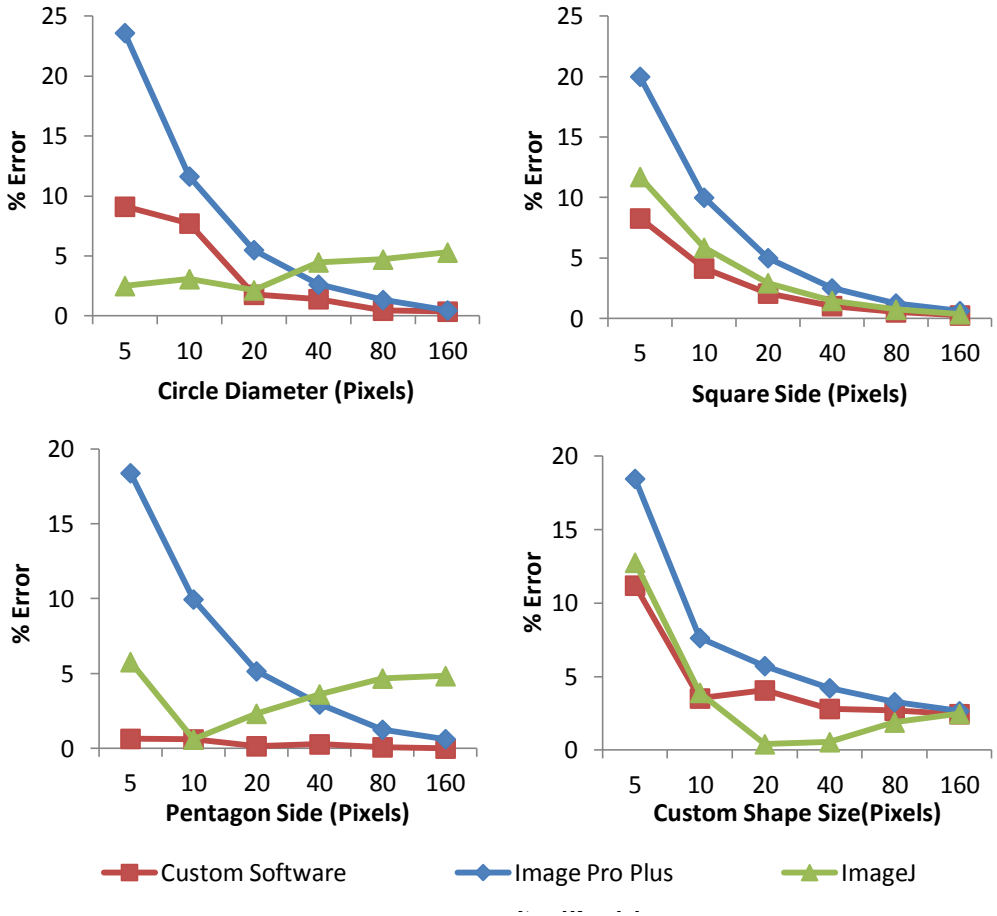

Figure 4.15 A comparison between percentage errors in perimeter measurement of test shapes using custom software, Image Pro Plus and ImageJ

4.4.1 Illustration of UHMWPE wear particle characterisation using custom software

This section demonstrates the coverage of entire range of size and shapes of UHMWPE wear particles by using custom SEM image analysis.

No	Particle	Dmax (µm)	ECD (µm)	AR	E	R	FF	CP	CX
1		0.053	0.040	1.500	1.634	0.565	0.739	0.250	0.941
2		0.083	0.047	2.667	3.181	0.330	0.571	0.226	0.884
3		0.162	0.149	1.181	1.702	0.844	0.838	0.264	0.953
4		0.260	0.100	3.349	9.484	0.148	0.271	0.187	0.616
5		0.272	0.166	1.578	7.703	0.374	0.319	0.207	0.591
6		0.523	0.402	1.440	2.703	0.590	0.619	0.236	0.884
7		0.562	0.213	1.729	33.831	0.144	0.087	0.163	0.261
8		0.779	0.576	1.145	12.434	0.548	0.216	0.170	0.593
9		1.434	0.870	1.271	16.971	0.368	0.165	0.160	0.512

10		1.837	1.024	2.352	11.453	0.310	0.232	0.161	0.705
11		7.290	2.817	1.568	31.675	0.149	0.093	0.161	0.285
12	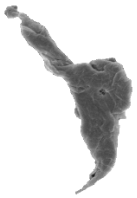	8.808	4.715	2.308	10.157	0.287	0.256	0.171	0.700
13		9.981	1.639	3.235	81.219	0.027	0.038	0.178	0.095
14		58.786	24.669	3.175	27.512	0.176	0.096	0.116	0.573

As noticed from the table above, UHMWPE wear debris had a range of size and shapes. Size and shape descriptors were able to characterise particles in detail as mentioned below:

- Dmax and equivalent circular diameter were able to quantify the size of particles from 25 nanometres to 100 microns. Particle 1 and 2 were nanoscale particles with Dmax of 53nm and 83nm respectively. Particle 14 was a very large micron scale particle with Dmax of 58.786µm.
- Elongated particles with high aspect ratio (AR) were Particle 2, 4, 10, 12, 13, and 14. Moreover, these particles could be fibrillar when elongation (E) values were higher and complexity values were lower such as Particle 7, 11, 13.
- Particle 4, 5 and 9 were partially fibrillar.
- Particle 1, 3, 6 were round and compact with higher roundness, form factor, compactness and complexity values.
- Complex agglomerated particles such as Particle 8 and 10 had marginally higher elongation and marginally lower complexity values.

Chapter 5 - **Results**

In this section, UHMWPE wear particles produced by multidirectional pin-on-plate, ankle, knee and hip simulator testing of conventional UHMWPE as well as latest generation UHMWPE were compared for size and morphology.

- All joint simulator wear testing was conducted according to ISO standards (ISO14242-1 and ISO14243-1) [157], [158]. Loads and contact stresses in each joint articulation were comparable to those encountered in human body.
- Multidirectional pin-on-plate was run at 1Hz using a flat UHMWPE pin against cobalt chrome plate with a 40N load (contact stress 2MPa).
- Newborn calf serum diluted with deionised water was used as lubricant during wear testing as specified in ISO standards [157], [158]. The lubricant also contained EDTA to minimize precipitation of calcium phosphate onto the bearing surface and sodium azide to retard any bacterial growth.
- The lubricant was replaced every 0.5 million cycles and used lubricant containing wear debris was stored at -4°C. The particles were isolated from stored simulator lubricants using the novel isolation method described in Section 3.3.1. SEM images of wear particles were characterised using custom image analysis software described in Section 4.3.
- Wear testing from 0 to 0.5 million cycles in ankle, knee, and hip simulators was representative of early wear of a joint implant and was termed as **Early wear** in subsequent sections of this chapter.
- Wear testing from 4.5 to 5 million cycles in ankle, knee, and hip simulators were representative of steady state wear in joint simulators and were termed as **Long-term wear**.
- Wear testing from 0 to 0.5 million cycles in multidirectional pin-on-plate was representative of early wear in a joint and wear testing from 3 million cycles and beyond was representative of long-term wear.
- Each 1 million cycle was representative of approximately one year of a natural human walking at a frequency of 1 Hz.
- Conventional direct compression moulded UHMWPE is abbreviated by its commercial name ArCom® in the following sections of this chapter.

- Highly crosslinked Vitamin E diffused UHMWPE is abbreviated by its commercial name E1® in the following sections of this chapter.
- Vitamin E blended cold irradiated mechanically annealed UHMWPE is abbreviated by its commercial name ECiMa™ in the following sections of this chapter.
- Skewness and Kurtosis values were calculated for each size and shape descriptor. None of the size and shape descriptors were found to be normally distributed. Therefore, non-parametric testes were used for statistical analysis. Kolmogorov-smirnov Z test was used to compare different size distributions. Mann-Whitney test was used to compare the shape descriptors in each size range of the shape analysis plots. Statistically significant differences ($p < 0.05$) were highlighted by black outlines.

5.1 Influence of change in processing conditions and addition of vitamin E as an antioxidant on size and morphology of wear debris

All of the comparisons done in this section are listed in Table 5.1. Section 5.1.1 and Section 5.1.2 tested the influence of crosslinking and addition of vitamin E by diffusion on size and morphology of wear debris. Section 5.1.3 tested the influence of addition of vitamin E by blending followed by crosslinking and addition of vitamin E to highly crosslinked UHMWPE by diffusion on the size and morphology of wear debris. Section 5.1.4 tested the effect of change in moulding temperature in direct compression moulded UHMWPE on size and shape of wear debris.

Table 5.1 List of all comparisons described in Section 5.1

Section	Type of comparison	Stage of wear	Type of tribological testing
5.1.1	ArCom vs. E1	Early wear and Long-term wear	Knee simulator
5.1.2	ArCom vs. E1	Long-term wear	Multidirectional pin-on-plate wear tester
5.1.3	E1 vs. ECiMa	Early wear and Long-term wear	Hip simulator
5.1.4	Conventional UHMWPE moulded at 145°C vs. Conventional UHMWPE moulded at 175°C	Long-term wear	Multidirectional pin-on-plate wear tester

5.1.1 ArCom Knee vs. E1 Knee

In this section, wear particles isolated from UHMWPE-on-CoCr knee simulator testing of ArCom® Vanguard (Biomet) inserts and E1® Vanguard (Biomet) inserts were compared. Particles generated during early wear and long-term wear of both materials were compared for size and morphology.

5.1.1.1 Early Wear

During early wear, UHMWPE particles isolated from lubricant serum retrieved after 0.5 million cycles of knee simulator tests using ArCom and E1 liners were analysed for size and morphology.

5.1.1.1.1 Size analysis

A comparison between percentage number distributions of ArCom and E1 is shown in Figure 5.1. Statistical analysis using Kolmogorov-smirnov Z test indicated that both size distributions were significantly different from each other ($p < 0.05$). E1 had a marginally higher percentage of particles larger than 2µm, while ArCom had a higher percentage of particles in 250-500 nm size range.

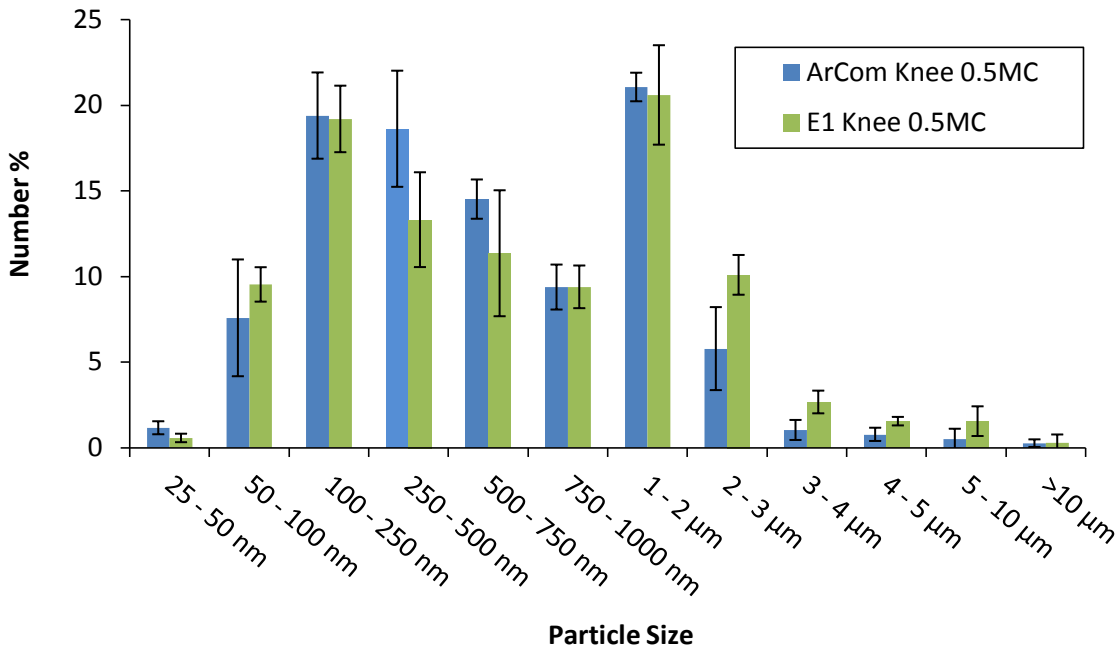

Figure 5.1 A comparison between percentage number size distributions according to maximum Feret's diameter (dmax) of ArCom knee and E1 knee wear particles during early wear. Error bars show standard deviation.

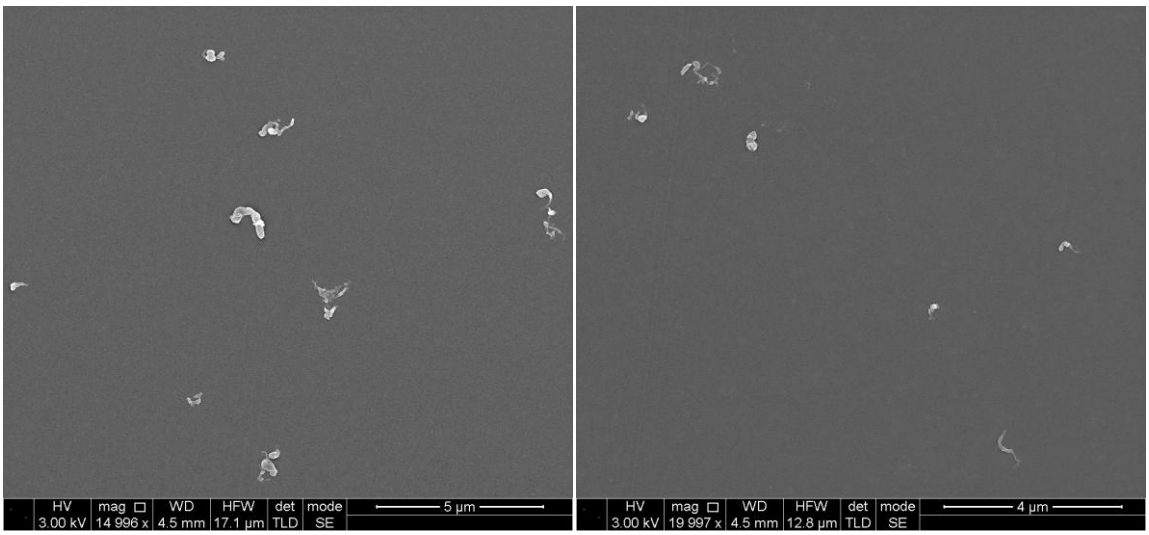

A) **B)**

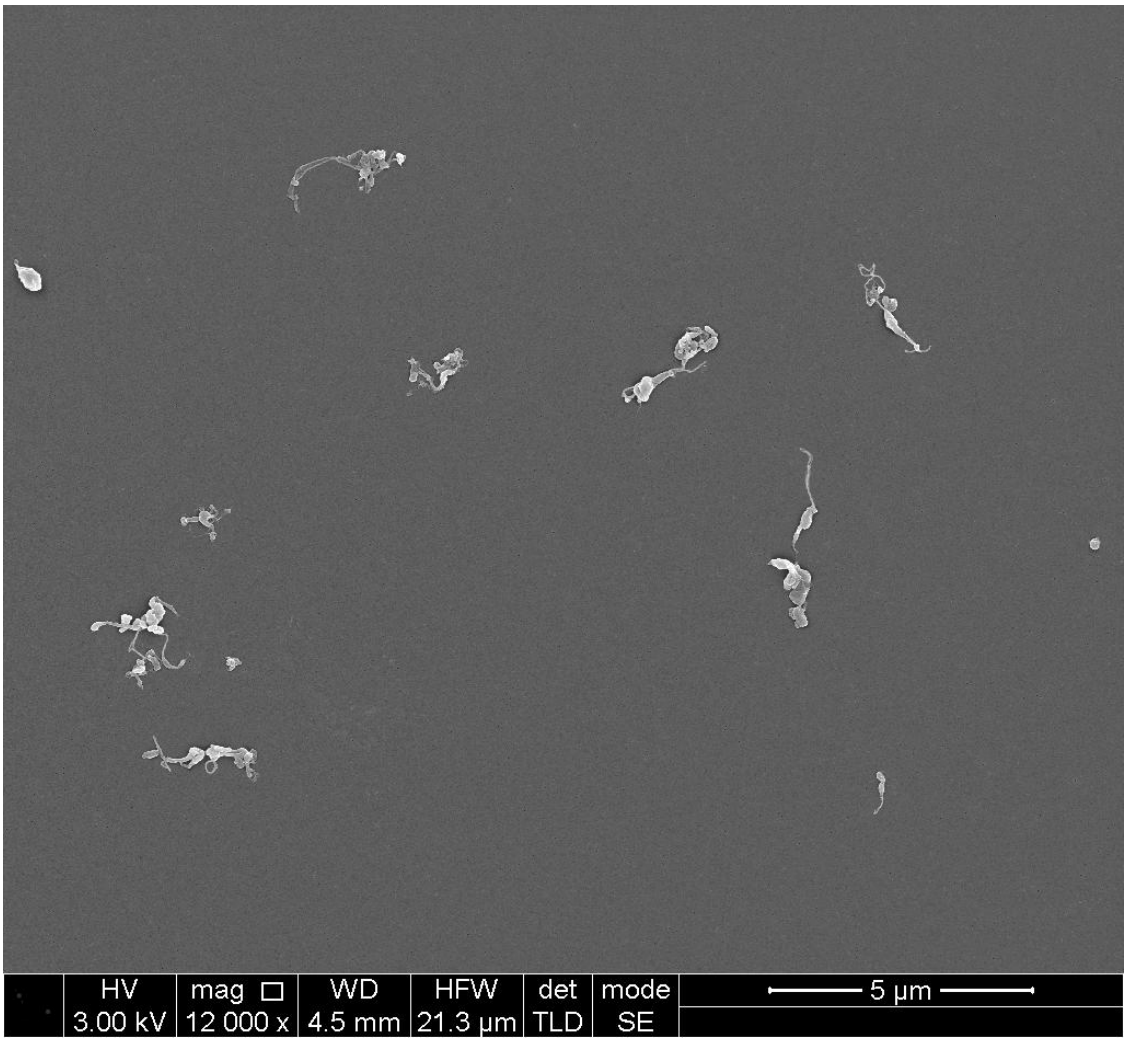

C)

Figure 5.2 Scanning electron micrographs of ArCom Knee during early wear. A) 15000x magnification, Scale = 5µm B) 20000x magnification, Scale = 4µm C) 12000x magnification, Scale = 5µm.

E1 Knee Early Wear

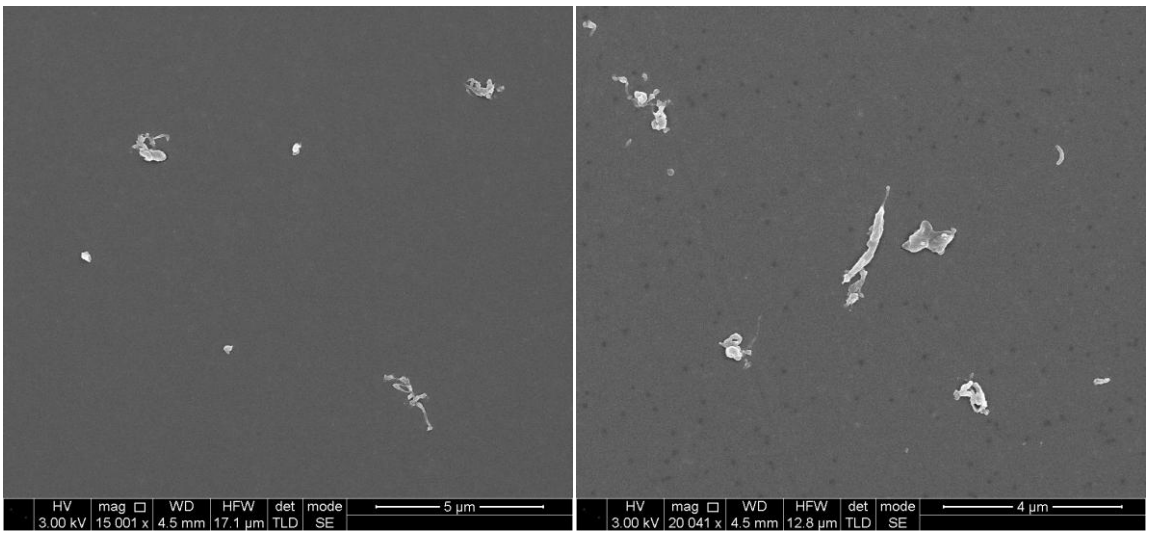

A) **B)**

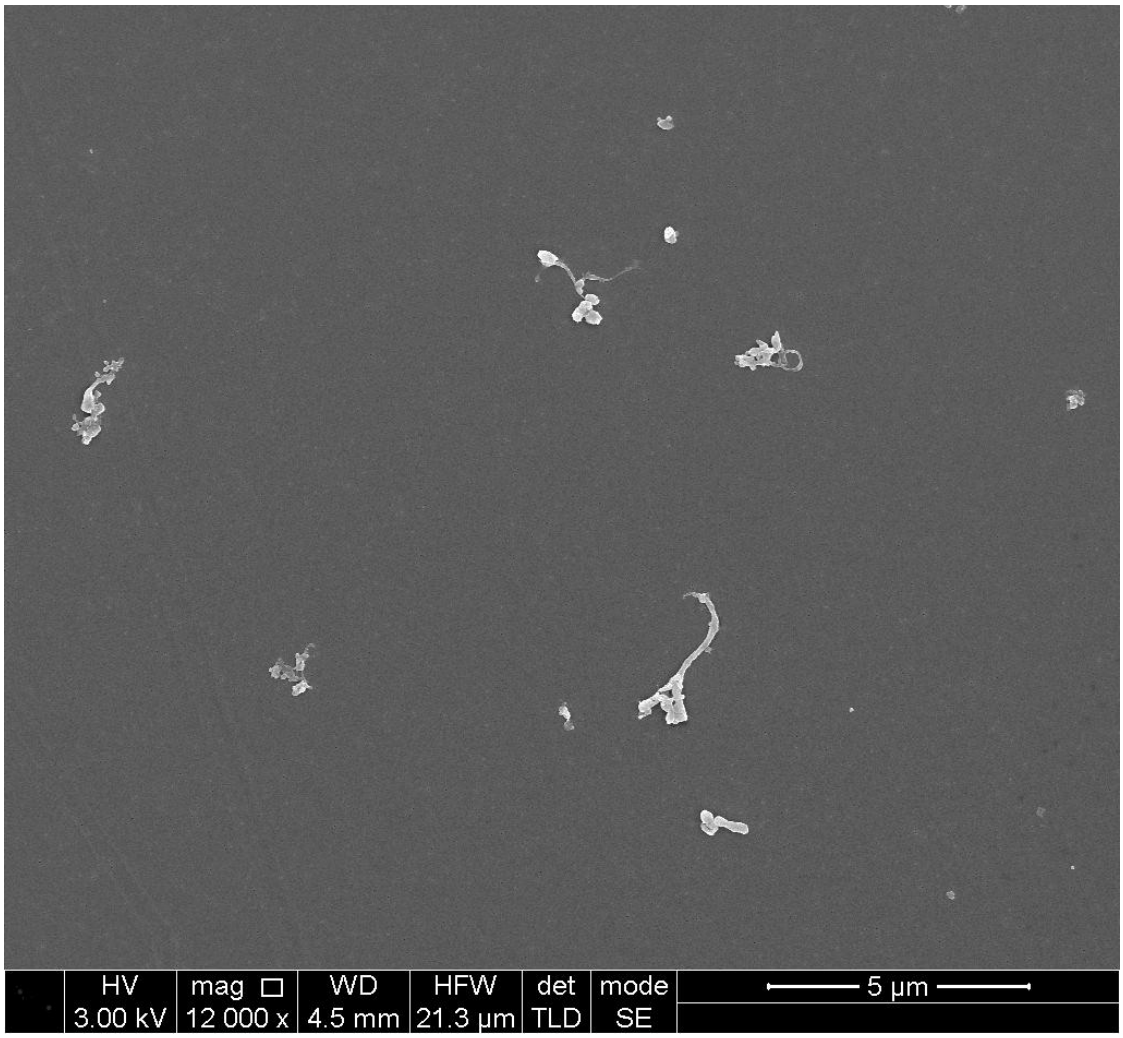

C)

Figure 5.3 Scanning electron micrographs of E1 Knee during early wear. A) 15000x magnification, Scale = 5µm B) 20000x magnification, Scale = 4µm C) 12000x magnification, Scale = 5µm.

5.1.1.1.2 Shape analysis

For comparison of the morphology of wear particles, aspect ratio, elongation, roundness, form factor, compactness and complexity were plotted against particle size. More specifically, the value of each shape factor in a size range indicated the mean value in the column chart. Error bars showed standard deviation of each shape factor from this mean value.

Figure 5.4 shows a comparison between aspect ratio values of ArCom knee and E1 knee after 0.5 million cycles. A gradual increase in aspect ratio values of both samples was noticed. Moreover, no significant difference in aspect ratio values was noticed for both ArCom knee and E1 knee. Elongation data showed statistically higher elongation values for ArCom in 0.025 to 0.1 µm and 1 to 5 µm size ranges as shown in Figure 5.5.

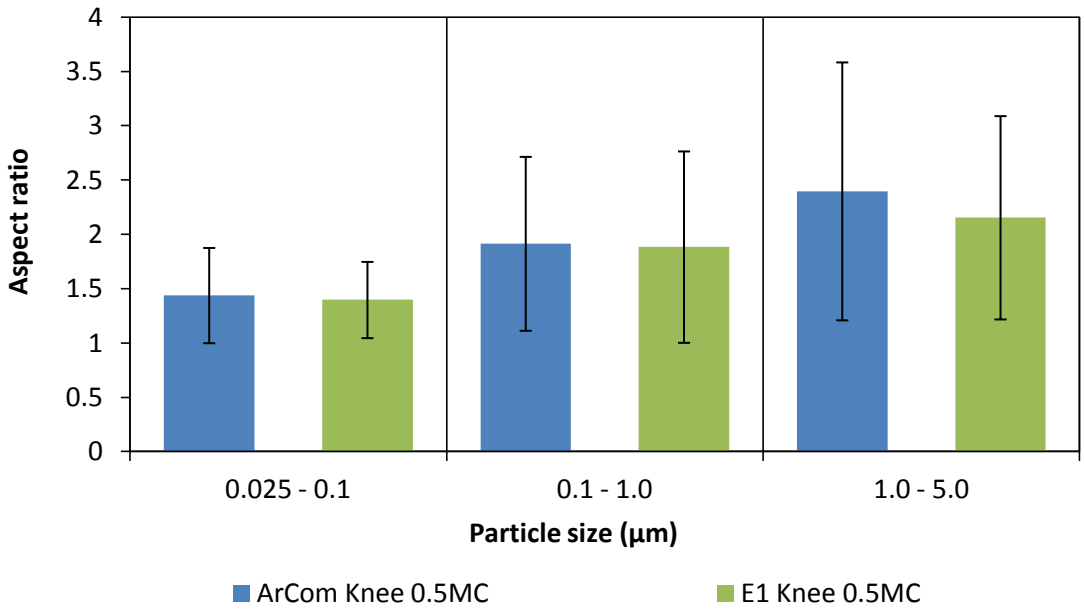

Figure 5.4 A plot showing aspect ratio versus particle size for early wear of ArCom and E1 Knee UHMWPE. Error bars indicate standard deviation from mean value in each size range. ArCom particles showed more elongated shape than E1.

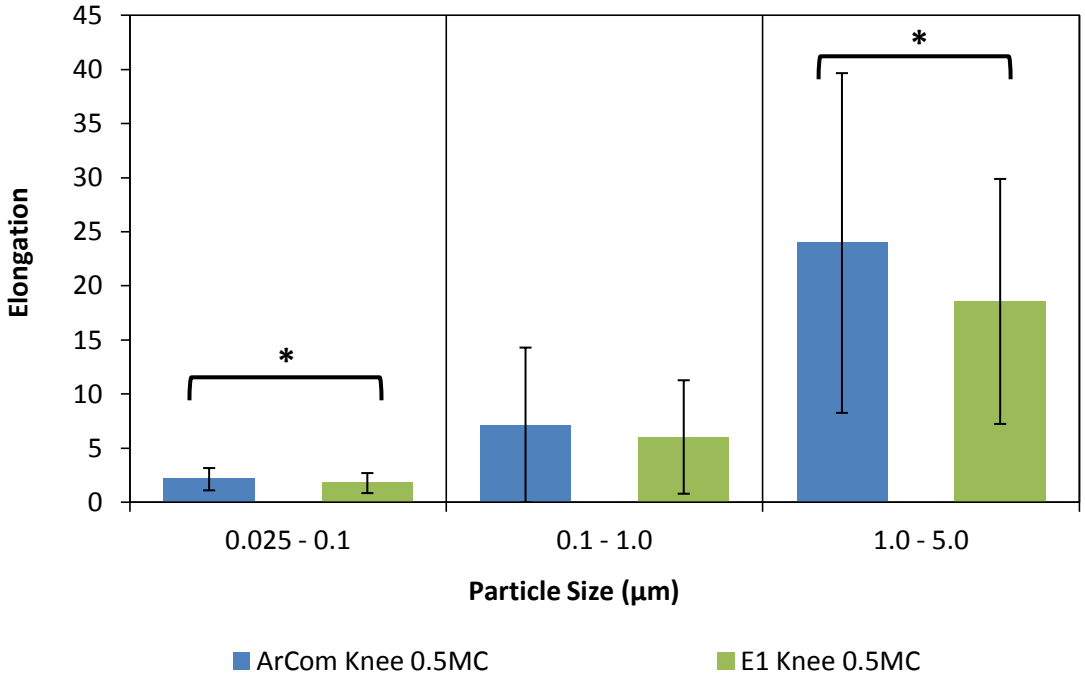

Figure 5.5 A plot showing elongation versus particle size for early wear of ArCom and E1 Knee UHMWPE. Error bars indicate standard deviation from mean value in each size range. Statistically significant differences ($p < 0.05$) are highlighted with a black outline. ArCom particles showed more elongated fibrillar shape than E1.

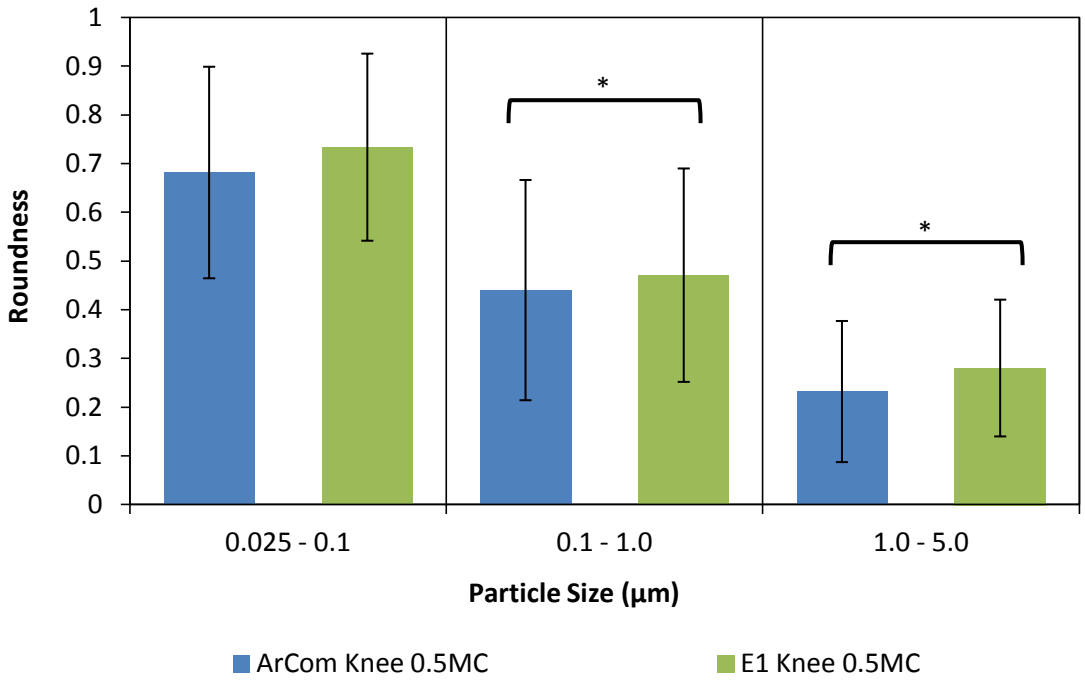

Figure 5.6 A plot showing roundness versus particle size for early wear of ArCom and E1 Knee UHMWPE.. Error bars indicate standard deviation from mean value in each size range. Statistically significant differences ($p < 0.05$) are highlighted with a black outline. E1 particles showed more rounded shape than ArCom.

When the roundness values of ArCom and E1 UHMWPE were compared, a gradual decrease in the roundness values with increrase in particle size was noticed as shown in Figure 5.6. Moreover, E1 particles in 0.1 to 5 µm size range had higher roundness values than ArCom, indicating more round morphology of E1 wear particles.

With regards to form factor, E1 knee showed higher form factor values in 0.025 to 0.1 µm and 1 to 5 µm size ranges compared to ArCom knee as shown in Figure 5.7.

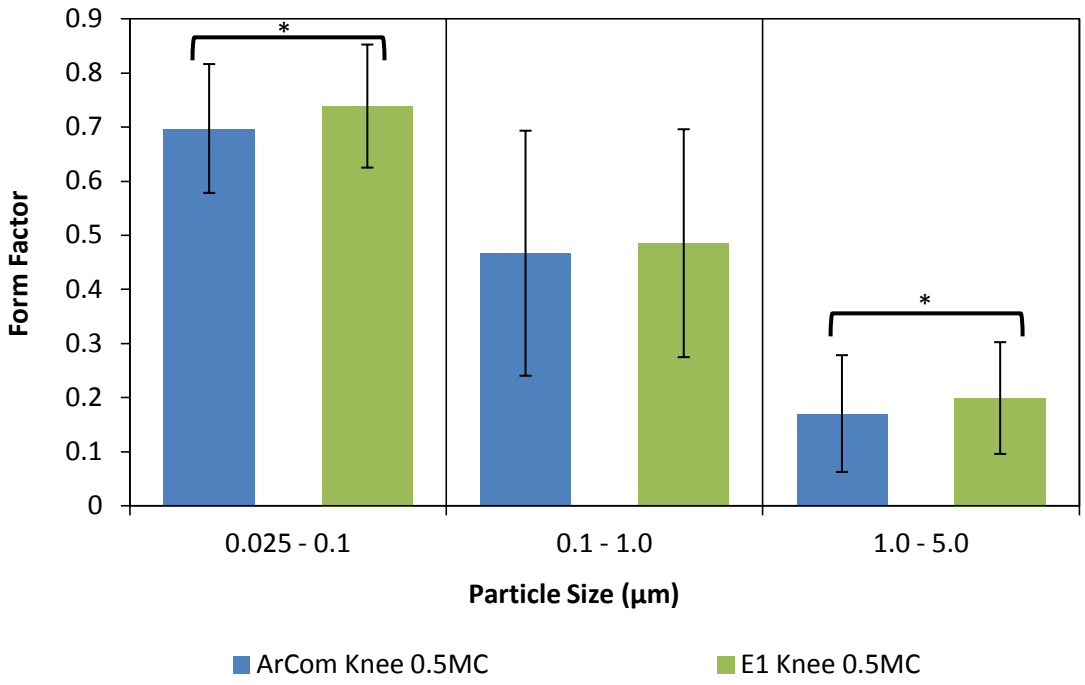

Figure 5.7 A plot showing form factor versus particle size for early wear of ArCom and E1 knee UHMWPE. Error bars indicate standard deviation from mean value in each size range. Statistically significant differences ($p < 0.05$) are highlighted with a black outline. E1 particles showed higher form factor values than ArCom in 0.025 to 0.1 µm and 1 to 5 µm size ranges.

A gradual decrease in compactness value was observed with increase in particle size for both ArCom and E1 UHMWPE as shown in Figure 5.8. This indicated that ArCom and E1 wear particles had less compact in shapes with an increase in their size. Moreover, no significant difference was noticed between the compactness values for both materials.

When complexity values of both ArCom and E1 UHMWPE were plotted against particle size, a gradual decrease in the complexity value was observed with increase in size as seen in Figure 5.9. As mentioned in Section 0, unlike other shape factors where a high value indicates greater occurrence of the shape characteristic attached to it, a low complexity value indicates more complex shape of the particle. Therefore, both ArCom and E1 UHMWPE showed more complex morphology of particles with increase in size. Moreover, ArCom particles showed more complex shape than E1 in 0.025 to 1 µm and 1 to 5 µm size ranges. This was also verified from SEM micrographs of both materials.

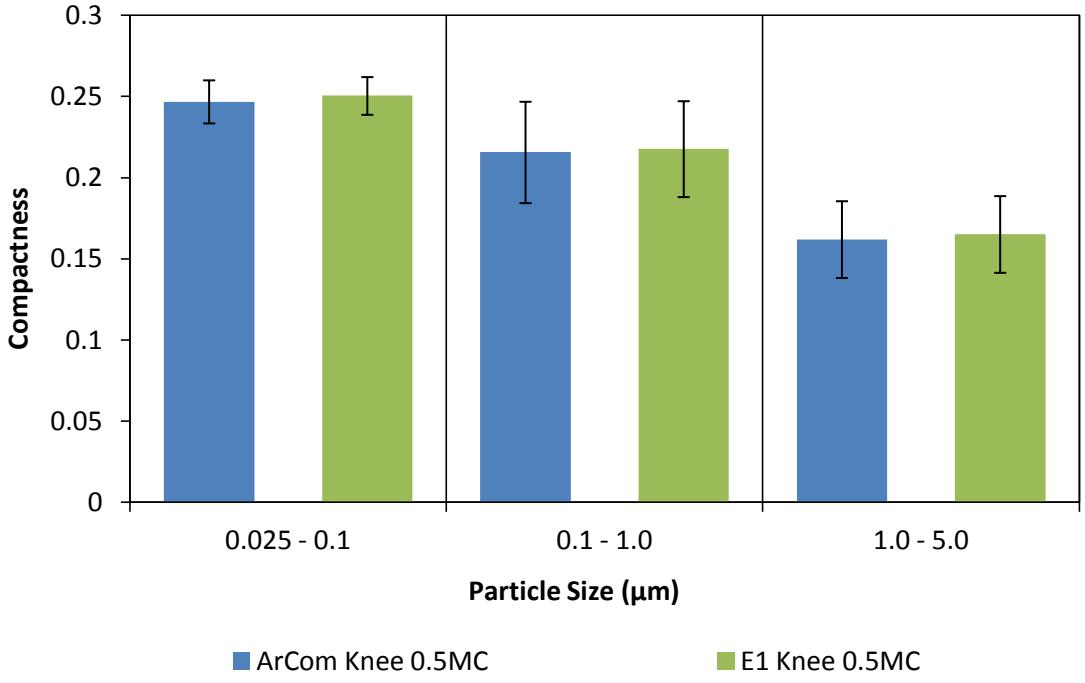

Figure 5.8 A plot showing compactness versus particle size for early wear of ArCom and E1 knee UHMWPE. Error bars indicate standard deviation from mean value in each size range. Both E1 and ArCom had similar compactness values.

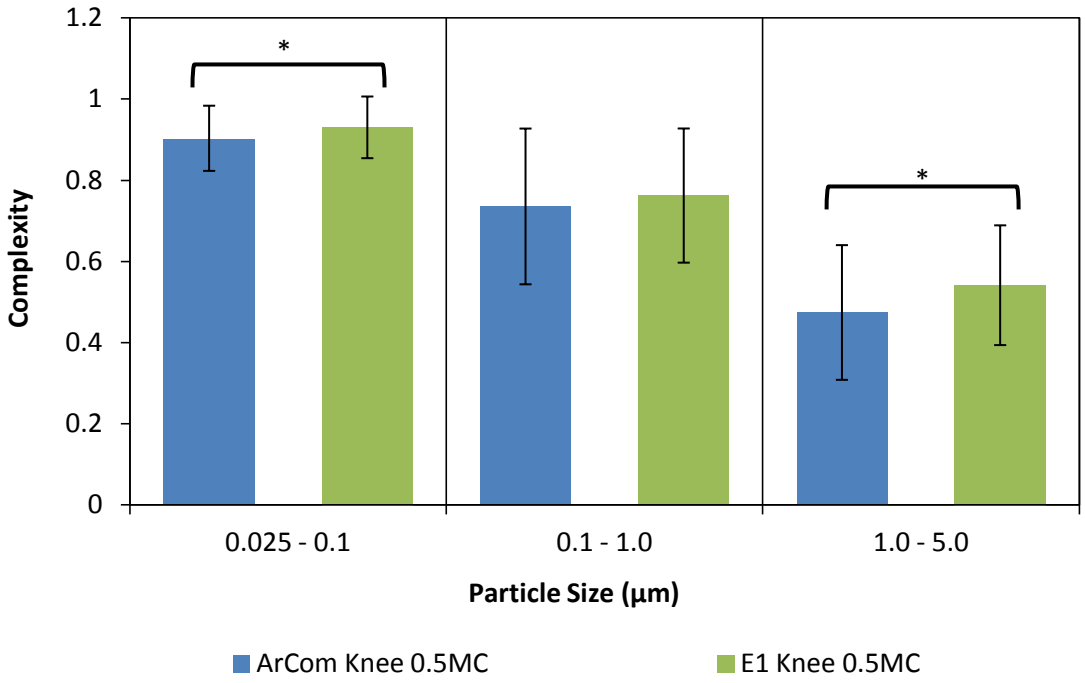

Figure 5.9 A plot showing complexity versus particle size for early wear of ArCom and E1 knee UHMWPE. Error bars indicate standard deviation from mean value in each size range. Statistically significant differences ($p < 0.05$) are highlighted with a black outline. ArCom particles showed more complex shape than E1 in 0.025 to 1 µm and 1 to 5 µm size ranges.

5.1.1.2 **Long-term Wear**

During long-term wear, UHMWPE wear particles isolated from lubricant serum samples retrieved after 4.5 million cycles of ArCom and E1 Knee simulator tests were characterised.

5.1.1.2.1 Size analysis

A comparison between number distributions of ArCom and E1 UHMWPE is shown in Figure 5.10. Although, overall size distribution of both materials looked similar, statistical analysis using Kolmogorov-smirnov Z test indicated that both size distributions were significantly different from each other ($p < 0.05$). Moreover, E1 had a higher percentage of particles smaller than 250nm, while ArCom had a higher percentage of particles in 250 – 750nm range. In addition, the percentage number of particles larger than 5µm was marginally higher in E1 samples compared to ArCom.

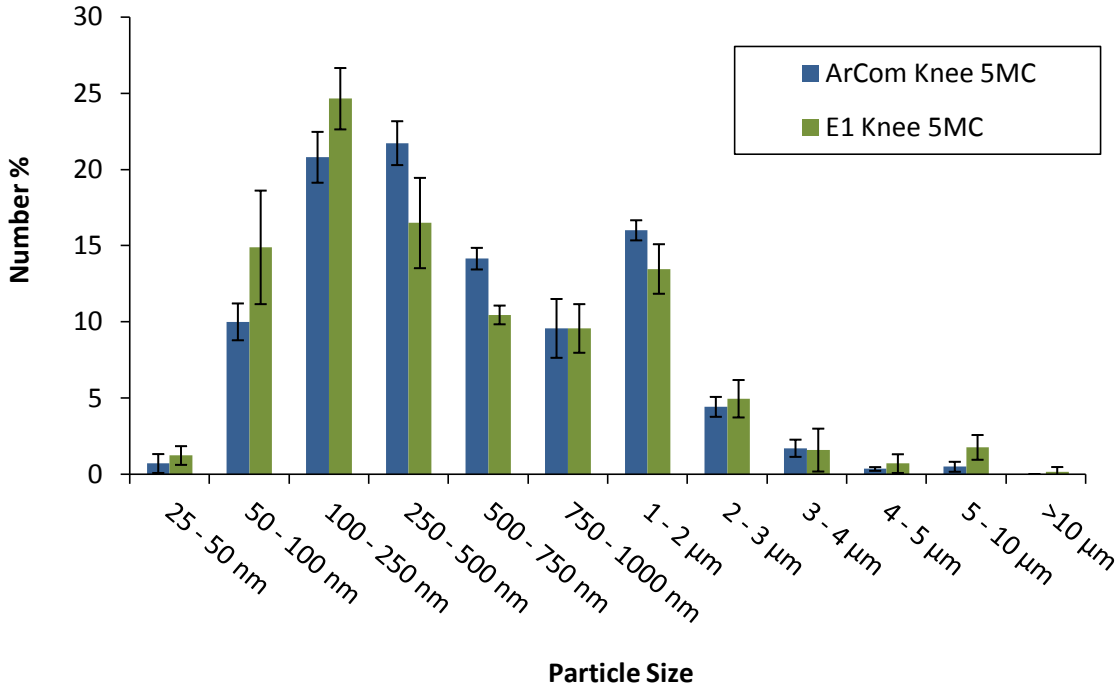

Figure 5.10 A comparison between percentage number size distributions according to maximum Feret's diameter (dmax) of ArCom knee and E1 knee wear particles during long-term wear. Error bars show standard deviation.

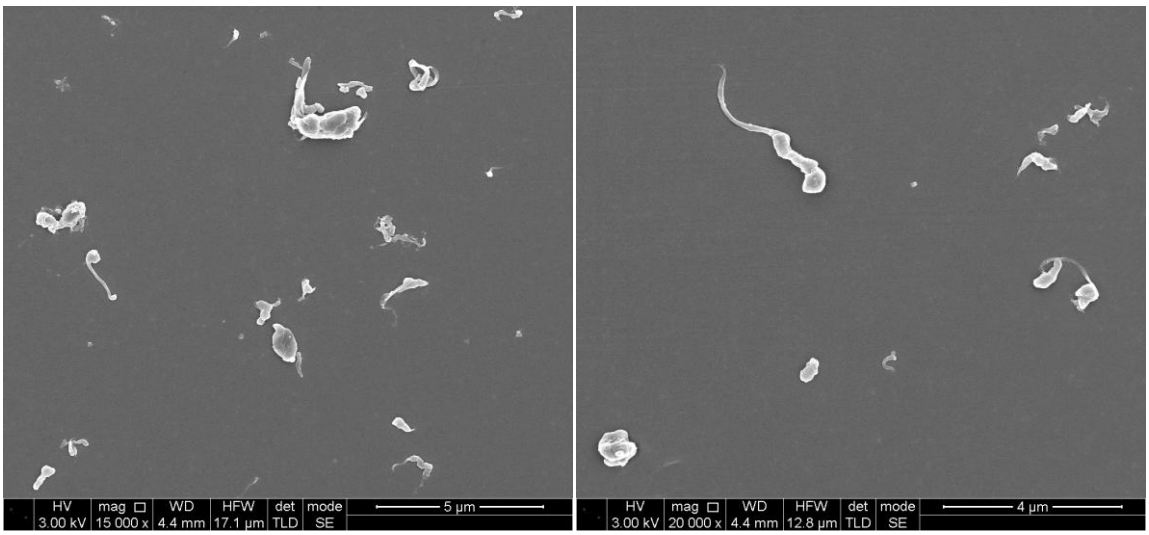

A) **B)**

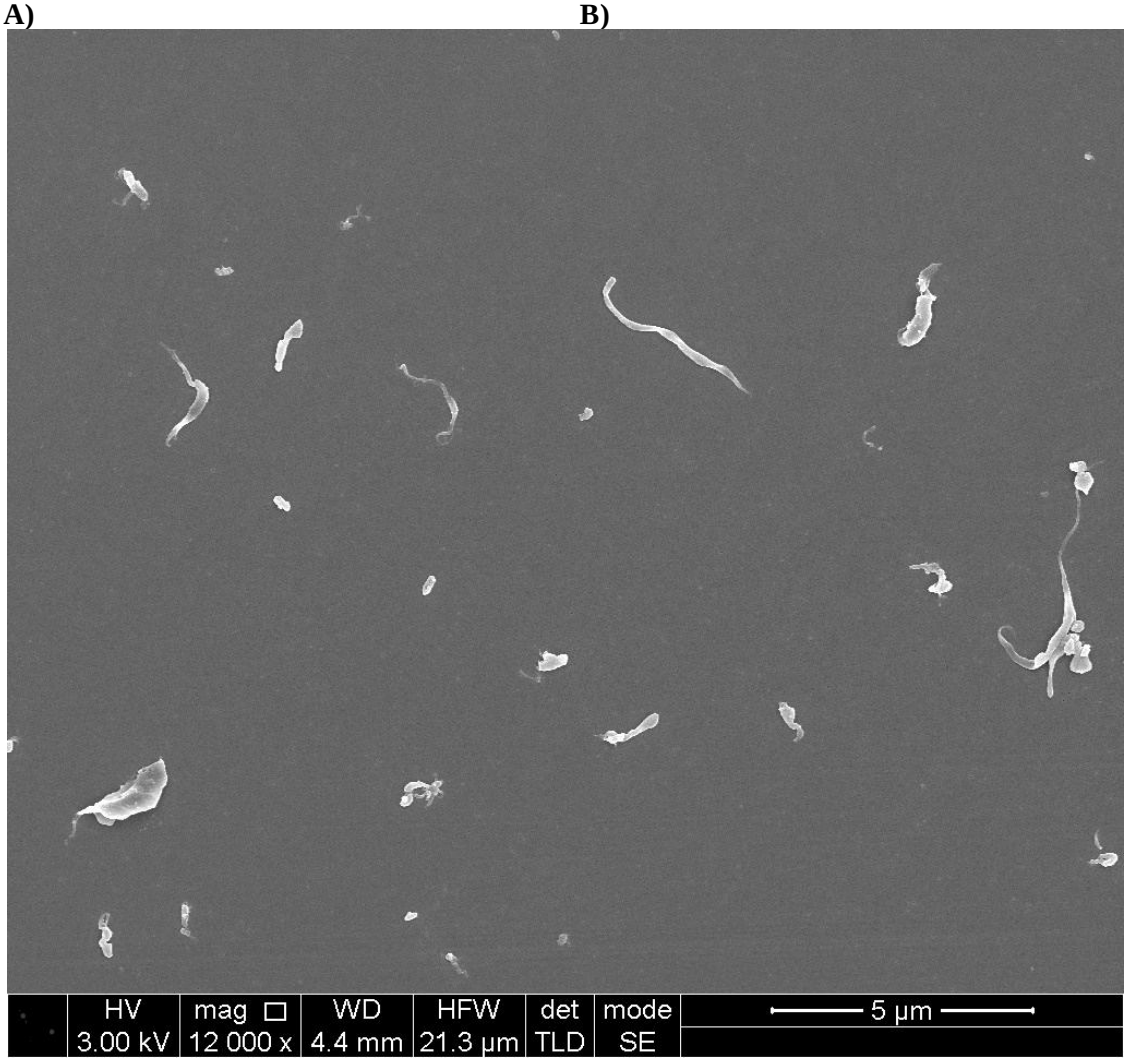

C)

Figure 5.11 Scanning electron micrographs of ArCom Knee during long-term wear. A) 15000x magnification, Scale = 5µm B) 20000x magnification, Scale = 4µm C) 12000x magnification, Scale = 5µm.

E1 Knee Long-term Wear

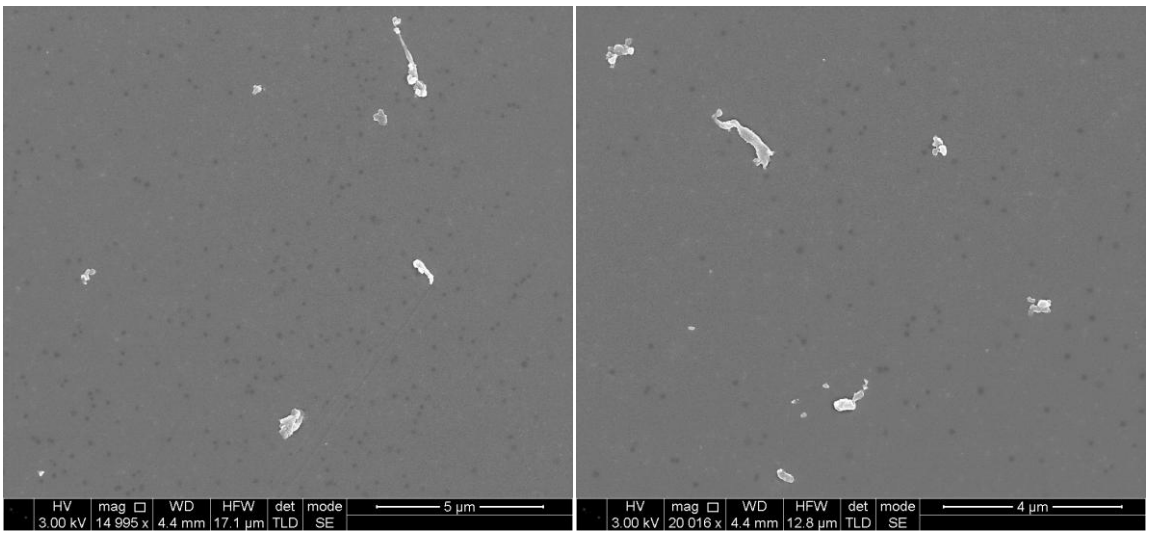

A) **B)**

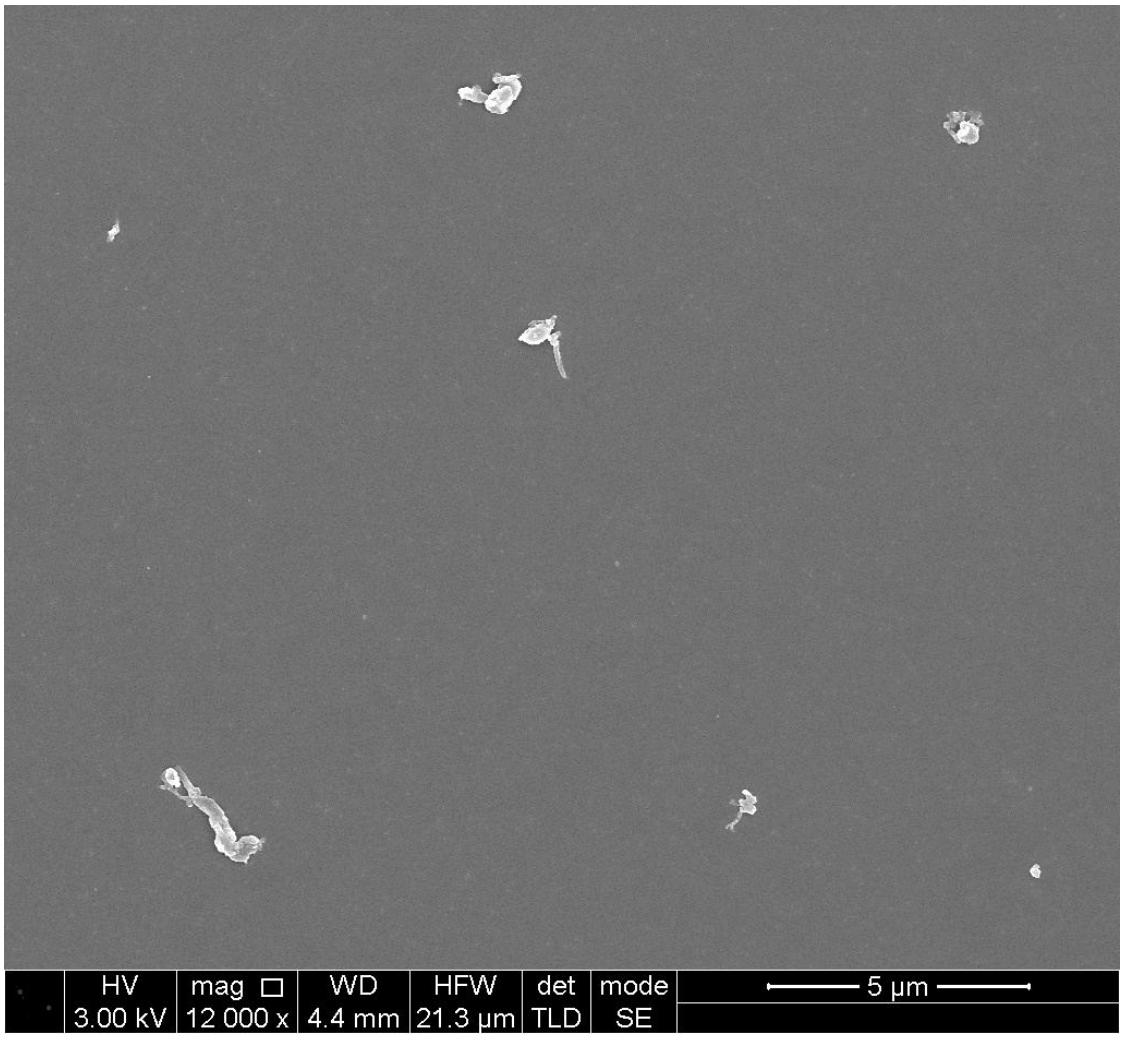

C)

Figure 5.12 Scanning electron micrographs of E1 Knee during long-term wear. A) 15000x magnification, Scale = 5µm B) 20000x magnification, Scale = 4µm C) 12000x magnification, Scale = 5µm.

5.1.1.2.2 Shape analysis

In terms of shape analysis, the aspect ratio values showed a gradual increase with increase in particle size as shown in Figure 5.13. Moreover, ArCom had significantly higher aspect ratio values compared to E1 for 0.1 to 1µm size range. For elongation, ArCom had higher elongation values in comparison to E1 for particles larger than 0.1 µm. Moreover, the difference in elongation values increased with an increase in size.

When the roundness values of ArCom and E1 UHMWPE were compared, a gradual decrease in the roundness value with increrase in particle size was noticed as shown in Figure 5.15. However, roundness values of E1 wear particles were higher than of ArCom for particles in 0.1 to 5 µm size range. This indicated more round morphology of E1 wear particles for above size range. Form factor showed a similar trend as shown in Figure 5.16. These results were similar to early wear of both ArCom and E1.

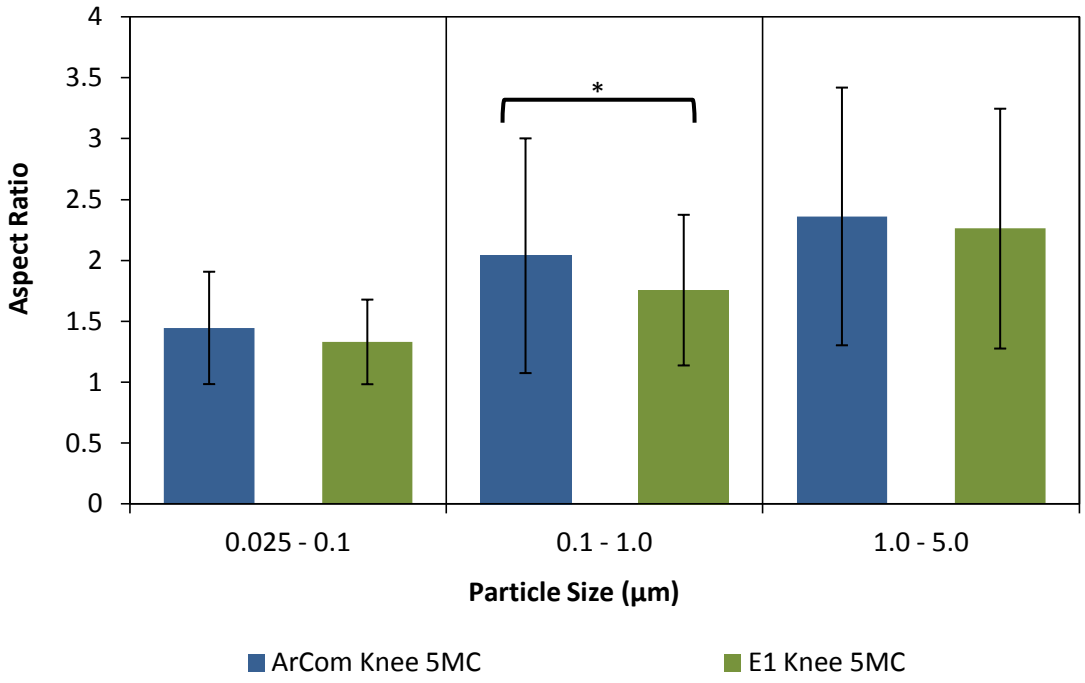

Figure 5.13 A plot showing aspect ratio versus particle size for long-term wear of ArCom and E1 Knee UHMWPE. Error bars indicate standard deviation from mean value in each size range. Statistically significant differences ($p < 0.05$) are highlighted with a black outline. ArCom particles showed more elongated shape than E1 in 0.1 to 1µm size range.

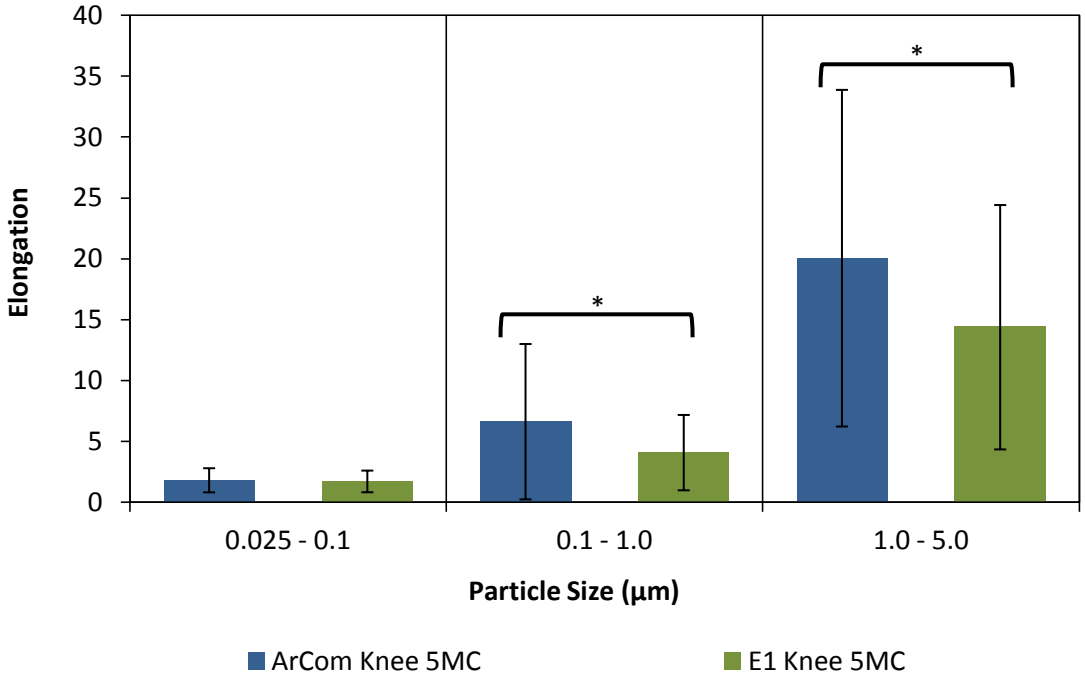

Figure 5.14 A plot showing elongation versus particle size for long-term wear of ArCom and E1 Knee UHMWPE. Error bars indicate standard deviation from mean value in each size range. Statistically significant differences ($p < 0.05$) are highlighted with a black outline. ArCom particles showed more elongated fibrillar shape than E1 for particles larger than 0.1µm.

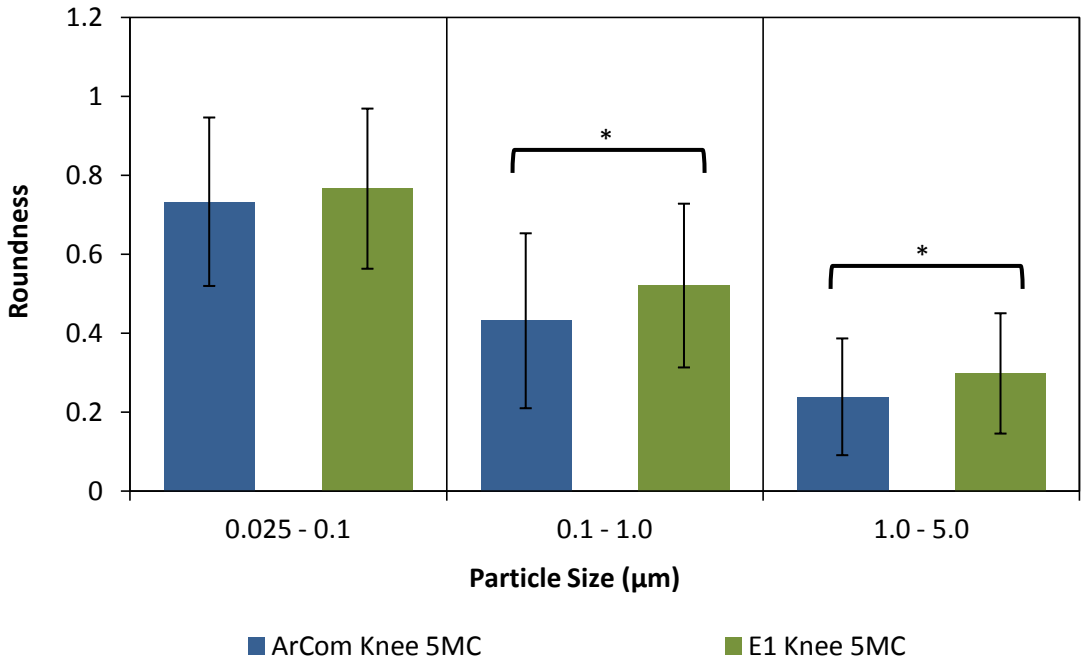

Figure 5.15 plot showing mean roundness versus particle size for long-term wear of ArCom and E1 Knee UHMWPE. Error bars indicate standard deviation from mean value in each size range. Statistically significant differences ($p < 0.05$) are highlighted with a black outline. E1 particles showed more round shape than ArCom in 0.1 to 5 µm size range.

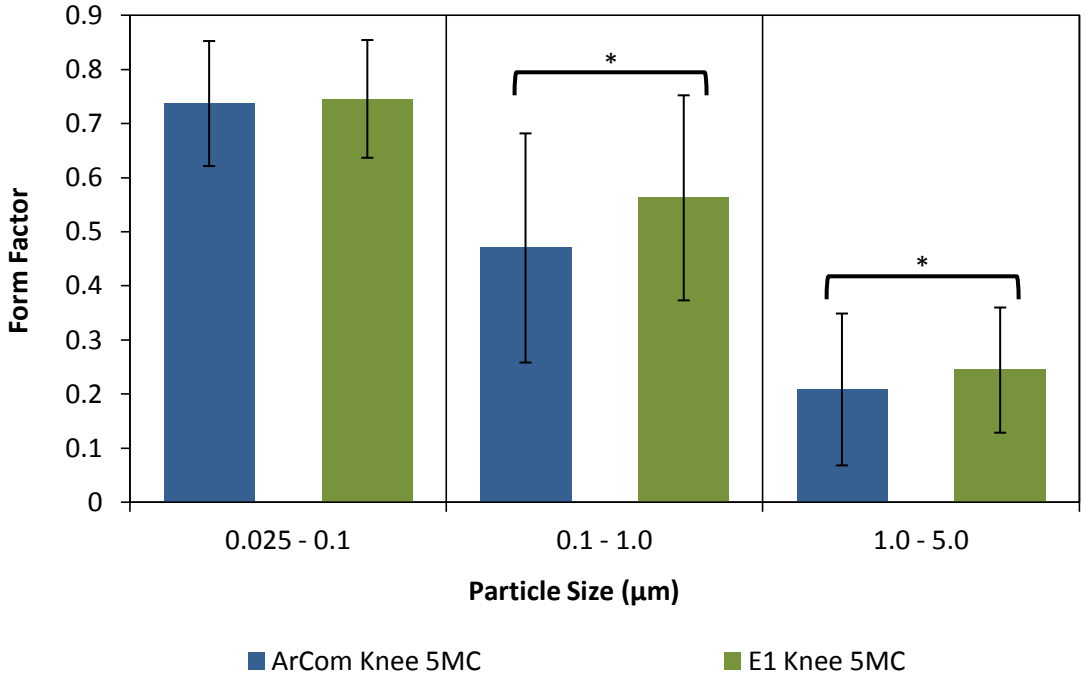

Figure 5.16 A plot showing form factor versus particle size for long-term wear of ArCom and E1 Knee UHMWPE. Error bars indicate standard deviation from mean value in each size range. Statistically significant differences ($p < 0.05$) are highlighted with a black outline. E1 showed higher form factor values than ArCom for particles larger than 0.1µm.

A gradual decrease in compactness value was observed with increase in particle size for both ArCom and E1 UHMWPE as shown in Figure 5.17. E1 showed higher compactness values than ArCom for particles in 0.1 - 1 µm size range.

When complexity values of both ArCom and E1 UHMWPE were plotted against particle size, both ArCom and E1 UHMWPE showed more complex morphology of particles with increase in size. Moreover, ArCom wear particles were slightly more complex in shape in comparison to E1 wear particles in 0.1 to 5 µm size range as shown in Figure 5.18.

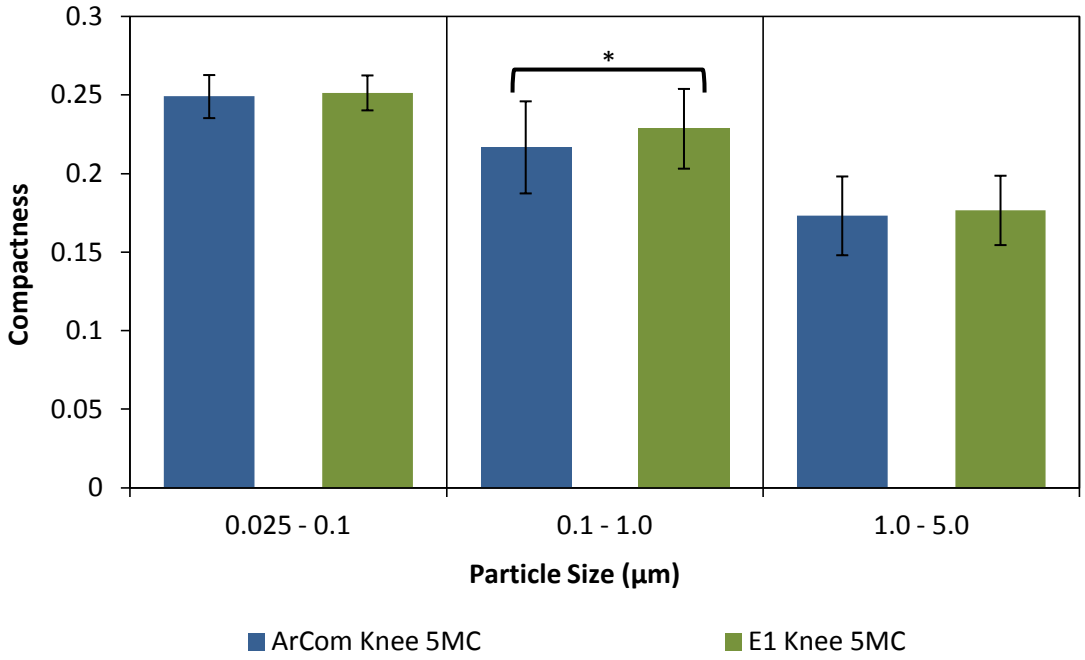

Figure 5.17 A plot showing compactness versus particle size for long-term wear of ArCom and E1 Knee UHMWPE. Error bars indicate standard deviation from mean value in each size range. Statistically significant differences ($p < 0.05$) are highlighted with a black outline. E1 showed more compact shape than ArCom for particles in 0.1 - 1 µm size range.

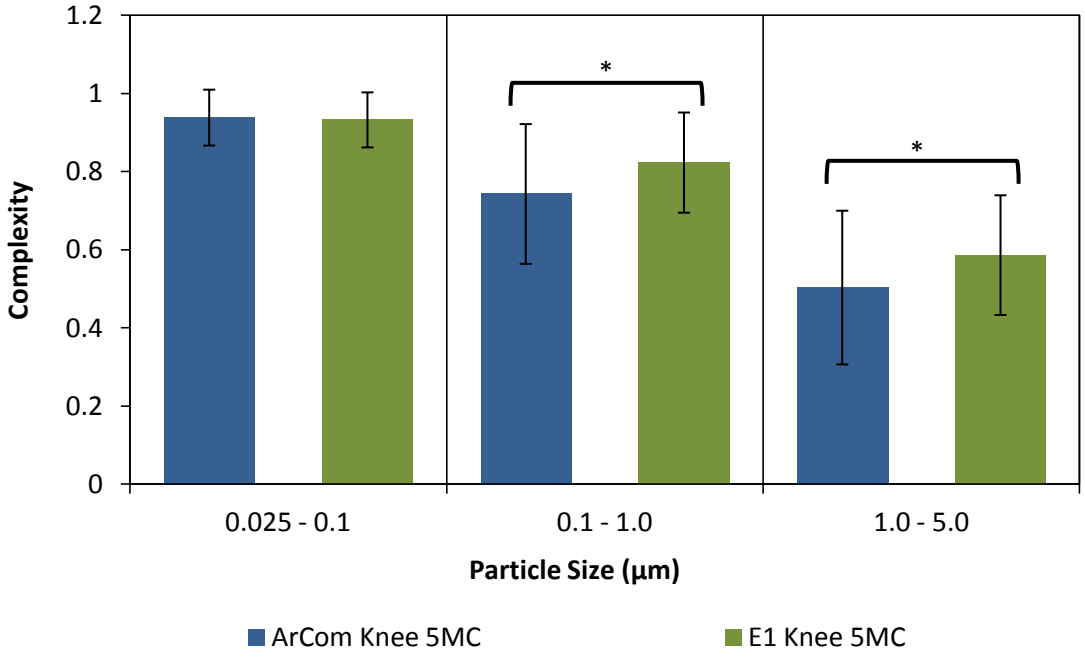

Figure 5.18 A plot showing complexity versus particle size for long-term wear of ArCom and E1 Knee UHMWPE. Error bars indicate standard deviation from mean value in each size range. Statistically significant differences ($p < 0.05$) are highlighted with a black outline. ArCom particles showed more complex shape than E1 in 0.1 to 5 µm size range.

5.1.2 ArCom multidirectional pin-on-plate vs. E1 multidirectional pin-on-plate

In this section, wear particles isolated from multidirectional pin-on-plate wear testing of ArCom® plates and E1® plates against CoCr flat pins were compared. Particles generated during long-term wear of both materials were compared for size and morphology.

5.1.2.1 Size analysis

ArCom generated a large number of particles greater then 1µm in size in comparison to E1 as shown in Figure 5.19. Alternatively, E1 generated a large fraction of submicron particles in 100-500nm size range. Statistical analysis using Kolmogorov-smirnov Z test indicated that both size distributions were significantly different from each other ($p < 0.05$).

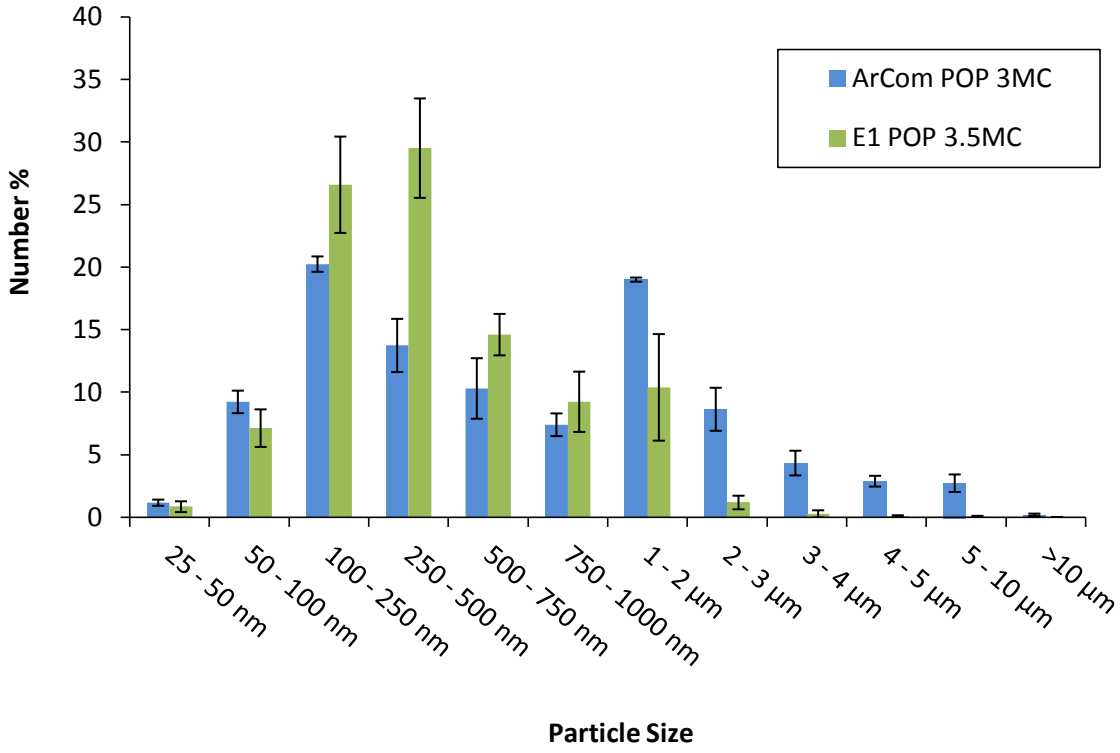

Figure 5.19 A comparison between percentage number size distributions according to maximum Feret's diameter (dmax) of ArCom multidirectional pin-on-plate (POP) and E1 multidirectional pin-on-plate(POP) wear particles during long-term wear. Error bars show standard deviation.

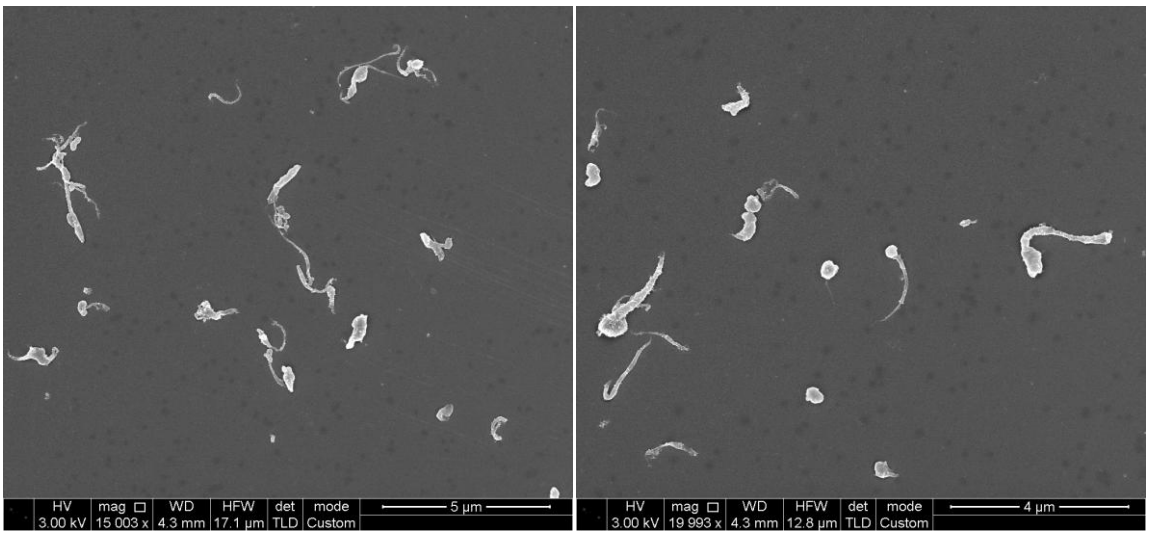

A) **B)**

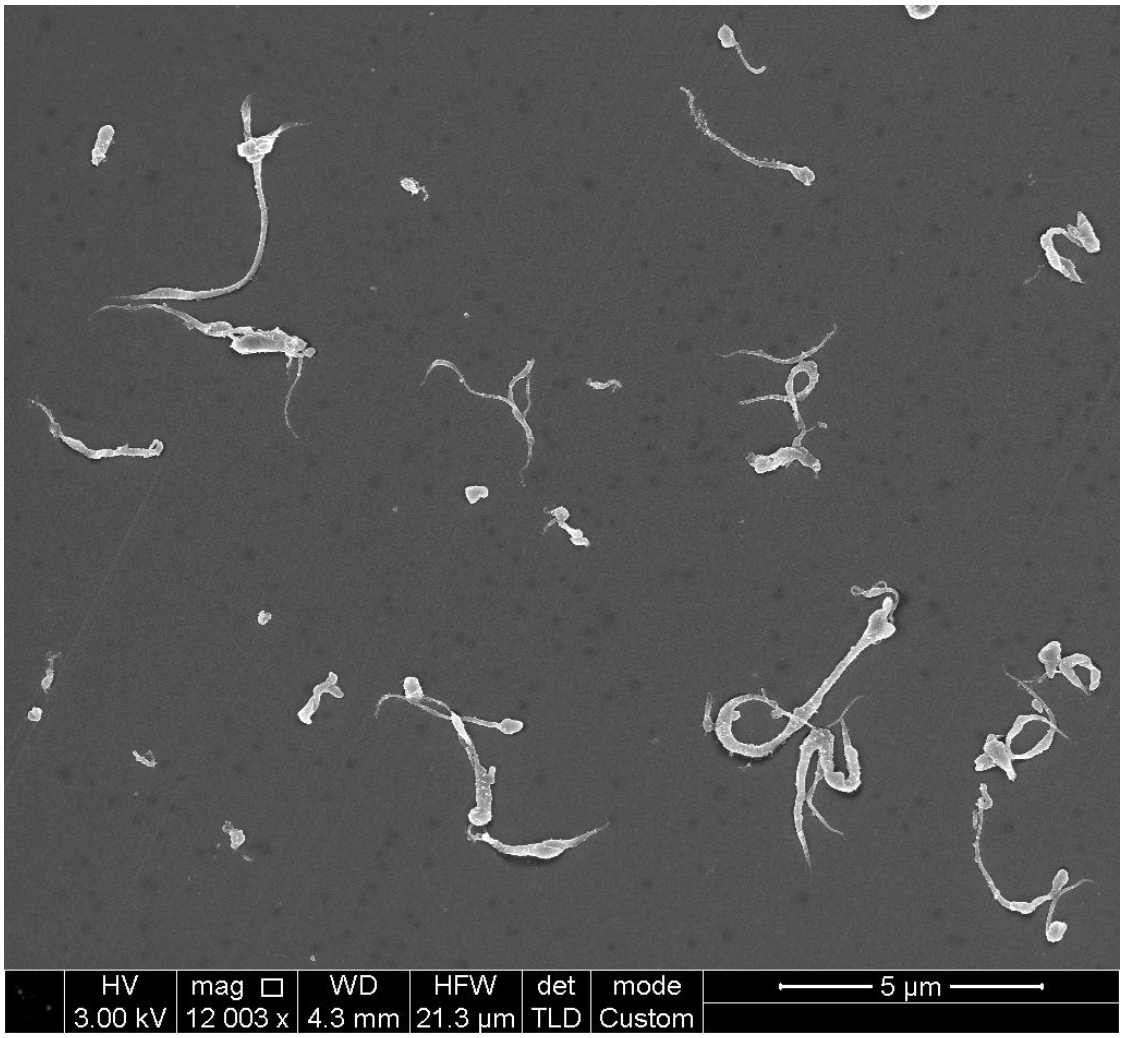

C)

Figure 5.20 Scanning electron micrographs of ArCom multistation pin-on-plate during long-term wear. A) 15000x magnification, Scale = 5µm B) 20000x magnification, Scale = 4µm C) 12000x magnification, Scale = 5µm.

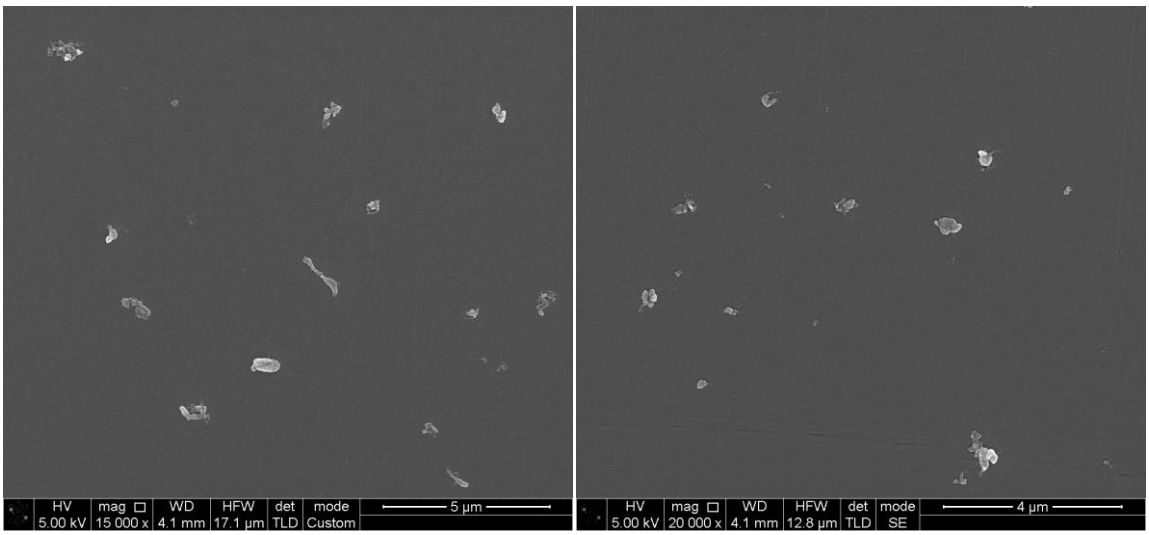

A) **B)**

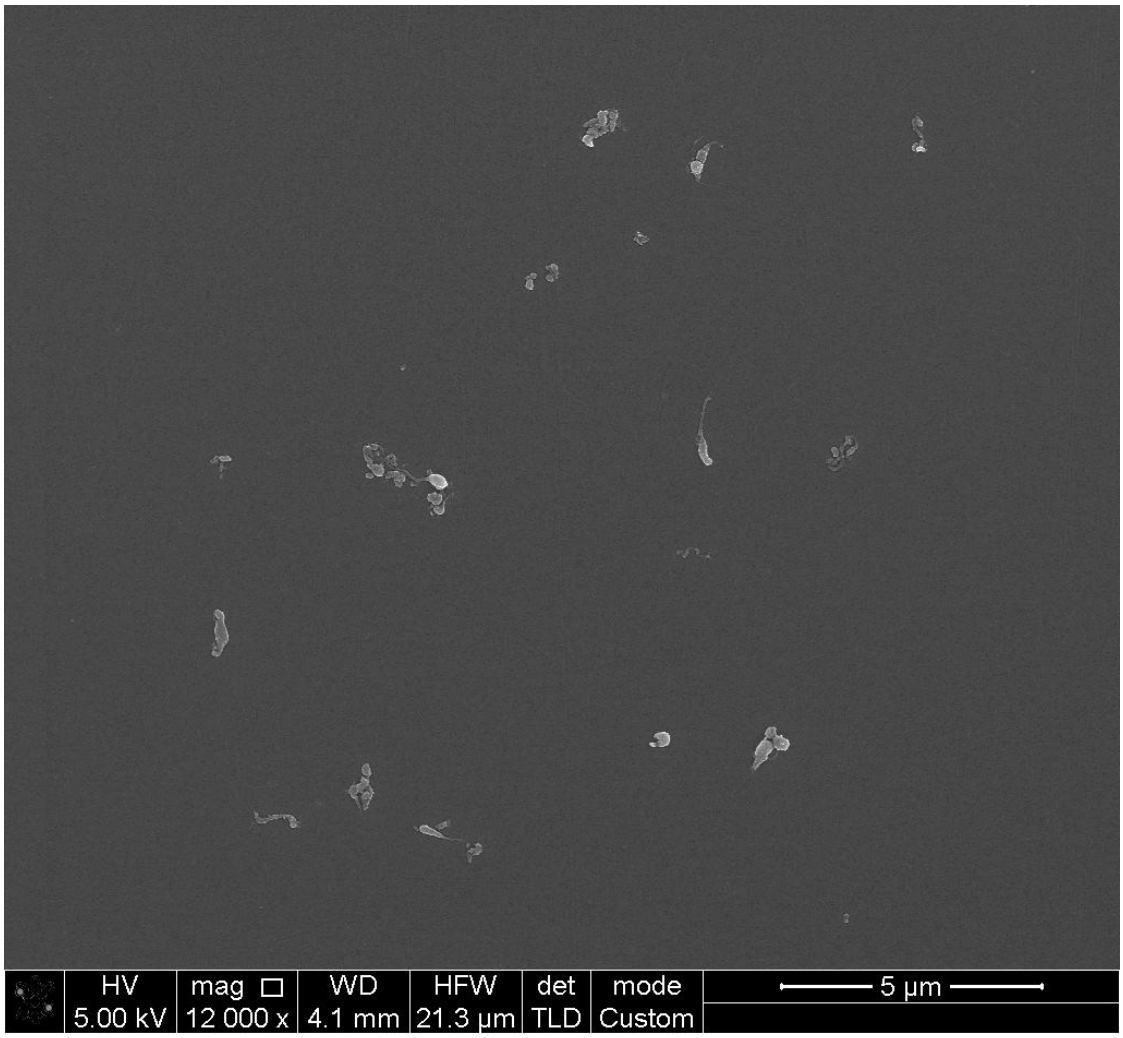

C)

Figure 5.21 Scanning electron micrographs of E1 multistation pin-on-plate during long-term wear. A) 15000x magnification, Scale = 5µm B) 20000x magnification, Scale = 4µm C) 12000x magnification, Scale = 5µm.

5.1.2.2 Shape analysis

A comparison between aspect ratio values of ArCom POP and E1 POP particles is shown in Figure 5.22. Aspect ratio value increased gradually with an increase in particle size for both samples. Moreover, ArCom particles in 0.1 to 5 µm size range showed higher aspect ratio values in comparison to E1.

Figure 5.23 shows a comparison between elongation values of both samples. There was an increase in elongation values with an increase in particle size for both samples. This increase was more noticeable for large particles (size greater than 1µm). ArCom particles showed higher elongation values in comparison to E1. This indicated that ArCom particles were more fibrillar in comparison to E1.

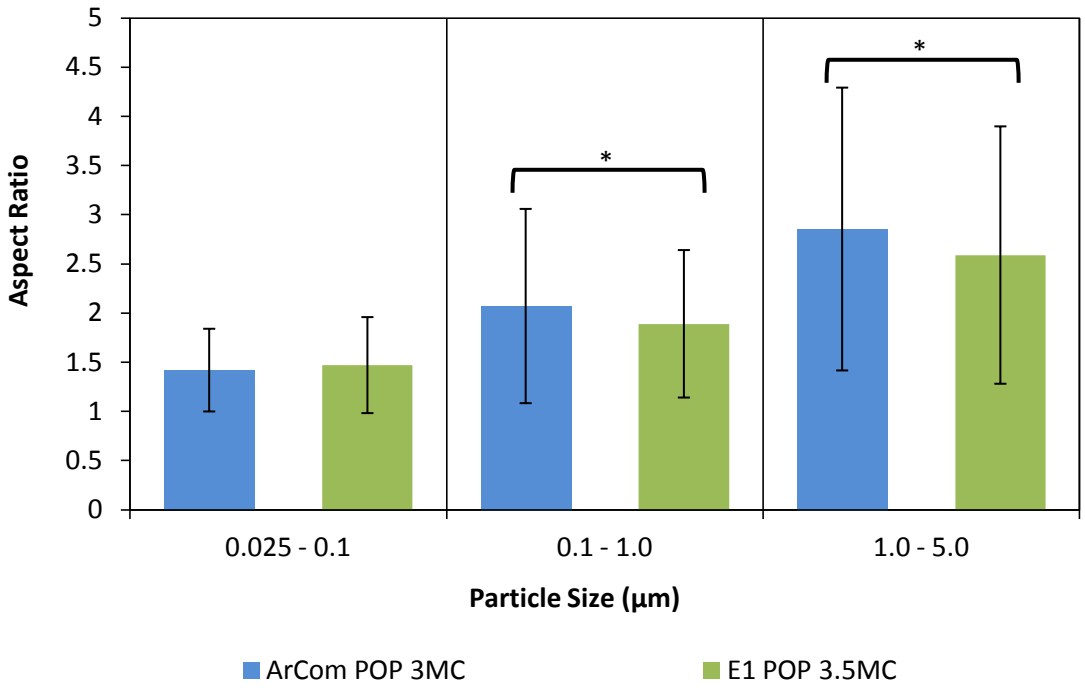

Figure 5.22 A plot showing aspect ratio versus particle size for long-term wear ArCom and E1 multidirectional pin-on-plate(POP) UHMWPE particles. Error bars indicate standard deviation from mean value in each size range. Statistically significant differences ($p < 0.05$) are highlighted with a black outline. ArCom particles showed more elongated shape than E1 in 0.1 to 5 µm size range.

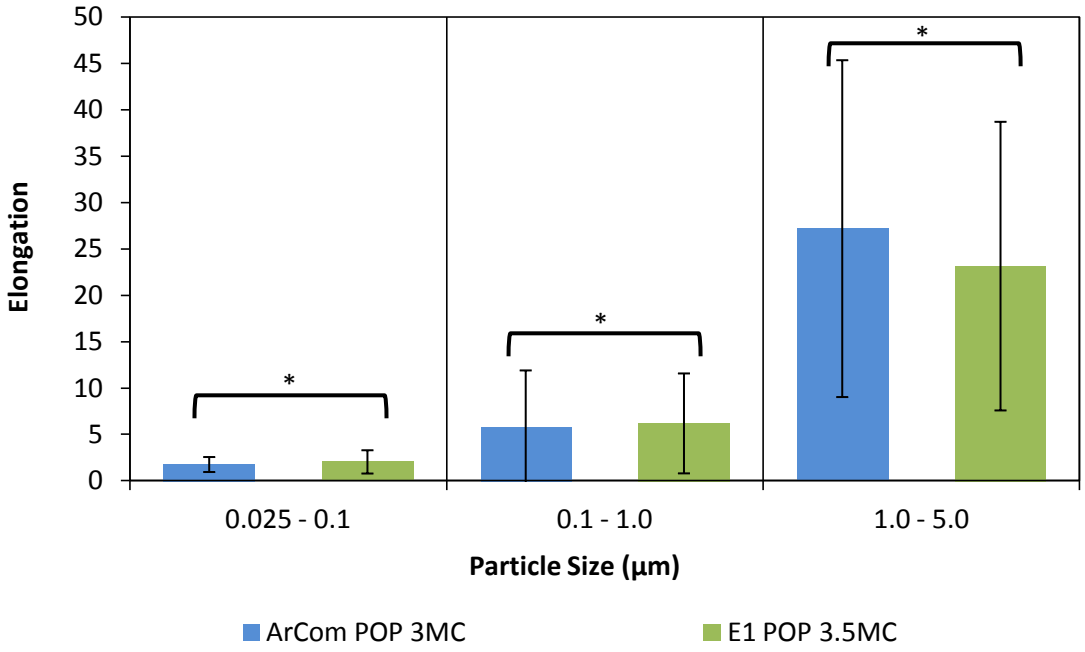

Figure 5.23 A plot showing elongation versus particle size for long-term wear ArCom and E1 multidirectional pin-on-plate (POP) UHMWPE particles. Error bars indicate standard deviation from mean value in each size range. Statistically significant differences ($p < 0.05$) are highlighted with a black outline. ArCom particles showed more elongated fibrillar shape than E1.

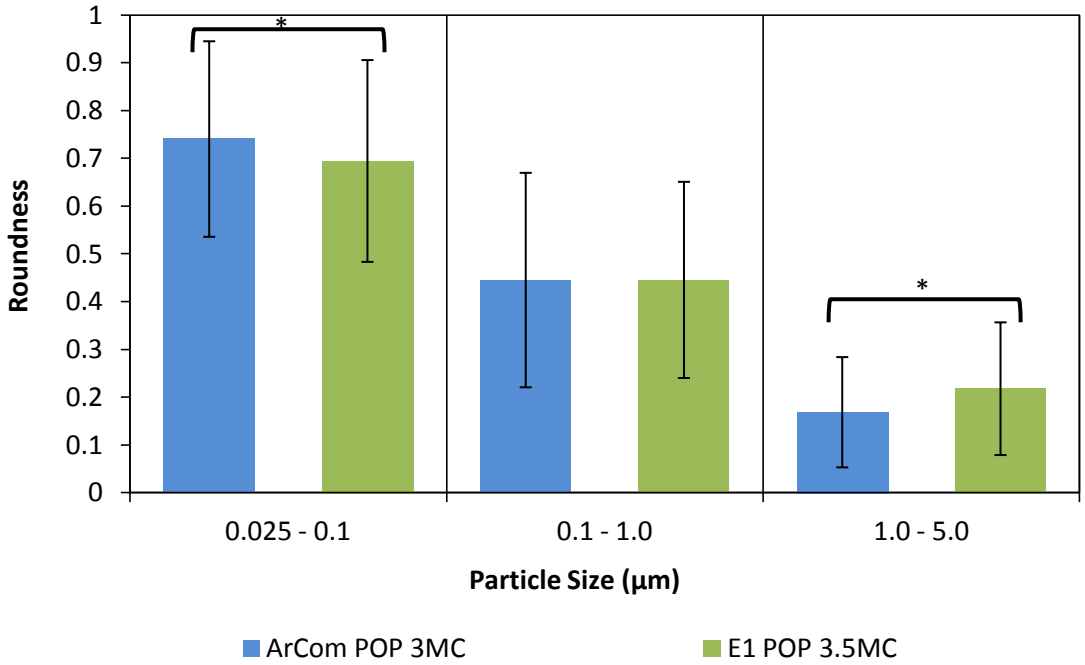

Figure 5.24 A plot showing roundness versus particle size for long-term wear ArCom and E1 multidirectional pin-on-plate (POP) UHMWPE particles. Error bars indicate standard deviation from mean value in each size range. Statistically significant differences ($p < 0.05$) are highlighted with a black outline. ArCom particles were more round shaped in 0.025 to 0.1 µm size range, while E1 particles were more round shaped in 1 to 5µm size range.

Figure 5.24 shows a comparison between roundness values of ArCom POP and E1 POP particles. A decrease in roundness values with an increase in particle size was noticed for both samples. ArCom particles were had higher roundness in 0.025 to 0.1 µm size range, while E1 particles had higher roundness in 1 to 5µm size range. In regards to form factor, ArCom particles showed higher form factor values than E1 for particles in 0.025 to 1 µm size range, while E1 particles had higher form factor in 1 to 5 µm size range as shown in Figure 5.25.

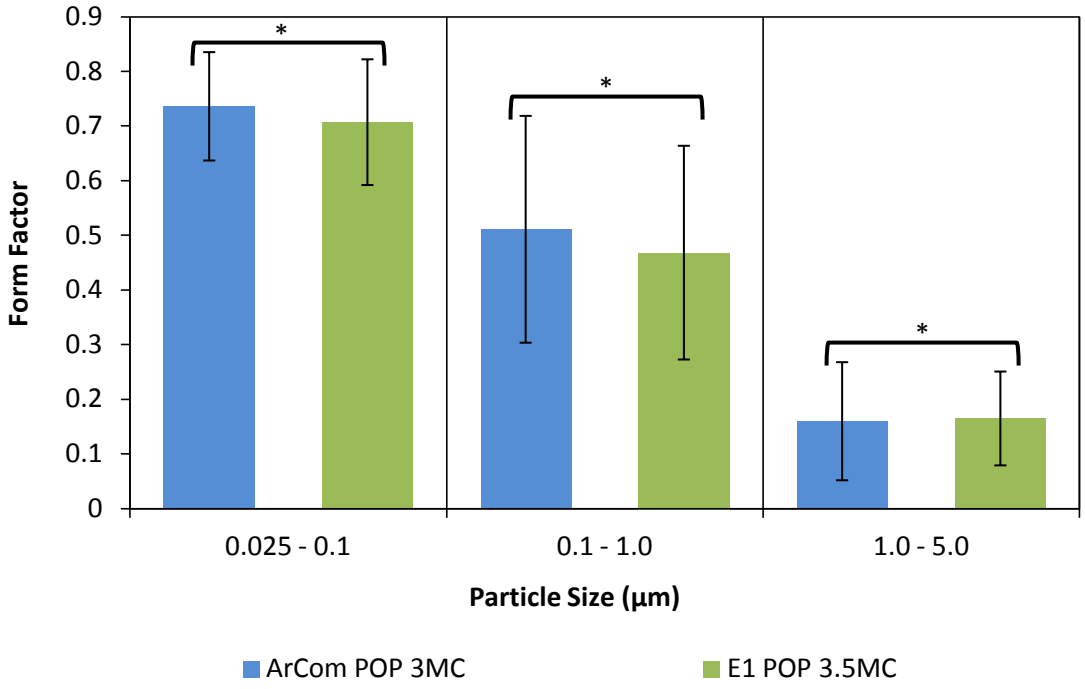

Figure 5.25 A plot showing form factor versus particle size for long-term wear ArCom and E1 multidirectional pin-on-plate (POP) UHMWPE particles. Error bars indicate standard deviation from mean value in each size range. Statistically significant differences ($p < 0.05$) are highlighted with a black outline. ArCom particles showed higher form factor values than E1 for particles in 0.025 to 1 µm size range, while E1 particles had higher form factor in 1 to 5 µm size range.

A comparison between compactness values of both ArCom POP and E1 POP is shown in Figure 5.26. There was a gradual decrease in compactness values with an increase in particle size. However, no significant difference was found between the compactness values of both ArCom and E1 particles.

Figure 5.27 shows complexity values of both ArCom POP and E1 POP particles. There was a decrease in complexity value with an increase in particle size for both samples indicating an increase complexity of particle shapes with size. ArCom showed marginally more complex shape for particles larger than 1µm, while E1 had more complex shape for particles in 0.025 to 1 µm size range.

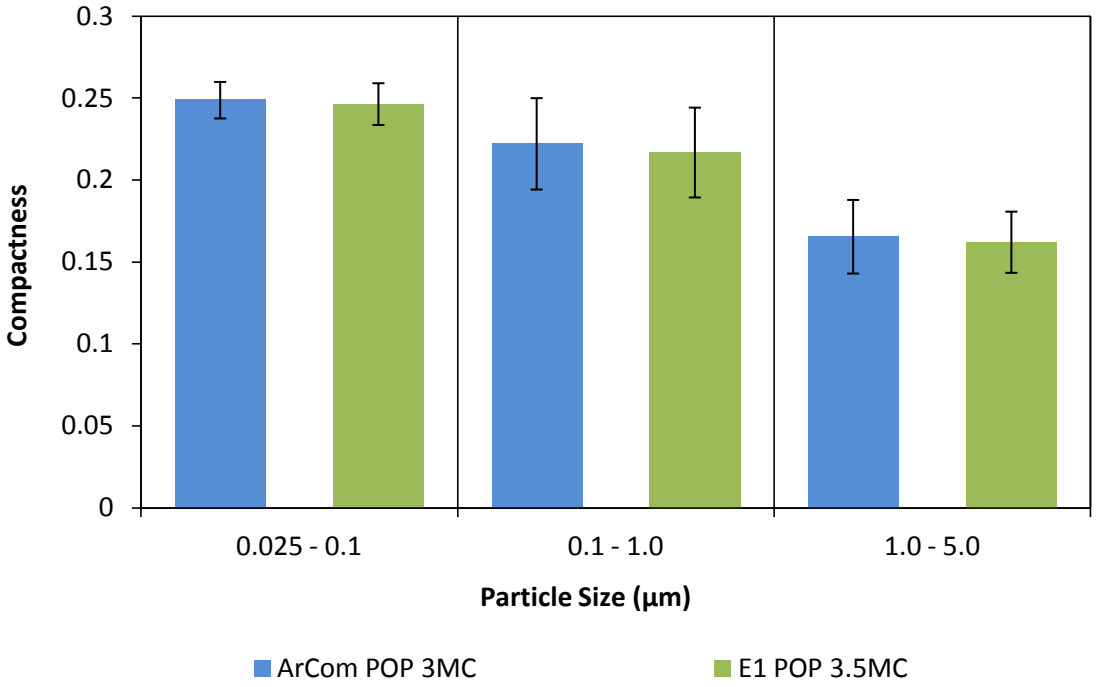

Figure 5.26 A plot showing compactness versus particle size for long-term wear ArCom and E1 multidirectional pin-on-plate (POP) UHMWPE particles. Error bars indicate standard deviation from mean compactness value in each size range. Both ArCom and E1 had similar compactness values.

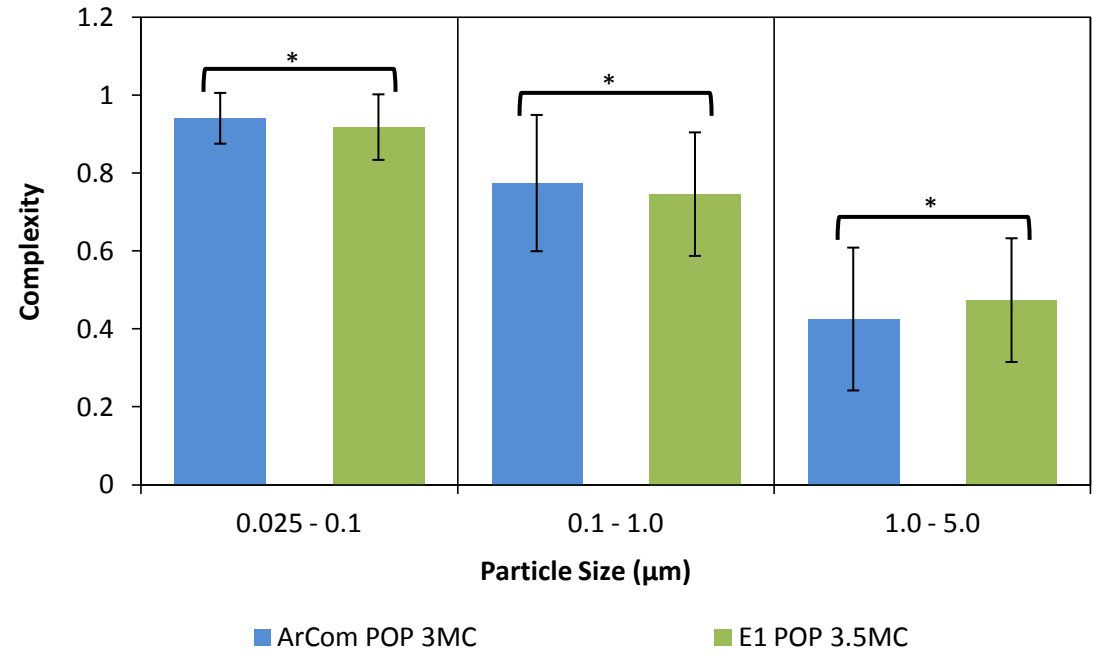

Figure 5.27 A plot showing complexity versus particle size for long-term wear ArCom and E1 multidirectional pin-on-plate (POP) UHMWPE particles. Error bars indicate standard deviation from mean value in each size range. ArCom particles had more complex shape for particles larger than 1µm, while E1 had more complex shape for particles in 0.025 to 1 µm size range.

5.1.3 E1 Hip vs. ECiMa Hip

In this section, wear particles isolated from UHMWPE-on-CoCr hip simulator wear testing of vitamin E diffused E1® (Active Articulation™) and vitamin E blended highly crosslinked ECiMa™ (Trinity™) were compared. Particles generated during early wear and long-term wear of both materials were compared for size and morphology.

5.1.3.1 Early wear

During early wear, E1 and ECiMa particles isolated from lubricant serum retrieved after 0.5 million cycles of hip simulator testing were used for particle analysis.

5.1.3.1.1 Size analysis

A comparison between number distributions of E1 and ECiMa is shown in Figure 5.28. Both size distributions were distinctly different. A bimodal size distribution was noticed for ECiMa, while E1 had a single mode size distribution. Statistical analysis using Kolmogorov-smirnov Z test also indicated that both size distributions were significantly different from each other ($p < 0.05$). Moreover, E1 generated a higher percentage of particles in 100 – 500 nm size range, while ECiMa generated a higher percentage of particles in 1 - 3µm size range.

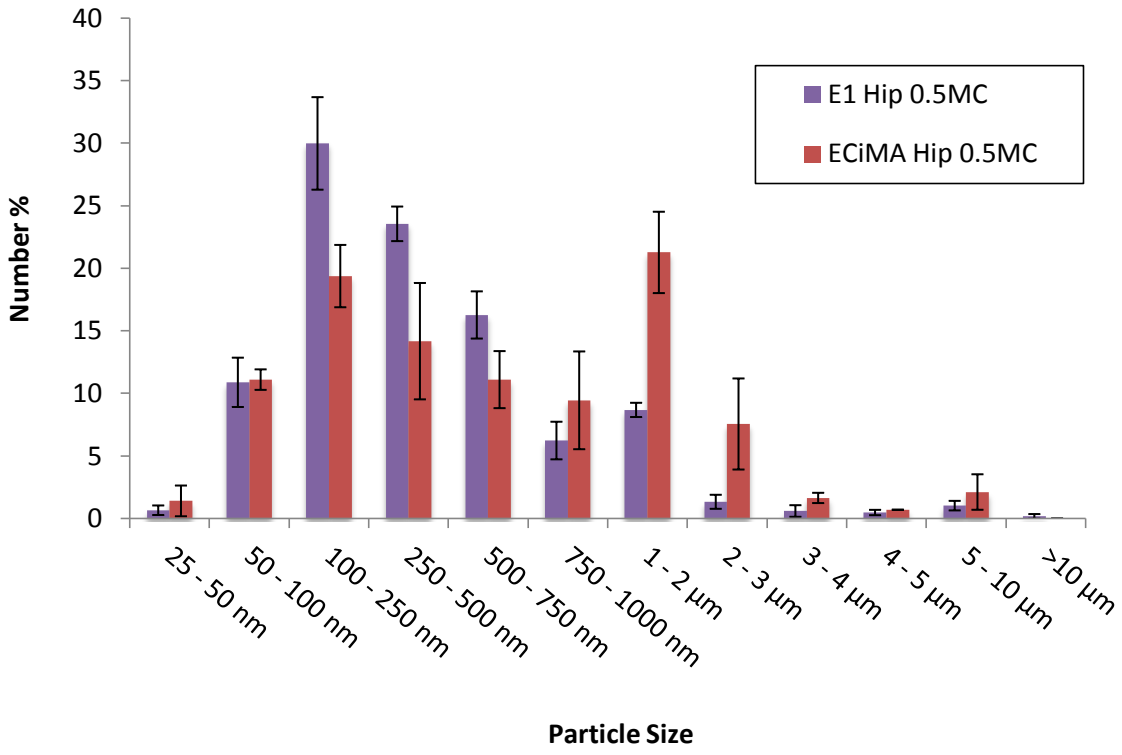

Figure 5.28 A comparison between percentage number size distributions according to maximum Feret's diameter (dmax) of E1 Hip and ECiMa hip wear particles during early wear. Error bars show standard deviation.

E1 Hip Early Wear

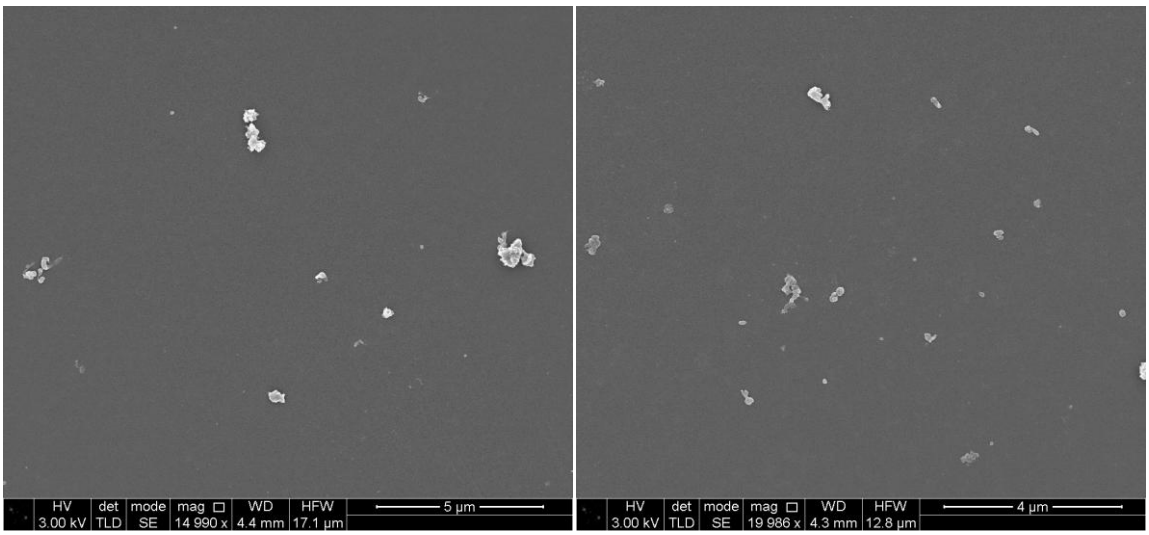

A) **B)**

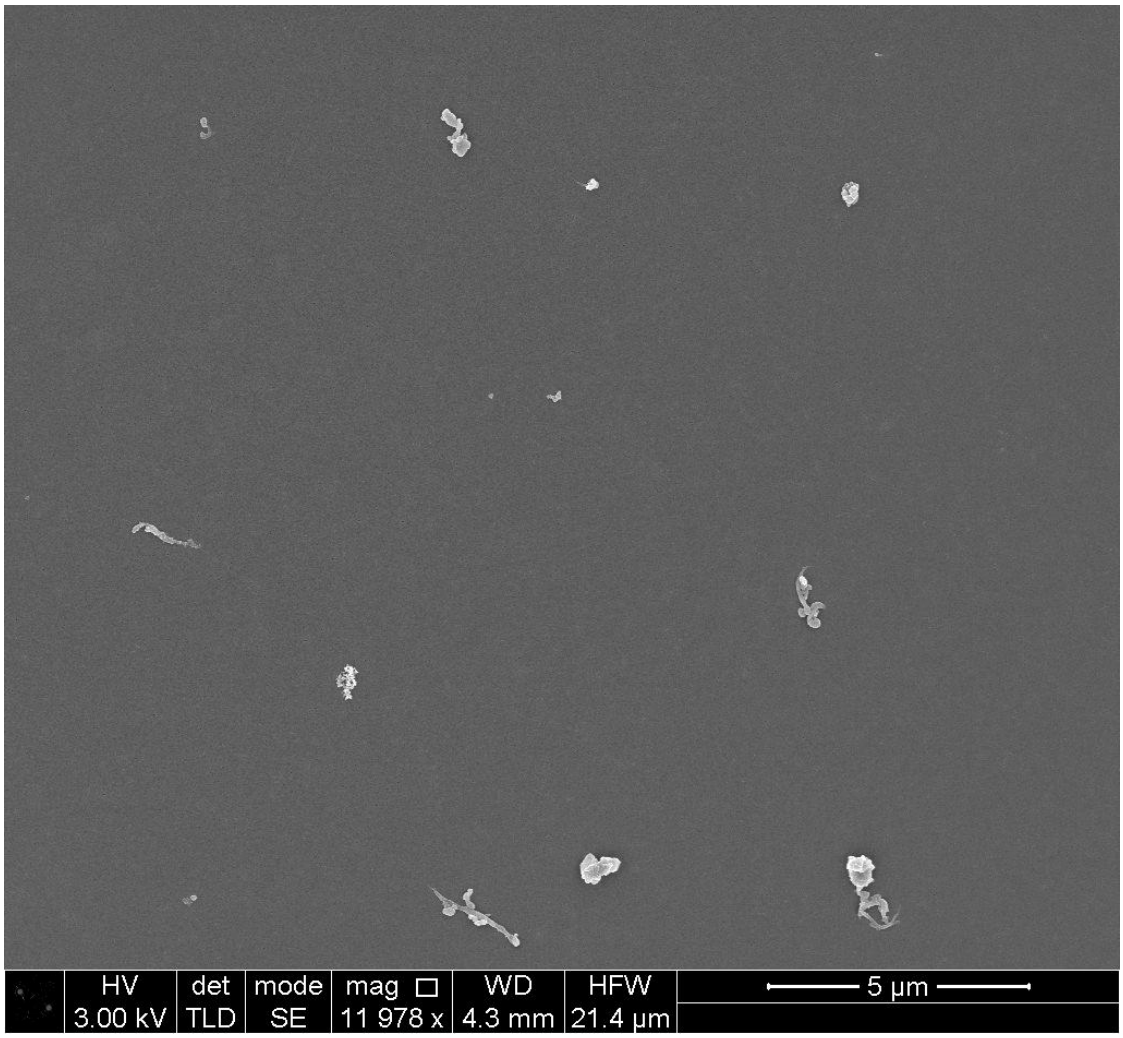

C)

Figure 5.29 Scanning electron micrographs of E1 hip during early wear. A) 15000x magnification, Scale = 5µm B) 20000x magnification, Scale = 4µm C) 12000x magnification, Scale = 5µm.

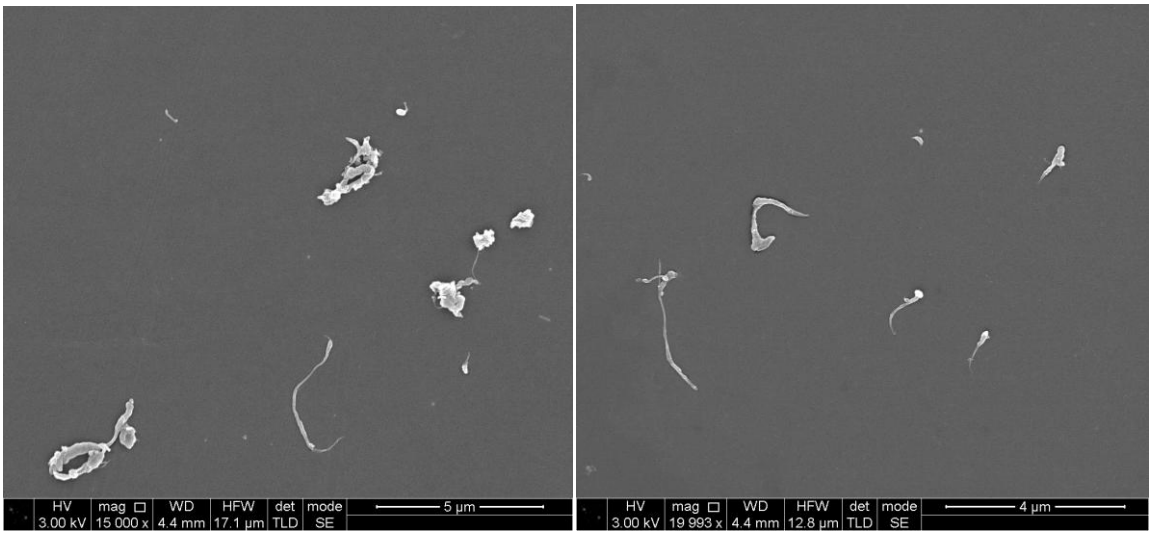

A) **B)**

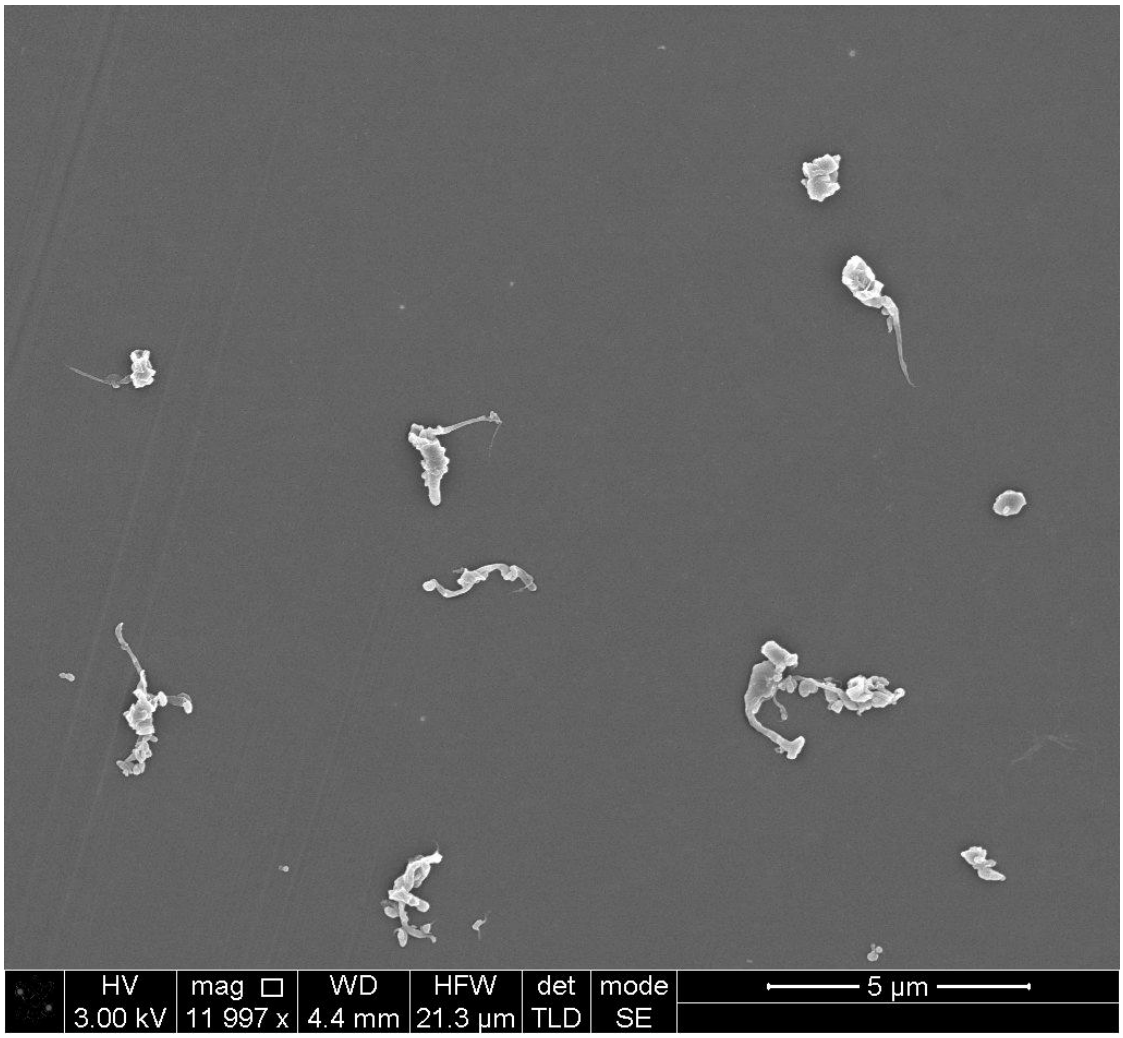

C)

Figure 5.30 Scanning electron micrographs of ECiMa hip during early wear. A) 15000x magnification, Scale = 5µm B) 20000x magnification, Scale = 4µm C) 12000x magnification, Scale = 5µm.

5.1.3.1.2 Shape analysis

Figure 5.31 shows a comparison between aspect ratio values of E1 hip and ECiMa hip particles. Both E1 and ECiMa showed a gradual increase in aspect ratio values with an increase in particle size. Moreover, ECiMa hip particles had higher aspect ratio values for particles in 0.025 to 1µm size range.

A comparison between elongation values of both samples is shown in Figure 5.32. Similar to aspect ratio there was an increase in elongation value with an increase in particle size for E1 and ECiMa. In addition, the elongation values of ECiMa particles were higher than E1 particles in 0.1 to 5µm size range.

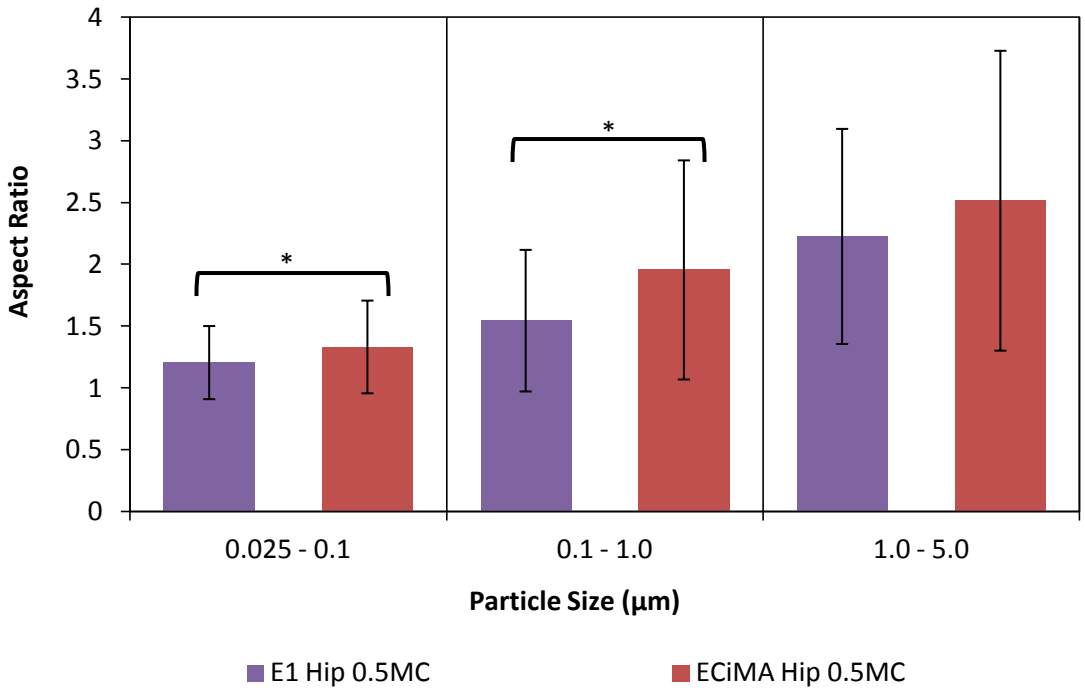

Figure 5.31 A plot showing aspect ratio versus particle size for early wear of E1 hip and ECiMA hip. Error bars indicate standard deviation from mean value in each size range. Statistically significant differences ($p < 0.05$) are highlighted with a black outline. ECiMa showed more elongated shape than E1 for submicron particles.

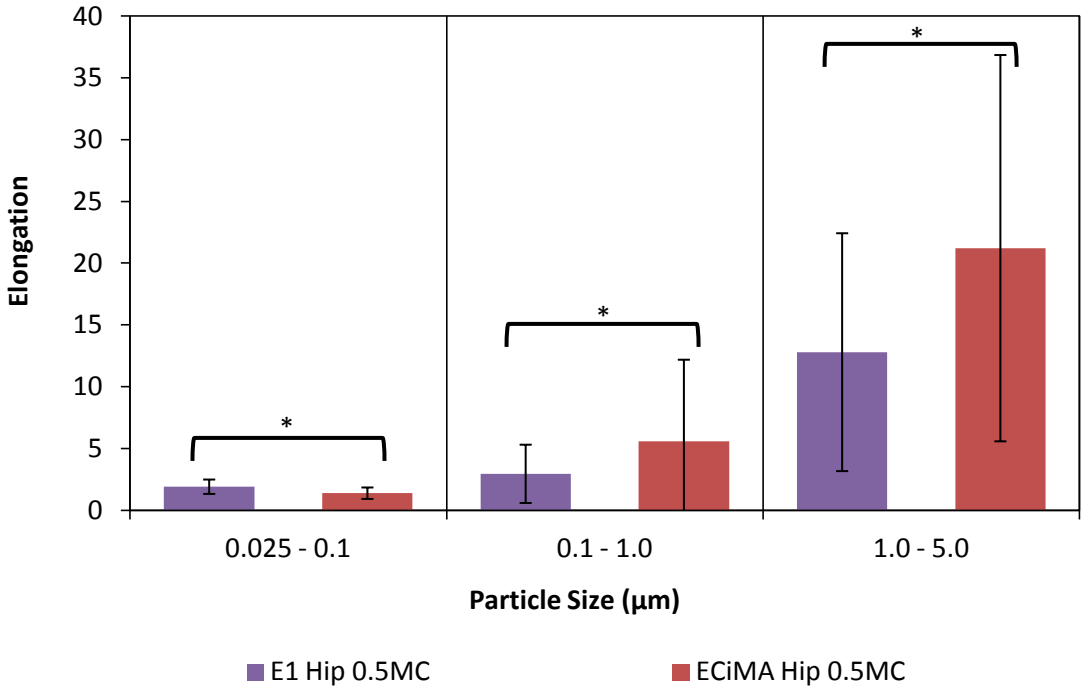

Figure 5.32 A plot showing elongation versus particle size for early wear of E1 hip and ECiMA hip. Error bars indicate standard deviation from mean value in each size range. Statistically significant differences ($p < 0.05$) are highlighted with a black outline. ECiMa showed more elongated fibrillar shaped particles in 0.1 to 5 µm size range.

Figure 5.33 shows a comparison between roundness values of E1 hip and ECiMa hip particles. There was a gradual decrease in roundness value with an increase in particle size.. Form factor values also decreased with an increase in particle size as shown in Figure 5.34. In addition, E1 particles had higher roundness and form factor values in comparison to ECiMa

Figure 5.35 shows change in compactness value with particle size for both E1 hip and ECiMa hip. A constant decrease with an increase in size was noticed for both samples. Moreover, E1 particles had higher compactness values in comparison to ECiMa hip.

A comparison between complexity values of E1 and ECiMa particles is shown in Figure 5.36. There was a constant decrease in complexity with an increase in particle size for both samples, indicating an increase in complex shape of particles with size. Furthermore, ECiMa particles showed lower complexity values in comparison to E1 for particles larger than 0.1µm. This indicated generation of more complex shape particles in ECiMa in the above size range.

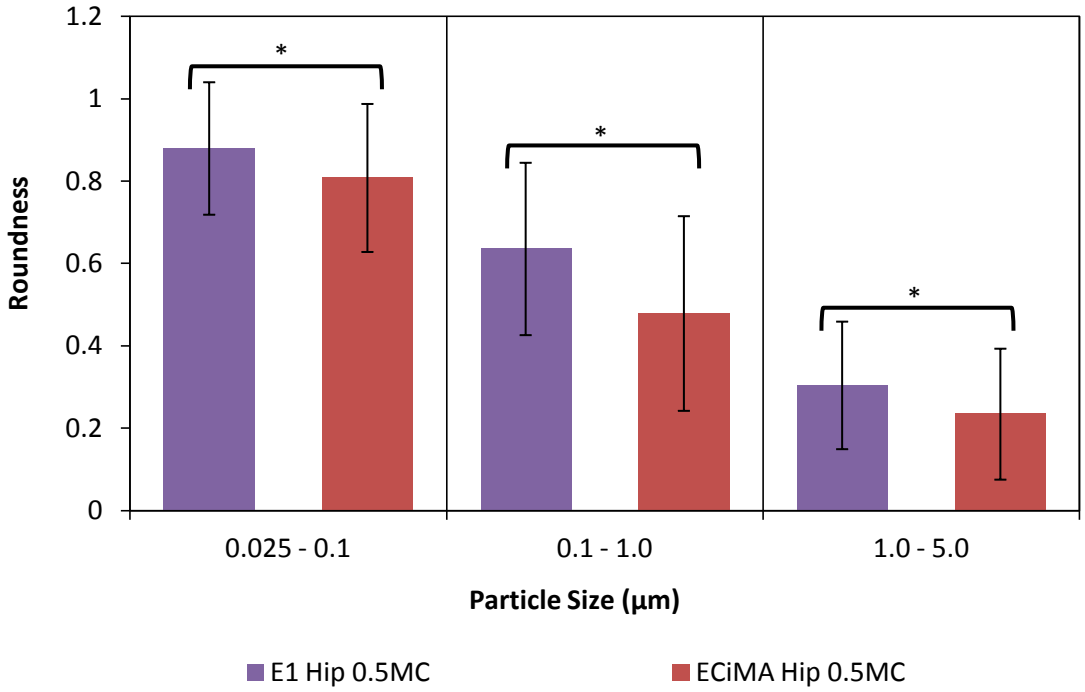

Figure 5.33 A plot showing roundness versus particle size for early wear of E1 hip and ECiMA hip. Error bars indicate standard deviation from mean value in each size range. Statistically significant differences ($p < 0.05$) are highlighted with a black outline. E1 showed more round shape than ECiMA.

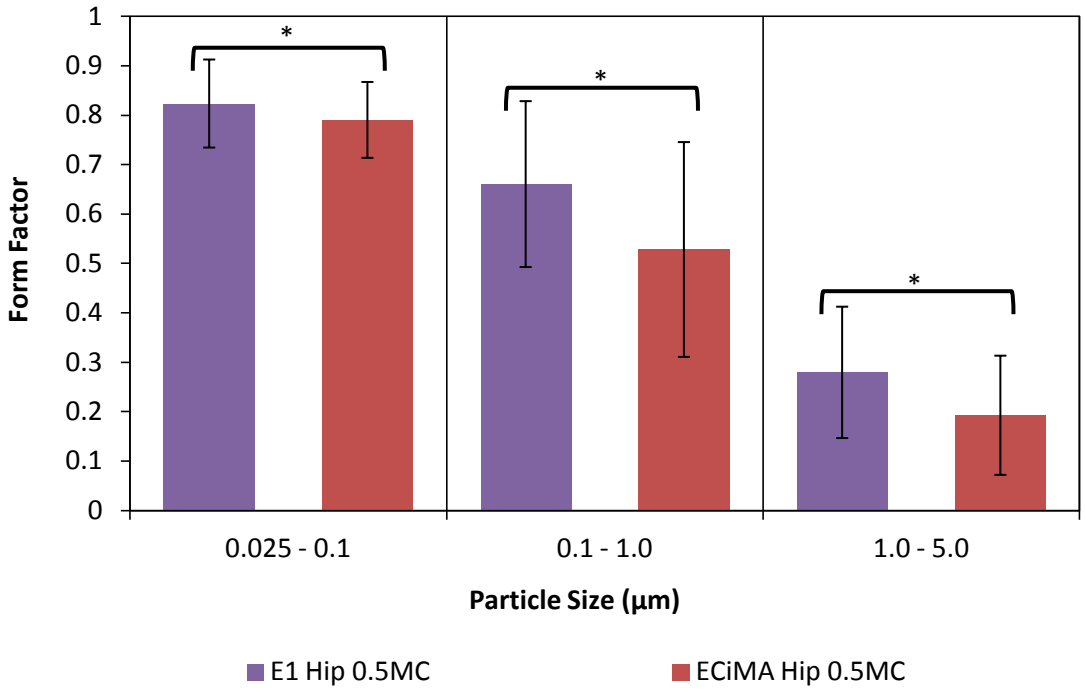

Figure 5.34 A plot showing form factor versus particle size for early wear of E1 hip and ECiMA hip. Error bars indicate standard deviation from mean value in each size range. Statistically significant differences ($p < 0.05$) are highlighted with a black outline. E1 showed higher form factor values than ECiMA.

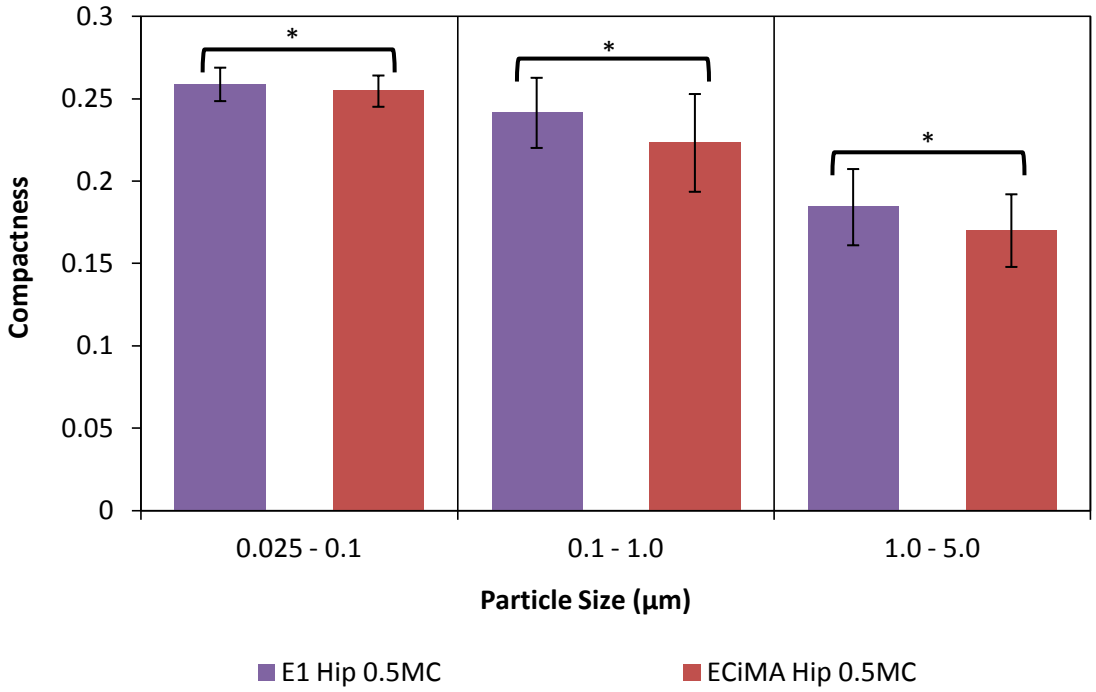

Figure 5.35 A plot showing compactness versus particle size for early wear of E1 hip and ECiMA hip. Error bars indicate standard deviation from mean value in each size range. Statistically significant differences ($p < 0.05$) are highlighted with a black outline. E1 showed more compact shape than ECiMA.

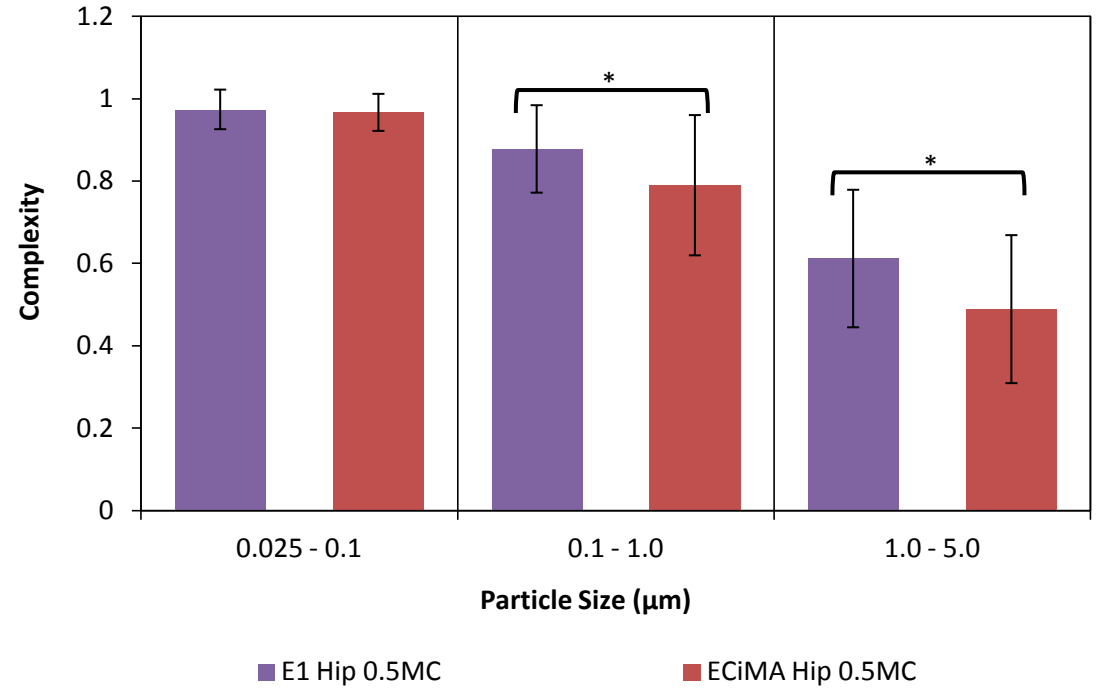

Figure 5.36 A plot showing complexity versus particle size for early wear of E1 hip and ECiMA hip. Error bars indicate standard deviation from mean value in each size range. Statistically significant differences ($p < 0.05$) are highlighted with a black outline. ECiMA showed more complex shape than E1 for particles larger than 0.1µm.

5.1.3.2 **Long-term wear**

During long-term wear, E1 and ECiMa particles isolated from simulator lubricant retrieved after 5 million cycles of hip simulator testing were compared for size and morphology.

5.1.3.2.1 Size analysis

A comparison between number distributions of E1 hip and ECiMa hip particles during long-term wear is shown in Figure 5.37. Statistical analysis using Kolmogorov-smirnov Z test indicated that both size distributions were significantly different from each other ($p < 0.05$). Moreover, the size distribution of E1 hip was slightly shifted towards smaller particle size in comparison to ECiMa hip. Majority of particles were generated in 100 - 750nm size range for both samples. E1 had a higher percentage of small particles (size below 250nm), whereas ECiMa had marginally higher percentage of particles in 250 - 750nm size range.

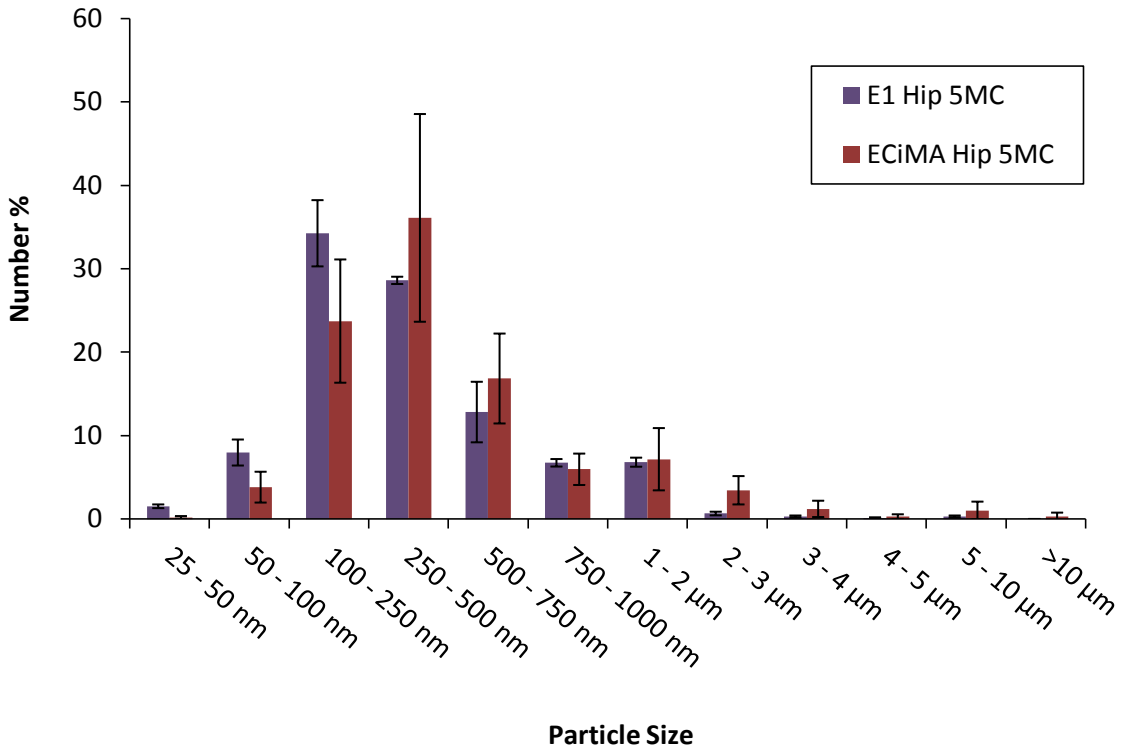

Figure 5.37 A comparison between percentage number size distributions according to maximum Feret's diameter (dmax) of E1 hip and ECiMa hip wear particles during long-term wear. Error bars show standard deviation.

E1 Hip Long-term Wear

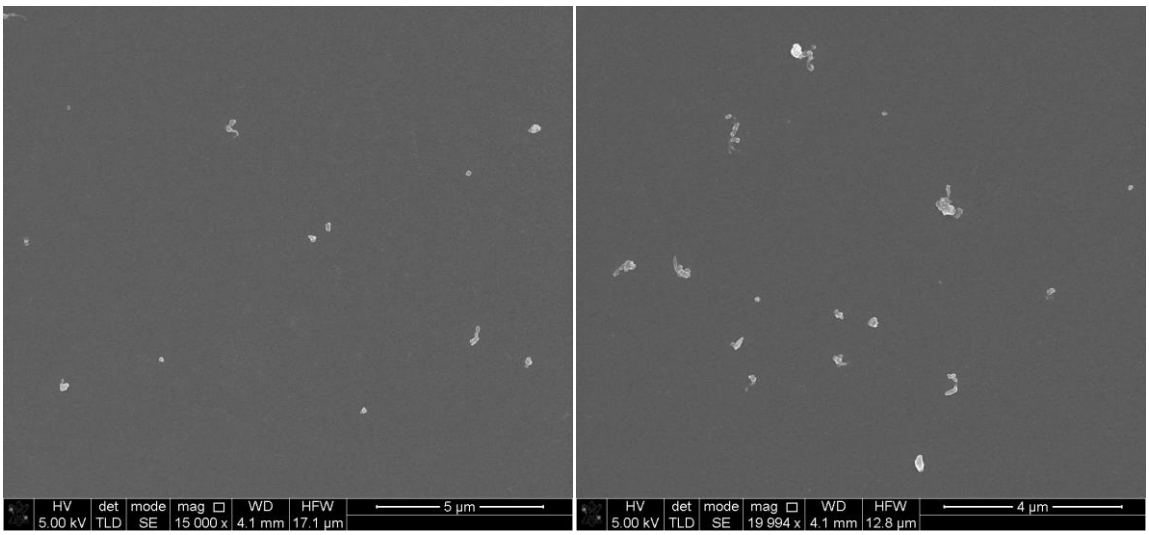

A) **B)**

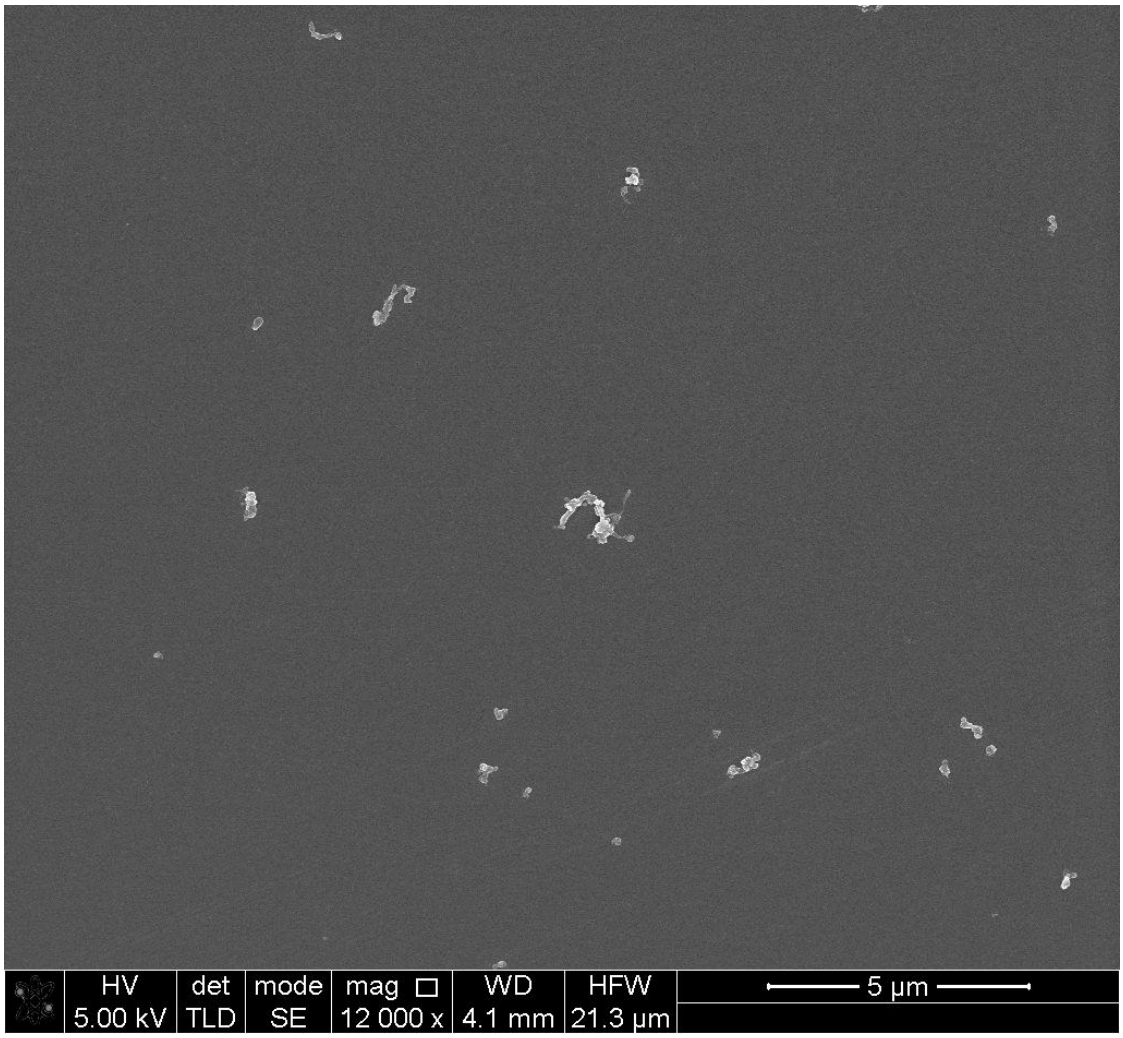

C)

Figure 5.38 Scanning electron micrographs of E1 hip during long-term wear. A) 15000x magnification, Scale = 5µm B) 20000x magnification, Scale = 4µm C) 12000x magnification, Scale = 5µm.

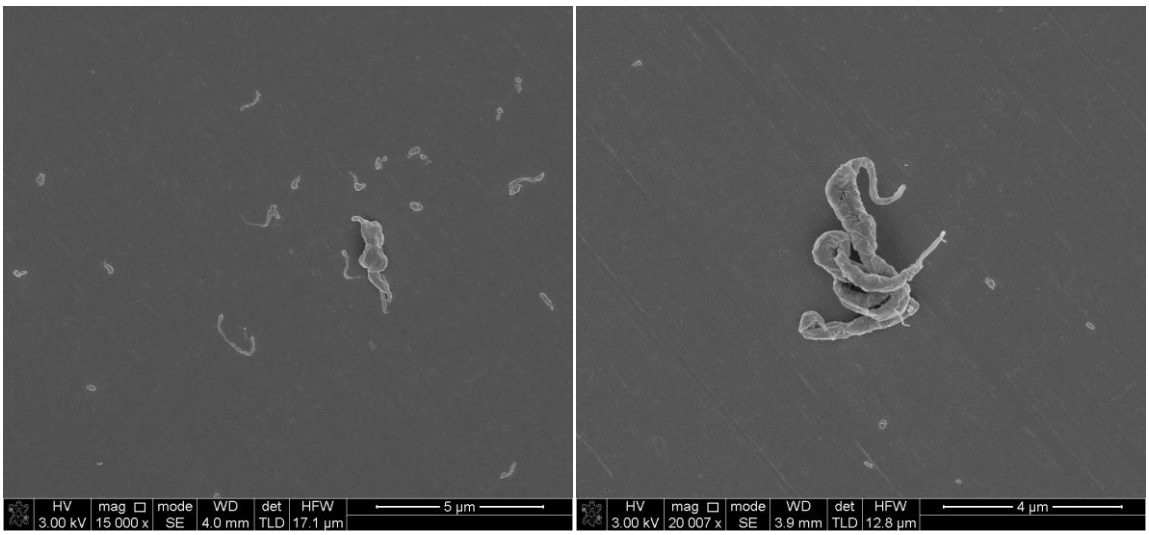

A) **B)**

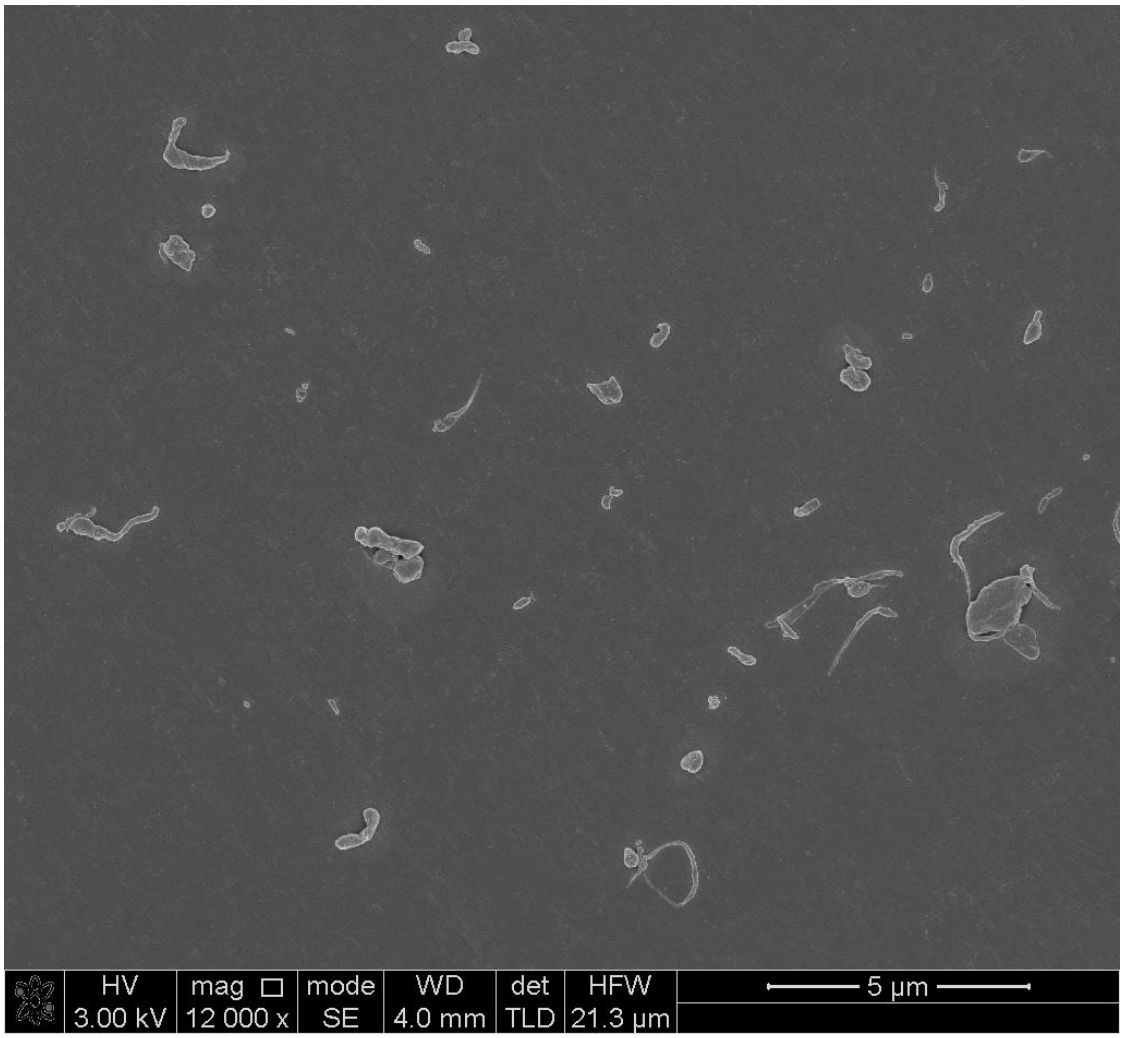

C)

Figure 5.39 Scanning electron micrographs of ECiMa hip during long-term wear. A) 15000x magnification, Scale = 5µm B) 20000x magnification, Scale = 4µm C) 12000x magnification, Scale = 5µm.

5.1.3.2.2 Shape analysis

Figure 5.40 shows a comparison between aspect ratio values of E1 Hip and ECiMa hip particles during long-term wear. A gradual increase in aspect ratio value with an increase in particle size was noticed for both samples. Moreover, aspect ratio values of ECiMa particles were mirginally higher than E1 particles in 0.1 to 5 µm size range.

A comparison between elongation values of both samples is shown in Figure 5.41. A gradual increase in elongation value with an increase in particle size was noticed for both samples. However, no significant difference was observed between elongation values of both samples.

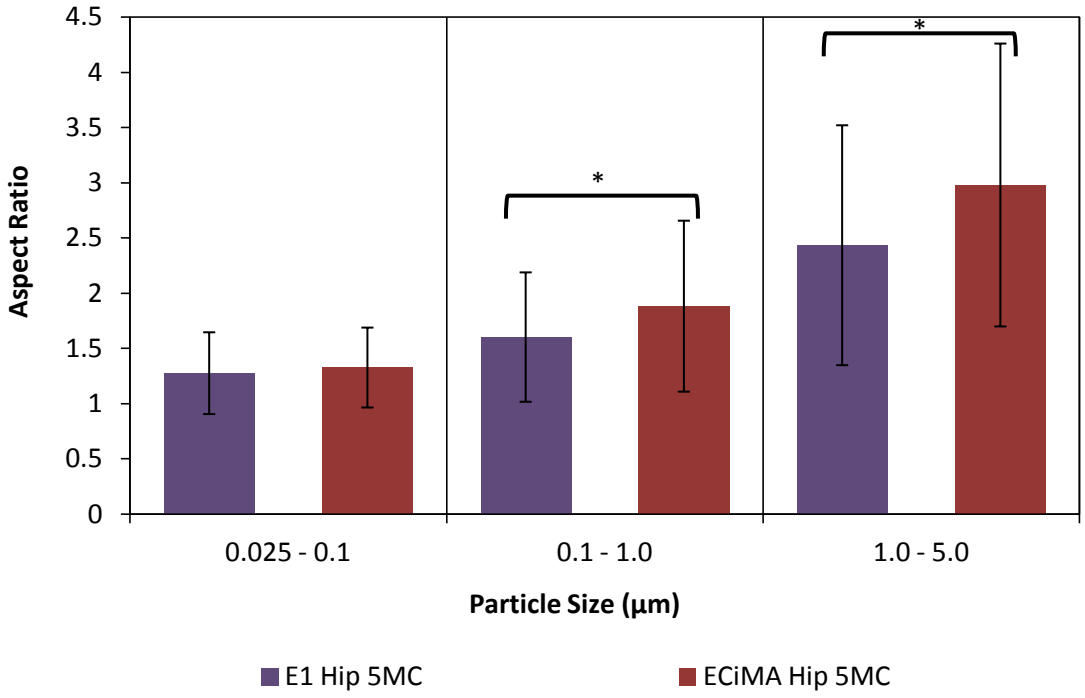

Figure 5.40 A plot showing aspect ratio versus particle size for long-term wear of E1 hip and ECiMA hip. Error bars indicate standard deviation from mean value in each size range. Statistically significant differences ($p < 0.05$) are highlighted with a black outline. ECiMa showed more elongated shape than E1 for particles larger than 0.1 µm.

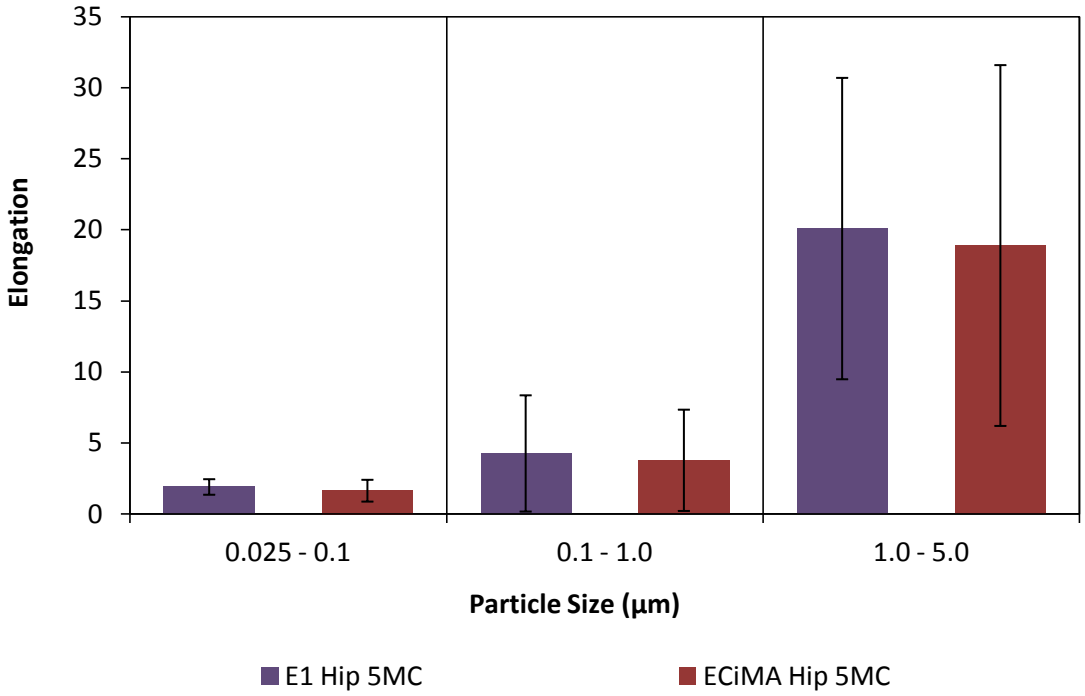

Figure 5.41 A plot showing elongation versus particle size for long-term wear of E1 hip and ECiMA hip. Error bars indicate standard deviation from mean value in each size range. Statistically significant differences ($p < 0.05$) are highlighted with a black outline. Both E1 and ECiMa had similar elongation values.

Figure 5.42 shows a comparison between roundness values of E1 Hip and ECiMa hip particles during long-term wear. There was a gradual decrease in roundness value with an increase in particle size for both samples. In addition, E1 particles in 0.1 to 5 µm size range had higher roundness values in comparison to ECiMa. Figure 5.43 shows a comparison between form factor values of both samples. E1 Hip particles had a marginally higher form factor value when particle size was smaller than 0.1 µm in comparison to ECiMa.

Figure 5.44 shows change in compactness value with particle size for both E1 Hip and ECiMa hip during long-term wear. A decrease in compactness value with an increase in size was noticed for both samples. E1 particles in 0.025 to 0.1 µm size range had more compact shape, while ECiMa particles in 1 to 5 µm size range had more compact shape.

A comparison between complexity values of E1 and ECiMa particles is shown in Figure 5.45. ECiMa particles in 0.025 to 0.1 µm size range were more complex shaped in comparison to E1 particles.

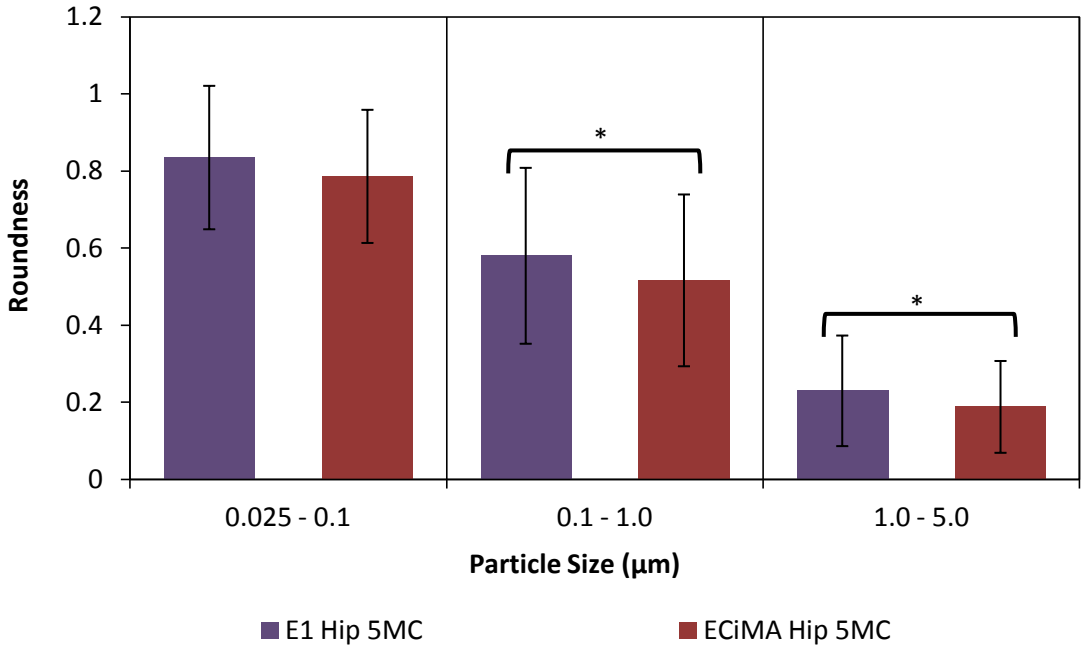

Figure 5.42 A plot showing roundness versus particle size for long-term wear of E1 hip and ECiMA hip. Error bars indicate standard deviation from mean value in each size range. Statistically significant differences ($p < 0.05$) are highlighted with a black outline. E1 showed more round shape than ECiMa for particles larger than 0.1 µm.

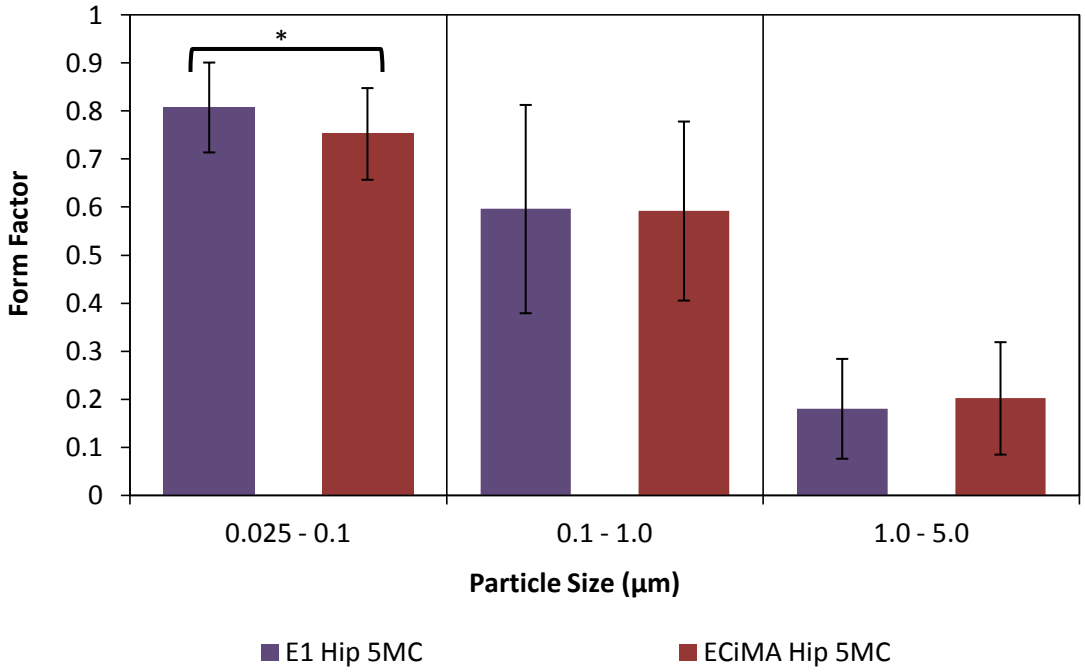

Figure 5.43 A plot showing form factor versus particle size for long-term wear of E1 hip and ECiMA hip. Error bars indicate standard deviation from mean value in each size range. Statistically significant differences ($p < 0.05$) are highlighted with a black outline. E1 showed marginally higher form factor values for particles smaller than 0.1 µm.

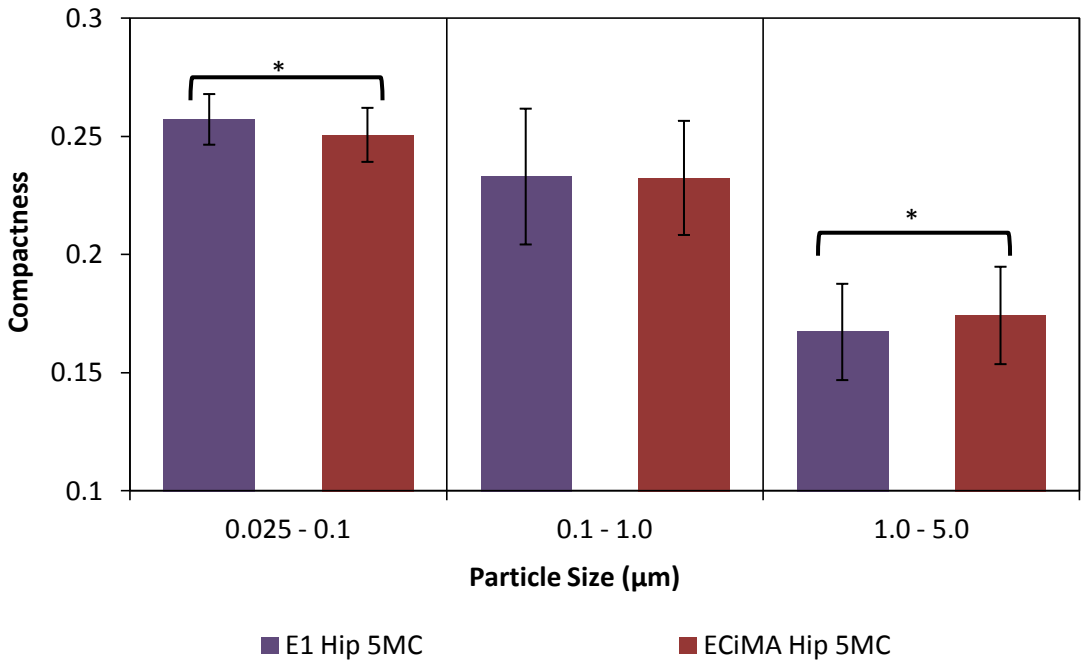

Figure 5.44 A plot showing compactness versus particle size for long-term wear of E1 hip and ECiMA hip. Error bars indicate standard deviation from mean value in each size range. Statistically significant differences ($p < 0.05$) are highlighted with a black outline. E1 particles in 0.025 to 0.1 µm size range were more compact shaped, while ECiMa particles in 1 to 5 µm size range had more compact shape.

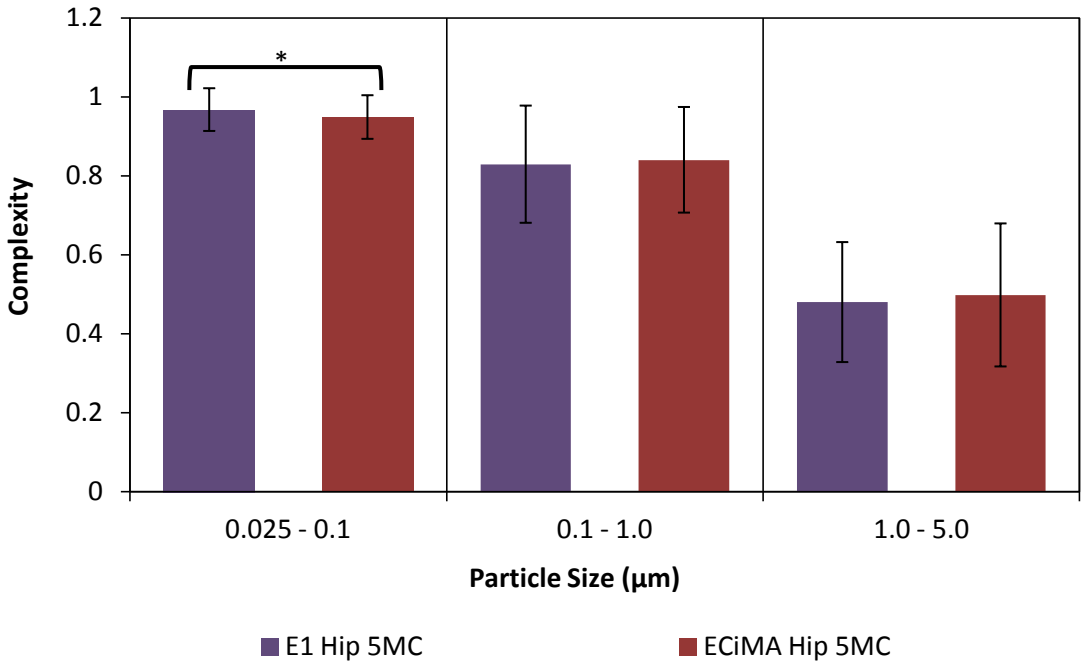

Figure 5.45 A plot showing complexity versus particle size for long-term wear of E1 hip and ECiMA hip. Error bars indicate standard deviation from mean value in each size range. Statistically significant differences ($p < 0.05$) are highlighted with a black outline. ECiMa particles in 0.025 to 0.1 µm size range were more complex shaped in comparison to E1 particles.

5.1.4 Conventional UHMWPE moulded at 145°C vs. Conventional UHMWPE moulded at 175°C

In this section, wear particles isolated from multidirectional pin-on-plate testing of two varieties of DCM UHMWPE plates manufactured at a moulding temperatures of 145°C and 175°C were compared. Effect of change in moulding temperature on size and shape of UHMWPE wear debris produced during multidirectional pin-on-plate testing of metal pins against direct compression moulded (DCM) UHMWPE plates was investigated. Lubricant serum collected after 3 million cycles of POP testing was used for particle analysis.

5.1.4.1 Size analysis

Figure 5.46 shows a comparison between number percentage size distributions of DCM UHMWPE moulded at 145°C and 175°C. Statistical analysis using Kolmogorov-smirnov Z test indicated that both size distributions were significantly different from each other ($p < 0.05$). Moreover, a marginally higher percentage of particles smaller than 250 nm were produced in UHMWPE moulded at 175°C, whereas a marginally higher percentage of particles in 250 – 500 nm size range were produced in UHMWPE moulded at 145°C.

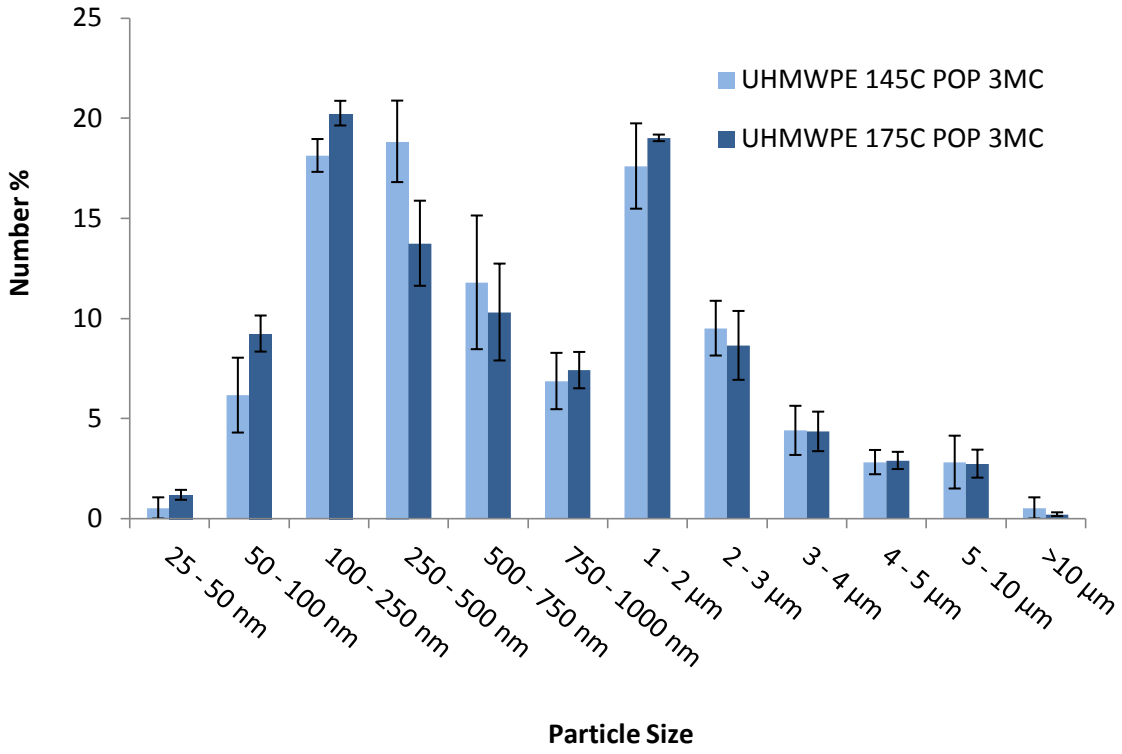

Figure 5.46 A comparison between percentage number size distributions of particles A comparison between percentage number size distributions according to maximum Feret's diameter (dmax) of 145°C DCM UHMWPE and 175°C DCM UHMWPE wear particles during early wear generated in a multidirectional pin-on-plate(POP). Error bars show standard deviation.

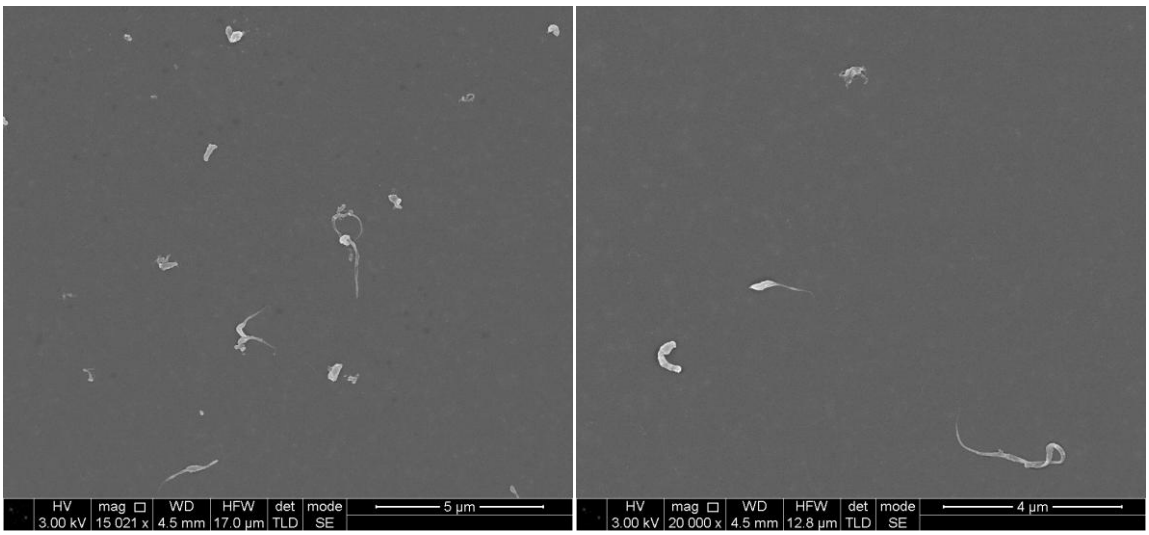

A) **B)**

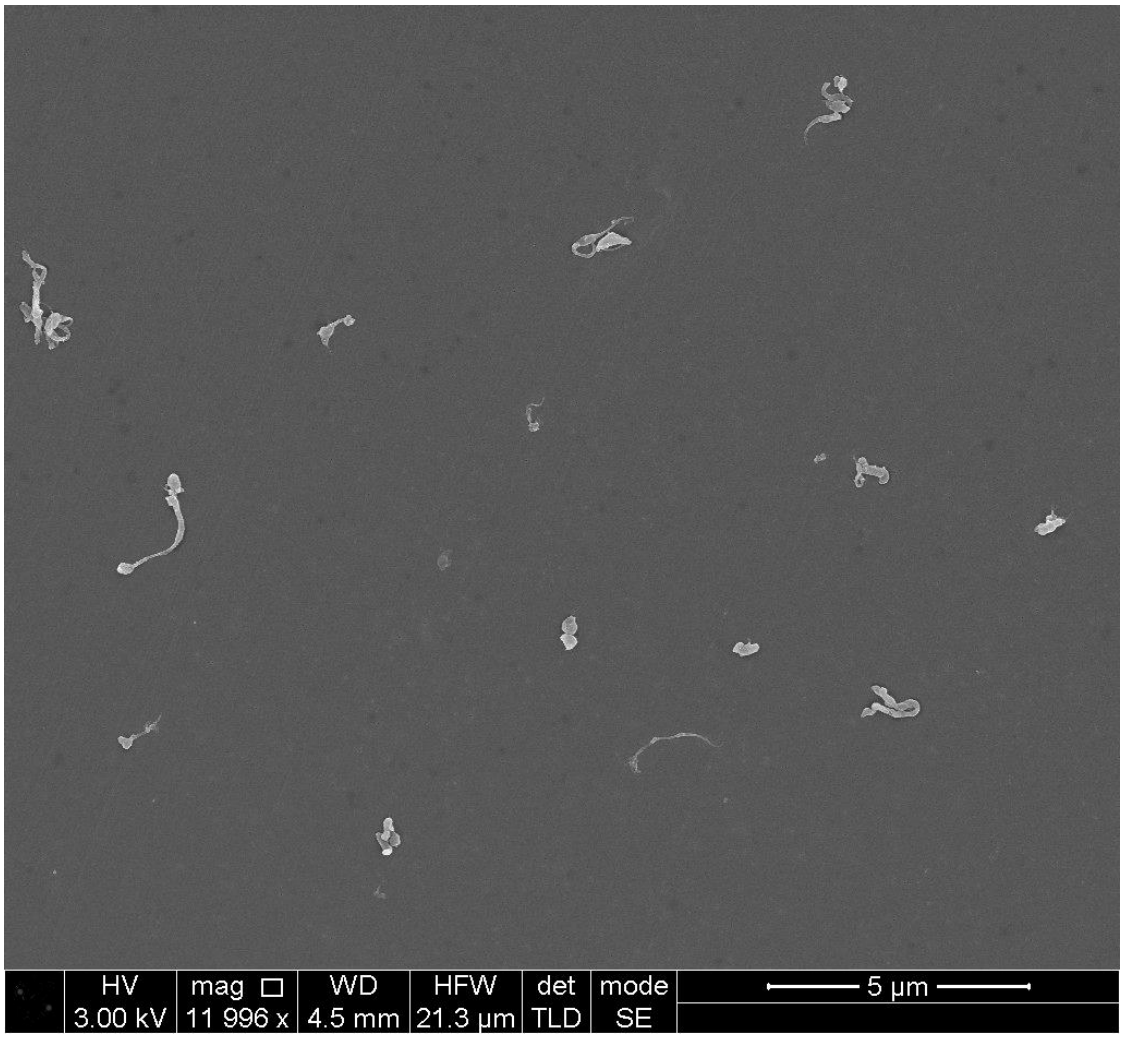

C)

Figure 5.47 Scanning electron micrographs of DCM UHMWPE 145°C multistation pin-on-plate during long-term wear. A) 15000x magnification, Scale = 5µm B) 20000x magnification, Scale = 4µm C) 12000x magnification, Scale = 5µm.

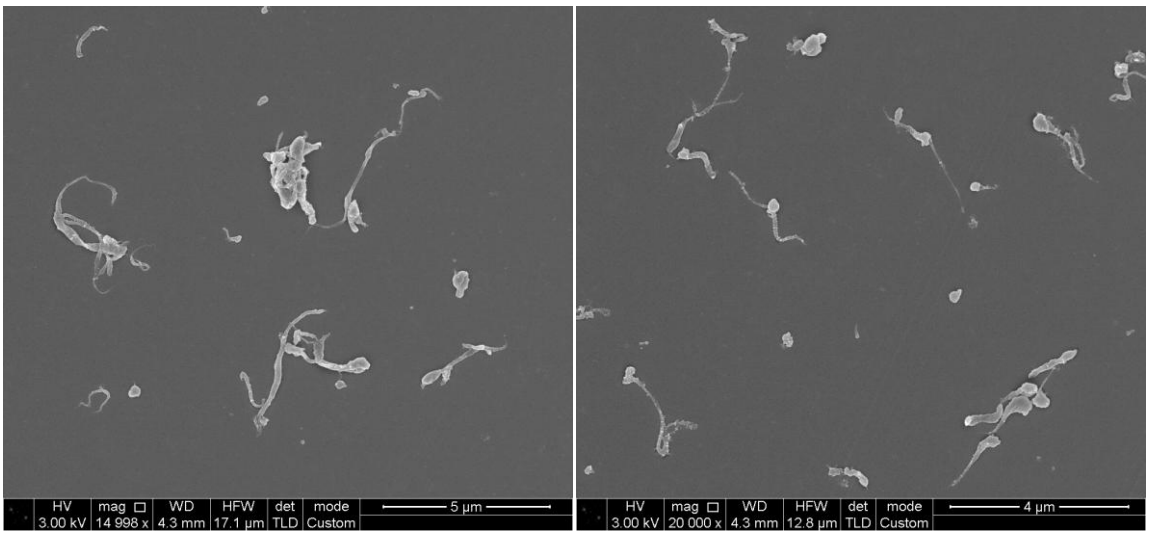

A) **B)**

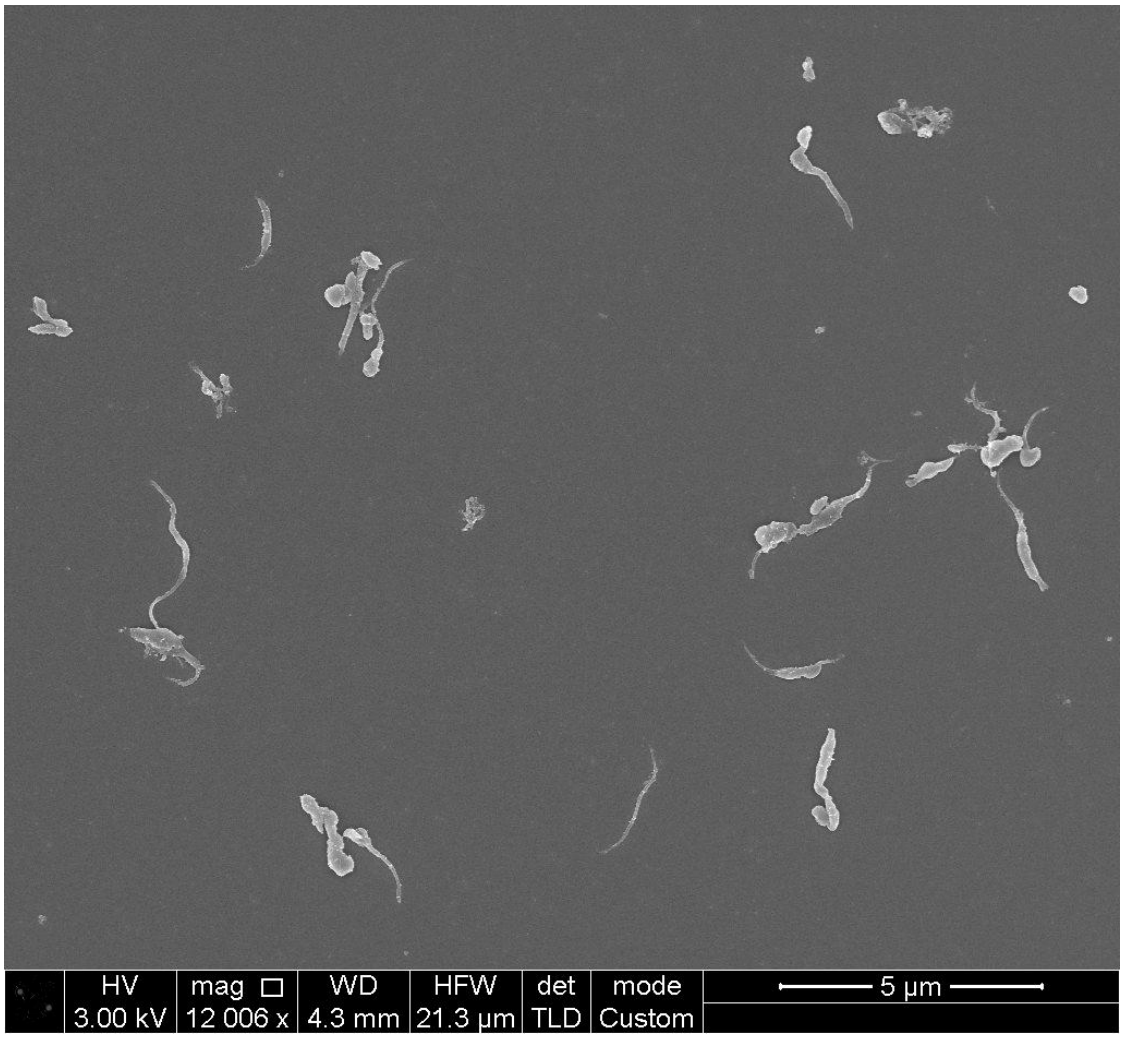

C)

Figure 5.48 Scanning electron micrographs of DCM UHMWPE 175°C multistation pin-on-plate during long-term wear. A) 15000x magnification, Scale = 5µm B) 20000x magnification, Scale = 4µm C) 12000x magnification, Scale = 5µm.

5.1.4.2 Shape analysis

A comparison between aspect ratio values of UHMWPE moulded at 145°C and 175°C is shown in Figure 5.49. No significant difference was observed between aspect ratio values of both samples. Figure 5.50 shows a comparison between elongation values of both samples. No significant difference was observed in elongation values.

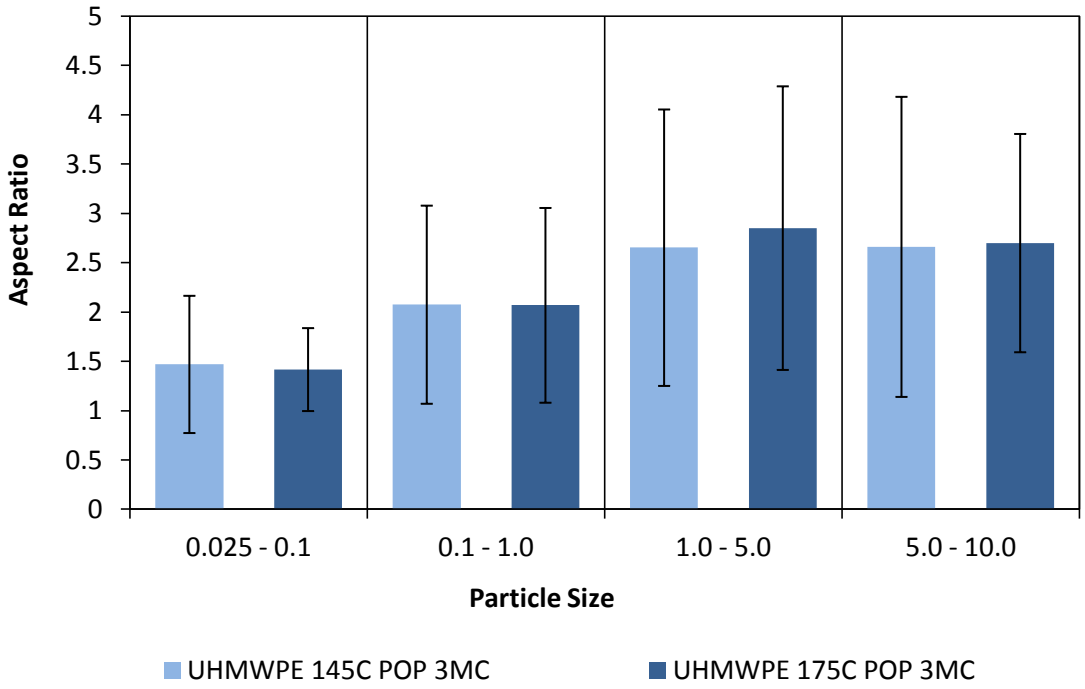

Figure 5.49 A plot showing aspect ratio versus particle size for long-term wear of 145°C DCM UHMWPE and 175°C DCM UHMWPE in a multidirectional pin-on-plate (POP). Error bars indicate standard deviation from mean value in each size range. No significant differences were observed in aspect ratio values.

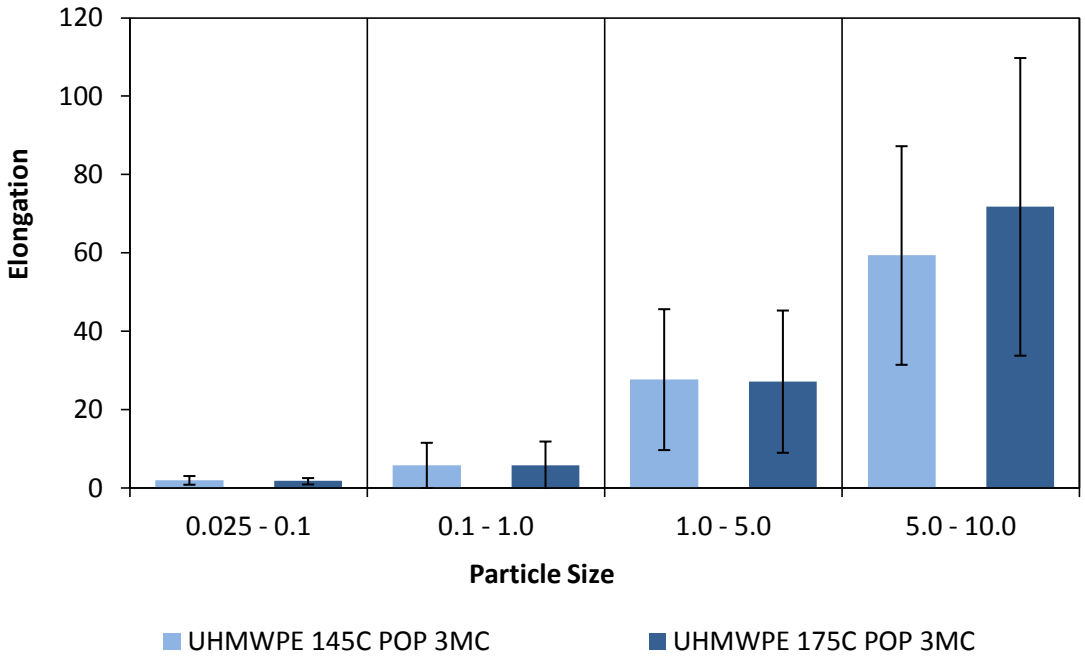

Figure 5.50 A plot showing elongation versus particle size for long-term wear of 145°C DCM UHMWPE and 175°C DCM UHMWPE in a multidirectional pin-on-plate (POP). Error bars indicate standard deviation from mean value in each size range. No significant differences were observed in elongation values.

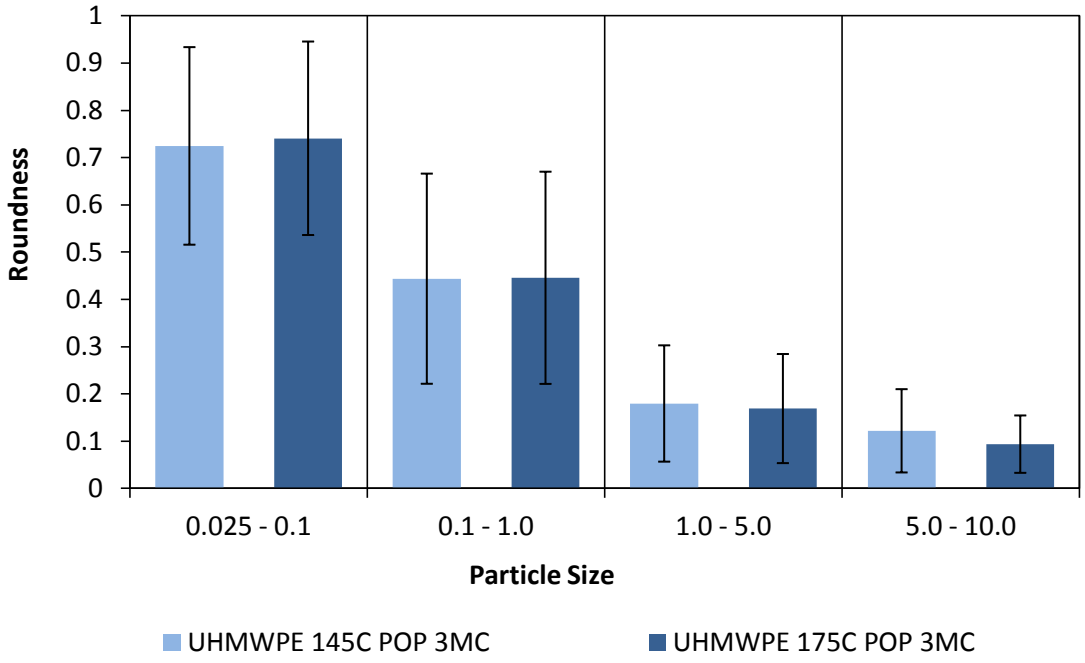

Figure 5.51 A plot showing roundness versus particle size for long-term wear of 145°C DCM UHMWPE and 175°C DCM UHMWPE in a multidirectional pin-on-plate (POP). Error bars indicate standard deviation from mean value in each size range. No significant differences were observed in roundness values.

Figure 5.51 shows a comparison between roundness values of UHMWPE moulded at 145°C and 175°C. No significant differences were observed in roundness values. In the similar manner, form factor values were similar for both samples as shown in Figure 5.52.

Figure 5.53 shows a comparison between compactness values. Both samples had nearly identical compactness values. No noticeable differences were noticed for complexity either as shown in Figure 5.54.

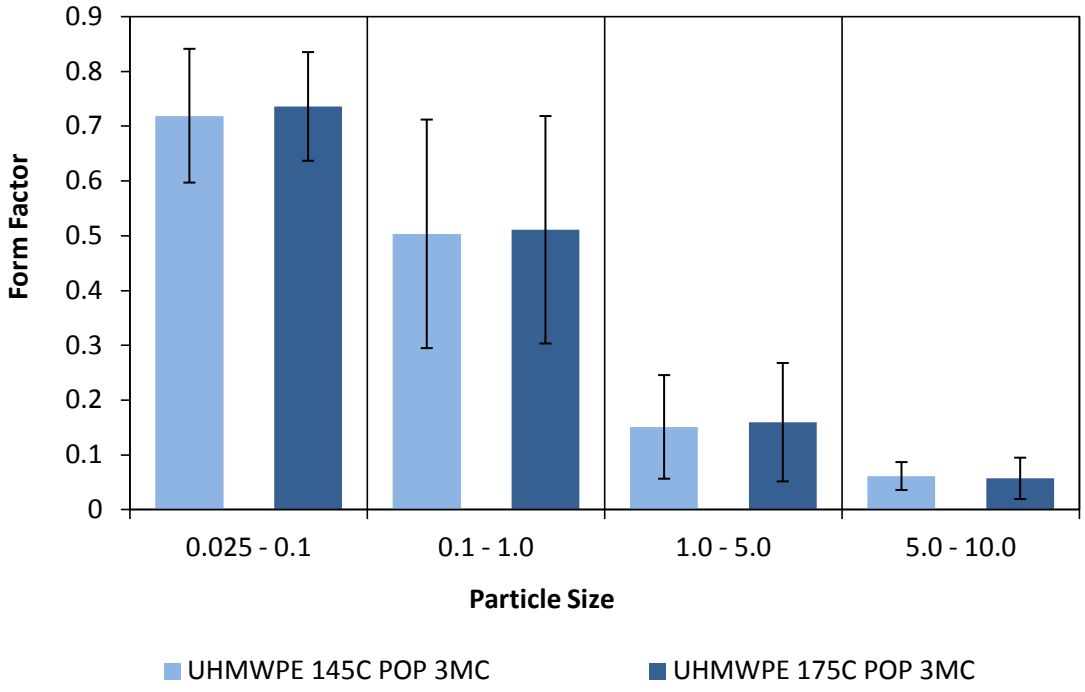

Figure 5.52 A plot showing form factor versus particle size for long-term wear of 145°C DCM UHMWPE and 175°C DCM UHMWPE in a multidirectional pin-on-plate (POP). Error bars indicate standard deviation from mean value in each size range. No significant differences were observed in form factor values.

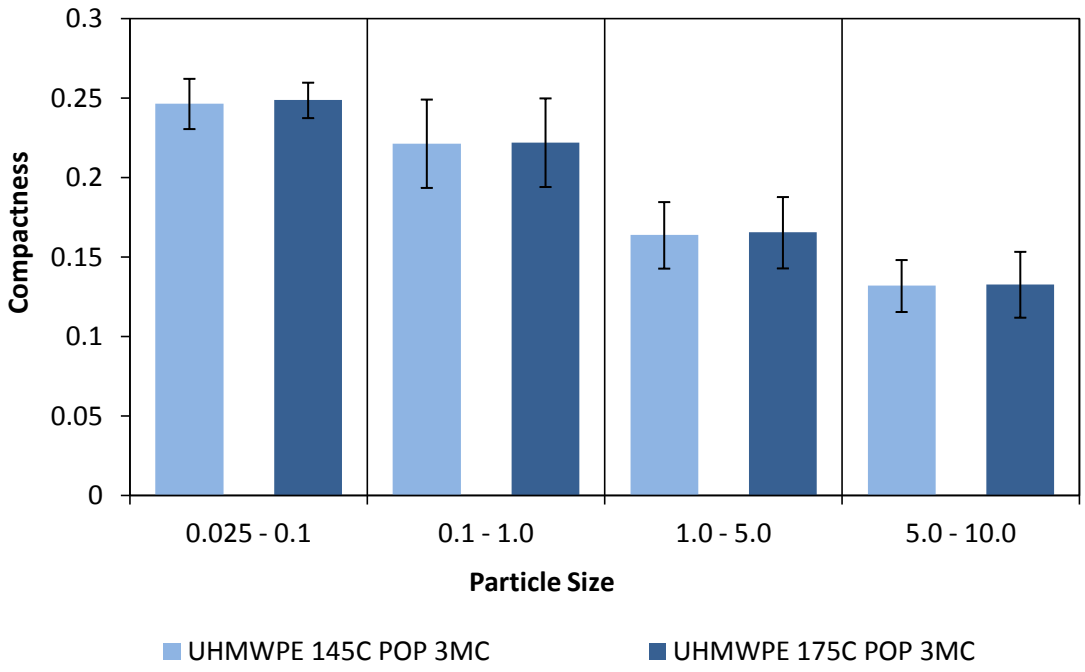

Figure 5.53 A plot showing compactness versus particle size for long-term wear of 145°C DCM UHMWPE and 175°C DCM UHMWPE in a multidirectional pin-on-plate (POP). Error bars indicate standard deviation from mean value in each size range. No significant differences were observed in compactness values.

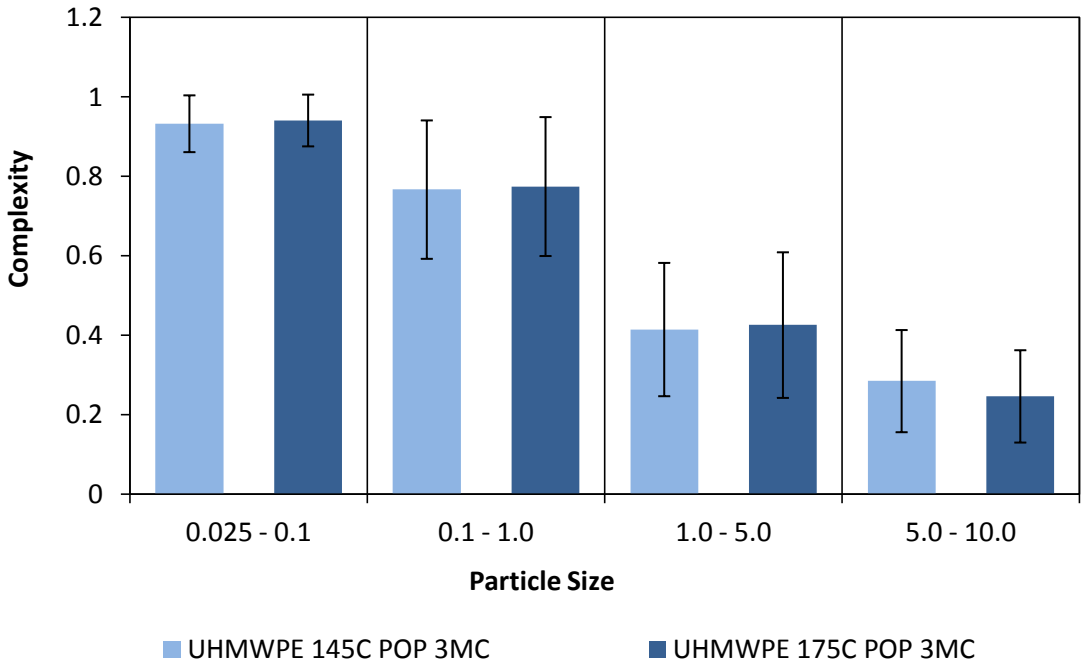

Figure 5.54 A plot showing complexity versus particle size for long-term wear of 145°C DCM UHMWPE and 175°C DCM UHMWPE in a multidirectional pin-on-plate (POP). Error bars indicate standard deviation from mean value in each size range. No significant differences were observed in complexity values.

5.2 Influence of different joint articulations on wear debris size and morphology

This section tested the influence of difference in type of joint articulation on wear particle size and morphology. All of the comparisons done in this section are listed in Table 5.2.

Table 5.2 A list of comparisons described in Section 5.2

Section	Description	Stage of wear
5.2.1	E1 Knee vs. E1 Ankle	Early wear and Long-term wear
5.2.2	E1 Knee vs. E1 Hip	Early wear and Long-term wear
5.2.3	E1 Multidirectional pin-on-plate vs. E1 Hip	Early wear and Long-term wear
5.2.4	E1 Multidirectional pin-on-plate vs. E1 Knee	Early wear and Long-term wear

5.2.1 E1 Knee vs. E1 Ankle

In this section, particles isolated from UHMWPE-on-metal knee and ankle simulator testing of E1 liners were compared for size and morphology.

5.2.1.1 Early wear

During early wear, E1 UHMWPE particles isolated from lubricant serum retrieved after 0.5 million cycles of knee simulator and ankle simulator tests were used for analysis.

5.2.1.1.1 Size analysis

The size distributions of both ankle and knee wear particles are shown in Figure 5.55. Statistical analysis using Kolmogorov-smirnov Z test indicated that both size distributions were significantly different from each other ($p < 0.05$).In addition, ankle generated a higher percentage of particles in 100-500 nm size range in comparison to knee.

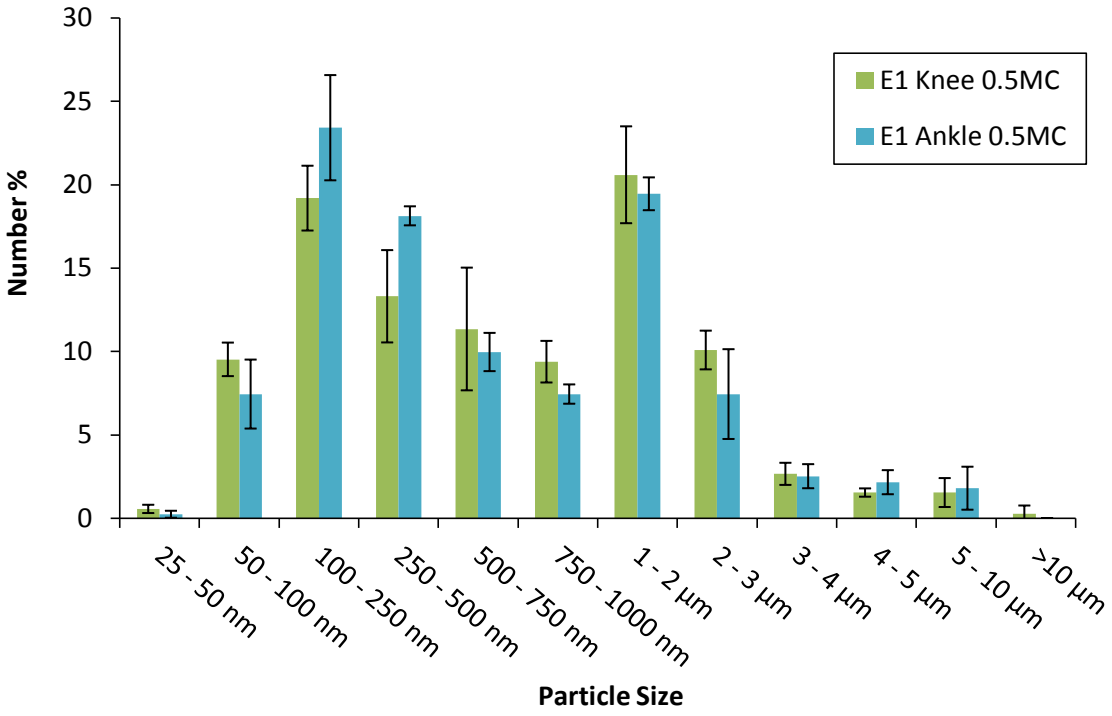

Figure 5.55 A comparison between percentage number size distributions according to maximum Feret's diameter (dmax) of E1 knee and E1 ankle wear particles during early wear. Error bars show standard deviation.

E1 Knee Early Wear

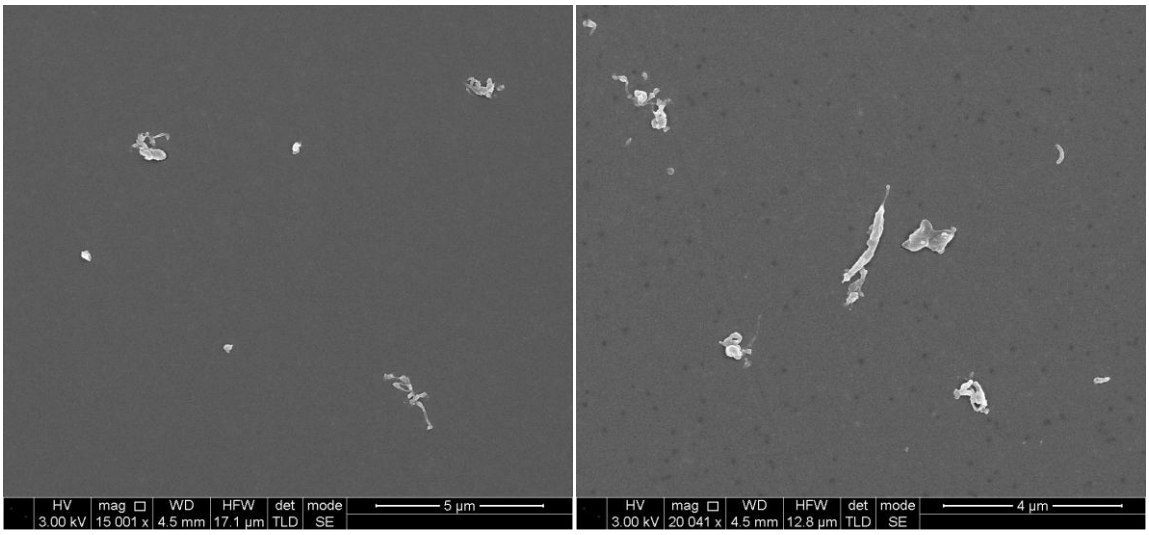

A) **B)**

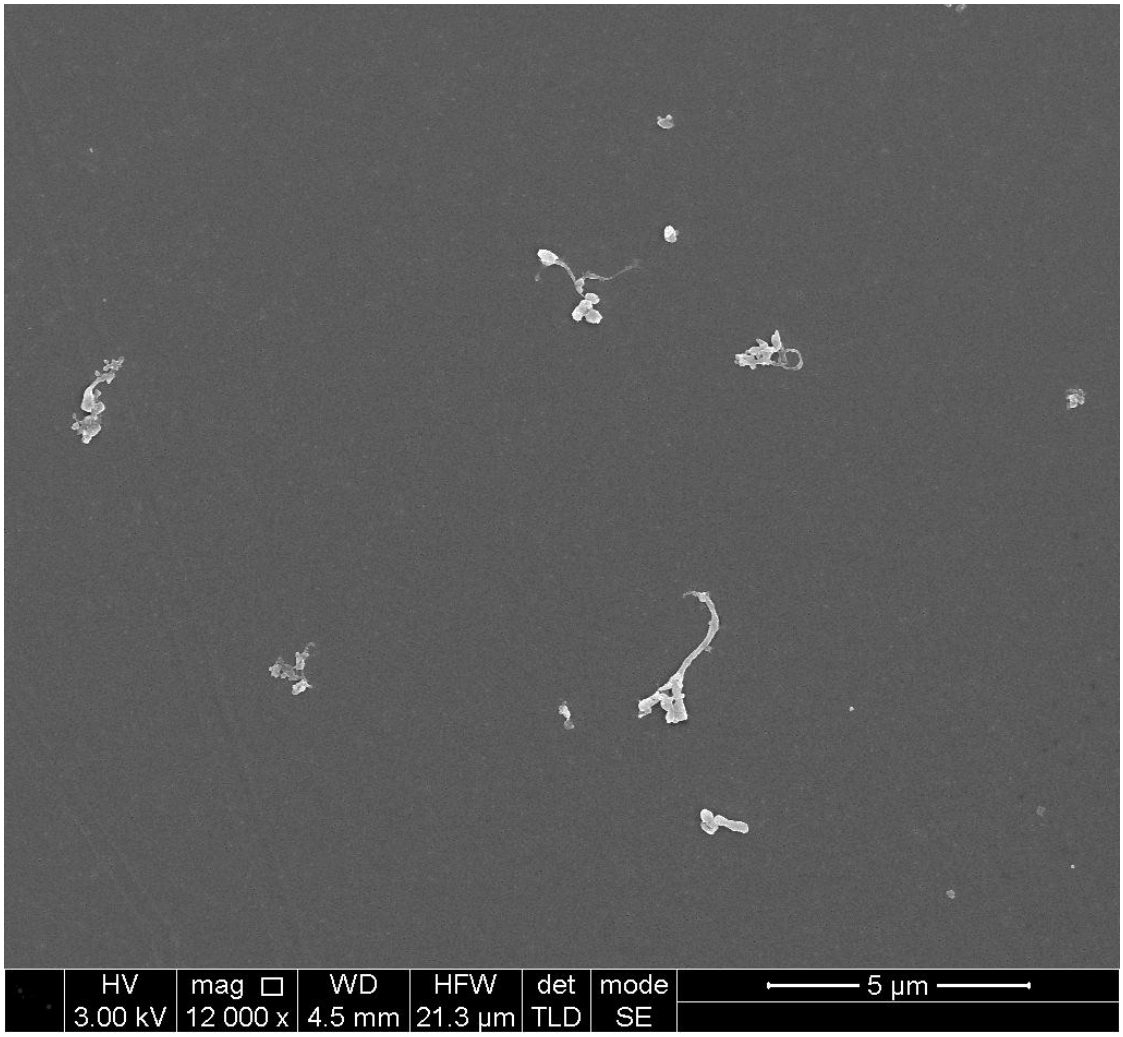

C)

Figure 5.56 Scanning electron micrographs of E1 Knee during early wear. A) 15000x magnification, Scale = 5µm B) 20000x magnification, Scale = 4µm C) 12000x magnification, Scale = 5µm.

E1 Ankle Early Wear

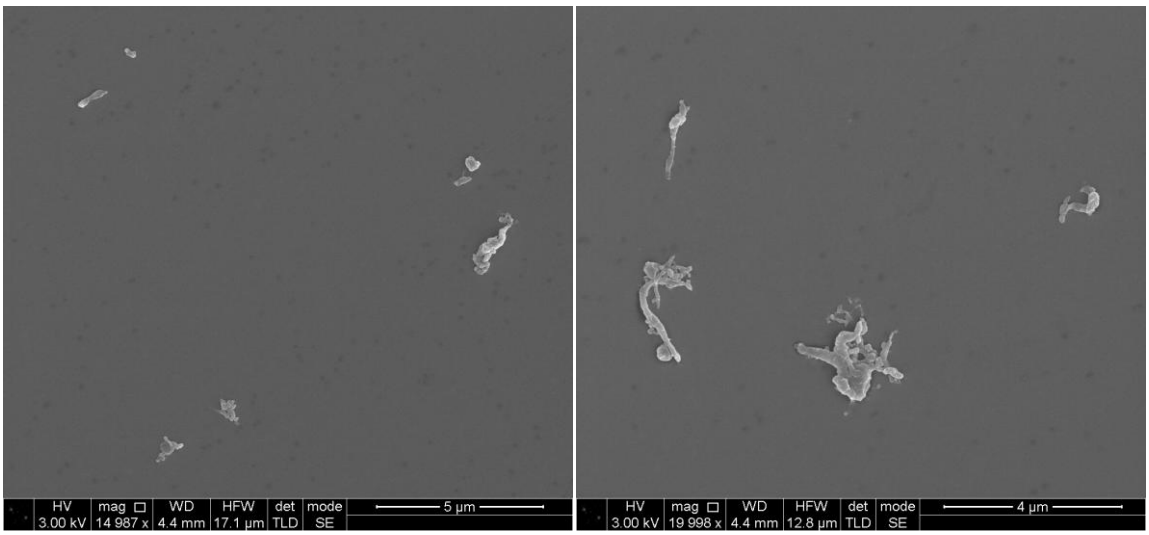

A) **B)**

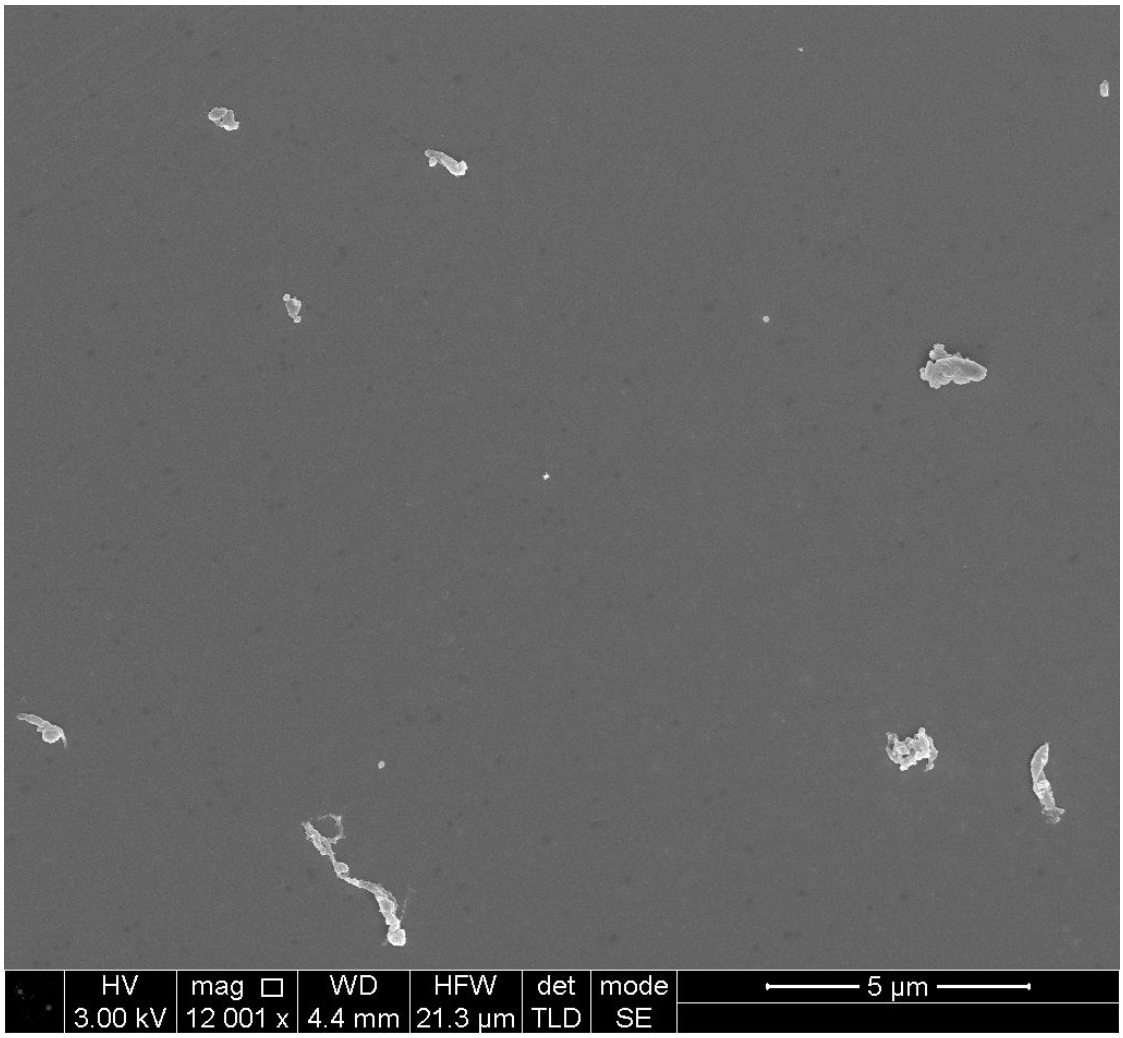

C)

Figure 5.57 Scanning electron micrographs of E1 Ankle during early wear. A) 15000x magnification, Scale = 5µm B) 20000x magnification, Scale = 4µm C) 12000x magnification, Scale = 5µm.

5.2.1.1.2 Shape analysis

Figure 5.58 shows a comparison between aspect ratio values of ankle and knee wear particles during early wear. Similar to the previous study of ArCom and E1 knee particles in section 5.1.1, there was a gradual increase in aspect ratio values with an increase in particle size for both samples. However, this trend was diminished in E1 knee particles for particles larger than 5µm. Consequently, E1 knee particles showed a lower aspect ratio value in 5-10 µm size range compared to E1 ankle.

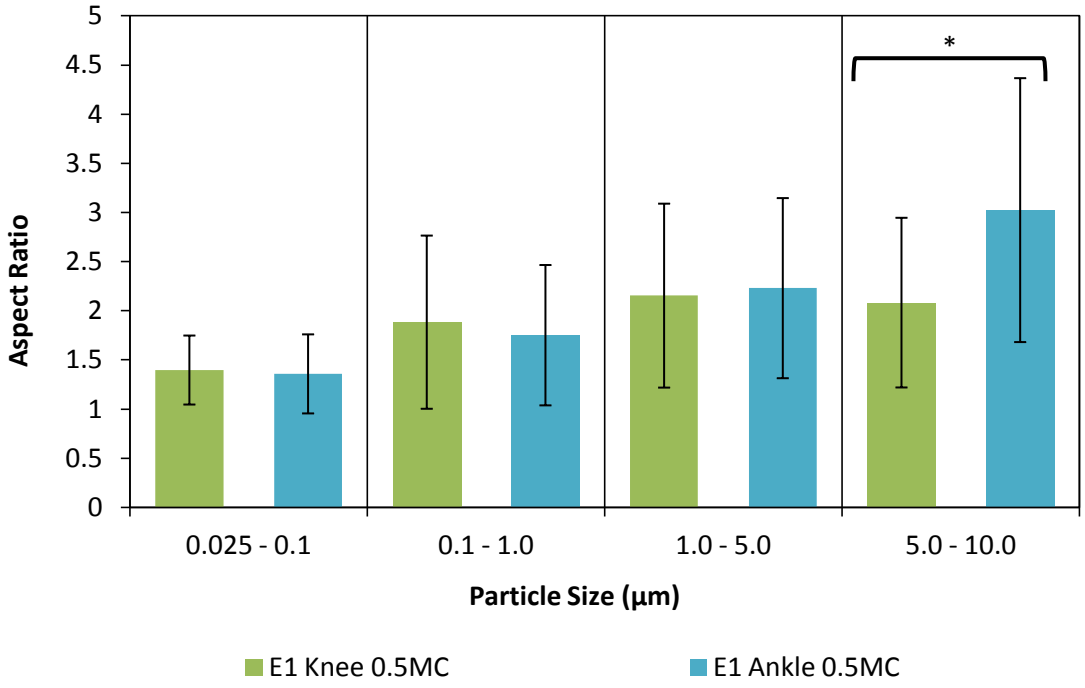

Figure 5.58 A plot showing aspect ratio versus particle size for early wear E1 knee and E1 ankle particles. Error bars indicate standard deviation from mean aspect ratio value in each size range. Statistically significant differences ($p < 0.05$) are highlighted with a black outline. Ankle showed more elongated shape than knee for particles larger than 5µm.

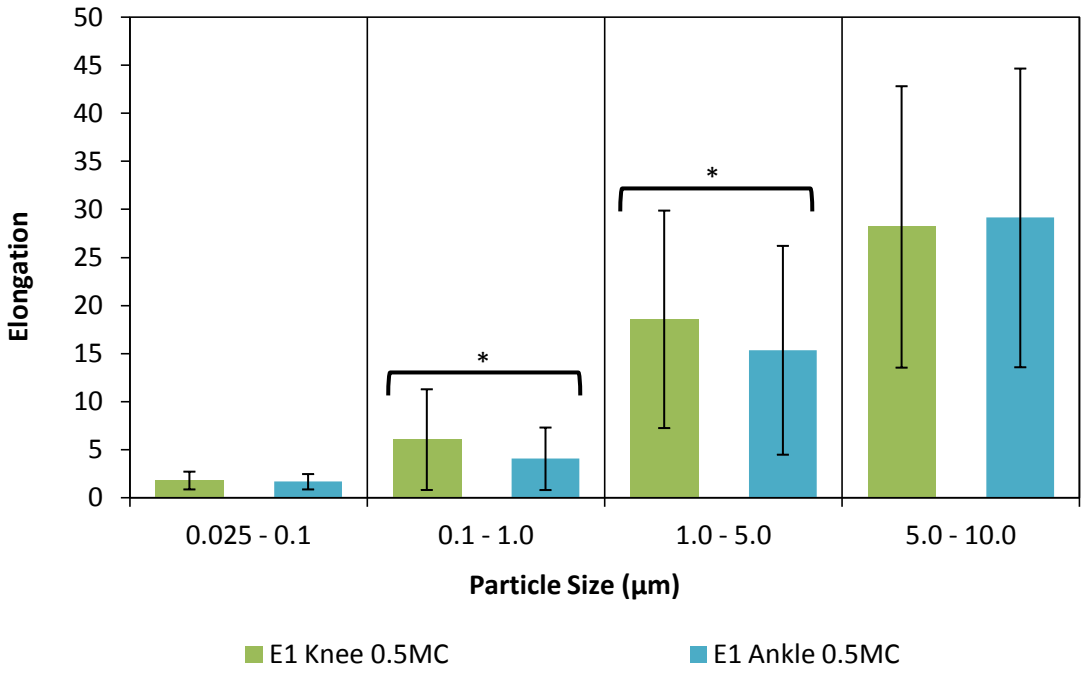

Figure 5.59 A plot showing elongation versus particle size from early wear E1 knee and E1 ankle particles. Error bars indicate standard deviation from mean elongation value in each size range. Statistically significant differences ($p < 0.05$) are highlighted with a black outline. Knee showed more elongated fibrillar shape than ankle for particles in 0.1 to 5µm size range.

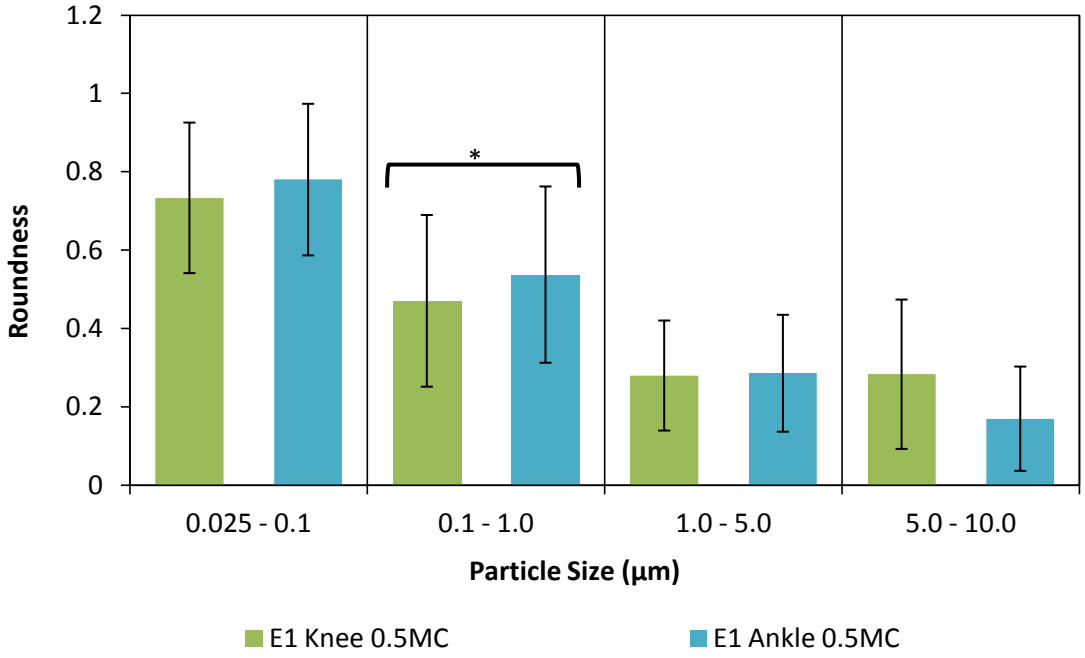

Figure 5.60 A plot showing roundness versus particle size for early wear E1 knee and E1 ankle particles. Error bars indicate standard deviation from mean roundness value in each size range. Statistically significant differences ($p < 0.05$) are highlighted with a black outline. Ankle showed more round shape than knee for particles in 0.1 to 1µm size range.

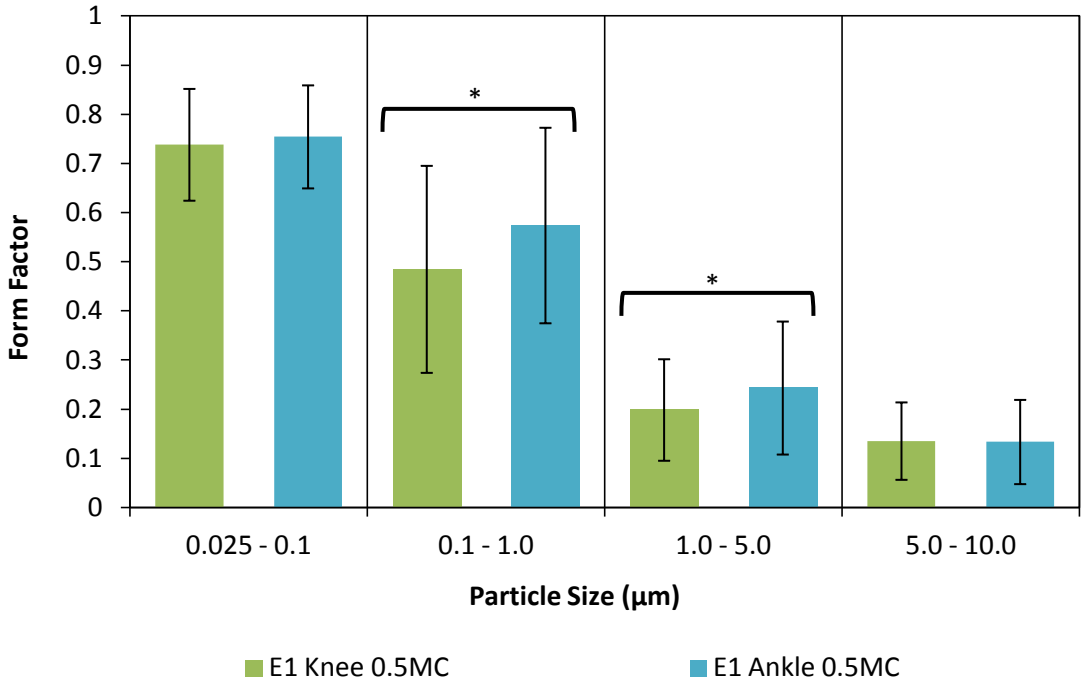

Figure 5.61 A plot showing form factor versus particle size from early wear of E1 knee and E1 ankle. Error bars indicate standard deviation from mean form factor value in each size range. Statistically significant differences ($p < 0.05$) are highlighted with a black outline. Ankle showed higher form factor values than knee for particles in 0.1 to 5µm size range.

Figure 5.59 shows a comparison between elongation values of E1 ankle and E1 knee wear particles during early wear. Elongation values increased with an increase in particle size in a similar manner as observed in previous knee samples. Moreover, knee wear particles in 0.1 to 5µm size range had higher elongation values in comparison to ankle, indicating more elongated fibrillar morphology of these particles.

A comparison between roundness values of both samples is shown in Figure 5.60. Roundness values decreased with an increase in particle size in a similar manner as in previous knee samples. Moreover, ankle particles in 0.1 to 1 µm size range had higher roundness values in comparison to knee.

Figure 5.61 shows form factor versus particle size for both ankle and knee. There was a gradual decrease in form factor values with an increase in particle size in a similar manner as in previous samples. Moreover, ankle particles had higher form factor values in comparison to knee for particles in 0.1 to 5 µm size range.

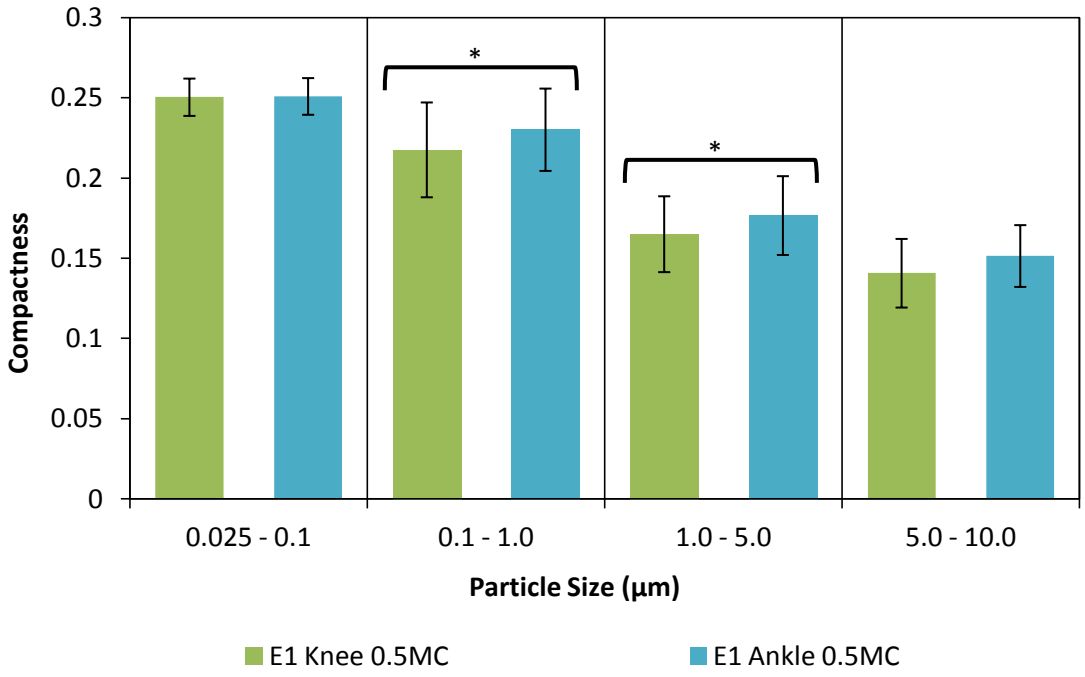

Figure 5.62 A plot showing compactness versus particle size from early wear of E1 knee and E1 ankle. Error bars indicate standard deviation from mean compactness value in each size range. Statistically significant differences ($p < 0.05$) are highlighted with a black outline. Ankle showed more compact shape than knee for particles larger than 0.1µm and smaller than 5µm.

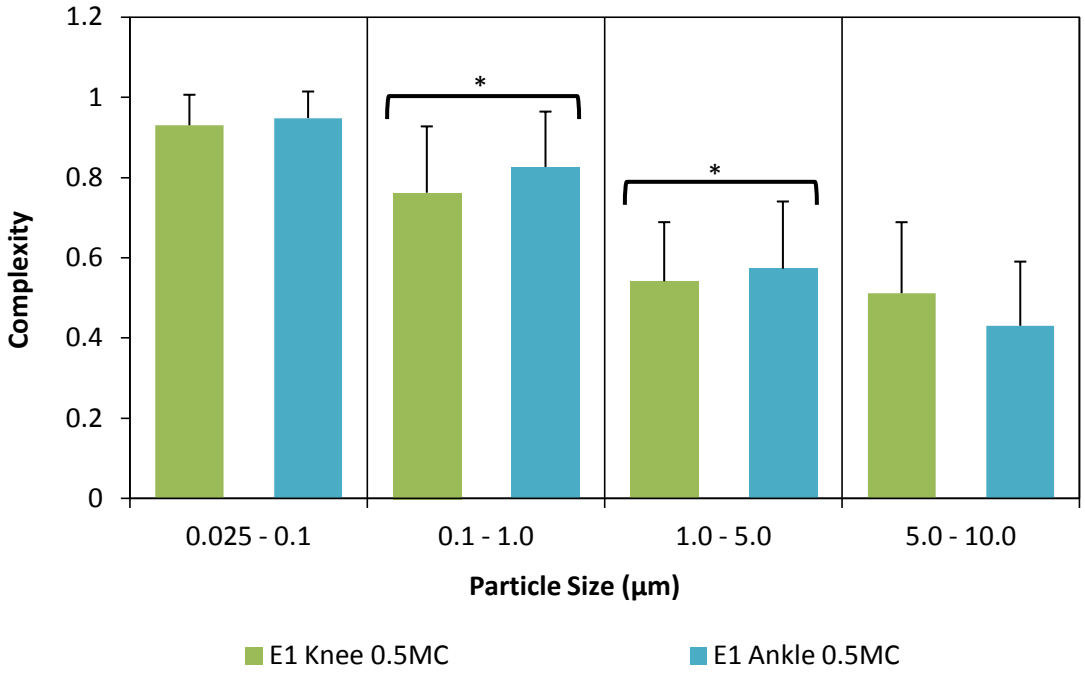

Figure 5.63 A plot showing complexity versus particle size from early wear of E1 knee and E1 ankle. Error bars indicate standard deviation from mean complexity value in each size range. Statistically significant differences ($p < 0.05$) are highlighted with a black outline. Knee showed more complex shape for particles in 0.1 to 5 µm size range.

Figure 5.62 shows a comparison between compactness values. There was a gradual decrease in compactness with an increase in size. Furthermore, ankle particles had higher compactness values for particles in 0.1 to 5 μm size range compared to knee.

Figure 5.63 shows change in complexity values with particle size for both ankle and knee particles. There was a gradual decrease in complexity value with an increase in particle size indicating an increase in complex shape of particles with increasing size. Also, knee particles were found to be more complex in shape for particles in 0.1 to 5 μm size range.

5.2.1.2 **Long-term wear**

During long-term wear, E1 UHMWPE particles isolated from lubricant serum retrieved after 5 million cycles of knee simulator and ankle simulator testing were used for analysis.

5.2.1.2.1 Size analysis

The size distributions of E1 UHMWPE particles produced in ankle and knee simulators during long-term wear were distinctly different from each other as shown in Figure 5.64. Statistical analysis using Kolmogorov-smirnov Z test also indicated that both size distributions were significantly different from each other ($p < 0.05$). Knee generated a higher percentage of E1 particles in 50-500 nm size range, whereas E1 ankle particles had a distinct peak in 500-750 nm size range. In addition, ankle also generated a greater percentage of large particles (size above 3µm) in comparison to knee.

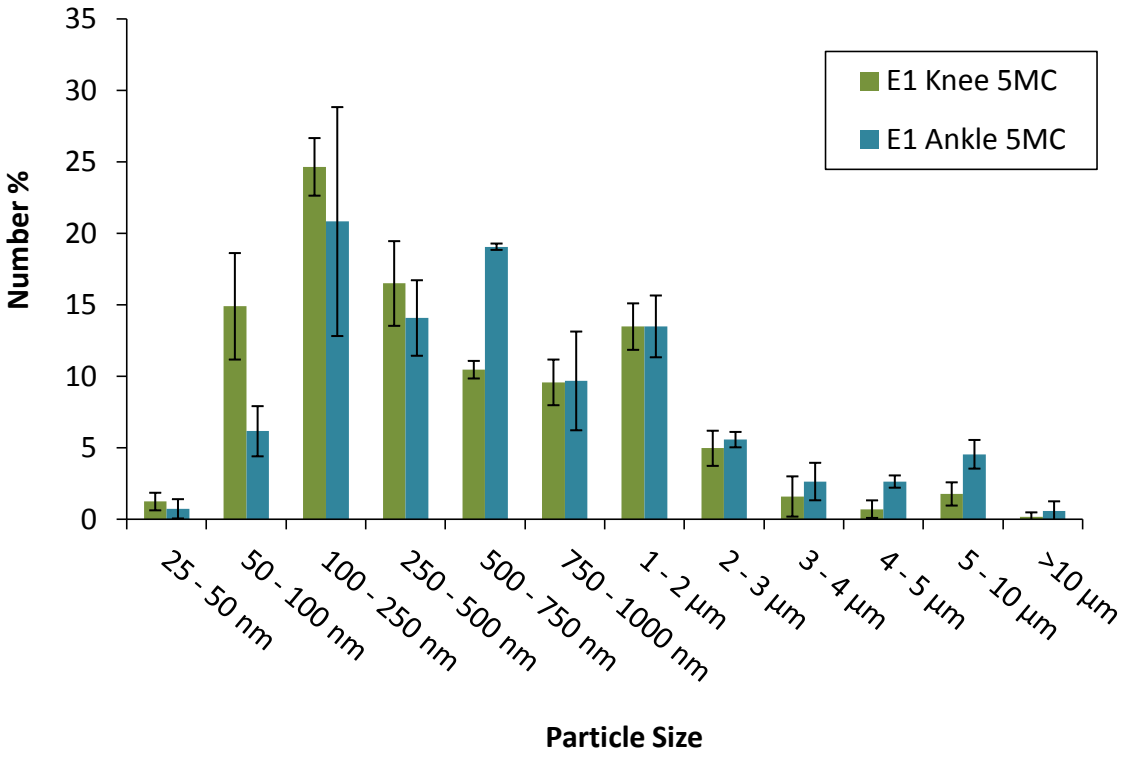

Figure 5.64 A comparison between percentage number size distributions according to maximum Feret's diameter (dmax) of E1 knee and E1 ankle wear particles during long-term wear. Error bars show standard deviation.

E1 Knee Long-term Wear

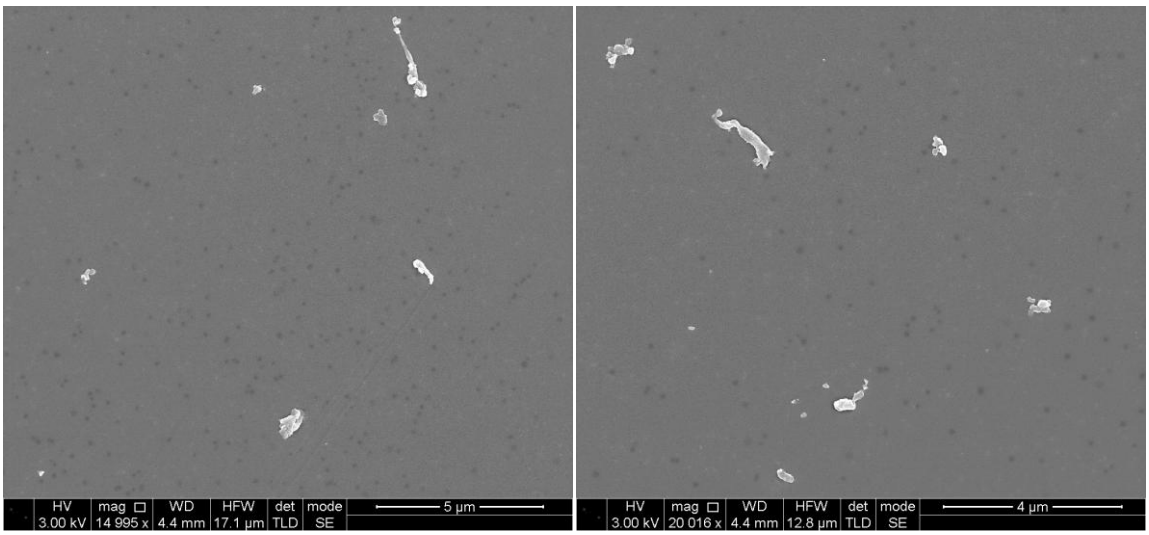

A) **B)**

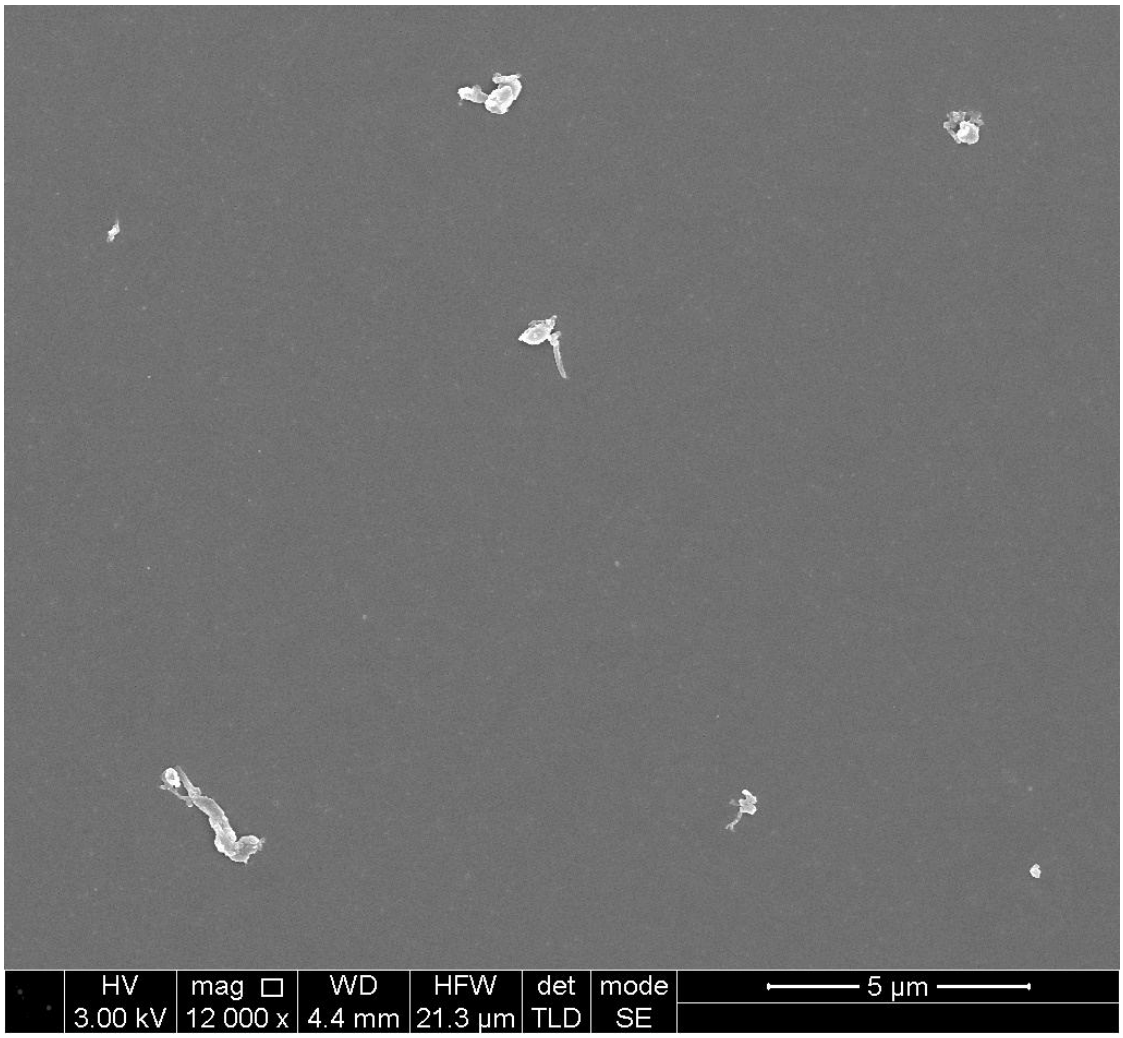

C)

Figure 5.65 Scanning electron micrographs of E1 knee during long-term wear. A) 15000x magnification, Scale = 5µm B) 20000x magnification, Scale = 4µm C) 12000x magnification, Scale = 5µm.

E1 Ankle Long-term Wear

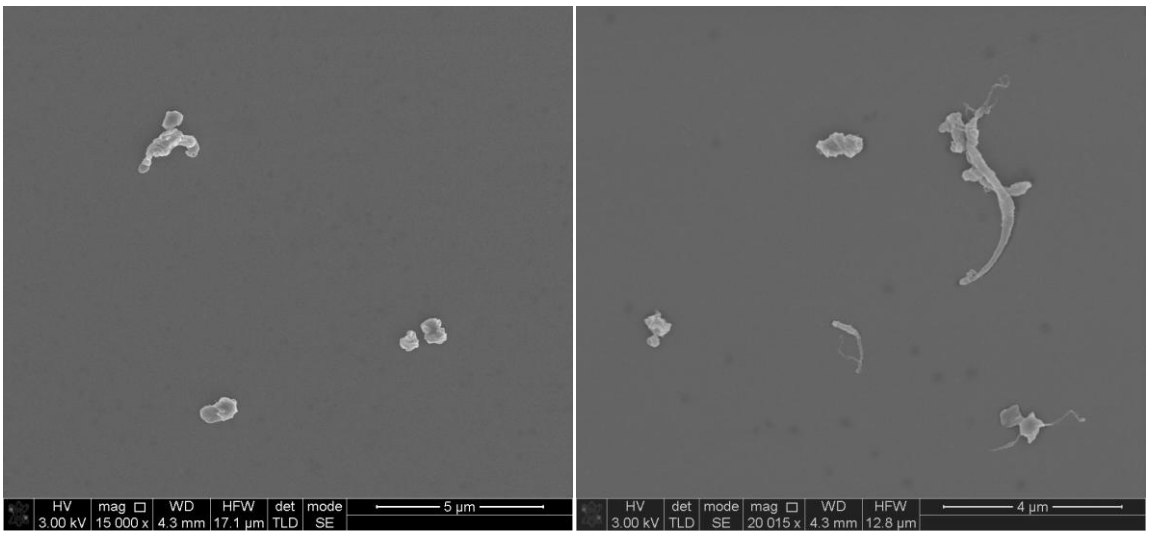

A) **B)**

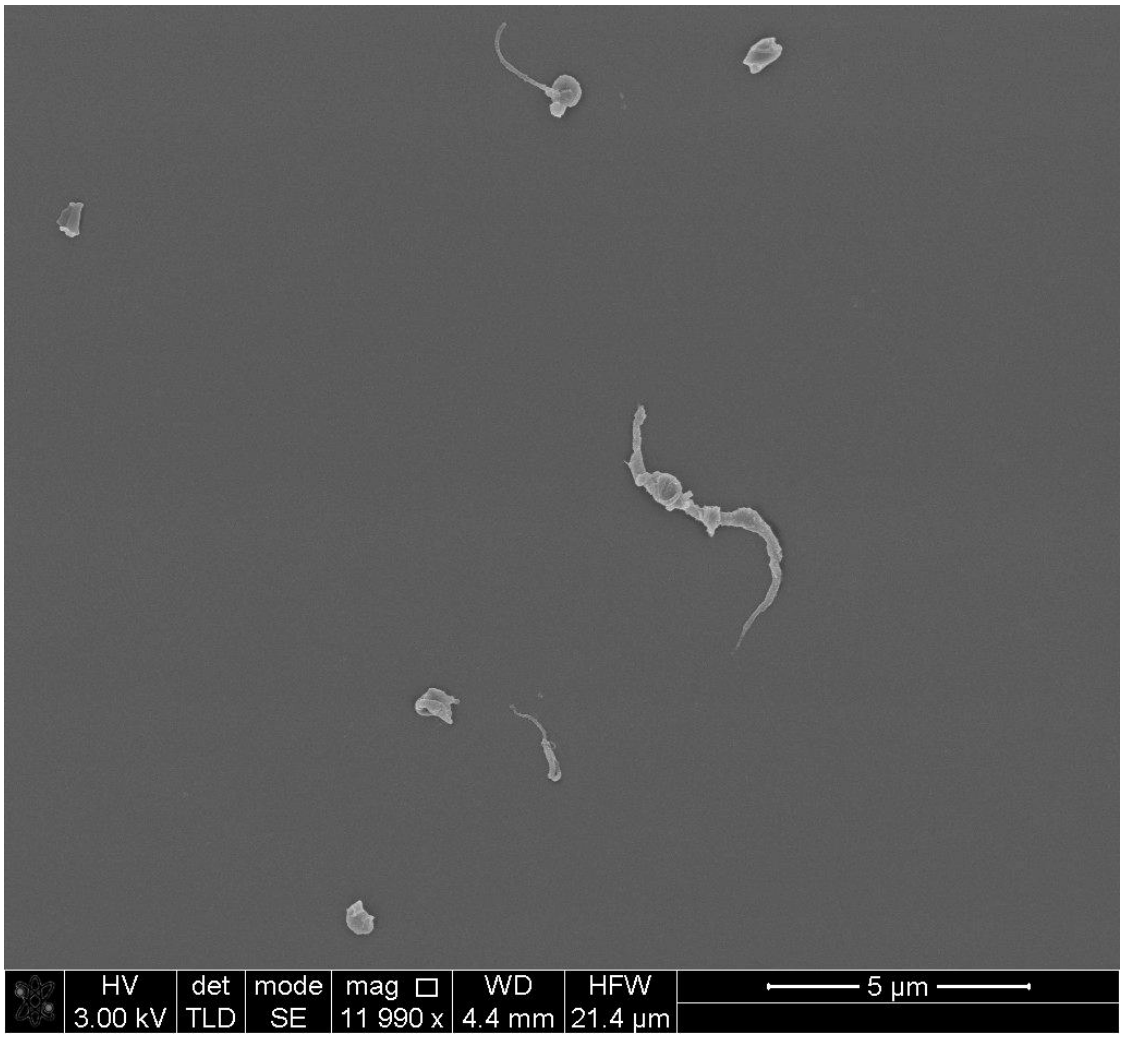

C)

Figure 5.66 Scanning electron micrographs of E1 ankle during long-term wear. A) 15000x magnification, Scale = 5µm B) 20000x magnification, Scale = 4µm C) 12000x magnification, Scale = 5µm.

5.2.1.2.2 Shape analysis

Figure 5.67 shows a comparison between aspect ratio values of E1 ankle and E1 knee particles produced during long-term wear. There was a gradual increase in aspect ratio value with an increase in particle size, similar to early wear. E1 Knee showed more elongated shape for particles in 0.1 to 1μm size range.

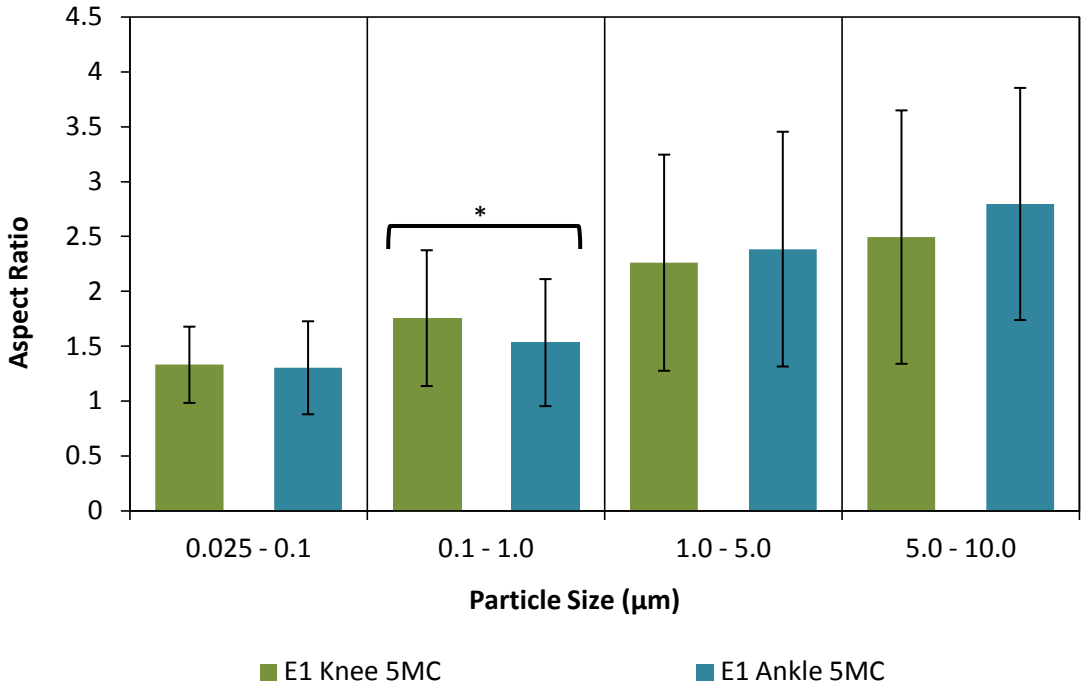

Figure 5.67 A plot showing aspect ratio versus particle size for long-term wear E1 knee and E1 ankle particles. Error bars indicate standard deviation from mean aspect ratio value in each size range. Statistically significant differences ($p < 0.05$) are highlighted with a black outline. Knee showed more elongated shape for particles in 0.1 to 1μm size range.

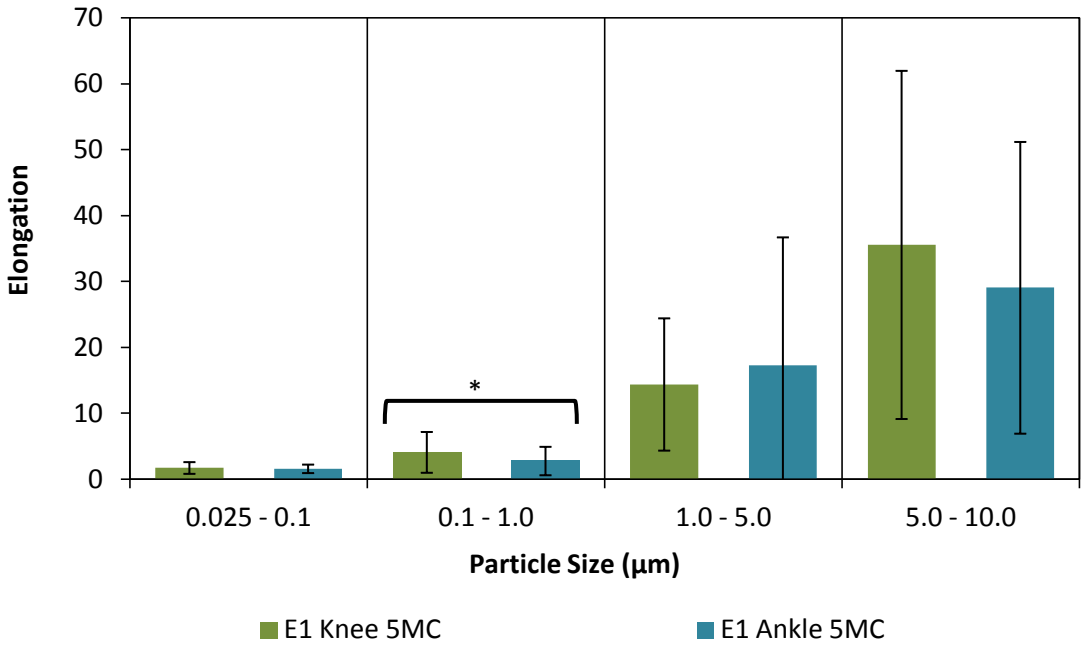

Figure 5.68 A plot showing elongation versus particle size for long-term wear E1 knee and E1 ankle particles. Error bars indicate standard deviation from mean elongation value in each size range. Statistically significant differences ($p < 0.05$) are highlighted with a black outline. Knee showed more elongated fibrillar shape for particles in 0.1 to 1 µm size range.

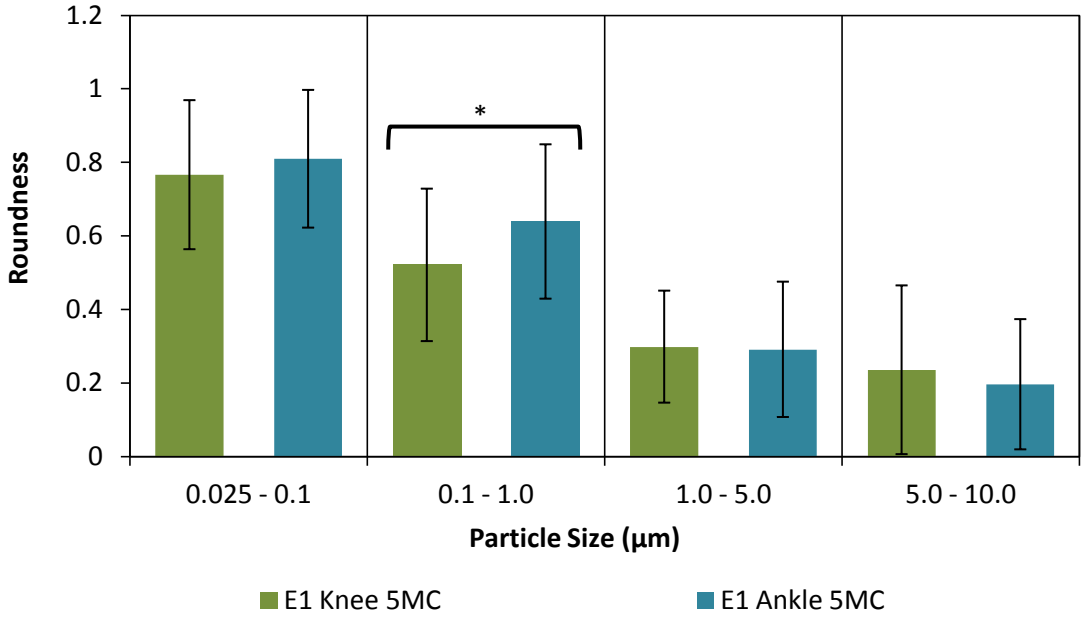

Figure 5.69 A plot showing roundness versus particle size for long-term wear E1 knee and E1 ankle particles. Error bars indicate standard deviation from mean roundness value in each size range. Statistically significant differences ($p < 0.05$) are highlighted with a black outline. Ankle showed more round shape for particles in 0.1 to 1µm size range.

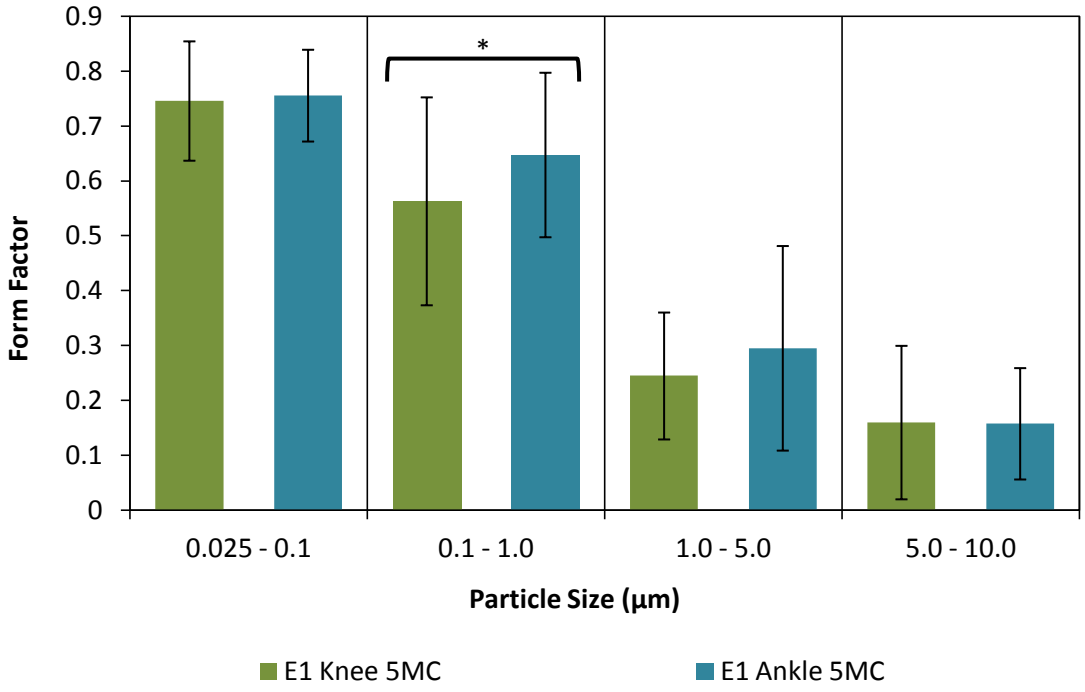

Figure 5.70 A plot showing form factor versus particle size for long-term wear E1 knee and E1 ankle particles. Error bars indicate standard deviation from mean form factor value in each size range. Statistically significant differences ($p < 0.05$) are highlighted with a black outline. Ankle showed higher form factor values for particles in 0.1 to 1µm size range.

Figure 5.68 shows change in elongation with particle size for E1 ankle and E1 knee wear particles during long-term wear. Elongation increased with an increase in particle size in a similar manner as in early wear. Moreover, knee particles showed a higher elongation value for particles in 0.1 to 1 µm size range. A higher elongation value indicated more fibrillar morphology.

A comparison between roundness values of both samples is shown in Figure 5.69. Similar to early wear, a gradual decrease in roundness with an increase in particle size was observed. Ankle particles in 0.1 to 1µm size range had more round shape in comparison to knee.

Figure 5.70 shows form factor versus particle size for both ankle and knee. There was a gradual decrease in form factor values with an increase in particle size in a similar manner as in early wear. Moreover, ankle particles showed a higher form factor value in comparison to knee for 0.1 - 1 µm size range.

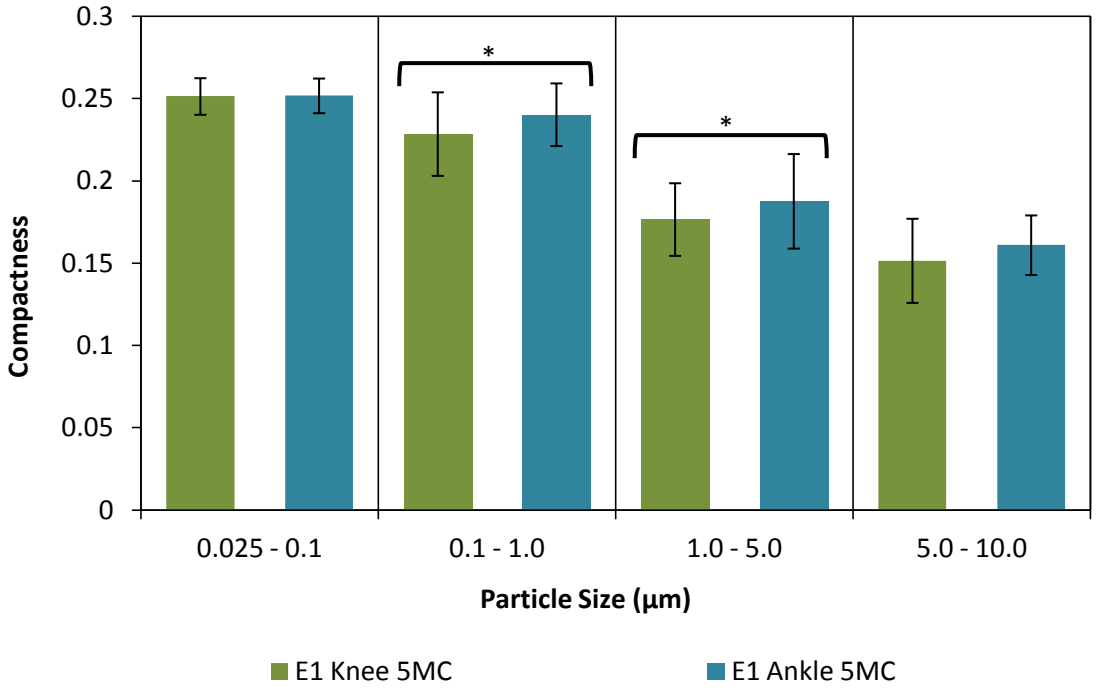

Figure 5.71 A plot showing compactness versus particle size for long-term wear E1 knee and E1 ankle particles. Error bars indicate standard deviation from mean compactness value in each size range. Statistically significant differences ($p < 0.05$) are highlighted with a black outline. Ankle showed higher compactness values for particles in 0.1 to 5 µm size range compared to knee.

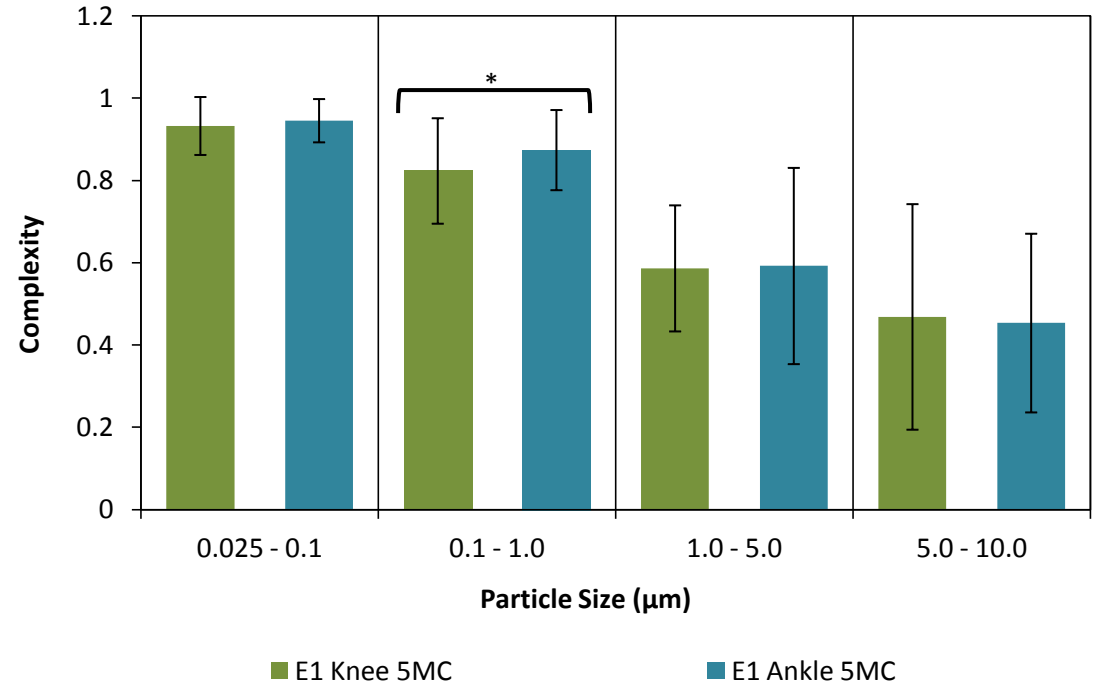

Figure 5.72 A plot showing complexity versus particle size for long-term wear E1 knee and E1 ankle particles. Error bars indicate standard deviation from mean complexity value in each size range. Statistically significant differences ($p < 0.05$) are highlighted with a black outline. Knee showed more complex shape for particles in 0.1 to 1µm size range.

Figure 5.71 shows compactness versus particle size for E1 ankle and E1 knee particles. Similar to early wear, a gradual decrease in compactness was observed with an increase in size. However, ankle particles had higher compactness in comparison to knee for particles in 0.1 to 5 μm size range.

Figure 5.72 shows change in complexity values with particle size for E1 ankle and E1 knee particles. There was a gradual decrease in complexity value with an increase in particle size indicating an increase in complex shape of particles with increasing size. In addition, knee particles were found to be slightly more complex in shape for particles in 0.1-1μm size range.

5.2.2 E1 Knee vs. E1 Hip

In this section, wear particles produced in UHMWPE-on-CoCr knee simulator testing of E1® vanguard (Biomet) inserts and UHMWPE-on-CoCr hip simulator testing of vitamin E diffused E1® advantage (Biomet) liners were compared for size and morphology.

5.2.2.1 Early wear

During early wear, E1 UHMWPE particles isolated from lubricant serum retrieved after 0.5 million cycles of knee simulator and hip simulator testing were used for analysis.

5.2.2.1.1 Size analysis

The size distributions of E1 UHMWPE wear particles produced in knee and hip during early wear are shown in Figure 5.73. Statistical analysis using Kolmogorov-smirnov Z test indicated that both size distributions were significantly different from each other ($p < 0.05$). Knee simulator generated a bimodal size distribution with two peaks at 100 - 250 nm and 1 - 2 µm. Alternatively, hip generated a size distribution with single mode peak at 100 - 250 nm. Moreover, hip generated a higher percentage of particles in 100 - 750 nm, while knee generated a higher percentage of particles in 1 - 2 µm size range.

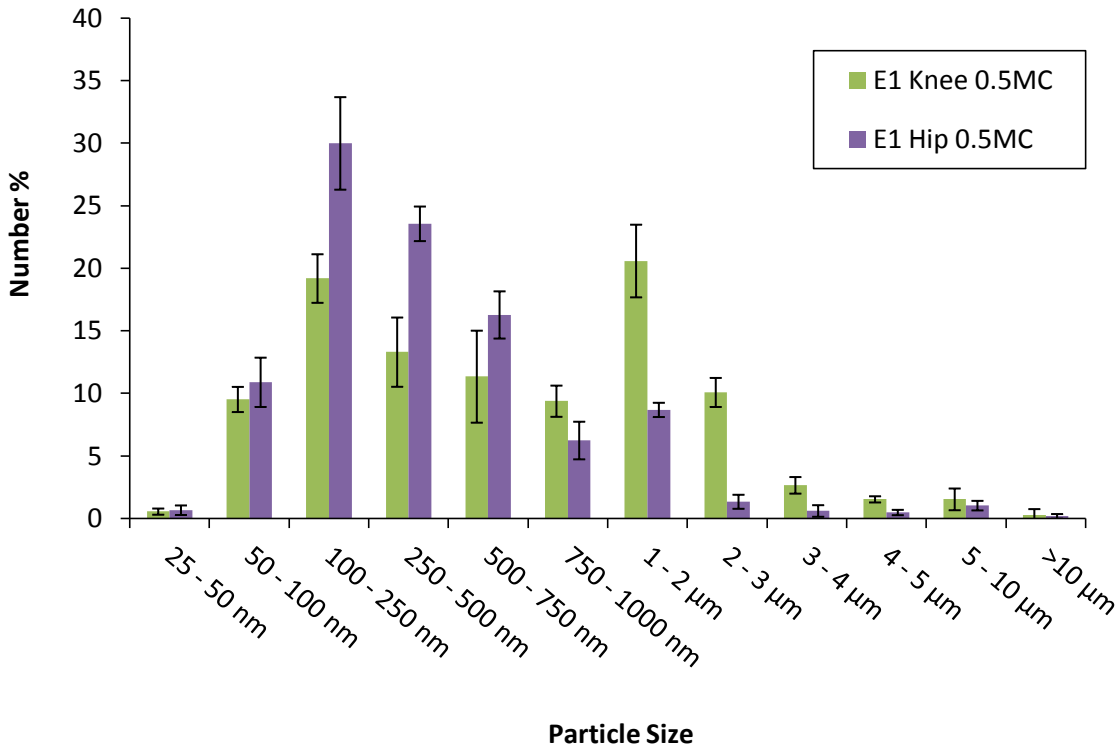

Figure 5.73 A comparison between percentage number size distributions according to maximum Feret's diameter (dmax) of E1 knee and E1 hip wear particles during early wear. Error bars show standard deviation.

E1 Knee Early Wear

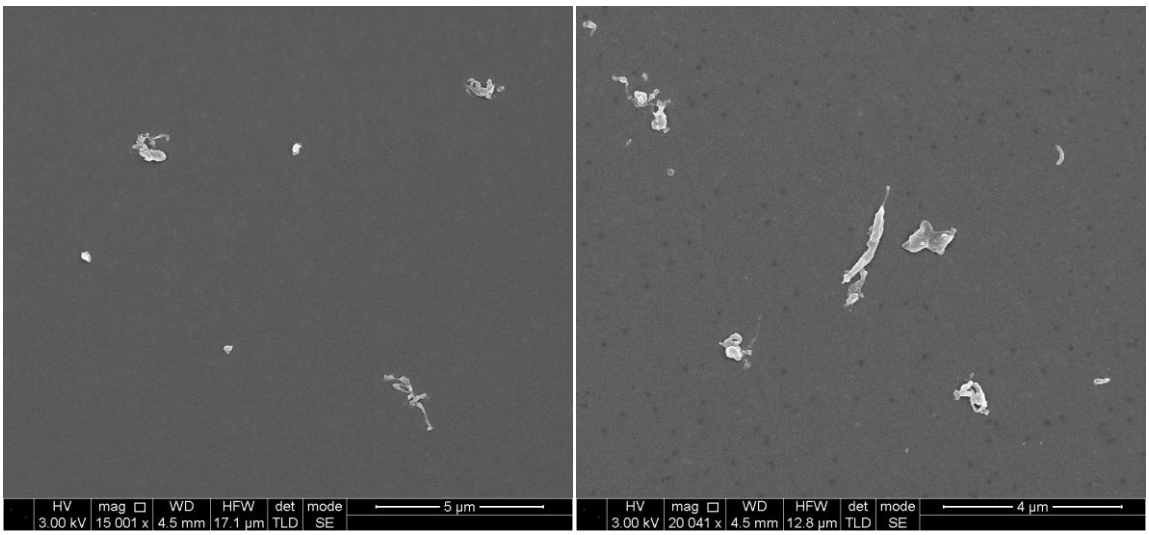

A) **B)**

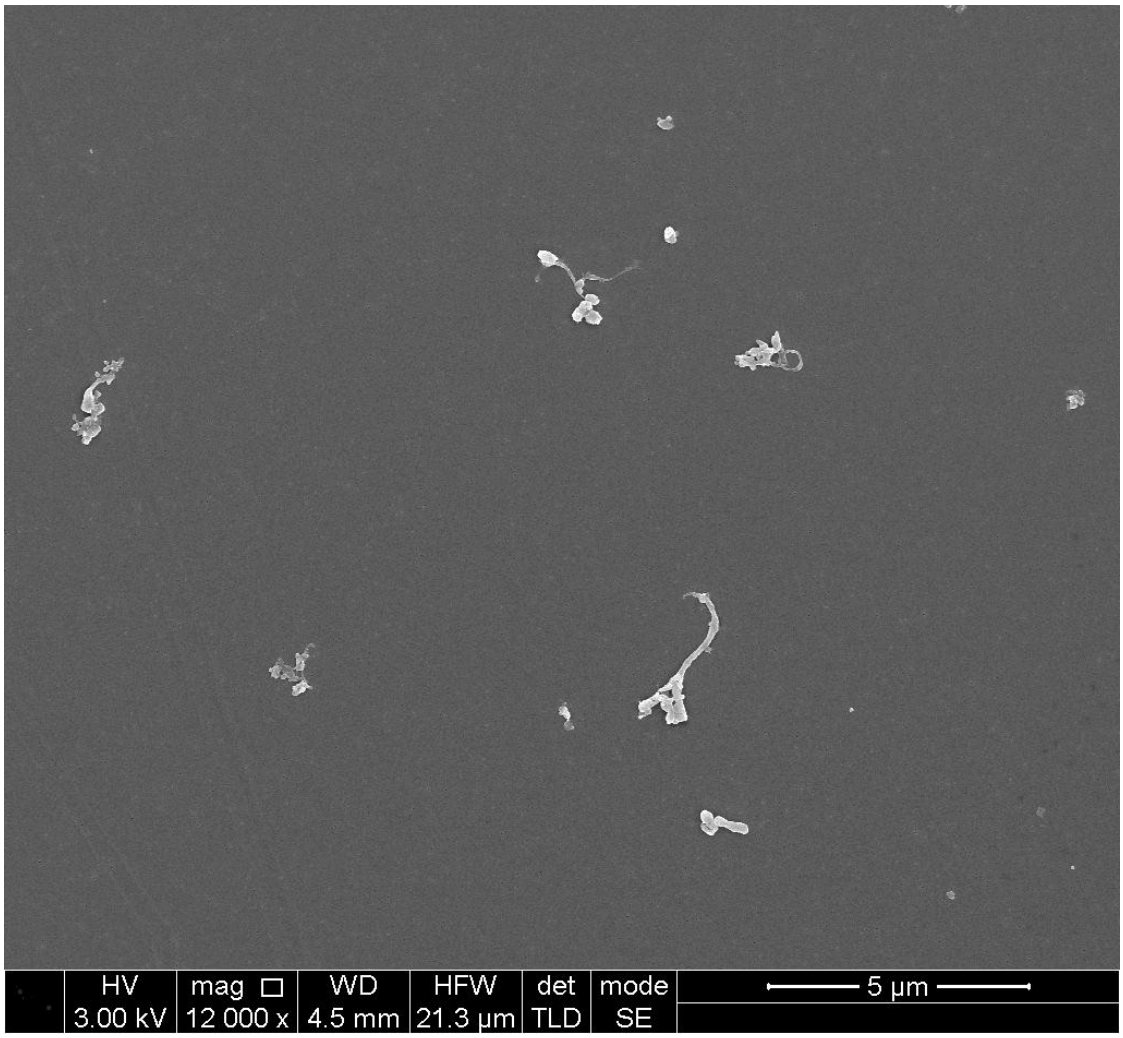

C)

Figure 5.74 Scanning electron micrographs of E1 knee during early wear. A) 15000x magnification, Scale = 5µm B) 20000x magnification, Scale = 4µm C) 12000x magnification, Scale = 5µm.

E1 Hip Early Wear

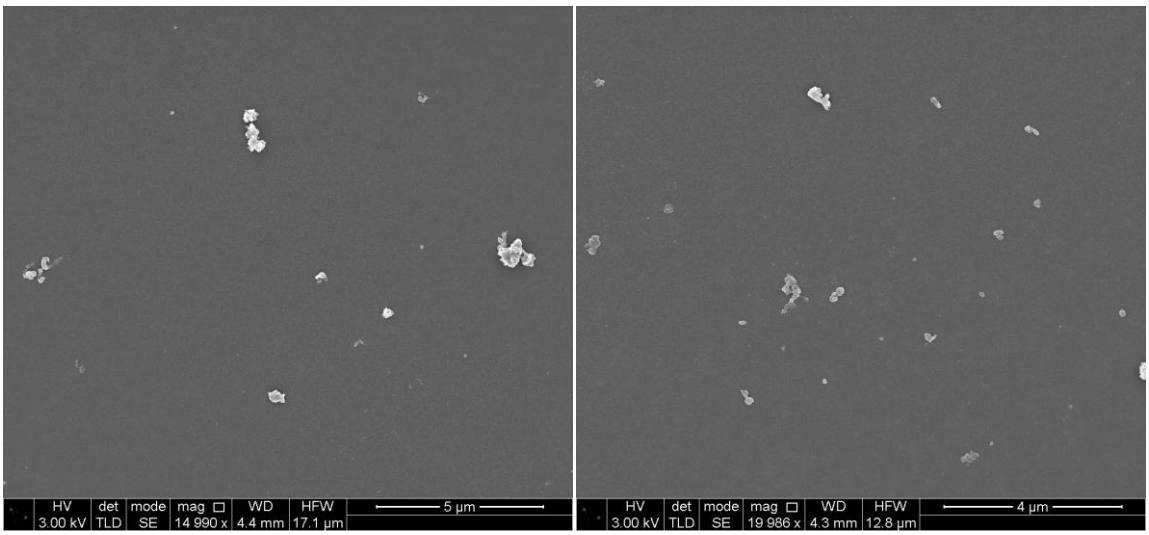

A) **B)**

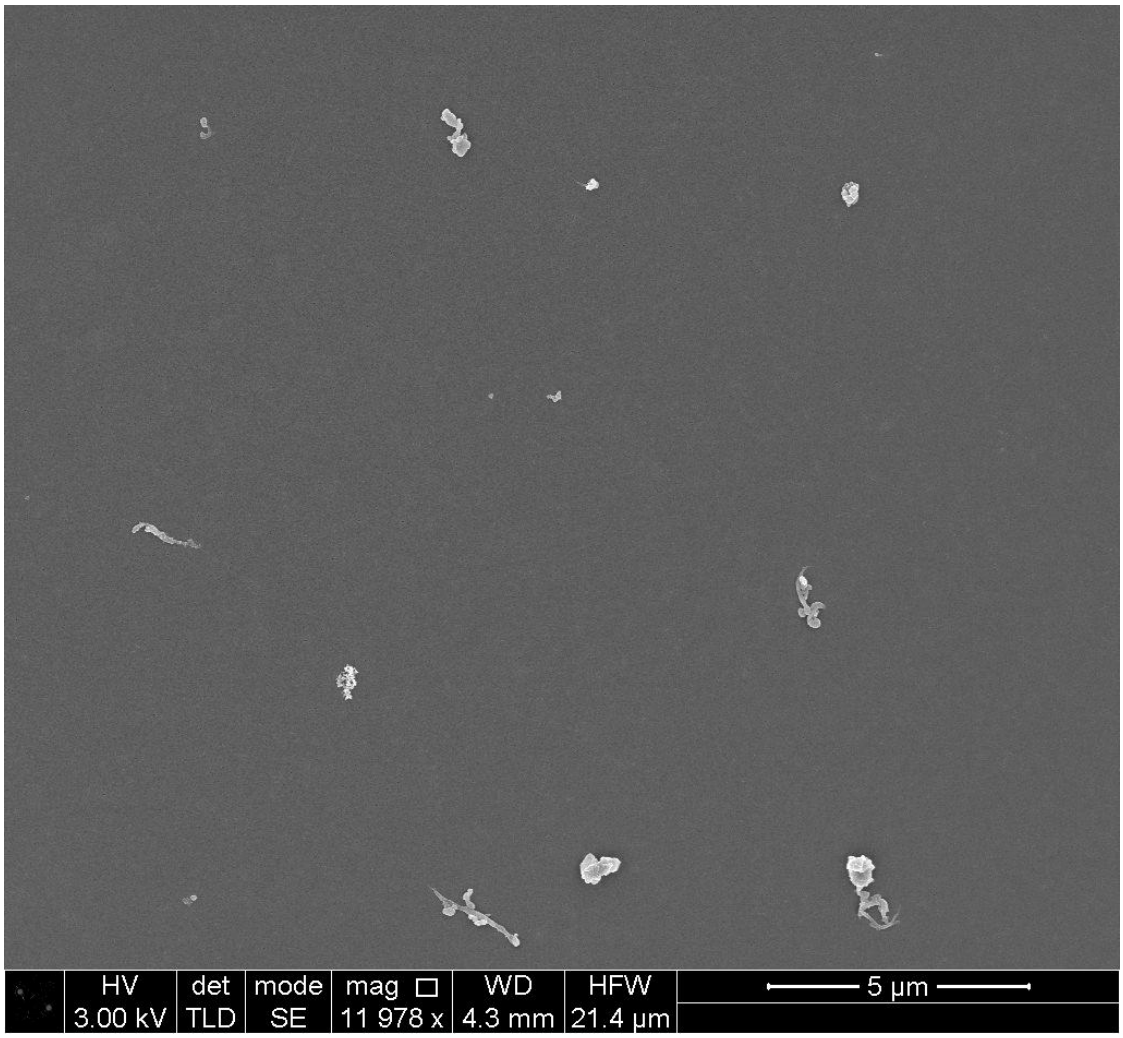

C)

Figure 5.75 Scanning electron micrographs of E1 hip during early wear. A) 15000x magnification, Scale = 5µm B) 20000x magnification, Scale = 4µm C) 12000x magnification, Scale = 5µm.

5.2.2.1.2 Shape analysis

Figure 5.76 shows a comparison between aspect ratio values of E1 UHMWPE particles produced during early wear of knee inserts and hip liners. Similar to the previous studies (Section 5.1.2 and Section 5.2.2), there was a gradual increase in aspect ratio values with an increase in particle size. Moreover, E1 knee particles had higher aspect ratio value in 0.025 to 1µm size range, indicating elongated morphology of particles in this size range.

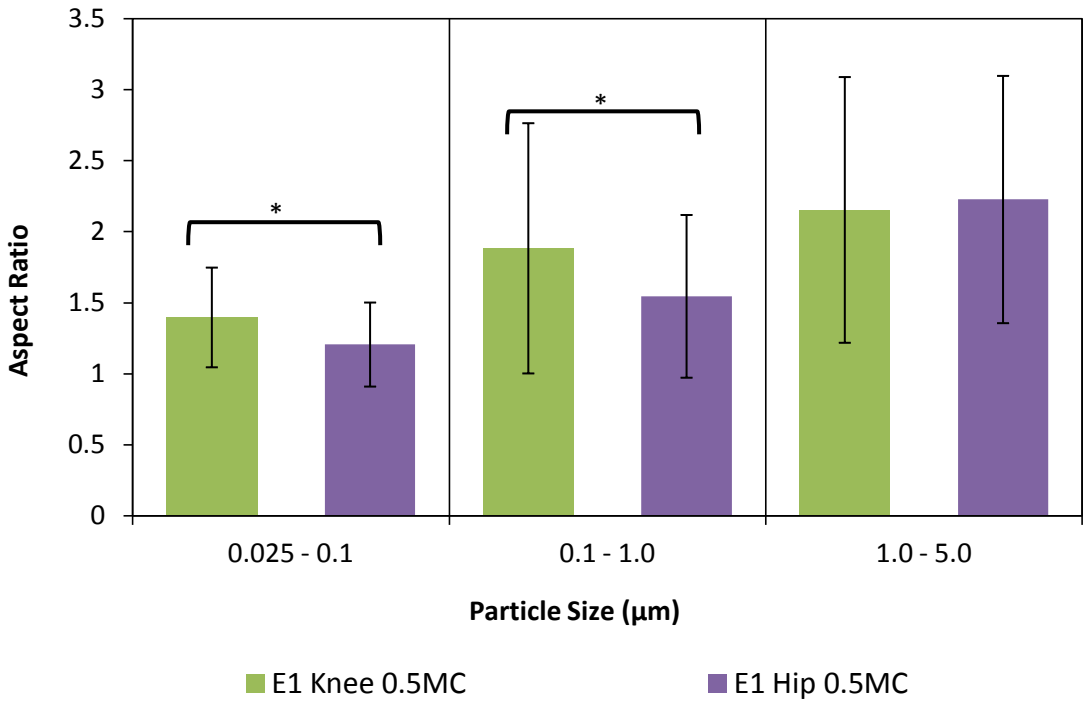

Figure 5.76 A plot showing aspect ratio versus particle size for early wear E1 knee and E1 hip particles. Error bars indicate standard deviation from mean aspect ratio value in each size range. Statistically significant differences ($p < 0.05$) are highlighted with a black outline. Knee showed more elongated shape for particles in 0.025 to 1µm size range compared to hip.

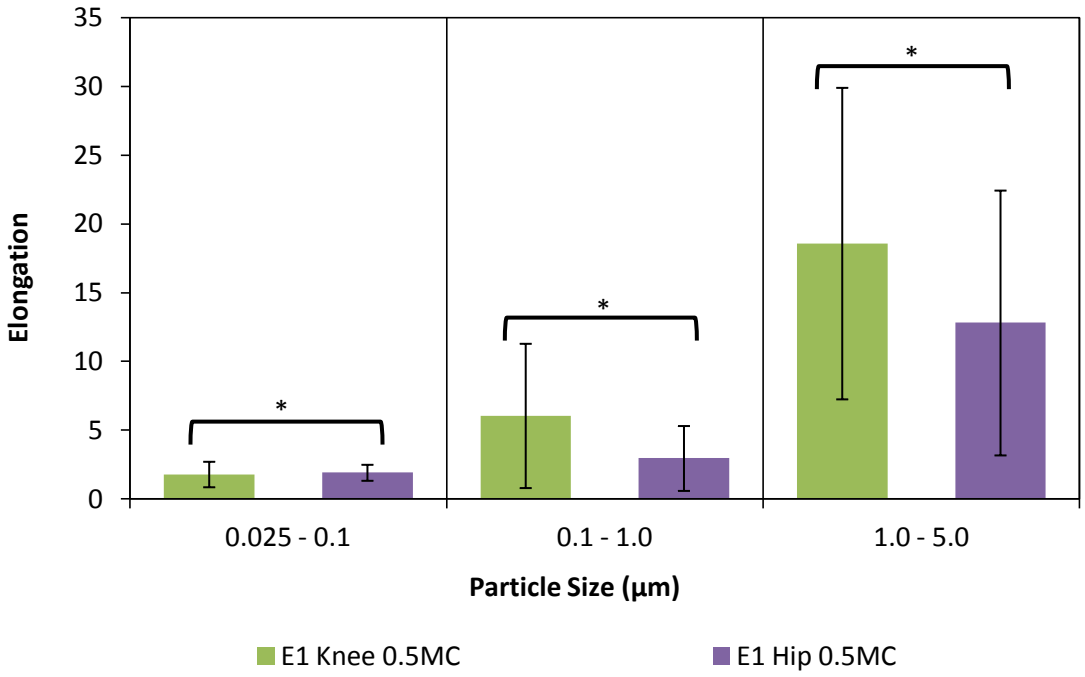

Figure 5.77 A plot showing elongation versus particle size for early wear of E1 knee and E1 hip. Error bars indicate standard deviation from mean elongation value in each size range. Statistically significant differences ($p < 0.05$) are highlighted with a black outline. Knee showed more elongated fibrillar shape for particles larger than 0.1µm, while hip showed more elongated particles in 0.025 to 0.1 µm size range.

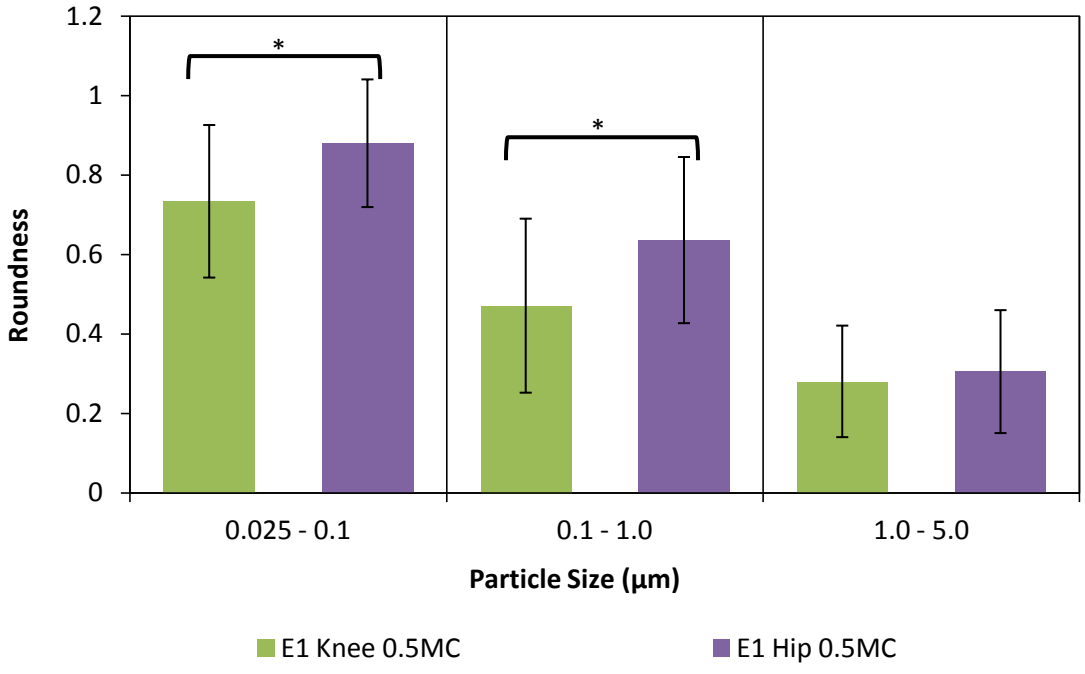

Figure 5.78 A plot showing roundness versus particle size for early wear of E1 knee and E1 hip. Error bars indicate standard deviation from mean roundness value in each size range. Statistically significant differences ($p < 0.05$) are highlighted with a black outline. Hip showed more round shape for particles in 0.025 to 1µm size range compared to knee.

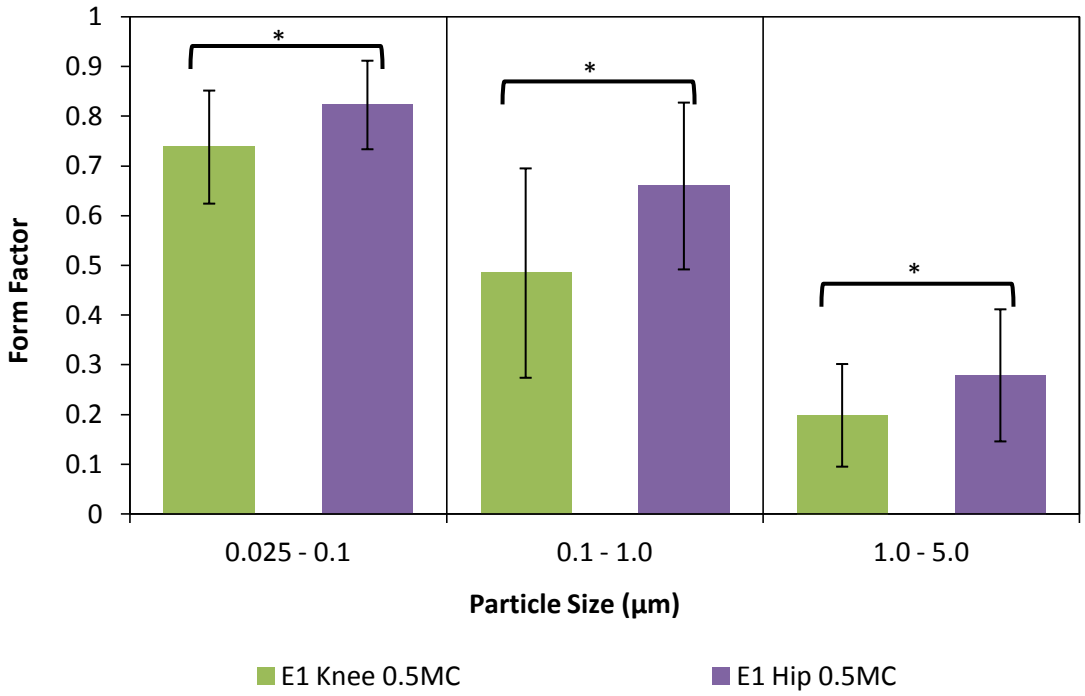

Figure 5.79 A plot showing form factor versus particle size for early wear of E1 knee and E1 hip. Error bars indicate standard deviation from mean form factor value in each size range. Statistically significant differences ($p < 0.05$) are highlighted with a black outline. Hip showed higher form factor values in comparison to knee.

Figure 5.77 shows a comparison between elongation values of E1 knee and E1 hip wear particles during early wear. Elongation values increased with an increase in particle size in both samples. However, E1 knee had higher elongation values for particles in 0.1 to 5 µm size range, while hip showed more elongated particles in 0.025 to 0.1 µm size range.

A comparison between roundness values of both samples is shown in Figure 5.78**.** Roundness values decreased with an increase in particle size. Moreover, E1 hip particles in 0.025 to 1µm size range had higher roundness values in comparison to E1 knee.

Figure 5.79 shows form factor versus particle size for both E1 hip and E1 knee. There was a gradual decrease in form factor values with an increase in particle size in a similar manner as in previous samples. Moreover, E1 hip particles had higher form factor values in comparison to knee for all size ranges.

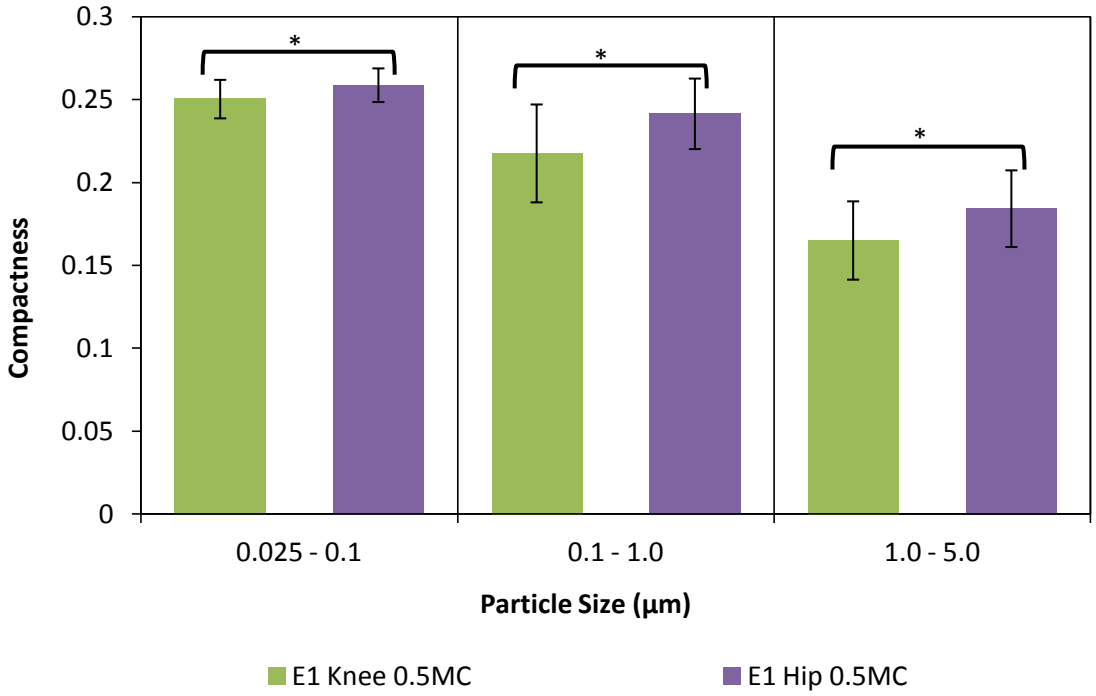

Figure 5.80 A plot showing compactness versus particle size for early wear of E1 knee and E1 hip. Error bars indicate standard deviation from mean compactness value in each size range. Statistically significant differences ($p < 0.05$) are highlighted with a black outline. Hip particles showed more compact shape in comparison to knee.

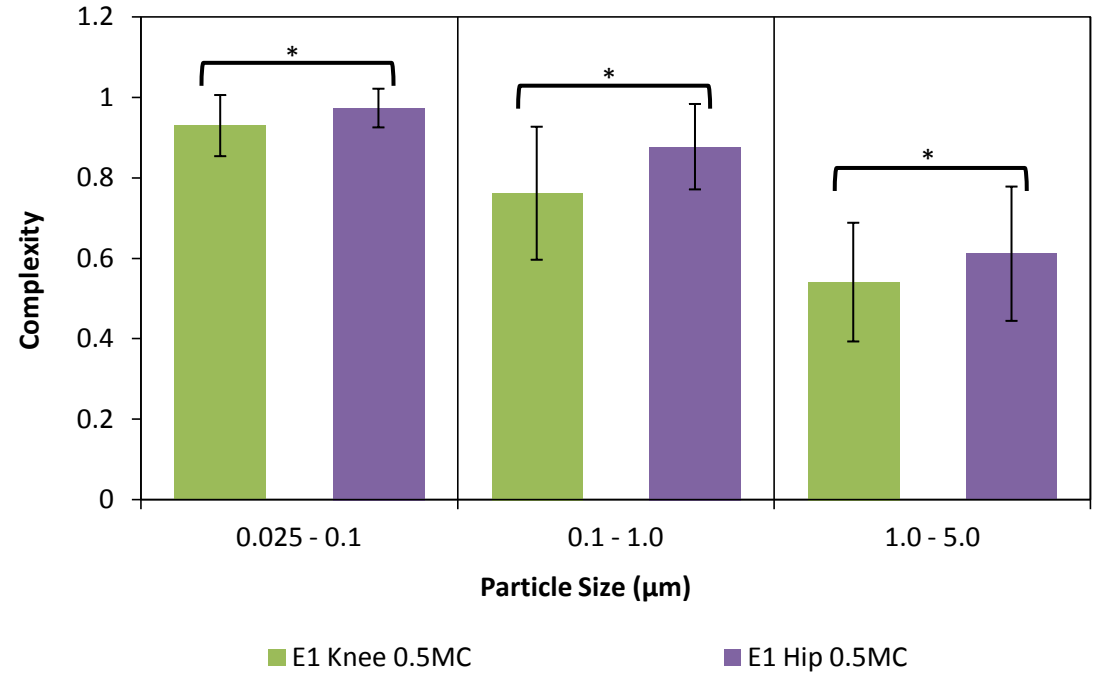

Figure 5.81 A plot showing complexity versus particle size for early wear of E1 knee and E1 hip. Error bars indicate standard deviation from mean complexity value in each size range. Statistically significant differences ($p < 0.05$) are highlighted with a black outline. Knee showed more complex shape in comparison to hip.

Figure 5.80 shows compactness versus particle size for E1 Hip and E1 knee particles. A gradual decrease in compactness was noticed with an increase in particle size. Moreover, E1 hip particles had higher compactness in comparison to knee.

Figure 5.81 shows change in complexity values with particle size for E1 Hip and E1 knee particles. There was a gradual decrease in complexity value with an increase in particle size indicating an increase in complex shape of particles with increasing size. In addition, knee particles were more complex in shape in comparison to E1 hip.

5.2.2.2 **Long-term wear**

During long-term wear, E1 UHMWPE particles isolated from lubricant serum retrieved after 5 million cycles of knee simulator and ankle simulator tests were used for analysis.

5.2.2.2.1 Size analysis

The size distributions of E1 UHMWPE wear particles produced in knee and hip during long-term wear are shown in Figure 5.82. Statistical analysis using Kolmogorov-smirnov Z test indicated that both size distributions were significantly different from each other ($p < 0.05$). Knee produced a higher number of nanoparticles in 50 - 100nm size range, whereas hip generated higher fraction of particles in 100 - 500 nm size range, similar to early wear. Moreover, knee generated a greater fraction of particles larger than 750nm in comparison to hip.

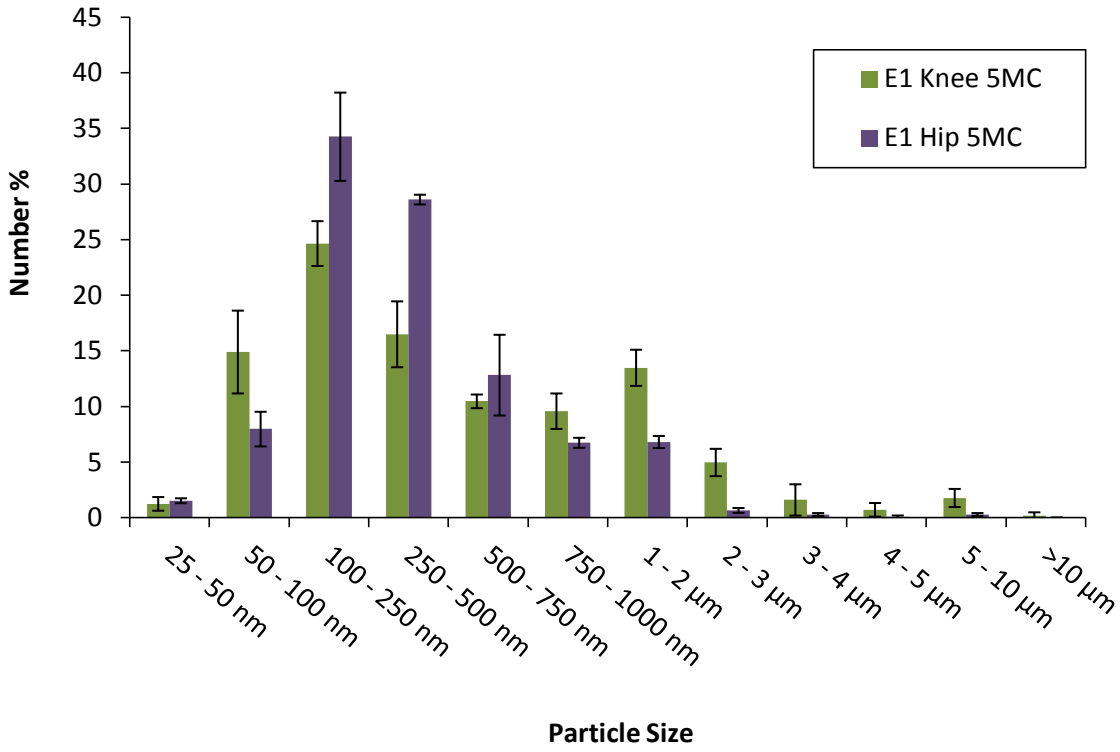

Figure 5.82 A comparison between percentage number size distributions according to maximum Feret's diameter (dmax) of E1 knee and E1 hip wear particles during long-term wear. Error bars show standard deviation.

E1 Knee Long-term Wear

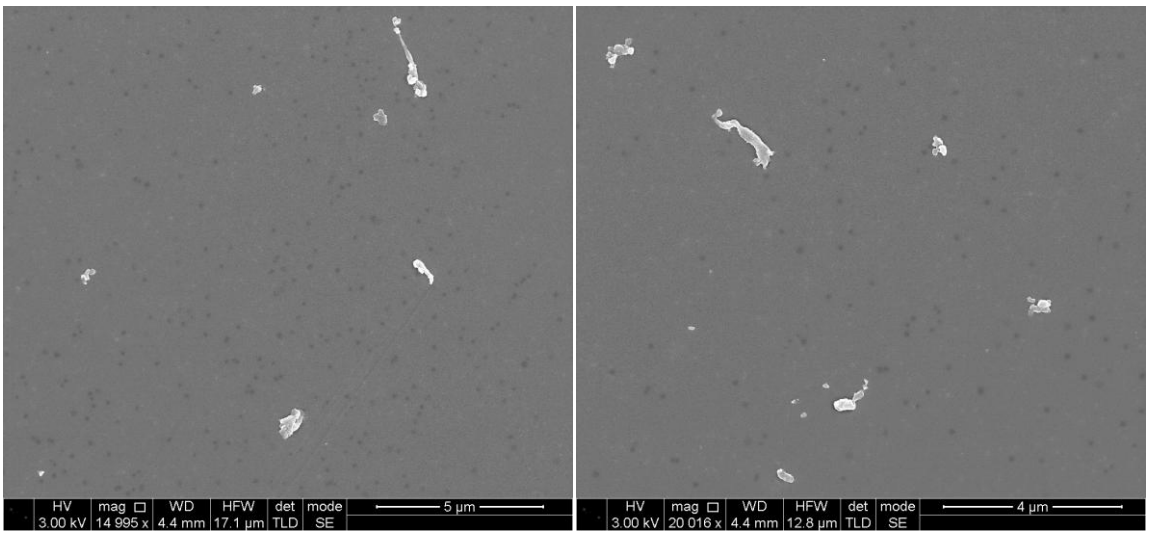

A) **B)**

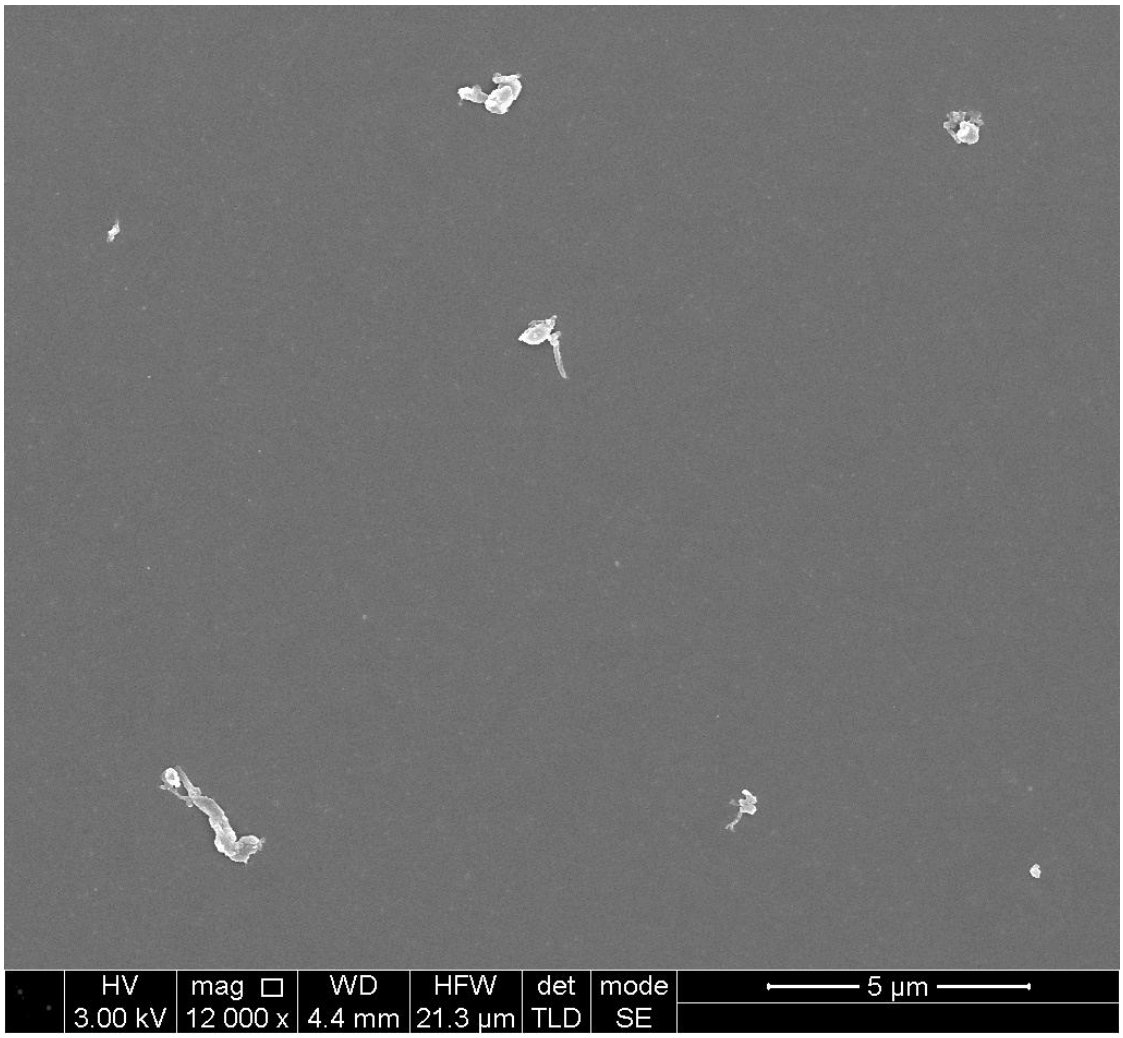

C)

Figure 5.83 Scanning electron micrographs of E1 knee during long-term wear. A) 15000x magnification, Scale = 5µm B) 20000x magnification, Scale = 4µm C) 12000x magnification, Scale = 5µm.

E1 Hip Long-term Wear

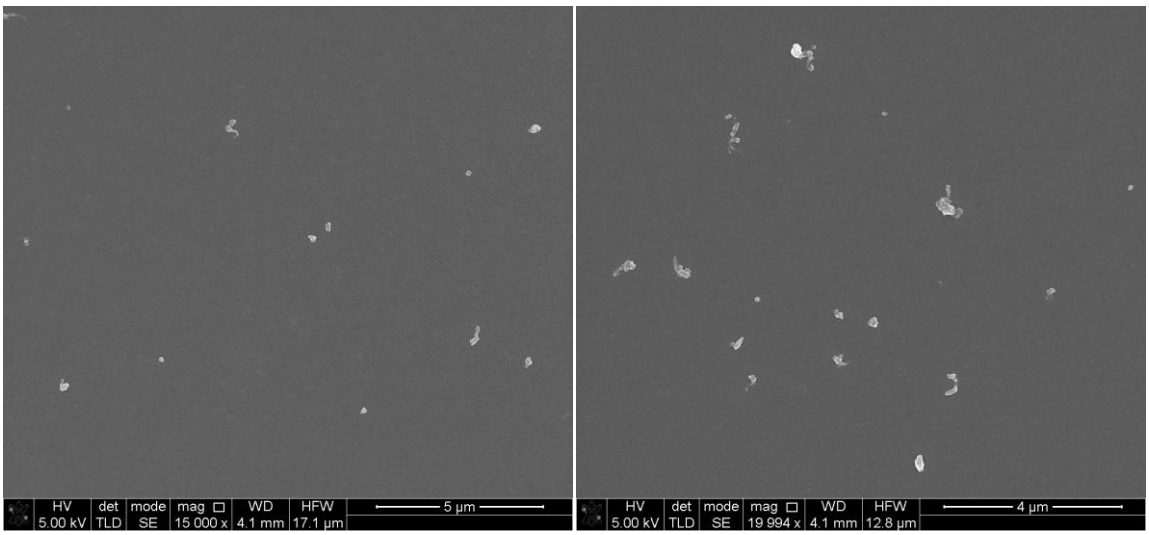

A) **B)**

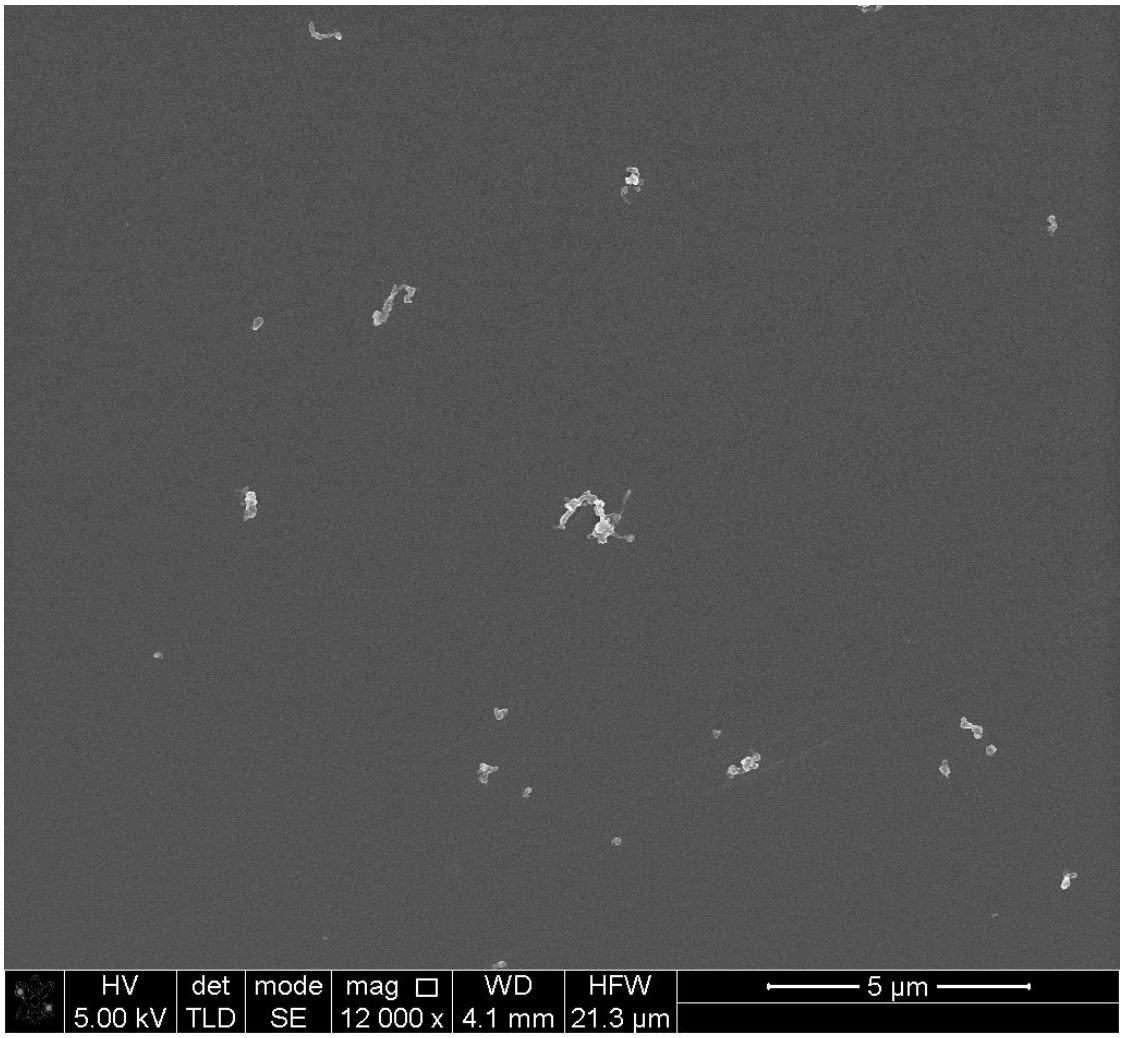

C)

Figure 5.84 Scanning electron micrographs of E1 hip during long-term wear. A) 15000x magnification, Scale = 5µm B) 20000x magnification, Scale = 4µm C) 12000x magnification, Scale = 5µm.

5.2.2.2.2 Shape analysis

Figure 5.85 shows a comparison between aspect ratio values of E1 UHMWPE particles produced during long-term wear of knee tibial inserts and hip liners. A gradual increase in aspect ratio values was noticed with an increase in particle size. Knee particles in 0.1 to 1 µm size range had higher aspect ratio value compared to hip. A higher aspect ratio value indicated more elongated particle shape.

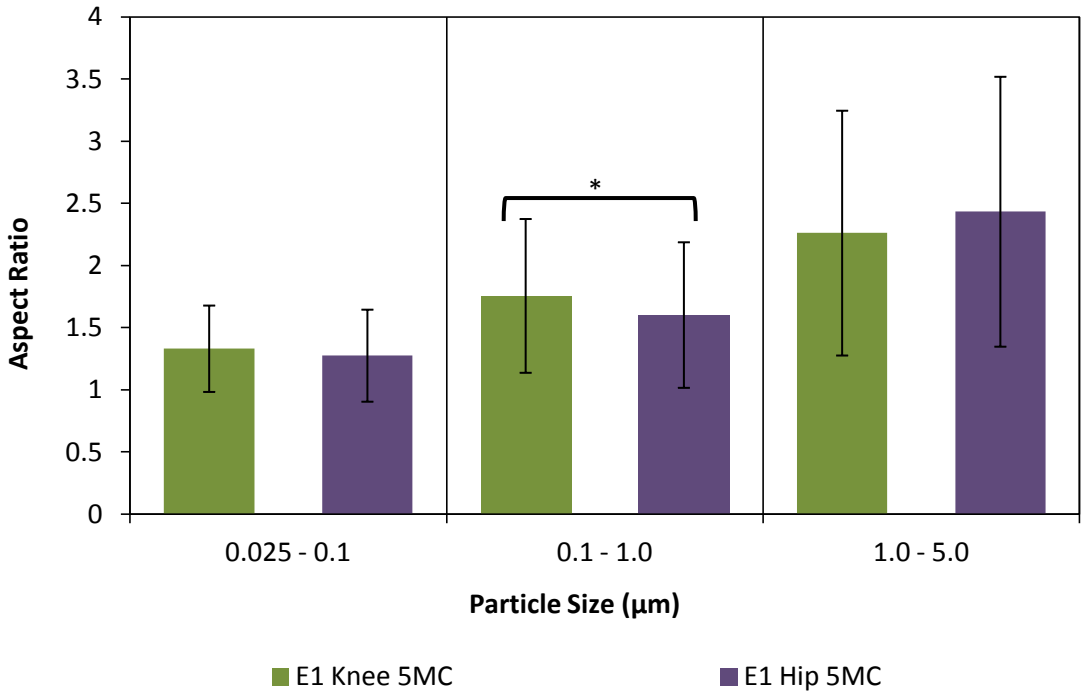

Figure 5.85 A plot showing aspect ratio versus particle size for long-term wear of E1 knee and E1 hip. Error bars indicate standard deviation from mean aspect ratio value in each size range. Statistically significant differences ($p < 0.05$) are highlighted with a black outline. Knee particles in 0.1 to 1 µm size range had more elongated shape compared to hip.

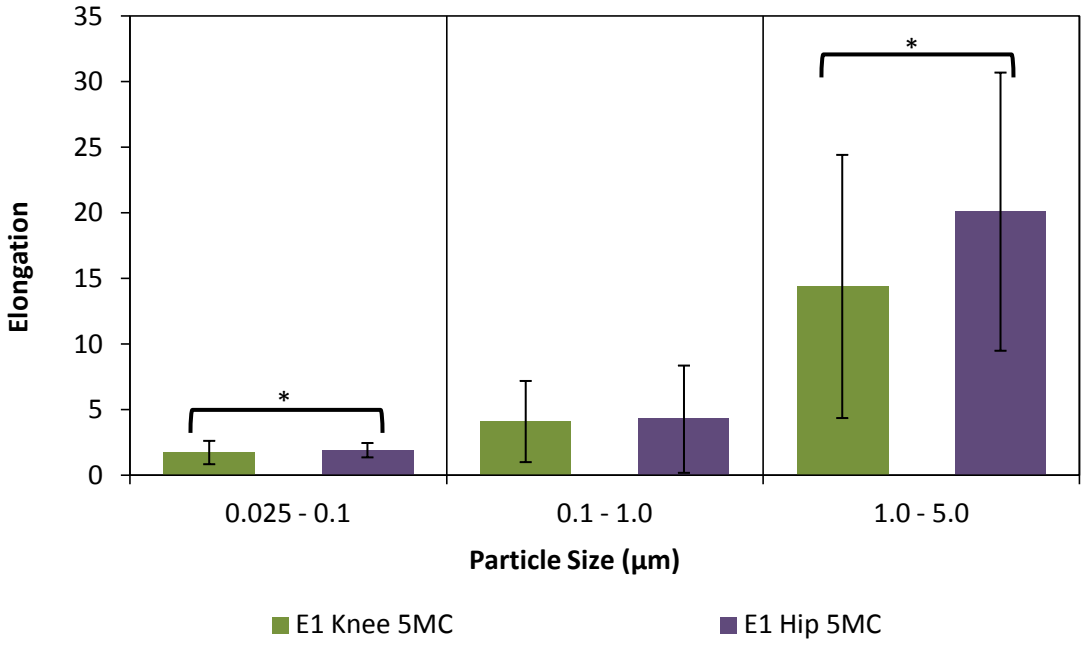

Figure 5.86 A plot showing elongation versus particle size for long-term wear of E1 knee and E1 hip. Error bars indicate standard deviation from mean elongation value in each size range. Statistically significant differences ($p < 0.05$) are highlighted with a black outline. Hip showed higher elongation for particles in 0.025 to 0.1 µm and 1 to 5 µm size ranges in comparison to knee.

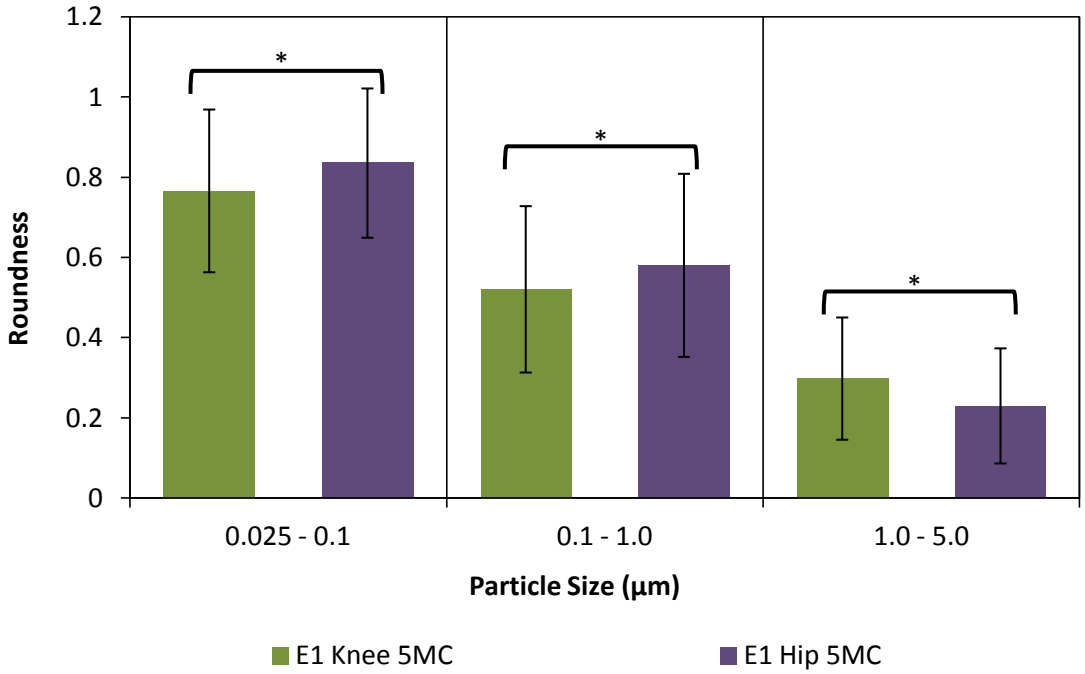

Figure 5.87 A plot showing roundness versus particle size for long-term wear of E1 knee and E1 hip. Error bars indicate standard deviation from mean roundness value in each size range. Statistically significant differences ($p < 0.05$) are highlighted with a black outline. Hip showed more round particles in 0.025 to 1 µm size range, while knee showed rounder particles in 1 to 5 µm size range.

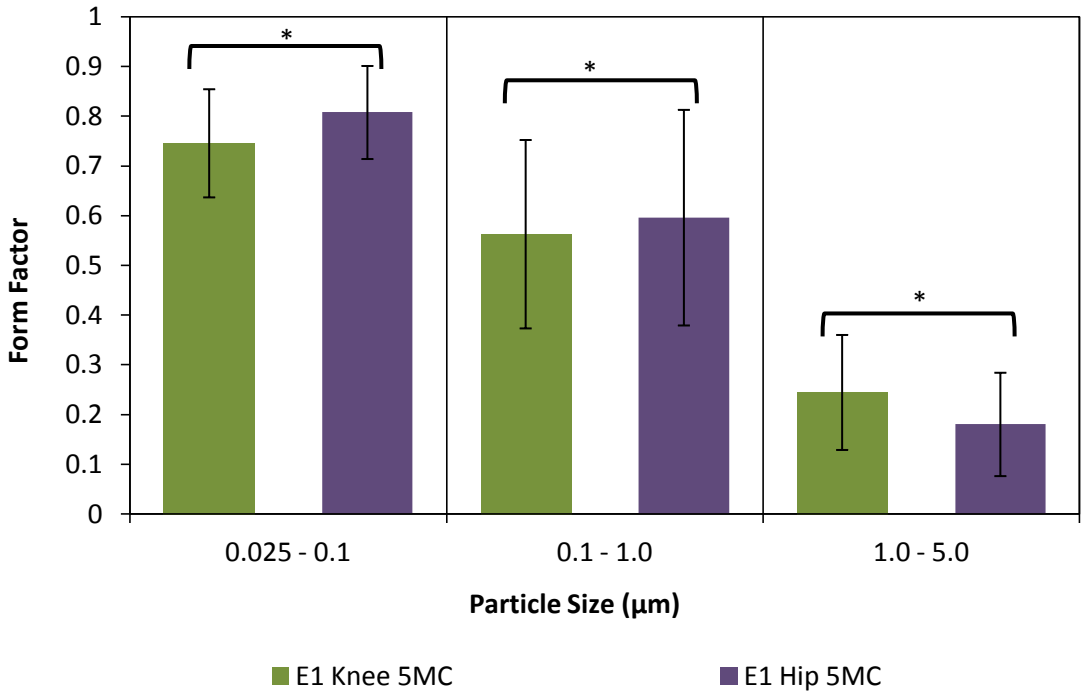

Figure 5.88 A plot showing form factor versus particle size for long-term wear of E1 knee and E1 hip. Error bars indicate standard deviation from mean form factor value in each size range. Statistically significant differences ($p < 0.05$) are highlighted with a black outline. Hip showed higher form factor values in 0.025 to 1 µm size range, while knee showed higher form factor values in 1 to 5 µm size range.

Figure 5.86 shows a comparison between elongation values of E1 knee and E1 hip wear particles during long-term wear. Elongation values increased with an increase in particle size in both samples. Moreover, E1 hip particles had higher elongation value for particles in 0.025 to 0.1 µm and 1 to 5 µm size ranges in comparison to knee. A higher elongation value indicated more elongated fibrillar particle shape.

A comparison between roundness values of both samples is shown in Figure 5.87**.** Roundness values decreased with an increase in particle size for E1 knee and E1 hip particles. Moreover, E1 hip particles in 0.025 to 1 µm size range had higher roundness values, while knee had higher roundness values for particles in 1 to 5 µm size range.

Figure 5.88 shows form factor versus particle size for both E1 hip and E1 knee during long-term wear. The differences between form factor values of knee and hip particles were found to be very similar to the differences in their roundness values (Figure 5.87).

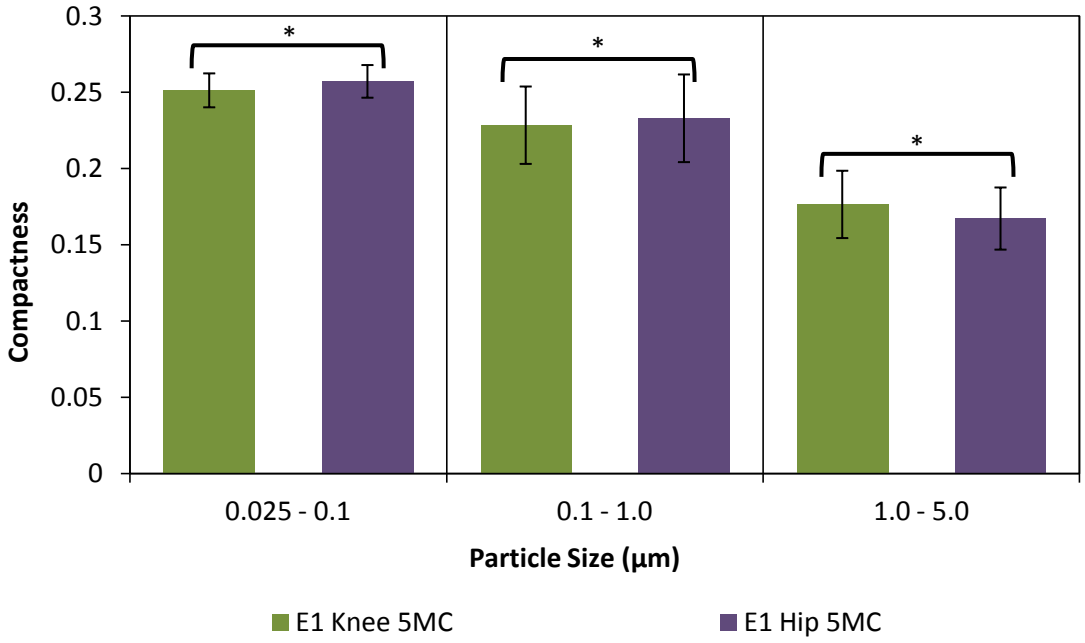

Figure 5.89 A plot showing compactness versus particle size for long-term wear of E1 knee and E1 hip. Error bars indicate standard deviation from mean compactness value in each size range. Statistically significant differences ($p < 0.05$) are highlighted with a black outline. Hip showed marginally higher compactness in 0.025 to 1 µm size range, while knee showed marginally higher compactness in 1 to 5 µm size range.

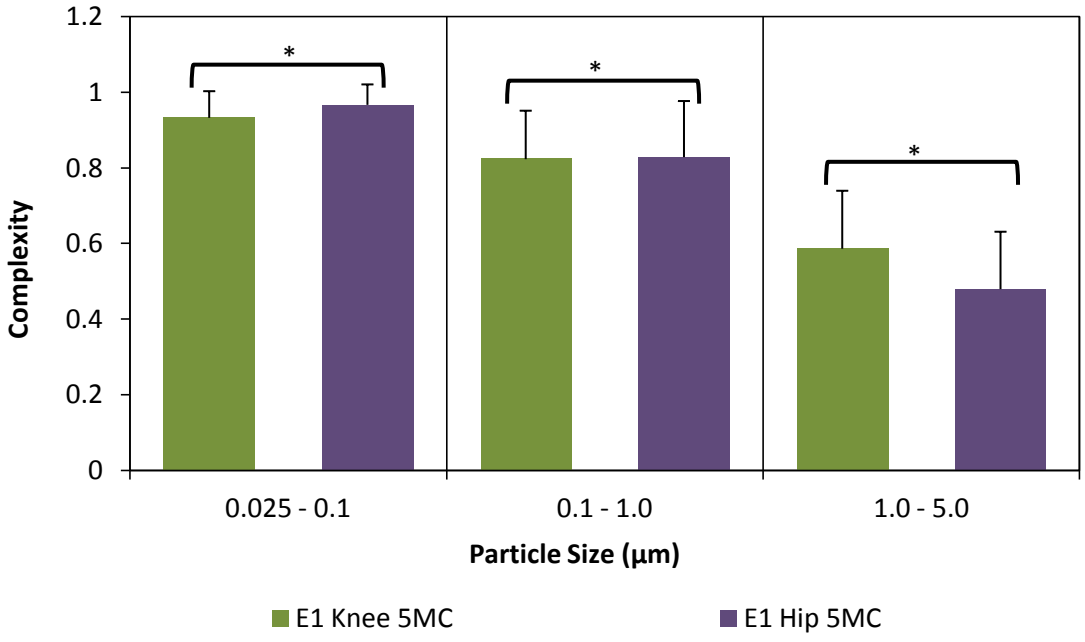

Figure 5.90 A plot showing complexity versus particle size for long-term wear of E1 knee and E1 hip. Error bars indicate standard deviation from mean complexity value in each size range. Statistically significant differences ($p < 0.05$) are highlighted with a black outline. Hip showed more complex particle shape in 1 to 5 µm size range, while knee showed complex shaped particles in 0.025 to 1µm size range.

Figure 5.89 shows compactness versus particle size for E1 knee and E1 Hip particles during long-term wear. A gradual decrease in compactness was noticed with an increase in particle size. E1 hip showed marginally higher compactness in 0.025 to 1 μm size range, while knee showed marginally higher compactness in 1 to 5 μm size range.

Figure 5.90 shows change in complexity values with particle size for E1 knee and E1 Hip particles. E1 knee and hip particles showed a decrease in complexity values with an increase in particle size, indicating an increase in complex shape of particles with increasing size. Moreover, E1 hip showed more complex particle shape in 1 to 5 μm size range, while knee showed complex shaped particles in 0.025 to 1μm size range.

5.2.3 E1 Multidirectional pin-on-plate vs. E1 Hip

In this section, E1 wear particles produced during multidirectional pin-on-plate testing of E1 UHMWPE pins against metal plates were compared with particles produced during hip simulator testing of E1 liners against metal counterparts. Wear particles generated during early wear and long-term wear of both materials were compared for size and morphology.

5.2.3.1 Early wear

During early wear, E1 UHMWPE particles isolated from lubricant serum retrieved after 0.5 million cycles of testing were used for analysis.

5.2.3.1.1 Size analysis

The size distribution of E1 wear particles produced in a hip simulator and multidirectional pin-on-plate simulator during early wear are compared as shown in Figure 5.91. Statistical analysis using Kolmogorov-smirnov Z test indicated that both size distributions were different from each other ($p < 0.05$). E1 hip generated higher percentage of particles in 100 to 250nm and 1 to 2 µm size range, while multidirectional pin-on-plate generated higher percentage of particles in 250 to 500 nm size range.

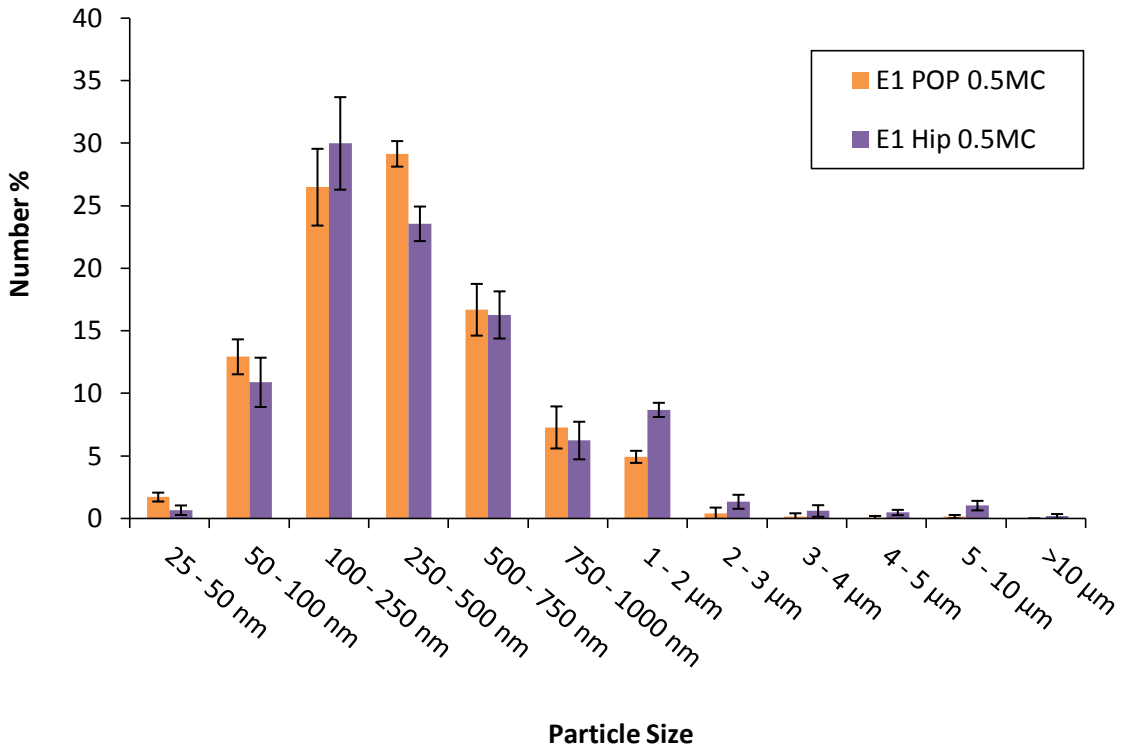

Figure 5.91 A comparison between percentage number size distributions according to maximum Feret's diameter (dmax) of E1 multidirectional pin-on-plate(POP) and E1 hip wear particles during early wear. Error bars show standard deviation.

E1 Multistation Pin-on-plate Early Wear

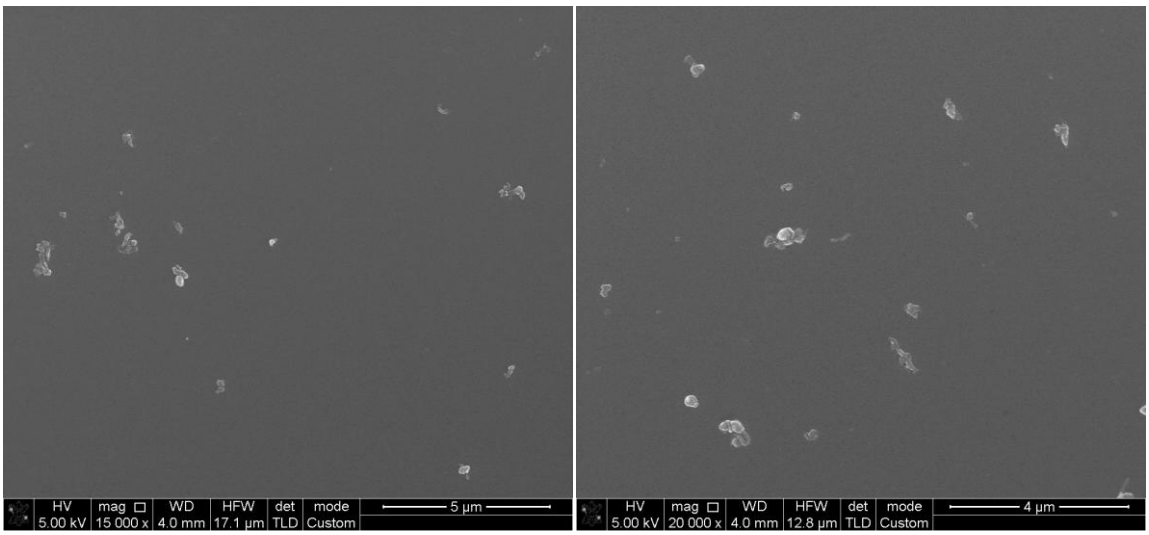

A) **B)**

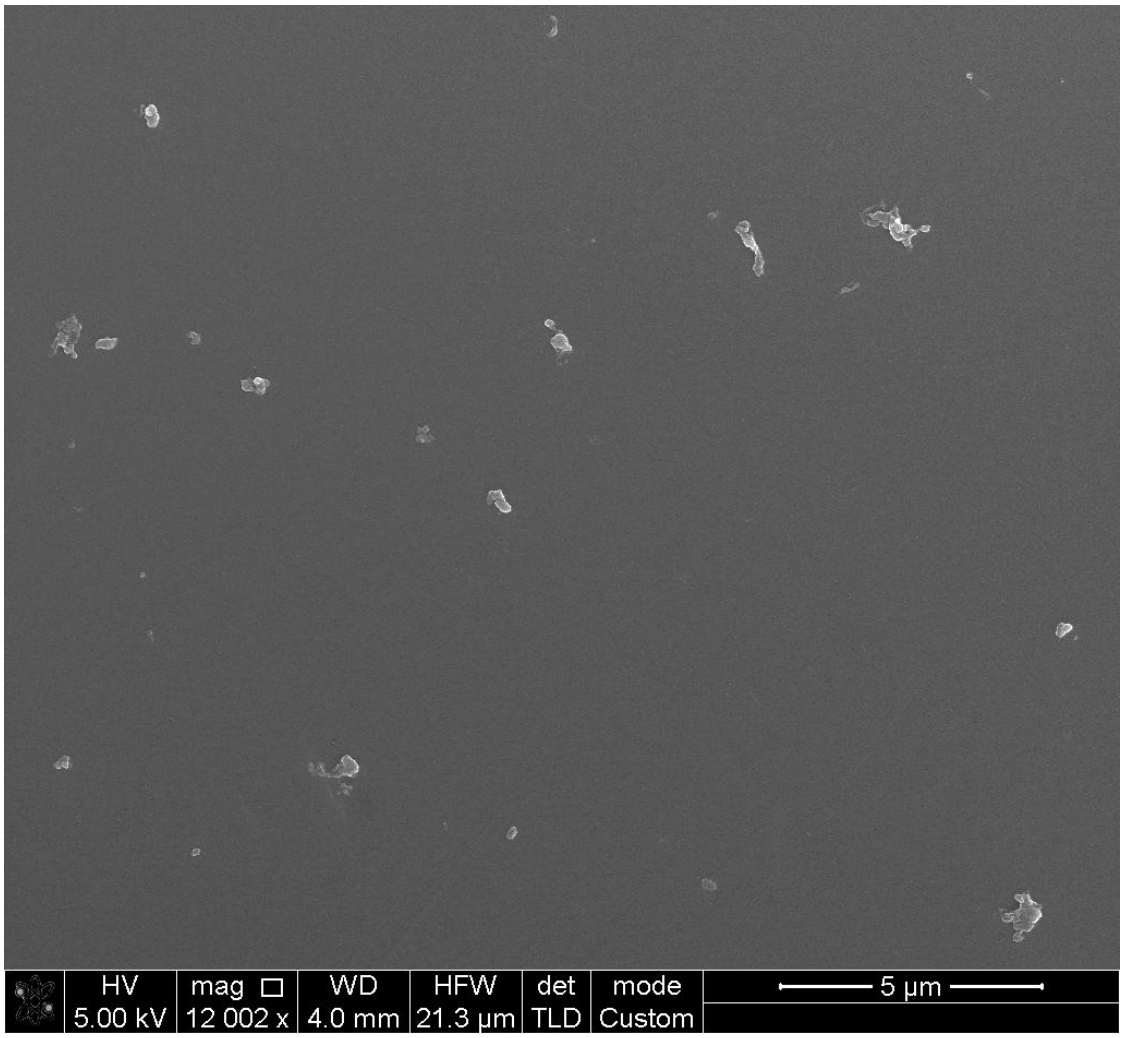

C)

Figure 5.92 Scanning electron micrographs of E1 multistation pin-on-plate during early wear. A) 15000x magnification, Scale = 5µm B) 20000x magnification, Scale = 4µm C) 12000x magnification, Scale = 5µm.

E1 Hip Early Wear

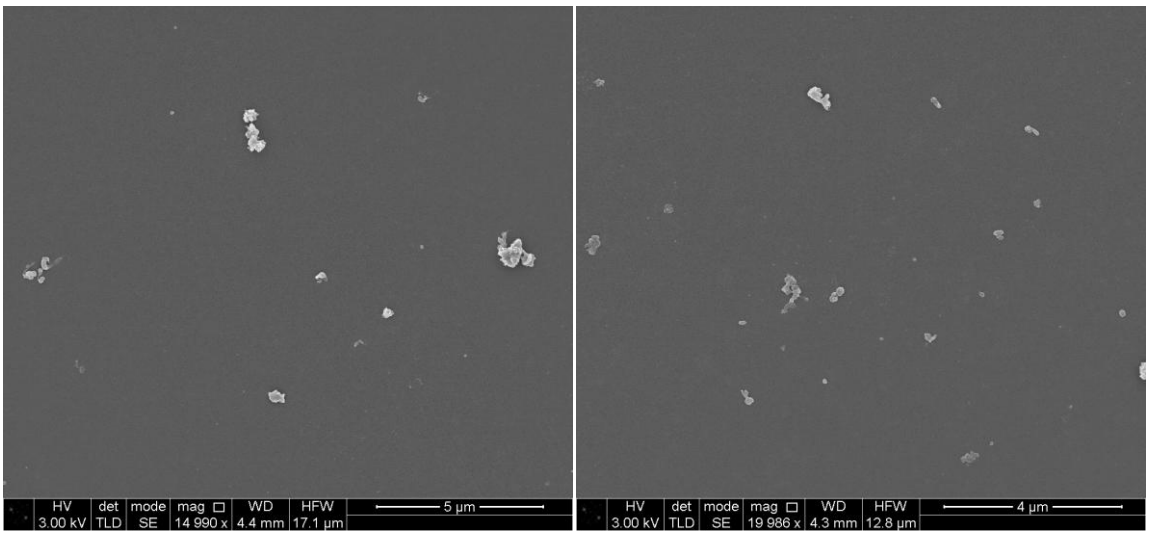

A) **B)**

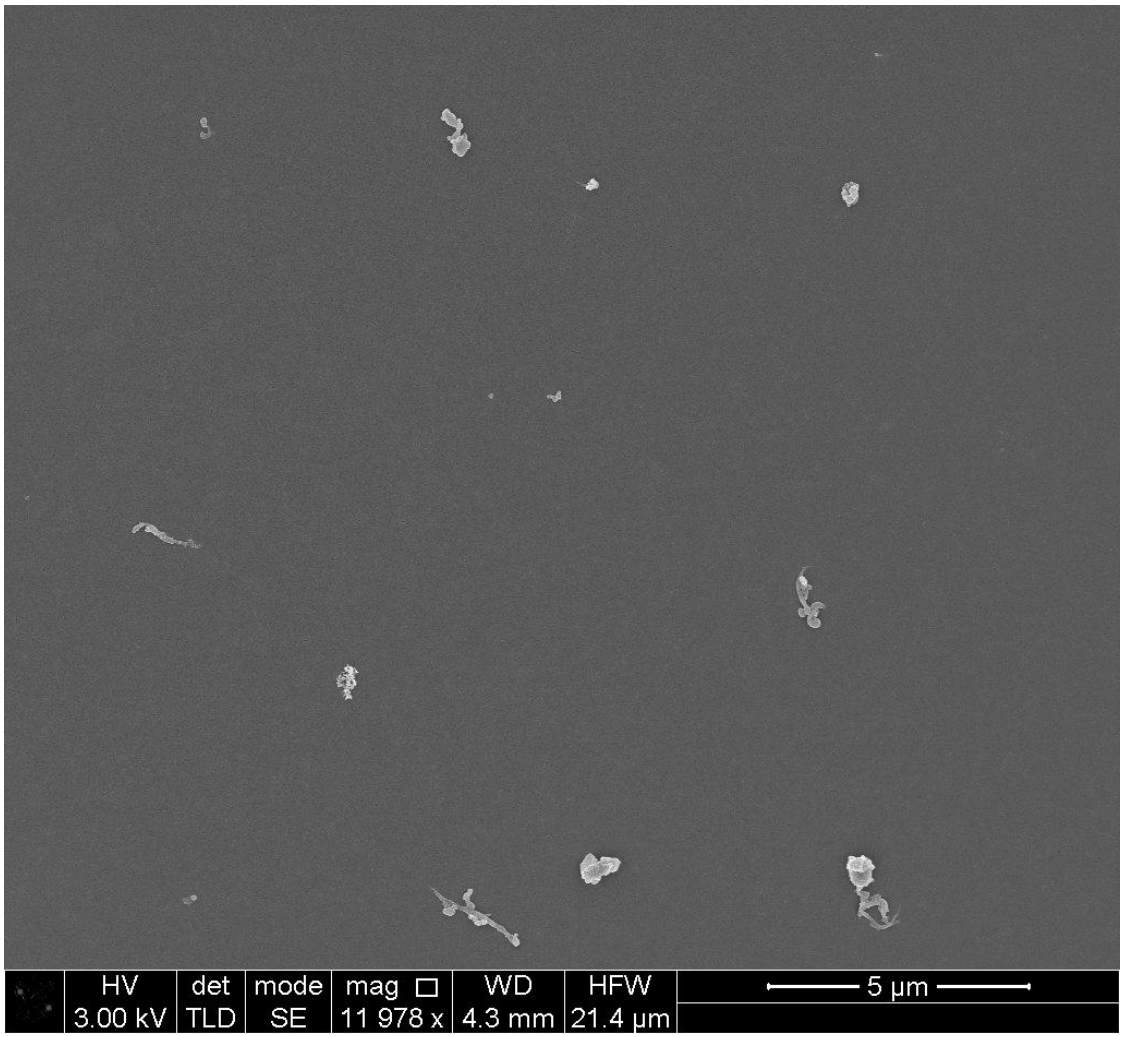

C)

Figure 5.93 Scanning electron micrographs of E1 hip during early wear. A) 15000x magnification, Scale = 5µm B) 20000x magnification, Scale = 4µm C) 12000x magnification, Scale = 5µm.

5.2.3.1.2 Shape analysis

A comparison between aspect ratio values of E1 POP and E1 hip particles during early wear is shown in Figure 5.94. A gradual increase in aspect ratio values was noticed with an increase in particle size. Moreover, aspect ratio values were higher for E1 POP particles in comparison to E1 hip.

Elongation values of both samples are shown in Figure 5.95. There was an increase in elongation values with an increase in particle size for both samples. However, E1 POP particles showed higher elongation values in comparison to E1 hip for particles larger than 100nm. This indicated presence of more elongated fibrillar particles in E1 POP compared to E1 hip.

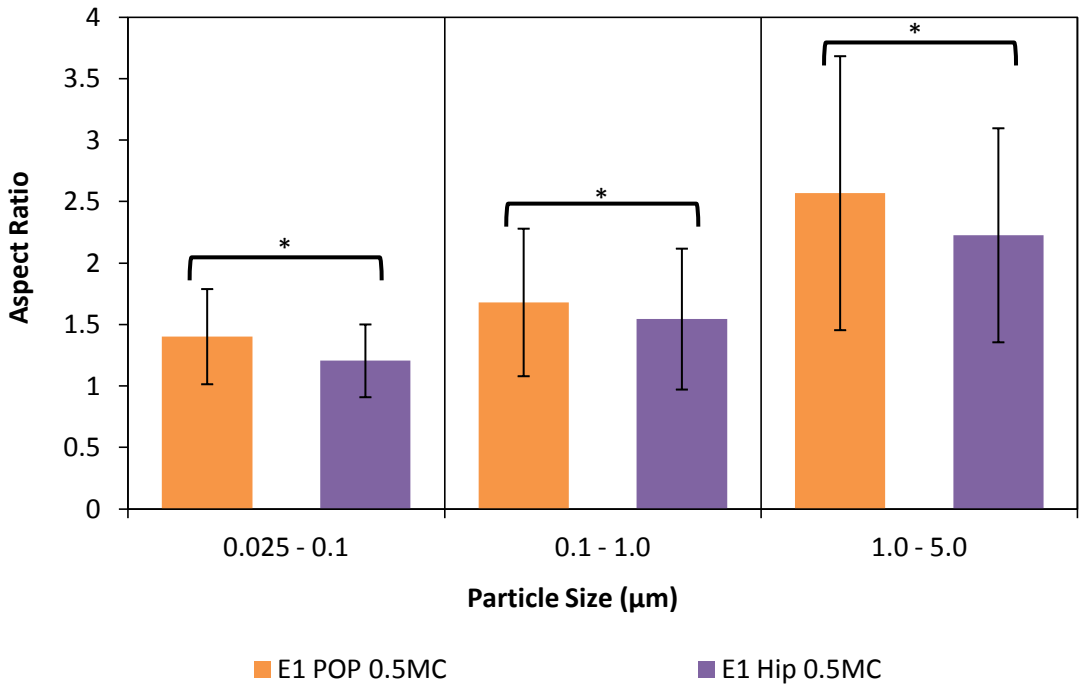

Figure 5.94 A plot showing aspect ratio versus particle size for early wear E1 multidirectional pin-on-plate (POP) and E1 hip particles. Error bars indicate standard deviation from mean aspect ratio value in each size range. Statistically significant differences ($p < 0.05$) are highlighted with a black outline. POP showed more elongated particles in comparison to hip.

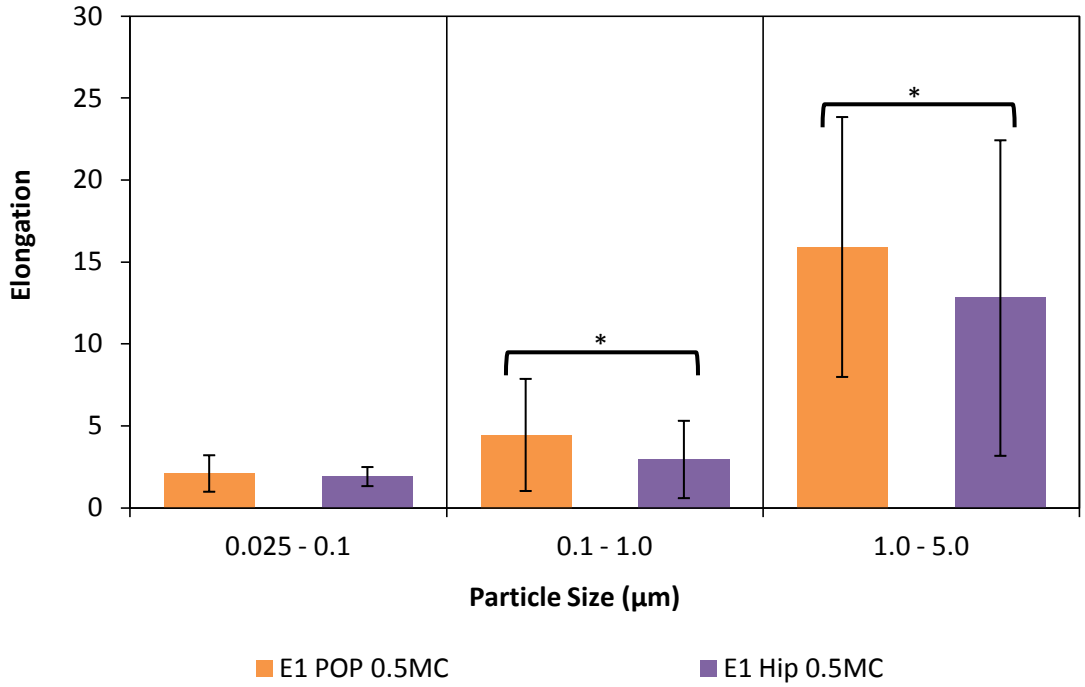

Figure 5.95 A plot showing elongation versus particle size for early wear E1 multidirectional pin-on-plate (POP) and E1 hip particles. Error bars indicate standard deviation from mean elongation value in each size range. Statistically significant differences ($p < 0.05$) are highlighted with a black outline. POP showed more elongated fibrillar particles in 0.1 to 5 µm size range in comparison to hip.

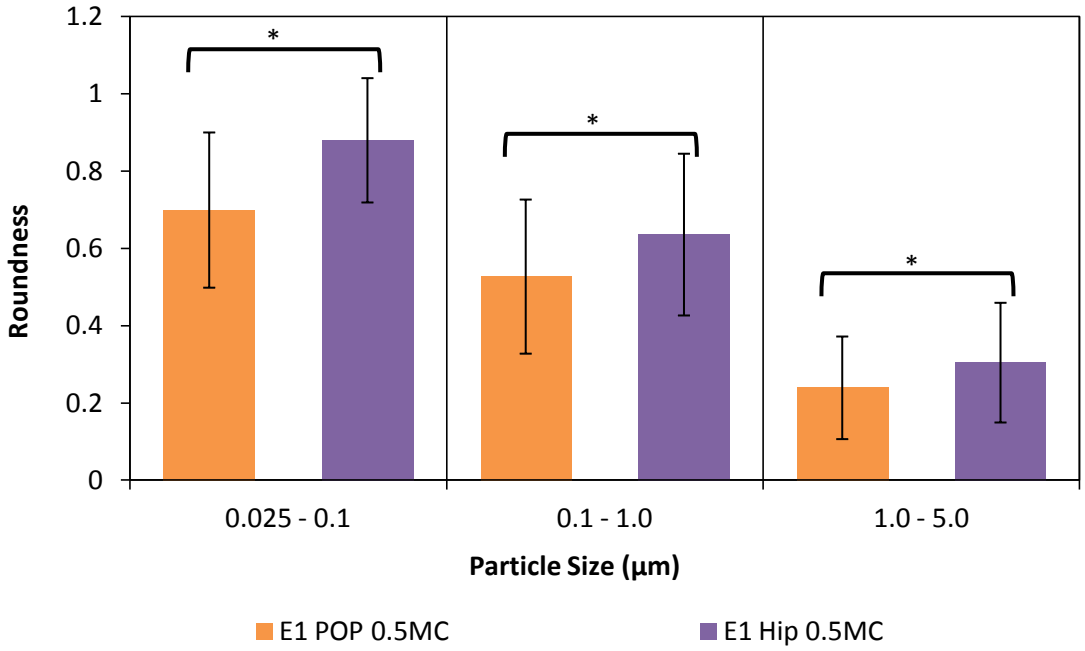

Figure 5.96 A plot showing roundness versus particle size for early wear E1 multidirectional pin-on-plate (POP) and E1 hip particles. Error bars indicate standard deviation from mean roundness value in each size range. Statistically significant differences ($p < 0.05$) are highlighted with a black outline. Hip showed more round particles in comparison to POP.

Figure 5.96 shows a comparison between roundness values of E1 POP and E1 hip particles during early wear. A decrease in roundness values with an increase in particle size was noticed for both samples. Moreover, hip particles had higher roundness values in comparison to POP, indicating that hip produced particles with more round morphology compared to POP. Form factor values also decreased with an increase in particle size in a similar manner as shown in Figure 5.97.

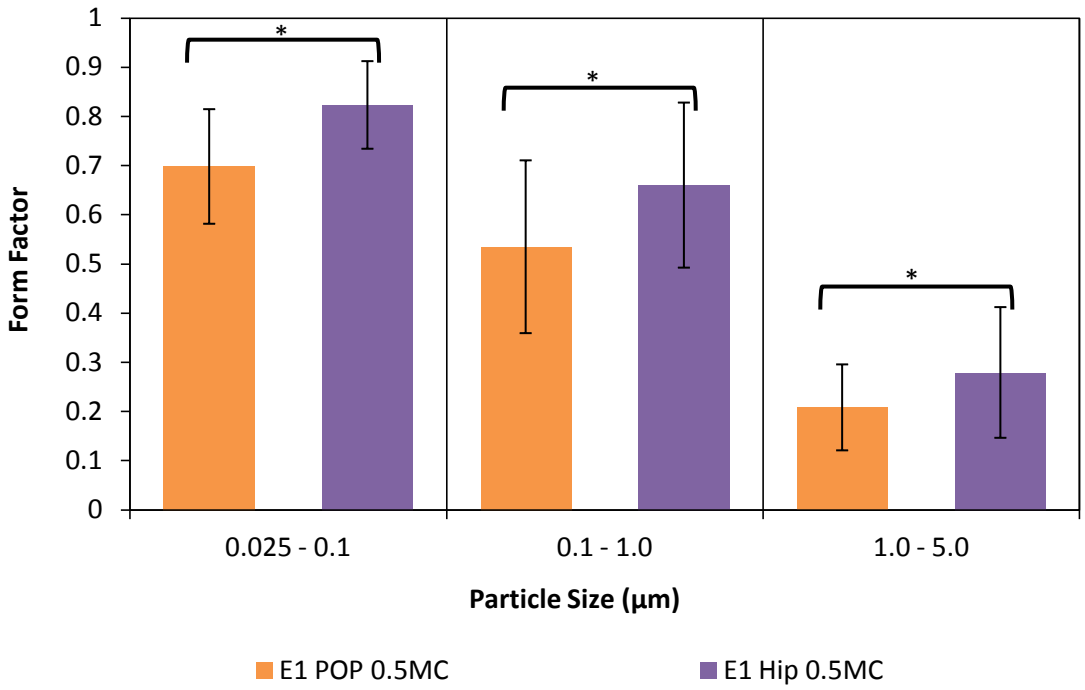

Figure 5.97 A plot showing form factor versus particle size for early wear E1 multidirectional pin-on-plate (POP) and E1 hip particles. Error bars indicate standard deviation from mean form factor value in each size range. Statistically significant differences ($p < 0.05$) are highlighted with a black outline. Hip showed higher form factor values in comparison to POP.

A comparison between compactness values of both samples during early wear is shown in Figure 5.98. There was a gradual decrease in compactness values with an increase in particle size. Moreover, E1 hip particles showed higher compactness values in comparison to E1 POP.

Figure 5.99 shows change in complexity values of both E1 POP and E1 hip particles with an increase in particle size. A decrease in complexity value with an increase in particle size for both samples indicated increasing complexity of particle shapes with size. Moreover, E1 POP particles had lower complexity values in comparison to E1 hip indicating generation of more complex shaped particles in POP compared to hip during early wear.

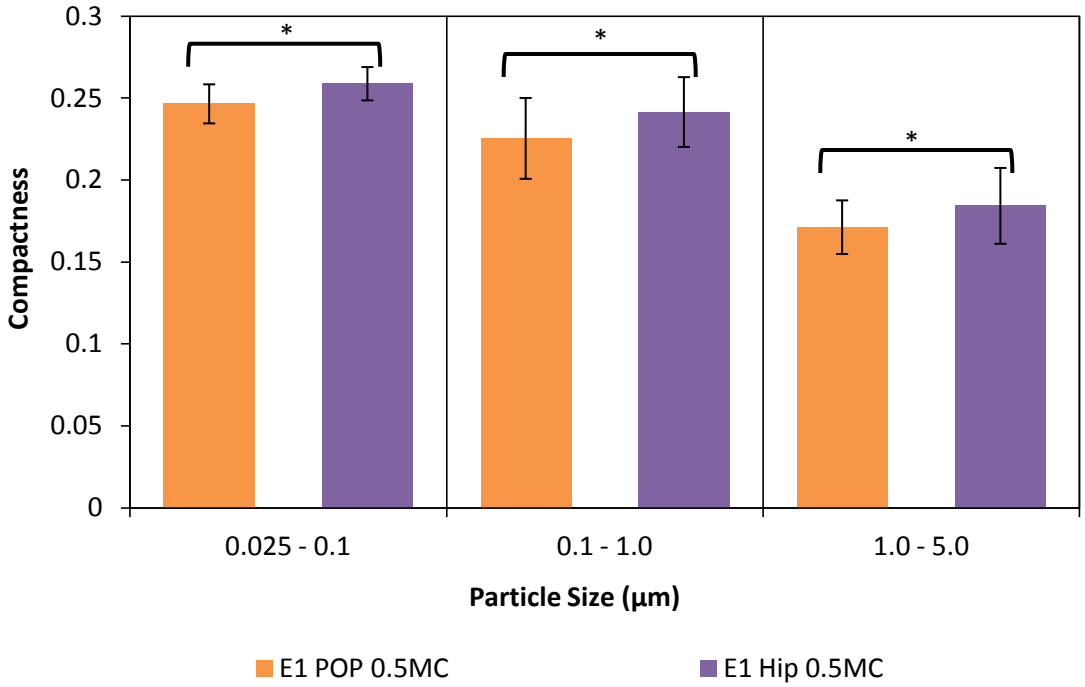

Figure 5.98 A plot showing compactness versus particle size for early wear E1 multidirectional pin-on-plate (POP) and E1 hip particles. Error bars indicate standard deviation from mean compactness value in each size range. Statistically significant differences ($p < 0.05$) are highlighted with a black outline. Hip showed more compact shape in comparison to POP.

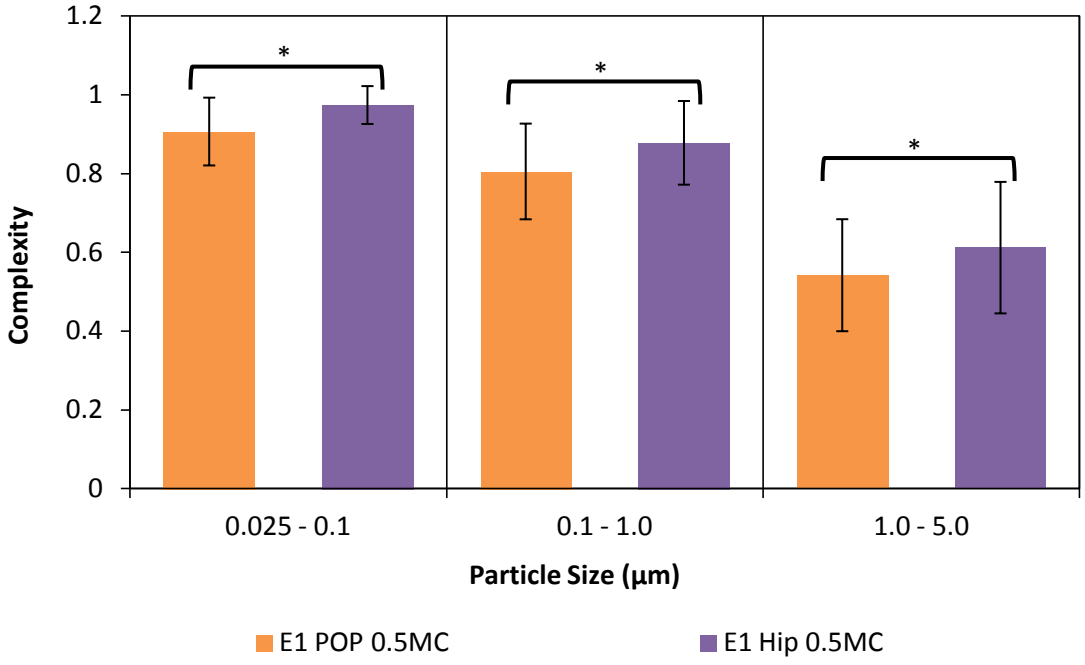

Figure 5.99 A plot showing complexity versus particle size for early wear E1 multidirectional pin-on-plate (POP) and E1 hip particles. Error bars indicate standard deviation from mean complexity value in each size range. Statistically significant differences ($p < 0.05$) are

highlighted with a black outline.POP showed particles with more complex shape in comparison to hip.

5.2.3.2 Long-term wear

During long-term wear, E1 UHMWPE particles isolated from lubricant serum retrieved after 3.5 million cycles of POP testing were compared with E1 UHMWPE particles isolated from lubricant serum retrieved after 5 million cycles of E1 Hip testing.

5.2.3.2.1 Size analysis

The size distributions of E1 UHMWPE wear particles produced in POP and hip during long-term wear is shown in Figure 5.100. Overall shape of both size distributions looked similar. However, statistical analysis using Kolmogorov-smirnov Z test indicated that both size distributions were different from each other ($p < 0.05$). Moreover, hip produced a higher percentage of particles with size smaller than 250nm.

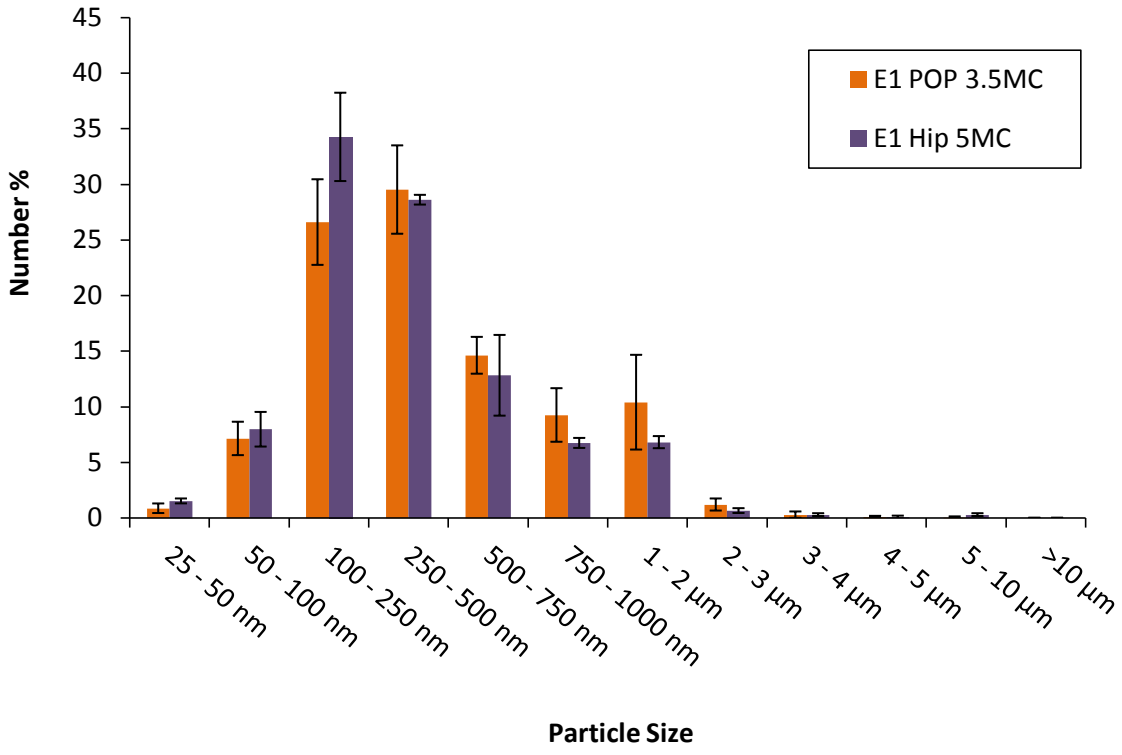

Figure 5.100 A comparison between percentage number size distributions according to maximum Feret's diameter (dmax) of E1 multidirectional pin-on-plate(POP) and E1 hip wear particles during long-term wear. Error bars show standard deviation.

E1 Multistation Pin-on-plate Long-term Wear

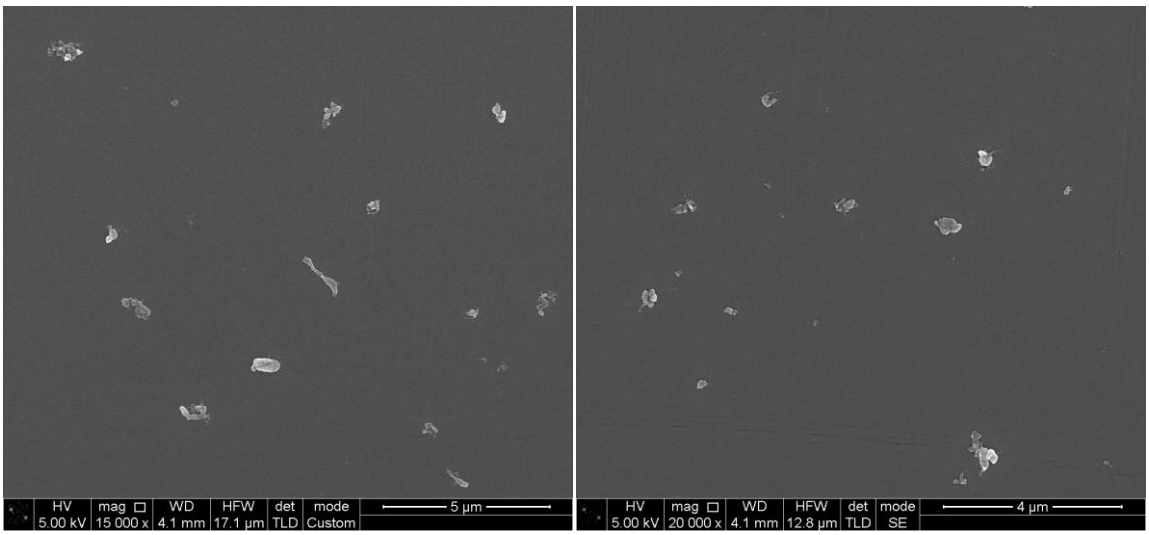

A) **B)**

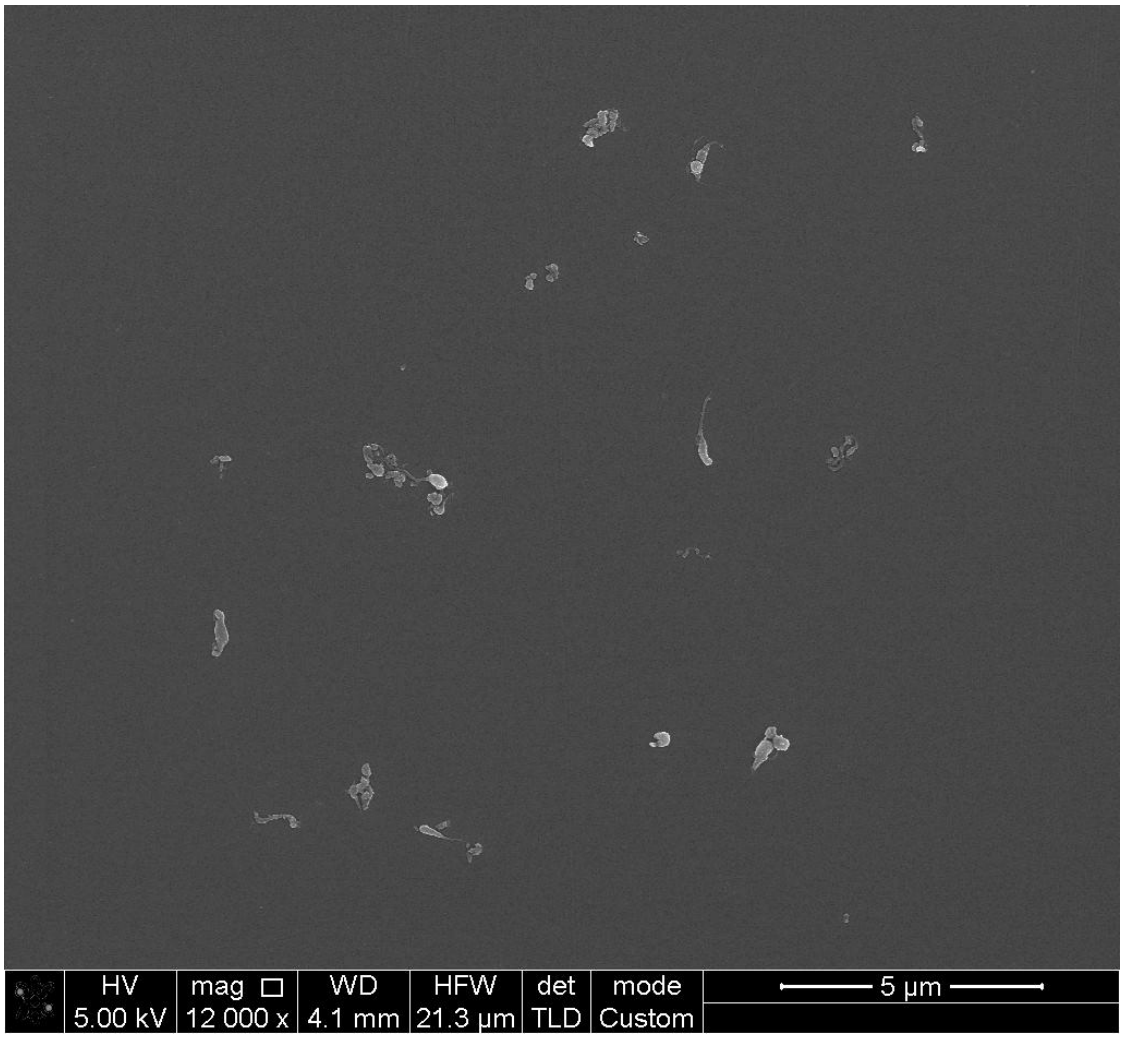

C)

Figure 5.101 Scanning electron micrographs of E1 multistation pin-on-plate during long-term wear. A) 15000x magnification, Scale = 5µm B) 20000x magnification, Scale = 4µm C) 12000x magnification, Scale = 5µm.

E1 Hip Long-term Wear

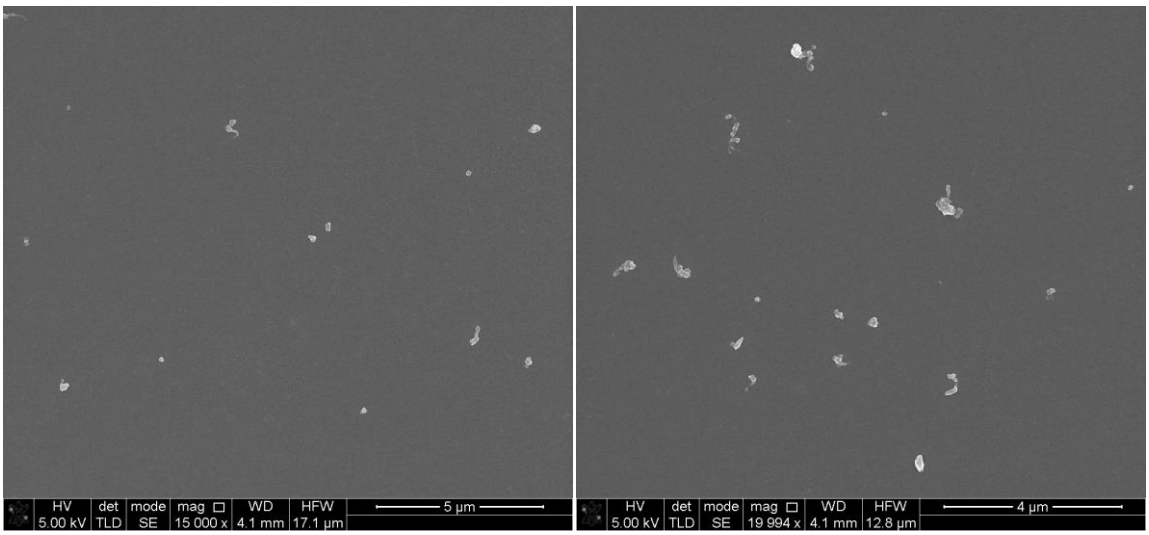

A) **B)**

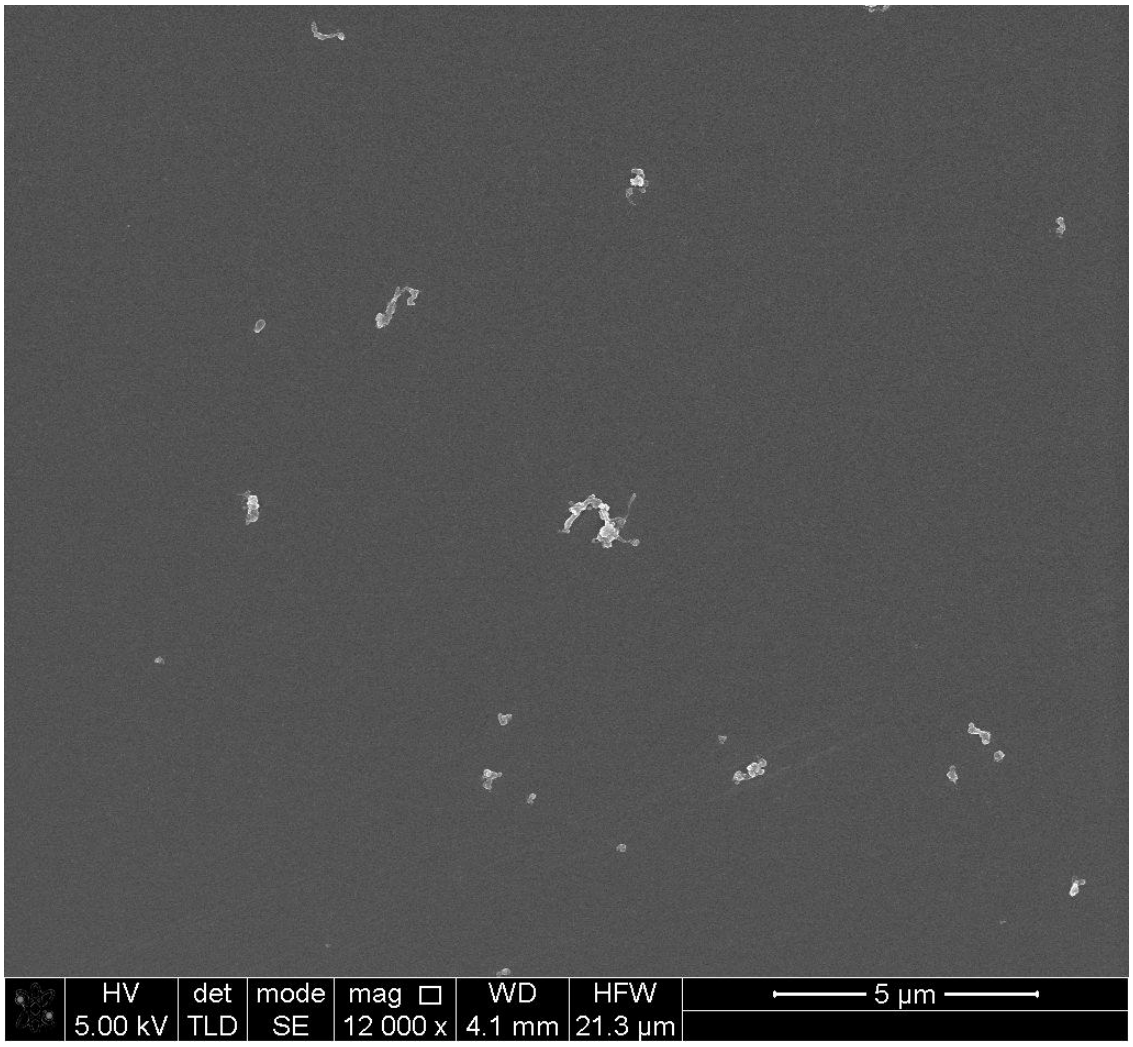

C)

Figure 5.102 Scanning electron micrographs of E1 hip during long-term wear. A) 15000x magnification, Scale = 5µm B) 20000x magnification, Scale = 4µm C) 12000x magnification, Scale = 5µm.

5.2.3.2.2 Shape analysis

A comparison between aspect ratio values of E1 POP and E1 hip particles during long-term wear is shown in Figure 5.103. A gradual increase in aspect ratio values was noticed with an increase in particle size. Moreover, E1 POP particles showed higher aspect ratio values for particles in 0.025 to 1 µm size range compared to E1 hip.

Elongation values of both samples are shown in Figure 5.95. There was an increase in elongation values with an increase in particle size for both samples. However, E1 POP particles showed higher elongation values in 0.1 to 1 µm size range compared to E1 hip. A higher elongation value indicated more elongated fibrillar shape.

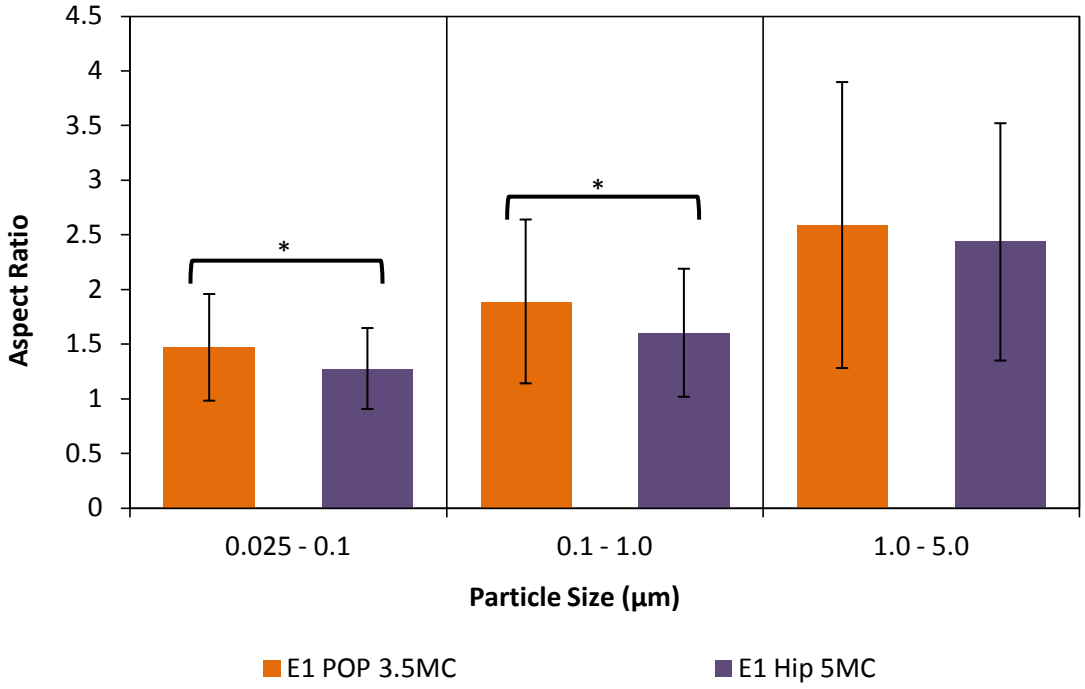

Figure 5.103 A plot showing aspect ratio versus particle size for long-term wear E1 multidirectional pin-on-plate (POP) and E1 hip particles. Error bars indicate standard deviation from mean aspect ratio value in each size range. Statistically significant differences ($p < 0.05$) are highlighted with a black outline. POP showed more elongated particles compared to hip for particles in 0.025 to 1 µm size range.

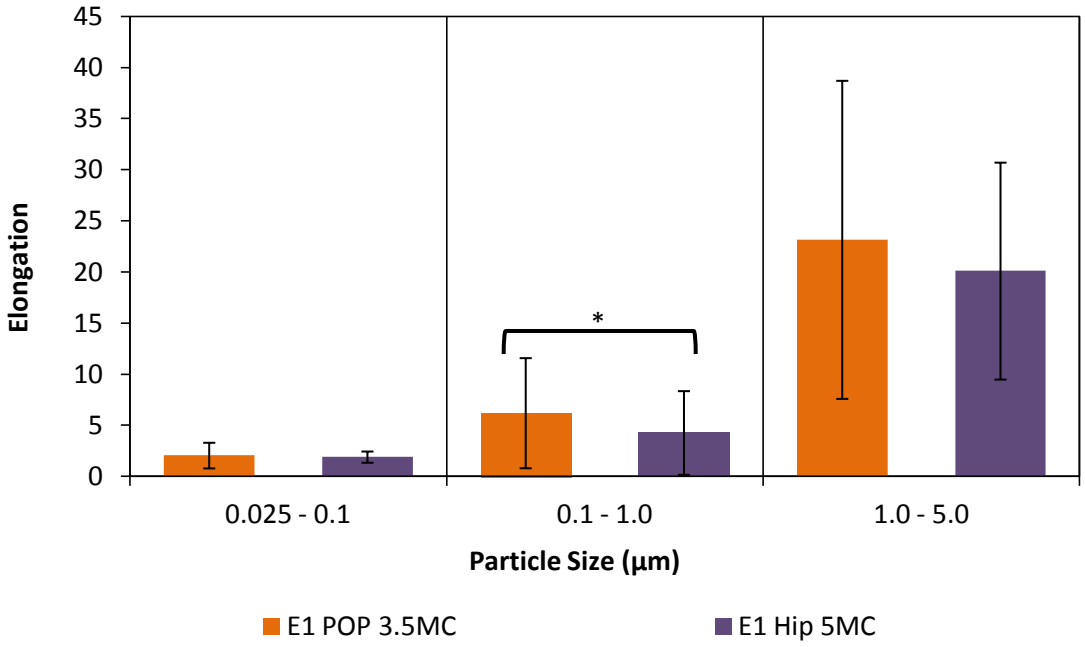

Figure 5.104 A plot showing elongation versus particle size for long-term wear E1 multidirectional pin-on-plate (POP) and E1 hip particles. Error bars indicate standard deviation from mean elongation value in each size range. Statistically significant differences ($p < 0.05$) are highlighted with a black outline. POP showed more elongated fibrillar particles in 0.1 to 1 µm size range compared to hip.

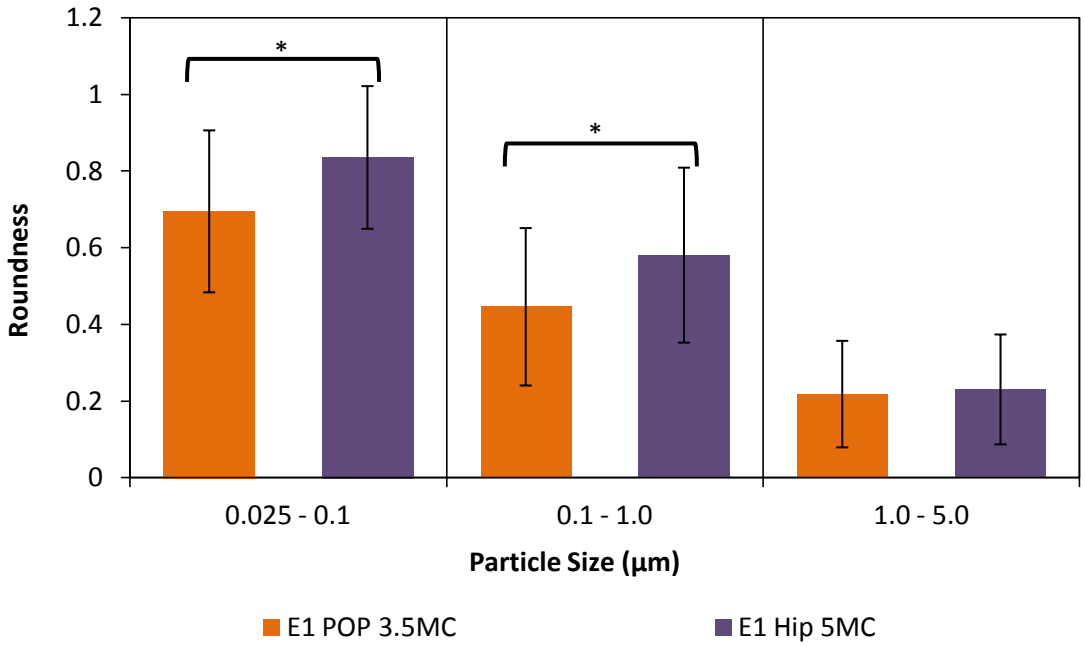

Figure 5.105 A plot showing roundness versus particle size for long-term wear E1 multidirectional pin-on-plate (POP) and E1 hip particles. Error bars indicate standard deviation from mean roundness value in each size range. Statistically significant differences ($p < 0.05$) are highlighted with a black outline. Hip showed more round shape compared to POP for particles in 0.025 to 1 µm size range.

Figure 5.105 shows a comparison between roundness values of E1 POP and E1 hip particles during long-term wear. A decrease in roundness values with an increase in particle size was noticed for both samples. However, E1 hip particles in 0.025 to 1 µm size range had higher roundness values in comparison to E1 POP. Form factor values also decreased with an increase in particle size in a similar manner as shown in Figure 5.97.

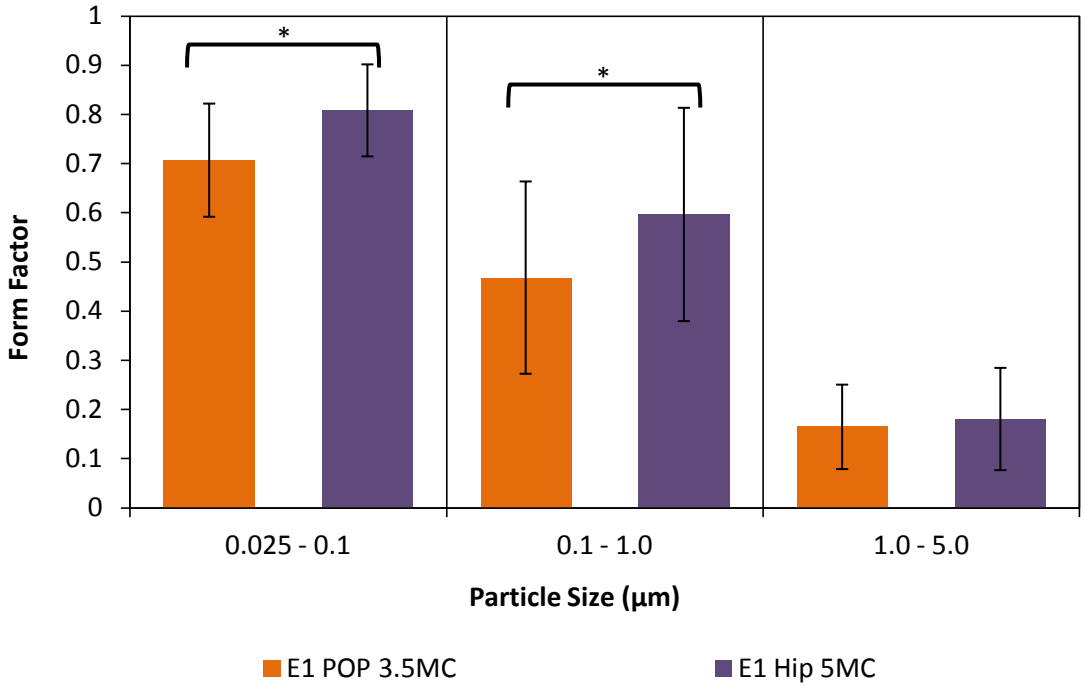

Figure 5.106 A plot showing form factor versus particle size for long-term wear E1 multidirectional pin-on-plate (POP) and E1 hip particles. Error bars indicate standard deviation from mean form factor value in each size range. Statistically significant differences ($p < 0.05$) are highlighted with a black outline. Hip showed higher form factor values for particles in 0.025 to 1 µm size range compared to POP.

A comparison between compactness values of both samples during early wear is shown in Figure 5.107. There was a gradual decrease in compactness values with an increase in particle size. Moreover, E1 hip particles in showed marginally higher compactness values in comparison to E1 POP. A higher compactness value indicated more compact particle shape.

Figure 5.108 shows change in complexity values of both E1 POP and E1 hip particles with an increase in particle size. A decrease in complexity value with an increase in particle size for both samples indicated increasing complexity of particle shapes with size. Moreover, E1 POP particles in 0.025 to 1 µm size range had lower complexity values in comparison to E1 hip indicating generation of more complex shaped particles in POP compared to hip in this size range.

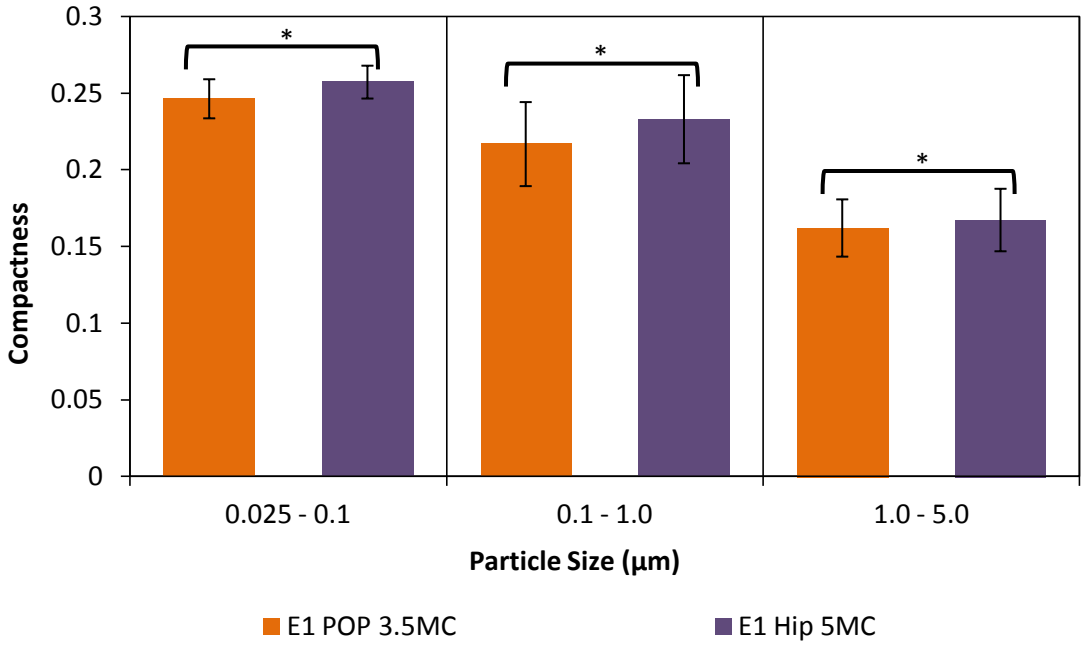

Figure 5.107 A plot showing compactness versus particle size for long-term wear E1 multidirectional pin-on-plate (POP) and E1 hip particles. Error bars indicate standard deviation from mean compactness value in each size range. Statistically significant differences ($p < 0.05$) are highlighted with a black outline. Hip showed more compact shape compared to POP.

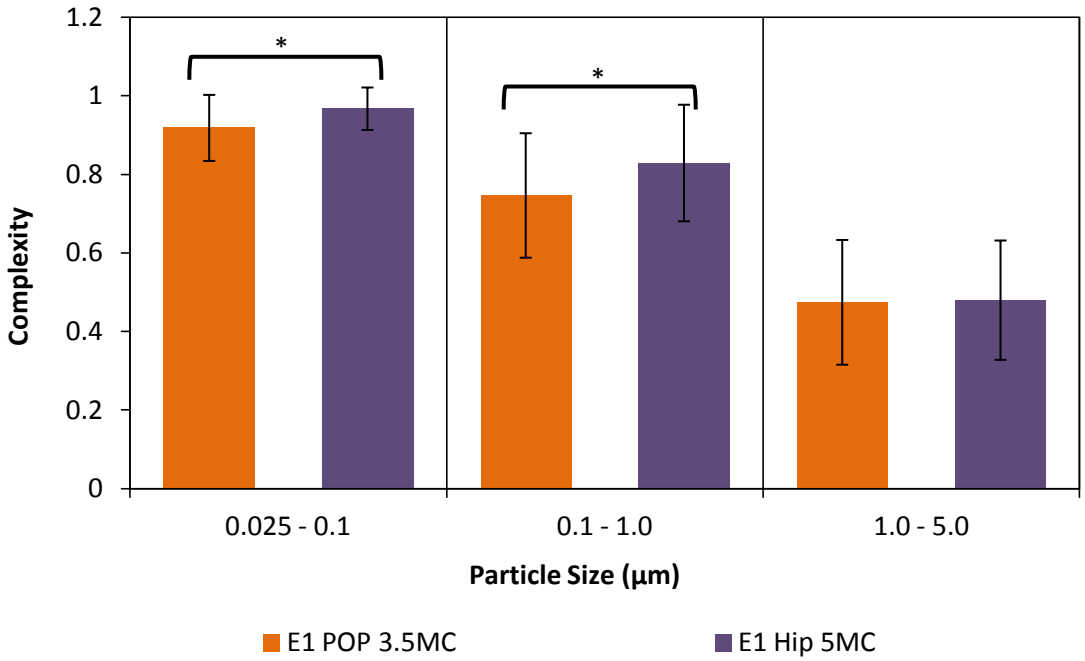

Figure 5.108 A plot showing complexity versus particle size for long-term wear E1 multidirectional pin-on-plate (POP) and E1 hip particles. Error bars indicate standard deviation from mean complexity value in each size range. Statistically significant differences ($p < 0.05$) are highlighted with a black outline. POP showed more complex shape compared to hip for particles in 0.025 to 1 µm size range.

5.2.4 E1 Multidirectional pin-on-plate vs. E1 Knee

In this section, E1 wear particles produced during multidirectional pin-on-plate testing of E1 UHMWPE pins against metal plates were compared with particles produced during knee simulator testing of E1 liners against metal counterparts. Wear particles generated during early wear and long-term wear of both materials were compared for size and morphology.

5.2.4.1 Early wear

During early wear, E1 UHMWPE particles isolated from lubricant serum retrieved after 0.5 million cycles of testing were used for analysis.

5.2.4.1.1 Size analysis

The size distribution of E1 wear particles produced in multidirectional pin-on-plate simulator and knee simulator during early wear is shown in Figure 5.109. Statistical analysis using Kolmogorov-smirnov Z test indicated that both size distributions were significantly different from each other ($p < 0.05$). Knee simulator generated a bimodal size distribution with two peaks at 100 to 250nm and 1 to 2µm respectively, while multidirectional pin-on-plate generated a single peak size distribution. Moreover, multidirectional pin-on-plate generated higher percentage of particles smaller than 750nm, while knee generated a higher percentage of particles larger than 750nm.

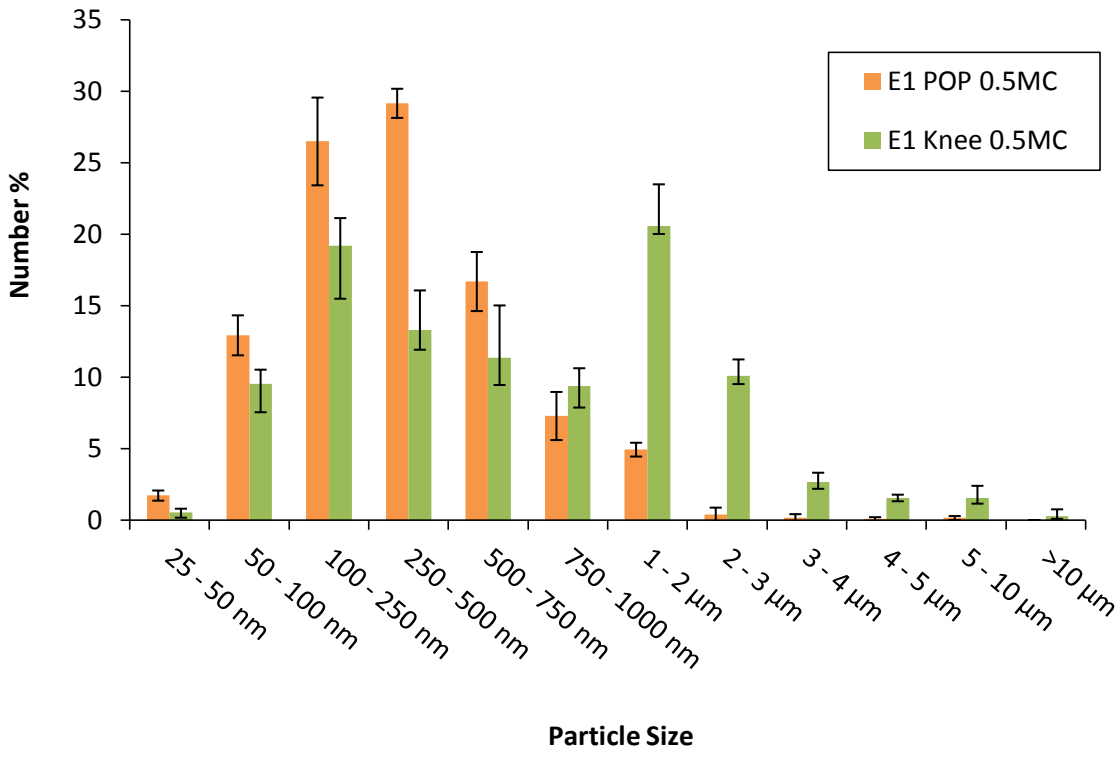

Figure 5.109 A comparison between percentage number size distributions according to maximum Feret's diameter (dmax) of E1 multidirectional pin-on-plate(POP) and E1 knee wear particles during early wear. Error bars show standard deviation.

E1 Multistation Pin-on-plate Early Wear

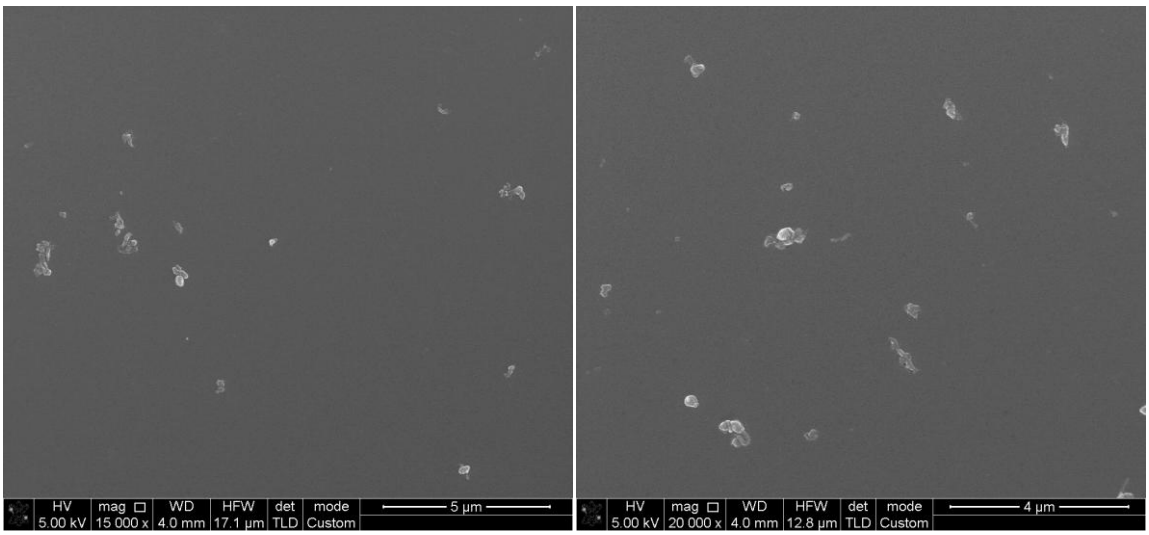

A) **B)**

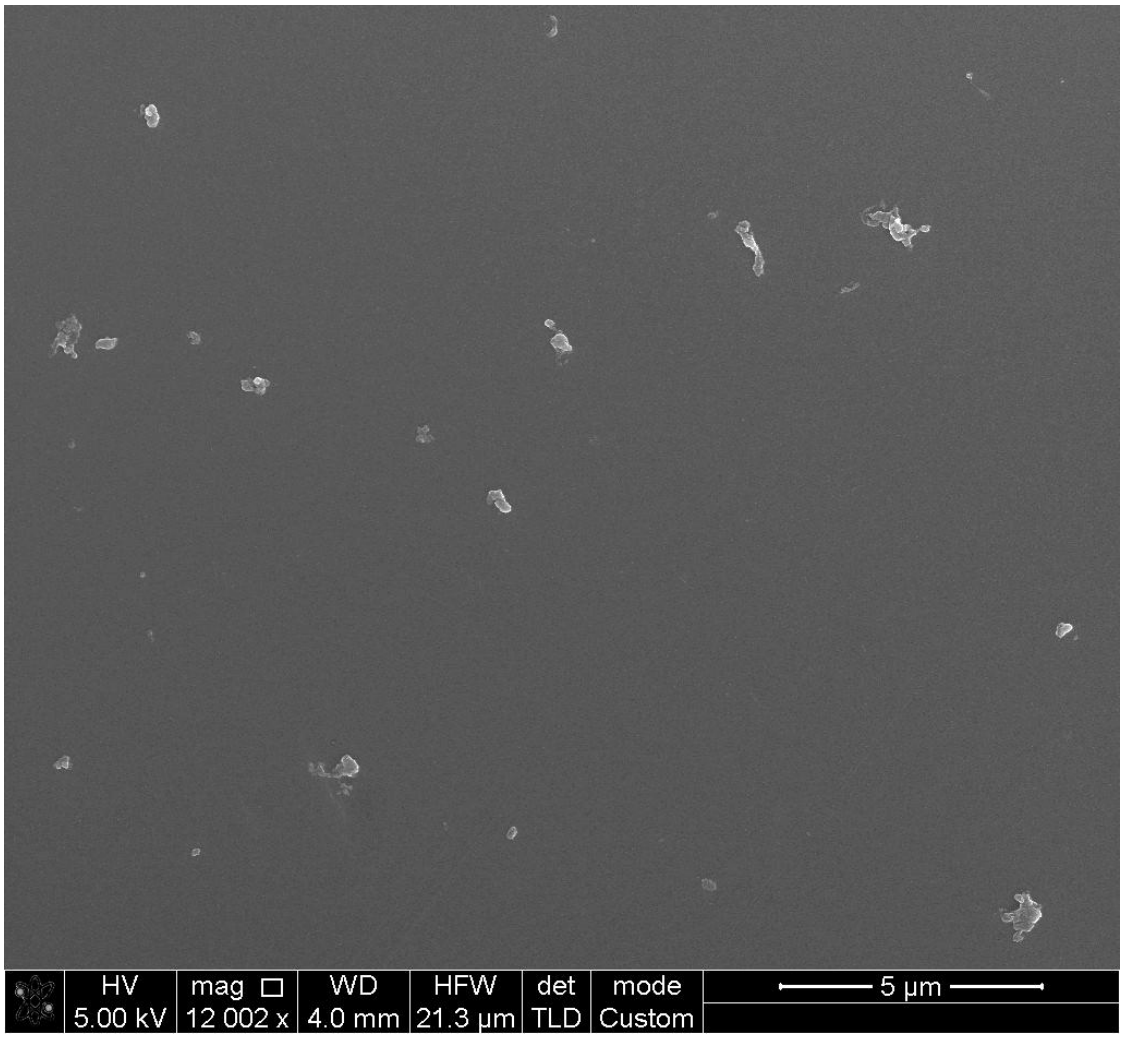

C)

Figure 5.110 Scanning electron micrographs of E1 multistation pin-on-plate during early wear. A) 15000x magnification, Scale = 5µm B) 20000x magnification, Scale = 4µm C) 12000x magnification, Scale = 5µm.

E1 Knee Early Wear

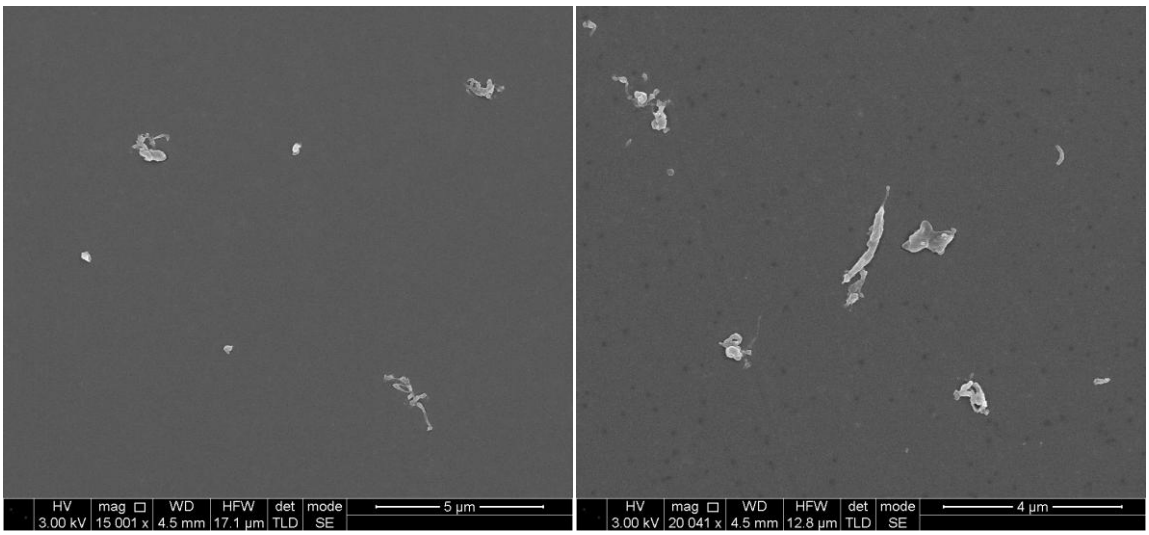

A) **B)**

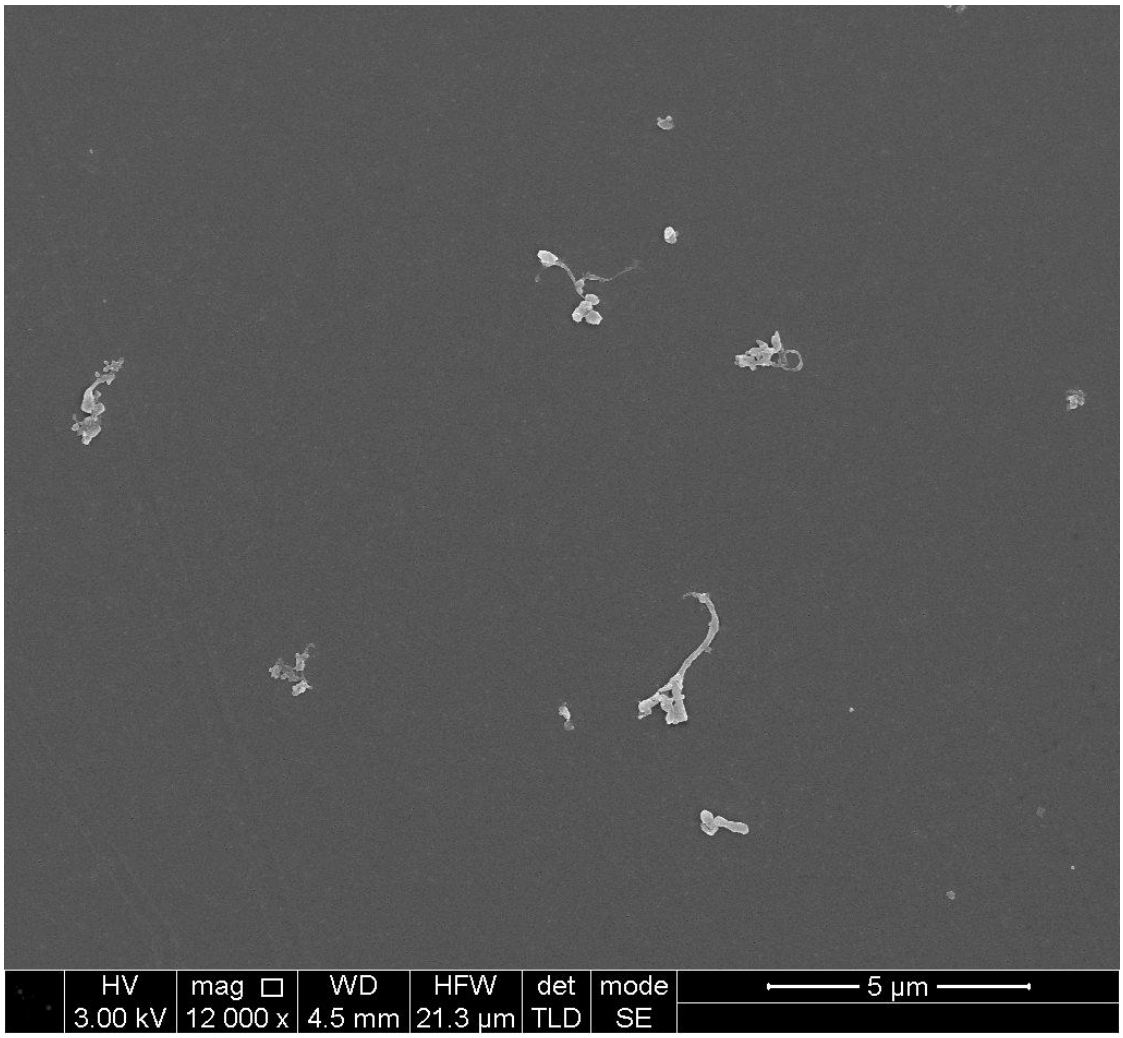

C)

Figure 5.111 Scanning electron micrographs of E1 Knee during early wear. A) 15000x magnification, Scale = 5µm B) 20000x magnification, Scale = 4µm C) 12000x magnification, Scale = 5µm.

5.2.4.1.2 Shape analysis

A comparison between aspect ratio values of E1 POP and E1 knee particles during early wear is shown in Figure 5.112. There was a gradual increase in aspect ratio value with an increase in particle size for both POP and knee. Moreover, E1 knee particles showed a higher aspect ratio value in 0.1 to 1µm size range, while E1 POP particles showed a higher aspect ratio value in 1 to 5µm size range.

Elongation values of both samples are shown in Figure 5.113. There was an increase in elongation value with an increase in particle size for both samples. E1 knee particles showed marginally higher elongation values in 0.1 to 1 µm size range, whereas E1 POP showed more elongated particles in 0.025 to 0.1 µm size range.

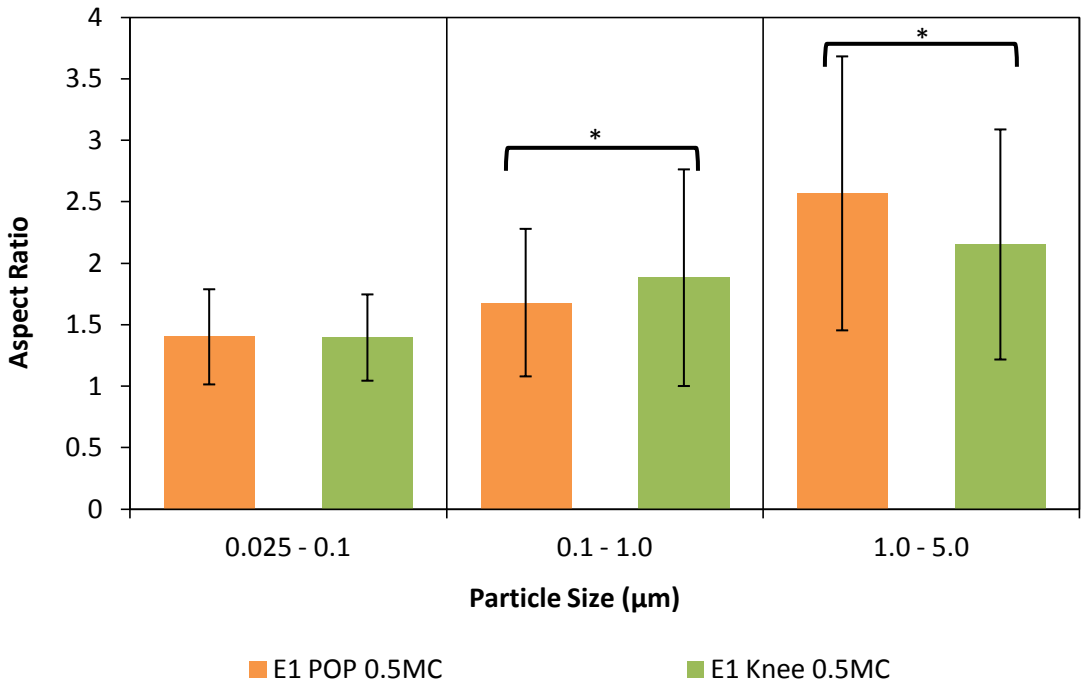

Figure 5.112 A plot showing aspect ratio versus particle size for early wear of E1 multidirectional pin-on-plate (POP) and E1 knee. Error bars indicate standard deviation from mean aspect ratio value in each size range. Statistically significant differences ($p < 0.05$) are highlighted with a black outline. Knee showed more elongated particles in 0.1 to 1 µm size range, while POP showed more elongated particles in 1 to 5 µm size range.

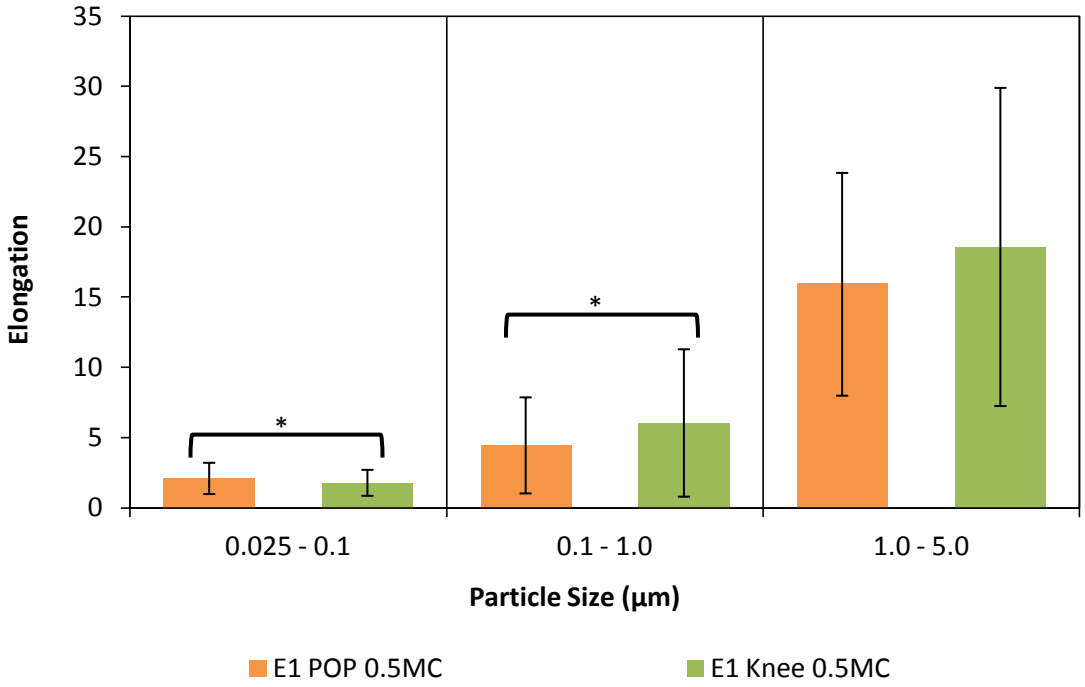

Figure 5.113 A plot showing elongation versus particle size during early wear of E1 multidirectional pin-on-plate (POP) and E1 knee. Error bars indicate standard deviation from mean elongation value in each size range. Statistically significant differences ($p < 0.05$) are highlighted with a black outline. Knee had more elongated fibrillar particles in 0.1 to 1 µm size range, while POP had more elongated fibrillar particles in 0.025 to 1 µm size range.

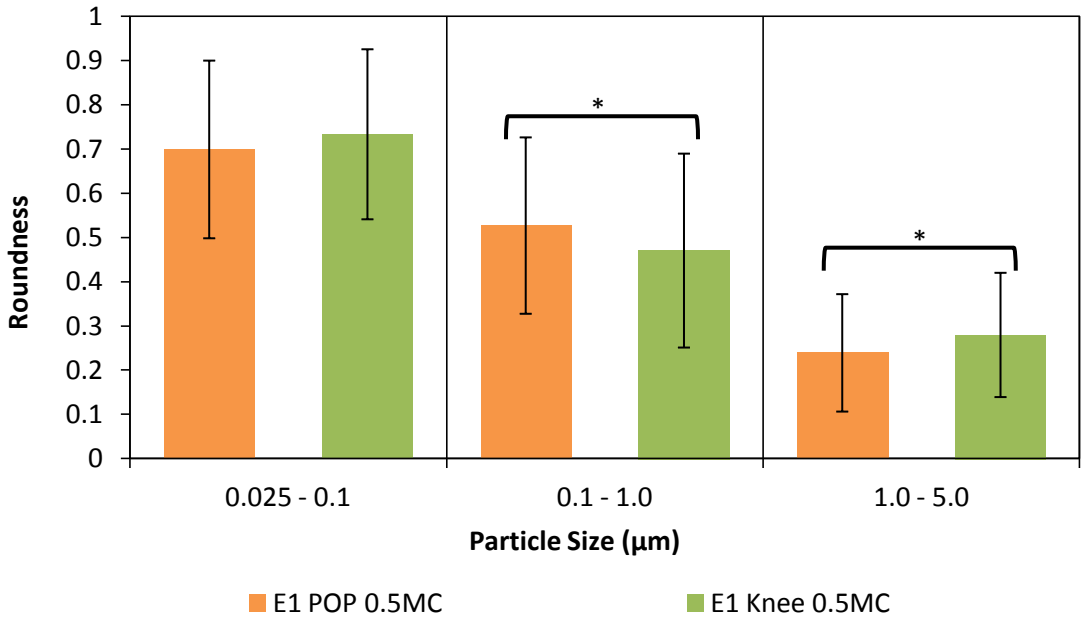

Figure 5.114 A plot showing roundness versus particle size during early wear of E1 multidirectional pin-on-plate (POP) and E1 knee. Error bars indicate standard deviation from mean roundness value in each size range. Statistically significant differences ($p < 0.05$) are highlighted with a black outline. Knee showed marginally more round particles in 1 to 5 µm size range, while POP showed marginally more round particles in 0.1 to 1 µm size range.

Figure 5.114 shows a comparison between roundness values of E1 POP and E1 knee particles during early wear. A decrease in roundness values with an increase in particle size was noticed for both samples. E1 knee showed marginally rounder particles in 1 to 5 µm size range, while POP showed marginally rounder particles in 0.1 to 1 µm size range. Form factor values showed a marginally higher form factor value for particles in 0.025 to 0.1 µm size range, while POP showed marginally higher form factor value for particles in 0.1 to 1 µm size range as shown in Figure 5.115.

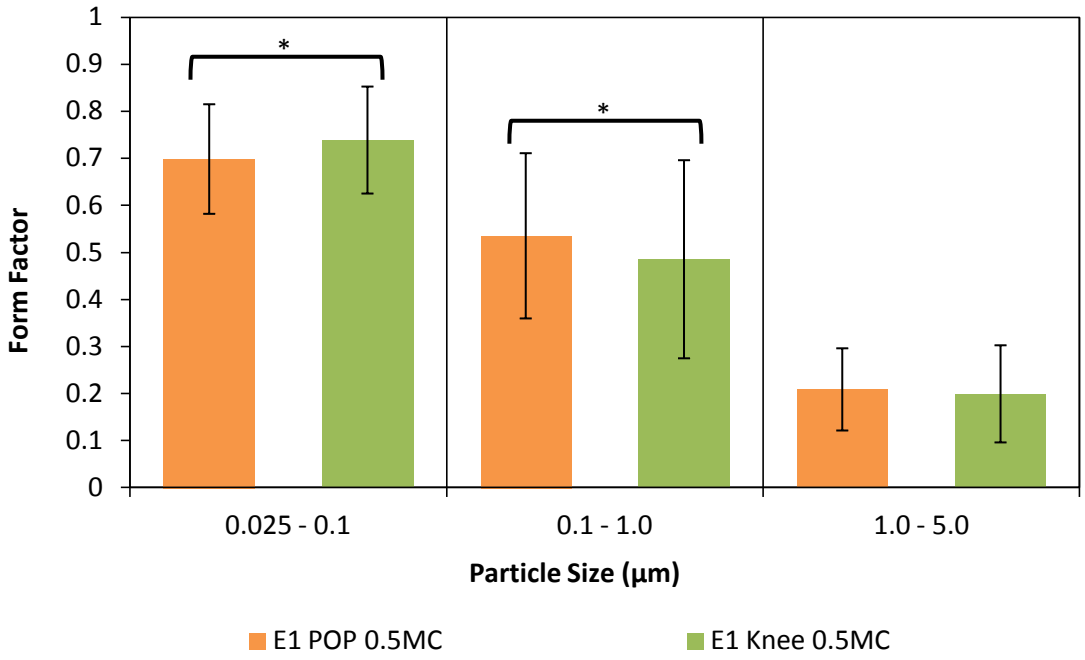

Figure 5.115 A plot showing form factor versus particle size during early wear of E1 multidirectional pin-on-plate (POP) and E1 knee. Error bars indicate standard deviation from mean form factor value in each size range. Statistically significant differences ($p < 0.05$) are highlighted with a black outline. Knee showed marginally higher form factor values for particles in 0.025 to 0.1 µm size range, while POP showed marginally higher form factor values for particles in 0.1 to 1 µm size range.

A comparison between compactness values of both E1 POP and E1 knee during early wear is shown in Figure 5.116. There was a gradual decrease in compactness values with an increase in particle size. Moreover, E1 knee particles were more compact in 0.025 to 0.1 µm size range, while E1 POP particles had more compact shaped particles in 0.1 to 5 µm size range.

Figure 5.117 shows complexity values of both E1 POP and E1 knee particles. A decrease in complexity value with an increase in particle size for both samples indicated increasing complexity of particle shapes with size. E1 POP had more complex shaped particles in 0.025 to 0.1 µm size range, while knee wear debris had more complex shaped particles in 0.1 to 1 µm size range.

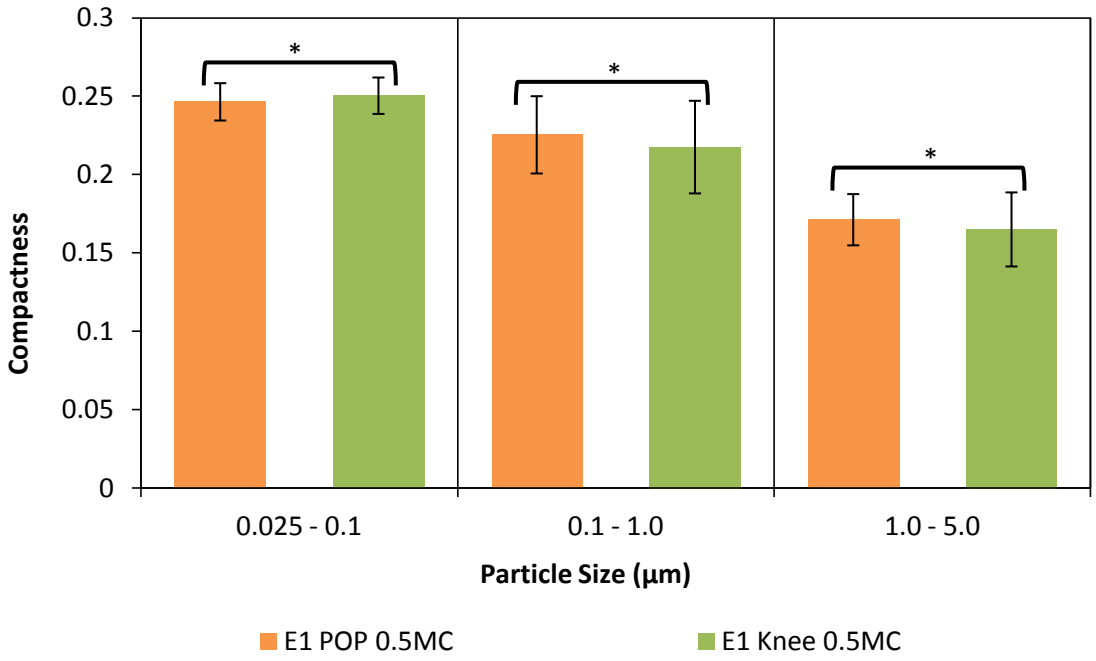

Figure 5.116 A plot showing compactness versus particle size during early wear of E1 multidirectional pin-on-plate (POP) and E1 knee. Error bars indicate standard deviation from mean compactness value in each size range. Statistically significant differences ($p < 0.05$) are highlighted with a black outline. Knee particles had more compact shape in 0.025 to 1 µm size range, while POP particles had more compact shape in 0.1 to 5 µm size range.

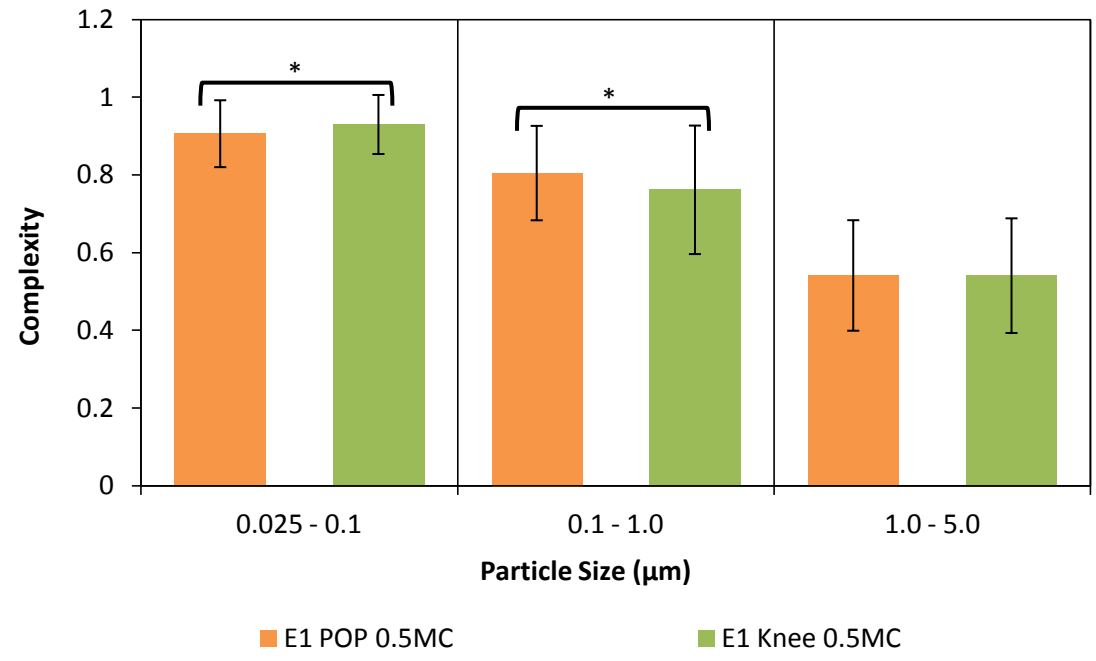

Figure 5.117 A plot showing complexity versus particle size during early wear of E1 multidirectional pin-on-plate (POP) and E1 knee. Error bars indicate standard deviation from mean form factor value in each size range. Statistically significant differences ($p < 0.05$) are highlighted with a black outline. E1 POP particles had more complex shape in 0.025 to 0.1 µm size range, while knee wear debris had more complex shape in 0.1 to 1 µm size range.

5.2.4.2 **Long-term wear**

During long-term wear, E1 UHMWPE particles isolated from lubricant serum retrieved after 3.5 million cycles of POP testing were compared with E1 UHMWPE particles isolated from lubricant serum retrieved after 5 million cycles of E1 knee testing.

5.2.4.2.1 Size analysis

The size distributions of E1 wear particles produced in multidirectional pin-on-plate simulator and knee simulator during long-term wear are shown in Figure 5.118. Statistical analysis using Kolmogorov-smirnov Z test indicated that both size distributions were different from each other ($p < 0.05$). Moreover, knee produced a larger percentage of particles in 50 - 100 nm size range, whereas POP higher percentage of particles in 250 - 500nm size range.

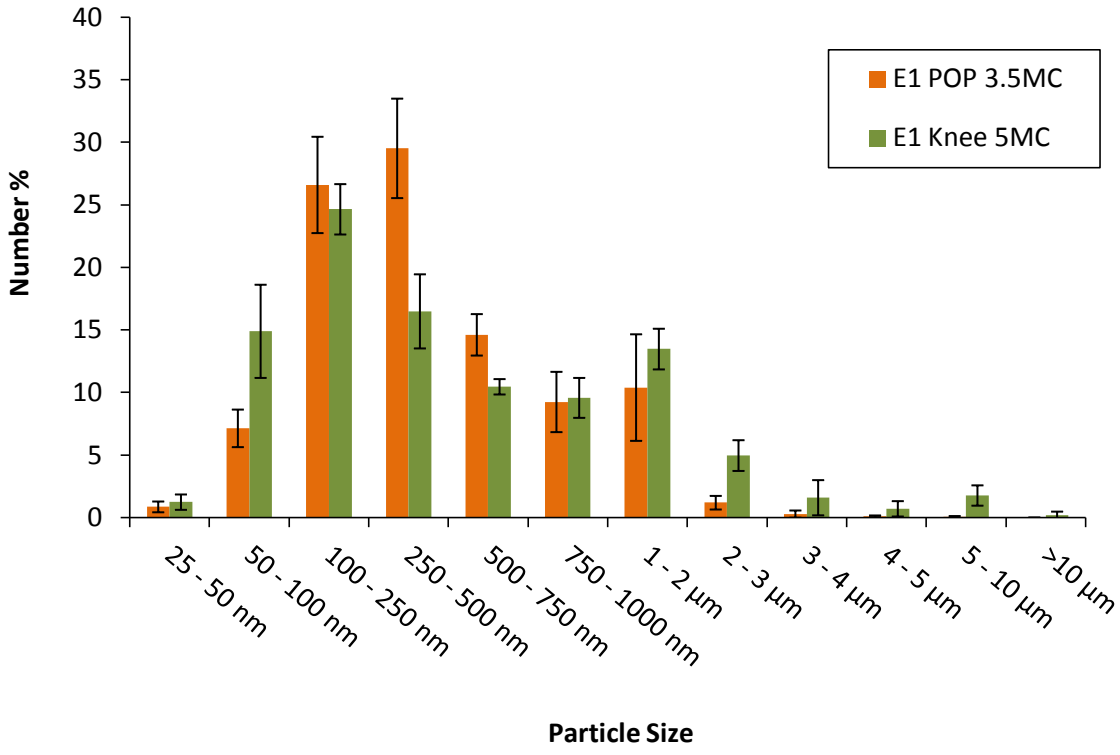

Figure 5.118 A comparison between percentage number size distributions according to maximum Feret's diameter (dmax) of E1 multidirectional pin-on-plate(POP) and E1 knee wear particles during long-term wear. Error bars show standard deviation.

E1 Multistation Pin-on-plate Long-term Wear

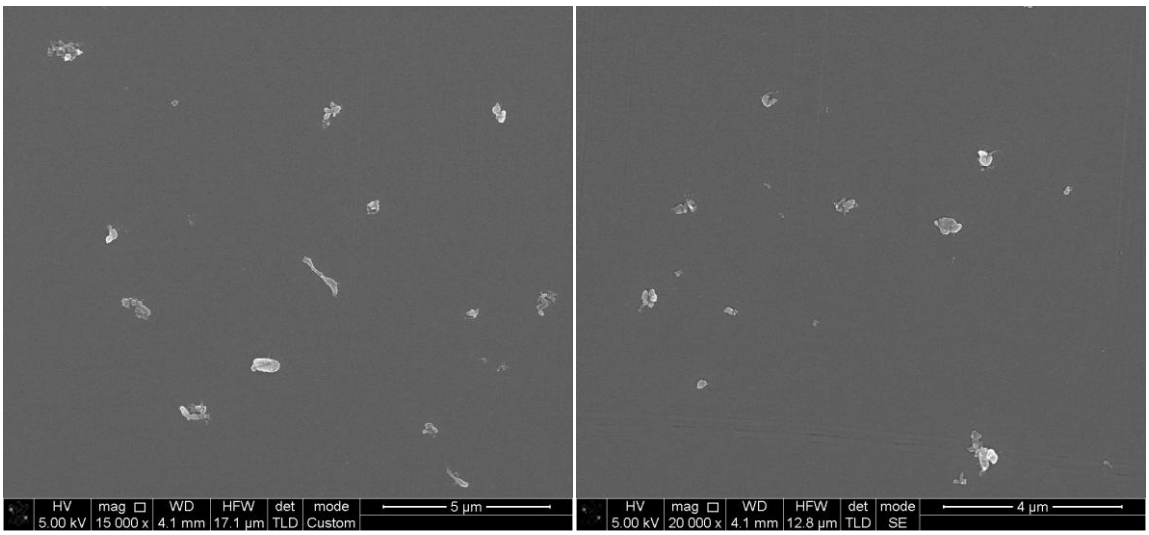

A) **B)**

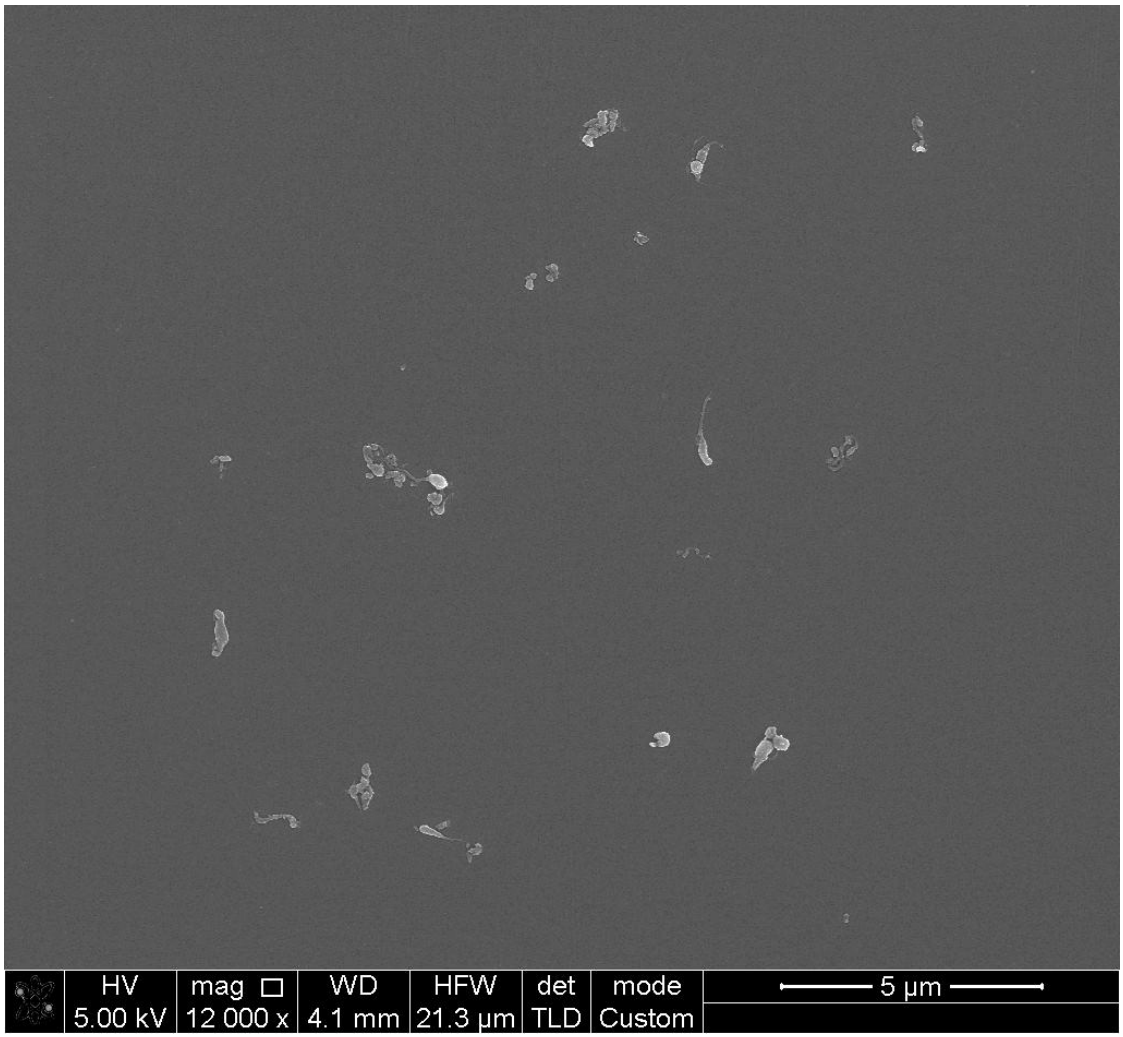

C)

Figure 5.119 Scanning electron micrographs of E1 multistation pin-on-plate during long-term wear. A) 15000x magnification, Scale = 5µm B) 20000x magnification, Scale = 4µm C) 12000x magnification, Scale = 5µm.

E1 Knee Long-term Wear

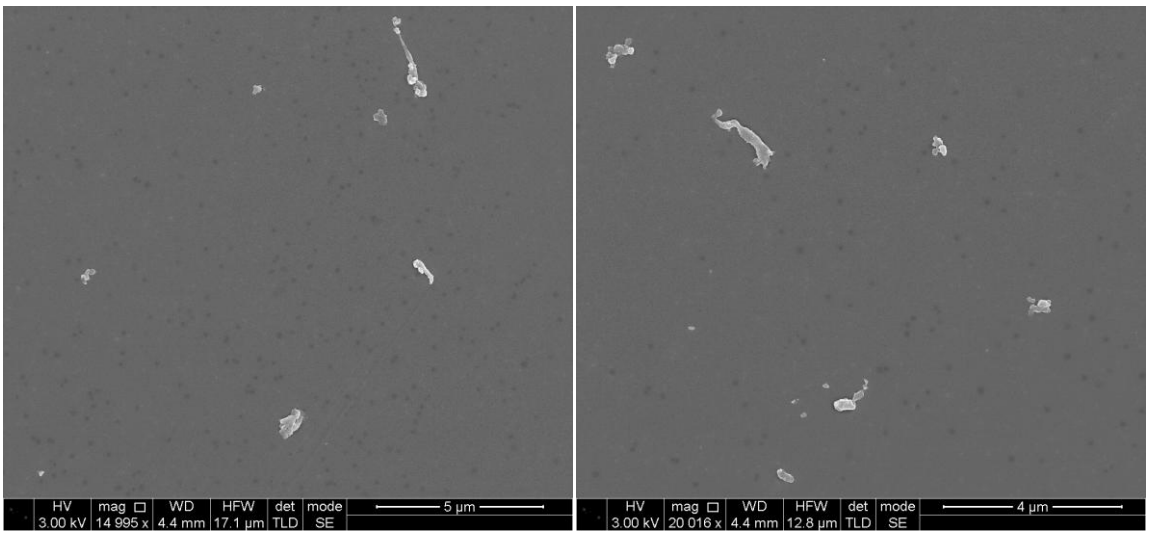

A) **B)**

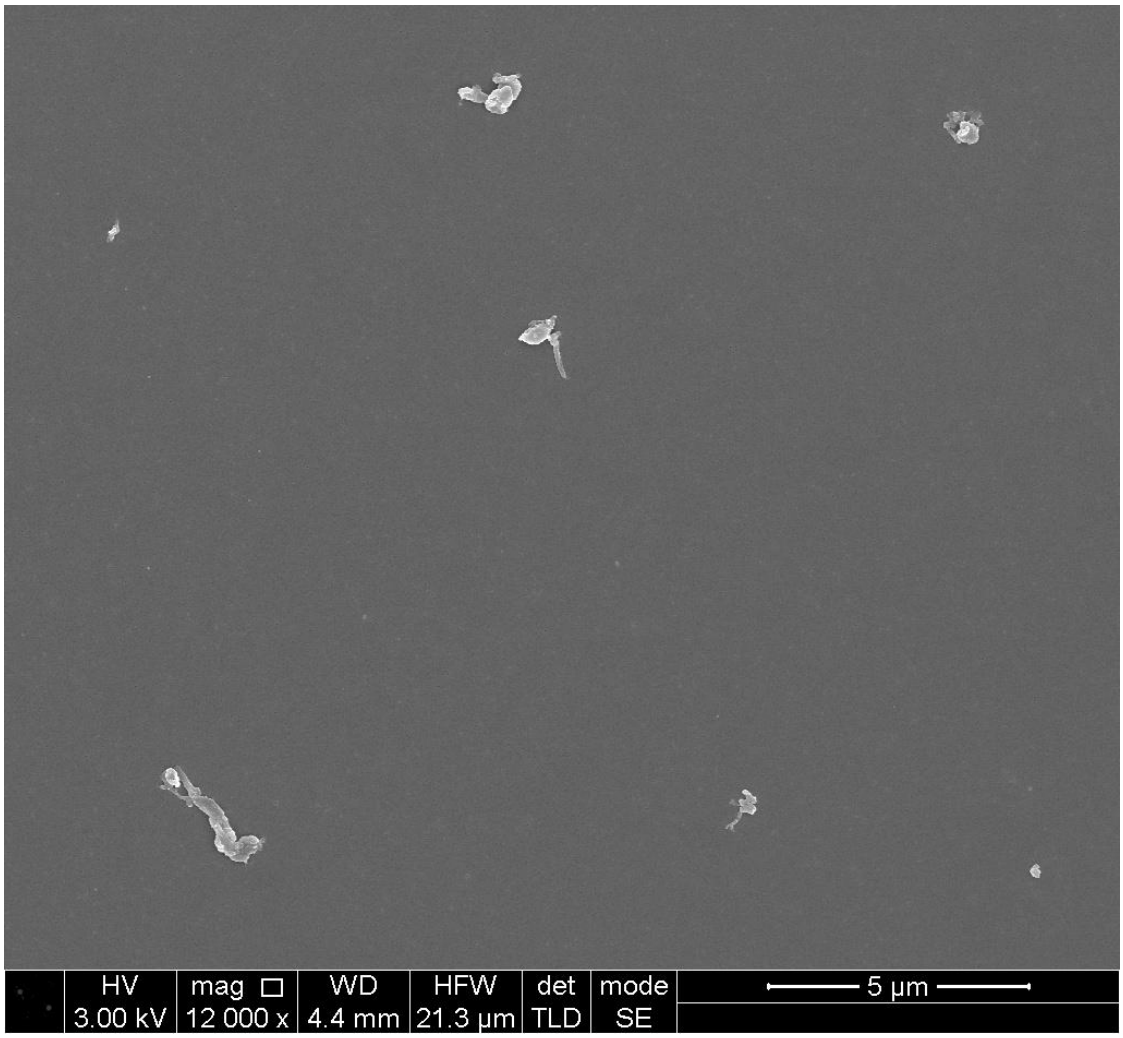

C)

Figure 5.120 Scanning electron micrographs of E1 knee during long-term wear. A) 15000x magnification, Scale = 5µm B) 20000x magnification, Scale = 4µm C) 12000x magnification, Scale = 5µm.

5.2.4.2.2 Shape analysis

A comparison between aspect ratio values of E1 POP and E1 knee particles during long-term wear is shown in Figure 5.121. There was a gradual increase in the aspect ratio values with an increase in particle size for both POP and knee. Moreover, E1 POP particles showed higher aspect ratio values in 1 to 5 µm size range compared to E1 knee.

Elongation values of both samples are shown in Figure 5.113. There was an increase in elongation value with an increase in particle size for both samples. Moreover, E1 POP particles showed higher elongation values in comparison to E1 knee indicating generation of more elongated fibrillar particles in POP.

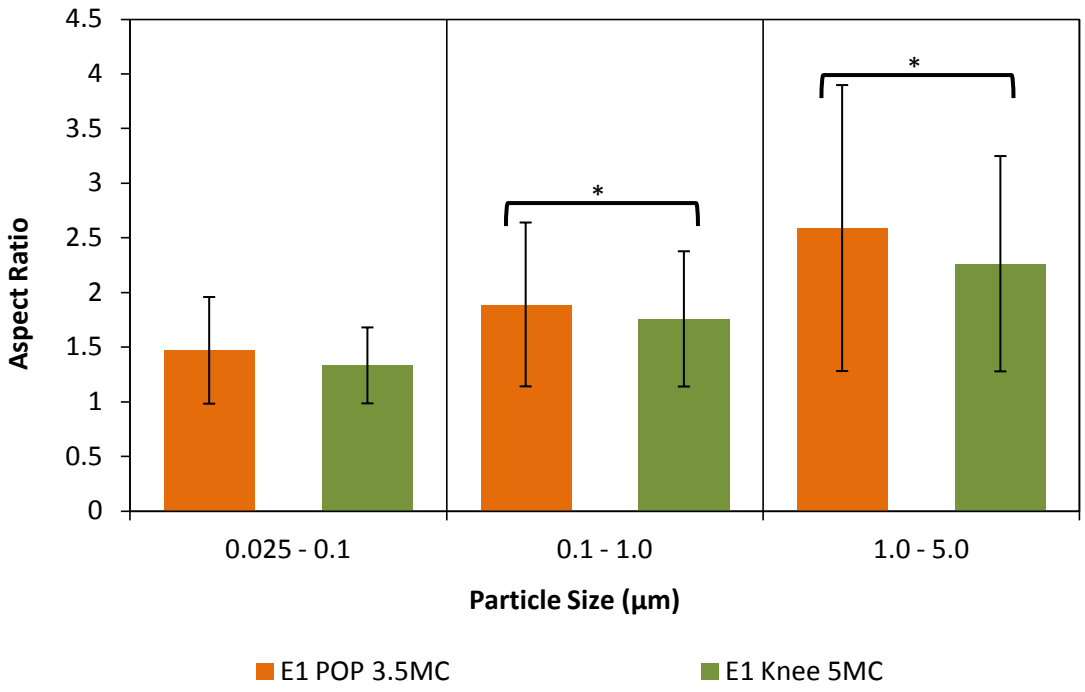

Figure 5.121 A plot showing aspect ratio versus particle size for later-stage wear of E1 multidirectional pin-on-plate (POP) and E1 knee. Error bars indicate standard deviation from mean aspect ratio value in each size range. Statistically significant differences ($p < 0.05$) are highlighted with a black outline. POP showed more elongated shape in comparison to knee for particles larger than 0.1µm.

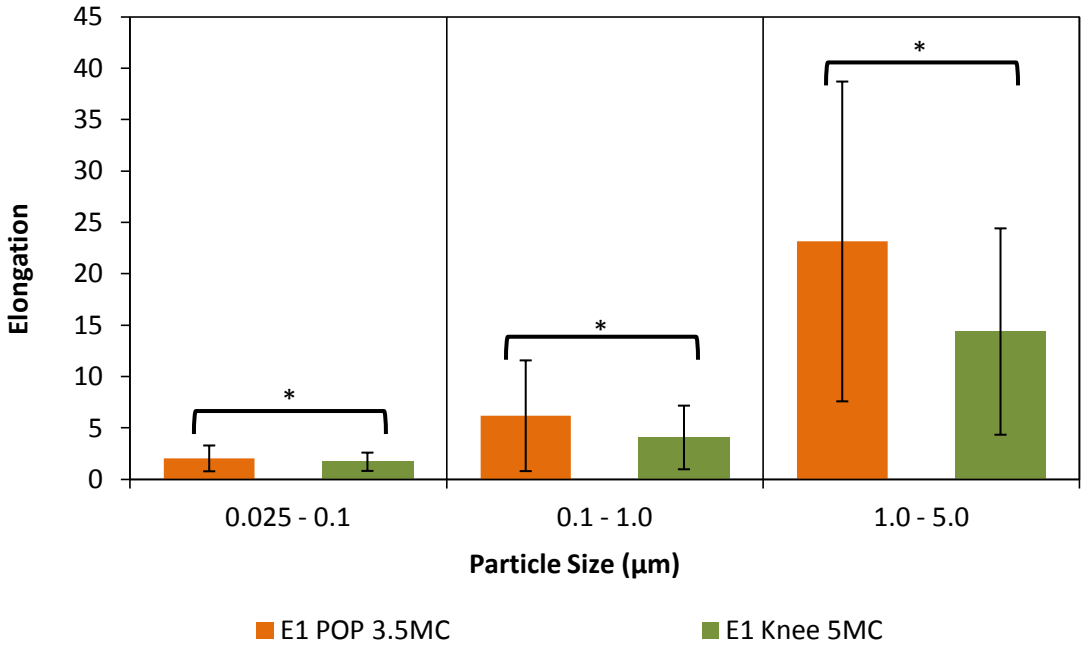

Figure 5.122 A plot showing elongation versus particle size for long-term wear E1 multidirectional pin-on-plate (POP) and E1 knee particles. Error bars indicate standard deviation from mean elongation value in each size range. Statistically significant differences ($p < 0.05$) are highlighted with a black outline. POP showed more elongated fibrillar particles in comparison to knee.

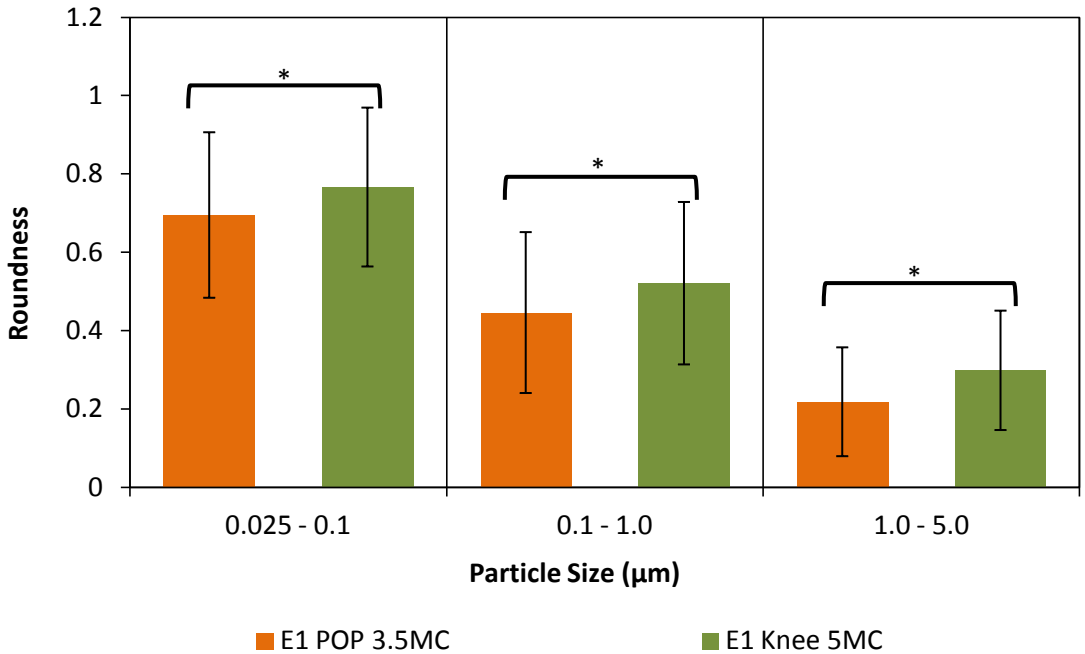

Figure 5.123 A plot showing roundness versus particle size for long-term wear E1 multidirectional pin-on-plate (POP) and E1 knee particles. Error bars indicate standard deviation from mean roundness value in each size range. Statistically significant differences ($p < 0.05$) are highlighted with a black outline. Knee showed more round particles compared to POP.

Figure 5.96 shows a comparison between roundness values of E1 POP and E1 knee particles during long-term wear. A decrease in roundness value with an increase in particle size was noticed for both samples. Moreover, E1 knee particles showed higher roundness values in comparison to E1 POP, indicating that knee produced particles with more round morphology in comparison to POP.

A comparison between form factor values of E1 POP and E1 knee had similar results to roundness as shown in Figure 5.124. Form factor value decreased with an increase in particle size. Moreover, E1 knee particles showed higher form factor values in comparison to POP.

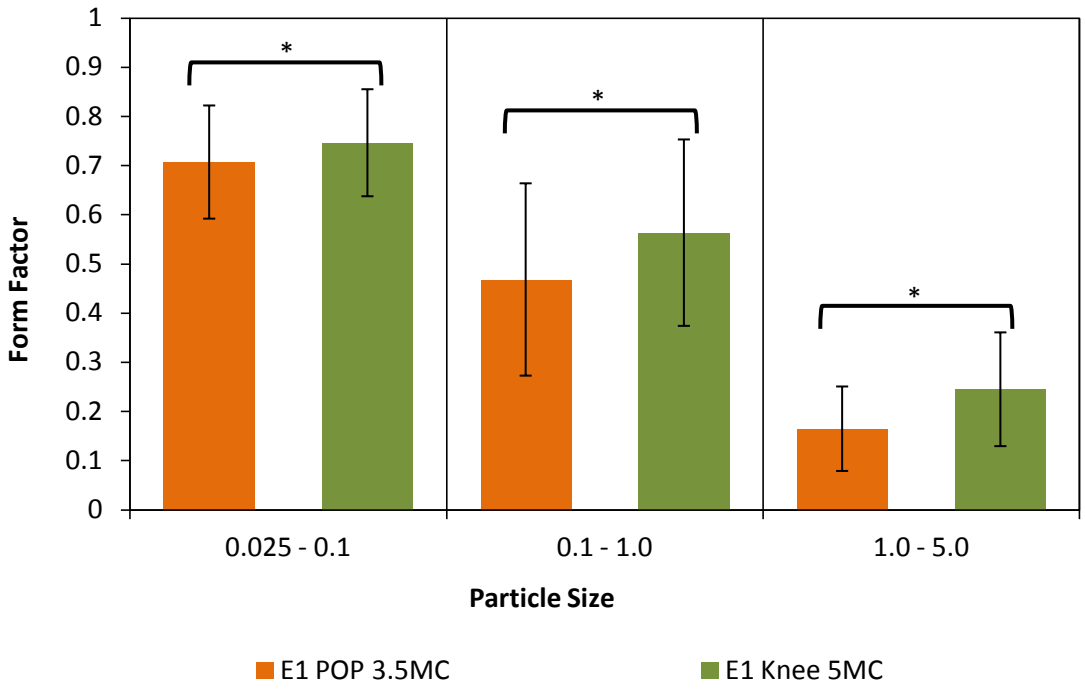

Figure 5.124 A plot showing form factor versus particle size for long-term wear E1 multidirectional pin-on-plate (POP) and E1 knee particles. Error bars indicate standard deviation from mean form factor value in each size range. Statistically significant differences ($p < 0.05$) are highlighted with a black outline. Knee showed higher form factor values compared to POP.

A comparison between compactness values of both E1 POP and E1 knee during long-term wear is shown in Figure 5.125. There was a gradual decrease in compactness values with an increase in particle size. Furthermore, compactness values of E1 knee particles was higher than E1 POP for all size ranges.

Figure 5.126 shows complexity values of both E1 POP and E1 knee particles. A decrease in complexity value with an increase in particle size for both samples indicated increasing complexity of particle shapes with size. Moreover, complexity values of E1 POP particles in 0.1 - 5µm size range were found to be higher than E1 knee particles indicating generation of more complex shaped particles in POP for above size range.

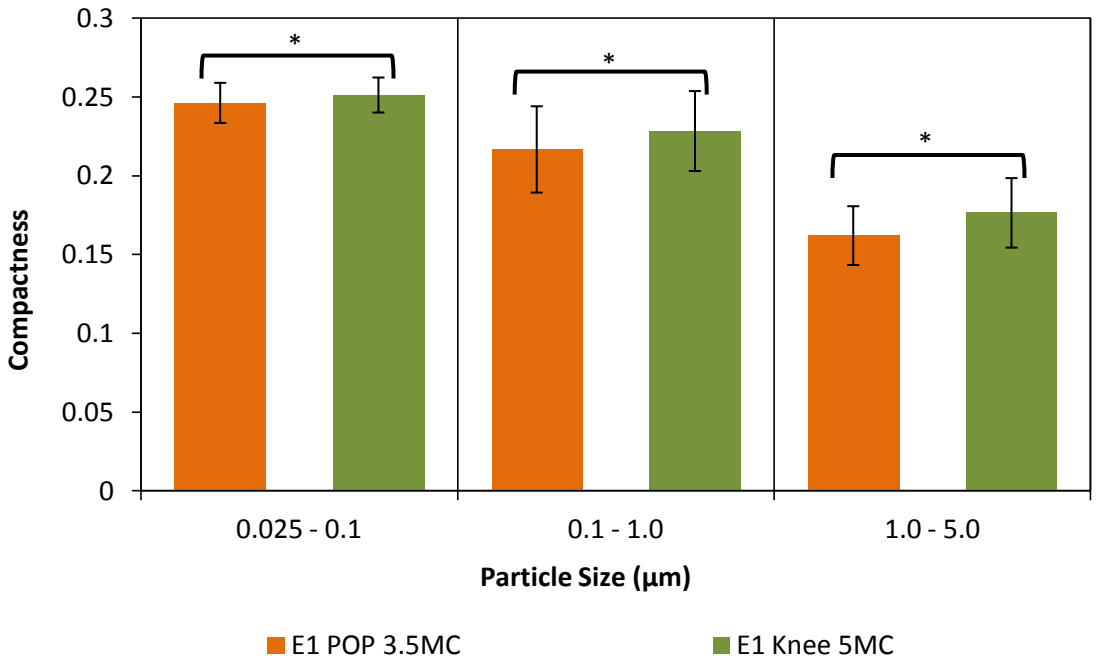

Figure 5.125 A plot showing compactness versus particle size for long-term wear E1 multidirectional pin-on-plate (POP) and E1 knee particles. Error bars indicate standard deviation from mean compactness value in each size range. Statistically significant differences ($p < 0.05$) are highlighted with a black outline. Knee showed more compact shaped particles in comparison to POP.

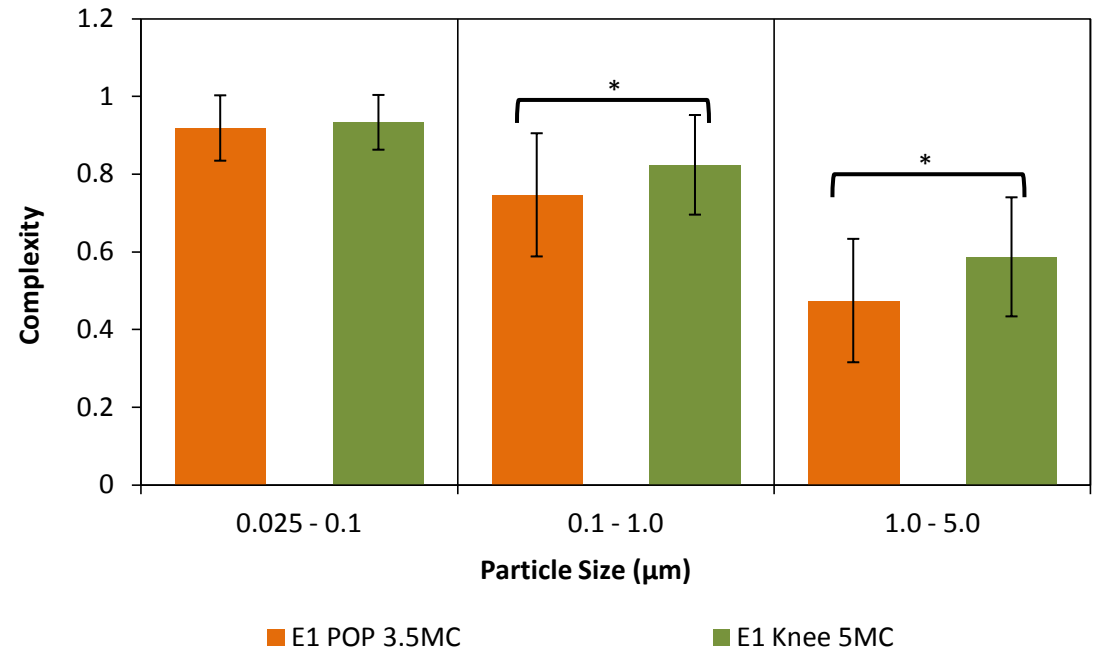

Figure 5.126 A plot showing complexity versus particle size for long-term wear E1 multidirectional pin-on-plate (POP) and E1 knee particles. Error bars indicate standard deviation from mean form factor value in each size range. Statistically significant differences ($p < 0.05$) are highlighted with a black outline. POP showed more complex shaped particles in 0.1 to 5 µm size range in comparison to knee.

Chapter 6 - **Discussion**

This thesis was divided into three parts. Firstly, the methodology for isolation of UHMWPE from serum lubricants. Secondly, the characterisation of wear debris from SEM images using image analysis. Thirdly, the analysis of a range of factors that could influence the size and morphology of UHMWPE wear debris. These factors included UHMWPE crosslinking, addition of antioxidants, material defects and nature of articulation. Novel methodologies were developed to isolate wear debris and to characterise wear particles for size and shape. Then, the wear debris isolation and characterisation was carried out for a range of serum lubricants. Finally, the above mentioned factors were investigated for their influence on wear debris size and morphology. Following sections discuss each of these parts in detail.

6.1 **Particle isolation methods**

Present study tested most recent state-of-the-art acid, base and enzymatic digestion based UHMWPE particle isolation methods. It was found that acid digestion method by Scott *et al.* and enzymatic digestion method by Niedzwiecki *et al.* were the easiest methods to implement. However, the purification of UHMWPE particles in these methods by membrane filtration had its limitations. The idea behind using filtration was to filter out all serum proteins and impurities, leaving particles behind on the membrane filter. This could hypothetically work in a situation where serum proteins were hydrolysed to the extent that protein molecules and small protein fragments could easily pass through the membrane pores. However, in reality it was difficult to achieve with 0.05µm pore size membrane filters, as demonstrated in Section 0. Nonetheless, acid digestion was found to be more efficient than enzymatic digestion in solubilising and hydrolysing the proteins. This was found in agreement with previous studies that compared a number of digestion and isolation methods [170], [195].

Recently developed method by Billi *et al.* [185] was found to be a relatively rigorous method. One could appreciate that each step used in this method was aimed at achieving high particle isolation efficiency. For instance, proteinase K was used in the presence of calcium ions, which acted as a stabiliser during digestion, unlike the method developed by Niedzwiecki et al [175]. Moreover, density gradients with protein denaturants were used to keep the proteins in their unfolded state during ultracentrifugation. However, the implementation of this method was not straightforward.

Firstly, it required custom components to secure a silicon chip suspended inside the centrifuge tubes. Although, this was achievable but there were safety concerns with high forces acting inside centrifuge tubes during ultracentrifugation. Secondly, sodium azide (mixed with urea and HEPES buffer) was lyophilised in one of the steps in the method. Although, the amount of sodium azide used in the solution prior to lyophilisation was only 0.04%, sodium azide is known to be a highly toxic compound in solid form. Since lyophiliser at labs in Durham were not inside a fume hood, there were concerns with the containment of sodium azide during the experiment. Thirdly, the method required to mix 3ml of serum sample to a large volume of lyophilised powder. This could have caused particle loss as described in Section 3.2.3, page66. Considering all these issues , this method was not chosen for further studies.

Particle isolation method developed by Tipper *et al.* was another method tested in the present study. This method has been around since late 1990s [173]. The implementation of this method was not as difficult as Billi's method. However, the use of a large number of lipid extraction steps at low centrifugation forces (500g) were believed to be the source of particle loss. This was verified by the SEM images of wear debris isolated by this method (Figure 3.12, Page 72). A few particles and large agglomerates were observed. Moreover, the morphology of particles looked relatively different compared to the particles isolated using other methods. Therefore, Tipper's method was not chosen for our studies either.

Another method tested in this study was developed by Elfick *et al.* The serum was digested using a strong base (5M NaOH) for 1 hour using ultrasonic agitation at 65°C. One major issue with implementation of this method was the first centrifugation step to concentrate particles in a top layer. Loss of particles was believed to occur at the end of centrifugation due to the sticking of particles to the ultracentrifuge tube walls (More details in Section 0). Moreover, impurities in SEM images suggested the need of a more complete digestion of serum proteins.

The novel particle isolation method was developed to overcome above mentioned limitations in current methods. Potassium hydroxide (5M) was chosen for serum digestion due to a number of reasons. Firstly, base digestion was found to be the most preferable digestion method for isolating UHMWPE wear debris. Over 25 studies had used base digestion in the past [25], [85], [89], [90], [95], [162], [166], [167], [169], [173], [175], [177], [178], [181], [184], [187], [189]–[191], [198]–[202], while seven studies used enzymatic digestion method [87], [172], [175], [185], [194], [195], [203] and six studies used acid digestion [84], [86], [171], [175], [176], [195]. Secondly, 5M potassium hydroxide it was shown to be among the most efficient digestion reagents by Baxter *et al.* [170]. Thirdly, the use of potassium hydroxide was cost effective in comparison to enzymes such as proteinase K or papain. Moreover, acid digestion was avoided because at the end of acid digestion the solution needed to be diluted by large volume of methanol. This was very time consuming if the use of 0.015µm pore size membrane was desired.

For purification of particles, a two-step density gradient centrifugation was used. The number of steps were minimised to avoid particle loss. Initially one-step purification was attempted during the development of the method and was found to be insufficient for complete purification of wear debris. Figure 6.1 shows a SEM image of particles that were lost in the bottom layers of the tube during single step isolation. For isolation steps, centrifugation speeds were decided based on sedimentation rate calculations using Stoke's law. According to Stoke's law [177] the sedimenation rate u_s of a particle of diameter d and density ρ_s going through a fluid of viscosity η and density ρ_f under a centrifugal force g is given by

$$u_s = \frac{(\rho_s - \rho_f)d^2 g}{18\eta}$$

Assuming the diameter of smallest particle as 0.02 µm, the density of UHMWPE as 930 kg/m^3, the density of digested serum as 1200 kg/m^3, the viscosity of water 1×10^{-3}Pa s and the centrifugal force of 165,000g, the sedimentation rate came out to be -37.0816 mm/hr. The negative sign was due to upwards motion for UHMWPE travelling in a centrifuge tube. Since the centrifugation was run for 4 hours in Step 1, the total displacement of particle would have been 148.326 mm for 4 hours. This displacement was larger than the height of a centrifuge tube. Therefore, the centrifugation speed and duration were considered more than sufficient for purification of 20nm or larger particles. At the end of purification, particles were harvested as a suspension in isopropanol from the interface between layers of 0.90gms/ml and 0.96gms/ml isopropanol. Moreover, this harvested liquid had purified UHMWPE particles in isopropanol with an approximate density of 0.93gms/ml and pH of 12.5 - 13.0. The basic pH helped in slowing down the bacterial growth during the storage before membrane filtration of particles. (Detailed description of isolation protocol in Appendix II).

A comparison between all of the above isolation methods was done based on reproducibility, isolation sensitivity, bacterial contamination and suitability for further analysis as shown in Table 6.1. Out of all methods the novel isolation method was found to be suitable when high isolation sensitivity and capability for further analysis was required, while acid digestion based Scott's method [176] was found suitable for quick isolation of UHMWPE particles with medium sensitivity.

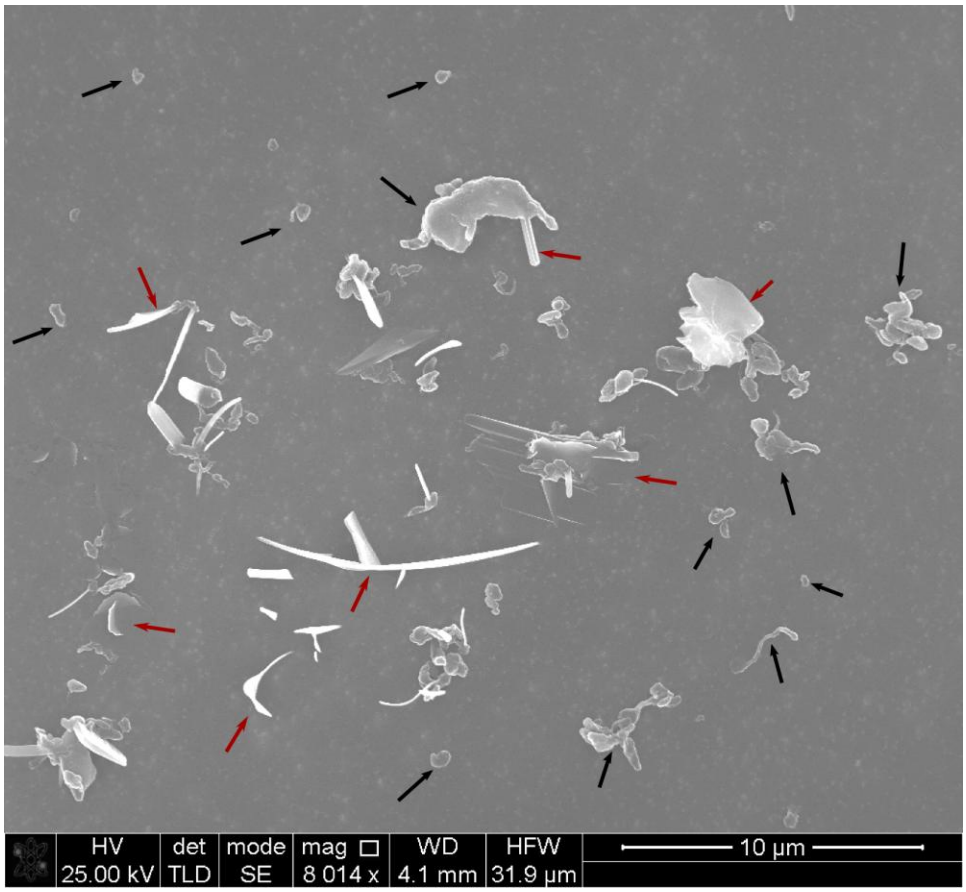

Figure 6.1 Particles lost in the bottom layers in an attempt to make single step purification method. Red arrows show impurities and black arrows show UHMWPE particles left in bottom layers.

Table 6.1 A comparison between current UHMWPE particle isolation methods

Particle Isolation Method	Reproducibility	Isolation Sensitivity	Bacterial Contamination	Availability of Isolated Particles
Acid digestion Scott *et al.*[176]	High	Medium	Very Low	No
Enzymatic digestion Niedzwiecki *et al.*[175]	Medium	Low	Low	No
Enzymatic digestion Billi *et al.*[185]	Low	High	High	No
Base Digestion Tipper *et al.*[178]	Low	Medium	Low	No
Base Digestion Elfick *et al.*[177]	Medium	Medium	Low	Yes
Novel Isolation Method (Current Work)	High	High	Low	Yes

6.2 Particle dispersion, display and image analysis

Right concentration and uniform dispersion of particles prior to imaging are important for accurate particle characterisation. Agglomeration was found to be dependent on the amount of particles filtered through the membranes by Slouf *et al.* [195]. Moreover, too low concentration of particles would display particles sparsely on filter. Although agglomeration may not be an issue at low concentrations, capturing extremely large number of SEM images would not be practical. For display of particles, the aim was to deposit maximum number of particles on the membrane filters, without a visible increase in agglomeration from SEM images.

For every 25 ml of serum isolated, about 6ml of particle concentrate was obtained at the end of isolation. It was experimentally found that 40 times dilution (250 µl in 9.750 ml) of the particle concentrate was optimum for the display of UHMWPE particles. Isopropanol was used to disperse particles because it was found to be a good dispersant for UHMWPE particles by Slouf *et al.* [195]. Isopropanol-water mixture with density 0.93 gms/ml was used as dispersant to match the density with UHMWPE wear particles for improved dispersion. The final volume of liquid before filtration was 10 ml. A low volume of feed helped quicker filtration using 0.015µm membrane (2-3 hours). Nanoscale pore size membrane filters are desirable for minimum loss of particles and a featureless background on SEM images with magnifications up to 20k.

During implementation of other methods such as Scott's method [176], filtration using 0.015µm membranes wasn't practical due to large filtration volume (250ml). Therefore, 0.05µm membrane filters were used for this method.

To achieve a uniform dispersion of UHMWPE, right amount of sonication along in combination with mechanical stirring was found to be an important factor. The mechanical stirring helped UHMWPE particles to stay suspended in the solution instead of sticking on the walls, while sonication helped them deagglomerate. Fifteen-minute sonication with mechanical stirring was found to be the optimum duration. Durations shorter than 15 minutes were found to be insufficient to deagglomerate the particles, whereas longer durations generated too much heat.

For SEM, coating thickness and type of coating were additional factors that could influence the quality of images. Gold coating of 5nm was found to be optimum for imaging UHMWPE debris. If the coating was too thin (3nm), a significant amount of contamination by electron beam was observed. If the coating was too thick (10nm or more), the nanoparticles were masked by coating and were not visible during imaging, which was not desirable.

In terms of image magnifications, 12000x, 15000x, and 20000x were chosen for particle analysis. Higher magnifications up to 200000x were used for qualitative analysis of particles. The reason behind choosing above magnifications for analysis was the typical size range of UHMWPE wear particles observed during SEM imaging. Majority of particles were 100 - 250 nm in size and very

few particles were larger than 10µm or smaller than 50nm. 12000x covered particles with size 100 nm to 18 µm in a single image, while 20000x was found to be sufficient for detecting particles as small as 25nm. A comparison between particle size distributions generated by 12000x, 15000x and 20000x images is shown in Figure 6.2. The sample used to generate these graphs was prepared by pooling particle size data from E1 UHMWPE particles generated in hip, knee and multidirectional multidirectional pin-on-plate. A large sample reduced the sampling errors to precisely show the differences due to change in magnifications.

Magnifications higher than 20000x significantly reduced the size of scanning window, and therefore required capturing of a very large number of images to get sufficient number of particles for analysis. Therefore, magnifications over 20000x were only used for qualitative purposes. In addition, as mentioned previously, magnifications of 20000x or lower, gave a featureless background with 0.015µm filter.

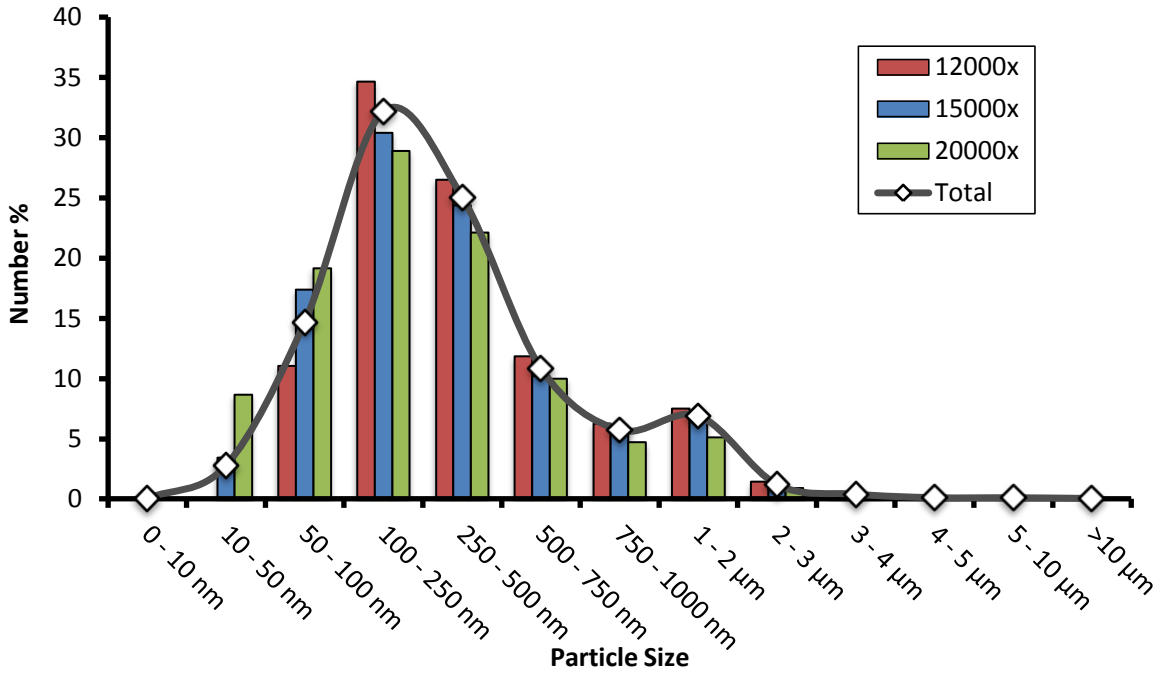

Figure 6.2 Effect of image magnification on the particle size distribution. Size distribution graphs obtained from particles imaged at 12000x, 15000x and 20000x are shown in the figure. E1 UHMWPE particle data from hip, knee and multidirectional pin-on-plate was pooled to generate a large sample used to generate above size distributions.

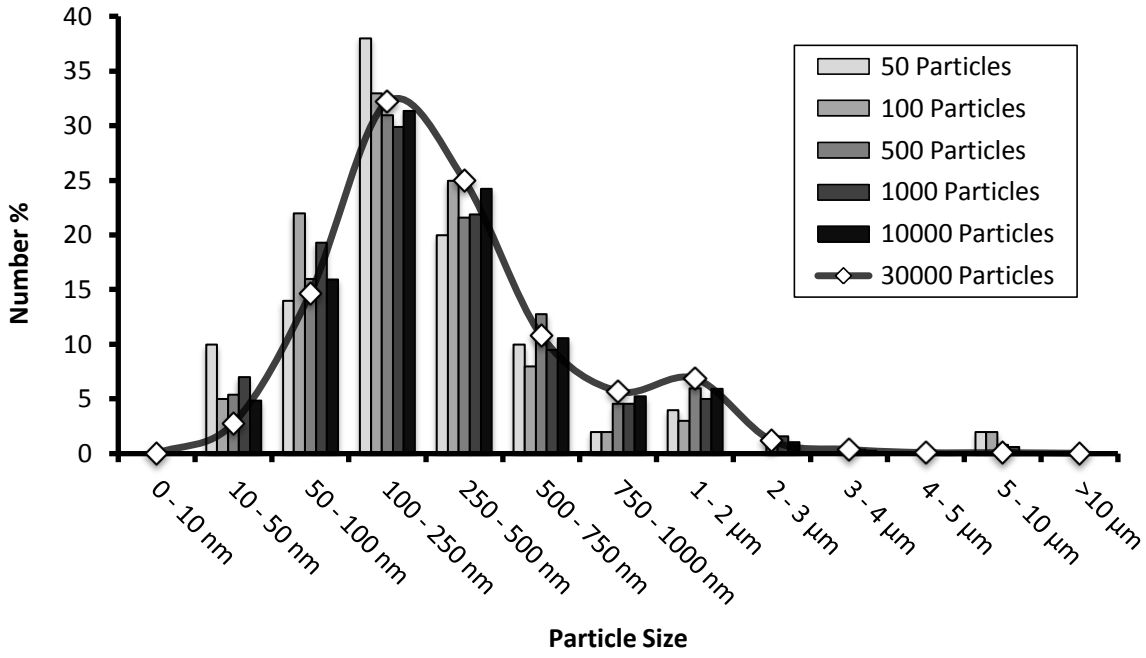

Figure 6.3 Effect of sample size on accuracy of size distribution. E1 UHMWPE particle data pooled from hip, knee and multidirectional pin-on-plate was used to generate above size distributions with total number of particles ranging from 50 to 30,000.

For image analysis based particle characterisation, it is necessary to know the minimum number of particles necessary for generation of accurate size and shape distribution data. ISO standard for polymer wear debris isolation and characterisation (ISO 17853) suggested a minimum of 100 particles for analysis [179]. This was verified by statistical analysis of a very large sample and its subsamples as shown in Figure 6.3. Kolmogorov-smirnov Z test was used on each sample and a sample size larger than 100 showed no statistical difference between the samples.

For increased accuracy, current study used a minimum of 500 particles to generate size distribution graphs. This was 5 times the number of particles recommended by ISO 17853 [179] and the number of particles computed experimentally using statistical analysis. Moreover, equal number of 12000x, 15000x and 20000x images were used for image analysis.

The next step after capturing images was the characterisation of wear debris using image analysis. Intel® OpenCV image processing library was chosen to implement image analysis features due to the availability of a large array of pre-built and well-documented image analysis functions. Moreover, the functions in the library were implemented using well-established algorithms in the area of image processing.

Analysis of UHMWPE wear debris using SEM images involved segmentation of particles from background. Image processing software such as Image Pro Plus and Image J failed to detect particles automatically. Although segmentation could have been straightforward for an image with a uniform background, SEM images are known for high background noise as well as shadowing on particle boundaries [204]. Simple segmentation methods such as thresholding required manual

input of threshold value and gave inaccurate results. Moreover, due to the fibrillar nature of UHMWPE wear particles, the region of interest contained thin fibrillar features with intensity values close to background. A marker-based watershed segmentation was chosen to segment the particles due to its ability to segment small features with good accuracy[205], [206]. The marker image was generated using background and foreground threshold values obtained by K-means clustering on intensity histogram data of the image. The particles were identified using contours as mentioned in Section 4.3.2. Contours were chosen as they give continuous segmentation of each particle and efficiently separate individual particles [207].

One key feature implemented was the storage of particle data as a vector of structures. This helped in easy organisation and accessibility of complete size and shape information of each individual particle. Particles were categorised into folders based on their size. Four size ranges chosen for categorisation were 0 to 100 nm, 100 nm to 1µm, 1µm to 5µm, 5 to 10µm and 10 to 100 µm. These size range effectively segregated nanoscale, submicron and micron sized particles as well as covered the complete size range of UHMWPE particles observed in current study and in literature. This helped in identifying key differences in shape within each size range when comparing different wear debris samples.

The size and shape descriptors calculated by the software not only covered ASTM F1877-05 specifications [192], but also calculated compactness and complexity. The addition of compactness and complexity in the present study helped in differentiating UHMWPE particles based on their level of compactness and complexity in shape. These descriptors have been used for geological image analysis [208] are dependent on the convex hull area of a particle. Compact shapes showed higher compactness values in UHMWPE particles as shown in Figure 6.4 and complex/fibrillar shapes showed lower complexity values as shown in Figure 6.5.

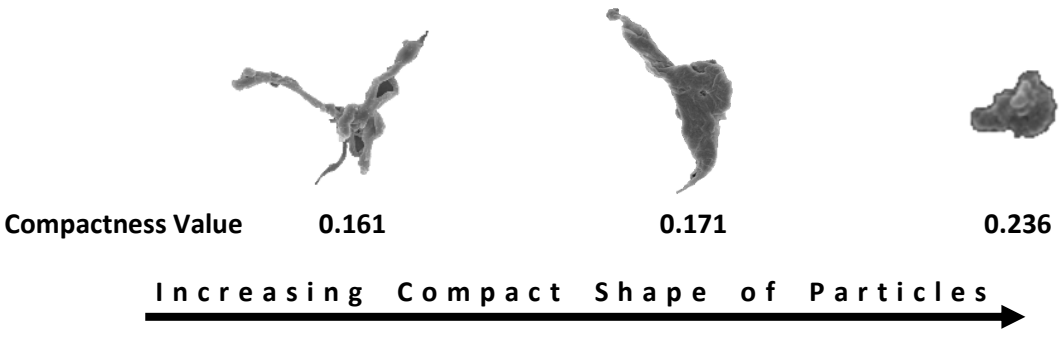

Figure 6.4 Compactness values of particles with increasing compact shape.

Complexity Value: **0.860** **0.430** **0.252**

Increasing Complex/fibrillar shape of particles

Figure 6.5 Complexity values of particles with increasing complex/fibrillar shape.

It was also advantageous to investigate the invariance of the shape descriptors during natural transformation of polymeric fibrillar particles, which could change their morphology by bending as shown in the Figure 6.6. In such situations, area and perimeter are constant. Out of the six shape descriptors used in this study, elongation and form factor are dependent on area and perimeter. Therefore, these two shape descriptors were found to be invariant to fibrillar particle transformations (Figure 6.6).

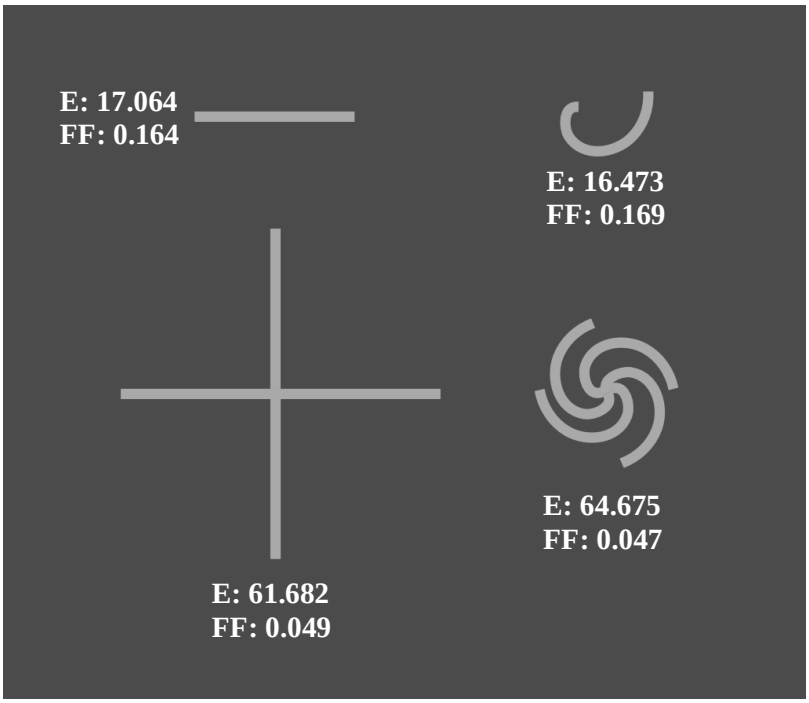

Figure 6.6 Elongation (E) and form factor (FF) invariance of fibrillar particles. Particle in top left represents a straight fibre, which is transformed into a bent fibre particle on top right. E and FF values for both particles are very similar. Particle on bottom left represents complex straight fibres, which are transformed into the fibrillar particle on the bottom right. E and FF values for both particles are very similar. Minor differences in the values are due to errors assicoated with the geometric transformation of particles and computation of area and perimeter by the custom software.

6.3 Influence of change in UHMWPE processing conditions and addition of Vitamin E antioxidant on size and morphology of wear debris

6.3.1 Conventional direct compression moulded UHMWPE vs. Highly crosslinked Vitamin E diffused UHMWPE

UHMWPE as an orthopaedic bearing material has gone through several stages of development. Based on modifications to the material, UHMWPE has been categorised into three major categories as conventional, first generation highly crosslinked UHMWPE and second generation highly crosslinked UHMWPE (More detail in Section 2.3.1, page 11). In this section, a comparison between conventional direct compression moulded ArCom UHMWPE and second generation highly crosslinked vitamin E infused E1 UHMWPE is discussed. Comparison between these two generations of UHMWPE gave more insight into combined effect of crosslinking and infusion of vitamin E in UHMWPE on wear debris generation.

Although wear rates of conventional direct compression moulded UHMWPE and E1 UHMWPE in a knee simulator have been compared previously [209], no comparison between wear debris generated by wear testing of conventional UHMWPE and vitamin E diffused UHMWPE was found in literature. One study by Bichara *et al.* used E1 wear particles commercially generated by Bioengineering Solutions, Inc. (Oak Park, IL) and compared the osteolytic potential of both materials [5]. However, no details were given about the particle generation methods. Therefore, the particle size distribution data from this study was not chosen for comparison. Nonetheless, significant amount of work has been done in the past on comparison of conventional UHMWPE and highly crosslinked UHMWPE wear debris. It has been shown in literature that addition of vitamin E through diffusion doesn't affect the mechanical properties and wear rates of highly crosslinked UHMWPE. Therefore, in present study, comparison of the results were compared to the studies that used conventional UHMWPE and highly crosslinked UHMWPE.

Both ArCom and E1 were tested at nearly identical conditions in an artificial knee simulator and a multidirectional pin-on-plate tester. Moreover, knee wear debris from early wear and long-term wear was analysed, while multidirectional pin-on-plate wear debris from only long-term wear was analysed because only long-term wear tests were conducted using multidirectional pin-on-plate.

6.3.1.1 **ArCom Knee vs. E1 Knee**

This section compared ArCom and E1 UHMWPE wear particles generated in a knee simulator during early wear and long-term wear.

Early stage wear

During early wear, a large number of particles in 1 - 2µm size range were noticed for both samples. Moreover, high aspect ratio and elongation values of these particles indicated generation of large elongated particles in both samples. This was verified by looking at particle morphology as shown in Figure 6.7. Campbell *et al.* showed similar large irregular elongated particles in her study and suggested an adhesive mechanism for generation of these particles, rather than abrasive mechanism[167]. Therefore, it is believed that majority of these particles were generated by adhesive wear.

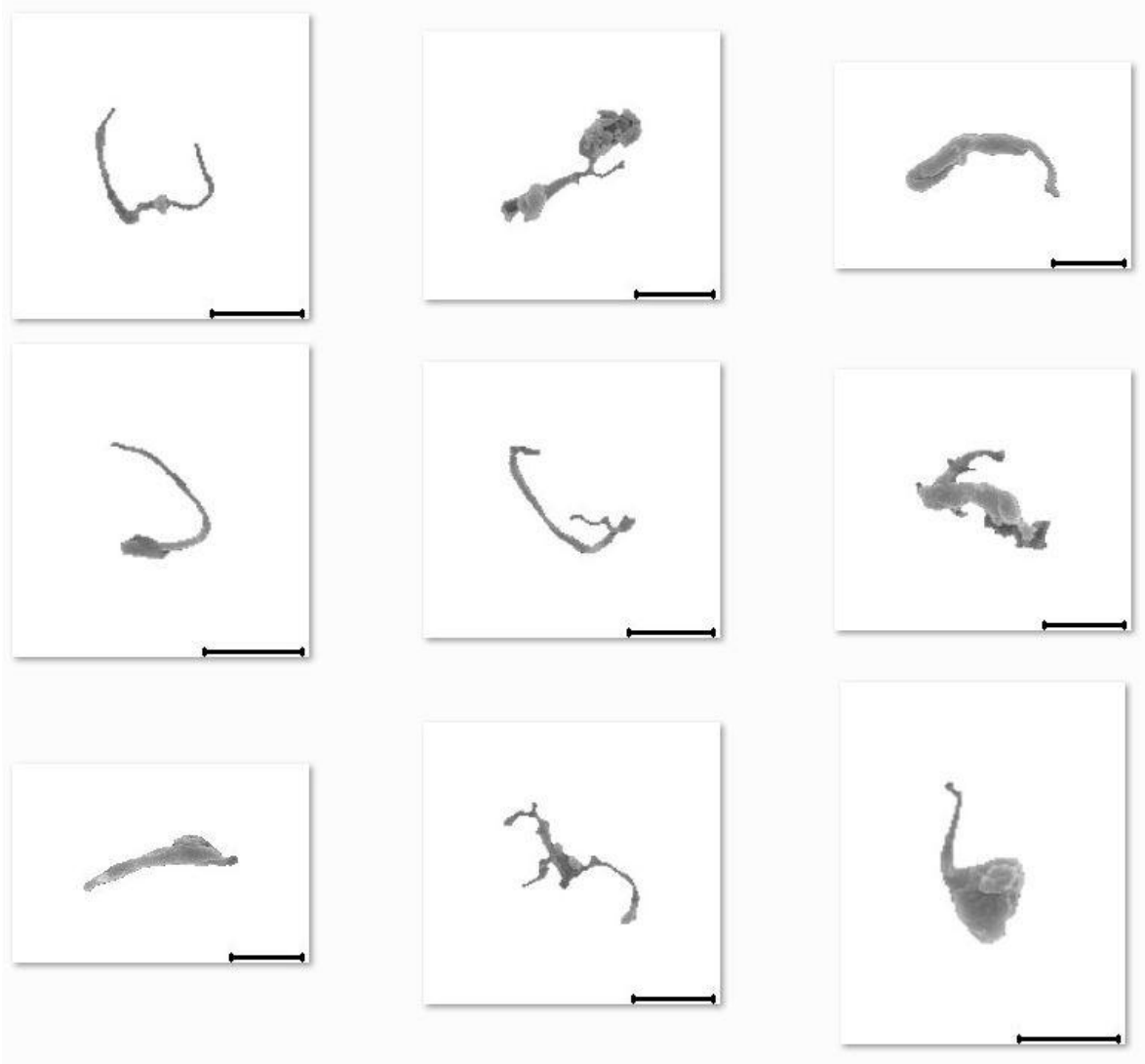

Figure 6.7 ArCom knee particles produced during early wear with size 1 to 2 µm. Majority of particles were observed as elongated / fibrillar. Scale = 1µm.

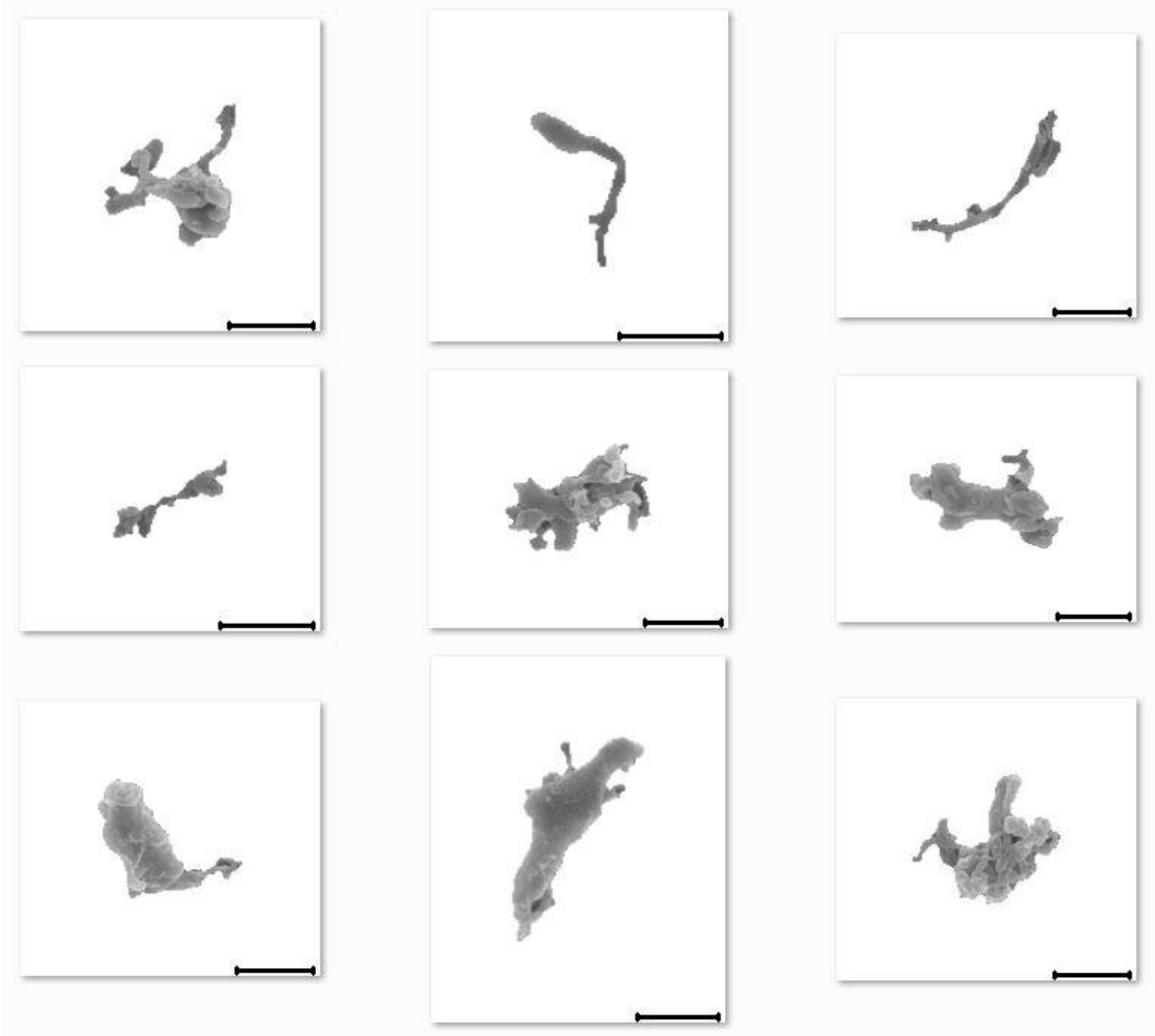

Figure 6.8 E1 knee particles produced during early wear with size 1 to 2 µm. Majority of particles were noticed as elongated / fibrillar. Scale = 1µm.

Long-term wear

During long-term wear, the number of particles in 1 - 2µm size range reduced for both ArCom and E1 in comparison to early wear and both showed majority of particles as submicron particles .

It is known that with the progression of a wear test, the burnishing (smoothening) of the articulating knee bearing surfaces happens due to micro abrasive/adhesive wear (as mentioned in Section 2.5.1.2, page 27). This causes generation of submicron sized wear debris. Therefore, with progression of test, a reduction in adhesive wear and an increase in micro abrasive/adhesive wear is believed to occur.

Moreover, within submicron size range E1 generated a larger fraction of particles smaller than 250 nm in comparison to ArCom. Highly crosslinked UHMWPE has been known to generate smaller wear particles in comparison to conventional UHMWPE [6], [185], [210].Therefore, above observation was in agreement with previous studies.

In terms of particle morphology, ArCom showed higher aspect ratio and elongation values in comparison to E1. This was caused by a generation of more elongated particles in ArCom as shown in Figure 6.9. Additionally, ArCom particles were found to be more complex in shape, due to the fibrillar/complex shape of the wear debris. It is believed that higher chain mobility in uncrosslinked ArCom was the reason behind more elongated and fibrillar/complex morphology of wear debris, while in E1 crosslinking may have reduced chain mobility causing generation of less elongated particles with simpler shapes. For the same reason, higher elongation to break was observed for uncrosslinked UHMWPE in comparison to vitamin E diffused UHMWPE by Oral *et al.* [211].

On the whole, as both materials were tested under knee articulation conditions, based on previous studies, adhesive/abrasive for submicron particles and a combination of adhesive and fatigue wear for large elongated particles were believed to be the primary mechanism of generation of wear particles [212]–[215]. Moreover, from early wear to long-term wear a change is surface roughness is believed to increase the generation of submicron sized particles.

A) ArCom Knee Long-term Wear

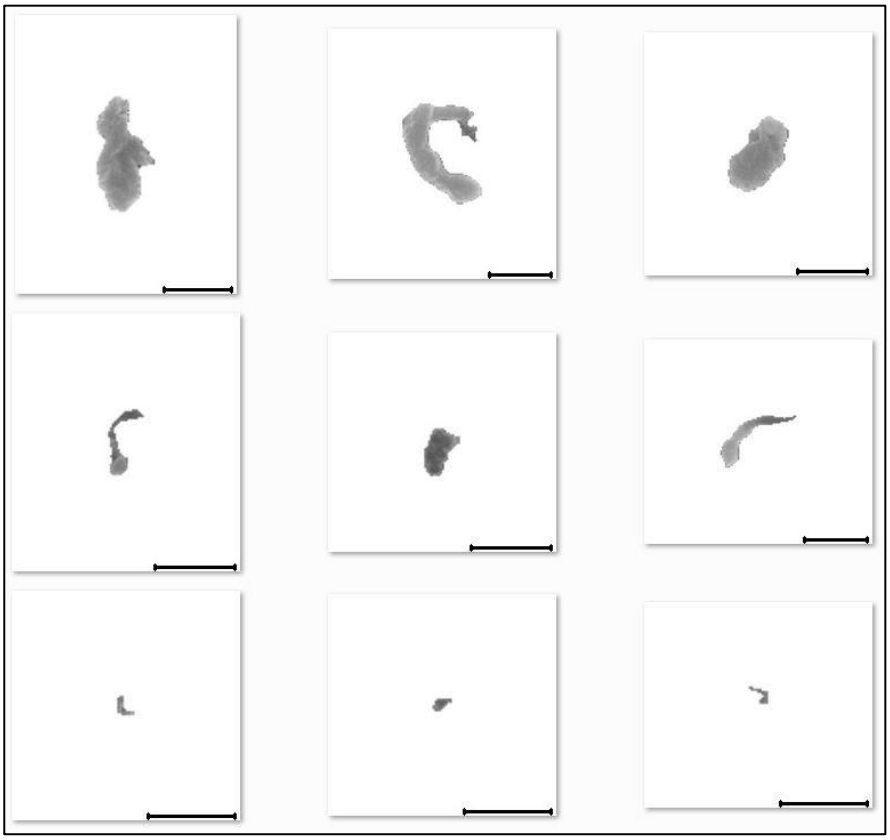

B) E1 Knee Long-term Wear

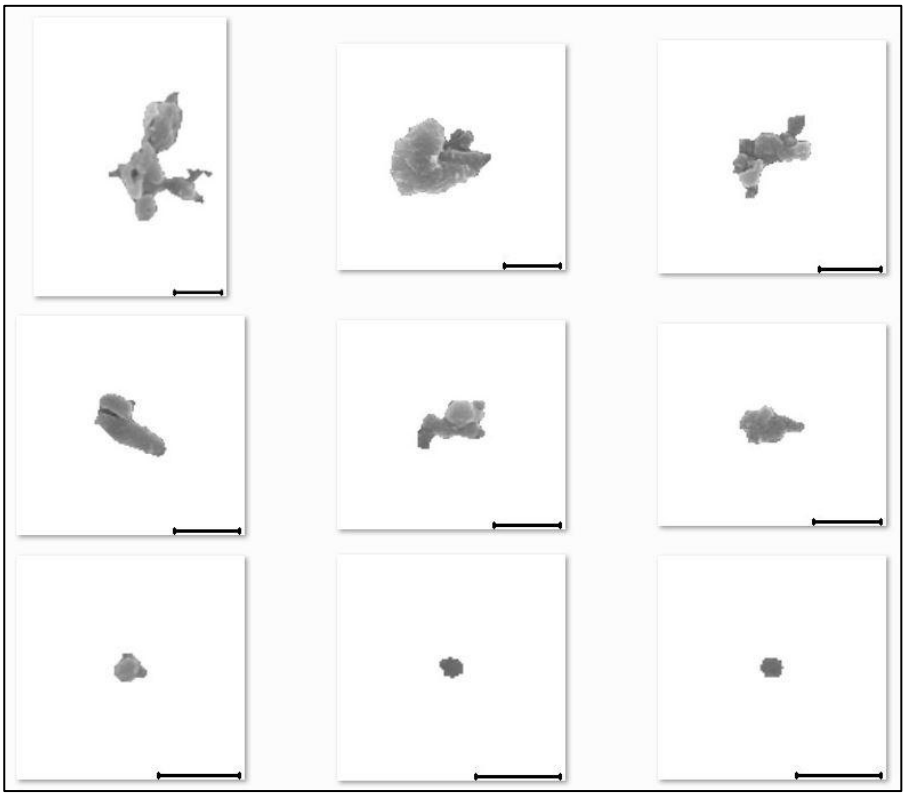

Figure 6.9 Different morphologies of submicron sized wear particles. Images show long-term wear particles of both E1 and ArCom knee. A) Elongated and fibrillar ArCom knee particles B) More compact and less elongated E1 particles. Scale = 500nm

6.3.1.2 ArCom multidirectional pin-on-plate vs. E1 multidirectional pin-on-plate

This section compared ArCom and E1 UHMWPE wear particles generated in a Multidirectional pin-on-plate tester during long-term wear. The Multidirectional pin-on-plate articulation during the wear test was a combination of translation motion along with rotational motion to simulate multidirectional wear (More information in Section 2.6, page 33).

Although the articulation conditions were identical for both materials, the particles generated by ArCom had a significantly different size distribution compared to E1. A bimodal distribution was observed for ArCom particles. The mode size ranges were 100 - 250 nm and 1 - 2 µm, which indicated generation of submicron particles as well as large micron sized particles. Alternatively, E1 had majority of particles smaller than 1µm, and over 50% particles in 100 - 500 nm size range.

A previous study by Tipper *et al.* compared non crosslinked and highly crosslinked UHMWPE wear debris generated in a multidirectional pin-on-plate tester [216]. A higher number percentage of nanoscale wear debris were reported for non crosslinked UHMWPE and a higher number percentage of particles in 0.1 to 1µm size range were reported for highly crosslinked UHMWPE. Current study observed similar pattern for non crosslinked ArCom and highly crosslinked E1 UHMWPE.

In regards to the shape of wear particles, submicron particles had similar elongated shapes for both ArCom and E1. However, large ArCom particles (size above 1 µm) were more elongated and fibrillar than E1. The reason behind this difference in morphology as well as generation of larger particles in ArCom is the effect of crosslinking on chain mobility and ductility. As mentioned in previous section, crosslinking reduces chain mobility and elongation to break. Moreover, this difference in both materials was amplified by the nature of motion in multidirectional pin-on-plate tester. As observed by several studies, multidirectional pin-on-plate creates cross shear due to combined effect of translational and rotational movement [210], [217], [218]. Softer materials such as UHMWPE can undergo adhesive/abrasive wear when sliding against metal (Section 2.4.3.1, page 21). A combination of these effects can cause pulling out and shearing of the material at the same time. Therefore, differences in chain mobility and ductility were clearly noticeable.

A) ArCom Multistation Pin-on-plate Long-term Wear

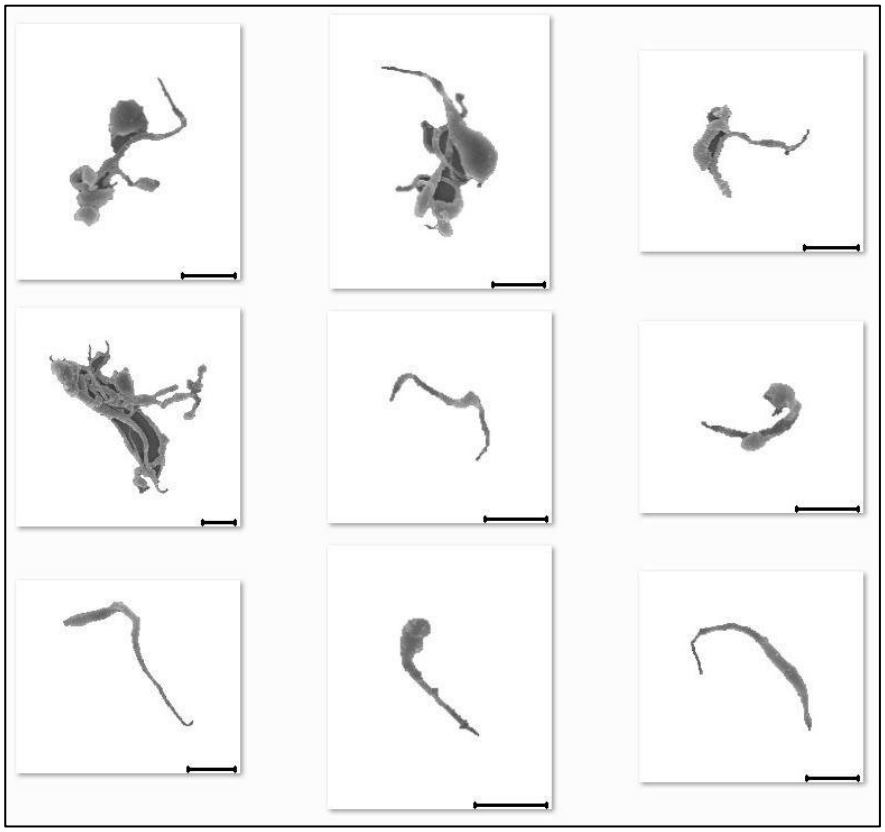

B) E1 Multistation Pin-on-plate Long-term Wear

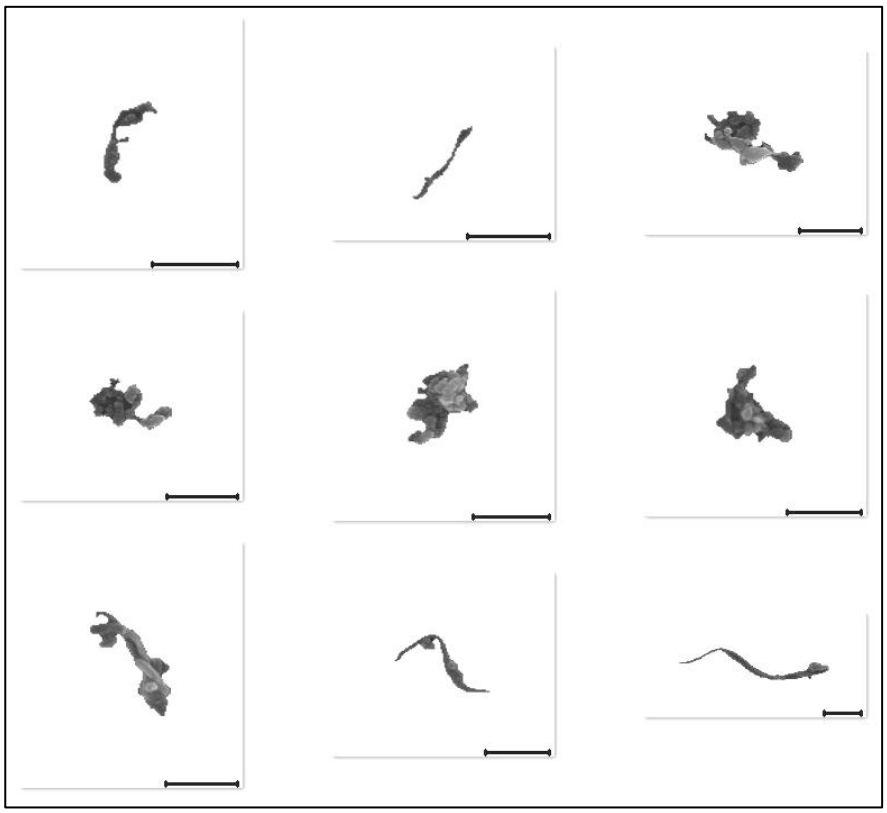

Figure 6.10 Difference in morphology of ArCom and E1 wear debris in 1 to 5µm size range during long-term wear. A) ArCom multistation pin-on-plate. B) E1 multistation pin-on-plate. More fibrillar and elongated particles were produced by ArCom in comparison to E1. Scalebar = 1µm

6.3.2 Highly Cross-linked Vitamin E Diffused E1 UHMWPE vs. Vitamin E Blended Highly Cross-linked ECiMa UHMWPE

Recent modifications in UHMWPE include addition of Vitamin E as an antioxidant. Two methods by which Vitamin E has been added to UHMWPE are by blending vitamin E into UHMWPE resin before consolidation or by diffusing it through crosslinked UHMWPE. It has been shown that blending vitamin E may reduce the extent of crosslinking by irradiation [51]. Moreover, wear rates of vitamin E blended UHMWPE were found to be higher than highly crosslinked UHMWPE by Affatato *et al.* [219]. The effect of a change in the vitamin E addition process was investigated in current study by comparing size and shape of wear debris produced by hip simulator wear testing of vitamin E blended cold irradiated mechanically annealed UHMWPE (ECiMa) and vitamin E diffused highly crosslinked UHMWPE (E1). Moreover, the wear debris were compared during early wear as well as long-term wear.

Early wear

During early wear, ECiMa produced larger wear debris than E1. Moreover, a bimodal size distribution was produced by ECiMa wear debris, with mode size ranges 100 - 250 µm and 1 - 2 µm. Alternatively, E1 particles were mostly submicron in size. A comparison of shape analysis showed higher aspect ratio/elongation for ECiMa particles, while higher roundness/form factor values were observed for E1. Moreover, ECiMa particles were found to have lower complexity values, indicating complex/fibrillar particles produced by ECiMa.

Long-term wear

During long-term wear, ECiMa generated smaller size wear debris in comparison to early wear and both E1 and ECiMa had majority of particles smaller than 2 µm. However, the mode size range for E1 was 100 - 250 µm, while mode size range for ECiMa was 250 - 500 µm. The morphology of long-term wear particles was found to be more elongated in ECiMa in comparison to E1. Moreover, particles larger than 1µm were mostly long fibres in ECiMa, whereas in E1 particles were complex/fibrillar. The reason behind generation of more elongated particles in ECiMa was found to be its 15% higher elongation at break in comparison to highly crosslinked UHMWPE [220]. Since the extent of crosslinking was not affected by diffusion of vitamin E [52], the mechanical properties of E1 were assumed similar to highly crosslinked UHMWPE.

ECiMa also generated few very large (size above 10µm) particles (Figure 6.12) during long-term wear indicative of fatigue and delamination wear.

E1 Hip Long-term Wear

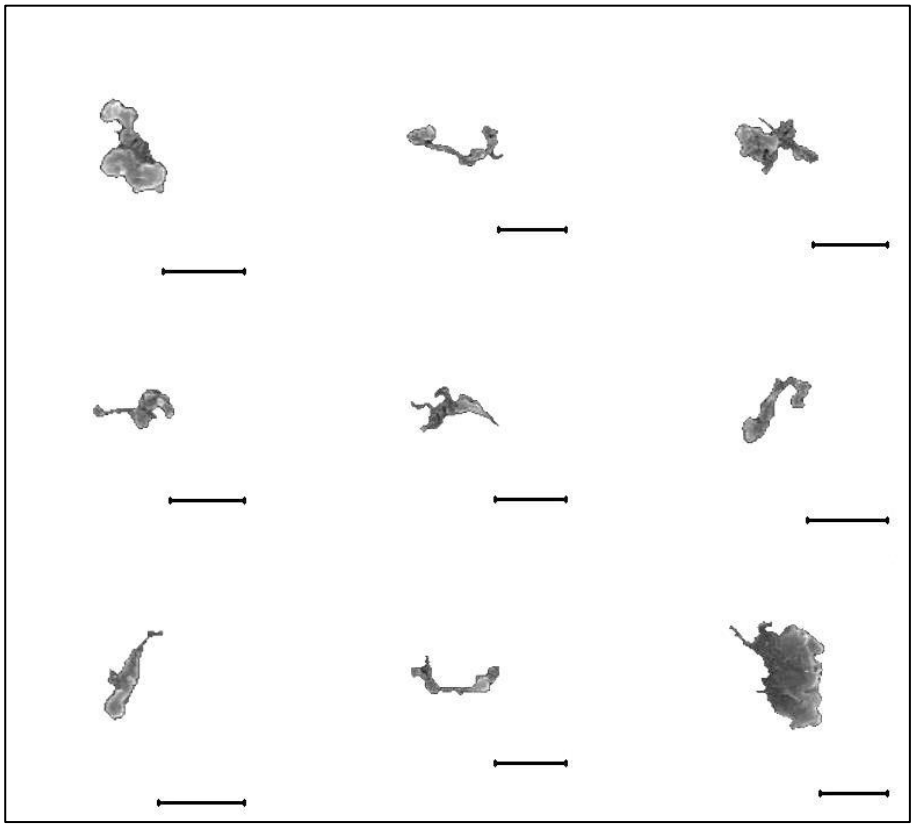

ECiMa Hip Long-term Wear

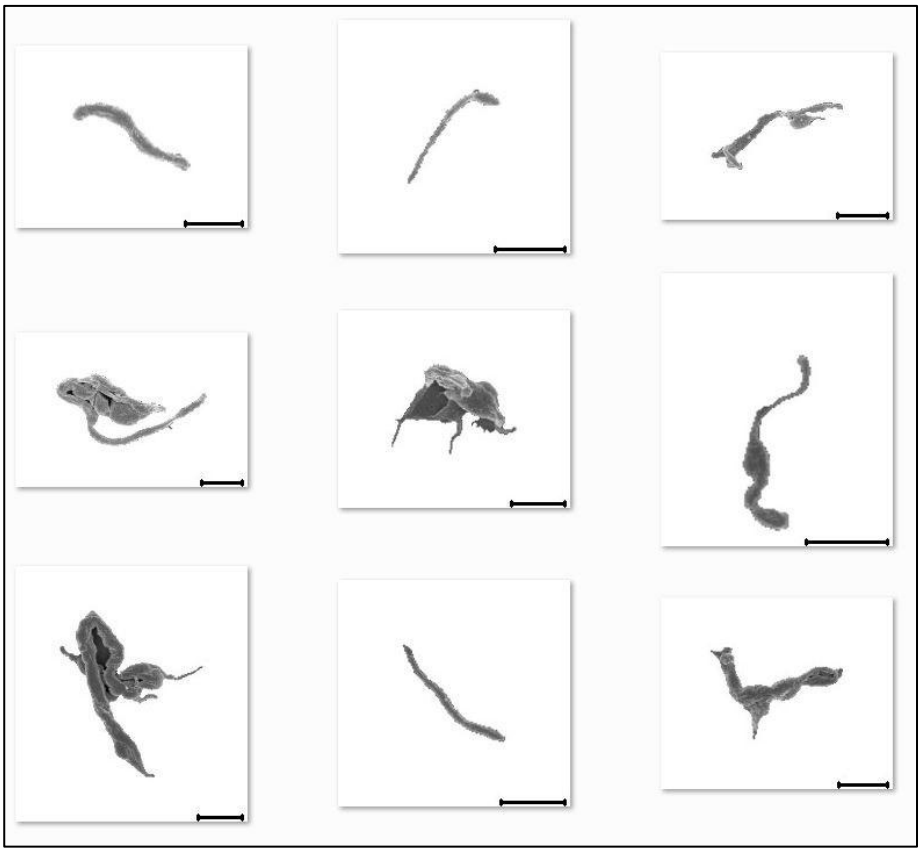

Figure 6.11 Difference in morphology of E1 and ECiMa wear debris in 1 to 5µm size range during long-term wear. A) E1 hip. B) ECiMa hip. More elongated fibrillar particles were produced from ECiMa in comparison to E1. Scalebar = 1µm

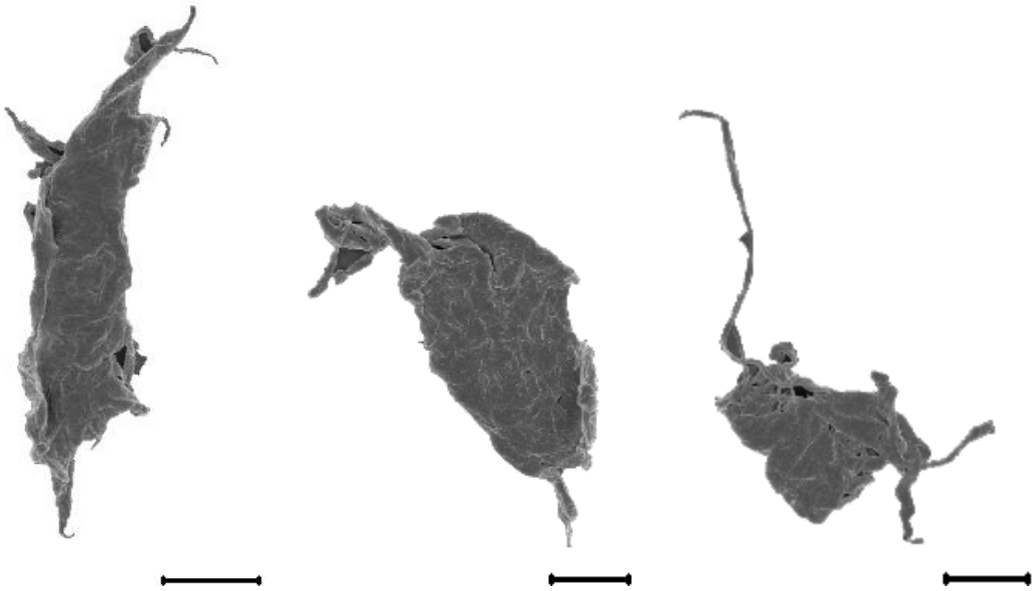

Figure 6.12 Very large particles (size >10µm) generated in ECiMa during long-term wear. These particles were believed to be produced by delamination of the bearing surface. Scale = 2µm.

6.3.3 Conventional UHMWPE moulded at 145°C vs. Conventional UHMWPE moulded at 175°C

With a change in moulding temperature, there is a structural difference in terms of type of defect and the extent of defect present in the compression moulded UHMWPE. A previous study by Wu *et al.* stated that the UHMWPE samples moulded at 175°C were less crystalline compared to the samples moulded at 145°C and had higher elongation to break [221]. Effect of a change in moulding temperature of direct compression moulded UHMWPE was investigated.

Multidirectional pin-on-plate wear tester was used to assess the wear debris generated during long-term wear of direct compression moulded (DCM) UHMWPE moulded at 145°C and DCM UHMWPE moulded at 175°C. No effect of these imperfections on size and morphology was noticed. Therefore, it is believed that irrespective of the amount of wear, the size and morphology of wear debris remains the same with a change in moulding temperature.

UHMWPE moulded at 145°C Multistation Pin-on-plate Long-term Wear

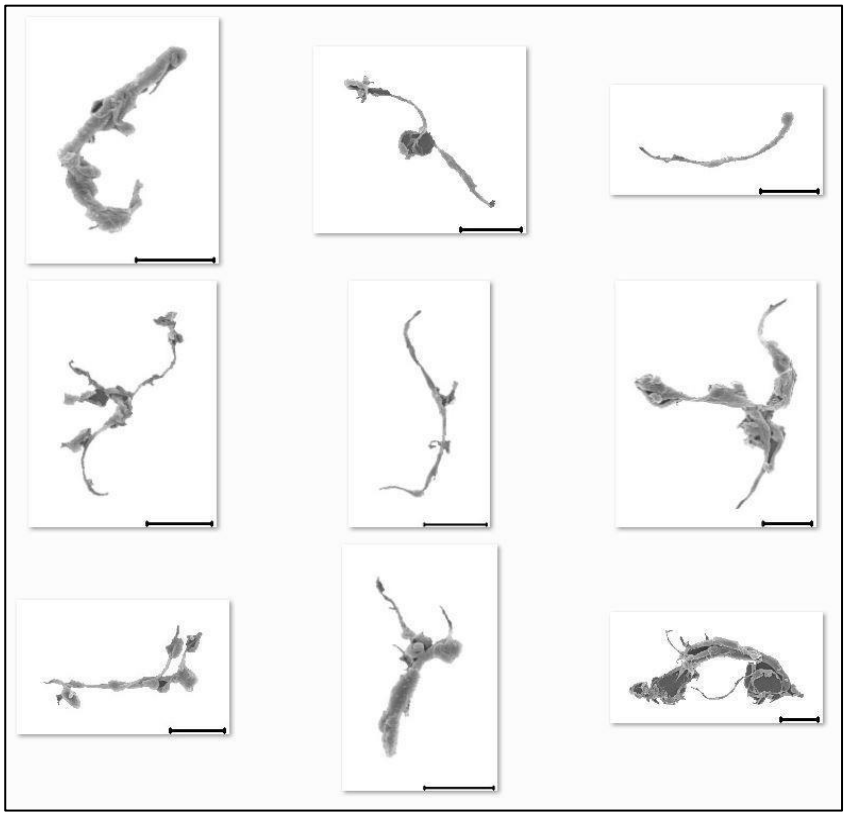

UHMWPE moulded at 175°C Multistation Pin-on-plate Long-term Wear

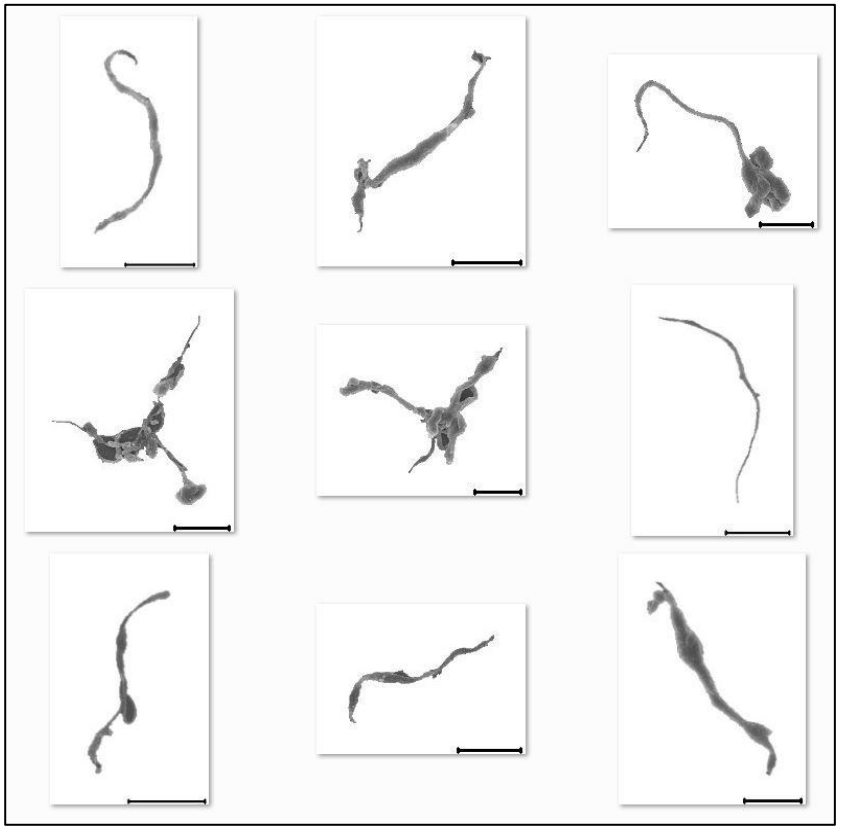

Figure 6.13 Difference in morphology of UHMWPE wear debris in 5 to 10μm size range, with change in moulding temperature during long-term wear. A) DCM UHMWPE 145°C. B) DCM UHMWPE 145°C. No significant differences in morphology were observed. Scalebar = 2μm

6.4 Influence of different joint articulations on wear debris size and morphology

Second part of the study compared the influence of the type of joint articulation on size and morphology of wear debris produced by the wear of highly crosslinked E1 UHMWPE. A number of studies done in the past have compared wear debris produced in knee, hip, ankle and shoulder (2.5.1.3.1, page 30). This section will discuss the comparison between size and morphology of E1 wear debris produced in Knee, Ankle, Hip and multidirectional pin-on-plate tester.

6.4.1 E1 Knee vs. E1 Ankle

In this section, the size and morphology of E1 wear particles produced by artificial ankle articulation and artificial knee articulation were compared.

Early wear

During early wear, the particles generated by both ankle and knee were mostly similar in size. However, ankle produced a higher number of particles in 100 - 500 nm size range, while knee produced a marginally higher number of particles in 500 nm - 3µm size range. Upon closer inspection of the particle morphology and shape factor graphs, it was found that knee generated more complex fibrillar particles, whereas ankle produced more compact and round particles as shown in Figure 5.62 (page 152) and Figure 5.60 (page 150).

Long-term wear

During long-term wear, there were notable differences between the size distributions of wear debris generated by both articulations. Ankle produced a large number of particles (≈19%) in 500 - 750 nm size range, whereas no peak was observed for knee in this size range. In order to identify the reasons for these differences, the morphology and shape factor data of particles in each of these size ranges were investigated. It was found that the particles generated by ankle articulation in 500 - 750 nm size range were noticeably different from usual shapes of UHMWPE debris in this size range. Their morphology was round and compact as shown in Figure 6.14. As these particles were generated only during long-term wear, it is believed that these particles were generated due to fatigue wear triggered by cyclic loading at higher contact stresses.

Another noticeable difference was in 50 - 100 nm size range where knee generated almost 15% of wear debris, while ankle generated only about 6%. The morphology of these particles looked similar (small granular). Therefore, it is possible that both articulations had similar wear mechanism in this size range. Adhesive/abrasive wear is believed to be the wear mechanism.

Overall ankle produced more round and compact particles in comparison to knee, which is in agreement with the previous study by Kobayashi *et al.* [222]. A marginally higher number of large

particles, with size greater than 4µm, were also noticed in ankle than knee. These particles were either flaky, irregular elongated or long fibrillar morphology. Large flakes were indicative of fatigue and delamination wear, while elongated, irregular and fibrillar particles were indicative of adhesive wear.

E1 Ankle Long-term Wear

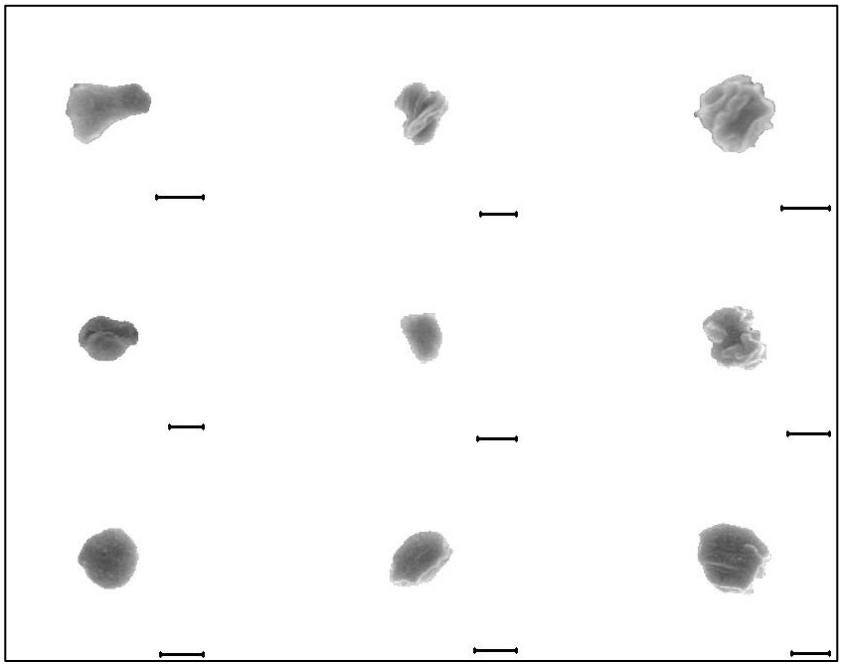

E1 Knee Long-term Wear

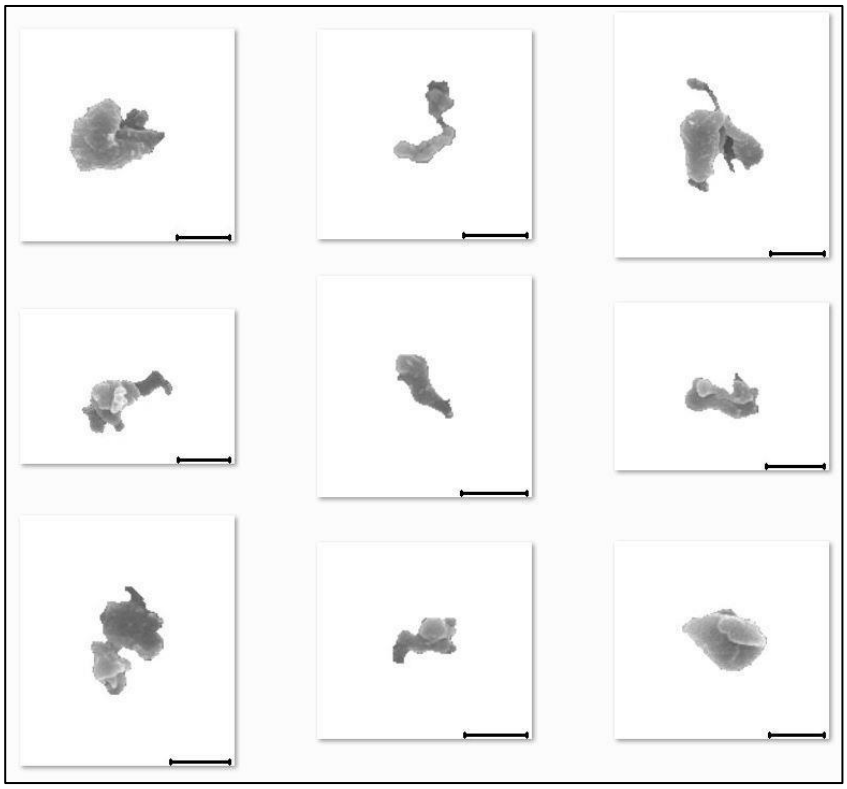

Figure 6.14 E1 wear particles (500 - 750 nm) generated during long-term wear of E1 ankle and E1 knee. Round and compact shapes were observed for ankle particles, while less compact and complex shapes for knee particles. Scale bar = 500nm

E1 Ankle Long-term Wear

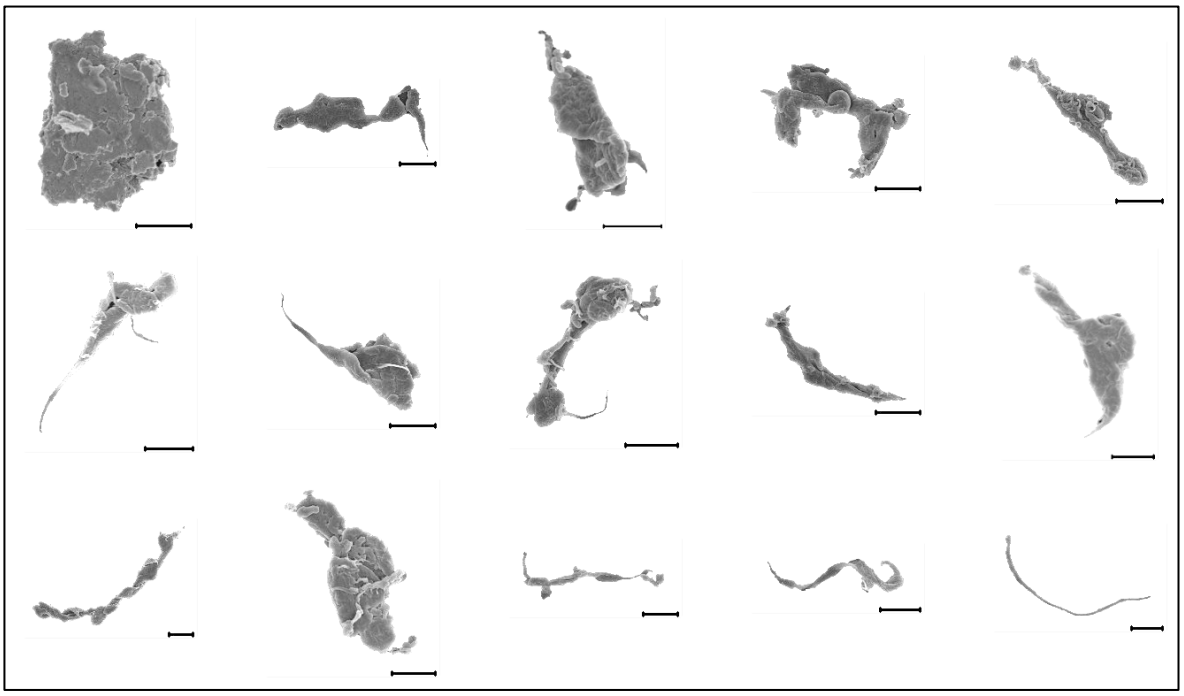

E1 Knee Long-term Wear

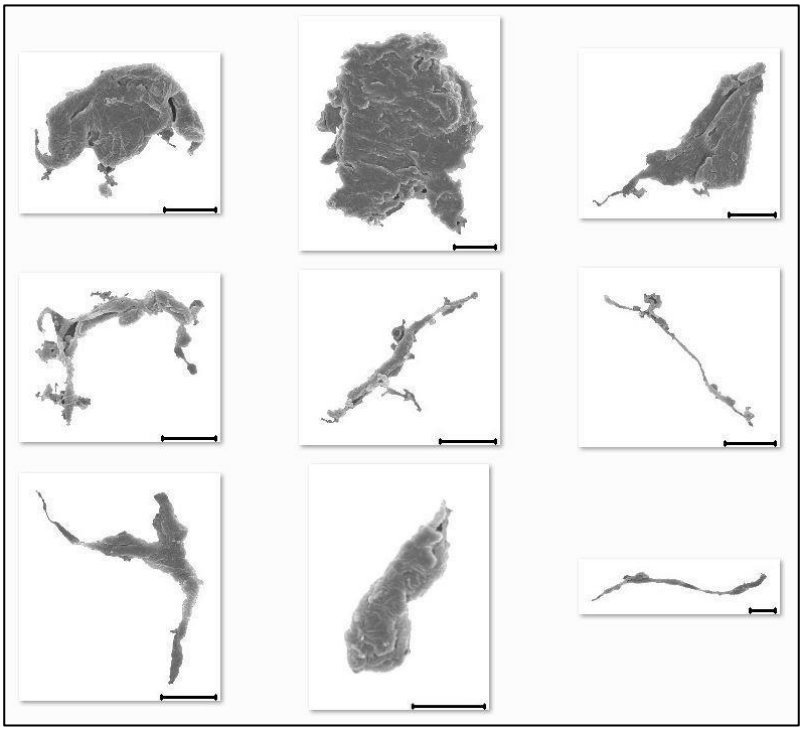

Figure 6.15 Large microscale UHMWPE wear debris produced by E1 ankle and E1 knee during long-term wear. Scale = 2µm. Both ankle and knee showed long fibrillar particles as well as few large flaky particles.

6.4.2 **E1 Knee vs. E1 Hip**

This section discusses the comparison between size and morphology of wear debris produced by E1 knee and E1 hip.

Particles from early wear and long-term wear were characterised for size and morphology. During early wear, particles generated by E1 hip were smaller than particles produced in knee (Section 5.2.2.1.1, page 162). Moreover, majority (over 87%) of the particles produced in E1 hip were submicron in size. On the other hand, knee generated a bimodal size distribution with mode size ranges of 100 - 250 µm and 1 - 2 µm. Over 63% of knee particles were submicron in size. The shape analysis of both E1 hip and Knee during early wear also showed differences in their morphology. Submicron knee particles had higher aspect ratio values, while submicron E1 hip particles were rounder and compact in morphology, indicating differences in particle generation mechanisms (Figure 6.16).

During long-term wear, majority of wear debris produced by both E1 hip and E1 Knee were submicron in size. In addition, over 60% of the E1 hip particles were in 100 - 500 nm size range, while knee produced a wider size distribution of particles, with higher percentage of particles in 50 – 100 nm and 1- 2 µm size ranges in comparison to E1 hip. The shape analysis of both samples indicated similar shapes, apart from marginally rounder morphology in E1 hip for submicron-sized particles.

Concerning particle generation mechanisms, previous studies suggest adhesive and microabrasive wear mechanisms for generation of smaller wear particles in hip [95], [167]. Therefore, early wear submicron particles in E1 hip with round and compact morphology were believed to be generated by more micro-abrasive and less adhesive wear. In knee during early wear, a combination of adhesion and abrasion was believed as the wear mechanism (mentioned previously in Section 6.3, page 215). During the long-term wear, E1 hip wear particles had complex/elongated morphology similar to knee wear particles, indicative of a shift to less microabrasive and more adhesive wear. This was particularly noticeable from difference in morphology of larger sized particles between early wear and long-term wear in 0.1 - 1 µm size range as shown in Figure 6.16 and Figure 6.17. Large flakes were rarely noticed in both samples, indicating that delamination and fatigue wear was not significant in E1 hip and E1 knee.

A) E1 Knee Early Wear

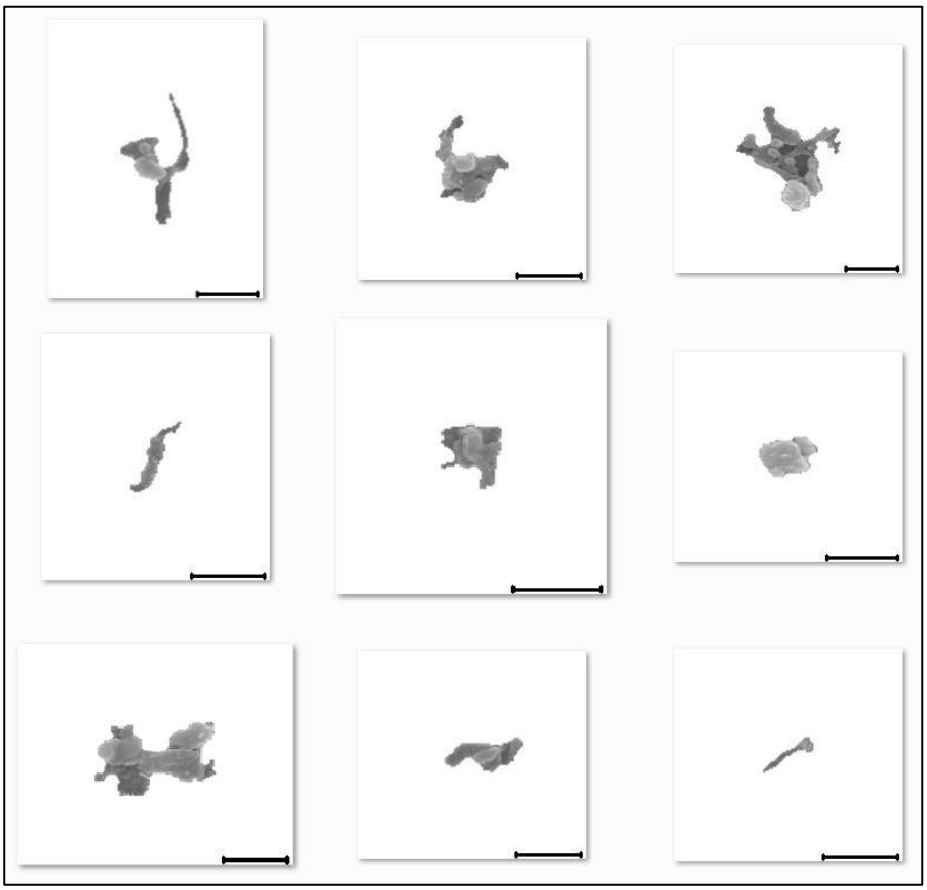

B) E1 Hip Early Wear

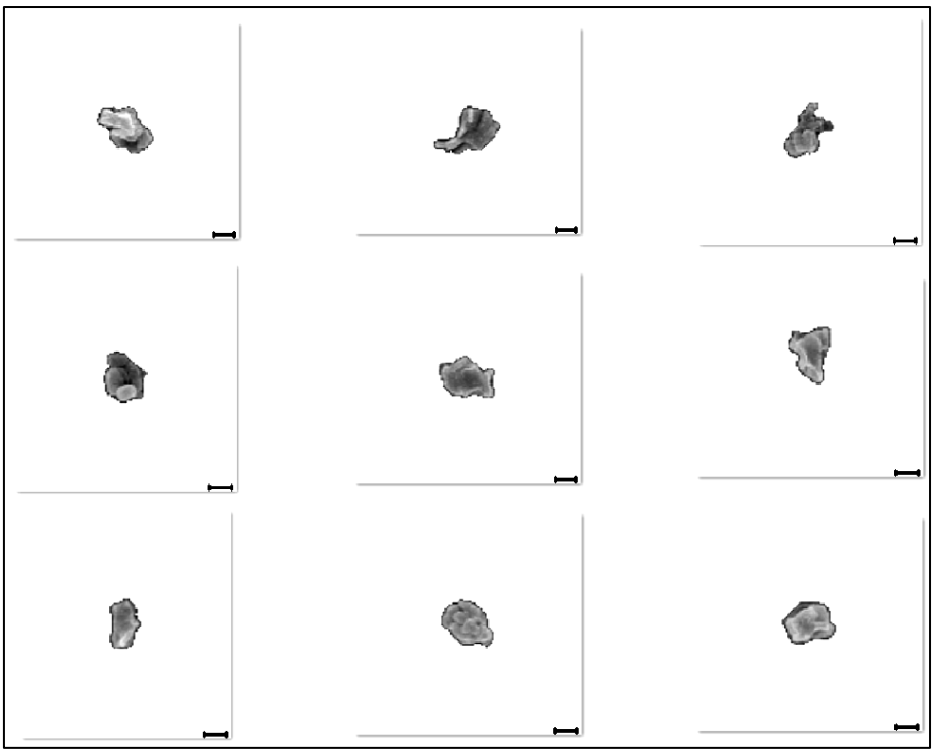

Figure 6.16 Difference in morphology of E1 knee and E1 hip wear debris in 0.1 - 1um size range during early wear. A) E1 knee. Scalebar = 500nm B) E1 hip, Scalebar = 200nm. E1 hip had rounder and more compact morphology in comparison to E1 knee.

A) E1 Knee Long-term Wear

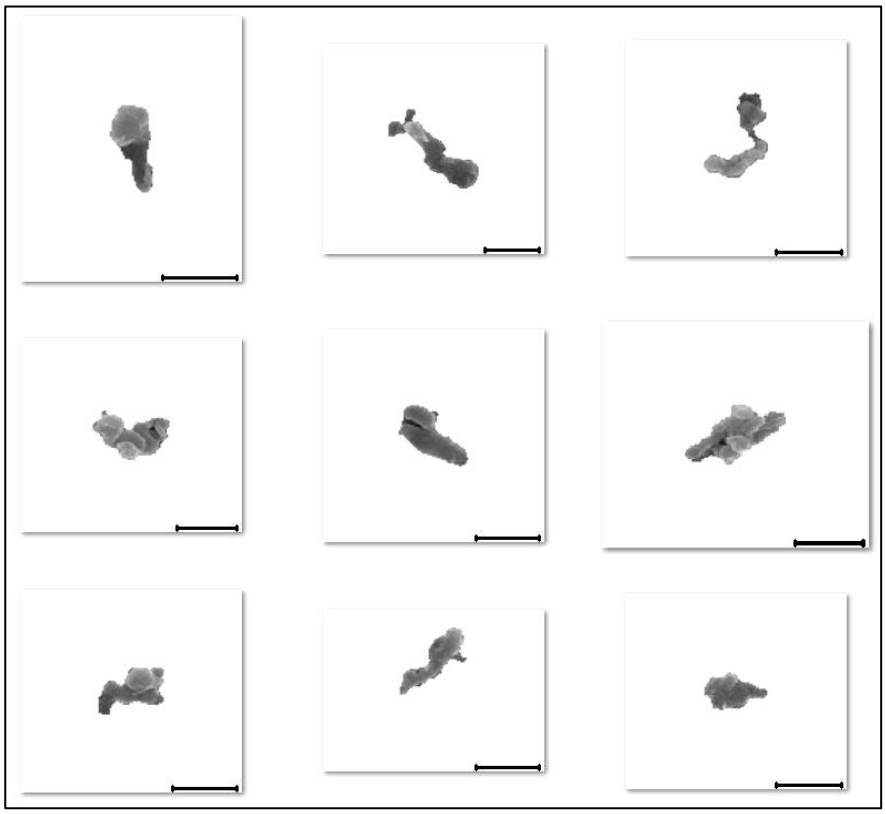

B) E1 Hip Long-term Wear

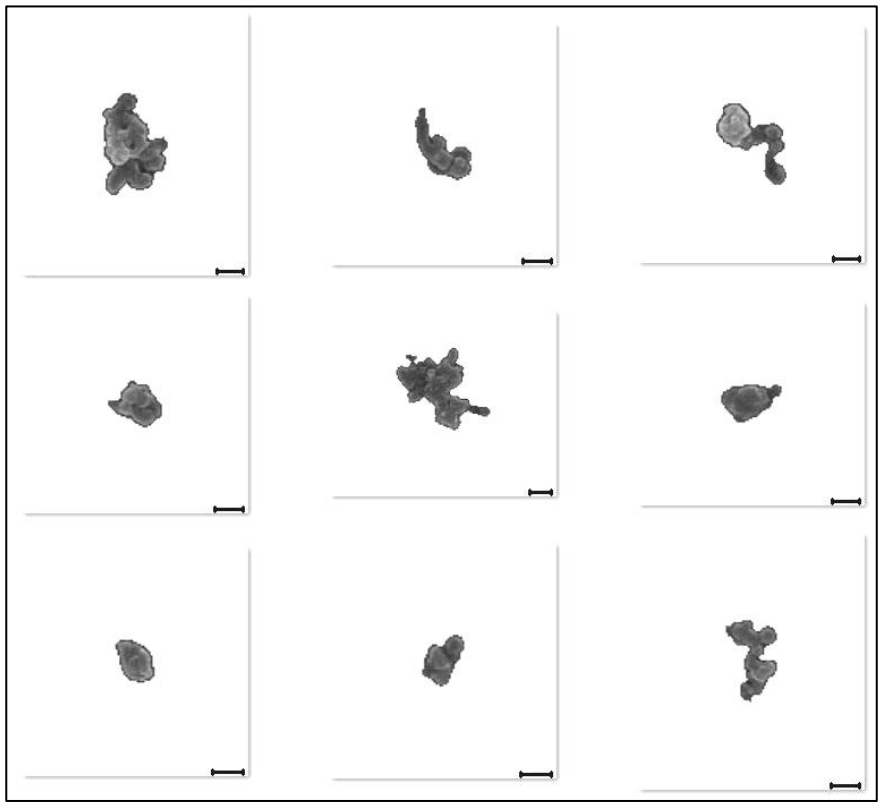

Figure 6.17 Morphology of E1 knee and E1 hip wear debris in 0.1 - 1um size range during early wear. A) E1 knee. Scalebar = 500nm B) E1 hip, Scalebar = 200nm. Both had similar morphology, except for a few more rounder particles in E1 hip.

Table 6.2 Comparisons of wear debris size and shape between different joint arthoplasties

Source	Material	Percent size less than 1µm (%)	Mean Size (µm)	AR	R	Reference
Hip tissue	UHMWPE	88	0.7	1.626 ±0.015	0.707 ±0.003	Mabrey *et al.*
Hip tissue	UHMWPE	85	0.43			Schmalzried *et al.*
Hip tissue	UHMWPE		0.72			Hirakawa *et al.* [223]
Hip, Serum	UHMWPE	≈94	Dmax - 0.9			Billi *et al.*
Hip, Serum	UHMWPE (7.5-Mrad XL)	≈98	Dmax - 0.5			Billi *et al.*
Hip, Serum	**E1 UHMWPE**	**92**	**ECD - 0.28 Dmax - 0.44**	**1.629 ±0.035**	**0.538 ±0.023**	
Knee, tissue	UHMWPE	43	1.2	1.935 ±0.015	0.612 ±0.003	Mabrey *et al.*
Knee, tissue	UHMWPE	36	1.7			Shanbhag *et al.*
Knee, tissue	UHMWPE		0.74			Hirakawa *et al.* [223]
Knee, tissue	UHMWPE	71	0.52			Schmalzried *et al.*
Knee, synovial fluid	UHMWPE	---	ECD - 0.78	2.300 ±0.220	0.397 ±0.35	Kobayashi *et al.* [222]
Knee, Serum	**ArCom UHMWPE**	**76**	**ECD - 0.37 Dmax - 0.72**	**2.064 ±0.064**	**0.413 ±0.020**	
Knee, Serum	**E1 UHMWPE**	**77**	**ECD - 0.43 Dmax - 0.79**	**1.820 ±0.065**	**0.504 ±0.028**	
Ankle, synovial fluid	UHMWPE	---	ECD - 0.81	1.570 ±0.040	0.676 ±0.03	Kobayashi *et al.* [222]
Ankle, Serum	**E1 UHMWPE**	**70**	**ECD - 0.63 Dmax - 1.23**	**1.802 ±0.058**	**0.541 ±0.022**	

A number of studies have compared wear debris generated in hip, knee and ankle joint arthoplasties as mentioned in Section 2.5.1.3.1 (page 30). A comparison between size and shape of wear debris

characterised in these studies and wear debris characterised in current study of E1 Ankle, Knee and Hip is shown in . Both had similar morphology, except for a few more rounder particles in E1 hip.

Table 6.2 Majority of the comparisons between knee and hip wear debris indicated a higher mean particle size for knee in comparison to hip. Correspondingly, in current study, wear debris from E1 knee also generated a higher mean particle size compared to E1 hip. Moreover, a higher aspect ratio in knee compared to hip was observed by Mabrey *et al.* Similarly, a higher aspect ratio was observed for E1 Knee wear debris in comparison to E1 hip. Furthermore, ankle wear particles were found to be rounder in comparison to knee by Kobayashi et al[222]. Similar pattern was found between E1 ankle and E1 knee wear debris in current study. However, the differences in aspect ratio and roundness values were relatively smaller.

Overall, this comparison demonstrates the similarity in dominant wear mechanisms responsible for generation of UHMWPE wear debris for a particular joint arthroplasty. Moreover, it validates the use of *in vitro* simulation to replicate *in vivo* wear in terms of size and shape of wear debris.

Although the general trends were similar, the actual mean size values were not similar in few cases. In several studies, it was not indicated whether the size was Feret diameter (Dmax) or equivalent circular diameter (ECD). This may have caused the differences noticed in particle size. Moreover, with the improvement in imaging technology and isolation methods, the ability to isolate and detect nanometre size wear debris has increased. This was investigated by comparing the mean Dmax of E1 hip with highly crosslinked UHMWPE (7.5-Mrad XL) in Billi *et al.* The similarity between two mean Dmax values demonstrated the comparability of the data produced in this study with literature data.

6.4.3 **E1 Multidirectional pin-on-plate vs. E1 Hip**

This section discusses the comparison between wear debris produced by E1 multidirectional pin-on-plate tester and E1 hip. The wear particle generation mechanisms of E1 hip during early wear and long-term wear have already been discussed in section 6.3.2. Therefore, this discussion would be primarily based on the size and shape differences between E1 hip and E1 multidirectional pin-on-plate wear debris.

It was noticed that overall size distribution of wear particles generated using multidirectional pin-on-plate during early wear as well as long-term wear was similar to hip particles. Majority of particles were submicron in size, with a large fraction of particles within 0 - 500 nm size (Figure 5.91, page 178 and Figure 5.100, page 185). However, mode size of wear debris generated by multidirectional pin-on-plate was slightly shifted to 250 - 500 nm in comparison to hip, where mode size of particles was 100 - 250 nm. In addition, there were very few particles larger than 5µm in multidirectional pin-on-plate samples in comparison to hip.

Concerning morphology, E1 multidirectional pin-on-plate particles were more elongated than E1 hip for all size ranges shown by higher aspect ratio/elongation and lower roundness/form factor. Moreover complexity values of these particle were lower than hip even for particles smaller than 100nm. This indicated fibrillar nature of these particles even at nanometre scales, which was confirmed by visual analysis of the wear particle morphology. A comparison between morphology of E1 multidirectional pin-on-plate and E1 hip particles smaller than 500 nm is shown in Figure 6.18.

The absence of large particles in multidirectional pin-on-plate samples could be explained by the occurrence of a combination of reciprocating and rotational movements during the test, which may have caused significant amount of cross-shear. Materials such as highly crosslinked UHMWPE have reduced chain mobility and chain stretch which lowers their ductility. It is believed that as the material was pulled by the asperities on counter surface, the crosslinked polymer got detached quickly when tensile forces acted on it. This may have caused the generation of small and more fibrillar wear particles.

A) E1 POP Long-term Wear

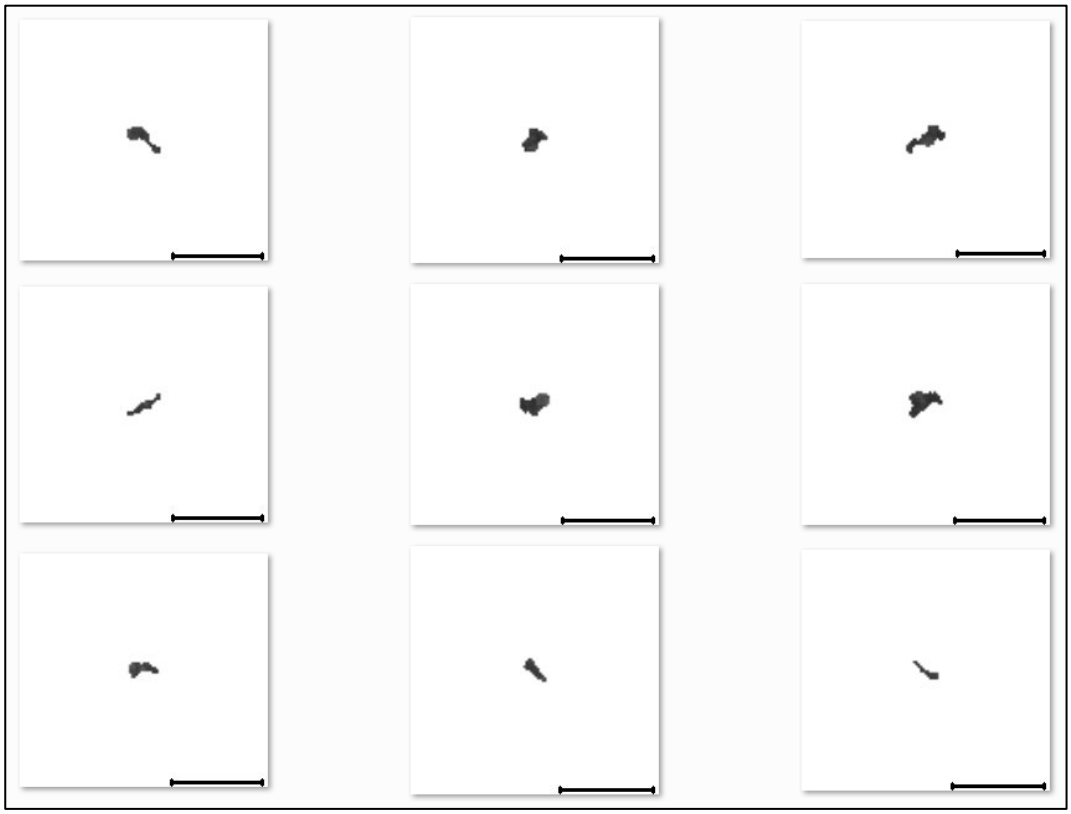

B) E1 Hip Long-term Wear

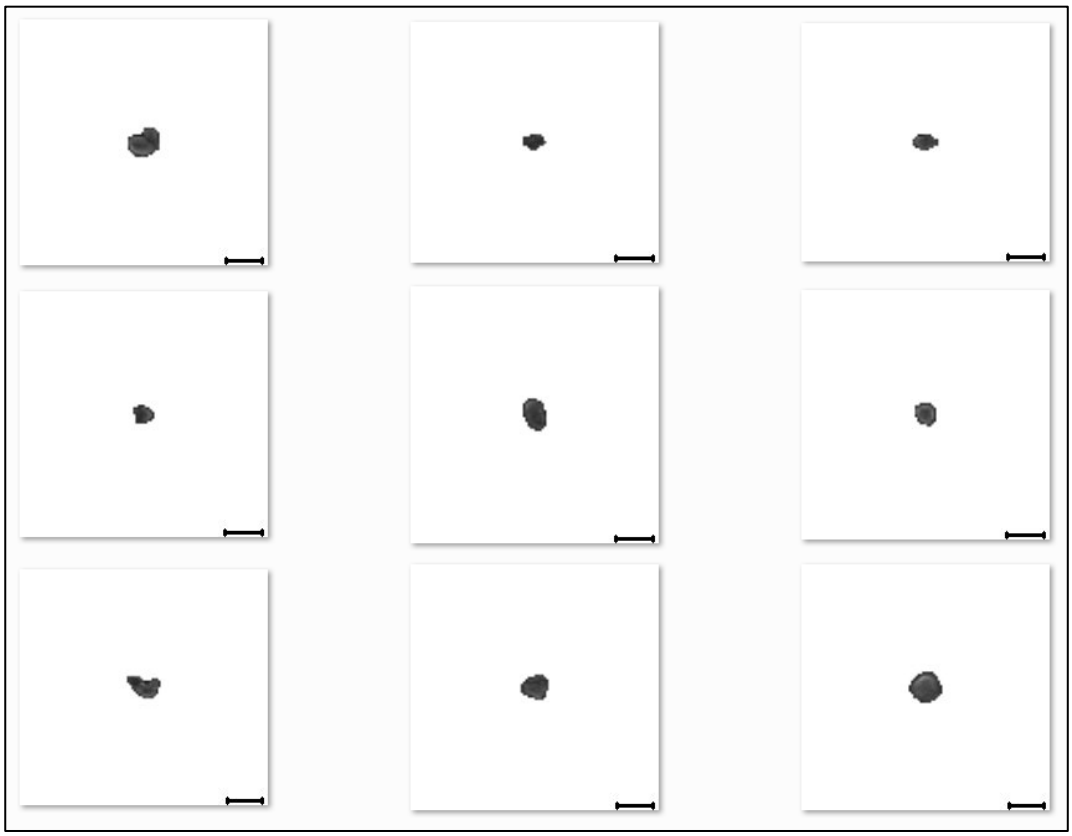

Figure 6.18 Comparison of nanometre and submicron sized E1 particles generated during long-term wear. A) Wear particles generated in multidirectional pin-on-plate. Scale = 500nm. B) Wear particles generated in hip simulator, Scale = 200nm

6.4.4 **E1 Multidirectional Pin-on-plate vs. E1 Knee**

This section discusses the comparison between size and morphology of wear debris produced by Multidirectional pin-on-plate and Knee simulator. As both E1 Knee and E1 Multidirectional pin-on-plate were discussed previously in this section, only differences between the two will be highlighted here.

During early wear, wear debris produced in knee had considerable different size distribution compared to multidirectional pin-on-plate. Particles larger than 1µm were significantly more in Knee than multidirectional pin-on-plate (Figure 5.109, page 192). However, long-term wear produced similar size distribution, except in 250 - 500 nm size range where multidirectional pin-on-plate produced significantly larger percentage of particles (≈30%).

The particle morphology of wear debris showed no significant difference between multidirectional pin-on-plate and knee. However, there were small differences in each size range. As discussed in previous comparison, multidirectional pin-on-plate produced more elongated fibrillar particles throughout all size ranges. On the other hand, knee produced elongated fibrillar particles as well as complex/elongated particles.

In terms of wear mechanisms, as previously mentioned for multidirectional pin-on-plate, adhesive/abrasive wear with significant amount of cross shear is believed to be responsible for majority of wear debris. For knee, adhesive/abrasive wear with less cross shear than multidirectional pin-on-plate as well as fatigue wear is believed to be the dominant wear mechanism.

A) E1 POP Long-term Wear

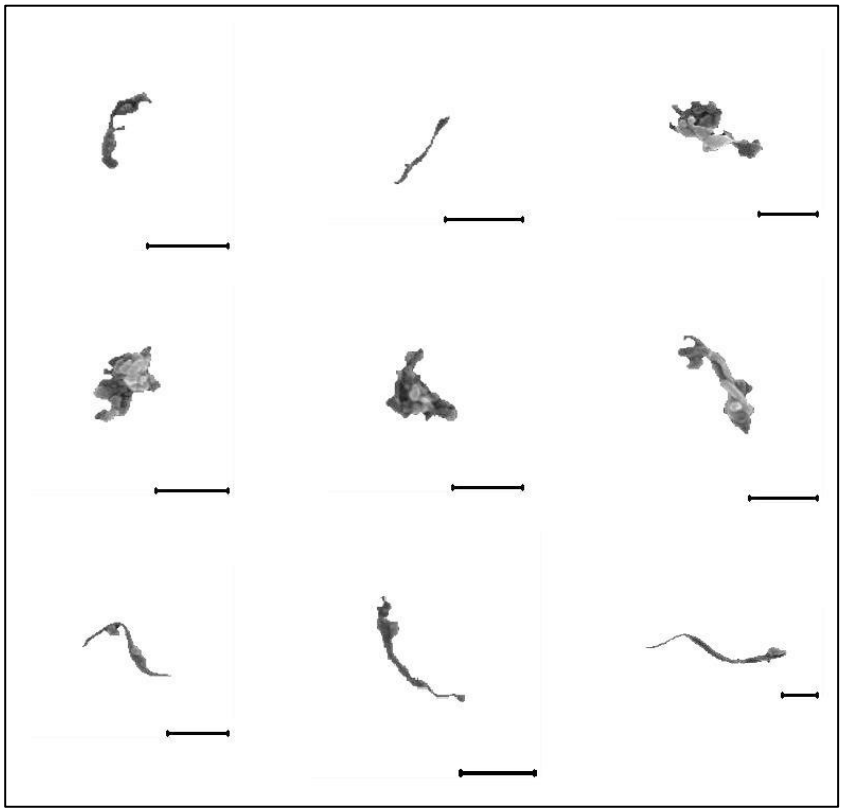

B) E1 Knee Long-term Wear

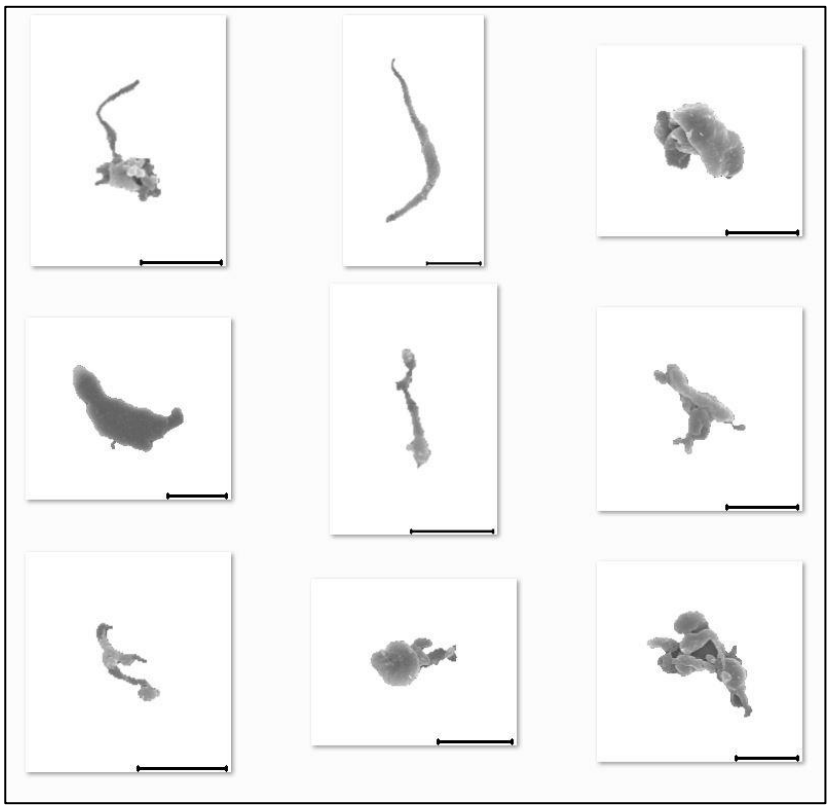

Figure 6.19 Morphology of E1 POP and E1 knee wear debris in 1 - 5 μm size range during long-term wear. A) E1 POP. Scale bar = 500nm B) E1 knee, Scale bar = 200nm.

6.5 Overall comparison of the morphology of UHMWPE particles using shape descriptors

Shape descriptors help in standardising the characterisation process. Manual interpretation of a shape could vary from one person to another, which may cause inconsistent characterisation of identical samples. Shape descriptors used in the present study characterised the particles based on their overall shape and morphological characteristics such as fibrillar, complex aggregated, flaky and granular shapes. Aspect Ratio and Roundness provided information about the overall shape of particles. Elongated particles showed higher aspect ratio values, while round particles showed higher roundness values. As the particle size increased, the presence of more elongated and fibrillar particles caused an increase in the Aspect Ratio values as shown in Figure 6.20. Roundness, on the other hand, decreased with an increase in particle size due to the decreased presence of compact round particles (Figure 6.21).

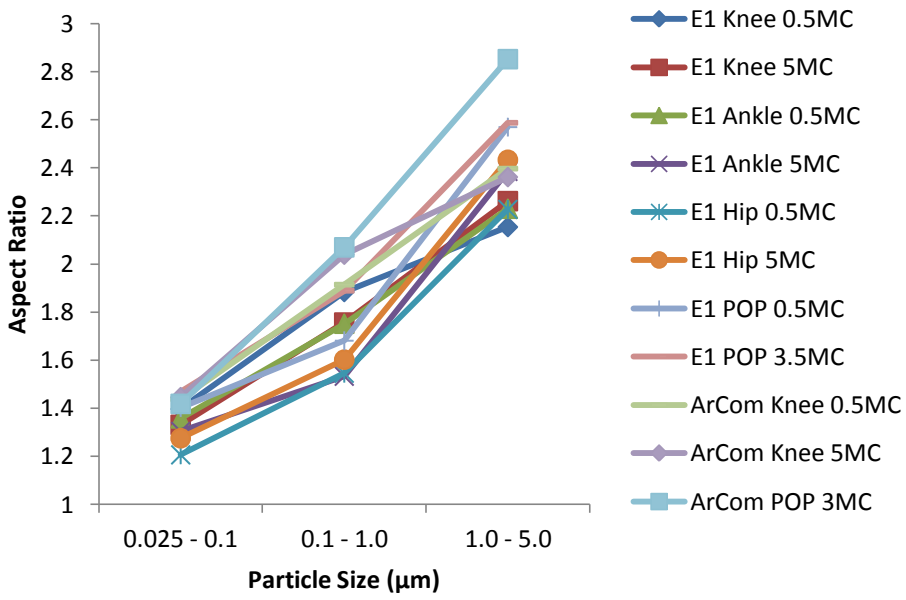

Figure 6.20 A comparison of average aspect ratio of E1 and ArCom UHMWPE wear particles generated under various test conditions in small (0.025 - 0.1 µm), medium (0.1 - 1 µm) and large (1 - 5 µm) size ranges. Average aspect ratio values increased with an increase in particle size.

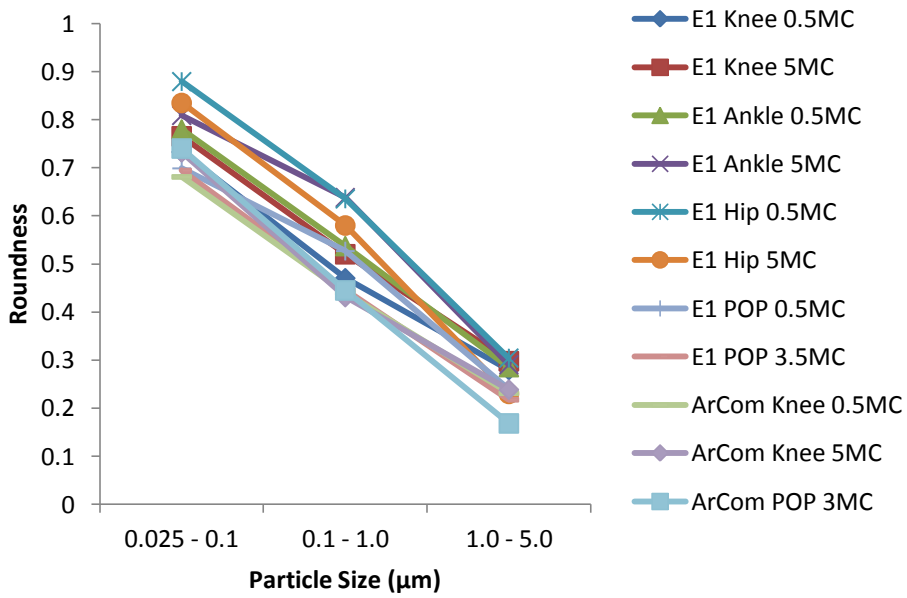

Figure 6.21 A comparison of average roundness of E1 and ArCom UHMWPE wear particles generated under various test conditions in small (0.025 - 0.1 µm), medium (0.1 - 1 µm) and large (1 - 5 µm) size ranges. Average roundness values decreased with an increase in particle size.

Form factor is more sensitive to the boundary roughness due to its dependence on particle perimeter. It is more likely to give lower values in comparison to roundness for particles with irregular boundaries. For the same reason, in present study, form factor values were marginally lower than roundness (Figure 6.22).

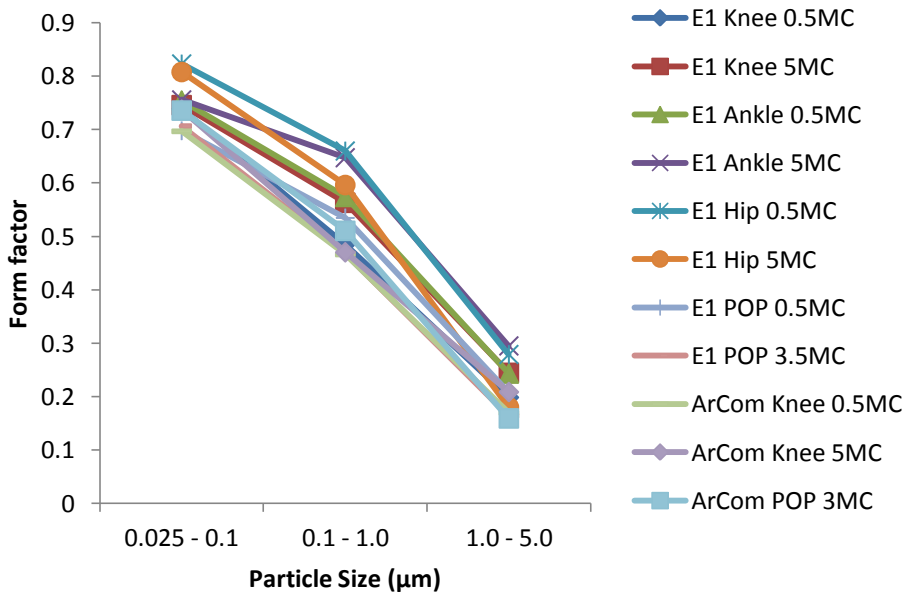

Figure 6.22 A comparison of average form factor of E1 and ArCom UHMWPE wear particles generated under various test conditions in small (0.025 - 0.1 µm), medium (0.1 - 1 µm) and large (1 - 5 µm) size ranges. Average form factor values decreased with an increase in particle size.

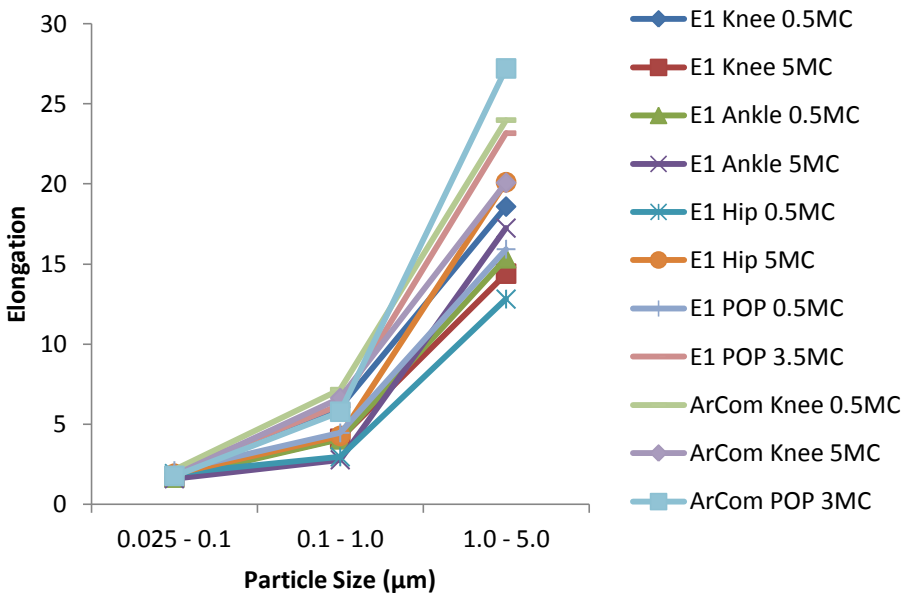

Figure 6.23 A comparison of average elongation of E1 and ArCom UHMWPE wear particles generated under various test conditions in small (0.025 - 0.1 µm), medium (0.1 - 1 µm) and large (1 - 5 µm) size ranges. Average elongation values increased with an increase in particle size. The increase in elongation was much higher for particles larger than 1 µm.

Elongation provided information about fibrillar nature of particles and higher elongation values indicated increased presence of fibrillar particles. Average elongation values for UHMWPE wear particles increased with an increase in particle size (Figure 6.23). Moreover, particles larger than 1 µm had much higher elongation values and had greater variability between the samples. This also indicated that the amount of fibrillar particles can vary significantly between the samples for large micron sized wear particles.

Compactness gives information about the compact shape of particles (Section 6.2). Compactness value is high for compact particles with smooth boundary. Average compactness value of UHMWPE wear debris decreased with an increase in particles size (Figure 6.24). This was due to the greater presence of complex fibrillar aggregates.

Complexity is useful for differentiating between simple shapes such as granules, flakes or shards, and complex shapes such as complex fibrillar and aggregated particles (Section 6.2). Complexity value is high for samples with simple shapes and low for samples with complex shapes. Unlike compactness, it is less sensitive to the roughness of particle boundary. Average complexity values of UHMWPE wear debris decreased with an increase in particle size. This indicated the higher occurrence of complex fibrillar shapes when the particle size was increased (Figure 6.25).

To summarise the above findings, the morphology of UHMWPE wear particles was different in each size range. Smaller nanoscale particles were more compact and very round, while micron

sized particles (100 - 1000 nm) were more elongated and fibrillar. Large particles with size greater than 1 µm were mostly fibrillar aggregates with complex morphologies. Very few particles were observed as single fibres, flaky, or shard-like in shape. Particles in each size range are shown in Appendix I.

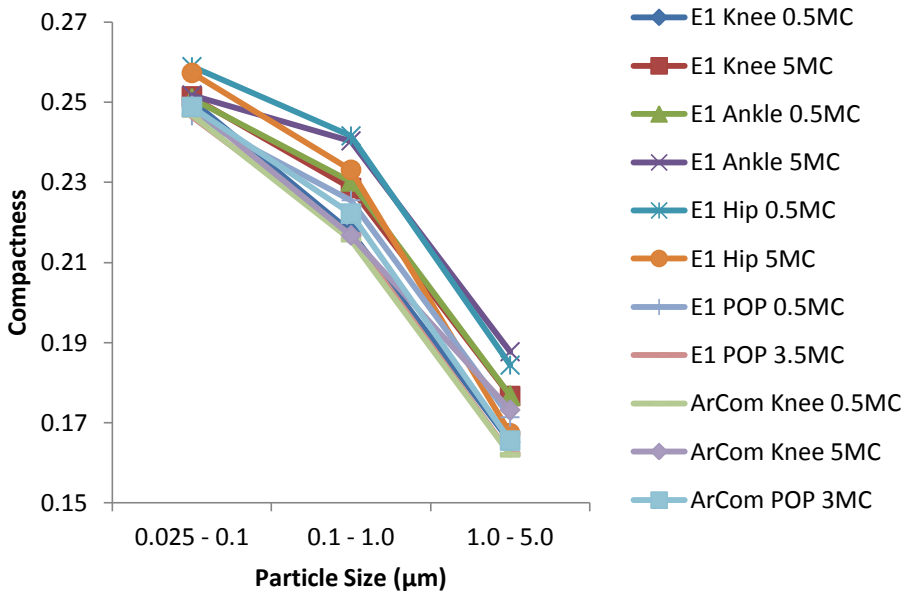

Figure 6.24 A comparison of average compactness of E1 and ArCom UHMWPE wear particles generated under various test conditions in small (0.025 - 0.1 µm), medium (0.1 - 1 µm) and large (1 - 5 µm) size ranges. Average compactness values decreased with an increase in particle size.

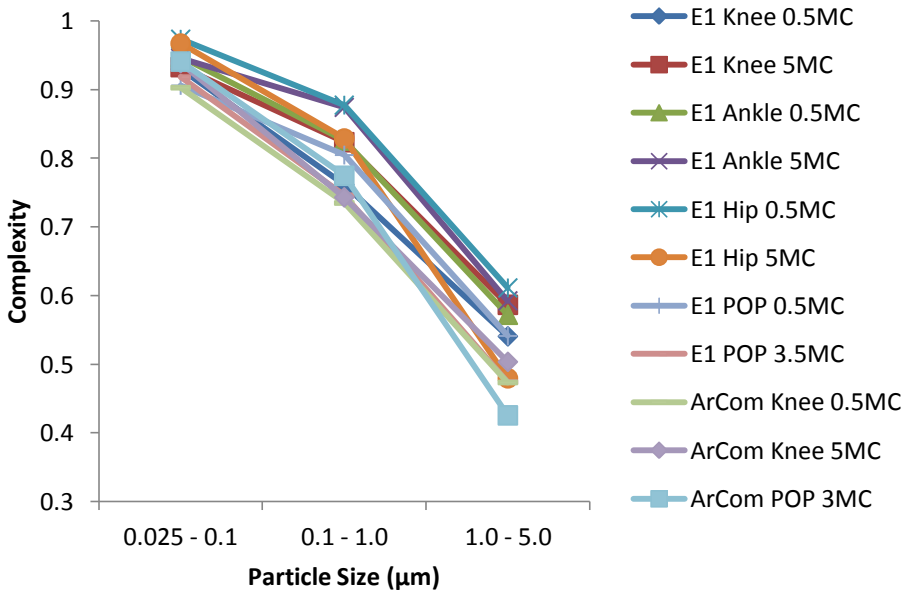

Figure 6.25 A comparison of average complexity of E1 and ArCom UHMWPE wear particles generated under various test conditions in small (0.025 - 0.1 µm), medium (0.1 - 1 µm) and large (1 - 5 µm) size ranges. Average complexity values decreased with an increase in particle size.

6.6 Summary

6.6.1 Effect of change in processing conditions of UHMWPE and addition of Vitamin E as an antioxidant on wear debris shape and size

6.6.1.1 Effect of crosslinking and addition of vitamin E by diffusion in UHMWPE

- A comparison between size distributions of ArCom and E1 showed generation of higher percentage of smaller submicron particles (size less than 250 nm) in E1, which was in agreement with previous studies comparing noncrosslinked UHMWPE to highly crosslinked UHMWPE.
- E1 wear particles were found to be less elongated and less fibrillar in comparison to ArCom. A reduction in chain mobility with crosslinking was believed to be the reason behind this difference in particle morphology.
- Adhesive/abrasive wear was predicted to be the dominant wear mechanism in knee. As the test progressed to long-term wear, a reduction in adhesive wear was predicted based on change in size and morphology of wear debris.
- A comparison between wear debris from ArCom and E1 tested under multidirectional pin-on-plate tester validated the effect of crosslinking on reduced chain mobility. ArCom generated submicron particles as well as large micron sized elongated and fibrillar particles. Conversely, E1 generated mostly submicron sized particles.

6.6.1.2 Effect of addition of vitamin E as an antioxidant by blending instead of diffusion in UHMWPE

- Wear debris generated by hip simulator testing of vitamin E blended highly crosslinked ECiMa and E1 hip testing of vitamin E diffused E1 were compared for size and morphology.
- ECiMa was found to generate larger sized particles in comparison to E1. Moreover, particles larger than 1 micron were found to be more fibrillar in ECiMA in comparison to E1. In addition, very large particles with flake-like or irregular morphology were noticed, suggesting fatigue and delamination wear in ECiMa during long-term wear.
- Higher ductility and higher elongation to break values of ECiMa in comparison to highly crosslinked UHMWPE was suggested as the reason behind generation of more elongated and fibrillar wear particles.

6.6.1.4 Effect of change in moulding temperature of direct compression moulded (DCM) UHMWPE

- Wear debris generated in multidirectional pin-on-plate testing of DCM UHMWPE moulded at 145°C and 175°C were compared for size and morphology.
- No difference in size and morphology was observed.
- The mechanism of wear in both samples was believed to be cross shear induced adhesive/abrasive wear.

6.6.2 Effect of the type of joint simulation on wear debris size and morphology

6.6.2.1 Comparison of E1 wear debris generated by artificial knee and ankle simulation

- Overall size and morphology of wear debris was similar for both ankle and knee, in agreement with literature.
- During long-term wear, ankle generated a higher number of compact and round wear debris in 500 - 750 nm size range. Fatigue wear was the suggested wear mechanism for these particles.
- A marginally higher number of particles larger than 2 µm were noticed for ankle in comparison to knee. Adhesive wear in combination with fatigue and delamination were considered as the dominant wear mechanisms for these large particles.
- Particles smaller than 500nm in both hip and knee were believed to be generated by adhesive/abrasive wear.

6.6.2.2 Comparison of E1 wear debris generated by artificial knee and hip simulation

- E1 hip generated predominantly submicron sized particles, with majority of particles in 100 - 500 nm size range. Knee generated submicron as well as large micron sized particles. Therefore, on the whole, knee generated particles larger than E1 hip, which was in agreement with previous studies.
- E1 hip submicron particles had marginally rounder morphology in comparison to knee.
- During early wear, microabrasion and adhesion were believed to be the primary wear mechanisms, with majority of wear generated by microabarasion. During long-term wear adhesion was suggested as dominant wear mechanism and microabrasion as second dominant wear mechanism.

6.6.2.4 Comparison of E1 wear debris generated by multidirectional pin-on-plate simulation and artificial hip simulation

- Overall size distribution of both multidirectional pin-on-plate and E1 hip was similar with over 90% particles submicron in size and majority of particles (over 50%) in 0 - 500 nm size range. Moreover, very few particles larger than 5µm in Multidirectional pin-on-plate samples in comparison to E1 hip.
- Multidirectional pin-on-plate generated more elongated and fibrillar particles in comparison to E1 hip, including nanofibrillar particles.
- Significant amount of cross shear in combination with adhesion was believed to cause generation of fibrillar and elongated particles in multidirectional pin-on-plate.

6.6.2.5 Comparison of E1 wear debris generated by multidirectional pin-on-plate simulation and artificial knee simulation

- Wear debris generated in multidirectional pin-on-plate was submicron in size, while knee generated submicron particles as well as large particles with size over 1 micron.
- Particle morphology was elongated fibrillar for multidirectional pin-on-plate. Knee wear debris was elongated fibrillar as well as complex elongated.
- Elongated and fibrillar particles in multidirectional pin-on-plate were believed to be generated by cross shear induced adhesive wear.
- Round and compact shaped submicron particles were believed to be produced by microabrasive wear in both multidirectional pin-on-plate and knee.

6.7 **Limitations**

Wear particles characterised in this study were generated in artificial joint simulators. Although, *in vitro* wear testing was designed to replicate the *in vivo* articulation and bearing lubrication, it might not have entirely represented the characteristics of wear debris produced *in vivo*.

Particle isolation method developed in current study was assumed to recover the entire particle size range of UHMWPE wear debris. However, particles might have been lost during the isolation process. Scanning electron microscopy was used to image wear particles. As this is a two dimensional imaging method, no information about particle volume or particle morphology in 3D was available. In addition, particles smaller than 25nm were not included for analysis to avoid any potential errors associated with calculation of size and shape descriptors.

The volumetric wear rate data of the wear tests that generated particles isolated and characterised in the present study was not accessible. Therefore, particle size distributions were reported as percentage number (frequency) and volumetric wear data from literature was used for comparison of implant wear between different bearing materials and joint simulations.

Despite great efforts to disperse the UHMWPE particles prior to SEM imaging, there might have been a possibility of particle aggregation. Analysis of agglomerated particles as single particles might bias the size distribution towards larger particles and could also change the values of shape descriptors.

The prediction of wear mechanisms was based on size and shape of wear debris and information available in literature. Since wear and generation of wear debris is a complex process, the wear mechanisms proposed here may not fully represent the real wear debris generation scenario.

Chapter 7 - **Conclusions**

The novel UHMWPE isolation method presented in this thesis and the custom software developed for detailed particle characterisation have made it possible to analyse size and morphology of wear particles isolated from joint simulator testing of current state-of-the-art crosslinked and non-crosslinked UHMWPE implants.

This is the first study ever:

- To carry out detailed wear debris analysis by using custom software with an ability to access a range of size and shape descriptors, along with visual image of each individual particle. This helped in identifying key differences in size and morphology, which gave insights into the fundamental wear mechanisms behind the generation of wear particles.
- To compare the wear debris characteristics of gold standard direct compression moulded UHMWPE with the latest generation vitamin E diffused UHMWPE and further compared wear debris characteristics of vitamin E blended ECiMa and vitamin E diffused E1 UHMWPE.
- To compare vitamin E diffused E1 UHMWPE wear debris produced by all primary artificial joint articulations i.e. ankle, knee and hip in a single study. Moreover, it gave insights into the effect of type of articulations on size and morphology of wear debris.
- To compare the size and morphology of wear debris generated during early wear as well as long-term wear. This helped in identifying key changes in wear characteristics and wear mechanisms with the progression of the test.

Key findings:

- UHMWPE is known to produce predominantly submicron sized particles [25], [169], [185], [216]. Wear particles in the current study were found to be predominantly submicron in size for all variants of UHMWPE isolated and characterised in this thesis.
- The morphology of UHMWPE wear debris was similar to the morphology reported in literature. Submicron particles mainly consisted of granular, fibrillar, bead-like, complex fibrillar and irregular elongated shapes. Particles larger than 1 micron mainly consisted of complex fibrillar particles. A few particles also had irregular elongated, large flaky and shard-like shapes.

- Cross-linking was found to reduce the size of UHMWPE wear debris. Noncrosslinked UHMWPE generated more elongated and fibrillar wear debris due to higher chain mobility and higher elongation to break. Alternatively, highly crosslinked UHMWPE generated less elongated and more compact particles.
- Wear particles in knee were primarily generated by adhesive/abrasive wear. During long-term wear, a reduction in adhesive wear was predicted based on change in size and morphology of wear debris.
- ECiMa generated more elongated/fibrillar and larger sized particles in comparison to E1. The reason behind above differences was believed to be higher ductility and higher elongation to break due to reduced crosslinking efficiency in vitamin E blended ECiMa.
- DCM UHMWPE moulded at 175°C and DCM UHMWPE moulded at 145°C showed no changes in similar size and morphology. Therefore, it is believed that fusion defects do not influence any change in particle size and morphology.
- Overall size and morphology of wear particles generated in ankle and knee were found to be similar. Both generated submicron as well as large micron sized particles. Adhesive/abrasive wear was believed to be the dominant wear mechanism. In ankle, the presence of compact and round particles during long-term wear was believed to be caused by fatigue wear. The presence of a marginally higher number of very large particles (size above 4μm) was also indicative of fatigue wear.
- E1 hip generated predominantly submicron sized particles, while knee generated submicron as well as large micron sized particles. Moreover, E1 hip submicron particles had marginally rounder morphology in comparison to knee. During early wear, microabrasion and adhesion were believed to be the primary wear mechanisms in hip, with majority of wear generated by microabarasion. During long-term wear adhesion was suggested as dominant wear mechanism and microabrasion as second dominant wear mechanism.
- Multidirectional pin-on-plate and E1 hip generated predominantly submicron sized particles. Multidirectional pin-on-plate generated more elongated and fibrillar particles in comparison to E1 hip. Some of these particles were observed as nanofibrillar particles. Significant amount of cross shear in combination with adhesion was believed to cause generation of fibrillar and elongated particles in multidirectional pin-on-plate.

Future Impact

- Second-generation vitamin E containing UHMWPE such as E1 and ECiMa were developed to overcome oxidative degradation after implantation and to reduce wear. E1 has been in clinical use since its introduction in 2007 for knee and hip. Although *in vitro* work and *in vivo* animal studies have demonstrated good biocompatibility and reduced inflammation with these materials [5], [6], there is no direct method to measure the *in vivo*

compatibility of these new generation implants in patients. Therefore, extensive *in vitro* assessment of the performance and compatibility of these implants is of utmost importance. Current study characterised wear debris produced in different joints and gave insights into the wear characteristics of these latest generation materials.

- The wear debris size and morphology results obtained in this thesis have potential to provide insights into future *in vitro* biological evaluations and *in vivo* performance of these state-of-the-art joint implants.
- Scanning electron microscopy in combination with image analysis is a powerful tool to analyse materials from nanoscale to microscale. The image analysis methodologies developed in this thesis could be potentially used in a number of areas involving particle characterisation.

Future Work

This thesis isolated and characterised UHMWPE wear debris from serum lubricants used in artificial joint simulators and multidirectional pin-on-plate tester under standard testing conditions. Isolation and analysis of wear debris from periprosthetic tissue samples would facilitate a comparison between particle size and morphology of wear debris produced *in vitro* and *in vivo*. This would allow a direct assessment of artificial joint simulation for production of clinically relevant wear debris. In addition, analysis of wear debris produced by more realistic artificial testing of implants would help in assessment and development of novel joint simulation techniques.

Biological activity evaluations in the following topics would be valuable for assessing the clinical performance of UHMWPE.

- Differences in the biological activity between early wear and long-term wear of UHMWPE.
- Influence of the type of articulation on biological activity of E1 UHMWPE by comparing wear particles generated in hip, knee and ankle.
- Studies have shown the positive effects of vitamin E on reduction of inflammation and osteolysis (Section 2.6.2, page 38). Present study compared wear debris generated by vitamin E diffused E1 UHMWPE and vitamin E blended ECiMa UHMWPE. Effect of addition of Vitamin E by diffusion and blending on biological activity of UHMWPE could be further investigated.
- Influence of UHMWPE wear debris size and shape on its biological activity. Methods already exist for separation of particles by size using membrane filtration. Separation of particles by shape is a challenging area and needs further development.

Isolation and characterisation of wear particles from novel implant materials such as latest generation ceramics, surface engineered ceramic coatings and polymer composites would allow further insight into wear characteristics and associated biological activity of these materials.

Appendices

Appendix I - UHMWPE Wear Debris Morphologies

This section has a compilation of the particle morphologies observed in polymeric particles isolated from wear testing of UHMWPE-on-metal implants using knee, ankle and hip joint simulators.

UHMWPE ArCom Knee 0.5MC			
0 – 0.1µm (Scale = 200nm)	0.1 - 1µm (Scale = 500nm)	1- 5µm (Scale = 1µm)	5 - 10µm (Scale = 2µm)
			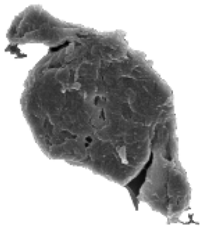
			
			
			

UHMWPE ArCom Knee 4.5MC			
0 – 0.1µm (Scale = 200nm)	0.1 - 1µm (Scale = 500nm)	1- 5µm (Scale = 1µm)	5 - 10µm (Scale = 2µm)
			
			
			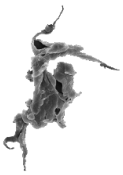
			

UHMWPE E1 Knee 0.5MC			
0 – 0.1µm (Scale = 200nm)	0.1 - 1µm (Scale = 500nm)	1- 5µm (Scale = 1µm)	5 - 10µm (Scale = 2µm)
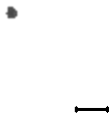			
			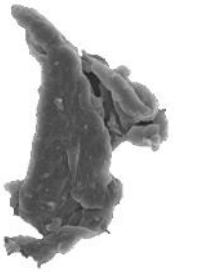
			
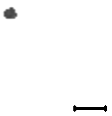			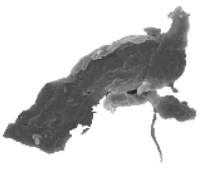

UHMWPE E1 Knee 5MC			
0 – 0.1µm (Scale = 200nm)	0.1 - 1µm (Scale = 500nm)	1- 5µm (Scale = 1µm)	5 - 10µm (Scale = 2µm)
		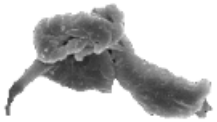	
		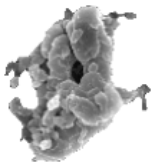	
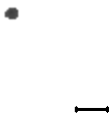			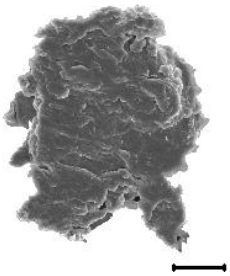
			

UHMWPE E1 Ankle 0.5MC			
0 – 0.1µm (Scale = 200nm)	0.1 - 1µm (Scale = 500nm)	1- 5µm (Scale = 1µm)	5 - 10µm (Scale = 2µm)
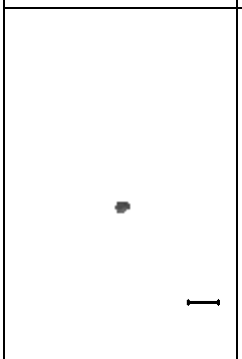			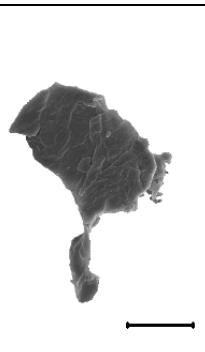
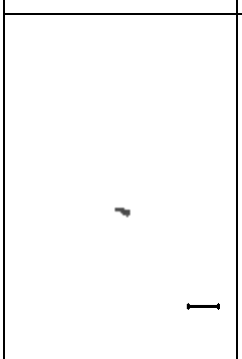			
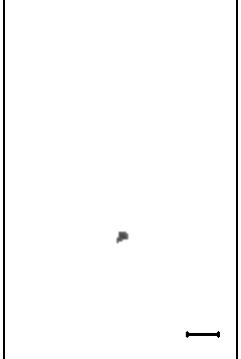		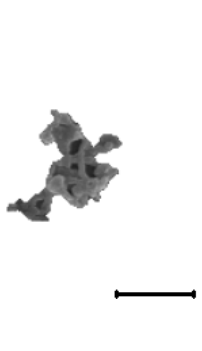	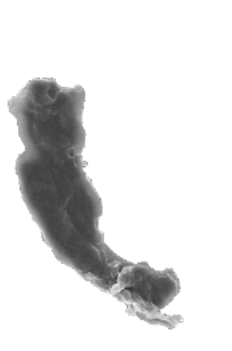
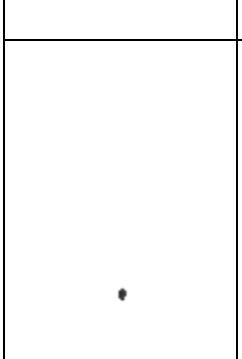			

UHMWPE E1 Ankle 5MC			
0 – 0.1µm (Scale = 200nm)	0.1 - 1µm (Scale = 500nm)	1- 5µm (Scale = 1µm)	5 - 10µm (Scale = 2µm)
			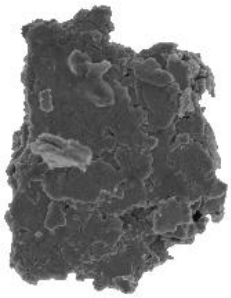
			
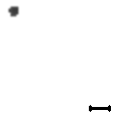			
		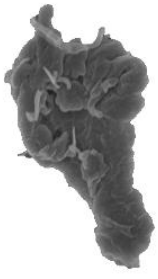	

UHMWPE E1 Hip 0.5MC			
0 – 0.1µm (Scale = 200nm)	0.1 - 1µm (Scale = 500nm)	1- 5µm (Scale = 1µm)	5 - 10µm (Scale = 2µm)
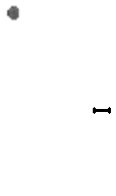		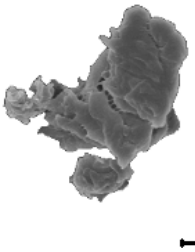	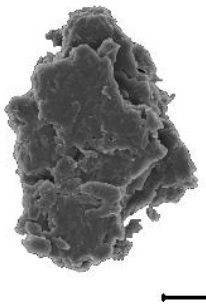
			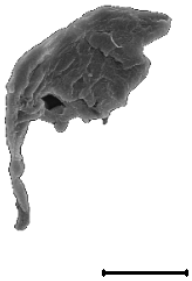
			
			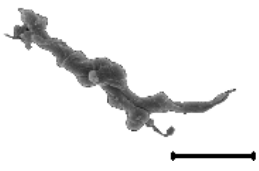

UHMWPE E1 Hip 5MC			
0 – 0.1µm (Scale = 200nm)	0.1 - 1µm (Scale = 500nm)	1- 5µm (Scale = 1µm)	5 - 10µm (Scale = 2µm)
			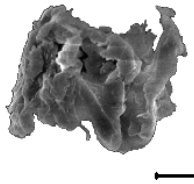
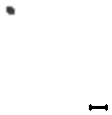			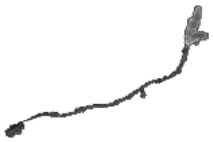
			
			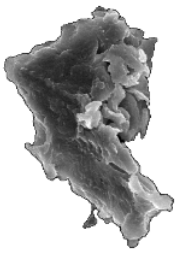

Appendix II Particle isolation protocol

Modified base digestion method

Part A - Serum Digestion

Duration: 2 days

1. Frozen serum is taken out of the freezer and thawed out at room temperature.
2. The serum is mixed well with mechanical motion as well as a using a 25ml pipette until visibly homogeneous. (Note: It is important for the serum to be homogeneous to have a representative sub sample)
3. The serum sample is taken in the multiples of 25ml. In present case, we take out 75ml in total (3x25ml).
4. Each 25ml sample is stored in a 50ml falcon tube.
5. 7 grams of KOH pellets are added to each tube to make 5M KOH solution in individual tubes.
6. All the falcon tubes are put together in a rack and placed in a closed water bath with temperature set to 60°C.
7. After 24 hours, the falcon tubes are vortexed, sonicated (10 minutes) and vortexed consecutively.
8. The tubes are then digested again in water bath at 60°C for further 24 hours.
9. At the end of digestion, the tubes are taken out and cooled down at room temperature.
10. The tubes are again vortexed, sonicated (10 minutes) and vortexed consecutively and used immediately for centrifugation or stored at room temperature.

Part B - Particle Concentration

Duration: 4 Hours

1. Make sure the 50ml falcon tubes are vortexed, sonicated (10 minutes) and vortexed consecutively before moving further.
2. Beckman Optiseal Polyallomer 32.4ml tubes (Item No:361625 at www.beckmancoulter.com) are used for centrifugation.
3. These tubes are used with a black rubber seal in order to confine the basic KOH solution inside the tubes.
4. Tube spacers are used on top of each tube to fit them securely inside the buckets.
5. SW32Ti or SW28 rotor can be used for centrifugation of samples. Both rotors along with their buckets are located in the cold room next to centrifuge room in Biology.
6. Since a total of 6 samples can be centrifuged together, we used 3 particle and 3 control samples.

7. 25ml of the digested serum is pipetted out of each falcon tube and put into each Optiseal tube.
8. The weight of each tube is measured after step 7 to make sure they have equal weight.
9. 2ml of 50nm filtered ultrapure water is carefully layered on top of the serum digest for each tube.
10. 0.90 gm/ml isopropanol is layered on top of water up to the base of the neck as shown in the Figure 0.1.

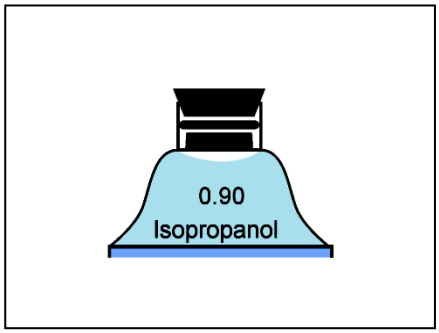

Figure 0.1 Top section of the Optiseal tube

11. Make sure the inner surface of the neck of tube is dry by wiping any drops of liquid using a tissue.
12. The rubber seal is secured on each tube as shown in Figure 1.
13. Tubes are placed in their respective rotor buckets with the matching numbers.
14. Tube spacers are placed on top of each tube.
15. Each bucket is closed with its cap making sure the numbers match.
16. **The weight of each tube is checked to make sure they have identical weight. (Note: It is essential for proper distribution of weight during the centrifugation).**
17. For SW32Ti rotor - The rotor is placed inside the centrifuge first and then the buckets are put inside each slot with matching numbers.
18. For SW28 - The buckets are carefully attached to the rotor at the correct position with matching numbers. Then the rotor is placed carefully inside the centrifuge.
19. The samples are centrifuged at 32000 rpm (For SW32Ti) or 27000rpm (For SW28) for 4 hours at 15°C.
20. After centrifugation the Optiseal tubes are taken out of the buckets.
21. The rubber seals are carefully taken out by hands. In case the rubber seal is stuck, wait for few minutes and it will loosen up.
22. The concentrated particles can be seen as white layer between isopropanol layer and brownish yellow serum layer.
23. The concentrated particles are taken out using a sterile pasteur pipette and stored in 15ml tubes.

24. For each tube approximately 5-6ml of particle concentrate is taken out from the isopropanol-serum interface.
25. The 15ml tubes are stored at room temperature.

Part C - Particle Isolation

Duration 4 hours

1. The concentrated serum obtained from Part B is vortexed, sonicated (10 minutes) and vortexed consecutively.
2. Equal volume of 50nm filtered ultrapure water is added to each tube containing serum concentrate to dilute it by a factor of 2.
3. The diluted particle concentrate is then vortexed, sonicated (10 minutes) and vortexed consecutively until the solutions are visibly homogeneous.
4. Beckman SW41 rotor is used for centrifugation in this part.
5. Beckman Open-Top Thinwall Polyallomer 13.2ml tubes (Item No: 331372 at www.beckmancoulter.com) are used inside the rotor buckets.
6. 5ml of the particle concentrate obtained after step 3 is pipetted into the bottom of each tube.
7. 2ml of 0.98gm/ml isopropanol is carefully layered on top of particle concentrate layer.
8. 2ml of 0.96gm/ml isopropanol is carefully layered on top of 0.98gm/ml layer.
9. Finally 0.90gm/ml isopropanol is carefully layered on top of 0.96gm/ml layer until the tube is filled to the brim (meniscus just covering the "Beckman" imprinted on top of the tube).
10. The buckets are carefully attached to the rotor at the correct position with matching numbers. Then the rotor is placed carefully inside the centrifuge.
11. **The weight of each tube is checked to make sure they have identical weight. (Note: It is essential for proper distribution of weight during the centrifugation).**
12. The samples are centrifuged at 40000 rpm for 4 hours at 15°C.
13. At the end of centrifugation the rotor is taken out carefully and the tubes are carefully placed in a rack.
14. The pure UHMWPE particles can be seen as a faint white banding between 0.90gm/ml and 0.96gm/ml layer.
15. The pure UHMWPE particles are taken out using a sterile Pasteur pipette and stored in sterile 15ml tubes. Approx. 3ml of particle solution is obtained from each tube.
16. The tubes are vortexed, sonicated (10 minutes) and vortexed consecutively and used immediately or stored in the fridge.

Appendix III

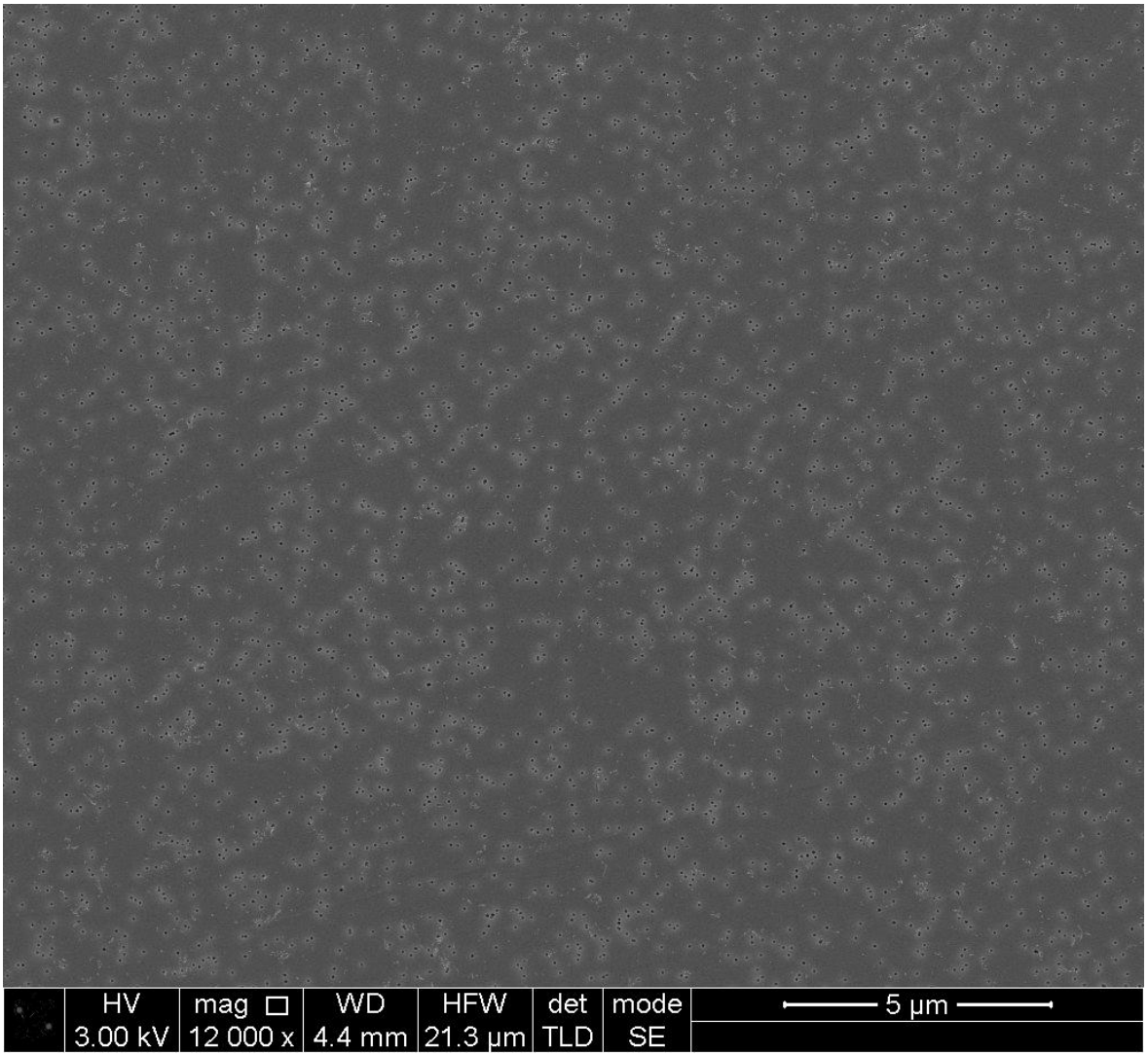

Figure 8.0.2 Scanning electron micrograph of 50nm pore size membrane filter without particles. Bright circular visual artifacts surrounding the pores were produced during imaging.

Appendix IV

Figure 8.0.3 Radiological zones of Gruen and DeLee[12]

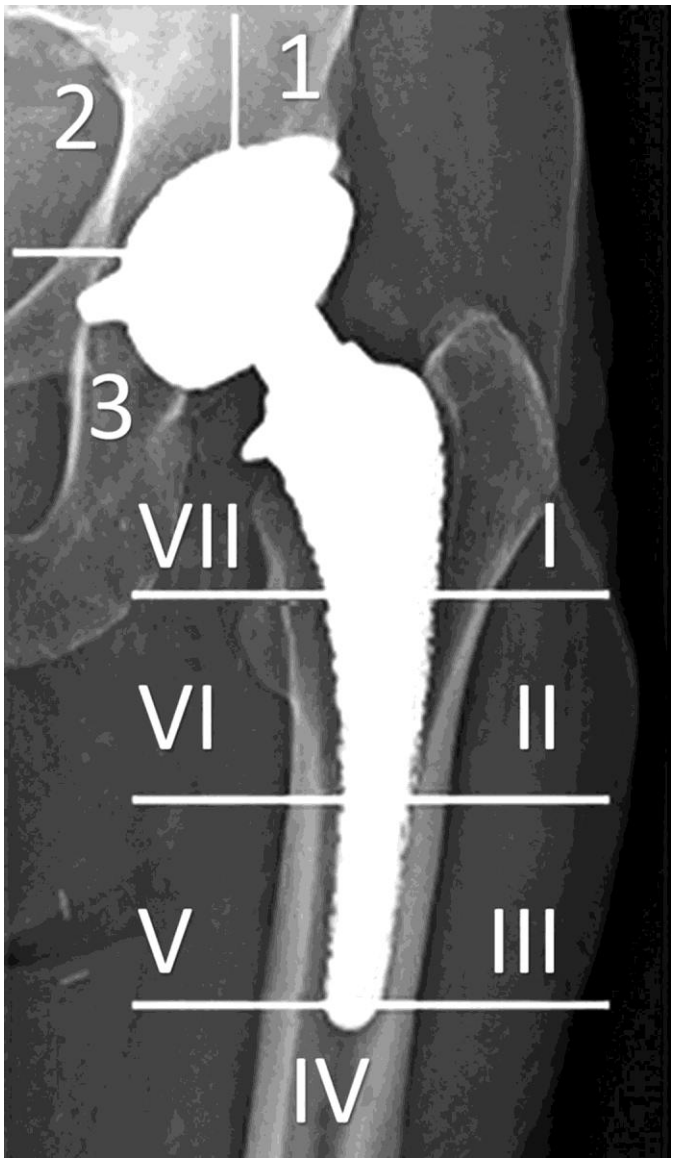

[12] J Bone Joint Surg Am, 2011 Jun 01; 93 (11): 1039 -1044 . http://dx.doi.org/10.2106/JBJS.I.01757

References

[1] Laura Helmuth, “Why Are You Not Dead Yet?,” *Slate*, 2013.

[2] G. Labek, M. Thaler, W. Janda, M. Agreiter, and B. Stöckl, “Revision rates after total joint replacement: cumulative results from worldwide joint register datasets.,” *J. Bone Joint Surg. Br.*, vol. 93, no. 3, pp. 293–7, Mar. 2011.

[3] I. S. Vanhegan, a K. Malik, P. Jayakumar, S. Ul Islam, and F. S. Haddad, “A financial analysis of revision hip arthroplasty: the economic burden in relation to the national tariff.,” *J. Bone Joint Surg. Br.*, vol. 94, no. 5, pp. 619–23, May 2012.

[4] O. Muratoglu and S. M. Kurtz, “Hip replacement: current trends and controversies,” *New York Marcel Dekker*, pp. 1 – 46, 2002.

[5] D. A. Bichara, E. Malchau, N. H. Sillesen, S. Cakmak, G. P. Nielsen, and O. K. Muratoglu, “Vitamin E-diffused highly cross-linked UHMWPE particles induce less osteolysis compared to highly cross-linked virgin UHMWPE particles in vivo.,” *J. Arthroplasty*, vol. 29, no. 9 Suppl, pp. 232–7, Sep. 2014.

[6] C. L. Bladen, S. Teramura, S. L. Russell, K. Fujiwara, J. Fisher, E. Ingham, N. Tomita, and J. L. Tipper, “Analysis of wear, wear particles, and reduced inflammatory potential of vitamin E ultrahigh-molecular-weight polyethylene for use in total joint replacement.,” *J. Biomed. Mater. Res. B. Appl. Biomater.*, vol. 101, no. 3, pp. 458–66, Apr. 2013.

[7] S. M. Kurtz, *UHMWPE Biomaterials Handbook*. 2009.

[8] G. K. McKee and J. Watson-Farrar, “Replacement of arthritic hips by the McKee-Farrar prosthesis.,” *J. Bone Joint Surg. Br.*, vol. 48, no. 2, pp. 245–59, May 1966.

[9] P. A. Ring, “Complete replacement arthroplasty of the hip by the ring prosthesis.,” *J. Bone Joint Surg. Br.*, vol. 50, no. 4, pp. 720–31, Nov. 1968.

[10] P. S. Walker and B. L. Gold, “The tribology (friction, lubrication and wear) of all-metal artificial hip joints,” *Wear*, vol. 17, no. 4, pp. 285–299, Apr. 1971.

[11] M. Kothari, D. Bartel, and J. Booker, “Surface geometry of retrieved McKee-Farrar total hip replacements.,” *Clin. Orthop. Relat. Res.*, vol. 329, pp. S141–S147, 1996.

[12] J. Charnley, “Long Term Results of Low Friction Arthroplasty of Hip as Primary Intervention,” *J. Bone Jt. Surg.*, vol. 54, pp. 61 – 76, 1972.

[13] “NIH Consens Statement: Total Hip Replacement,” in *National Institutes of Health Technology Assessment Conference*, pp. 12(5):1–31.

[14] T. Shikata, H. Oonishi, and Y. Hashimato, “Wear resistance of irradiated UHMW polyethylenes to Al2O3 ceramics in total hip prosthesis,” *Trans 3rd Annu Meet Soc Biomater*, p. 118, 1977.

[15] F. Higuchi, A. Inoue, and M. Semlitsch, “Metal-on-metal CoCrMo McKee-Farrar total hip arthroplasty: characteristics from a long-term follow-up study.,” *Arch. Orthop. Trauma Surg.*, vol. 116, no. 3, pp. 121–4, Jan. 1997.

[16] S. A. Jacobsson, K. Djerf, and O. Wahlström, “A comparative study between McKee-Farrar and Charnley arthroplasty with long-term follow-up periods.,” *J. Arthroplasty*, vol. 5, no. 1, pp. 9–14, Mar. 1990.

[17] H. C. Amstutz, P. Campbell, H. McKellop, T. P. Schmalzreid, W. J. Gillespie, D. Howie, J. Jacobs, J. Medley, and K. Merritt, “Metal on metal total hip replacement workshop consensus document.,” *Clin. Orthop. Relat. Res.*, no. 329 Suppl, pp. S297–303, Aug. 1996.

[18] D. R. Boardman, F. R. Middleton, and T. G. Kavanagh, “A benign psoas mass following metal-on-metal resurfacing of the hip.,” *J. Bone Joint Surg. Br.*, vol. 88, no. 3, pp. 402–4, Mar. 2006.

[19] R. A. E. Clayton, I. Beggs, D. M. Salter, M. H. Grant, J. T. Patton, and D. E. Porter, “Inflammatory pseudotumor associated with femoral nerve palsy following metal-on-metal resurfacing of the hip. A case report.,” *J. Bone Joint Surg. Am.*, vol. 90, no. 9, pp. 1988–93, Sep. 2008.

[20] F. W. Gruber, A. Böck, S. Trattnig, F. Lintner, and P. Ritschl, “Cystic lesion of the groin due to metallosis: a rare long-term complication of metal-on-metal total hip arthroplasty.,” *J. Arthroplasty*, vol. 22, no. 6, pp. 923–7, Sep. 2007.

[21] H. Pandit, S. Glyn-Jones, P. McLardy-Smith, R. Gundle, D. Whitwell, C. L. M. Gibbons, S. Ostlere, N. Athanasou, H. S. Gill, and D. W. Murray, “Pseudotumours associated with metal-on-metal hip resurfacings.,” *J. Bone Joint Surg. Br.*, vol. 90, no. 7, pp. 847–51, Jul. 2008.

[22] N. J. Registry, “National Joint Registry for England and Wales: 4th Annual report,” 2007.

[23] D. Synthes, “DePuy ASR™ Hip Recall,” 2010. [Online]. Available: http://www.depuysynthes.com/asrrecall.

[24] T. R. Green, J. Fisher, M. Stone, B. M. Wroblewski, and E. Ingham, “Polyethylene particles of a ‘critical size’ are necessary for the induction of cytokines by macrophages in vitro.,” *Biomaterials*, vol. 19, no. 24, pp. 2297–302, Dec. 1998.

[25] L. Richards, C. Brown, M. H. Stone, J. Fisher, E. Ingham, and J. L. Tipper, “Identification of nanometre-sized ultra-high molecular weight polyethylene wear particles in samples retrieved in vivo.,” *J. Bone Joint Surg. Br.*, vol. 90, no. 8, pp. 1106–13, Aug. 2008.

[26] K. J. Jepsen, “Systems Analysis of Bone,” *Wiley Interdiscip. Rev. Syst. Biol. Med.*, vol. 1, no. 1, pp. 73–88, 2009.

[27] R. L. Drake, V. A. Wayne, and A. W. M. Mitchell, *Gray’s Anatomy for Students*, 2e ed. Churchill Livingstone, 2010.

[28] J. Hamill and K. M. Knutzen, *Biomechanical Basis of Human Movement*. 2009.

[29] S. Affatato, *Wear of orthopaedic implants and artificial joints*. 2012.

[30] “Arthritis in the UK - key facts,” 2008. [Online]. Available: www.arthritisresearchuk.org.

[31] T. Scheerlinck and P.-P. Casteleyn, “The design features of cemented femoral hip implants.,” *J. Bone Joint Surg. Br.*, vol. 88, no. 11, pp. 1409–18, Nov. 2006.

[32] T. W. Bauer and J. Schils, “The pathology of total joint arthroplasty I . Mechanisms of implant fixation,” *Skeletal Radiol.*, vol. 28, pp. 423–432, 1999.

[33] S. Nag and R. Banerjee, “Fundamental of Medical Implant Materials,” *ASM Handb.*, vol. 23, pp. 6 – 17, 2012.

[34] J. Charnley and D. K. Halley, “Rate of wear in total hip replacement.,” *Clin. Orthop. Relat. Res.*, no. 112, pp. 170–9, Oct. 1975.

[35] C. BASTIAANSEN, H. MEYER, and P. LEMSTRA, “Memory effects in polyethylenes: influence of processing and crystallization history,” *Polymer (Guildf).*, vol. 31, no. 8, pp. 1435–1440, Aug. 1990.

[36] R. . Olley, I. . Hosier, D. . Bassett, and N. . Smith, “On morphology of consolidated UHMWPE resin in hip cups,” *Biomaterials*, vol. 20, no. 21, pp. 2037–2046, Nov. 1999.

[37] M. Kurth, P. Eyerer, R. Ascherl, K. Dittel, and U. Holz, “An evaluation of retrieved UHMWPE hip joint cups.,” *J. Biomater. Appl.*, vol. 3, no. 1, pp. 33–51, Jul. 1988.

[38] C. M. Rimnac, R. W. Klein, F. Betts, and T. M. Wright, “Post-irradiation aging of ultra-high molecular weight polyethylene.,” *J. Bone Joint Surg. Am.*, vol. 76, no. 7, pp. 1052–6, Jul.

1994.

[39] S. M. Kurtz, C. M. Rimnac, and D. L. Bartel, “Degradation rate of ultra-high molecular weight polyethylene.,” *J. Orthop. Res.*, vol. 15, no. 1, pp. 57–61, Jan. 1997.

[40] L. C. Sutula, J. P. Collier, K. A. Saum, B. H. Currier, J. H. Currier, W. M. Sanford, M. B. Mayor, R. E. Wooding, D. K. Sperling, and I. R. Williams, “The Otto Aufranc Award. Impact of gamma sterilization on clinical performance of polyethylene in the hip.,” *Clin. Orthop. Relat. Res.*, no. 319, pp. 28–40, Oct. 1995.

[41] J. P. Collier, D. K. Sperling, J. H. Currier, L. C. Sutula, K. A. Saum, and M. B. Mayor, “Impact of gamma sterilization on clinical performance of polyethylene in the knee.,” *J. Arthroplasty*, vol. 11, no. 4, pp. 377–89, Jun. 1996.

[42] A. A. Edidin, C. W. Jewett, A. Kalinowski, K. Kwarteng, and S. M. Kurtz, “Degradation of mechanical behavior in UHMWPE after natural and accelerated aging.,” *Biomaterials*, vol. 21, no. 14, pp. 1451–60, Jul. 2000.

[43] M. Matsubara and M. Watanabe, “The Wear Properties of High-density polyethylene irradiated by gamma rays,” *Wear*, vol. 10, pp. 214–222, 1967.

[44] S. J. Gencur, C. M. Rimnac, and S. M. Kurtz, “Fatigue crack propagation resistance of virgin and highly crosslinked, thermally treated ultra-high molecular weight polyethylene.,” *Biomaterials*, vol. 27, no. 8, pp. 1550–7, Mar. 2006.

[45] S. S. Tower, J. H. Currier, B. H. Currier, K. A. Lyford, D. W. Van Citters, and M. B. Mayor, “Rim cracking of the cross-linked longevity polyethylene acetabular liner after total hip arthroplasty.,” *J. Bone Joint Surg. Am.*, vol. 89, no. 10, pp. 2212–7, Oct. 2007.

[46] D. Halley, A. Glassman, and R. D. Crowninshield, “Recurrent dislocation after revision total hip replacement with a large prosthetic femoral head. A case report.,” *J. Bone Joint Surg. Am.*, vol. 86-A, no. 4, pp. 827–30, Apr. 2004.

[47] H.-N. Pang, D. D. R. Naudie, R. W. McCalden, S. J. MacDonald, and M. G. Teeter, “Highly Crosslinked Polyethylene Improves Wear But Not Surface Damage in Retrieved Acetabular Liners.,” *Clin. Orthop. Relat. Res.*, Aug. 2014.

[48] D. T. Schroder, N. H. Kelly, T. M. Wright, and M. L. Parks, “Retrieved highly crosslinked UHMWPE acetabular liners have similar wear damage as conventional UHMWPE.,” *Clin. Orthop. Relat. Res.*, vol. 469, no. 2, pp. 387–94, Feb. 2011.

[49] L. Packer, “Protective role of vitamin E in biological systems.,” *Am. J. Clin. Nutr.*, vol. 53, no. 4 Suppl, p. 1050S–1055S, Apr. 1991.

[50] M. Parth, N. Aust, and K. Lederer, “Studies on the effect of electron beam radiation on the molecular structure of ultra-high molecular weight polyethylene under the influence of alpha-tocopherol with respect to its application in medical implants.,” *J. Mater. Sci. Mater. Med.*, vol. 13, no. 10, pp. 917–21, Oct. 2002.

[51] E. Oral, C. Godleski Beckos, A. S. Malhi, and O. K. Muratoglu, “The effects of high dose irradiation on the cross-linking of vitamin E-blended ultrahigh molecular weight polyethylene.,” *Biomaterials*, vol. 29, no. 26, pp. 3557–60, Sep. 2008.

[52] E. Oral, E. S. Greenbaum, A. S. Malhi, W. H. Harris, and O. K. Muratoglu, “Characterization of irradiated blends of alpha-tocopherol and UHMWPE.,” *Biomaterials*, vol. 26, no. 33, pp. 6657–63, Nov. 2005.

[53] S. Kurtz, *PEEK Biomaterials Handbook*. Elsevier Inc., 2012.

[54] D. Xiong, L. Xiong, and L. Liu, “Preparation and tribological properties of polyetheretherketone composites.,” *J. Biomed. Mater. Res. B. Appl. Biomater.*, vol. 93, no. 2, pp. 492–6, May 2010.

[55] S. C. Scholes and A. Unsworth, “The wear properties of CFR-PEEK-OPTIMA articulating against ceramic assessed on a multidirectional pin-on-plate machine.,” *Proc. Inst. Mech.*

Eng. H., vol. 221, no. 3, pp. 281–9, Apr. 2007.

[56] S. C. Scholes and A. Unsworth, "Wear studies on the likely performance of CFR-PEEK/CoCrMo for use as artificial joint bearing materials.," *J. Mater. Sci. Mater. Med.*, vol. 20, no. 1, pp. 163–70, Jan. 2009.

[57] Q. Q. Wang, J. J. Wu, A. Unsworth, A. Briscoe, M. Jarman-Smith, C. Lowry, D. Simpson, and S. Collins, "Biotribological study of large diameter ceramic-on-CFR-PEEK hip joint including fluid uptake, wear and frictional heating.," *J. Mater. Sci. Mater. Med.*, vol. 23, no. 6, pp. 1533–42, Jun. 2012.

[58] H. P. Sieber, C. B. Rieker, and P. Köttig, "Analysis of 118 second-generation metal-on-metal retrieved hip implants.," *J. Bone Joint Surg. Br.*, vol. 81, no. 1, pp. 46–50, Jan. 1999.

[59] G. H. Isaac, J. Thompson, S. Williams, and J. Fisher, "Metal-on-metal bearings surfaces: materials, manufacture, design, optimization, and alternatives.," *Proc. Inst. Mech. Eng. H.*, vol. 220, no. 2, pp. 119–33, Feb. 2006.

[60] G. Dearnaley and J. H. Arps, "Biomedical applications of diamond-like carbon (DLC) coatings: A review," *Surf. Coatings Technol.*, vol. 200, no. 7, pp. 2518–2524, Dec. 2005.

[61] S. Williams, J. L. Tipper, E. Ingham, M. H. Stone, and J. Fisher, "In vitro analysis of the wear , wear debris and biological activity of surface-engineered coatings for use in metal-on-metal total hip replacements," *Proc. Inst. Mech. Eng. Part H J. Eng. Med.*, vol. 217, pp. 155–163, 2003.

[62] J. Olofsson, T. M. Grehk, T. Berlind, C. Persson, and S. Jacobson, "Evaluation of silicon nitride as a wear resistant and resorbable alternative for THR," vol. 2, no. 2, pp. 94–102, 2012.

[63] P. Boutin, "Total arthroplasty of the hip by fritted alumina prosthesis. Experimental study and 1st clinical applications.," *Rev Chir Orthop Reparatrice Appar Mot*, vol. 58, pp. 229–246, Feb. 1972.

[64] G. T. Evangelista, E. Fulkerson, F. Kummer, and P. E. Di Cesare, "Surface damage to an Oxinium femoral head prosthesis after dislocation.," *J. Bone Joint Surg. Br.*, vol. 89, no. 4, pp. 535–7, Apr. 2007.

[65] J. S. Hou, M. H. Holmes, W. M. Lai, and M. V.C., *Squeese film lubrication for articular cartilage with synovial fluid*. Springer, Verlang New York, 1990.

[66] D. G. Poitout, *Biomechanics and Biomaterials in Orthopedics*. Springer-Verlang London, 2004.

[67] J. F. Archard, "Contact and Rubbing of Flat Surfaces," *J. Appl. Phys.*, vol. 24, no. 8, p. 981, Jun. 1953.

[68] M. Caligaris, C. E. Canal, C. Ahmad, T. R. Gardner, and G. A. Ateshian, "Investigation of the Frictional Response of Osteoarthritic Human Tibiofemoral Joints and the Potential Beneficial Tribological Effect of Healthy Synovial Fluid," *Osteoarthr. Cartil.*, vol. 17, no. 10, pp. 1327 – 1332, 2009.

[69] J. H. Dumbleton, *Tribology of Natural and Artificial Joints*. Elsevier, 1981.

[70] P. A. Revell, *Joint Replacement Technology*. Woodhead Publishing, 2008.

[71] T. W. Bauer and J. Schils, "The pathology of total joint arthroplasty II . Mechanisms of implant failure," *Skeletal Radiol.*, vol. 28, pp. 483–497, 1999.

[72] A. Wang, C. Stark, and J. H. Dumbleton, "Role of cyclic plastic deformation in the wear of UHMWPE acetabular cups.," *J. Biomed. Mater. Res.*, vol. 29, no. 5, pp. 619–26, May 1995.

[73] S. Teoh, "Fatigue of biomaterials: a review," *Int. J. Fatigue*, vol. 22, no. 10, pp. 825–837, Nov. 2000.

[74] C. G. Mohler, J. J. Callaghan, D. K. Collis, and R. C. Johnston, "Early loosening of the femoral

component at the cement-prosthesis interface after total hip replacement.," *J. Bone Joint Surg. Am.*, vol. 77, no. 9, pp. 1315–22, Sep. 1995.

[75] B. S. Bal, M. N. Rahaman, T. Aleto, F. Miller, F. Traina, and A. Toni, "Surface Changes to Alumina Femoral Heads after Metal Staining during Implantation, and after Recurrent Dislocations of the Prosthetic Hip," in *Bioceramics and Alternative Bearings in Joint Arthroplasty*, 2005, pp. 147–154.

[76] R. W. Hood, T. M. Wright, and A. H. Burstein, "Retrieval analysis of total knee prostheses: a method and its application to 48 total condylar prostheses.," *J. Biomed. Mater. Res.*, vol. 17, no. 5, pp. 829–42, Sep. 1983.

[77] B. M. Wroblewski, M. Lynch, J. R. Atkinson, D. Dowson, and G. H. Isaac, "External wear of the polyethylene socket in cemented total hip arthroplasty.," *J. Bone Joint Surg. Br.*, vol. 69, no. 1, pp. 61–3, Jan. 1987.

[78] E. Ingham and J. Fisher, "Biological reactions to wear debris in total joint replacement," *Proc. Inst. Mech. Eng. Part H J. Eng. Med.*, vol. 214, no. 1, pp. 21–37, Jan. 2000.

[79] J. Black, H. Sherk, J. Bonini, W. R. Rostoker, F. Schajowicz, and J. O. Galante, "Metallosis associated with a stable titanium-alloy femoral component in total hip replacement. A case report.," *J. Bone Joint Surg. Am.*, vol. 72, no. 1, pp. 126–30, Jan. 1990.

[80] W. J. Maloney, M. Jasty, W. H. Harris, J. O. Galante, and J. J. Callaghan, "Endosteal erosion in association with stable uncemented femoral components.," *J. Bone Joint Surg. Am.*, vol. 72, no. 7, pp. 1025–34, Aug. 1990.

[81] J. D. Witt and M. Swann, "Metal wear and tissue response in failed titanium alloy total hip replacements.," *J. Bone Joint Surg. Br.*, vol. 73, no. 4, pp. 559–63, Jul. 1991.

[82] T. P. Schmalzried, M. Jasty, and W. H. Harris, "Periprosthetic bone loss in total hip arthroplasty. Polyethylene wear debris and the concept of the effective joint space.," *J. Bone Joint Surg. Am.*, vol. 74, no. 6, pp. 849–63, Jul. 1992.

[83] R. A. Cooper, C. M. McAllister, L. S. Borden, and T. W. Bauer, "Polyethylene debris-induced osteolysis and loosening in uncemented total hip arthroplasty. A cause of late failure.," *J. Arthroplasty*, vol. 7, no. 3, pp. 285–90, Sep. 1992.

[84] K. J. Margevicius, T. W. Bauer, J. T. McMahon, S. A. Brown, and K. Merritt, "Isolation and characterization of debris in membranes around total joint prostheses.," *J. Bone Joint Surg. Am.*, vol. 76, no. 11, pp. 1664–75, Nov. 1994.

[85] A. S. Shanbhag, J. J. Jacobs, T. T. Glant, J. L. Gilbert, J. Black, and J. O. Galante, "Composition and morphology of wear debris in failed uncemented total hip replacement.," *J. Bone Joint Surg. Br.*, vol. 76, no. 1, pp. 60–7, Jan. 1994.

[86] K. Hirakawa, T. W. Bauer, B. N. Stulberg, A. H. Wilde, and M. Secic, "Characterization and comparison of wear debris from failed total hip implants of different types.," *J. Bone Joint Surg. Am.*, vol. 78, no. 8, pp. 1235–43, Aug. 1996.

[87] W. J. Maloney, R. L. Smith, T. P. Schmalzried, J. Chiba, D. Huene, and H. Rubash, "Isolation and characterization of wear particles generated in patients who have had failure of a hip arthroplasty without cement.," *J. Bone Joint Surg. Am.*, vol. 77, no. 9, pp. 1301–10, Sep. 1995.

[88] P. Campbell, P. Doorn, F. Dorey, and H. C. Amstutz, "Wear and morphology of ultra-high molecular weight polyethylene wear particles from total hip replacements.," *Proc. Inst. Mech. Eng. H.*, vol. 210, no. 3, pp. 167–74, Jan. 1996.

[89] T. P. Schmalzried, P. Campbell, a K. Schmitt, I. C. Brown, and H. C. Amstutz, "Shapes and dimensional characteristics of polyethylene wear particles generated in vivo by total knee replacements compared to total hip replacements.," *J. Biomed. Mater. Res.*, vol. 38, no. 3, pp. 203–10, Jan. 1997.

[90] a Kobayashi, W. Bonfield, Y. Kadoya, T. Yamac, M. a Freeman, G. Scott, and P. a Revell, "The size and shape of particulate polyethylene wear debris in total joint replacements.," *Proc. Inst. Mech. Eng. H.*, vol. 211, no. 1, pp. 11–5, Jan. 1997.

[91] J. Fisher, P. S. . Barbour, M. King, A. . Besong, J. L. Hailey, J. . Tipper, E. Ingham, M. H. Stone, and B. M. Wroblewski, "Wear of ultrahigh molecular weight polyethylene in artificial joints: A new approach to the quantification of wear debris," in *PROCEEDINGS OF THE 5TH EUROPEAN CONFERENCE ON ADVANCED MATERIALS AND PROCESSES AND APPLICATIONS: MATERIALS, FUNCTIONALITY & DESIGN*, 1997, pp. 543–545.

[92] R. M. Urban, J. J. Jacobs, M. J. Tomlinson, J. Gavrilovic, J. Black, and M. Peoc'h, "Dissemination of wear particles to the liver, spleen, and abdominal lymph nodes of patients with hip or knee replacement.," *J. Bone Joint Surg. Am.*, vol. 82, no. 4, pp. 457–76, Apr. 2000.

[93] D. Pokorný, M. Slouf, F. Veselý, P. Fulín, D. Jahoda, and A. Sosna, "[Distribution of UHMWPE wear particles in periprosthetic tissues of total hip replacements].," *Acta Chir. Orthop. Traumatol. Cech.*, vol. 77, no. 2, pp. 87–92, Apr. 2010.

[94] G. I. Howling, P. I. Barnett, J. L. Tipper, M. H. Stone, J. Fisher, and E. Ingham, "Quantitative characterization of polyethylene debris isolated from periprosthetic tissue in early failure knee implants and early and late failure Charnley hip implants.," *J. Biomed. Mater. Res.*, vol. 58, no. 4, pp. 415–20, Jan. 2001.

[95] J. D. Mabrey, A. Afsar-Keshmiri, G. a Engh, C. J. Sychterz, M. a Wirth, C. a Rockwood, and C. M. Agrawal, "Standardized analysis of UHMWPE wear particles from failed total joint arthroplasties.," *J. Biomed. Mater. Res.*, vol. 63, no. 5, pp. 475–83, Jan. 2002.

[96] C.-H. Cho, T. Murakami, and Y. Sawae, "Influence of microscopic surface asperities on the wear of ultra-high molecular weight polyethylene in a knee prosthesis," *Proc. Inst. Mech. Eng. Part H J. Eng. Med.*, vol. 224, no. 4, pp. 515–529, Apr. 2010.

[97] H. Ito, C. M. Maloney, R. D. Crowninshield, J. C. Clohisy, D. J. McDonald, and W. J. Maloney, "In vivo femoral head damage and its effect on polyethylene wear.," *J. Arthroplasty*, vol. 25, no. 2, pp. 302–8, Feb. 2010.

[98] M. Jasty, C. R. Bragdon, K. Lee, A. Hanson, and W. H. Harris, "Surface damage to cobalt-chrome femoral head prostheses.," *J. Bone Joint Surg. Br.*, vol. 76, no. 1, pp. 73–7, Jan. 1994.

[99] A. Kusaba and Y. Kuroki, "Femoral component wear in retrieved hip prostheses.," *J. Bone Joint Surg. Br.*, vol. 79, no. 2, pp. 331–6, Mar. 1997.

[100] P. a Revell, "The combined role of wear particles, macrophages and lymphocytes in the loosening of total joint prostheses.," *J. R. Soc. Interface*, vol. 5, no. 28, pp. 1263–78, Nov. 2008.

[101] P. Campbell, E. Ebramzadeh, S. Nelson, K. Takamura, K. De Smet, and H. C. Amstutz, "Histological features of pseudotumor-like tissues from metal-on-metal hips.," *Clin. Orthop. Relat. Res.*, vol. 468, no. 9, pp. 2321–7, Sep. 2010.

[102] C. P. Case, V. G. Langkamer, C. James, M. R. Palmer, A. J. Kemp, P. F. Heap, and L. Solomon, "Widespread dissemination of metal debris from implants.," *J. Bone Joint Surg. Br.*, vol. 76, no. 5, pp. 701–12, Sep. 1994.

[103] H. J. Griffiths, J. Burke, and T. A. Bonfiglio, "Granulomatous pseudotumors in total joint replacement.," *Skeletal Radiol.*, vol. 16, no. 2, pp. 146–52, Jan. 1987.

[104] W. F. Scully and S. M. Teeny, "Pseudotumor Associated With Metal-on-Polyethylene Total Hip Arthroplasty," *Orthopedics*, vol. 36, no. 5, pp. E666–E670, 2013.

[105] C. A. Cipriano, P. S. Issack, B. Beksac, A. G. Della Valle, T. P. Sculco, and E. A. Salvati, "Metallosis after metal-on-polyethylene total hip arthroplasty.," *Am. J. Orthop. (Belle Mead. NJ).*, vol. 37, no. 2, pp. E18–25, Feb. 2008.

[106] A. R. Hsu, C. E. Gross, and B. R. Levine, “Pseudotumor from modular neck corrosion after ceramic-on-polyethylene total hip arthroplasty.,” *Am. J. Orthop. (Belle Mead. NJ).*, vol. 41, no. 9, pp. 422–6, Sep. 2012.

[107] X. Mao, G. H. Tay, D. B. Godbolt, and R. W. Crawford, “Pseudotumor in a well-fixed metal-on-polyethylene uncemented hip arthroplasty.,” *J. Arthroplasty*, vol. 27, no. 3, pp. 493.e13–7, Mar. 2012.

[108] G. McKee and J. Farrar, “Joint Replacement of Arthritic Hips by the McKee-Farrar Prosthesis,” *J. Bone Jt. Surg.*, vol. 48, pp. 245 – 259, 1966.

[109] S. Leclercq, “Charnley-Kerboull-Bousquet hybrid THR after 10 years,” in *Total Hip Arthroplasty; 3rd International Symposium*, 2000.

[110] J. McKee, “Reducing the risk of recurrent dislocation,” *AAOS Now*, 2011. [Online]. Available: http://www.aaos.org/news/aaosnow/jan11/clinical2.asp.

[111] A. G. Gristina and J. W. Costerton, “Bacterial adherence to biomaterials and tissue. The significance of its role in clinical sepsis.,” *J. Bone Joint Surg. Am.*, vol. 67, no. 2, pp. 264–73, Feb. 1985.

[112] C. A. Engh, T. F. McGovern, J. D. Bobyn, and W. H. Harris, “A quantitative evaluation of periprosthetic bone-remodeling after cementless total hip arthroplasty.,” *J. Bone Joint Surg. Am.*, vol. 74, no. 7, pp. 1009–20, Aug. 1992.

[113] S. Kumari, S. Mg, and S. Mayor, “Endocytosis unplugged: multiple ways to enter the cell.,” *Cell Res.*, vol. 20, no. 3, pp. 256–75, Mar. 2010.

[114] S. Conner and S. Schmid, “Regulated portals of entry into the cell,” *Nature*, vol. 422, no. March, pp. 37–44, 2003.

[115] J. A. Swanson, “Shaping cups into phagosomes and macropinosomes.,” *Nat. Rev. Mol. Cell Biol.*, vol. 9, no. 8, pp. 639–49, Aug. 2008.

[116] D. M. Underhill and H. S. Goodridge, “Information processing during phagocytosis,” *Nat. Rev. Immunol.*, vol. 12, no. 7, pp. 492–502, 2012.

[117] N. Doshi and S. Mitragotri, “Macrophages recognize size and shape of their targets.,” *PLoS One*, vol. 5, no. 4, p. e10051, Jan. 2010.

[118] J. A. Champion and S. Mitragotri, “Role of target geometry in phagocytosis.,” *Proc. Natl. Acad. Sci. U. S. A.*, vol. 103, no. 13, pp. 4930–4, Mar. 2006.

[119] G. J. Cannon and J. a Swanson, “The macrophage capacity for phagocytosis.,” *J. Cell Sci.*, vol. 101 (Pt 4, pp. 907–913, 1992.

[120] S. Yang, W. Ren, Y. Park, A. Sieving, S. Hsu, S. Nasser, and P. H. Wooley, “Diverse cellular and apoptotic responses to variant shapes of UHMWPE particles in a murine model of inflammation,” *Scan. Electron Microsc.*, vol. 23, pp. 3535–3543, 2002.

[121] J. Mercer and A. Helenius, “Virus entry by macropinocytosis.,” *Nat. Cell Biol.*, vol. 11, no. 5, pp. 510–20, May 2009.

[122] J. L. Tipper, “The Biological Response to Nanometer-Sized Particles,” in *Transactions of the 4th UHMWPE International Meeting, UHMWPE for Arthroplasty: from Powder to Debris.*, 2009.

[123] E. Ingham and J. Fisher, “The role of macrophages in osteolysis of total joint replacement.,” *Biomaterials*, vol. 26, no. 11, pp. 1271–86, Apr. 2005.

[124] N. Cobelli, B. Scharf, G. M. Crisi, J. Hardin, and L. Santambrogio, “Mediators of the inflammatory response to joint replacement devices,” *Nat. Rev. Rheumatol.*, vol. 7, no. 10, pp. 600–608, 2011.

[125] K. D. Merkel, J. M. Erdmann, K. P. McHugh, Y. Abu-Amer, F. P. Ross, and S. L. Teitelbaum, “Tumor necrosis factor-alpha mediates orthopedic implant osteolysis.,” *Am. J. Pathol.*, vol.

154, no. 1, pp. 203–10, Jan. 1999.

[126] J. W. Xu, Y. T. Konttinen, J. Lassus, S. Natah, A. Ceponis, S. Solovieva, P. Aspenberg, and S. Santavirta, “Tumor necrosis factor-alpha (TNF-alpha) in loosening of total hip replacement (THR).,” *Clin. Exp. Rheumatol.*, vol. 14, no. 6, pp. 643–8, Jan. .

[127] K. J. Kim, H. E. Rubash, S. C. Wilson, J. A. D’Antonio, and E. J. McClain, “A histologic and biochemical comparison of the interface tissues in cementless and cemented hip prostheses.,” *Clin. Orthop. Relat. Res.*, no. 287, pp. 142–52, Feb. 1993.

[128] A. Sabokbar and N. Rushton, “Role of inflammatory mediators and adhesion molecules in the pathogenesis of aseptic loosening in total hip arthroplasties.,” *J. Arthroplasty*, vol. 10, no. 6, pp. 810–6, Dec. 1995.

[129] J. W. Xu, T. F. Li, G. Partsch, A. Ceponis, S. Santavirta, and Y. T. Konttinen, “Interleukin-11 (IL-11) in aseptic loosening of total hip replacement (THR).,” *Scand. J. Rheumatol.*, vol. 27, no. 5, pp. 363–7, Jan. 1998.

[130] J. Chiba, H. E. Rubash, K. J. Kim, and Y. Iwaki, “The characterization of cytokines in the interface tissue obtained from failed cementless total hip arthroplasty with and without femoral osteolysis.,” *Clin. Orthop. Relat. Res.*, no. 300, pp. 304–12, Mar. 1994.

[131] S. B. Goodman, P. Huie, Y. Song, D. Schurman, W. Maloney, S. Woolson, and R. Sibley, “Cellular profile and cytokine production at prosthetic interfaces. Study of tissues retrieved from revised hip and knee replacements.,” *J. Bone Joint Surg. Br.*, vol. 80, no. 3, pp. 531–9, May 1998.

[132] J. B. Matthews, T. R. Green, M. H. Stone, B. M. Wroblewski, J. Fisher, and E. Ingham, “Comparison of the response of three human monocytic cell lines to challenge with polyethylene particles of known size and dose.,” *J. Mater. Sci. Mater. Med.*, vol. 12, no. 3, pp. 249–58, Mar. 2001.

[133] T. R. Green, J. Fisher, J. B. Matthews, M. H. Stone, and E. Ingham, “Effect of size and dose on bone resorption activity of macrophages by in vitro clinically relevant ultra high molecular weight polyethylene particles.,” *J. Biomed. Mater. Res.*, vol. 53, no. 5, pp. 490–7, Sep. 2000.

[134] J. B. Matthews, T. R. Green, M. H. Stone, B. M. Wroblewski, J. Fisher, and E. Ingham, “Comparison of the response of primary murine peritoneal macrophages and the U937 human histiocytic cell line to challenge with in vitro generated clinically relevant UHMWPE particles.,” *Biomed. Mater. Eng.*, vol. 10, no. 3–4, pp. 229–40, Jan. 2000.

[135] J. B. Matthews, T. R. Green, M. H. Stone, B. M. Wroblewski, J. Fisher, and E. Ingham, “Comparison of the response of primary human peripheral blood mononuclear phagocytes from different donors to challenge with model polyethylene particles of known size and dose.,” *Biomaterials*, vol. 21, no. 20, pp. 2033–44, Oct. 2000.

[136] S. Tanaka, N. Takahashi, N. Udagawa, T. Tamura, T. Akatsu, E. R. Stanley, T. Kurokawa, and T. Suda, “Macrophage colony-stimulating factor is indispensable for both proliferation and differentiation of osteoclast progenitors.,” *J. Clin. Invest.*, vol. 91, no. 1, pp. 257–63, Jan. 1993.

[137] W. S. Simonet, D. L. Lacey, C. R. Dunstan, M. Kelley, M. S. Chang, R. Lüthy, H. Q. Nguyen, S. Wooden, L. Bennett, T. Boone, G. Shimamoto, M. DeRose, R. Elliott, A. Colombero, H. L. Tan, G. Trail, J. Sullivan, E. Davy, N. Bucay, L. Renshaw-Gegg, T. M. Hughes, D. Hill, W. Pattison, P. Campbell, S. Sander, G. Van, J. Tarpley, P. Derby, R. Lee, and W. J. Boyle, “Osteoprotegerin: a novel secreted protein involved in the regulation of bone density.,” *Cell*, vol. 89, no. 2, pp. 309–19, Apr. 1997.

[138] D. L. Lacey, E. Timms, H. L. Tan, M. J. Kelley, C. R. Dunstan, T. Burgess, R. Elliott, A. Colombero, G. Elliott, S. Scully, H. Hsu, J. Sullivan, N. Hawkins, E. Davy, C. Capparelli, A. Eli, Y. X. Qian, S. Kaufman, I. Sarosi, V. Shalhoub, G. Senaldi, J. Guo, J. Delaney, and W. J. Boyle,

"Osteoprotegerin ligand is a cytokine that regulates osteoclast differentiation and activation.," *Cell*, vol. 93, no. 2, pp. 165–76, Apr. 1998.

[139] D. M. Anderson, E. Maraskovsky, W. L. Billingsley, W. C. Dougall, M. E. Tometsko, E. R. Roux, M. C. Teepe, R. F. DuBose, D. Cosman, and L. Galibert, "A homologue of the TNF receptor and its ligand enhance T-cell growth and dendritic-cell function.," *Nature*, vol. 390, no. 6656, pp. 175–9, Nov. 1997.

[140] I. Itonaga, A. Sabokbar, D. W. Murray, and N. A. Athanasou, "Effect of osteoprotegerin and osteoprotegerin ligand on osteoclast formation by arthroplasty membrane derived macrophages.," *Ann. Rheum. Dis.*, vol. 59, no. 1, pp. 26–31, Jan. 2000.

[141] F. von Knoch, A. Heckelei, C. Wedemeyer, G. Saxler, G. Hilken, J. Brankamp, T. Sterner, S. Landgraeber, F. Henschke, F. Löer, and M. von Knoch, "Suppression of polyethylene particle-induced osteolysis by exogenous osteoprotegerin.," *J. Biomed. Mater. Res. A*, vol. 75, no. 2, pp. 288–94, Nov. 2005.

[142] L. C. Hofbauer, D. L. Lacey, C. R. Dunstan, T. C. Spelsberg, B. L. Riggs, and S. Khosla, "Interleukin-1beta and tumor necrosis factor-alpha, but not interleukin-6, stimulate osteoprotegerin ligand gene expression in human osteoblastic cells.," *Bone*, vol. 25, no. 3, pp. 255–9, Sep. 1999.

[143] R. B. Kimble, S. Srivastava, F. P. Ross, A. Matayoshi, and R. Pacifici, "Estrogen deficiency increases the ability of stromal cells to support murine osteoclastogenesis via an interleukin-1and tumor necrosis factor-mediated stimulation of macrophage colony-stimulating factor production.," *J. Biol. Chem.*, vol. 271, no. 46, pp. 28890–7, Nov. 1996.

[144] K. Kobayashi, N. Takahashi, E. Jimi, N. Udagawa, M. Takami, S. Kotake, N. Nakagawa, M. Kinosaki, K. Yamaguchi, N. Shima, H. Yasuda, T. Morinaga, K. Higashio, T. J. Martin, and T. Suda, "Tumor necrosis factor alpha stimulates osteoclast differentiation by a mechanism independent of the ODF/RANKL-RANK interaction.," *J. Exp. Med.*, vol. 191, no. 2, pp. 275–86, Jan. 2000.

[145] E. Ingham, T. R. Green, J. B. Matthews, M. H. Stone, and J. Fisher, "Influence of TNF-alpha in polyethylene particle stimulated macrophage bone resorption," in *45th Annual Meeting, Orthopaedic Research Society*, 1999, vol. 44, no. 0, p. 899.

[146] C.-T. Wang, Y.-T. Lin, B.-L. Chiang, S.-S. Lee, and S.-M. Hou, "Over-expression of receptor activator of nuclear factor-kappaB ligand (RANKL), inflammatory cytokines, and chemokines in periprosthetic osteolysis of loosened total hip arthroplasty.," *Biomaterials*, vol. 31, no. 1, pp. 77–82, Jan. 2010.

[147] W. Ren, "Distinct gene expression of receptor activator of nuclear factor-κB and rank ligand in the inflammatory response to variant morphologies of UHMWPE particles," *Biomaterials*, vol. 24, no. 26, pp. 4819–4826, Nov. 2003.

[148] J. Fisher, H. M. J. McEwen, J. L. Tipper, A. L. Galvin, J. Ingram, A. Kamali, M. H. Stone, and E. Ingham, "Wear, debris, and biologic activity of cross-linked polyethylene in the knee: benefits and potential concerns.," *Clin. Orthop. Relat. Res.*, no. 428, pp. 114–9, Nov. 2004.

[149] I. E. Adamopoulos and E. D. Mellins, "Alternative pathways of osteoclastogenesis in inflammatory arthritis.," *Nat. Rev. Rheumatol.*, vol. 11, no. 3, pp. 189–94, Mar. 2015.

[150] D. Berry and J. Lieberman, *Surgery of the Hip*. 2013.

[151] S. C. Scholes and A. Unsworth, "Pin-on-plate studies on the effect of rotation on the wear of metal-on-metal samples," vol. 2, pp. 299–303, 2001.

[152] T. J. Joyce, P. Thompson, and a. Unsworth, "The wear of PTFE against stainless steel in a multi-directional pin-on-plate wear device," *Wear*, vol. 255, no. 7–12, pp. 1030–1033, Aug. 2003.

[153] A. Liu, E. Ingham, J. Fisher, and J. L. Tipper, "Generation of a large volume of clinically relevant nanometre-sized ultra-high-molecular-weight polyethylene wear particles for cell

culture studies.," *Proc. Inst. Mech. Eng. H.*, vol. 228, no. 4, pp. 418–26, Apr. 2014.

[154] C. J. Bell and J. Fisher, "Simulation of polyethylene wear in ankle joint prostheses.," *J. Biomed. Mater. Res. B. Appl. Biomater.*, vol. 81, no. 1, pp. 162–7, Apr. 2007.

[155] S. Affatato, M. Spinelli, M. Zavalloni, C. Mazzega-Fabbro, and M. Viceconti, "Tribology and total hip joint replacement: current concepts in mechanical simulation.," *Med. Eng. Phys.*, vol. 30, no. 10, pp. 1305–17, Dec. 2008.

[156] P. I. Barnett, J. Fisher, D. D. Auger, M. H. Stone, and E. Ingham, "Comparison of wear in a total knee replacement under different kinematic conditions," *J. Mater. Sci. Mater. Med.*, vol. 12, no. 10–12, pp. 1039–1042, Dec. 2001.

[157] ISO, "ISO 14242 Implants for surgery — Wear of total hip-joint prostheses," 2002.

[158] ISO, "ISO 14243 Implants for surgery — Wear of total knee joint prostheses," 2002.

[159] A. Ochsner and W. Ahmed, *Biomechanics of Hard Tissues*. Wiley, 2011.

[160] H.-W. Fang, M.-L. Shih, J.-H. Zhao, H.-T. Huang, H.-Y. Lin, H.-L. Liu, C.-H. Chang, C.-B. Yang, and H.-C. Liu, "Association of polyethylene friction and thermal unfolding of interfacial albumin molecules," *Appl. Surf. Sci.*, vol. 253, no. 16, pp. 6896–6904, Jun. 2007.

[161] M. Al-Hajjar, I. J. Leslie, J. Tipper, S. Williams, J. Fisher, and L. M. Jennings, "Effect of cup inclination angle during microseparation and rim loading on the wear of BIOLOX® delta ceramic-on-ceramic total hip replacement.," *J. Biomed. Mater. Res. B. Appl. Biomater.*, vol. 95, no. 2, pp. 263–8, Nov. 2010.

[162] S. Affatato, G. Bersaglia, M. Rocchi, P. Taddei, C. Fagnano, and A. Toni, "Wear behaviour of cross-linked polyethylene assessed in vitro under severe conditions.," *Biomaterials*, vol. 26, no. 16, pp. 3259–67, Jun. 2005.

[163] J. M. Brandt, L. K. Brière, J. Marr, S. J. MacDonald, R. B. Bourne, and J. B. Medley, "Biochemical comparisons of osteoarthritic human synovial fluid with calf sera used in knee simulator wear testing," *J. Biomed. Mater. Res. - Part A*, vol. 94, no. 3, pp. 961–971, 2010.

[164] Y.-S. Liao, D. McNulty, and M. Hanes, "Wear rate and surface morphology of UHMWPE cups are affected by the serum lubricant concentration in a hip simulation test," *Wear*, vol. 255, no. 7–12, pp. 1051–1056, Aug. 2003.

[165] A. Wang, A. Essner, V. . Polineni, C. Stark, and J. . Dumbleton, "Lubrication and wear of ultra-high molecular weight polyethylene in total joint replacements," *Tribol. Int.*, vol. 31, no. 98, pp. 17–33, 1998.

[166] H. Fang, Y. Su, C. Huang, and C. Yang, "Influence of biological lubricant on the morphology of UHMWPE wear particles generated with microfabricated surface textures," *Mater. Chem. Phys.*, vol. 95, no. 2–3, pp. 280–288, Feb. 2006.

[167] H. A. McKellop, P. Campbell, S. H. Park, T. P. Schmalzried, P. Grigoris, H. C. Amstutz, and A. Sarmiento, "The origin of submicron polyethylene wear debris in total hip arthroplasty.," *Clin. Orthop. Relat. Res.*, no. 311, pp. 3–20, Feb. 1995.

[168] J.-M. Lee, A. Salvati, F. Betts, B. Doty, F. Dicarlo, and G. Bullough, "Size of metallic and polyethylene debris in failed cemented total hip replacements," *J. Bone Jt. Surg.*, vol. 74B, pp. 380–384, 1992.

[169] P. Campbell, S. Ma, B. Yeom, H. McKellop, T. P. Schmalzried, and H. C. Amstutz, "Isolation of predominantly submicron-sized UHMWPE wear particles from periprosthetic tissues.," *J. Biomed. Mater. Res.*, vol. 29, no. 1, pp. 127–31, Jan. 1995.

[170] R. M. Baxter, M. J. Steinbeck, J. L. Tipper, J. Parvizi, M. Marcolongo, and S. M. Kurtz, "Comparison of periprosthetic tissue digestion methods for ultra-high molecular weight polyethylene wear debris extraction.," *J. Biomed. Mater. Res. B. Appl. Biomater.*, vol. 91, no. 1, pp. 409–18, Oct. 2009.

[171] M. Lapcikova, M. Slouf, J. Dybal, E. Zolotarevova, G. Entlicher, D. Pokorny, J. Gallo, and A. Sosna, “Nanometer size wear debris generated from ultra high molecular weight polyethylene,” *Biomaterials*, vol. 266, pp. 349–355, 2009.

[172] D. D. Dean, Z. Schwartz, Y. Liu, C. R. Blanchard, C. M. Agrawal, J. D. Mabrey, V. L. Sylvia, C. H. Lohmann, and B. D. Boyan, “The Effect of Ultra-High Molecular Weight Polyethylene Wear Debris on MG63 Osteosarcoma Cells in Vitro The Effect of Ultra-High Molecular Weight Polyethylene Wear Debris on,” *J. Bone Jt. Surg.*, 2011.

[173] a a Besong, J. L. Tipper, E. Ingham, M. H. Stone, B. M. Wroblewski, and J. Fisher, “Quantitative comparison of wear debris from UHMWPE that has and has not been sterilised by gamma irradiation.,” *J. Bone Joint Surg. Br.*, vol. 80, no. 2, pp. 340–4, Mar. 1998.

[174] S. Niedzwiecki, J. Short, S. Jani, W. Sauer, L. Pruitt, and M. Ries, “Isolation of UHMWPE wear debris: a comparison of three viable methods.,” in *Society for Biomaterials, editor. Proceedings of the 22nd Annual Meeting of the Society for Biomaterials*, 1999, p. 150.

[175] S. Niedzwiecki, C. Klapperich, J. Short, S. Jani, M. Ries, and L. Pruitt, “Comparison of three joint simulator wear debris isolation techniques: Acid digestion, base digestion, and enzyme cleavage,” *Techniques*, 2001.

[176] M. Scott, K. Widding, and S. Jani, “Do current wear particle isolation procedures underestimate the number of particles generated by prosthetic bearing components?,” *Wear*, vol. 251, no. 1–12, pp. 1213–1217, Oct. 2001.

[177] A. P. D. Elfick, “The quantitative assessment of UHMWPE wear debris produced in hip simulator testing: the influence of head material and roughness, motion and loading,” *Wear*, vol. 249, no. 5–6, pp. 517–527, Jun. 2001.

[178] J. L. Tipper, A. L. Galvin, S. Williams, H. M. J. McEwen, M. H. Stone, E. Ingham, and J. Fisher, “Isolation and characterization of UHMWPE wear particles down to ten nanometers in size from in vitro hip and knee joint simulators.,” *J. Biomed. Mater. Res. A*, vol. 78, no. 3, pp. 473–80, Sep. 2006.

[179] ISO, “ISO 17853 Wear of implant materials — Polymer and metal wear particles — Isolation and characterization,” 2011.

[180] M. Scott, M. Morrison, S. R. Mishra, and S. Jani, “Particle analysis for the determination of UHMWPE wear.,” *J. Biomed. Mater. Res. B. Appl. Biomater.*, vol. 73, no. 2, pp. 325–37, May 2005.

[181] A. Wang, A. Essner, C. Stark, and J. H. Dumbleton, “Comparison of the size and morphology of UHMWPE wear debris produced by a hip joint simulator under serum and water lubricated conditions,” *Biomaterials*, vol. 17, no. 9, pp. 865–871, Jan. 1996.

[182] J. . Tipper, P. . Firkins, a. . Besong, P. S. . Barbour, J. Nevelos, M. . Stone, E. Ingham, and J. Fisher, “Characterisation of wear debris from UHMWPE on zirconia ceramic, metal-on-metal and alumina ceramic-on-ceramic hip prostheses generated in a physiological anatomical hip joint simulator,” *Wear*, vol. 250, no. 1–12, pp. 120–128, Oct. 2001.

[183] A. L. Galvin, J. L. Tipper, L. M. Jennings, M. H. Stone, Z. M. Jin, E. Ingham, and J. Fisher, “Wear and biological activity of highly crosslinked polyethylene in the hip under low serum protein concentrations,” *Eng. Med.*, vol. 221, pp. 1–10, 2007.

[184] S. Affatato, G. Bersaglia, I. Foltran, P. Taddei, G. Fini, and a Toni, “The performance of gamma- and EtO-sterilised UHWMPE acetabular cups tested under severe simulator conditions. Part 1: role of the third-body wear process.,” *Biomaterials*, vol. 23, no. 24, pp. 4839–46, Dec. 2002.

[185] F. Billi, P. Benya, A. Kavanaugh, J. Adams, E. Ebramzadeh, and H. McKellop, “The John Charnley Award: an accurate and sensitive method to separate, display, and characterize wear debris: part 1: polyethylene particles.,” *Clin. Orthop. Relat. Res.*, vol. 470, no. 2, pp.

329–38, Feb. 2012.

[186] M. Scott, M. Morrison, S. R. Mishra, and S. Jani, “Particle analysis for the determination of UHMWPE wear.,” *J. Biomed. Mater. Res. B. Appl. Biomater.*, vol. 73, no. 2, pp. 325–37, May 2005.

[187] D. L. Wolfarth, D. W. Han, G. Bushar, and N. L. Parks, “Separation and characterization of polyethylene wear debris from synovial fluid and tissue samples of revised knee replacements.,” *J. Biomed. Mater. Res.*, vol. 34, no. 1, pp. 57–61, Jan. 1997.

[188] F. Billi, P. Benya, A. Kavanaugh, J. Adams, H. McKellop, and E. Ebramzadeh, “The John Charnley Award: an accurate and extremely sensitive method to separate, display, and characterize wear debris: part 2: metal and ceramic particles.,” *Clin. Orthop. Relat. Res.*, vol. 470, no. 2, pp. 339–50, Mar. 2012.

[189] A. P. D. Elfick, S. M. Green, S. Krikler, and A. Unsworth, “The nature and dissemination of UHMWPE wear debris retrieved from periprosthetic tissue of THR.,” *J. Biomed. Mater. Res. A*, vol. 65, no. 1, pp. 95–108, Apr. 2003.

[190] A. P. D. Elfick, S. M. Green, I. M. Pinder, and A. Unsworth, “A novel technique for the detailed size characterization of wear debris.,” *J. Mater. Sci. Mater. Med.*, vol. 11, no. 5, pp. 267–71, May 2000.

[191] D. W. Hahn, D. L. Wolfarth, and N. L. Parks, “Analysis of polyethylene wear debris using micro-Raman spectroscopy: a report on the presence of beta-carotene.,” *J. Biomed. Mater. Res.*, vol. 35, no. 1, pp. 31–7, Apr. 1997.

[192] ASTM, “F1877 - 05 Standard Practice for Characterisation of Particles,” 2010.

[193] G. W. Stachowiak, G. B. Stachowiak, and P. Campbell, “Application of numerical descriptors to the characterization of wear particles obtained from joint replacements.,” *Proc. Inst. Mech. Eng. H.*, vol. 211, no. 1, pp. 1–10, Jan. 1997.

[194] M. A. Wirth, C. M. Agrawal, J. A. Y. D. Mabrey, D. D. Dean, C. R, M. A. Miller, and C. A. Rockwood, “Isolation and Characterization of Polyethylene Wear Debris Associated with Osteolysis Following Total Shoulder Arthroplasty,” *J. Bone Jt. Surg.*, 2011.

[195] M. Slouf, S. Eklova, J. Kumstatova, S. Berger, H. Synkova, A. Sosna, D. Pokorny, M. Spundova, and G. Entlicher, “Isolation, characterization and quantification of polyethylene wear debris from periprosthetic tissues around total joint replacements,” *Wear*, vol. 262, no. 9–10, pp. 1171–1181, Apr. 2007.

[196] D. Zhang, J. R. Page, A. E. Kavanaugh, and F. Billi, “A new method for shape and texture classification of orthopedic wear nanoparticles,” *J. Appl. Biomater. Funct. Mater.*, no. jabfm vol. 10 issue 2, 2012, pp. 141–148, Sep. 2012.

[197] J. Fisher, J. Bell, P. S. Barbour, J. L. Tipper, J. B. Matthews, a a Besong, M. H. Stone, and E. Ingham, “A novel method for the prediction of functional biological activity of polyethylene wear debris.,” *Proc. Inst. Mech. Eng. H.*, vol. 215, no. 2, pp. 127–32, Jan. 2001.

[198] J. L. Hailey, E. Ingham, M. Stone, B. M. Wroblewski, and J. Fisher, “Ultra-high molecular weight polyethylene wear debris generated in vivo and in laboratory tests; the influence of counterface roughness.,” *Proc. Inst. Mech. Eng. H.*, vol. 210, no. 1, pp. 3–10, Jan. 1996.

[199] J. L. Tipper, E. Ingham, J. L. Hailey, A. A. Besong, J. Fisher, B. M. Wroblewski, W. Hospital, and M. H. Stone, “Quantitative analysis of polyethylene wear debris, wear rate and head damage in retrieved Charnley hip prostheses,” *Most*, vol. 1, pp. 117–124, 2000.

[200] J. L. Tipper, P. J. Firkins, E. Ingham, J. Fisher, M. H. Stone, and R. Farrar, “Quantitative analysis of the wear and wear debris from low and high carbon content cobalt chrome alloys used in metal on metal total hip replacements.,” *J. Mater. Sci. Mater. Med.*, vol. 10, no. 6, pp. 353–62, Jun. 1999.

[201] B. Fernandes, A. Tucci, L. Esposito, and A. Toni, “Isolation and morphological

characterisation of UHMWPE wear debris generated in vitro," *Bone*, vol. 22, 2001.

[202] S. Affatato, D. Emiliani, G. Bersaglia, F. Traina, and A. Toni, "An easy technique to digest and isolate UHMWPE wear particles from a hip joint simulator.," *Int. J. Artif. Organs*, vol. 27, no. 5, pp. 424–32, May 2004.

[203] H. Koseki, T. Matsumoto, S. Ito, H. Doukawa, H. Enomoto, and H. Shindo, "Analysis of polyethylene particles isolated from periprosthetic tissue of loosened hip arthroplasty and comparison with radiographic appearance.," *J. Orthop. Sci.*, vol. 10, no. 3, pp. 284–90, May 2005.

[204] H. L. Jang and I. Y. Suk, "An effective image segmentation technique for the SEM image," *Proc. IEEE Int. Conf. Ind. Technol.*, pp. 3–7, 2008.

[205] H. Q. Sun and Y. J. Luo, "Adaptive watershed segmentation of binary particle image.," *J. Microsc.*, vol. 233, no. 2, pp. 326–30, Mar. 2009.

[206] S. Beucher and C. Lantuejoul, "Use of Watershed in Contour Detection," in *International workshop on image processing*, 1979, pp. 17 – 21.

[207] J. C. Russ, *The Image Processing handbook*. CRC Press, 2011.

[208] S. J. Gardoll, D. I. Groves, C. M. Knox-Robinson, G. Y. Yun, and N. Elliott, "Developing the tools for geological shape analysis, with regional- to local-scale examples from the Kalgoorlie Terrane of Western Australia," *Aust. J. Earth Sci.*, vol. 47, no. 5, pp. 943–953, Oct. 2000.

[209] H. Haider, J. N. Weisenburger, S. M. Kurtz, C. M. Rimnac, J. Freedman, D. W. Schroeder, and K. L. Garvin, "Does Vitamin E-Stabilized Ultrahigh-Molecular-Weight Polyethylene Address Concerns of Cross-Linked Polyethylene in Total Knee Arthroplasty?," *J. Arthroplasty*, vol. 27, no. 3, pp. 461–469, 2012.

[210] M. M. Endo, D. C. Barton, J. Fisher, J. L. Tipper, E. Ingham, and M. H. Stone, "Comparative wear and wear debris under three different counterface conditions of crosslinked and non-crosslinked ultra high molecular weight polyethylene," vol. 11, pp. 23–35, 2001.

[211] E. Oral, S. D. Christensen, A. S. Malhi, K. K. Wannomae, and O. K. Muratoglu, "Wear resistance and mechanical properties of highly cross-linked, ultrahigh-molecular weight polyethylene doped with vitamin E.," *J. Arthroplasty*, vol. 21, no. 4, pp. 580–91, Jun. 2006.

[212] O. K. Muratoglu, B. R. Burroughs, C. R. Bragdon, S. Christensen, A. Lozynsky, and W. H. Harris, "Knee simulator wear of polyethylene tibias articulating against explanted rough femoral components.," *Clin. Orthop. Relat. Res.*, no. 428, pp. 108–13, Nov. 2004.

[213] M. M. Landy and P. S. Walker, "Wear of ultra-high-molecular-weight polyethylene components of 90 retrieved knee prostheses.," *J. Arthroplasty*, vol. 3 Suppl, pp. S73–85, Jan. 1988.

[214] M. S. Kuster and G. W. Stachowiak, "Factors affecting polyethylene wear in total knee arthroplasty.," *Orthopedics*, vol. 25, no. 2 Suppl, pp. s235–42, Feb. 2002.

[215] J. P. Collier, M. B. Mayor, J. L. McNamara, V. A. Surprenant, and R. E. Jensen, "Analysis of the failure of 122 polyethylene inserts from uncemented tibial knee components.," *Clin. Orthop. Relat. Res.*, no. 273, pp. 232–42, Dec. 1991.

[216] A. Galvin, J. L. Tipper, E. Ingham, and J. Fisher, "Nanometre size wear debris generated from crosslinked and non-crosslinked ultra high molecular weight polyethylene in artificial joints," *Wear*, vol. 259, no. 7–12, pp. 977–983, Jul. 2005.

[217] L. Kang, A. L. Galvin, T. D. Brown, Z. Jin, and J. Fisher, "Quantification of the effect of cross-shear on the wear of conventional and highly cross-linked UHMWPE.," *J. Biomech.*, vol. 41, no. 2, pp. 340–6, Jan. 2008.

[218] A. Abdelgaied, C. L. Brockett, F. Liu, L. M. Jennings, J. Fisher, and Z. Jin, "Quantification of the effect of cross-shear and applied nominal contact pressure on the wear of moderately

cross-linked polyethylene.," *Proc. Inst. Mech. Eng. H.*, vol. 227, no. 1, pp. 18–26, Jan. 2013.

[219] S. Affatato, P. Bracco, L. Costa, T. Villa, V. Quaglini, and A. Toni, "In vitro wear performance of standard, crosslinked, and vitamin-E-blended UHMWPE.," *J. Biomed. Mater. Res. A*, vol. 100, no. 3, pp. 554–60, Mar. 2012.

[220] A. Traynor, D. Simpson, P. Ellison, and S. Collins, "ECIMA AS A NEXT GENERATION, ADVANCED BEARING MATERIAL," *J. Bone Jt. Surgery, Br. Vol.*, vol. 94-B, no. SUPP XXXVII, p. 142, Sep. 2012.

[221] J. J. Wu, C. . Buckley, and J. . O'Connor, "Mechanical integrity of compression-moulded ultra-high molecular weight polyethylene: effects of varying process conditions," *Biomaterials*, vol. 23, no. 17, pp. 3773–3783, Sep. 2002.

[222] A. Kobayashi, Y. Minoda, Y. Kadoya, H. Ohashi, K. Takaoka, and C. L. Saltzman, "Ankle arthroplasties generate wear particles similar to knee arthroplasties.," *Clin. Orthop. Relat. Res.*, no. 424, pp. 69–72, Jul. 2004.

[223] K. Hirakawa, T. W. Bauer, B. N. Stulberg, and A. H. Wilde, "Comparison and quantitation of wear debris of failed total hip and total knee arthroplasty.," *J. Biomed. Mater. Res.*, vol. 31, no. 2, pp. 257–63, Jun. 1996.